



**Politecnico
di Torino**

ScuDo
Scuola di Dottorato ~ Doctoral School
WHAT YOU ARE, TAKES YOU FAR

Doctoral Dissertation
Doctoral Program in Civil and Environmental Engineering (36.th cycle)

Machine Learning Perspectives in Structural Health Monitoring

From traditional operational modal analysis to
intelligent-based methods

Marco Martino Rosso

* * * * *

Supervisors

Prof. Giuseppe Carlo Marano, Tutor and Supervisor, Politecnico di Torino

Prof. Giansalvo Cirrincione, Thesis Co-Advisor, University of Picardie Jules Verne

Prof. Giuseppe Quaranta, Thesis Co-Advisor, Sapienza University of Rome

Politecnico di Torino
June, 2024

I hereby declare that, the contents and organisation of this dissertation constitute my own original work and does not compromise in any way the rights of third parties, including those relating to the security of personal data.

Marco Martino Rosso
Turin, June, 2024

Summary

The term Structural Health Monitoring (SHM) identifies all those activities aimed at periodically inspecting the health status of a structural system over time in operating conditions. In particular, operational modal analysis (OMA) identifies all those techniques based on the analysis of output-only vibrational responses during in-service situations without measuring the input excitation. The main goal of OMA is to determine the modal properties, i.e. natural frequencies, damping ratios, and mode shapes of a structure. These parameters define the dynamics of the so-called combined system, i.e. comprising both the actual structural system and the loading system, this latter typically conceived as a stationary white noise excitation. The current Thesis document summarizes the research activities conducted during the current Ph.D. program mainly focused on SHM vibration-based approaches improved by innovative machine learning (ML) techniques. The mathematical framework at the base of OMA has been initially reviewed, exploring both time-domain and frequency-domain methods, and differentiating between parametric and nonparametric procedures. The PyOMA software was developed with a fruitful collaboration with two other institutions. PyOMA represented the first Python-based open-source package collecting a suite of the most used and well-established conventional OMA methods, thus delivering an essential tool for both researchers and practitioners working in this sector. Furthermore, due to the growing demand for automatic and continuous SHM monitoring systems, a novel framework named intelligent automatic operational modal analysis (i-AOMA) has been developed by leveraging the potentialities offered by nowadays artificial intelligence (AI) solutions. The i-AOMA method combines quasi-Monte Carlo sampling to reduce the impacts of the user's arbitrary choice of OMA control parameters, and postprocessing the identification results with effective ML-based data-driven solutions. This methodology can reliably identify actual physical recurrent modal properties whilst discarding those spurious ones. Moreover, it also provides an uncertainty evaluation of the modal parameter results. Generally speaking, an ideal SHM paradigm can be formalized at least into 5 levels, depending on the depth of investigation and understanding of any occurring structural damage. Therefore, the main research efforts have been herein devoted to the purpose of integrating ML innovative data-driven procedures into the SHM Level 1, i.e. referred to as

the damage detection task. This is a crucial aspect because it determines the amount of economic and time resources to be earmarked for further deeper damage diagnosis and/or prognosis evaluations, and even for optimizing and prioritizing maintenance activities and safety restoration interventions. Nondestructive testing (NDT) procedures have been herein effectively integrated with deep learning (DL) methods, e.g. focusing on computer vision automatic classification of tunnel linings defects based on ground penetrating radar (GPR) surveys. Vibration-based NDT for damage detection tasks has been also analyzed, especially focusing on subspace-based damage-sensitive features derived from the mathematical framework of the OMA stochastic subspace identification (SSI) algorithm. Several research efforts should be still spent to provide further deeper insights into the above-mentioned aspects. Moreover, since the scope of applicability of conventional OMA approaches is limited to linear structures under operational stationary white noise excitation, future promising research paths should additionally explore the field of nonlinear and nonstationary OMA methods. This means exploring the methods of the actual procedure for analyzing time-varying evolving modal parameter histories computed from vibration responses of structures under transient loads, e.g. under earthquake excitation, and potentially damaging over time.

Acknowledgements

In conclusion to the current Ph.D. program, I believe it is essential to dedicate the current brief section to express my sincere gratitude to everyone who supported me during this three-year journey.

Foremost, I would like to thank Professor Marano for being my tutor, mentor, and supervisor. He guaranteed fundamental independence with all its related pros and cons. Nevertheless, this allowed me to autonomously gain such a precious experience, not only from the professional standpoint, which is essential to successfully address the everyday new challenges of the Ph.D. life. I would also like to express my gratitude to Professor Cirrincione for co-supervising my Thesis and for being my valuable “tour guide” in the world of artificial intelligence. Last but not least, I would like to express all my sincere gratitude to Professor Quaranta for his great support and for his noteworthy dedication to co-supervising my Thesis with his inestimable advice, which instilled me with his knowledge, enthusiasm, and research devotion.

A special tribute must be dedicated to my wife Simona, especially for her patience and her incredible support in every aspect of my life. This latter vital factor permitted us to write down our own story in the last years, allowing us to weave a new and unique plot successfully combining the strings of sentimental and working life aspects. I would like to dedicate a special thank to all my family members, i.e. to my beloved parents, my brothers, my sister and their corresponding life partners, Simona’s family and relatives, and to all our four nieces and four nephews who constantly fill our hearts with their love.

Finally, I would like to express my gratitude to whom I made a lasting impression in their hearts and souls, to all the people that I was familiar with, such as lifelong friends, my friends from the University studying period, my middle and high school professors who have always been meaningful contacts in my life, and to all those people whom I met during this three-year journey. I am grateful for making such new bonds, specifically considering how some of them have become sincerely deep relationships with some special genuine people to share with all the joys and pains of this Ph.D. without any reservation.

I would like to dedicate a closing homage to knowledge itself, to the learning activity, and the study, which I have always considered my deeply-rooted passions. These are essential elements in my life to which I have dedicated and will continue dedicating the required time and cares, so that my desire for knowledge and inexhaustible curiosity may accompany me during my entire lifetime.

Ringraziamenti

Al termine di questo percorso di Dottorato di Ricerca, reputo fondamentale dedicare questo spazio, seppur breve, per esprimere i miei più sinceri e profondi ringraziamenti a tutte le persone che mi hanno circondato e sostenuto in questi ultimi tre anni.

Desidero innanzitutto esprimere la mia gratitudine al Prof. Marano per essere stato il mio tutor e mentore, garantendomi quell'indipendenza fondamentale che, con gli annessi benefici e svantaggi, mi ha permesso non solo di crescere personalmente e professionalmente, ma anche di vivere appieno tutte le sfide di questo percorso dottorale. Ringrazio sentitamente il Prof. Cirrincione per essere stato la mia autorevole guida nel mondo dell'intelligenza artificiale ed aver svolto il ruolo di correlatore di questa Tesi. Esprimo inoltre la mia sincera riconoscenza al Prof. Quaranta per tutto il suo immenso supporto, per aver svolto con dedizione il ruolo di correlatore di questa Tesi, e per avermi trasmesso con energia, la sua conoscenza e passione.

Un ringraziamento speciale va a mia moglie Simona, per avermi sempre sopportato ma, soprattutto, supportato in ogni ambito. Questo è stato uno dei fattori chiave che ci ha permesso di poter scrivere la nostra storia, consentendomi anche di poter intrecciare in maniera unica i fili che legano la vita affettiva con quella lavorativa. Vorrei dedicare un grazie speciale anche a tutta la mia famiglia, ai miei genitori, ai miei fratelli, a mia sorella, e ai loro rispettivi partner, all'intera famiglia di Simona, e a tutti i nostri otto nipotini che ci riempiono costantemente la vita di amore e gioia immensi.

Vorrei infine dedicare un omaggio a tutte le persone a cui ho lasciato anche solo una piccola parte di me, a tutte le persone che già conoscevo come gli amici di una vita, i miei amici dell'università, i miei professori delle medie e delle superiori che sono sempre stati per me un importante riferimento di vita, e anche a tutte le persone che ho avuto modo di conoscere durante questo percorso. Sono grato di aver potuto stringere molti nuovi legami durante questo viaggio, ed in particolare di constatare come talvolta questi si siano trasformati in rapporti profondi e autentici con persone genuine con cui condividere gioie e dolori di questo Dottorato senza riserve.

Un ultimo pensiero lo rivolgo alla conoscenza e allo studio che da sempre ritengo mie passioni radicate, elementi imprescindibili della mia vita a cui ho dedicato e continuerò a dedicare tutta la cura ed il tempo necessari affinché la curiosità ed il desiderio di sapere le cose del mondo possano accompagnarmi per sempre.

*To whom I made a lasting
impression on heart and soul*

Contents

Contents	xi
List of Tables	xiv
List of Figures	xvii
1 Introduction	1
1.1 Scope and Motivations	1
1.2 Machine learning perspectives in structural engineering	18
1.2.1 Machine learning techniques remarks	20
1.2.2 Deep learning subfield	36
1.3 Contents' outline	52
2 Conventional approaches for operational modal analysis	53
2.1 Historical highlights and OMA fundamentals	54
2.1.1 Brief history of OMA	54
2.1.2 Signal processing basics for OMA	56
2.1.3 Vibration tests and experimental campaigns	66
2.2 Conventional OMA stationary methods	68
2.2.1 Several potential classifications of OMA methods	68
2.2.2 Frequency domain methods	70
2.2.2.1 Peak-peaking method	70
2.2.2.2 Frequency domain decomposition	72
2.2.3 Time domain methods	74
2.2.3.1 Stochastic state-space models	74
2.2.3.2 Covariance-equivalent representation of stochastic state space model	78
2.2.3.3 Kalman filter representation of stochastic state space model	79
2.2.3.4 Covariance-based stochastic-subspace identification	82
2.2.3.5 Data-driven-based stochastic-subspace identification	89

2.2.3.6	Quality assessment of the dynamic identification results	94
2.2.4	Notes about other OMA methods	96
2.3	PyOMA: a Python package for operational modal analysis	97
2.4	PyOMA for model-updating-related studies	101
2.4.1	Indirect estimate of concrete strength: The Corvara Bridge case study	103
2.4.2	Cables force estimate in cable-stayed bridges: The Marghera Bridge case study	111
2.4.3	Train-track-bridge-interaction model in railway bridges: The Orte-Falconara bridge case study	119
2.5	Conventional OMA conclusive remarks	126
3	Machine-learning-aided operational modal analysis	129
3.1	Automatic Operational Modal Analysis	130
3.2	Intelligent automatic operational modal analysis	133
3.2.1	i-AOMA Phase 1a: stabilization diagram processing through kernel density estimation	135
3.2.2	i-AOMA Phase 1b: the random forest intelligent core	139
3.2.3	i-AOMA Phase 2: intelligent-guided automatic modal identification and uncertainty propagation	141
3.2.4	i-AOMA recap and Python implementation	142
3.3	i-AOMA validation: numerical shear-type planar frame benchmark case study	144
3.4	i-AOMA application: the Hardanger Bridge case study in Norway	153
3.4.1	Long-term monitoring system description and open database	153
3.4.2	Dynamic identification under sustained wind conditions	156
3.5	i-AOMA application: the Al-Hamra Firduos Tower case study in Kuwait	174
3.5.1	General description, sensor network for dynamic monitoring and finite element analysis	174
3.5.2	Identification under ambient vibrations	177
3.6	i-AOMA conclusive remarks	188
4	Machine-learning-aided damage detection strategies for civil structures	191
4.1	Structural damage detection	192
4.1.1	Maintenance philosophies	195
4.1.2	Nondestructive Testing and Evaluation, SHM, and OMA for damage detection	200
4.2	Tunnel linings damage detection with ground penetrating radar	203

4.3	Neural-based damage detection with subspace features and statistical indicators	228
4.3.1	Effects of noise on the proposed subspace-based damage detection strategies	250
4.4	Damage detection conclusive remarks	257
5	Future developments and conclusions	259
5.1	Notes about nonstationary operational modal analysis	261
5.1.1	Recursive stochastic subspace identification	265
5.2	Final remarks	271
	Bibliography	275
	Appendix	296
A	Output block Hankel matrix in stochastic subspace identification	297
B	Tunnel linings damage detection: training curves and interpretable maps	303
B.1	Training curves	303
B.1.1	Convergence curves for ResNet-50	303
B.1.2	Convergence curves for EfficientNet-B0	304
B.1.3	Convergence curves for ViT	305
B.1.4	Convergence curves for CCT	306
B.2	Interpretable class activation maps and attention maps	308
C	Dissemination activity	315
C.1	Journal Papers	315
C.2	Conference Papers	317

List of Tables

1.1	Confusion matrix for a binary classification problem.	26
2.1	Corvara case study: OMA results of the seven spans: f_i and ξ_i are the natural frequency and damping ratio of the i -th mode.	106
2.2	Corvara case study: nominal values in MPa of concrete mechanical parameters, being f_k the characteristic nominal strength.	108
2.3	Variance-based sensitivity analysis results (Sobol Indicators).	108
2.4	Comparison between experimental and optimized numerical natural frequencies [Hz].	109
2.5	Estimated mechanical parameters and related variances.	109
2.6	Averaged parameters among the spans.	110
2.7	Comparison between the concrete resistance estimated from the FE model updating (indirect) and that estimated from concrete samples (direct).	110
2.8	Marghera bridge case study: cable forces identified from vibration data in the tests of 2011 [138].	114
2.9	Marghera bridge case study: sensitivity indicators S_1 for the error function Eq. (2.148) and for the cable forces.	115
2.10	Sensitivity indicators S_1 for $\mathcal{F}_2(\boldsymbol{\theta})$, $f_1(\boldsymbol{\theta})$ and $f_2(\boldsymbol{\theta})$, and for the frequency of each modes (see Fig. 2.19).	117
2.11	Sensitivity indicators S_1 for for the MAC of each modes (see Fig. 2.19).	117
2.12	Cable forces and modal parameters associated with the optimum set of parameters and percentage error before and after the updating. In the bottom right part of the table, the optimum parameters are listed with the upper (U.B) and lower (L.B.) bounds. In the cable notation, M indicates the Mestre side, whereas V is the Venice side. Instead, in the mode labels, letters V, M, and T indicate the prevalent mode nature, i.e. Bending, Mixed, or Torsional respectively.	118
2.13	Input parameters of the deterministic model updating optimization algorithm.	125
3.1	Hardanger Bridge: location of the accelerometers.	155

3.2	Hardanger Bridge: comparison between the modal results reported by Petersen et al. [207, 205, 201] and those obtained in the present study by means of the i-AOMA algorithm for sustained wind case 2 (November 12th, 2015 at 23:54:31 with a wind speed of 14.02 ± 2.28 m/s). Note that f is the natural frequency, whereas ξ indicates the damping ratio.	168
3.3	Hardanger Bridge: comparison between the modal results of the i-AOMA method for wind cases 1, 2 and 3. Note that f is the natural frequency, whereas ξ indicates the damping ratio.	173
3.4	Al-Hamra Tower: location of the accelerometers.	176
3.5	Al-Hamra Tower: numerical values of the modal properties estimated from finite element analysis (T is the natural period; f is the natural frequency; UX and UY represent the participating mass ratio along X direction and Y direction, respectively; RX, RY and RZ denote the participating rotational mass ratio along X direction, Y direction and vertical direction, respectively; the symbol Σ stands for cumulative sum of the participating mass ratios up to that mode number).	177
3.6	Al-Hamra Tower: comparison between the results reported by Sun et al. [211] and those obtained in the present study by means of the i-AOMA algorithm (f is the natural frequency, whereas ξ indicates the damping ratio).	186
4.1	Confusion matrices and classification metrics for ResNet-50 model trained with raw image data.	216
4.2	Confusion matrices and classification metrics for ResNet-50 model trained with bi-dimensional Fourier pre-processed image data.	217
4.3	Confusion matrices and classification metrics for EfficientNet model trained with raw image data.	218
4.4	Confusion matrices and classification metrics for EfficientNet model trained with bi-dimensional Fourier pre-processed image data.	219
4.5	Confusion matrices and classification metrics for ViT model trained with raw image data.	220
4.6	Confusion matrices and classification metrics for ViT model trained with bi-dimensional Fourier pre-processed image data.	221
4.7	Confusion matrices and classification metrics for CCT model trained with raw image data.	222
4.8	Confusion matrices and classification metrics for CCT model trained with bi-dimensional Fourier pre-processed image data.	223
4.9	Global average accuracy for the three analyzed neural models.	224
4.10	Modes in the undamaged case of the numerical beam under study retrieved from an eigenvalue analysis and an OMA analysis conducted with the PyOMA module.	234

4.11	Summary of the properties of the implemented MLP. None means variable dimension, depending on the batch chosen size (in this case empirically set to 200). In this case, input units are referred to method (B).	237
4.12	Summary of the properties of the implemented MLP for the experimental case study. None means variable dimension, depending on the batch chosen size (in this case empirically set to 200). In this case, input units are referred to method (A).	246
4.13	Summary of the properties of the implemented 1D-CNN for studying noise effects.	251
4.14	Summary of the properties of the implemented MLP for studying noise effects.	251

List of Figures

1.1	Bridges collapse causes in the USA, reprinted from [6].	4
1.2	Some sadly known collapses occurred in USA. (a) Tacoma Narrow Bridge, courtesy of PRI’s Studio 360; (b) Silver Bridge (Point Pleasant Bridge), courtesy of Bob Smerecki Art; (c) I-35W Bridge, courtesy of Marion Doss; (d) Champlain Towers South Surfside Florida, reprinted from [12].	5
1.3	ISTAT 15th Population and housing census 2011 results: (a) Absolute number of new constructions for various time spans. (b) Overview of how structural typologies proportions varied for existing residential building heritage over time; (c) Pie chart of the structural typologies of proportions at the 2011 census time.	8
1.4	Some sadly collapses occurred in Italy. (a) Polcevera Bridge, Liguria, courtesy of Maurizio Boi; (b) Fossano Bridge, Piedmont, reprinted from [17]; (c) Caprigliola Bridge, Tuscany; (d) Former Porta Susa Station, Piedmont, reprinted from LA STAMPA.	10
1.5	Infographic chart of nowadays USA infrastructure state and recent investment efforts to support bridge rehabilitation programs.	13
1.6	Infographic chart of Italy infrastructures and recent European investment support.	17
1.7	Conceptual relationship Venn graph among the fields of Artificial Intelligence, Machine Learning, Deep Learning, Reinforcement Learning, and Generative Intelligence, and their connections with Data Science and Big Data.	20
1.8	Different learning methods in ML.	22
1.9	The typical ML project workflow.	24
1.10	List of some ML algorithms according to the learning methods.	32
1.11	Number of documents published from 2012 until 2021 (a) and Pie chart of the main area of recent years studies (b). Data retrieved from Scopus search service with query “Deep Learning” and “Structural Health Monitoring”.	37

1.12	Pareto chart of the number of documents published on Scopus related to the most active countries, with a limit placed to 80% of the cumulative frequency. Data retrieved from Scopus search service with query “Deep Learning” and “Structural Health Monitoring” from year 2012 until 2021.	38
1.13	MCP neuron model and Rosenblatt’s perceptron model.	39
1.14	CNN example workflow.	44
1.15	Illustration of convolutional layer working mechanism with two filters.	47
1.16	Global and local receptive field concepts, with an example of two consecutive applications of the filters showed in Fig. 1.15.	48
2.1	Combined system identified within the OMA context.	56
2.2	Direct computation of auto-correlation function according to Eq. (2.18) on a sinusoidal signal.	61
2.3	Spectral leakage attenuation through the windowing procedure.	62
2.4	Fourier transform of rectangular and Hanning windows to show side-lobe attenuation.	62
2.5	Several potential classifications of OMA methods.	69
2.6	SVD graph of the PSD within the FDD method, showing the intrinsic noise separation effect provided by the SVD method.	74
2.7	Stabilization diagram. The colors of the poles, identified by the numbers 0.0 to 4.0 in the legend, indicate respectively: unstable, stable in frequency, stable in frequency and mode shape, stable in frequency and damping, stable in frequency damping and mode shape.	88
2.8	Stabilization diagram with overlapped SVD graph of the PSD, from synthetic data used in the example shown in Fig. 2.6.	88
2.9	PyOMA research project overview.	98
2.10	PyOMA implemented algorithms.	99
2.11	“PyOMA_GUI” graphical user interface software general overview.	100
2.12	The new PyOMA2 logo.	101
2.13	Corvara bridge case study: (a) Global and side view of the; (b) Transverse and longitudinal cross-section of the bridge.	105
2.14	Corvara bridge case study: (a) experimental setup overview; (b) stabilization diagram.	106
2.15	Corvara case study: visualization of the experimental mode shapes of a sample bridge span.	107
2.16	Corvara case study: (a) FE model view with marked accelerometers positions; (b)-(e) first four FE mode shapes corresponding to the experimental ones.	107
2.17	Marghera bridge case study: proposed step-wise model updating procedure for cable-stayed bridges.	112
2.18	Marghera bridge case study: global overview.	113
2.19	Marghera bridge case study: dynamic identification results from [138].	114

2.20	Marghera bridge case study: SAP2000 FE model overview.	115
2.21	Marghera bridge case study: graphical representation of the sensitivity of the objective functions in Eq. (2.148) with two different views (a)-(b) according to the concrete Young's modulus of the tower (E_c, t), the vertical stiffness of the bearings (k_a) and the mass of the concrete deck (ρ_c).	116
2.22	Orte-Falconara bridge case study: TTBI model illustration.	120
2.23	Orte-Falconara bridge case study: moving train loading model.	121
2.24	Orte-Falconara bridge case study: viaduct overview and ambient vibration testing.	123
2.25	Orte-Falconara bridge case study: cross-section details with beams numbering.	124
2.26	Orte-Falconara bridge case study: modal parameter estimates obtained with PyOMA software.	124
3.1	Statistical-based criterion for the automatic definition of the prominence threshold and the detection of significant peaks from the normalized KDE.	138
3.2	The i-AOMA workflow: i-AOMA Phase 1 (top row) and i-AOMA Phase 2 (bottom row).	143
3.3	Numerical benchmark case: synthetic monitoring data (a) and singular value decomposition of the power spectral density (b).	146
3.4	Numerical benchmark case i-AOMA Phase 1: normalized KDE together with the identified peaks (a) and certainly stable poles falling within the retaining bands (b) obtained from the sets of control parameters generated for training the intelligent core of i-AOMA.	147
3.5	Numerical benchmark case: numerical values of IC obtained from the sets of control parameters generated for training the intelligent core of i-AOMA.	148
3.6	Numerical benchmark case i-AOMA Phase 2: the normalized KDE together with the identified peaks (a) and certainly stable poles falling within the retaining bands (b) obtained at the end of the i-AOMA.	149
3.7	Numerical benchmark case: convergence analysis of the relative total sample variance for each mode.	149
3.8	Numerical benchmark case: numerical values of IC obtained from all the feasible sets of control parameters generated during i-AOMA.	150
3.9	Numerical benchmark case: joint probability density functions of the control parameters samples that have been classified as feasible from the intelligent core of i-AOMA.	150
3.10	Numerical benchmark case: median mode shapes and corresponding uncertainty level in terms of boxplot's whiskers.	151

3.11	Numerical benchmark case: average (a) and standard deviation (b) of natural frequencies over the feasible samples of the control parameters.	152
3.12	Numerical benchmark case: average (a) and standard deviation (b) of damping ratios over the feasible samples of the control parameters.	152
3.13	The Hardanger Bridge (Norway), picture courtesy of Sami Haidar (CC BY-NC 2.0).	154
3.14	Illustration of the Hardanger Bridge and its long term monitoring sensors layout.	154
3.15	Wind speed recordings of the A6 anemometer located in the midspan for the three selected cases under investigation.	156
3.16	Hardanger Bridge: accelerations recorded on November 12th, 2015 at midspan accelerometer on the west side H5W (a) and singular value decomposition of the power spectral density limited to the first ten singular values (b).	157
3.17	Hardanger Bridge: overlapped stabilization diagram at the end of Phase 1 of the i-AOMA method.	158
3.18	Hardanger Bridge: i-AOMA Phase 1, normalized KDE together with the identified peaks (a) and certainly stable poles falling within the retaining bands (b) obtained from the sets of control parameters generated for training the intelligent core of i-AOMA.	159
3.19	Hardanger Bridge: i-AOMA Phase 1, numerical values of IC obtained from the sets of control parameters generated for training the intelligent core of i-AOMA.	160
3.20	Hardanger Bridge: convergence analysis of the relative total sample variance for each mode.	161
3.21	Hardanger Bridge: overlapped stabilization diagram at the end of Phase 2 of the i-AOMA method.	161
3.22	Hardanger Bridge: i-AOMA Phase 2, normalized KDE together with the identified peaks (a) and certainly stable poles falling within the retaining bands (b) obtained from the sets of control parameters generated for training the intelligent core of i-AOMA.	162
3.23	Hardanger Bridge: i-AOMA Phase 2, numerical values of IC obtained from the sets of control parameters generated for training the intelligent core of i-AOMA.	163
3.24	Hardanger Bridge: joint probability density functions of the control parameters that have been classified as feasible from the intelligent core of i-AOMA.	164
3.25	Hardanger Bridge: i-AOMA Phase 2, simplified geometrical mode shape visualization for modes from 1 to 9.	165
3.26	Hardanger Bridge: i-AOMA Phase 2, simplified geometrical mode shape visualization for modes from 10 to 18.	166

3.27	Hardanger Bridge: MAC matrix of the median mode shapes finally retrieved by i-AOMA, with a special focus on the first 11 modes. . .	169
3.28	Hardanger Bridge: i-AOMA uncertainty level in terms of boxplot's median components and whiskers for the horizontal mode 1 (a), for the vertical mode 2 (b), and for the torsion mode 11 (c) of the bridge.	170
3.29	Hardanger Bridge: i-AOMA average (a) and standard deviation (b) of natural frequencies over the feasible samples of the control parameters.	171
3.30	Hardanger Bridge: i-AOMA average (a) and standard deviation (b) of damping ratios over the feasible samples of the control parameters.	172
3.31	Al-Hamra Tower: general view (a) and finite element model adopted for the modal analysis (b).	175
3.32	Al-Hamra Tower: typical monitored floor of the Al-Hamra Tower (left) and view of the biaxial accelerometers (right).	175
3.33	Al-Hamra Tower: accelerations recorded on May 2, 2022 at 6th, 42th, and 76th floor (a) and singular value decomposition of the power spectral density limited to the first six singular values (b). . .	178
3.34	Al-Hamra Tower: normalized KDE together with the identified peaks (a) and certainly stable poles falling within the retaining bands (b) obtained from the sets of control parameters generated for training the intelligent core of i-AOMA.	179
3.35	Al-Hamra Tower: numerical values of IC obtained from the sets of control parameters generated for training the intelligent core of i-AOMA.	179
3.36	Al-Hamra Tower: the normalized KDE together with the identified peaks (a) and certainly stable poles falling within the retaining bands (b) obtained at the end of the i-AOMA.	180
3.37	Al-Hamra Tower: convergence analysis of the relative total sample variance for each mode.	181
3.38	Al-Hamra Tower: numerical values of IC obtained from all the feasible sets of control parameters generated during i-AOMA.	181
3.39	Al-Hamra Tower: joint probability density functions of the control parameters that have been classified as feasible from the intelligent core of i-AOMA.	182
3.40	Al-Hamra Tower: numerical mode shape (a), median experimental mode shape (b) and corresponding uncertainty level in terms of boxplot's whiskers (c) for the first mode of the tower.	183
3.41	Al-Hamra Tower: numerical mode shape (a), median experimental mode shape (b) and corresponding uncertainty level in terms of boxplot's whiskers (c) for the second mode of the tower.	183

3.42	Al-Hamra Tower: numerical mode shape (a), median experimental mode shape (b) and corresponding uncertainty level in terms of boxplot's whiskers (c) for the third mode of the tower.	183
3.43	Al-Hamra Tower: numerical mode shape (a), median experimental mode shape (b) and corresponding uncertainty level in terms of boxplot's whiskers (c) for the fourth mode of the tower.	184
3.44	Al-Hamra Tower: numerical mode shape (a), median experimental mode shape (b) and corresponding uncertainty level in terms of boxplot's whiskers (c) for the fifth mode of the tower.	184
3.45	Al-Hamra Tower: numerical mode shape (a), median experimental mode shape (b) and corresponding uncertainty level in terms of boxplot's whiskers (c) for the sixth mode of the tower.	184
3.46	Al-Hamra Tower: numerical mode shape (a), median experimental mode shape (b) and corresponding uncertainty level in terms of boxplot's whiskers (c) for the seventh mode of the tower.	185
3.47	Al-Hamra Tower: numerical mode shape (a), median experimental mode shape (b) and corresponding uncertainty level in terms of boxplot's whiskers (c) for the eighth mode of the tower.	185
3.48	Al-Hamra Tower: numerical mode shape (a), median experimental mode shape (b) and corresponding uncertainty level in terms of boxplot's whiskers (c) for the ninth mode of the tower.	185
3.49	Al-Hamra Tower: numerical mode shape (a), median experimental mode shape (b) and corresponding uncertainty level in terms of boxplot's whiskers (c) for the tenth mode of the tower.	186
3.50	Al-Hamra Tower: average (a) and standard deviation (b) of natural frequencies over the feasible samples of the control parameters. . . .	187
3.51	Al-Hamra Tower: average (a) and standard deviation (b) of damping ratios over the feasible samples of the control parameters.	188
4.1	Levels of SHM paradigms based on the knowledge depth of damage identification process, with Levels 1-5 based on Rytter (1993) [219].	194
4.2	Schematic visualization of the time-dependent behavior of a performance index (such as the reliability index) during the life-cycle of a structure, evidencing preventive and essential maintenance interventions effects on extending the in-service lifetime (a); illustration of the two possible updating cases for time-dependent behavior of a performance index leveraging SHM monitoring data (b).	197
4.3	Illustration of the typically surveyed GPR tunnel lining profiles for different tunnel's widths (different number of road lanes).	205
4.4	Human interpretation of GPR tunnel lining profiles' defects.	206
4.5	Data collection, preliminary preparations and the final obtained dataset with and without Fourier pre-processing.	207

4.6	Hierarchical framework for the multi-level tunnel defects GPR profiles classification.	209
4.7	Resulting magnitude pre-processed images with bi-dimensional Fourier transform of two samples belonging to class C4 (reinforcement bars) and C13 (excavation) respectively.	211
4.8	Illustrative representation of the neural models with hyperparameters herein adopted.	212
4.9	ViT-L16 model architecture visualization, highlighting the pre-trained part and the fine-tuned part.	213
4.10	Comparative analysis of the various DL models' classification accuracy with and without Fourier pre-processing among the classification levels.	224
4.11	Scatter plot of classification accuracy with and without Fourier pre-processing among the classification levels.	225
4.12	Flowchart of the various data-driven damage detection proposed strategies based on statistical information and subspace-based DIs.	232
4.13	Numerical beam model studied for testing damage detection procedures proposed in Fig. 4.12.	233
4.14	Sensitivity analysis on active space dimensions and, consequently the complementary null space dimensions, compared with the time shift user's defined choice.	235
4.15	MLP multiclass classification results for method (A). (a) MLP convergence curves; (b) MLP confusion matrix on the test set.	239
4.16	MLP multiclass classification results for method (B). (a) MLP convergence curves; (b) MLP confusion matrix on the test set.	239
4.17	MLP multiclass classification results for method (C). (a) MLP convergence curves; (b) MLP confusion matrix on the test set.	240
4.18	MLP with dropout regularization multiclass classification results for method (B). (a) MLP convergence curves; (b) MLP confusion matrix on the test set.	241
4.19	MLP multiclass classification results for method (B)-worsened. (a) MLP convergence curves; (b) MLP confusion matrix on the test set.	242
4.20	Experimental steel beam case study. (a) Beam monitoring setup with measures; (b) Beam cross section dimensions; (c) Damage induced with a localized cross section reduction. (d) Velocimeter sensors.	244
4.21	OMA analysis for undamaged conditions of the experimental beam. (a) Monitored signals expressed in Volt [V]; (b) Resulting stabilization diagram.	245
4.22	MLP training performances for method (A) on simulated I-beam. (a) 20 epochs due to early stopping to avoid overfitting; (b) Confusion matrix on the test set.	247

4.23	MLP training performances for method (B) on simulated I-beam. (a) 300 epochs without any evidence of overfitting; (b) Confusion matrix on the test set.	247
4.24	MLP training performances for method (C) on simulated I-beam. (a) 20 epochs due to early stopping to avoid overfitting; (b) Confusion matrix on the test set.	248
4.25	After training MLP predictions on experimental measurements collected from the steel-I beam for one undamaged and four damaged scenarios. (a) predictions of MLP trained with method (A); (b) predictions of MLP trained with method (B); (c) Predictions of MLP trained with method (C).	249
4.26	Classification results of the MLP models exploring varying noise effects.	252
4.27	Classification results of the CNN models exploring varying noise effects.. . . .	253
4.28	60-dB noise level CNN training performances history during the epochs.	254
4.29	Classification results of the 20dB CNN models on other SNR levels in all three methods.	255
4.30	Classification results of the 60dB CNN models on other SNR levels in all three methods.	256
5.1	RSSI recursive updating procedure with sliding windows of analysis.	270
B.1	(a-g) ResNet-50 trained with raw images: loss versus accuracy during the training iterations.	303
B.2	(a-g) ResNet-50 trained with Fourier pre-processed images: loss versus accuracy during the training iterations.	304
B.3	(a-g) EfficientNet-B0 trained with raw images: loss versus accuracy during the training iterations.	304
B.4	(a-g) EfficientNet-B0 trained with Fourier pre-processed images: loss versus accuracy during the training iterations.	305
B.5	(a-g) ViT trained with raw images: loss versus accuracy during the training epochs.	305
B.6	(a-g) ViT trained with Fourier pre-processed images: loss versus accuracy during the training epochs.	306
B.7	(a-g) CCT trained with raw images: loss versus accuracy during the training epochs.	306
B.8	(a-g) CCT trained with Fourier pre-processed images: loss versus accuracy during the training epochs.	307
B.9	Class activation maps for ResNet-50 and EfficientNet, and attention maps for ViT compared to original images for each class.	308
B.9	Class activation maps for ResNet-50 and EfficientNet, and attention maps for ViT compared to original images for each class.	309

B.9	Class activation maps for ResNet-50 and EfficientNet, and attention maps for ViT compared to original images for each class.	310
B.9	Class activation maps for ResNet-50 and EfficientNet, and attention maps for ViT compared to original images for each class.	311
B.9	Class activation maps for ResNet-50 with Fourier pre-processing compared to Fourier pre-processed images for each class.	312
B.9	Class activation maps for ResNet-50 with Fourier pre-processing compared to Fourier pre-processed images for each class.	313

Chapter 1

Introduction

In this first introductory section, the main research areas of the present Thesis are stated. The three-year Ph.D. program has been conducted under the guidance of Prof. Giuseppe Carlo Marano, full professor of Structural Design at Politecnico di Torino (Italy), with the co-supervision of two international collaborators, i.e. Prof. Giansalvo Cirrincione, associate professor at University of Picardie “Jules Verne” (France), and Prof. Giuseppe Quaranta, associate professor in Structural Engineering at Sapienza University of Rome (Italy). The topic of structural health monitoring (SHM) covers an important segment of the nowadays Structural Engineering challenges. Being this field strongly inter- and multi-disciplinary, this introductory part aims to mainly underline the public interest in this topic. Catastrophic consequences arise when there is a lack of proper engineering solutions, and analyzing past disasters helps all of us to be more aware of both the severe economic and social impacts that involve the entire community and the public interest, not only a prerogative of technical professional circles. Therefore the essential motivations of the present study are presented in the following.

1.1 Scope and Motivations

Monitoring the health status of existing structures and infrastructures over time is an essential and extremely topical issue worldwide. Recent collapses have particularly shaken public opinion, rekindling the general interest in investing in the Structural Civil Engineering sector, especially for risk mitigation strategies and promoting smart and innovative solutions to ensure and preserve the safety levels of our existing heritage [1]. Severe economic and life losses are usually associated with structural failures, especially when strategic constructions are involved [2]. Nonetheless, they sadly represent a crucial opportunity to grow our engineering experience and improve our understanding in order to move toward a new mentality,

focused on performance-based, risk-prevention solutions, increasing safety and reliability [3]. Indeed, the history of structural collapses often follows the “pendulum principle” [4]. If the greater impact on public opinion is, thus greater academic and economic resources are usually rapidly allocated for preventing similar events by deeply studying and understanding the catastrophe-triggering causes.

The USA counts over 617,000 bridges and about 42% are at least 50 years old [5], an increased statistics from 39% in 2016. The bridge heritage’s average age is estimated at about 44 years, however, 12% of highway bridges are aged 80 years or older. In 2018, the Federal Highway Administration (FHWA) defined a “structurally deficient” bridge when one of the key structural elements, i.e. culvert, substructure, superstructure, and deck, is assessed in poor conditions. The quadrennial *Report Card for America’s Infrastructure* 2021 edition [5] documented that 7.5% of the total bridges are considered structurally deficient, and their average age is about 69 years. A total of 1,062 bridge collapses occurred between 1980-2012 in the US [6], some of them depicted in Fig. 1.2, whereof 503 occurred between 1989 and 2000 [2]. The bridge design and maintenance mindset radically changed after the catastrophic suspension Tacoma Narrows Bridge collapse occurred on November 7th, 1940, in Washington State, thankfully with no human losses [7, 8]. The subsequent failure analyses and studies on the physical interaction of aerodynamics and aeroelastic phenomena permitted the consciousness-raising and the introduction of new design rules when conceiving similar long-span suspension bridges [9]. Nowadays, to ensure new infrastructure resilient design, the American Society of Civil Engineers (ASCE) strongly encourages federal agencies to incentive the adoption of up-to-date structural codes and standards, such as e.g.:

- ASCE 7, Minimum Design Loads and Associated Criteria for Buildings and Other Structures (ASCE/SEI 7-22);
- ASCE 24, Flood Resistant Design and Construction;
- ASCE 41, Seismic Evaluation and Retrofit of Existing Buildings;
- ASCE Manual of Practice 140, Climate-Resilient Infrastructure: Adaptive Design and Risk Management.

Instead, the bridge inspection attitude was completely overturned after the Silver Bridge collapse, better acknowledged as Point Pleasant Bridge, on December 15th, 1967, over the Ohio River in West Virginia, causing 46 deaths during rush-hour heavy load traffic conditions [7]. Indeed, the federal government mandated national bridge inspections periodically from 12 to 48 months to preserve the public’s safety [5]. The inspection’s goals are to identify the location and type of the bridge, its age, and its actual conditions, including the traffic loadings. According to the degree of structural deficiencies evidenced by the bridge inspector, the structure

can be posted for load, speed, or weight restrictions on one side, otherwise undergoing repairing interventions, or closed to traffic in the most serious scenarios. According to the 2021 ASCE’s report [5], about 10% of all the US bridges experienced such restrictions in 2019. A non-robust design combined with the increase of load levels and undetected damages may dreadfully threaten the structural integrity, recalling e.g. the I-35W Bridge failure in Minneapolis, Minnesota State, on August 1st, 2007, resulting in 13 deaths [10]. Analyzing the US past collapses, it is worth evidencing that design loads levels computed by designers are responsible for only 4% of structural collapses [6], thus being in line with an expected failure probability of $10^{-4} \div 10^{-5}$ considering an initial failure probability of 10^{-6} curtailed by execution uncertainties. For the sake of mentioning the order of magnitude of the economic aspects associated with bridge collapses, the I-35W Bridge catastrophe induced costs about 17 million USD in 2007 and additional 43 million USD in 2008, without accounting indirect costs [2]. Among the different causes of bridge failure reported in Fig. 1.1, natural phenomena represent the preponderant source, principally floods and scour [2, 6], even though the human factors are another decisive aspect affecting the bridges’ remaining life and safety levels. The destructive impact of natural hazards is often multiplied by maintenance negligence and/or inadequacy of old structures [11]. Furthermore, the human factors, especially regarding the proper attention to design and construction methods on one side, and even regarding effective inspection and maintenance programs on the other side, are the aspects on which we can proactively improve, since natural disasters are often unavoidable and not fully controllable by humans [2]. This may also mean that overloads, scour, or internal causes such as mistakes at the design or at execution level are not properly accounted for by the designer and/or by partial safety factors of actual design codes [6]. Another possible source of neglected maintenance could be ascribed to inadequate inspections with under-reported negative externalities [11]. Instead, referring to buildings, one of the most recent and catastrophic collapses occurred on June 24th, 2021, in Champlain Towers South, a 12-story condominium located in Surfside, Florida State, which claimed 98 deceased [12]. The real causes of failure are still unclear nowadays, however, it seems that a non-robust design combined with differential settlements caused by water infiltration and rebar corrosion of RC elements in the parking at the basement level produced a progressive collapse mechanism with such disproportionate consequences [12, 13].

On the other hand, considering the Italian panorama, it is worth noting that probably Italy has the most complex transportation network in the world due to its varied and widespread orographic and hydro-graphic features [11]. In addition, Italy hosts about 50% of all the tunnels in the EU [11]. The total railway heritage length is about 17,000 km, with a total number of 9,660 artifacts between bridges and viaducts, and 10,162 underpasses. Instead, the Italian roadway system presents globally about 837,493 km divided into five categories, viz., in decreasing importance order, highways, state roads, regional roads, provincial roads, and municipal

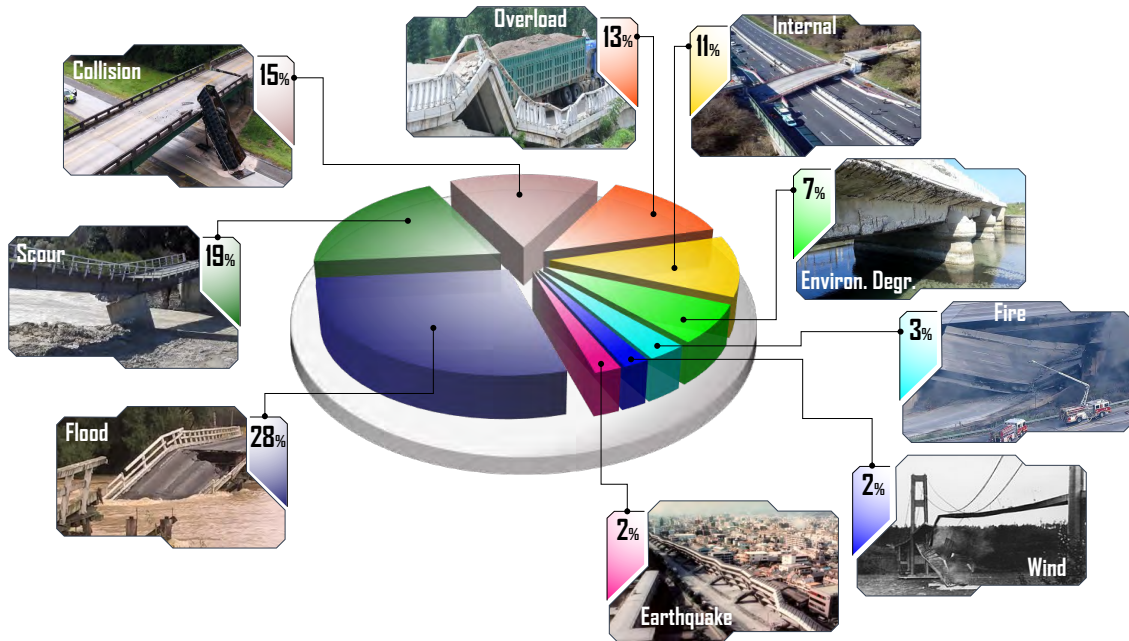


Figure 1.1: Bridges collapse causes in the USA, reprinted from [6].

roads. Moreover, it is worth evidencing that the infrastructure heritage is entrusted to several management companies [6]. 23 different companies are involved within the railways field, despite the dominant player is the Italian Railway Infrastructure (RFI) company, holding about 83% of the total railway length. Formed in 2001, RFI management was always more prone to address durability issues, since the overall Italian railway scenario is quite old, referring e.g. to the first Italian railway line established in Naples in 1839 [6]. Therefore, modern inspection techniques and progressive digitization have led to a railway bridge management system (BMS) in 2019 acknowledged as DOMUS system (in Italian “*Diagnostica Opere d’arte Manutenzione Unificata Standard*”) [14]. Focusing on roadway system, the dominant company is the National Autonomous Agency for the roads (ANAS), in Italian “*Azienda Nazionale Autonoma delle Strade*”, owned by FS Group company (in Italian “*Gruppo Ferrovie dello Stato*”), thus entirely financed by the Ministry of Economics and Finance (MEF). ANAS holds in total 30,000 km of roads and a number of 14603 bridges, and more than 2000 tunnels. Nonetheless, considering only the highway roads, the 7472 km are controlled by 32 different companies, and ANAS only holds 12% of the total length [6]. About 80% of Italy’s highway roadways was built in the time-span 1960-1970, whereas more ancient and often in worst conditions are provincial and municipal roads [11].

One of the most recent and tragically iconic infrastructure failures uppermost in our mind is the Polcevera Viaduct collapse in Genoa, which occurred on August 14th, 2018 and caused 43 victims [1]. Completed in 1967 after only 4 years

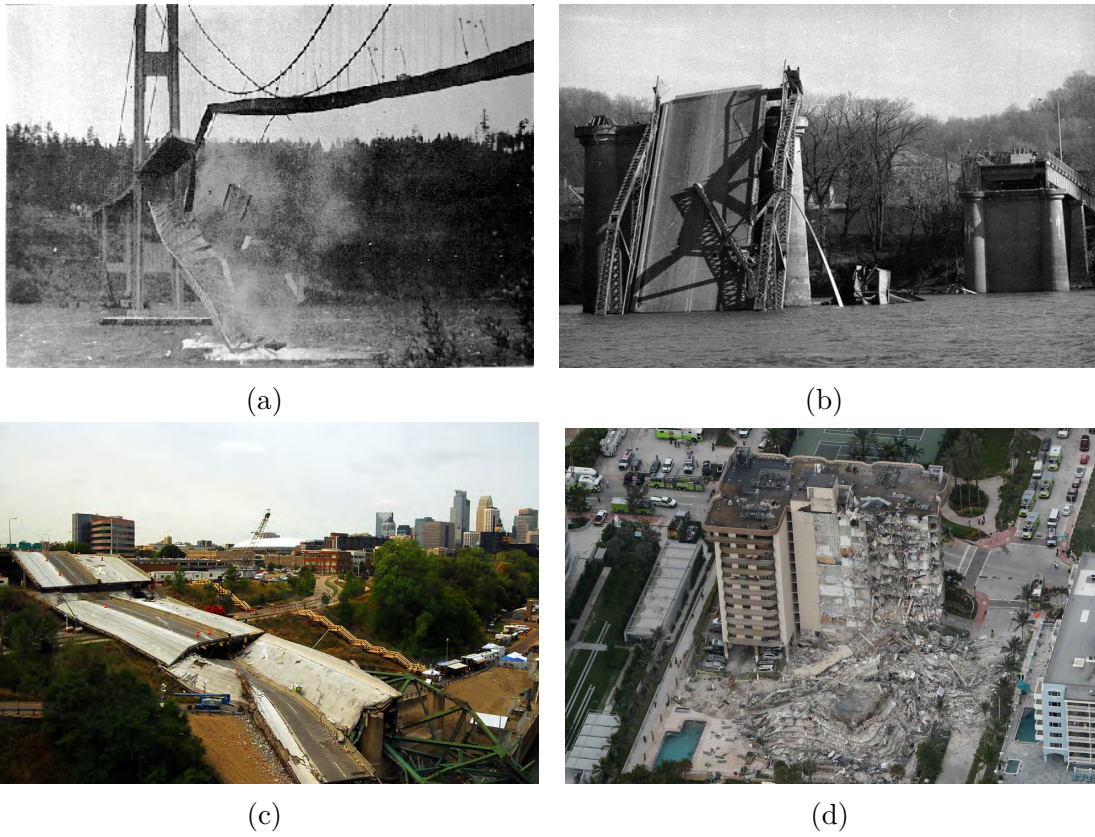


Figure 1.2: Some sadly known collapses occurred in USA. (a) Tacoma Narrows Bridge, courtesy of [PRI's Studio 360](#); (b) Silver Bridge (Point Pleasant Bridge), courtesy of [Bob Smerecki Art](#); (c) I-35W Bridge, courtesy of [Marion Doss](#); (d) Champlain Towers South Surfside Florida, reprinted from [12].

of construction, the Riccardo Morandi's bridge was a masterpiece of Italian engineering planetary known, composed of three prestressed reinforced concrete (PRC) cable-stayed balanced systems [3, 15]. Other recent and probably less internationally notorious bridge collapses occurred in Italy in recent years, as illustrated in Fig. 1.4. Indeed, in almost 18 months from late 2016 until mid-2018 five road bridges collapsed [16]. It is worth mentioning the Fossano ring road in Piedmont which collapsed without any traffic loading condition on April 18th, 2017 [17]. Despite apparent healthy external conditions, the possible failure causes have been addressed as systematic human errors due to inadequate post-tensioned prestressing cable grouting. Indeed, the damage patterns surveyed by visual inspection on cables immediately afterwards the failure evidenced a degradation scenario not compatible with the expected one for a 20-year-old in-service condition [17, 18]. As documented in Losanno et al. [19], in Italy approximately the 18% of bridge collapse is related to human factors, specifically 7% is attributable to degradation

of structural components, whereas the remaining part related to design or construction errors. These statistics are in agreement with US scenario in the time range 1989-2000, as declared in Deng et al. [2]. As reported in [16], it is worth reminding also the failures of the highway overpass in Camerano, Marche on March 9th, 2017, the roadway bridge crossing the Fiumara Allaro river, in Calabria on January 23rd, 2017, and the viaduct bridge between Annone and Cesana Brianza, in Lombardy October 28th, 2016. The excessive number of different companies, jointly with the complex and long-standing Italian red tape, may be sometimes one of the causes of the degradation of Italian infrastructures. About 1,425 bridges have unclear ownership even though they should be under ANAS control [6]. For instance, this is the case of the Annone overpass in Lombardy, because for Lecco province the bridge purview was transferred to ANAS, however, the existing documentation proved that the administrative transfer was never formalized. Only after several collision accidents due to unsatisfied overpass clearance height evidence of the bureaucratic technicality. Finally, it collapsed in 2016 due to excessive degradation in the Gerber half-joint, jointly with maintenance deficiencies, and overloading traffic not foreseen in the original design. Additionally, the administrative unclear ownership affected the readiness and coordination in post-emergency management [20]. On April 8th, 2020, a domino-type progressive collapse occurred for the 111-year-old slender RC arch Caprigliola bridge located in Massa and Carrara, in Tuscany, on Magra river [21]. No fatalities took place gratefully to the COVID-19 traveling restrictions of that time. The most accredited chronicle of the disaster concerns local damage which rapidly spread to the entire bridge. The true reasons for the collapse are still unknown, nonetheless, the literature studies revealed a possible combination of adverse conditions due to material degradation phenomena, overloading during decades, Caprigliola-side slope slippage, and foundation differential settlements [21]. In fact, the lack of proper robustness in the original design has meant that the collapse of one span provoked a rapid spread of damage. This was because the mutual arch stability conditions restraining the horizontal thrust among the spans were missing. The “pendulum effect” [4] of all these bridge collapses led to a gradual introduction of new structural codes to approach again the scientific world with the practical structural engineering domain. Indeed, as a direct consequence of the Polcevera Bridge collapse, the Italian Infrastructure Ministry and Transportation promulgated on December 17th, 2020, the Decree No. 578, entitled “Guidelines for the classification and management of risk, for the evaluation of safety and for the monitoring of existing bridges”, in Italian, “*Linee Guida per la classificazione e gestione del rischio, la valutazione della sicurezza ed il monitoraggio dei ponti esistenti*” (LG20) [22]. These guidelines provide systematic rules to ensure homogeneity in assessing risks and triaging the maintenance interventions of bridges [11]. According to them, the vulnerability assessment has been split in a five-level process:

- Level 0: census and geolocalization;
- Level 1: direct visual inspections both of the structure and the characteristics of the area (geomorphological, hydrological, and hydraulic);
- Level 2: definition of the Attention Class (AC) related to potential risks on parameters of hazard, vulnerability, and exposure, and multi-hazard hierarchical analysis;
- Level 3: carrying out preliminary assessments;
- Level 4: execution of accurate assessments (according to the Technical Standards for Construction);
- Level 5: network resilience, to be applied to bridges considered to be of strategic importance.

Concerning the Italian buildings existing heritage, a short premise should be made. Based on the OERCO2¹ technical report “1.2.1. *Study Of Most Used Materials In Italian Construction Sector*”², the Italian existing building heritage is in a generalized old conservation state. Before 1920s, the most used building typologies for residential purposes were exclusively masonry structures, combined with timber employed for slabs and roofs. Starting around 1920s, load bearing masonry began to be replaced even more often by reinforced concrete (RC) frames, and afterwards leading to the RC frames predominance for new constructions after 1970s. As reported in Fig. 1.3, it is worth underlining that following the 15th Italian National Institute of Statistics (ISTAT) general census of 2011³ the prevalent structural typology of existing building heritage is nowadays still represented by masonry structures combined with timber slabs and roof, which are also the oldest ones, and probably the most vulnerable ones. Luckily no recent catastrophic failure occurred on buildings collapse due to degradation effects only in Italy, even though two roof collapses have been documented in the literature lately. In Pieraccini et al. [23], the collapse of a long-span steel trusses roof covering a school building in Northern Italy collapsed in 2010 after an ordinary snowfall. Its completion dates back to 2008, and despite the school was opened few month before the collapse in 2010, gratefully no fatalities occurred. The main probable causes were attributed to the use of inadequate spherical joints and the use of an excessively brittle steel material for bolts, spheres and members. Once again the anthropogenic factor was pointed out as the responsible. Another partial roof collapse without causalities

¹European Project Open Educational Resource (for CO2 emissions in construction industry).

²OERCO2 online technical report resource.

³Online data warehouse resource from the *ISTAT 15th Population and housing census 2011*.

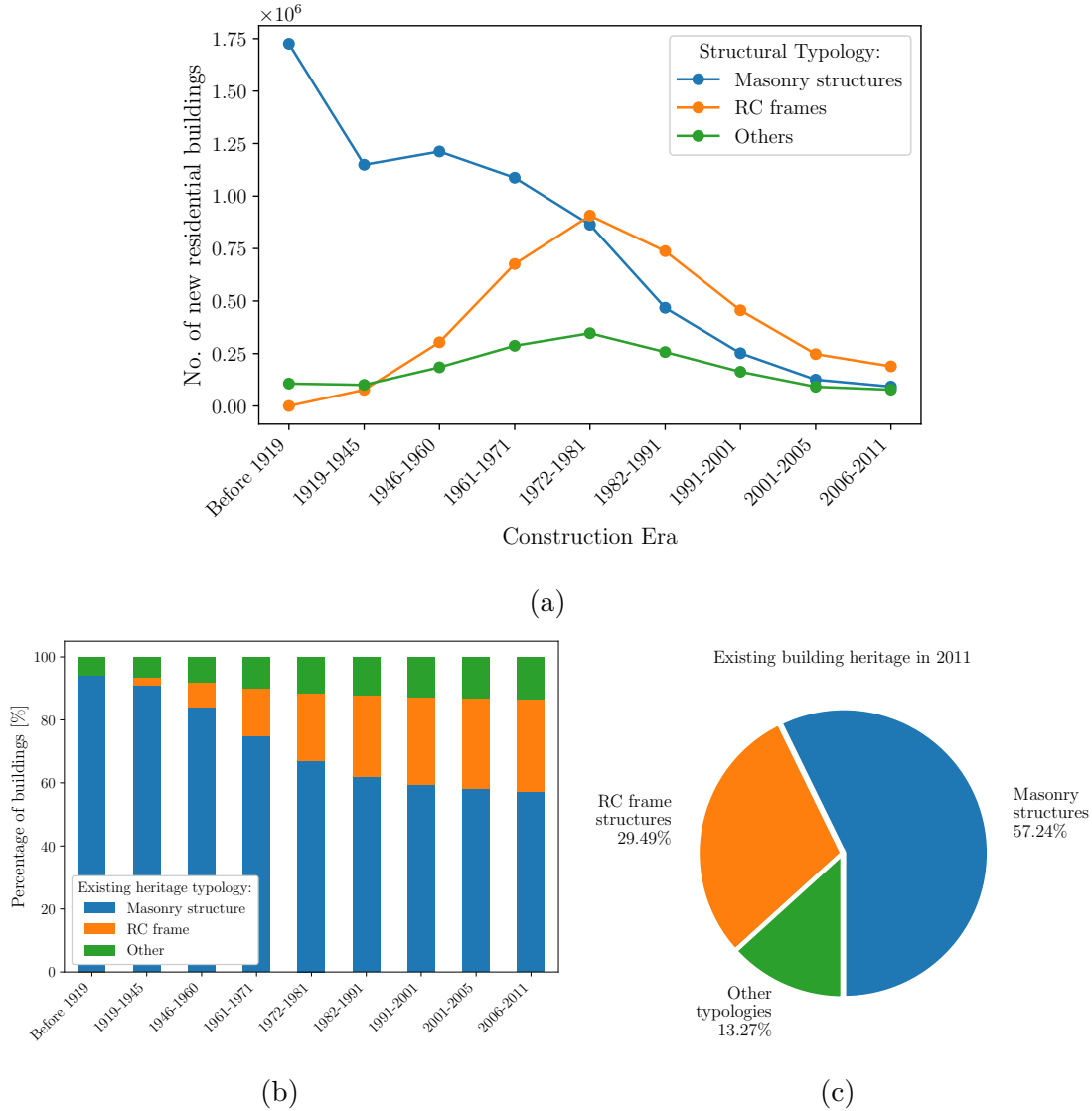


Figure 1.3: ISTAT 15th Population and housing census 2011 results: (a) Absolute number of new constructions for various time spans. (b) Overview of how structural typologies proportions varied for existing residential building heritage over time; (c) Pie chart of the structural typologies of proportions at the 2011 census time.

occurred in 2004 in a two-story building located in Palermo, Sicily, during ordinary maintenance activities aiming to realize a waterproofing layer [24]. The long-span in-situ cast RC roof was constructed around 1950 and this time the collapse under its self-weight was attributed to materials degradation issues, especially due to corrosion of beams reinforced bars due to high carbonation levels.

Focusing on building existing heritage implies mentioning another emerging

concern, i.e. related to the soil consumption issue. Land consumption is defined as the transformation from a natural condition to an artificial ground covering [25]. The human activities involved are distinguished into permanent artificial covering (e.g. urbanization) and non-permanent one (e.g. mining areas). Soil provides the fundamental ecosystem for humankind’s survival and development. Nonetheless, the often scarce mindfulness about the real intangible value of the soil led to human activities with degradation drawbacks resulting in prohibitive rehabilitation costs. Therefore, nowadays conceptions impose to rethink the land as a limited and non-renewable natural resource [25, 26]. The monitoring of soil consumption is performed by the Italian National Institute for Environmental Protection and Research (ISPRA) which yearly publishes official reports about the Italian situation [26]. Excessive soil consumption has strong and multiple impacts, for instance, soil sealing resulting in the increase in hydro-geological risks, and social-economical impacts with the reduction of agriculture activities, besides the climate and ecological impacts with the biodiversity reduction. Due to Italy’s multi-colored geomorphology, it is estimated that 91% of Italian Municipalities are affected by hydro-geological risks [11]. European Commission in 2021 has compiled four cornerstones to be followed in the soil consumption hierarchy attempting to accomplish with the United Nations (UN) 2030 Agenda for Sustainable Development launched in 2015 [27]: 1. Avoid soil consumption when it is possible; 2. Reuse already impermeable soils before consuming new natural ones; 3. Reduce at the minimum the use of highly natural land (such as forests or highly fertile grounds); 4. Compensation measures should be activated to point toward the ideal zero consumption. Focusing on the second point, an effective possible strategy to cope with the soil consumption mitigation, and even prompting sustainability aspects, should be promoting restoration of the ancient existing building heritage, e.g. focusing on preserving historical centers from long-term degradation effects [28, 29]. On June 15th, 2023, in Turin (Piedmont) the timber roof of the former Porta Susa railway station suddenly collapsed⁴. The masonry construction built in 1856 was dismissed in 2009, after the completion and opening of the new neighbouring Porta Susa underground railway station. After hosting some convivial events, the historical building was definitely abandoned in 2017. Despite some mild attempts to recover the nineteenth-century historical building, the aging effects prevailed with the ancient timber roof collapse in June 2023, probably due to water leakage. This represents one of the countless examples in Italy of historical buildings that should be worthy of restoring and rehabilitating to ensure once again usability with today’s safety requirements [29]. Other iconic examples still located in Turin are represented by two Pier Luigi Nervi’s masterpieces which are completely abandoned nowadays, i.e. the Turin Exhibition Center [30] and the Palace of Labour [31].

⁴From the Italian newspaper [LA STAMPA](#).

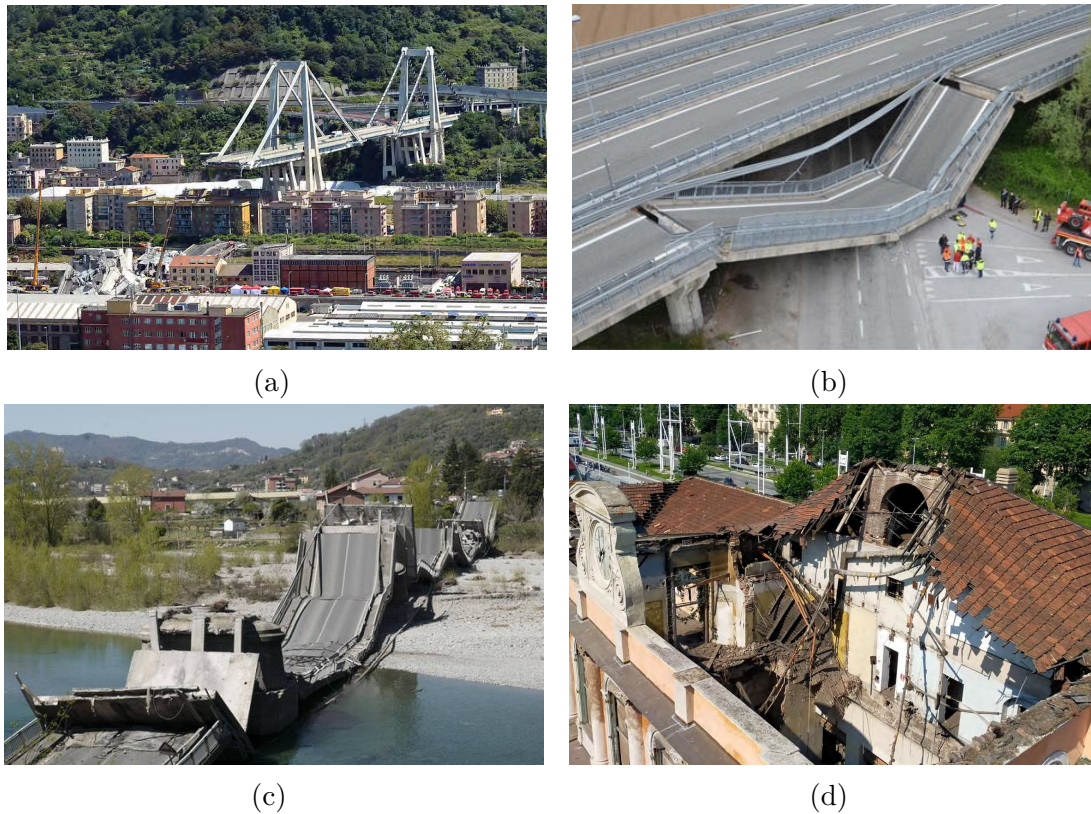


Figure 1.4: Some sadly collapses occurred in Italy. (a) Polcevera Bridge, Liguria, courtesy of [Maurizio Boi](#); (b) Fossano Bridge, Piedmont, reprinted from [17]; (c) Caprigliola Bridge, Tuscany; (d) Former Porta Susa Station, Piedmont, reprinted from [LA STAMPA](#).

All the so far debated social and economic aspects motivate the growing and significant demand for the scientific community to develop effective and innovative smart SHM solutions to be implemented also in historical buildings and infrastructures, bestowing them smart features to increase their conservation ensuring enough safety levels. In Japan, due to the severe seismicity, the SHM deployment on buildings already started in the 1950s, but it actually began rapidly widespread in recent years, afterward the 1995 Kobe earthquake [32]. In particular, before the 2011 Tohoky earthquake, only 150 buildings were equipped with an SHM system, and the number sharply rose to 500 in 2016. In 2018, it was estimated that about 850 buildings were equipped with an SHM system, often installed voluntarily by owners in the private sector, counting about 700 out of the estimated 850 [32]. The previously documented bridge collapse cases evidenced how existing bridges and viaducts are extremely vulnerable, especially to aging effects. Indeed, the increasing load demand over time and in-situ structural material properties changes adversely combine with environmental agents, often leading to rapid and

extreme localized degradation phenomena when not properly treated. These unwanted events directly influence their load-bearing capacity, threatening their reliability and safety degrees. The lack of proper and timely maintenance programs increases the probability of collapse of aged structures and infrastructures. For instance, in 1979, Riccardo Morandi himself alerted about the durability aspects of the Polcevera Viaduct. He foregrounded the highly aggressive environmental issues of chloride attacks and elevated salinity rates due to geomorphological aspects of the proximity to the seaside, and moreover, highlighting the aggressive chemicals within polluted air due to the industrial activities of the surrounding area [3, 15]. Lack of proper and timely maintenance may have also a strong social impact. The “social” costs of all road accidents in Italy, fatal or not, have been evaluated by the Ministry of Infrastructures as 15 billion EUR in 2019. A percentage between 5-20% of this latter can be attributed to the poor road conditions, or indirectly to the lack of sufficient driver’s time reaction to those unexpected road defects [11].

As reported in the infographic chart in Fig. 1.5, in the USA, the last decades’ governments efforts and investments within the infrastructure sector encouraged to reducing the number of highway structurally deficient bridges from 12.1% in 2009 to 7.5% in 2019. The mentality progressively evolved from a total replacement of old bridges toward a predictive maintenance approach [5]. However, there is still a great deal to be done since the rate of improvements shrunk to only 0.1 annually in last years. The FHWA estimated that the backlog for repairing the existing bridge amounts to 125 billion USD, warning that the current rate of deterioration is exceeding the rate of rehabilitation. Nonetheless, federal investments in bridges remained quite stagnant in the last years. The Highway Trust Fund which historically funded US bridges and road projects is primarily financed by fuels tax which remained stable at 18.3 cents per gallon since 1993 [5]. In the 2021 ASCE’s report, an economic measure was suggested to increase the federal motor fuel tax over the next five years to 24.4 cents. This may attempt fixing the Highway Trust Fund deficit, and further ensuring reliable future funding, even accounting inflation rates [5]. Anyway, the increasing mindfulness of maintaining the existing bridges instead of building new ones has prompted also new attitudes concerning durability issues. Foremost, the American Association of State Highway and Transportation Officials now mandates that new bridges must be designed with a nominal life of 75 years rather than the common 50-year approach. Secondly, the adoption of non-destructive evaluation techniques, such as the ones fostered in the current Thesis, ensures minimal impact on the existing structure whilst delivering the current health state of the structure. Dynamic characterization and new technologies such as ground penetrating radar (GPR), thermography and tomography, and unmanned aerial vehicles (UAVs) inspections, provide key insights to support optimal and efficient decision-making processes. New bridges should be designed as “living structures” since sensors are predisposed and embedded from the beginning, ensuring continuous feedback for a global life-cycle assessment. Since it accounts for ongoing long-term costs besides

upfront capital ones (e.g. construction cost), the life-cycle cost analysis (LCCA) is nowadays vital for infrastructure asset management since it provides more realistic economic predictions for stakeholders' optimal budget allocation purposes [11]. The identification of damage at early stages ensures the prioritization of maintenance interventions on the entire infrastructure network with an optimal allocation of the limited resources, whilst guaranteeing generalized public safety. Moreover, fair maintenance in the early stages of damage ensures repairing interventions at a fraction of the cost rather than incipient-collapse rehabilitation operations [11, 33]. This efficient maintenance program timely preserving bridges in fair conditions is estimated to reduce the number of structurally deficient bridges in the US below 5%, besides decreasing the future maintenance backlogs [5]. Moreover, the adoption of innovative materials may improve the infrastructure network resilience and durability, using e.g. high-performance steel and composite structures, corrosion-resistant reinforcements, and ultra-high-performance concrete. Another challenge to overcome is that every single structure is deteriorating at its own pace. Therefore, a systematic database approach is required to effectively manage the US National Bridge Inventory (NBI). Novel Transportation Asset Management Plans (TAMPs) are now required in the US to predict fair or poor bridges conditions in a 10-year future horizon, aiding cost-effective ways to timely addressing deterioration phenomena [5]. NBI no longer tracks those bridges considered functionally obsolete that do not comply with roadway geometry design or vertical/horizontal clearance. However, it is estimated that these about 94,000 bridges in the US still represent bottlenecks from a transportation standpoint [5], inducing traffic congestion and higher traveling time, especially considering strategic transportation functions such as fire trucks, ambulances, school buses, etc. As a direct consequence of the 2021 ASCE's report card, the US Congress issued the Federal Infrastructure Bill Public Law No. 117-58 on November 15th, 2021, better acknowledged as the Infrastructure Investment and Jobs Act (IIJA) [34]. This five-year investment plan recently boosted the infrastructure sector earmarking globally 1.2 trillion USD across the 17 infrastructure categories studied by the ASCE in its quadrennial comprehensive assessment of America's infrastructures compiled since 1998. Concerning bridge structures, the aim of IIJA is to modernize the asset management promoting life cycle cost analysis, maintain and improving existing assets. 500 billion USD have been designated in total over five years to road and bridge programs, whereof 40 billion in investments for the nation's bridges. 27 billion USD have been immediately devoted to about 15,000 most urgent bridges for replacement, rehabilitation, preservation and construction programs. This will ensure that the number of structurally deficient bridges will not increase despite those bridges will continue aging. In ASCE's *IIJA Recommendations for Effective Implementation*, it is claimed that the investment will boost over 100 new programs to improve and modernize the existing infrastructure assets, including the Bridge Replacement, Rehabilitation, Preservation, Protection, and Construction Program, the Rebuilding

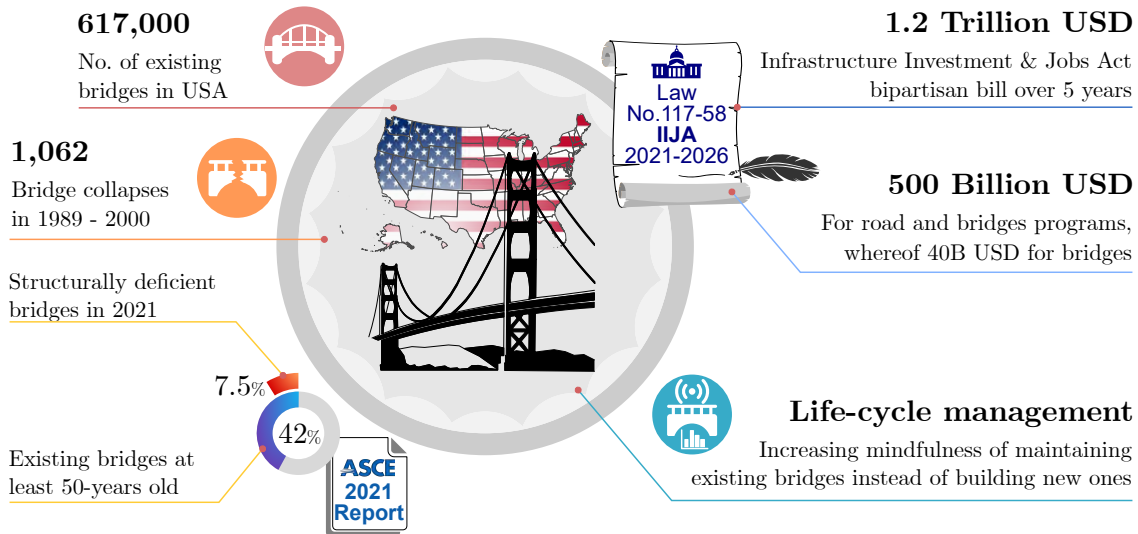


Figure 1.5: Infographic chart of nowadays USA infrastructure state and recent investment efforts to support bridge rehabilitation programs.

American Infrastructure with Sustainability and Equity (RAISE) grant program, and the Federal-State Partnership for State of Good Repair Grant Program, Federal Emergency Management Agency’s (FEMA) Building Resilient Infrastructure and Communities (BRIC) grant program.

Considering the European continent, the comparative report “*Overview of transport infrastructure expenditures and costs*” of EU commission [35] provided a survey of earmarking for operation and maintenance for roadways (OMR) over time. In 1995, when the EU counted 15 Member States, the OMR expenditures were about 44 billion EUR. Consider that in 1990s EU launched the Trans-European Transport Network (TEN-T) program to develop Europe-wide transportation network promoting safety, energy efficiency, and digitization [11]. However, due to the financial crisis in 2008, a steady decrease was registered in the time interval 2009-2016. About 38 billion for OMR expenditures has been recorded for the 28 EU Member States in 2016, just 86% than twenty years before [11, 35]. In fact, the Great Recession and the following austerity policies reduced the available resources for both new public works and maintaining the existing ones. It is estimated that the infrastructure funding gap affects a reduction of at least about 1% yearly of gross domestic product (GDP) of Member states [11]. Considering a public policy perspective, one of the reasons for the infrastructure sector funding backlog can be ascribed as an information deficit. It is often difficult to retrieve quality data related to infrastructure maintenance. These data involve the asset’s inventory such as location, current health status, age, exposure to hazards, usage volumes, etc. This knowledge is essential to prioritize multi-year budgeting for ordinary and extraordinary maintenance [11]. Also in the American context,

there is a similar issue, since there are still infrastructure sectors where data is scarce or unreliable (e.g. school facilities), still suffer from a lack of inventory of assets or robust condition information [5]. An important challenge for next future is to improve information transparency avoiding potential asymmetry at all levels of governments, state-owned enterprises, and private companies to improve budgeting preparation and consistency in infrastructure expenditures for multi-year strategic plans [11]. Focusing on the Italian scenario, the first attempt to gather all the critical information of the whole portfolio of national infrastructure network assets occurred in 2018 with the establishment of the National Archive of Public Infrastructures (AINOP), in Italian, “*Archivio Informativo Nazionale delle Opere Pubbliche*”, Law Decree No. 109 of 28 September 2018 (“*Decreto Genova*”). Nonetheless, in Italy there are some intrinsic governance issues producing a slow approach to investment decision-making, i.e. the progressive decentralization of infrastructure spending on one side, and a progressive depowering of the institutional agencies on the other side. In Italy, sub-national public administrations are responsible for over half of public investments, however, their role did not always achieve local financing empowerment, thus justifying the necessity of maintain a certain degree of centralization, especially for EU funding opportunities [11]. Indeed, Italy as a Member State should accomplish to EU directives and programs. Therefore, there is also a progressive transition from emergency or episodic maintenance toward a more systematic predictive maintenance mindfulness. Nonetheless, there is still a great deal to be done especially in the roadway system rather than the railway one. A few years ago, 250 million EUR were yearly earmarked for ANAS. However, without any multi-year strategic financial plan, this funding was just enough to cover the most urgent critical issues, thus preventing any long-term strategy [6]. Unfortunately, Italy faced a longstanding infrastructure investment gap, further intensified after the 2008 financial crisis, registering a decrease in public expenditure on capital investments from 4.6% of GDP in 2009 to only 2.9% of GDP in 2019 [11]. Moreover, the multiple numbers of different companies acting on road asset management jointly with Italian bureaucracy complexity represent an obstacle to shared and common conservation rules, resulting in lengthiness and countless downtime of authorization paths. Italian Agency for Territorial Cohesion estimated that, for projects under 100,000 EUR costs, the authorization process last on average more than 2 years, whereas it lasts over 15 years for more expensive works [11]. In 2016, the Italian legislation attempted to modernize the bridge inspection procedures which dated back to Ministerial Circular n°6736/61/A1 of July 19th, 1967 [6], involving filling out inspection reports. In order to seek transparency, simplification, and reduction of works completion time, Italian legislation enacted the Legislative Decree 50/2016 “New Code of Public Contracts”, and later in 2019 Law Decree 32/2019 Decree “Unlock Construction Sites”, in Italian “*Sblocca Cantieri*” which reformed of Public Contracts Code to simplify public works procedures, followed by Law decree 76/2020 converted into Law 120/2020 denoted as

Simplification Decree, in Italian “*Decreto Semplificazione*” which promoted digitization of public administration and envisaging the transfer of ownership of bridges and overpasses on secondary roads to ANAS. Therefore, as a consequence of the latter law, the number of bridges under the ANAS control reached 18,602 in total. In July 2016 a new multi-year financial plan for ANAS allocated 23 billion EUR over the 2016-2020 time-span, ten times the normal yearly funding for maintenance purposes [6]. This permitted the introduction of the ANAS’s BMS in 2017 within the predictive maintenance Road Asset Management (RAM) model, envisaging the large scale adoption of structural health monitoring systems divided into multiple levels of control and deepening. The term asset management identifies all those procedures acted to ensure that an asset (structure) operates in a way that enhances the asset’s life, in order to fulfill present and long-term requirements, whilst optimizing its maintenance and management costs, balancing among competing priorities [36]. An SHM system is not a decision-making tool per se, but it can provide real-time crucial information to support an effective asset management policy. This latter strongly depends on the decision-making process performed at each stage of an asset’s lifecycle, thus impacting subsequent stages and the entire lifetime asset’s organization. Other data and information that bridge managers can obtain to support decision-making are visual inspections and non-destructive evaluation. Bridges within an asset management network are categorized into three classes, i.e. core, intermediate, or advanced, based on their risk profile and every special criticality. A continuous and fully operational SHM system requires a significant money investment to deploy sensors and maintain the data collection and interpretation system over time. An example of a cost-benefit analysis is reported in [37], which discusses the implementation of a long-term SHM system on the cable-stayed Mezcala bridge case study in Mexico. The SHM economical effort represents the main drawback that limits its large-scale application. Therefore, in an optimal asset management strategy only strategic structures, i.e. those belonging to the advanced class, should be equipped with a complete SHM system that justifies the capital investment [33, 36]. In fact, high-risk artifacts have the potential to result in considerable cost savings for the stakeholders. SHM is not meant to replace visual inspection but provides more objective insight which combined with visual inspections, thus delivering important elements to support decision-making tasks. Furthermore, it is advisable to perform a decision-mapping procedure in advance to optimize the SHM system plan accounting for the major vulnerabilities of the specific artifact under investigation. It is worth underlining that it should be clear in mind that infrastructure is a system of systems, interconnected and interdependent, therefore an effective challenge for next years is to encourage the creation and utilization of infrastructure data sets across classes [5, 11]. Similarly, SHM is a part of the entire infrastructure preservation chain to which it is delegated the important task of dynamically “understanding” the risk evolution and identifying when and where any damage occurs [36]. Considering those aspects, smart investment

will ensure an SHM transition into commercially viable asset management policies, with a clear future vision for our infrastructure heritage. Recently, Europe financed several research and innovation projects to address significant improvements and renewals of the infrastructure sector. For instance, the European Commission Joint Research Centre (JRC) established an exploratory research project denoted Monitoring Transport Infrastructures with Connected and Automated Vehicles (MIT-ICA), carried out in the period 2020-2022, to investigate the indirect SHM (iSHM) [38]. The main idea is to explore innovative infrastructure motoring methods based on vehicle-bridge interaction and the deployment of sensor-equipped vehicles to indirectly retrieve the bridges' health state. In 2019 European Green Deal introduced a set of policies and directives leading toward a green transition. This is in line with the Sustainable Development Goals (SDGs) stated in the UN 2030 Agenda, as summarized in Fig. 1.6. Public administrations and rating agencies started adopting Environmental, social, and corporate governance (ESG) standards to evaluate a potential investment in the infrastructure sector, even incorporating key social and economic aspects to forecast future service demands [11]. Italy is currently implementing the National Recovery and Resilience Plan (NRRP), or in Italian "*Piano Nazionale di Ripresa e Resilienza*" (*PNRR*) to be fulfilled by 2026. This massive investment program of 235.14 billion EUR for Italy, part of the Next Generation EU (NGEU) program, has been allocated to 6 missions aiming to three principal aims, viz. digitization, ecological transition, and social inclusion. In particular mission 3 denoted "Infrastructure for sustainable mobility" earmarks 31.4 billion EUR for empowering the railways system, especially regional tracks in Southern Italy and high-speed lines [11]. However, the main EU funding limitation is often an unintended effect of investing in new goals whilst daunting maintenance expenditure for existing assets, in fact, not prioritized within the NRRP program. The infrastructure maintenance funds are currently financed by the Italian Complementary Fund with 300 million EUR [11]. Nonetheless, among the emerging priorities of safety and modernization, these investments can be effectively introduced in the infrastructure sector for smart SHM solutions with InfraTech solutions and new technologies [11]. Investing policies for higher resiliency and modern infrastructure presents benefit-to-costs ratios greater than 1, opening new opportunities to optimize the assets' diagnostic monitoring and risk assessment, enabling cheaper and less invasive repairing interventions, reducing environmental impacts and fostering innovation friendly and sustainable management frameworks [11].

Another crucial aspect of the current historical period is represented by the overwhelming digital revolution which fosters innovative and original artificial-intelligence-based (AI) solutions. The roles of smart cities are rapidly changing and drastically evolving due to the effective integration of Internet of Things (IoT) technologies and Machine Learning (ML) solutions. The digital revolution is rapidly affecting the Civil Engineering sector since new mobility technologies, increase public safety and quality of life, whilst accomplishing new requirements for environmental

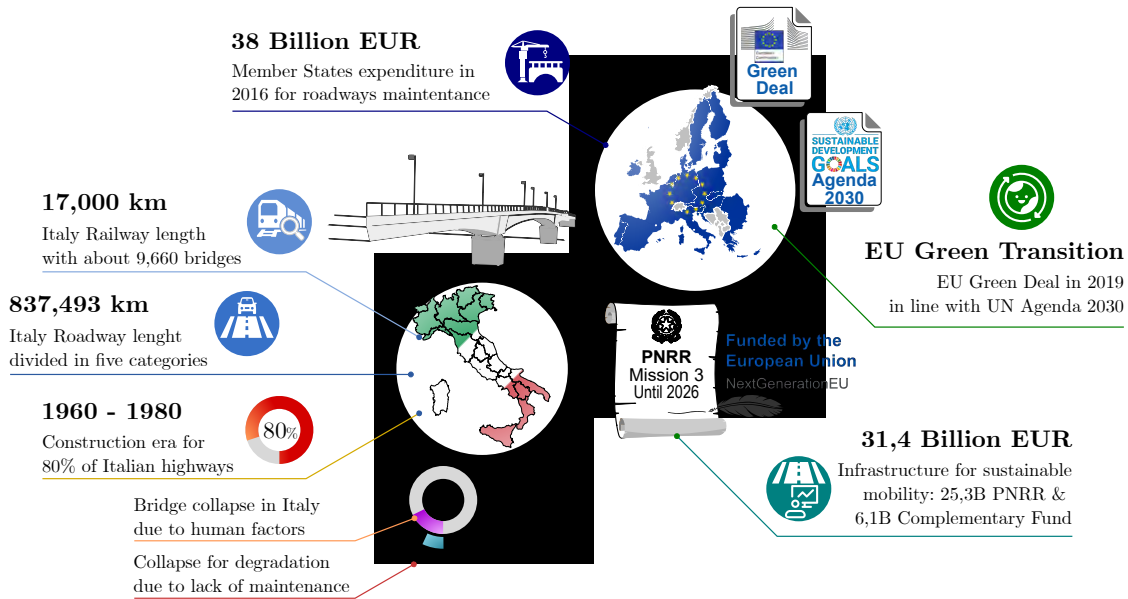


Figure 1.6: Infographic chart of Italy infrastructures and recent European investment support.

protection, and in the meanwhile still ensuring economic growth opportunities and contained cost of living [39]. New and emerging InfraTech and digital technologies, such as digital twins, AI, ML, IoT, and UAVs among the others, can revolutionize the way our structures and infrastructures are designed, build and maintained [38]. Novel AI-assisted SHM can be applied to all the different stages of structure and infrastructure life cycles, i.e. considering the construction phase, in-service and management conditions, maintenance, etc. heightening the infrastructures to a new intelligent transportation systems (ITS) [40].

Therefore, with those motivations and big picture perspective, the present Thesis encloses the results of research conducted during the three-year Ph.D. Program at Politecnico di Torino. The present document attempts in its own way to contribute with some new slight step forward within this vast and multidisciplinary research field unpretentious of being completely exhaustive. Once again, it is worth emphasizing that every implication, related aspect, and consequence of developing innovative research in the SHM field involves the entire society at different levels and not only a prerogative of technical professional circles. Supporting research for innovation and modernize our structure and infrastructure heritage prompts cost saving in the digital era, whilst promoting long-term sustainability in economic, social and environmental terms [5].

1.2 Machine learning perspectives in structural engineering

In the last decades, the increase of computational capabilities increasingly promoted the adoption of data-driven methodologies in structural engineering, fostered by the advent of innovative Artificial Intelligence (AI) solutions [41]. However, these latter are often blamed to be black box methods with the lack of proper interpretability, in contrast to the traditional structural engineering field characterized by transparent analytical, numerical, experimental, or phenomenological methods [41].

AI and ML are strongly related fields. Specifically, ML represents a sub-field of the vastest AI world, as depicted in Fig. 1.7. The term AI identifies that computer science branch attempting to artificially reproduce biological processes like human intelligence, thus synthetically replicating cognition and logic [41]. Conversely, the term Machine Learning (ML) indicates a family of methods that automatically permits acquiring information and knowledge from the unformed mass of available data, then allowing to make predictions (inference) for new and previously unobserved quantities [42, 43]. ML is often described also as those methods whose rules have not to be explicitly implemented (hard-coding), but they are derived directly from the information contained in the data under investigation [43]. From a terminology standpoint, the term data denotes any raw collected quantity that hardly conveys any meaning as it is, whereas information represents the outcome of the data-processing task delivering meaningful summaries of interest [44]. Instead, in the broader conception of the term information, knowledge means the human understanding of a certain phenomenon resulting from an integration of human perspectives and the conducted analyses to obtain some meaningful conclusions [44]. Knowledge can be described as a tripartite concept [44]: 1. Know-why, denoting the understanding of the phenomenon under investigation; 2. Know-what, denoting cognition or recognition of the underlying mechanisms occurring, thus describing the phenomenon under study; 3. Know-how, meaning the resulting capacity of choosing a proper action based on the acquired understanding of the phenomenon under study.

Since the huge amount of prolific studies and applications in the last decades sharing the adoption of artificial neural networks and their variants and derivatives, the Deep Learning (DL) subfield has been separately recognized within the ML area. In recent years, an evolving area of study has been identified as the Data Science subject, being the diminutive of data-driven science [44]. It comprises theories and multidisciplinary application-domain techniques drawn from mathematics, statistics, computer science, machine learning, and database fundamentals, encompassing all those methods aimed to extract knowledge from data, i.e. from the data preparation, reasoning, and mining, until the interpretation of the applied intelligent models' outcomes. Furthermore, as illustrated in Fig. 1.7, since the nowadays

availability of low-cost sensor devices and fast communication technologies, a new multidisciplinary field called Big data has emerged within the Data science area, and the methods, tools, and technologies developed to deal with those data have been formalized into the data analytics domain [44].

ML is preferred when dealing with complex problems with large amounts of data, in which traditional approaches do not yield good solutions, or because hard coding is an impracticable way since a huge number of complicated rules should be carefully explicitly programmed. Furthermore, ML reveals another its great potential when working in a fluctuating environment, i.e. when the model has to adapt to new data [43]. In their literature review [41], Tapeh and Naser explained that first traces of research studies concerning AI applications in structural engineering date back to late 1980s, and considering last 20-year studies, four main research themes transpired:

- Definition of data-driven phenomenological models;
- Prediction of structural behavior;
- Analytical description of physical phenomena;
- Computer vision applications for image or video data.

Computational methods can be classified in two main groups, denoted respectively as hard computing and soft computing. Whilst the foremost adopt hard-coding and explicit analytical forms, the latter employs approximate or implicit methods. Moreover, the various computational techniques can differently categorized into [41, 45]:

- White box: uses explicit and well-established functional relationships;
- Grey box: partially based on theoretical understanding or prior knowledge and on a data-driven part;
- Black box: based on complex implicit relationship hard to interpret, often completely data-driven.

Often, the majority of AI procedures, especially the ones concerning the use of DL architectures, fall within the black box procedures. As stated in Tapeh and Naser [41], AI has been extensively adopted to address three main structural engineering problems. The foremost concerns modeling problems, especially to predict the structural behavior or the mechanical properties of structures. Secondly, the majority number of studies were about simulation problems, including simulated damage and SHM of structures, even encompassing seismic effects. Thirdly, another densely populated research field is represented by structural optimization problems. It is worth mentioning that soft-computing methods, especially the meta-heuristic

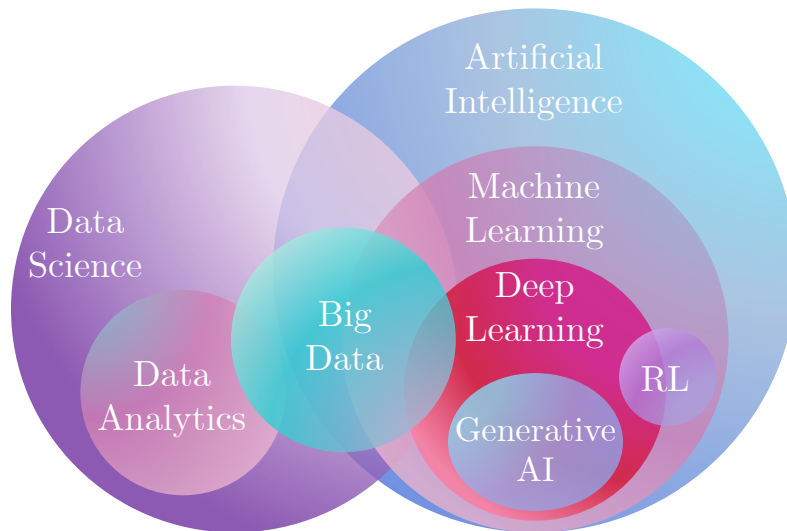


Figure 1.7: Conceptual relationship Venn graph among the fields of Artificial Intelligence, Machine Learning, Deep Learning, Reinforcement Learning, and Generative Intelligence, and their connections with Data Science and Big Data.

optimization algorithms, represent another branch of AI related to computational intelligence, since they are inspired by Mother Nature’s intelligence mimicking inherent mechanism of biology, physics, genetics, etc. [46, 47, 48, 49, 50]

The following subsections constitute a useful basis for the further chapters of the present Thesis, introducing a brief theoretical review, reporting the main fundamentals and general remarks about ML and DL fields.

1.2.1 Machine learning techniques remarks

In essence, a ML method frequently deals with defining a generic model $\mathbf{y}(\bullet)$ whose variable parameters are inferred in a data-driven way on the so-called training set \mathbf{x} . The input data are usually preprocessed and often undergo a feature extraction stage. The training data are usually expressed in a tabular form [41], and each row is called an instance, or an observation, or a data sample. The total number of rows indicates the size of the dataset, whereas the number of columns denotes the dimensionality of the feature space. The features are also named attributes, or measurements, and they characterize each sample. The precise form of $\mathbf{y}(\mathbf{x})$ is established through the training phase by quantifying how well the optimized model predicts the observed data. The training phase is the learning process, whereas the capacity to predict well new and previously unseen test set data is acknowledged as the generalization capabilities of the model [51]. The ML approaches are intrinsically statistical and probabilistic-based since the uncertain nature of the learning

task [42]. The ML approaches can be categorized into three main different procedures according to the type of available data, thus also influencing the learning process peculiarities:

- Supervised learning : describes the relationship between input data and their known targets (labeled data);
- Unsupervised learning : labels do not exist for data (unlabeled), therefore it attempts to describe intrinsic relationships among data;
- Reinforcement learning : conceptually different than the other ones, it is based on an intelligent agent that learns the optimal action policy to receive the maximum reward based on feedback retrieved by the environment [52].

Focusing on supervised learning, a classification problem is when the goal is to assign input data to a finite number of targets, whereas a regression problem is when the output target consists of one or more continuous variables [51]. In unsupervised learning, a clustering problem is set when the goal is to discover groups' similarities within the data, whereas it is a density distribution estimation task when the distribution of data is investigated. A dimensional reduction problem is an unsupervised learning technique that projects data from their original domain toward a new subspace. It may be useful both for visualization purposes or because it is hoped that the ML problem would be easier to solve in the new resulting subspace [51]. Other unsupervised learning applications include detecting anomalies or novelties for new incoming instances based on the information learned from starting available data [43]. The term ML becomes a synonym of data mining when it is used to deeply explore large amounts of data with the aim of discovering new insights and hidden patterns [43]. It is worth mentioning that there exists also another branch between supervised and unsupervised learning denoted as semi-supervised learning. This latter involves datasets where only a few instances are labeled, whereas the majority of them are available without any a priori label [43].

As depicted in Fig. 1.8, other criteria exist to categorize the different types of ML methods besides the nature of the available data [43]. The learning process is known as online learning when the ML model can learn incrementally from a stream of incoming data. In this case, data instances are feeding the model sequentially, or in small groups defined mini-batches. Online learning is ideal when dealing with continuous flow of data which require rapid and autonomous adaptations. In this case, it is fundamental to control the learning rate parameter, i.e. governing the adaptation speed rate of the ML model. Online learning is called out-of-core learning when the user is forced to use it due to physical limitations of computational resources, e.g. when it is necessary to train big datasets which cannot fit all together at one time the machine memory. On the other hand, when the ML system is incapable of learning incrementally, the learning process is acknowledged

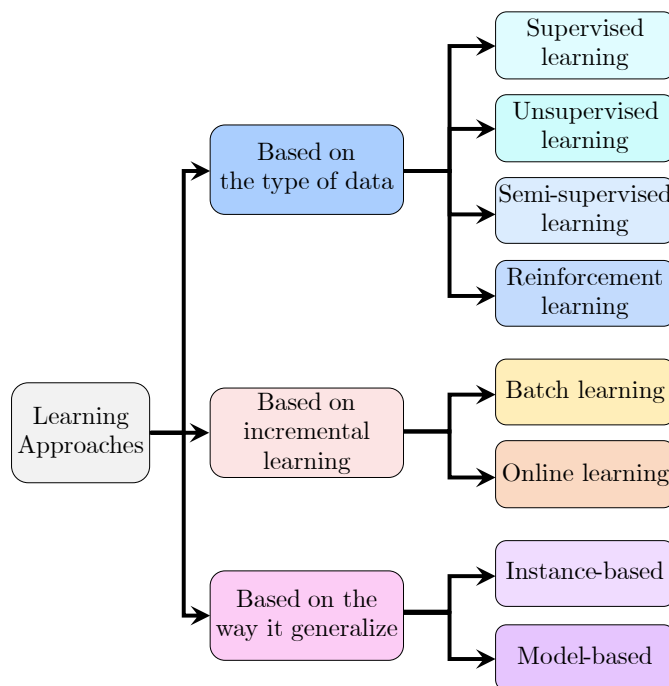


Figure 1.8: Different learning methods in ML.

as batch or offline learning. In this case, the model has to be trained on all data, thus often requiring larger computational resources and time. However, when new input data become available, the old trained system with batch learning must be completely replaced, i.e. a totally new model should be trained from scratch again. Another possible way to categorize ML methods is based on the way they generalize, which directly involves how input data samples are used to build knowledge [43]. The most trivial approach is named instance-based learning, meaning that the ML learns from available examples, and then generalizes to new instances by comparing them with previously learned samples based on some similarities metrics. Instead, a model-based learning approach rely on a trained and optimized mathematical model on available data, and uses it to make inference and predictions for new previously unseen instances. In this case, a model selection phase must be performed to find the optimal model based on a utility or fitness function, or conversely, usually based on a cost function.

The typical workflow in ML project is depicted in Fig. 1.9. The first step concerns the input features preparation involving incomplete samples elimination or imputing missing values, the selection of relevant features for the problem under study, and the reduction of the dimensionality of the data. A ML model should be trained on a sufficient amount of data to work properly, otherwise, the sampling noise may largely affect the pattern recognition task rather than the information contained in the available data [43]. Moreover, these data must be representative

of the problem under investigation in order to generalize well on new instances. A significant time investment is normally pursued to clean up raw data and to perform feature engineering tasks, i.e. selecting and extracting relevant features. An essential preprocessing transformation is converting all raw data attributes into numerical data to properly feed the ML model. Various options are available when dealing with categorical features. The most trivial method is converting the feature using a one-hot encoding scheme. This produces an increase of the feature space creating a sparse matrix for every single categorical attribute, thus introducing several dummy features equal to the number of possible categories. For each sample, only one dummy attribute is equal to 1 and all the others are 0, hence the name one-hot encoding. However, if the number of categories is large, as a rule of thumb greater than 50 [43], the one-hot encoding will result in an excessive number of input features, possibly compromising the training process performance. When one-hot encoding is no longer a doable option, it is advisable, especially in the DL field, to replace each category with a learnable and low-dimensional vector, designated as embedding. Special categorical features are named ordinal categorical attributes since an ordered relationship among categories exists. In this case, a label-to-integer encoding scheme could be a viable option, once the user has sorted the feature categories in increasing order of importance. Conversely, categorical features are named nominal variables when any existing ordering relationship among categories do not exist. For nominal categorical variables another possibility could be performing a label-to-integer encoding, followed by a proper scaling procedure. In this way, the categories converted into integer values are scaled to a common scale to avoid a possible biased learning, i.e. preventing categories associated with greater integers will affect more the training process [43]. Indeed, with few exceptions, the best practice is always to scale every single feature column to a common order of magnitude range [53, 54]. Two main scaling schemes are usually adopted. The min-max scaling converts each j -th numerical feature column in a way that each i -th sample lie in a $[0,1]$ support, i.e.

$$x'_{ij} = \frac{x_{ij} - \min(\mathbf{x}_j)}{\max(\mathbf{x}_j) - \min(\mathbf{x}_j)}, \quad (1.1)$$

whereas, the standard scaling normalizes the feature column in a $[-1,1]$ range, being $\mu_{\mathbf{x}_j}$ and $\sigma_{\mathbf{x}_j}$ the mean and the standard deviation of the j -th feature column respectively, i.e.

$$x'_{ij} = \frac{x_{ij} - \mu_{\mathbf{x}_j}}{\sigma_{\mathbf{x}_j}}, \quad (1.2)$$

Subsequently to the data preparation phase, the next step is to split the data into a training set and a hold-out test set. Indeed, the best way to check how the model generalizes well is to test the trained model on new previously unseen data [51, 55], and calculate the resulting generalization error rate through specific

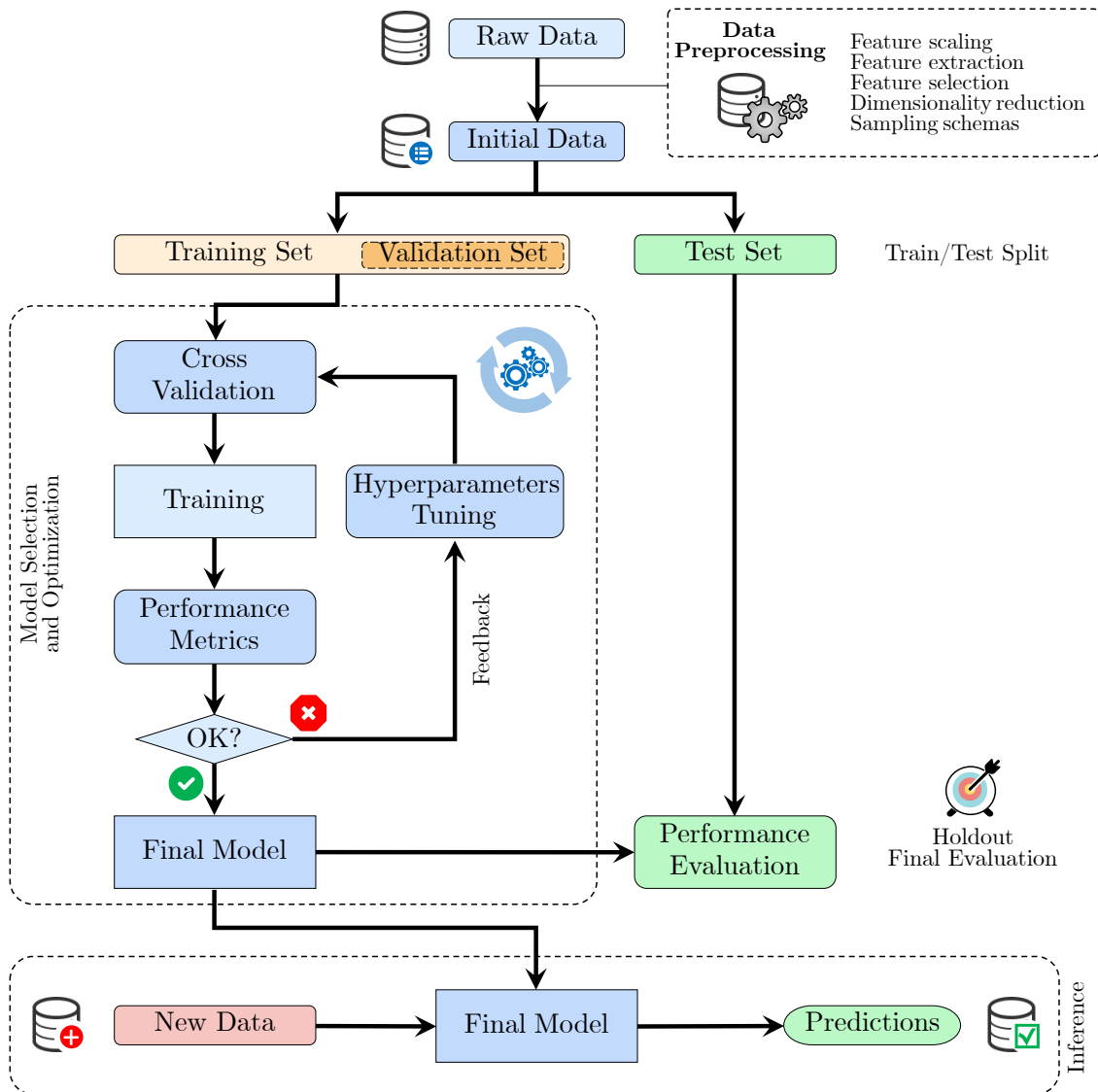


Figure 1.9: The typical ML project workflow.

metrics. However, generally a ML model should be trained using as much as possible of the available data to maximize its training performance [43]. Therefore, the preponderant part of the dataset is designated to the training set, with a common split rate of 80%, and consequently, the remaining 20% of the dataset is assigned to the test set. As illustrated in Fig. 1.9, the term hold-out means that the test set is hidden away and it does not contribute at all in the entire learning process. The test set comes into play only in the final evaluation part, i.e. when the ML model has been already trained and optimized and its generalization capabilities are checked. The training/test splitting proportions are not strictly fixed and they depend on the size of the dataset. For instance, considering a very large dataset of

dozen millions of instances, then even holding the 1% could be enough to estimate generalization errors. It is worth underlining that the specific manner to split data depends on their internal distribution. In fact, for an imbalance classification problem [56, 57], it may be necessary to adopt specific sampling schemas, such as e.g. a stratified sampling strategy, in order to pseudo-randomly assign data to the training and test sets, but maintaining the initial proportions among classes of the original dataset. Moreover, to avoid a biased split of data, it is advisable to perform a random shuffling before the training/test split step.

Generally, ML models should be trained using as much as possible of the available training data. As defined in [43], a model is a simplified representation of the observations. This means that superfluous information has been discarded, by making some assumptions, to push better generalization capabilities to new instances. In 1997, Wolpert and Macready [58] stated the famous “No-Free Lunch Theorem”, explaining that whether no assumptions a priori are made on the data, there is no reason to prefer a model over the other alternatives. Therefore, there is no model that a priori works better than others, and the user should ideally test all existing models to choose the best one. However, since it is not practically possible to test all the algorithms, the user should make some reasonable assumptions and choose a bunch of algorithms expected to work fine for the specific problem under study, and eventually compare them to choose the best performer. The hold-out test set metrics could be used to contrast various ML models in order to select the best one. Nonetheless, since the definition of the specific form of a ML model is often characterized by a wide choice of hyperparameters a priori, it may be preferable to automatize the comparisons among different models whilst considering their hyperparameter tuning directly embedded along the training phase. It is worth reminding that a hyperparameter is a parameter controlling the learning algorithm and not the model itself, despite they characterize the exact form of the ML model [43]. Therefore, the training process optimizes the parameters of the model whilst the chosen hyperparameters are not changed because of the training procedure. Therefore, a further hold-out split with a usual size proportion of about 10% is performed within the training set only, thus separating a validation set used for the model selection purposes [43, 59, 60, 61]. Nevertheless, if the extracted validation set is too small, it can provide a noisy and non-representative estimate of the predictive performances [51]. Furthermore, training and evaluating the models always on the same validation set may bias the choice for the best performer, preferring the one which works better on that particular validation set only rather than the one with the maximum generalization capabilities [43]. Accordingly, the training set is divided into a number k of equally sized folds. Each fold then serves as a training set and validation set throughout a process known as k -fold cross-validation [55]. Therefore, the training set should be split into k equal subsets, and each fold was used for training and validation. Specifically, one fold is chosen as a validation set while the remaining $k - 1$ folds are used for training. It has

Table 1.1: Confusion matrix for a binary classification problem.

		Predicted Class	
		Positive (P) or class 1	Negative (N) or class 0
Actual Class	Positive (P) or class 1	True Positive (TP)	False Negative (FN)
	Negative (N) or class 0	False Positive (FP)	True Negative (TN)

been demonstrated in previous studies that the stratified cross-validation with 10 folds delivers smaller bias whilst limiting the variance even when computational capabilities virtually permit for more folds [62]. Anyway, this process leads to k different models constructed with different hyperparameters sets, and each one is trained on a distinct subset of data. The exploration of the hyperparameters possible values is denoted as hyperparameter tuning process. In contrast to the naive empirical trial-and-error hyperparameter exploration procedures, some systematic techniques have been developed in the last decades, such as e.g. the grid search method or the random search approach combined with cross-validation procedures [43, 42, 60, 61]. Classification metrics across the various folds are then collected and averaged to enable a fair comparison of such different ML models. In practice, the cross-validation procedure offers a means to compare entirely distinct ML models, thereby pinpointing the predictors that consistently deliver the best performance on average and exhibit robust responses across different segments of the training set [63]. Finally, afterward the training phase and the final evaluation on the hold-out test set, the final model can be deployed for the inference stage, also named as the recall phase, i.e. using the optimal model to deliver its predictions based on the learned knowledge for new incoming data.

Several evaluation metrics are used in ML context depending on the type of problem. According to Ferri et al. [64] nomenclature, evaluation metrics can be regrouped in three main categories: threshold, ranking, and probabilistic metrics. The foremost threshold metrics are used commonly with ML classifiers and they are based on a qualitative description of error, on which an acceptable threshold could be set to minimize the error. Focusing on a supervised binary classification problem, the most adopted way to inspect the results is through a confusion matrix which counts the number of actual predicted samples with respect to the actual labels ground truth, as reported in Tab. 1.1 [43, 61]. The classification error rate E_r can be computed as

$$E_r = \frac{FP + FN}{FP + FN + TP + TN}, \quad (1.3)$$

whereas the classification accuracy A_c can be computed as

$$A_c = \frac{TP + TN}{FP + FN + TP + TN} = 1 - E_r, \quad (1.4)$$

Out of the total classifications, accuracy reflects what percentage is truly positive. Accuracy has some well-known limitations when dealing with imbalanced datasets.

This is because high accuracy values are achieved when the classifier is completely biased toward the majority class. Therefore, the true positive rate TP_r and false negative rate FN_r are preferred when dealing with imbalance classification problems, i.e.

$$TP_r = \frac{TP}{FP + TN}, \quad (1.5)$$

$$FN_r = \frac{TP}{FN + TP}, \quad (1.6)$$

Similar definition can be obtained for the TN_r , which is also called specificity.

Moreover, the precision and recall metrics have been considered associated with the confusion matrices of the current trained models. The precision estimates the number of samples that were correctly classified in a certain class over the total number of samples which have been truly associated with that class

$$P = \frac{TP}{TP + TN}, \quad (1.7)$$

whereas, the recall metric, or even known as sensitivity, indicates the number of samples correctly associated with a certain class over the number of samples which actually truly belongs to that class

$$R = \frac{TP}{TP + FN}. \quad (1.8)$$

Recall gives the true positive rate. This is typically used to measure the coverage of the minority class of major interest in imbalanced learning problems. The F1-score represents a sort of harmonic mean of precision and recall metrics, therefore it is widely used as a synthetic evaluation metric of the performances

$$\text{F1-score} = \frac{2}{\frac{1}{P} + \frac{1}{R}} = \frac{2 \cdot P \cdot R}{P + R}, \quad (1.9)$$

and its generalization is also known as $F\beta$ -score or F-measure

$$F\beta\text{-score} = \frac{(1 + \beta^2) \cdot P \cdot R}{\beta^2 P + R}. \quad (1.10)$$

For handling with imbalanced datasets [56, 57], the balanced accuracy computes the average of the percentage of positive and negative class instances correctly classified, representing i.e. the average of the recall of the majority and minority classes. This is commonly recognized as one of best metrics to synthesize the classification performance over both classes in terms of recall values.

The ranking metrics are the second category of metrics according to Ferri et al. [64], and they are based on how well the model ranks the examples. The receiver

operating characteristic (ROC) curve is a positive-slope diagnostic graph used to evaluate the performance of a classifier based on FP_r reported on the abscissa and TP_r reported on the ordinate axis. The ROC curve is computed by shifting the decision threshold of the classifier, thus evaluating the models at different error rates, delivering the proportions of instances correctly classified for a given false positive rate (FP_r). Each model evaluated at different thresholds represents a single point on the ROC graph. The main diagonal bisector line represents the no-skill classifier, i.e. a classifier that provides a complete random guess on the resulting prediction. Any point below the no-skill classifier performs worse than a random guess. Instead, the perfect classifier would lie on the left upper corner of the graph, i.e. when $TP_r = 1$ and $FP_r = 0$. The area under the receiver operating characteristic curve (AUC-ROC) is the ranking metric resulting from computing the area under the curve, whose ideal value is 1. A specular alternative to the ROC curve is the negative-slope precision-recall curve (PRC), especially useful for imbalance learning problems. The PRC is constructed computing precision obtained for various degree of recall [56, 57]. This diagnostic graph explores the trade-off between the well classified positive examples and the number of misclassified negative ones. The slope of PRC is negative since P decrease as R increase. In this case, the no-skill classifier is represented by an horizontal line whose precision corresponds to the positive class proportion over the entire dataset. For a balance dataset it would be 0.5. In this case, the perfect classifier is represented by the upper right corner of the graph, i.e. when $P = 1$ and $R = 1$. Even in this case, a quantitative metric is represented by the area under the curve (AUC-PRC).

The probabilistic metrics are the third typology of metrics according to Ferri et al. [64], specifically designed to quantify the uncertainty in the predictions of a classifier. For instance, the mean absolute error (MAE) is the average absolute deviation between between paired predictions \hat{y}_i and ground truth observations y_i ,

$$\text{MAE} = \frac{1}{n} \sum_{i=1}^n |\hat{y}_i - y_i|, \quad (1.11)$$

in which n is the number of samples in the test set. In practice, MAE measures the distance between two vectors corresponding to the $L1$ -norm, also denoted as $\|\bullet\|_1$, and even named Manhattan norm [43]. The mean squared error (MSE), also known as Brier score [64], is the squared version of MAE, i.e.

$$\text{MSE} = \frac{1}{n} \sum_{i=1}^n (\hat{y}_i - y_i)^2, \quad (1.12)$$

The root mean squared error (RMSE) corresponds to the Euclidean norm, the typical notion of distance, denoted as $L2$ -norm or $\|\bullet\|_2$. MAE and MSE could be considered a probability metrics when the predictions probabilities are compared with the true probabilities [64]. The most widespread probability metrics is the

cross-entropy or also named negative log likelihood (LogLoss) which measures the difference between two probability distributions. For a binary classification problems it is given by

$$H(\mathbf{y}, \hat{\mathbf{y}}) = \text{LogL} = -\frac{1}{n} \left[\sum_{i=1}^n y_i \cdot \log(\hat{y}_i) + (1 - y_i) \cdot \log(1 - \hat{y}_i) \right]. \quad (1.13)$$

MAE, MSE, and RMSE are typically employed to evaluate regression problems. Moreover, besides all the traditional statistical diagnostic tools such as the residual graphs, the classical indicator of goodness of fit, i.e. the coefficient of determination \mathcal{R}^2 , is also typically employed with regression problems.

Overgeneralization represents a pitfall that has to be carefully checked and controlled. Technically speaking, the overfitting problem occurs when a selected model performs outstandingly on the training set, but it dramatically fails in generalization over hold-out test samples [43, 42]. The overfitting issue may appear due to the adoption of an excessively complex model, i.e. with a high number of parameters, relative to a noisy and small training set [43]. Indeed, it may happen that the noise level will contribute mostly to the learning process, hiding the real information carried on by the data, thus losing sight of the real learning goal. In other words, the overfitting issue arises when prediction errors exhibit low bias on training data but with a high variance with test data, [42]. The term bias indicates the non-negative squared difference between the target average output and the algorithm average output, whereas variance is a non-negative quantity that measures the predictions' variability concerning the targets [65]. In other words, the bias can be attributed to that part of generalization error due to wrong assumptions, whereas variance indicates if the model is highly susceptible to small variations in training data [43]. The curse of dimensionality may be another cause for overfitting, i.e. arising when training set have a huge number of features with respect to the number of available samples [43]. Besides gathering more training data which is often costly or even impossible, a viable option to mitigate overfitting issues is to constrain the model parameters' values. This method is denoted as regularization and it works by imposing certain hyperparameters directly to govern and limit the level of complexity of the model. On the contrary, the underfitting problem arises when an excessively simple model is used to learn the actual hidden patterns underlined by training data [43]. In other terms, underfitting arises when training samples are characterized by a high bias and the test predictions exhibit a low variance around the biased target [42]. The optimal model complexity should be obtained by minimizing the validation error, i.e. characterized by the best tradeoff between the prediction bias and variance, a condition known as bias-variance tradeoff [42, 65].

The training phase of a ML model involves solving a minimization problem for a learning cost function to find the best fitting parameters for the available training set [43]. Several optimization problems have been formalized in mathematics in the

last century, specifically within the Operation Research fields. The mathematical programming methods involve a set of design variables even subjected to a number of constraints. The stochastic method involves problems with a set of random variables with known probability distribution. Statistical methods involve experimental data analysis in order to create empirical models of which laws best represent the data. The classical optimization approaches are usually related to gradient-based or mathematical methods. They are called classical methods to distinguish them with respect to the modern meta-heuristic approaches and because they are mathematically “well-posed” methods. Despite an example of a closed-form learning cost function that could be represented by the least square method for linear regression problems, in the ML area it is typical to employ iterative optimization methods. The gradient descent algorithm is a classical optimization algorithm that measures the local gradients of the cost function for a certain model’s parameters vector and finds the negative steepest direction in which adjusting parameters in the next iteration to progressively minimize the learning cost function [43]. For a supervised ML problem, a simple example of cost function $J(\mathbf{w})$ could be the sum of squared errors (SSE) [61], being \mathbf{w} the m parameters of the model,

$$J(\mathbf{w}) = \frac{1}{2} \sum_{i=1}^n (y_i - \hat{y}_i)^2, \quad (1.14)$$

in which n is the number of training data. The gradient descent algorithm involves computing the gradient $\nabla J(\mathbf{w})$ at iteration j to update the weights at the next $(j + 1)$ -th iteration with the following update rule:

$$\mathbf{w}_{(j+1)} = \mathbf{w}_{(j)} + \Delta \mathbf{w} = \mathbf{w}_{(j)} - \eta \frac{\partial J(\mathbf{w})}{\partial \mathbf{w}} = \mathbf{w}_{(j)} - \eta \nabla J(\mathbf{w}), \quad (1.15)$$

$$\nabla J(\mathbf{w}) = \begin{bmatrix} \frac{\partial}{\partial w_0} J(\mathbf{w}) \\ \frac{\partial}{\partial w_1} J(\mathbf{w}) \\ \vdots \\ \frac{\partial}{\partial w_m} J(\mathbf{w}) \end{bmatrix}_{\{\mathbf{x}, \mathbf{y}\}_{\text{train}}}. \quad (1.16)$$

In the update rule in Eq. (1.15), the learning rate η is the key parameter of the gradient descent algorithm. It is crucial to properly tune this hyperparameter because it directly governs the size of update steps among the iterations. When the learning rate is excessively large, the algorithm will jump around the optimal set of parameters never reaching the real global optimum, whereas, conversely, if it is extremely small, the algorithm will require a huge amount of iterations to reach convergence [43, 61]. If the cost function is a convex function, this mathematically ensures the existence and uniqueness of a global minimum, and the gradient descent method is theoretically proven to always approach, sooner or later, the global minimum [43]. The above equations denote the so-called batch gradient descent or

full gradient descent algorithm, since the derivatives computed in Eq. (1.16) are evaluated over the whole training set at every iteration step. Nonetheless, since this method could be very slow, especially with large datasets, the stochastic gradient descent (SDG) method has been proposed. To overcome this limitation, it randomly selects only a single training sample (e.g. for online learning) or a small subset of samples (mini-batch gradient descent) at every step to compute gradients [43, 61]. However, the training process would be noisier because only a few pieces of information are used to update weights at every step. On the other hand, this method allows out-of-core learning for limited machine memory and huge datasets. Furthermore, SDG is preferred when dealing with irregular cost functions, since its randomness nature naturally aids the algorithm to avoid being stacked and entrapped into local minima. By convention, to not entrust only in a single instance, SDG algorithm is run with a round of various iterations, and each round is called an epoch [43]. Moreover, the training set should be composed of independent and identically distributed instances to ensure that SDG pushes parameters toward the global optimum. To approach this condition, it is advisable to perform a shuffling of the training set at every epoch. SDG has an indirect effect of regularization. In fact, despite it perform worse on training set than classical gradient descent, it often provide comparable or even better performance on test set [60]. In mini-batch SDG, the algorithm accounts for a batch $B = \{j_1, \dots, j_m\}$ of training points for the ML parameters update, providing a good trade-off among stability and speed of the algorithm [60],

$$\mathbf{w}_{(j+1)} = \mathbf{w}_{(j)} + \Delta \mathbf{w} = \mathbf{w}_{(j)} - \eta \sum_{i \in B} \frac{\partial J(\mathbf{w})|_{x_i}}{\partial \mathbf{w}} \quad (1.17)$$

To further optimize the algorithm, the learning rate can be adapted during iterations, enhancing exploration of the parameters' space at the beginning of the algorithm whilst improving local exploitation approaching the optimum. Therefore, the learning schedule is a function that adaptively adjusts the learning rate, similar to what happens in meta-heuristic algorithms [46].

As previously stated, due to the “No free lunch theorem”, the user has to select a number of ML classifiers in order to be quite confident of the choice of the best-performing model. Every ML algorithm comes with its own set of advantages and disadvantages, and it is not possible to know a priori how it will perform. Therefore, when working with ML, it is always extremely important to train and compare different models and not only entrust a uniquely individual learner. Fig. 1.10, illustrates some of the most widely adopted ML techniques. In brief, some of the most widely adopted classifiers are the following:

- *K*-nearest neighbors (KNN) [66]: it is a supervised ML algorithm that classifies data points based on the majority class among their *K*-nearest neighbours.

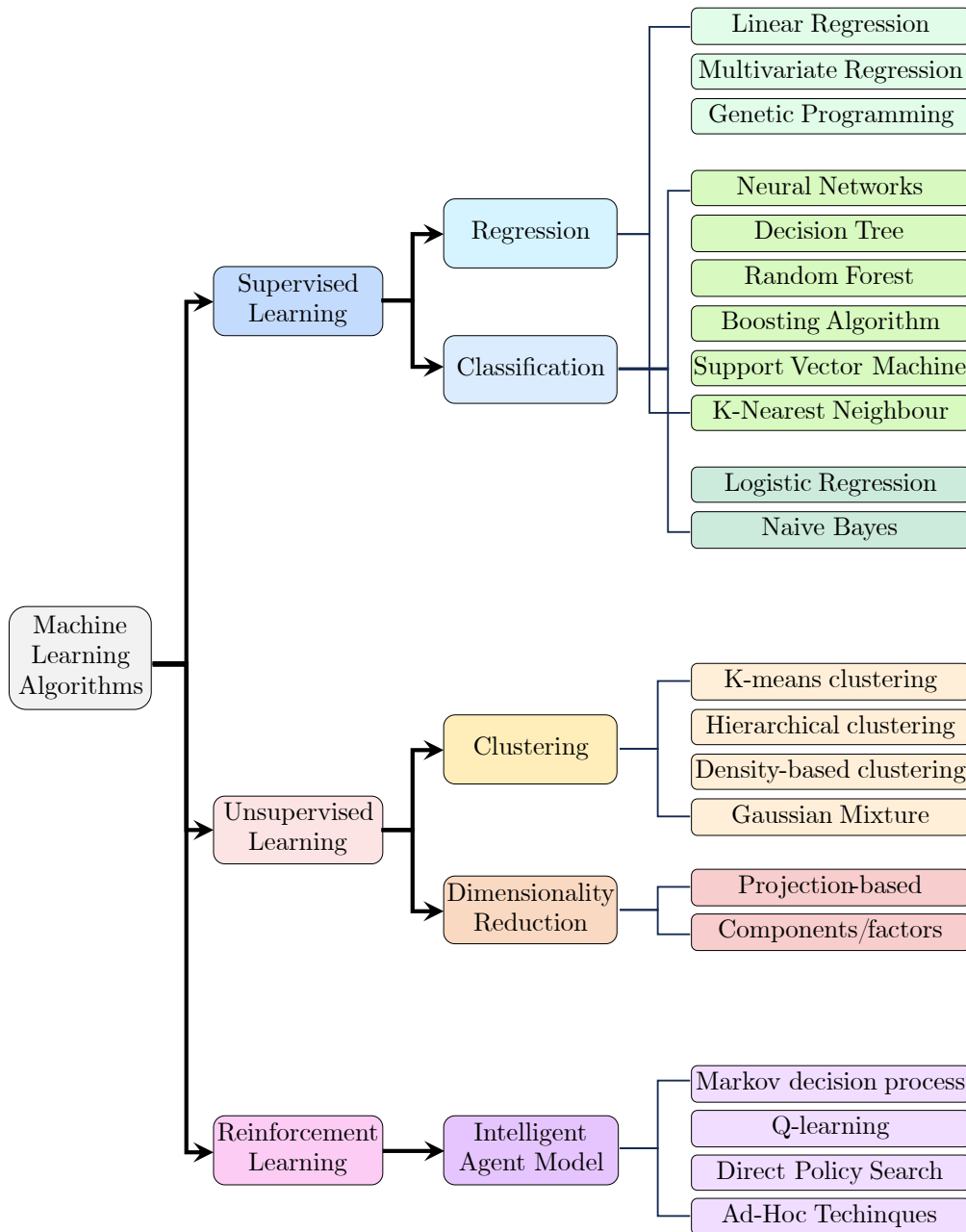


Figure 1.10: List of some ML algorithms according to the learning methods.

- Linear support vector machine (Linear SVM) [67]: it is a classification algorithm that finds a hyperplane that separates data into different classes. It is especially effective for linearly separable datasets.

- Radial basis function support vector machine (RBF SVM) [68]: it is a variant of the corresponding linear version that implements a radial basis function kernel to handle non-linearly separable data. It maps data to a higher-dimensional space in such a way to improve the separation among the classes.
- Decision tree (DT) [69]: it is a supervised algorithm in which the learning process implements a divide-and-conquer strategy by conducting a greedy search that identifies the optimal split points within a tree.
- Random forest (RF) [70]: it is an ensemble learning method that combines multiple decision trees to improve predictive accuracy and to reduce overfitting.
- Neural network (Neural Net) [71, 45]: they consist of layers of interconnected nodes (neurons) that mimic how the human brain works.
- Adaptive boosting (AdaBoost) [72]: it is an ensemble learning method that combines weak classifiers to create a strong classifier. It focuses on improving the classification of difficult-to-classify examples.
- Naive Bayes [73]: it is a probabilistic classification algorithm based on Bayes' theorem where the features are assumed to be conditionally independent each other.
- Quadratic discriminant analysis (QDA) [51]: it is a classification method that models the distribution of each class as a quadratic shape. It's a more flexible variant of the corresponding linear version and is especially suitable when the classes have different covariance matrices.
- Logistic regression (LR) [74, 51]: it is a supervised statistical-based method in which the posterior probability of one class is formulated as a logistic sigmoid function taking as argument a linear function of the features. Contrary to its name, the LR is a classification model born for binary classification tasks.
- Linear discriminant analysis (LDA) [75]: it is an analytical closed-form classifier that does not require any hyperparameter tuning. It represents a generalization of Fisher's linear discriminant method [51], and it aims to find a linear combination of features to linearly separate classes in a classification scheme.

Instead, the unsupervised learning techniques also deserve special attention since the vast majority of data are unlabeled. One of the most widespread methods is represented by clustering techniques [43]. Formally, the clustering analysis aims to group a dataset $\mathcal{D} = \{\mathbf{x}_1, \mathbf{x}_2, \dots, \mathbf{x}_n\}$ into k disjoint subsets denoted by C_1, C_2, \dots, C_k [76]. All samples are assigned to a finite number of groups, similarly

to a classification task, but this time in an unsupervised manner, i.e. identifying instances that are similar enough to be grouped together and simultaneously being sufficiently different from other groups. Practically speaking, based on some similarity metrics, the main idea is to minimize intra-cluster distances among similar samples, whereas maximizing inter-cluster distances among different groups [77]. Different types of clusters can be formalized. Hard or categorical clustering is the process of producing exhaustive clusters in which every sample belongs to one and only one cluster, and conversely, it is denoted as soft clustering when samples are associated with clusters with a certain degree of membership. K-means is an example of a hard clustering algorithm, whereas mixture modes are an example paradigm of soft clustering [76]. Both hard and soft clustering are also denoted as partitioning or flat clustering to distinguish them from hierarchical clustering. This latter produces a set of nested clusters organized in a hierarchical tree, also known as dendrogram [78], in a way that clusters can be regrouped into finer partitions of lower level or into super-clusters at higher levels [76]. The term relational or similarity-based clustering arises when data are organized in a way to establish pairwise relationships between data points instead of the traditional vector of features. Alternative distinctions among clustering methods can be stated according to the clustering criterion [76]. Probabilistic model-based clustering involves techniques to describe the distribution of data, such as finite mixture approaches or nonparametric Bayesian approaches. On the other hand, cost-based clustering methods minimize a cost function, and a further subdivision can be performed according to centroid-based algorithms, such as K-means, or spectral clustering which analyzes similarity metrics among data. A further distinction can be obtained considering between parametric and nonparametric clustering techniques.

Among unsupervised learning techniques, some of them are often used in the feature engineering phase, i.e. the dimensionality reduction techniques for the feature space. Two main approaches prevail within dimensionality reduction techniques [43]. The foremost are denoted as projection techniques since the training instances originally belonging to a high-dimensional space are projected toward a lower-dimensional subspace. The second branch is represented by manifold learning, meaning that a d -dimensional manifold is a portion of an n -dimensional space that locally can be assumed as a d -dimensional hyperplane, with $d < n$. Based on often observed empirically manifold hypothesis, the process of modeling the training space through manifolds is known as manifold learning. The principal component analysis (PCA) is the most famous dimensionality reduction projection method that aims at reducing the number of feature dimensions while preserving as much valuable information as possible while still able to describe the dataset with a controlled information loss [66, 79, 80]. Since the entropy is a measure of the information content, the basic assumption of PCA is that the total variance of the dataset is not explained equally by all dimensions of the dataset. Thus, through a singular value decomposition (SVD) of the dataset matrix, this latter

is projected with a linear transformation onto the eigenvector space [79, 80]. If some components have low variance, it is possible to truncate the SVD at a lower dimension delivering a projection onto a reduced subspace without a detrimental information loss. In order to contain the information loss associated with the dimensionality reduction, it is advisable to select a proper number of components providing a sufficient explained variance ratio (EVR). The EVR is the ratio of the variance explained by the single component over the total variance [79]. To further speed up the traditional PCA some alternatives have been formulated, e.g. the randomized PCA which reduced the computational complexity, or the incremental PCA which permitted using a mini-batch approach avoiding heavy computation using the whole dataset [42]. Alongside those linear projection techniques, many other nonlinear projection methods exist, such as the kernel PCA, the locally linear embedding (LLE), random projections, multidimensional scaling (MDS), isomap, t-distributed stochastic neighbor embedding (t-SNE), and linear discriminant analysis (LDA) [42].

According to Tapeh and Naser’s literature review [41], the most adopted AI-based algorithms within structural engineering studies are the artificial neural network, the genetic algorithm, the genetic programming, and the support vector machine, respectively. The first two appear in about 56% of the over 4000 research records of the last decade. This witnessed the still relevant and topical study subjects of SHM and structural optimization. Moreover, this underlined the large versatility of neural networks and genetic algorithms applicable for a wide range of problems, and even their well-established and mature development, often preferred over other black box solutions. The dataset size dimension in the structural engineering field exhibited remarkable variability. The majority of studies worked with a number of 100-300 instances, but there are also some sporadic studies dealing with over 10,000 samples [41]. This fact highlights the common difficulties experienced within Civil Engineering of acquiring sufficient high-quality data sources for properly training and tuning heavy and sophisticated ML models, thus forcing researchers to foster simple models or other statistical-based alternatives rather than testing the innovative and latest ML trends. Therefore, the scarce availability of open-access data for specialist structural engineering applications, jointly with missing AI code sharing, strongly limits the possibility of a fair comparison among similar studies based on shared validated benchmarks [41]. This challenge should be addressed as a priority in the next future to project AI-based structural engineering research toward a more transparent, ethical, and reproducible scenario. Indeed, a greater understanding of actual underlining physical and mechanical mechanisms, jointly with a clearer ML model interpretation which aid a deeper exploration and new insights, must be favored in AI-based structural engineering research field rather than embracing the “chased accuracy” culture, often unveiled in many nowadays AI-related studies [41].

1.2.2 Deep learning subfield

Despite the early origins of neural networks dating back to the 1940s, they were rediscovered in the 1990s, only when available technologies were able to satisfy the computational efforts required [81]. Many deep learning architectures were developed over years to cope with different demands in all aspects of human life which arises due to the astoundingly beginning of the digital revolution and artificial intelligence or information age [82, 83]. Considering the Scopus' literature search service, according to the search query "Deep Learning" and "Structural Health Monitoring" extended to all bibliographic fields, about 4000 documents have been found in total. Fig. 1.11 (a) illustrates how the research topic started to gain interest from 2012 and it is still nowadays a vibrant research area. Indeed, nowadays, the actual research level lies in the growing branch of this curve and it seems to exhibit an exponential growth with a very sharp slope, demonstrating that the research level is only at the beginning. This fact motivates the aim of the current study, i.e. it attempts to outline and critically discuss the adoption of the most recent DL techniques in SHM with a particular focus on civil engineering structures, emphasizing the pro and cons of the various techniques. Further mining the Scopus search results with the above-mentioned query, as depicted in Fig. 1.11 (b) the majority of the studies belongs to the Engineering field (about 35%), highlighting the wide range of successful DL applications to SHM. In the second place, the Computer Science field appears (about 20%) illustrating how the machine learning and deep learning architectures are still under development with everyday improvements to deliver more reliable models, with hopefully less computational efforts. This second place points out how the above two main sectors are nowadays strongly interconnected, with fruitful competencies exchange for the great aim to provide future smart structures and infrastructures, more reliable and safe. Most of the considered studies are journal articles (about 73%), whereas about 17% are conference papers and only the 7.6% is related to review papers, which indicates still few works to exhaustively catalog and discuss the most recent developments. Still focusing on the above-mentioned search query results, considering the Pareto chart illustrated in Fig. 1.12, it is possible to show that China appears to be the most prolific country which investigated DL applied to SHM (about 1652 published documents), followed by the USA (about 852 documents). Setting the limit of interest to 80% of the cumulative frequency value, the actual most active countries which riding high in that topic are 16 countries, in which Italy is placed at the 7th.

The deep learning subject represents a subpart of ML as illustrated in Fig. 1.7, standing out by the adoption of artificial neural networks (ANN) and its derivative architectures as learning models. The origins of ANN date back to early studies in Neuroscience and Biology (neurobiology) around the 1940s aimed to physiologically explain how the human brain and neurological system works [45]. In 1943, the

neurophysiologist McCulloch and the mathematician Pitts [83] described the first functional schema of human neuron cell, acquiring the name of McCulloch-Pitts (MCP) neuron [61]. As illustrated in Fig. 1.13, a biological neuron is an elongated-shaped cell composed of a cell body nucleus surrounded by branches called dendrites with a longer peripheral part protected by a myelin sheath denoted as the axon. This latter ends up with final branching extensions named telodentria with a micro-structure terminations denoted as synaptic terminals. Neuronal activity is provoked by electrical signals or chemical processes generally called synapses, which represent how stimuli and communication occur among neurons. Specifically, input signals coming from other neurons through synapses are captured toward dendrites and transferred to the cell nucleus to be processed. Afterwards, action potential signals, i.e. short electrical impulses, travel through axons reaching the neurotransmitters [43]. When the cumulated stimuli overcome a certain threshold in the axon terminals, the neuron is activated, meaning that new synapses are fired toward

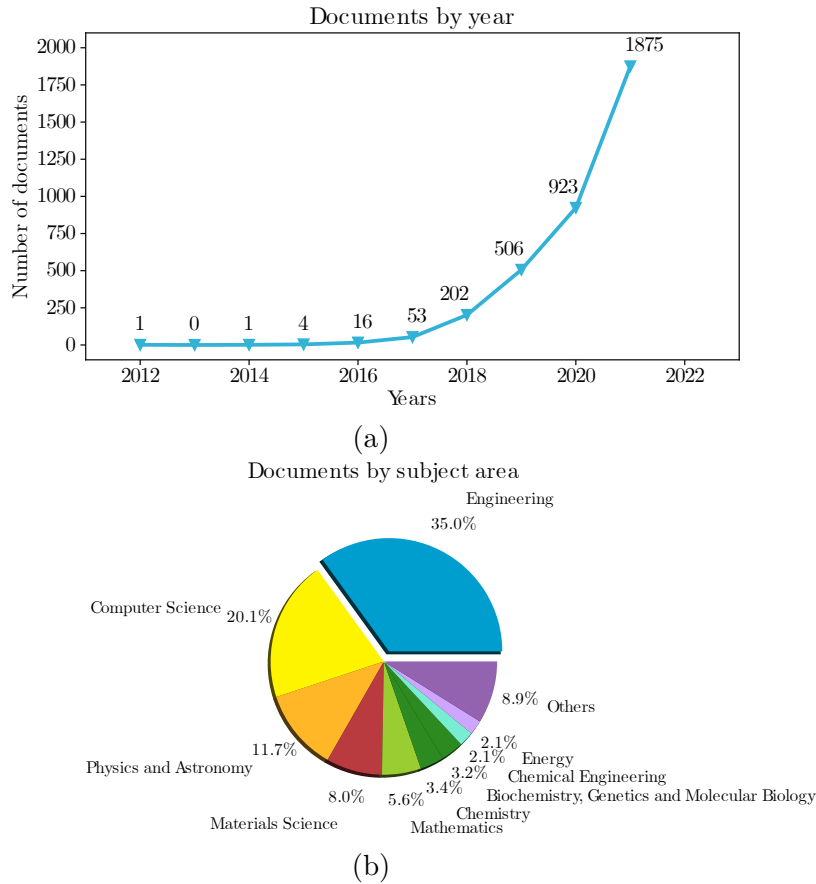


Figure 1.11: Number of documents published from 2012 until 2021 (a) and Pie chart of the main area of recent years studies (b). Data retrieved from Scopus search service with query “Deep Learning” and “Structural Health Monitoring”.

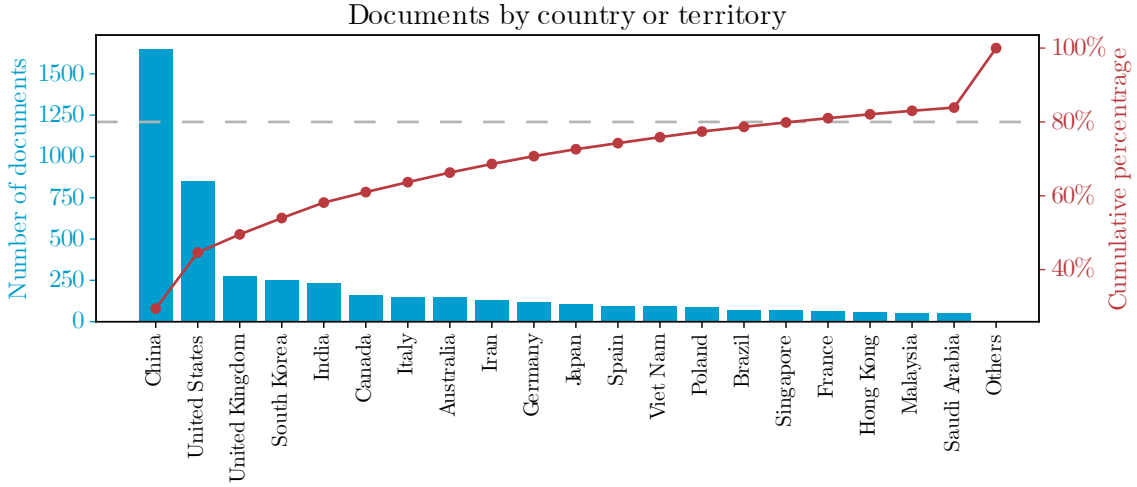


Figure 1.12: Pareto chart of the number of documents published on Scopus related to the most active countries, with a limit placed to 80% of the cumulative frequency. Data retrieved from Scopus search service with query “Deep Learning” and “Structural Health Monitoring” from year 2012 until 2021.

subsequent neurons. On the contrary, the neuron cell will inhibit the received stimuli without activating any synapses toward other neurons [83, 45]. MCP neuron’s mechanism evidences a one-way direction of information flow transmission. Moreover, it represented the strong basis of further neurocomputing studies, since it was employed to solve logical propositions. In 1957, Rosenblatt [82] introduced for the first time the perceptron, also denoted as threshold logic unit or linear threshold unit, i.e. the first artificial neuron considered as an information processing unit [43]. An illustration of the Rosenblatt model is reported in Fig. 1.13. In Rosenblatt’s perceptron rule, both input and output values are numerical values. The perceptron computes a weighted sum of input data \mathbf{x} , from all n input synapses, combined with learnable synaptic weights \mathbf{w} . Then, to evaluate if neuron is active or not, the perceptron output z is given by a nonlinear activation function $\phi(\bullet)$ evaluated on the previous linear combination. Specifically, in original Rosenblatt’s rule the activation function was the Heaviside or step function $H(\bullet)$, thus limiting the neuron output being only an hard class threshold ± 1 , i.e.

$$\phi(a) = H(a) = \begin{cases} 0 & \text{if } a < 0, \\ 1 & \text{otherwise.} \end{cases} \quad (1.18)$$

From a mathematical standpoint, in order to consider also possible constant values in the linear combination, a first weight w_0 , is normally incorporated with a fictitious unitary input $x_0 = 1$. This introduces a bias neuron representing the

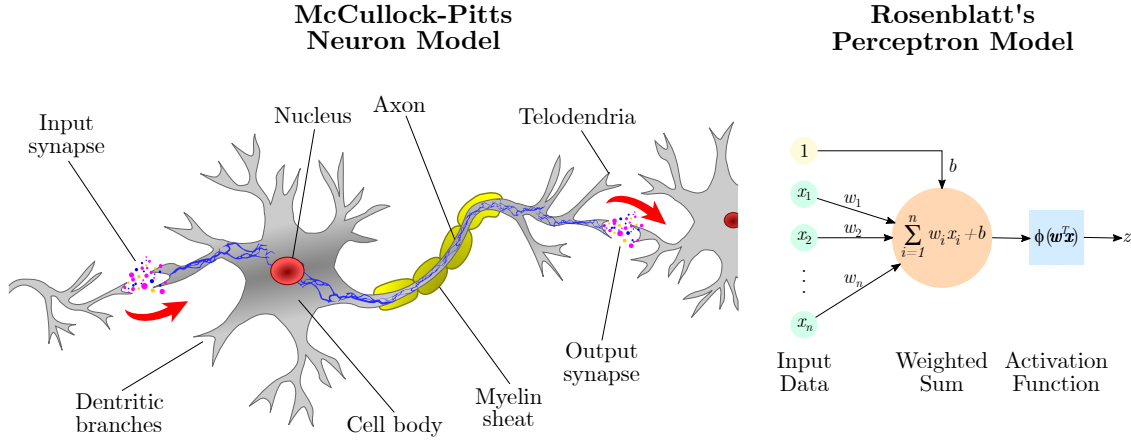


Figure 1.13: MCP neuron model and Rosenblatt’s perceptron model.

invariant part of the prediction, and w_0 is called bias b [60]. The perceptron input-output relationship can be formalized as follows [43, 45, 61]:

$$z = \phi(\mathbf{w}^T \mathbf{x}) = \phi \left(\sum_{i=0}^n w_i \cdot x_i \right) = \phi \left(\sum_{i=1}^n w_i \cdot x_i + b \right). \quad (1.19)$$

The training process of an ANN aims to find the best set of synaptic weights, following the update rule presented in Eq. (1.15). However, in original Rosenblatt neuron, the optimization was done heuristically by minimizing the number of misclassifications, e.g. considering a least square loss function [60]. Moreover, a single Rosenblatt neuron acts as a simple linear binary classifier, i.e. with linear decision boundary (similarly to logistic regression or decision tree algorithms). In fact, given a linearly separable dataset of observations, when the output is positive the sample will belong to a positive class, otherwise, it belongs to the negative class. Therefore, the Rosenblatt neuron was unable to solve even simple but slightly complex problems such as the “exclusive logical or” (XOR) classification tasks [43, 61]. To overcome this strong limitation and tackling more sophisticated problems, the multiple-layer perceptron (MLP) computational graph model has been formalized by stacking several perceptrons together, actually giving rise to the advent of deep learning field. In MLP, the computing units are arranged in various layers, viz. an initial input layer, a final output layer, and an arbitrary number of intermediate layers denoted as hidden layers [43, 61]. The number of hidden layers used defines the depth of an ANN [61]. The various neurons of each single layer are fully connected with all the other neurons in the immediately following layer, hence the name of feed-forward neural network (FNN). Within the DL field, an ANN is denoted shallow neural network when it presents one or two hidden layers, whereas it is a deep network when more hidden layers are configured. Dataset fed the ANN by the input layer, whose number of units is equal to the number of features. However,

these dummy neurons have no learnable weight associated since they only act to transmit data features to the subsequent computing layers. Layers spatially close to the input layer are described as lower layers, whereas on the opposite they are denoted as upper layers. The various k hidden layers fulfil the role of providing recursive non-linear transformations of the input features [84]. The output of the first hidden layer can be expressed as

$$\mathbf{h}_1 = \Phi(\mathbf{w}_1^T \mathbf{x}). \quad (1.20)$$

being \mathbf{w}_1 the weight connections vector of the first hidden layer, whereas the output of the i -th layer is accordingly given by

$$\mathbf{h}_i = \Phi(\mathbf{w}_i^T \mathbf{h}_{i-1}). \quad (1.21)$$

The results of the output layer \mathbf{o} can be expressed as

$$\mathbf{o} = \Phi(\mathbf{w}_{k+1}^T \mathbf{h}_k). \quad (1.22)$$

The success of MLP layer-wise architecture and also the subsequent unstoppable overwhelming improvements in the DL field owe their origins to the groundbreaking enhancement in the ANN training algorithm, which is still adopted nowadays. Indeed, in 1985, Rumelhart et al. [85] illustrated the backpropagation method to effectively optimize DL architectures. In practice, it is based on a two-step version of the gradient descent algorithm. Foremost, using the initial randomly initialized weights, the input data are transmitted into the network with the feed-forward approach until reaching the output layer and computing the loss or error function. It is crucial to initialize weights randomly to break the symmetry and avoiding that the entire layer behaves like a single unit [43]. Afterward, a backpropagation algorithm computes gradients based on the network's final error with a backward chain-rule process, i.e. with successive derivatives, until reaching the input layer. In this way, with the second backward passage, it is possible to quantify the actual contribution of each single weight connection to the final computed loss, and therefore adopting the above gradient descent parameter update rule at the end of every training epoch, see Eq. (1.15). This process also known as reverse-mode automatic differentiation, or reverse-mode autodiff, is particularly efficient when dealing with few outputs, in this case one single loss function, and many variables, i.e. all the synaptic weights connections [43]. In summary, the training dataset is divided into mini-batches, and one at a time, is forward passed computing loss for every instance. Backward pass with chain rule computes all weights' contributions to the final loss function until reaching the input layer. Through those iterative steps, gradient descent algorithm trains the MLP architecture until convergence. In fact, any ANN can be seen as a mere computational graph that establishes the composition of simple functions, which can be simply unpacked with nested chain rule in

the backpropagation process [60]. For MLP trained with the backpropagation rule, different activation functions can be adopted to both avoid discontinuities in the first derivatives, such as in the Heaviside function, and further introduce a more powerful nonlinear capabilities. Common monotonic activation functions include [84, 60, 61, 86]:

- Linear (or identity) activation function: it is the identity function with domain and codomain \mathbb{R} , useful for regression tasks,

$$\phi(z) = z; \quad (1.23)$$

- Logistic sigmoid function: it is a regular, i.e. continuous and differentiable, S-shaped function with domain \mathbb{R} and codomain $[0,1]$,

$$\sigma(z) = \frac{1}{1 + e^{-z}}; \quad (1.24)$$

- Hyperbolic tangent function: it is a regular S-shaped function with domain \mathbb{R} and codomain $[-1,1]$, it is a scaled version of the logistic sigmoid function $\sigma(\bullet)$ from which it depends in turn, i.e.

$$\tanh(z) = 2 \cdot \sigma(2z) - 1 = \frac{e^z - e^{-z}}{e^z + e^{-z}}; \quad (1.25)$$

- Rectified Linear Unit (ReLU): it is continuous but not differentiable in the origin and its derivative is zero in the negative part of abscissa axis, however it is fast to compute and widespread used,

$$\text{ReLU}(z) = \max(0, z); \quad (1.26)$$

- Softmax function: it is a generalization of the logistic sigmoid function, it is adopted only in the output layer, and it allows computing probabilities of belonging to a certain i -th output class than the other m possible ones for classification problems,

$$\phi_s(z) = \frac{e^{z_i}}{\sum_{j=1}^m e^{z_j}}. \quad (1.27)$$

All units in the same layer use the same activation function [60]. A two-layer MLP can theoretically approximate any function if a sufficient number of hidden units are employed, however, like any ML model, overfitting and underfitting issues may arise. Furthermore, despite their great capacity and versatility, their inner complexity requires careful design to avoid any issues even when dealing with large datasets [60]. Overfitting can be fostered by a large number of parameters, in this case, a regularization can be useful to constrain the model using few non-zero

parameters. A possible approach is the Tikhonov regularization, which consists of applying a penalty to the loss function of the type $\lambda\|\mathbf{w}\|^2$, with $\lambda > 0$. This regularization directly affects the parameter update rule, acting as a sort of gradual forgetting typical of biological neural networks, which forget less important, i.e. noisy, patterns progressively [60]. Another form of regularization is the early stopping process, which restricts the parameter space, and consequently stops the gradient descent algorithm before reaching convergence. In practice, holding out a validation set from the training set, when the error on the validation set starts rising, the early stopping terminates the learning process [60]. Moreover, increasing the depth of a MLP rather than increasing the number of neurons for every layer acts as a sort of regularization, since features in the last upper layers depend on the already processed information provided by the initial lower layers (hierarchical features). Nonetheless, besides longer training time required, deep ANN presents new two opposite issues, i.e. the problem of vanishing or exploding gradients. In fact, the chain-rule local derivatives in backpropagation process can exponentially decay or increase with backward pass with very long path, causing an unstable parameter updating process, especially affecting the initial lower layers [60]. Therefore, it is worth reminding that any ANN is merely a repeated composition of certain types of functions, and this fact increase the ANN capacity of representation power to approximate any arbitrary function [60]. However, not any function can be used in ANN, in fact the above examples of activation functions have been carefully designed with certain properties to works efficiently in the DL field. For instance, a MLP with only linear activation functions it was demonstrated that it trivially reduces to a single-layer MLP performing a linear regression task [60]. This fact enforces the importance of using nonlinear activation functions, which ensure nonlinear mapping of data pointing toward desirable behaviors, for instance, that non-separable data become linearly separable in the hidden feature space [60]. In traditional optimization, the main problem is stacking in local sub-optima rather than converging toward global optimum [46]. The optimization of ANN is a strongly nonlinear problem with several local optima. However, this latter issue is of secondary importance than the nonlinearities issues which can often compromise the convergence of the entire training process. However, in the ANN field, a good choice is sometimes starting from sub-optimized networks using an approach denoted pretraining [60].

Besides traditional MLP architecture presented so far, it is possible to relax the definition of ANN referring to any computational graph. In fact, it is possible to consider unconventional architectures where inputs are fed directly to hidden layers and not only in the first input layer, or conversely, retrieving the loss computation at any hidden nodes, especially for regularization purposes. Skip or residual connections represent a clever unconventional ANN architecture stratagem introduced to speed up the training process. Considering a certain layer with a set of incoming input features, these features are duplicated and follow two different fork paths.

One path fed the layer which traditionally processes them delivering the output results. Instead, the other path, i.e. the residual connection, directly transfer input features to be combined with the layer's processed output. This was demonstrated as being extremely helpful during training, especially at the beginning of the learning process, because of acted as a sort of identity function. The unprocessed information helps to speed up the learning process even when the weights of the layers are close to zero, when instead normally this fact would slow down the backpropagation process due to the vanishing gradient [43, 59].

Starting from MLP, massive research efforts and relevant developments provided some types of ANN architectures which rapidly became widespread and a common standard nowadays in the DL field. The perceptron represented the basic building block to construct more sophisticated ANN, whose architectures have been specialized in recent years often starting from insights and reasoning on the type of data and the problem to address [60]. For instance, text in a sentence requires considering a certain degree of correlation between successive words, or, focusing on an image example, pixels in a certain neighborhood are correlated with each other. Digital images are grid-structured data with a reference system origin in the upper-left corner, with the ordinate axis downward and the abscissa axis rightward [87]. Every grid position stores an integer numerical value called a pixel, and the pixels' grid density level defines the resolution of an image. In practice, gray-scale images with an 8-bit encoding are matrices with pixel values between 0 to 255 corresponding to its brightness level representation, from black to white respectively. Instead, colored images are encoded as three-dimensional tensors, with the first two dimensions defining its resolution, and the third dimension equal to three, called depth or number of channels, related to the red-green-blue (RGB) color scheme representation. Again, with an 8-bit color depth, pixels vary between 0 to 255 for each color channel defining their intensity. RGB images are based on the additive property of color space, meaning that the 256 resulting shading for every color channel permits representing about 16 millions of possible colors [87]. Any computer interprets two images as distinct when their pixel representation is different, even though for the human eye the same object is depicted but e.g. shot from different points of view or with varying brightness levels, a property of image data called translation invariance [60]. Convolutional neural networks (CNNs), in the early beginning named neocognitron, were inspired by the neurobiology studies about the brain's visual cortex starting in the 1960s. However, they rapidly emerged in the computer vision field only in the 1980s-1990s gratefully to the technological and computational power improvements making their training feasible [43]. Around the 1960s, thanks to experiments for mapping the visual cortex activity of cats and monkeys [88], scientists discovered the concept of a receptive field of a neuron. In practice, many surface neurons tend to react only to visual stimuli that lie in a small region of the visual field. Moreover, their receptive field may have different

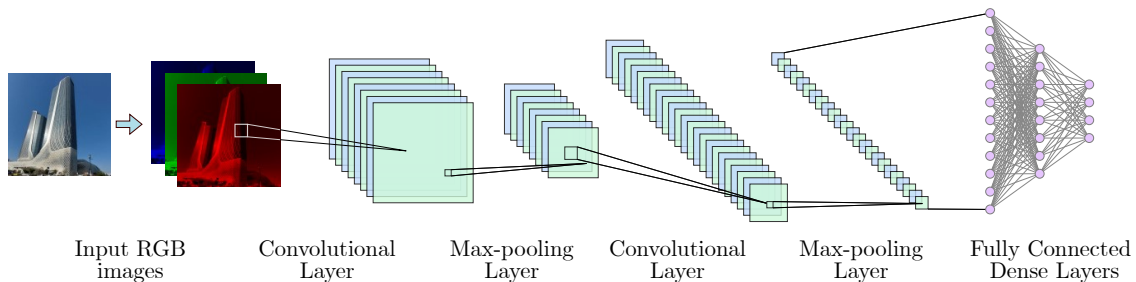


Figure 1.14: CNN example workflow.

sizes and tend to overlap each other in order to provide all together the total image in the visual field. Another biological-based insight was related to the specialized role of some neurons. For instance, some cells capture only horizontal lines, whereas some other else captures inclined lines, and so on. Furthermore, deeper neurons with larger receptive fields may capture complex patterns by combining patterns of specialized surface neurons with small receptive fields, thus evidencing a sort of hierarchy among visual cortex cells [43]. These neurobiological discoveries provided the basis for the development of CNNs, able to work with grid-structured or tensor-like datasets such as digital images. In general, as illustrated in Fig. 1.14, a CNN can be decomposed essentially into two parts: a first part acting as an automatic feature extractor essentially based on the convolution operation, and a second MLP-like part feed-forward dense final layers [61]. In the CNN context, every q -th layer can be represented as a three-dimensional tensor with height L_q , width B_q , and depth or number of channels d_q . The word depth is normally used to express the layer position q within the ANN, whereas the tensor third dimension d_q is preferably named as the number of channels. Without loss of generality, input images are located in the initial layer $q = 1$, typically characterized by the same L_1 and B_1 , and with depth equal to 3 or 1 for RGB or gray-scale images, respectively.

In the automatic feature extractor part, convolutional layers and pooling layers are two fundamental building blocks, firstly introduced in 1998 by Lecun et al. [89]. This initial part is demanded to provide a feature hierarchy from low-level feature patterns, such as capturing geometric primitives, vertical lines, horizontal lines, etc., to deliver high-level and more complex feature patterns in deeper layers, such as object shapes. Convolutional layers are designed to reproduce the receptive field concept of the visual cortex. In a convolutional layer, artificial neurons are conceived as a spatially arranged matrix to cover the input image spatial extension, in contrast to the vertical array deployment of MLPs' hidden layers. Since the number of neurons is considerably lower than the number of pixels in the image, the computational operations are characterized by relatively sparse connectivity [61]. Indeed, every unit is connected to the input image according to a certain receptive field area $F_q \times F_q \times d_q$, thus receiving information only from the patch of pixels of its competence $F_q \times F_q$ for all the input channels d_q . It is desirable

that neighboring neurons present some overlapping portions of their receptive field to reduce overfitting [60]. To control the level of overlap, a hyperparameter S_q denoted as stride can be defined, by default equal to 1 pixel. Therefore, the partially overlapped local receptive field regions dower the entire image, defining a certain number of neurons located in a spatially arranged matrix. Following the neural specialization to certain stimuli inspired by neurobiology studies, it is possible to think that an entire matrix of neurons shares the same set of weights denoted kernel or filter. In this way, every neuron focuses on a small part of the image, and according to their filter weights, they specialize to capture a specific pattern in that small region of interest. Every unit performs the convolution operation, i.e. the dot product between the monitored pixels patch and the related filter. To further inspect the input image for capturing a different pattern, a new matrix of neurons can be considered like before, but with a new filter, i.e. with a different set of weights. Therefore, in a convolutional layer, neurons can be conceptualized as a tensor with a number of channels equal to the number of filters n_F adopted. Typically, the number of adopted filters is a power of two [60]. Therefore, in general terms, the p -th filter in the q -th convolutional layer is a three-dimensional tensor $\mathbf{W}^{(p,q)} = [w_{i,j,k}^{(p,q)}]$, being i, j and k the height, width and depth of the filter, respectively. The convolution operation from the q -th convolutional layer to the next $(q + 1)$ -th one is formalized as the dot product of the p -th filter $F_q \times F_q \times d_q$ over the entire input image $\mathbf{H}^{(q)}$ repeated in every valid position (i, j) , i.e.

$$h_{i,j,p}^{(q+1)} = \sum_{r=1}^{F_q} \sum_{s=1}^{F_q} \sum_{k=1}^{d_q} w_{r,s,k}^{(p,q)} \cdot h_{i+r-1,j+s-1,k}^{(q)}, \quad (1.28)$$

where $\forall i \in \{1, \dots, L_q - F_q + 1\}$, $\forall j \in \{1, \dots, B_q - F_q + 1\}$, $\forall p \in \{1, \dots, d_{(q+1)}\}$, indicating the compound of all the dot products as a three-dimensional tensor $\mathbf{H}^{(q+1)} = [h_{i,j,p}^{(q+1)}]$ denoted as activation or feature map, the analog of hidden states in MLPs. It is noteworthy that, because of the duality between convolution and cross-correlation operations, the convolution operation is substantially a correlation operation in which the filter mask is rotated with a straight angle prior to the dot product, thus using a flipped kernel [90, 61]. The different feature maps produced by the adoption of n_F different filters are stacked in the output tensor, which will have a resulting number of channels $d_{(q+1)}$ equal to n_F . The feature maps actually represent pre-activation values which may undergo a one-to-one mapping through an activation layer. The most used one is the ReLU activation for its benefits affecting the training speed and accuracy. Therefore, the ReLU activation is usually performed instantly after the convolutional layer, often implicitly embedded in the convolutional layers' computational graph representations [60]. From a symmetrical perspective, the convolution operation can be interpreted as the procedure of placing the filter at each possible location on the image and computing the dot product. The total number of filter's possible spatial positions on the image,

i.e. consequently the number of neurons, is determined once the filter dimensions $F_q \times F_q \times d_q$ and the stride hyperparameter S_q have been fixed. The increase of the latter hyperparameter will reduce the granularity of the convolution operation, helpful when dealing with limited computing capacity machines. The output of the convolutional layer presents a reduced size than the input image, which is not desirable to avoid losing information at the border of the image. Therefore, in order to preserve the spatial input dimension in the resulting output volume, a half-padding may be introduced in the input image. This means that a lateral padding frame of entirely zero values of width $P_d = \lfloor (F_q - 1)/2 \rfloor$ is added to the original image, hence fictitiously increasing its size prior to the convolution operation. Another padding alternative is denoted full-padding, meaning that the $P_d = F_q - 1$ is used. In this way, the filter sticks out from the image in both directions leaving only $F_q - 1$ of both sides lying on the image in the first position, finally resulting in an increased output size [60]. This kind of increasing size “reversed convolution” is employed for autoencoders algorithm-type. On the other hand, a valid padding strategy means that no fictitious padding $P_d = 0$ is employed. Therefore, knowing the number of filters n_F used, the filters dimension $F_q \times F_q \times d_q$, the padding size P_q , and the stride hyperparameter S_q , the output volume from a convolutional layer will have an height $L_{(q+1)} = (L_q - F_q + 2 \cdot P_q) / S_q + 1$, a width $B_{(q+1)} = (B_q - F_q + 2 \cdot P_q) / S_q + 1$, and a number of channels equal to n_F . The number of learnable parameters n_W in a convolutional layer can be computed as

$$n_W = n_F \cdot (d_q \cdot F_q^2 + b), \quad (1.29)$$

in which b can be equal to 1 or 0 if accounting or not the presence of an external bias for every filter, likewise in MLP architectures. It is noteworthy that the above-defined convolution is characterized by the equivariance to translation property. This means that in order to capture a particular pattern or shape independently where it spatially is located in the image requires processing all the receptive fields in the same way. Indeed, this is done by sharing the weights of a certain filter to all the neurons which process singularly small portions of the image to capture that specific shape [60]. A schematic illustration of the working principles of the convolutional layers is depicted in Fig. 1.15. Specifically, an input RGB image is processed with two different 3x3 filters ($F_q = 3$), thus involving two layers of neurons with a sparse connection with the input image. Furthermore, pairwise neurons between the two layers share the same receptive field for all the channels of the input image. However, the two layers of neurons are characterized by two different sets of weights, which are shared among neurons belonging to the same layer. Every computational unit performs the convolution operation between the filter and its corresponding pixel patch, whose results are aggregated in the resulting feature map. In the specific example, one filter represents a possible weight set to specialize neurons in capturing horizontal lines in the input image, whereas the second filter captures better vertical edges. Because two filters have been used,

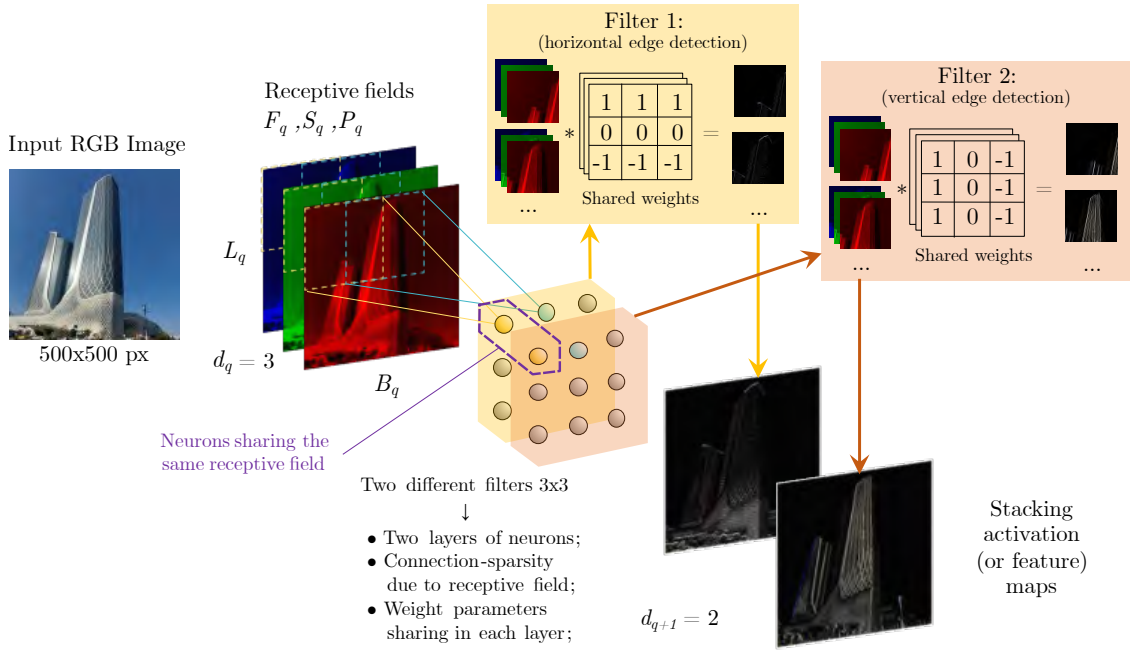


Figure 1.15: Illustration of convolutional layer working mechanism with two filters.

the output volume presents a stacking of two feature maps, i.e. with a number of channels $d_{(q+1)} = 2$. These resulting feature maps evidence the special role of the convolutional layer in performing an automatic feature extraction from the input image, since the filters are learned during the training process to automatically extract features of interest to address the problem under investigation. Moreover, it is worth observing that consecutive deeper convolutional layers will increase the global receptive field constructing a feature hierarchy. Every pixel of the feature maps in a layer $q + 1$ represents the results of neurons that already process a certain receptive field on the original image at layer q . Then, when a deeper convolutional layer $q + 1$ places new neurons with a new receptive field on the previous feature maps at layer $q + 1$, they are actually extracting new features leveraging information from an even larger receptive field on the original image q . Indeed, as shown in Fig. 1.16, despite three consecutive 3x3 filters being adopted on a 7x7 image, the global receptive field will increase from 3x3 to 5x5 and 7x7 respectively. As demonstrated in the example feature maps reported in Fig. 1.16, deeper convolutional layers will combine primitive features detected on small regions in early feature maps because of their enlarged global receptive field. In fact, two vertical or horizontal edge detection filters applied consequently highlight how the deeper feature maps will evidence longer detected vertical or horizontal lines.

The other building block of CNNs is represented by the pooling layer, at the early beginning defined as the sub-sampling layer. The pooling layer works on the activation map level by reducing the spatial volume in terms of height and width

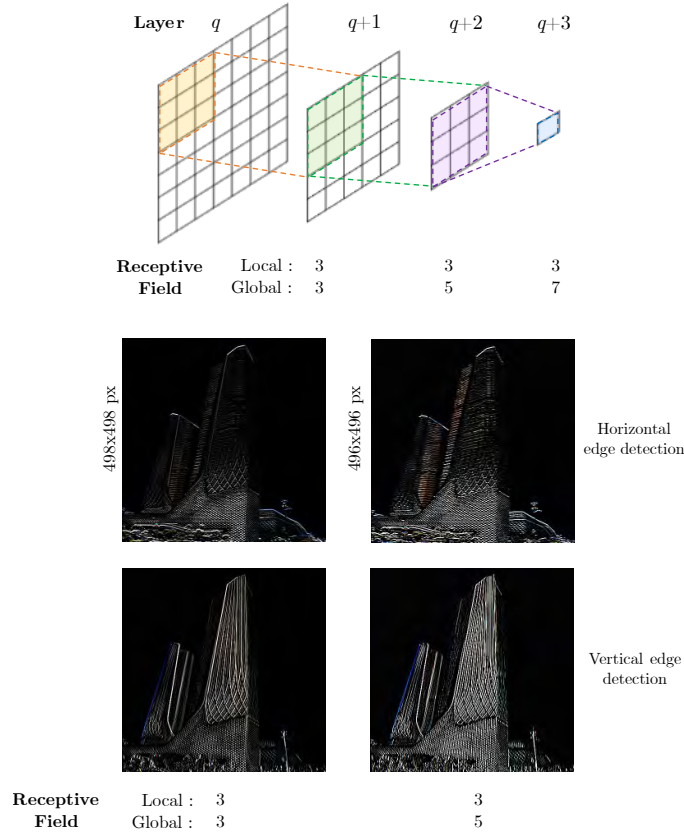


Figure 1.16: Global and local receptive field concepts, with an example of two consecutive applications of the filters showed in Fig. 1.15.

but preserving the starting number of channel d_q . In the max-pooling layer, every feature map from q -th layer is divided into several square regions of size $O_q \times O_q$ according to a certain stride S_q hyperparameter. A certain degree of overlap is again desirable to reduce possible overfitting issues [60]. Then, only the most remarkable feature information is maintained in every squared region by retaining the maximum value only. Therefore, the output size of the max-pooling layer will be $[(L_q - O_q)/S_q + 1] \times [(B_q - O_q)/S_q + 1] \times d_q$ [60]. Another possible pooling approach is denoted as average-pooling retaining the average of the features in every square region. However, max-pooling has been demonstrated to be more effective thanks to their stronger non-linear effects, which help enhancing most important information in activation maps whilst dropping the less important and probably useless data. Indeed, convolution layers increase the global receptive field only gently, requiring thus very deep networks to achieve satisfactory results, whilst the interleaved introduction of the pooling layer radically boosts the learning by drastically increasing the global receptive field [60]. In summary, the automatic feature extraction part of a CNN is composed of two or three set of convolutional and ReLU activation layers

followed by a max-pooling layer, as depicted in Fig. 1.14. This schema is repeated to deliver deeper ANN, integrating e.g. skip connections between layers attempting to mitigate the vanishing or exploding gradients. The last tensor of the feature extraction part is finally flattened before feeding a final dense fully connected part. This MLP-based tail performs the actual specialization of the network being able to solve classification or regression tasks, in the same manner as a MLP architecture. In fact, due to the above-mentioned neuron-units tensor-like interpretation of the feature maps, the flattening operation actually reshapes the last matrices of neurons (final feature maps) with dimension $L_q \times B_q \times d_q$ in a way to create a final hidden layer with a number of units equal to $L_q \cdot B_q \cdot d_q$. The next one or two hidden layers are fully connected in contrast to the sparse connections of the automatic feature extraction part. Furthermore, it is worth noting that this latter part evidences the highest computational burden of CNNs in terms of memory requirements, large number of activations, huge number of connections, and large number of weights to train. The training process of a CNN is based on the backpropagation rule, which has to be specialized for the new building blocks of convolutional layers and pooling layers. Considering the latter layer typology, the partial derivative of the loss considers directly the maximum value in the backward pass if no overlap is present in max-pooling layers, whereas it is necessary to consider effects proportionally to different contributing overlapped feature maps' patches [60]. On the other hand, the convolutional layer performs a linear transformation which can be seen as a form of matrix multiplication. Indeed, it is possible to demonstrate that the gradients at a layer $(q + 1)$ multiply the transpose of the filter, i.e. the weight matrix, to obtain gradients at layer q during the backpropagation procedure. With a simple intuitive explanation, during convolution filter acts as shifting on the input images, whereas during backpropagation, derivatives are computed with respect to the input volume, whose relative movements concerning the filter are opposite than before [60]. CNNs are computationally burdensome, and the usual millions of parameters to be trained may lead toward overfitting issues. Therefore, these models are ravenous for data, and a common stratagem attempting to reduce overfitting issues relies on a data augmentation procedure. As previously stated, since two images are different for a computer if their pixel representation is distinct, simple strategies such as translation, horizontal or vertical flipping, rotation, variation of brightness level or color intensity, etc. can be adopted as effective data augmentation tricks [43, 60]. The computational efforts required to effectively train CNNs limited their development, resulting in a research gap from 1998 until around 2010, when Graphical User Interface (GPU) computation revealed its great potential for overcoming the deep ANNs resource burden. Some CNN architecture milestones developed after LeNet-5 (1998) are e.g. AlexNet, developed in 2012, Visual Geometry Group VGG-16 and GoogLeNet, both released in 2014, DenseNet, conceived in 2016, and nowadays state-of-art EfficientNet, implemented in 2019 [43, 60].

Numerous different applications required to develop ML-based systems to work with sequence of data. For instance, in SHM area, it is common to deal with time-series data \mathbf{x}_t , i.e. streams of multivariate d -dimensional data collected over time t . Sequential data rely on the implicit assumption that data at every single time instant depend on past data. Furthermore, another implicit assumption is that time series exhibit a certain level of stationarity, since their underlining properties are practically constant over time. A mathematical model for dealing with time-series should be able to convert earlier input data into hidden states, and leveraging them to update the current hidden state \mathbf{h}_t . This latter for instance can be expressed as a function of the immediately previous hidden state \mathbf{h}_{t-1} and the current incoming information \mathbf{x}_t , i.e.

$$\mathbf{h}_t = f(\mathbf{h}_{t-1}, \mathbf{x}_t). \quad (1.30)$$

In the field of DL, recurrent neural networks (RNNs) were developed to deal with this kind of data stream [60]. Indeed, RNNs receive incoming data \mathbf{x}_t at each time-stamp and, accordingly, the current hidden state \mathbf{h}_t is adjusted at every time instant, see Eq. (1.30). This latter relationship imposes a recursive self-loop of the ANN architecture which progressively adjusts the hidden state whilst input data are gradually processed. In fact, the computational graph of a RNN can be represented with the so-called hidden representation, i.e. depicted as an MLP with an explicit self-loop symbol, or it can be illustrated in the so-called time-layered representation, meaning that the feed-forward MLP is unpacked explicitly showing all the hidden states for the finite-length time series under study. Furthermore, RNNs gives also the possibility to return an output result \mathbf{y}_t at every instant according to a distinct function $\mathbf{y}_t = g(\mathbf{h}_t)$, learning e.g. output probabilities from hidden states. The stationarity assumption imposes that the functions $f(\bullet)$ and $g(\bullet)$ are the same at every time instant. Despite this assumption may not be in perfect agreement with real-world scenarios, this reflects its benefits on greater learning stability and regularization effects [60]. To ensure using the same functions for the entire time series length, weight parameters are shared in all the recursive steps, clearly evidenced by the multiple connections depicted in a time-layered RNN representation. Therefore, backpropagation must take into account both the weight sharing and the temporal length of the time series, denoting a specific process called backpropagation through time (BPTT). The possibility to return outputs at every instant inspired RNNs to address forecasting applications, i.e. devoted to predicting future states of a system based on previous past observed states. For instance, RNNs have been applied to language modeling next-word prediction in a sentence. Instead, leveraging the recursive nature of Eq. (1.30), RNNs have been subsequently modified to model a function of variable-length inputs. Indeed, starting from an initial state initialized to a constant vector \mathbf{h}_0 , the next time-stamp state can be expressed as $\mathbf{h}_1 = f(\mathbf{h}_0, \mathbf{x}_1)$, and, consequently, the next state indirectly depends on the previous data and directly depends on the new inputs $\mathbf{h}_2 = f(f(\mathbf{h}_0, \mathbf{x}_1), \mathbf{x}_2)$, and so

on. Therefore, RNNs are considered Turing complete [60], meaning that if sufficient computational resources and data are provided, the RNN can theoretically simulate any algorithm. Nonetheless, the basic RNN structures evidenced severe generalization flaws when dealing with excessively long sequences of data, in addition to training issues like vanishing or exploding gradients. Therefore, special variants become famous in the last decades denoted as long short-term memory (LSTM), followed by a simplified version designated as gated recurrent units (GRUs) [60]. The most important advancements owing their origins to RNN is the development of an attention-based mechanism that enhanced the power of RNN-like architecture in dealing with very long sequences in a sequence-to-sequence approach, posing the basis for the most important milestone in the DL field, i.e. the implementation of neural transformers from 2017 and still evolving nowadays [91].

Another DL branch, i.e. the generative artificial intelligence, is radically revolutionizing all the AI panoramas and related fields lately [92]. Since 2014, generative adversarial networks (GAN) appeared as a novel ground-breaking approach in the DL area [93]. This kind of architecture was based on adversarial learning of two competing sub-models. A model named generator is demanded to learn the training probability space. In practice, the generator attempts modeling a mapping to transform a starting random noise latent space toward a certain probability distribution that, when sampled, provides new sample data quite similar to the ground truth available training data. The other competing sub-model is designated as the discriminator, and it is devoted to differentiating between real available training data and fake synthetic sampled data. The training of such a model resembles a minimax problem also known as a zero-sum game [92]. In fact, at the end of the training phase, both the generator and the discriminator reach a Nash trade-off equilibrium in which none of the two players prevails over the other. This means that the generator G learned how to map the probability distribution of input data $p_{data}(\mathbf{x})$ being able to produce such a realistic sample that the discriminator is no longer able to distinguish from actual real ones [93]. GAN models have been further applied in many scientific and engineering sectors e.g. in earthquake engineering [94], especially for data augmentation purposes. Despite basic GAN architecture being rather recently developed, different variants have been already proposed both for supervised and semi-supervised applications. For instance, it is noteworthy to mention deep convolutional GAN (DCGAN) based on convolutional layers implemented in the generator part, conditional GAN (cGAN) which leverages conditional supervised learning, and the Wasserstein GAN (WGAN), which adopts certain distance measure between synthetic and real training data distribution [92]. The integration of self-attention mechanisms, and therefore of neural transformers, in the generative AI solutions, recently led to the formalization of the acknowledged generative pre-trained transformer (GPT) models around 2020-2022, which represent the intrinsic core of the renowned ChatGPT, and of all the other similar outstanding generative AI tools alternative.

1.3 Contents' outline

The following of the present document are organized as follows.

Chapter 2 is dedicated to a review of structural health monitoring approaches, especially output-only operational modal analysis methods. In this chapter, a Python library for OMA denoted PyOMA is described. PyOMA package has been developed during the current three-year Ph.D. program with an international collaboration among three institutions. This open-source library is progressively getting attention in the international community of research and practitioners worldwide. In the conclusion of the chapter, some model-updating case studies have been illustrated in which the author leveraged the advantage offered by PyOMA to support the dynamic identification part.

Chapter 3 is mainly focused on the research studies conducted during the Ph.D. program for effectively integrating artificial intelligence procedures within conventional OMA techniques. Additionally, the aim was to also cope with automatic OMA (AOMA) solutions, a groundwork requirement of nowadays and efficient continuous SHM systems. The utmost outcome was the development of a new open-source paradigm for automatic OMA frameworks entitled intelligent automatic operational modal analysis (i-AOMA).

Besides dynamic identification strategies, in Chapter 4, the discussion moved oriented to damage detection strategies for civil structures. Specifically, several indirect non-destructive tests have been considered during the current Ph.D. program, some vibration-based integrated with neural networks, and others not vibration-funded, specifically referring to the ground penetrating radar (GPR) for tunnel lining health assessment, or even acoustic emission (AE) damage detection based on high-frequency elastic waves ranging between kHz to MHz released by the damaging material.

Eventually, before moving toward the conclusions, Chapter 5 illustrates some current and future perspectives regarding the most coherent and genuine continuation of this research activity. Specifically, the so far discussed OMA is mainly based on a dogmatic assumption of stationarity of the analyzed signals. Nonetheless, within signal processing fields, many other different techniques have been developed to analyze non-stationary and nonlinear signals. These kinds of signals are more common than it is thought, e.g. during transient loading periods followed by a free-decay response, during strong natural excitation such as wind or earthquake, or even considering the actual load distribution of isolated heavy traffic loading, which is really far from the stationary base hypothesis. Some of them have mildly started being studied for nonstationary OMA, however much still remains to be done and investigated, especially with the effective integration of AI solutions within this important area.

Chapter 2

Conventional approaches for operational modal analysis

The term *Operational modal analysis* (OMA) is defined as the field of study related to the techniques for dynamic identification of the modal properties of a structural system under ambient vibration or, generally speaking, exhibited during its normal operating life. Those techniques exclusively use the information contained in the vibration response only, so that is denoted as output-only [95, 96]. The *dynamic identification* process indicates those methods aimed to identify the governing parameters of a mathematical model used to describe the structural system's dynamical behavior in order to capture with the best fit the real vibration response collected during experimental campaigns [95]. Indeed, the actual vibration response depends on the physical properties of the structure under investigation, representing its tangible fingerprint. This aspect represents the cornerstone and the rationale behind the OMA research branch, i.e. searching for proper and reliable methodologies able to deliver the best estimation of the actual physical properties of the in-situ structure by processing the structure's vibration output response. The knowledge of the in-situ physical properties of the structure has important implications, for instance, for characterizing the level of change of material properties with respect to the nominal values declared at the era of construction due to the occurrence of degradation phenomena and long-term effects. One of the most important consequences of OMA is the derivation of damage detection strategies in order to monitor the evolution of the health state of a structural system by periodically inspecting its dynamic behavior over time. Therefore, in the OMA, it is crucial to achieve a sufficient understanding of the structural dynamics and structure's mechanics in order to capture its actual health state for SHM purposes. Several interdisciplinary challenges are generally involved in the OMA context, e.g. considering random vibration aspects such as linear or nonlinear vibration conditions, in-service life under stationary and either nonstationary situations, or even aspects concerning

solid technical knowledge from analog-to-digital data acquisition and related specific signal processing tools, which often requires application-oriented assumptions and tailored simplifications [95]. The current chapter is dedicated specifically to conventional OMA approaches whose main assumption is dealing with structural systems which can be defined as linear time-invariant (LTI) systems [96]. This basic hypothesis refers to structures exhibiting a linear behavior, i.e. in elastic conditions, usually in agreement during the operational in-service life situations, and characterized by constant parameters over time, denoted as stationary conditions. Considering the long-term continuous monitoring within the SHM field, the material properties vary in an extremely slow manner over a long period of time, meaning that their variation is slow enough to be approximately considered constant during each single experimental dynamic test session.

The present chapter is organized as follows. In the next section 2.1, a brief historical contextual overview is provided, recalling also some fundamental aspects of digital signal processing of random vibration signals. Subsequently, in section 2.2, conventional OMA techniques are discussed by distinguishing between frequency-domain-based and time-domain-based methods. Thereafter, in section 2.3, the PyOMA module is described. PyOMA is the first open-source python-based library developed during the current Ph.D. program in collaboration with other two institutions implementing a suite of conventional OMA techniques, whose theoretical background has been presented in section 2.2. Eventually, in section 2.4, some selected case study research works developed during the current Ph.D. program which remarkably used the PyOMA module have been presented. Specifically, these studies have been organized according to two different objectives which stimulated the research question, i.e. considering the dynamic identification goal on one side, and the model updating procedure on the other side.

2.1 Historical highlights and OMA fundamentals

2.1.1 Brief history of OMA

The branch of study regarding vibrations of bodies is rooted in ancient history, when e.g. the ancient Greek mathematicians and philosophers, specifically Pythagoras, set the origin of music by analyzing the sound emitted from strings fastened at different lengths, defining the concepts of notes and octaves [95]. During the Renaissance period, the Italian astronomer Galileo Galilei in his famous masterpiece entitled “Discourses Concerning Two New Sciences” (1638) essayed regarding the vibration of bodies, describing the resonance event of distant bodies characterized by the same natural frequency, and denoting it as the phenomenon of sympathetic vibration [95]. In 1755, the Swiss mathematician D. Bernoulli laid the foundation of the modal superposition principle, since he discovered that a vibrating string

can be described according to the overlapping of simple harmonics' oscillations, denoting by him as the “principle of coexistence” [95]. Probably, the most overwhelming impacts in the following centuries among every scientific and engineering field owe to Joseph Fourier, who developed his homonymous theorem when analyzing heat transmission principles in 1822. Referring to more recent eras, it is worth mentioning the British physicist J.W. Strutt, better acknowledged as 3rd Baron Rayleigh, whose contribution of the last two centuries represents the basic framework of the modern structural dynamics, condensing the damping definition accounting for both mass and stiffness quantities [95].

The first rudimentary OMA can be traced back to damage detection in railway lines in the 1800s [7], however, the main branch of study developed prior to modern OMA was denoted as the experimental modal analysis (EMA) [96]. Indeed, two main branches can be identified within dynamic identification strategies according to what is monitored, i.e. the input-output methods and output-only methods [95]. EMA is based on measuring both artificially impressed input-induced excitation and resulting vibration response, with the goal to characterize how the structural system acts as a filter, i.e. modifying the known input signal to obtain the output response. The input-output EMA methodologies are mainly prerogative of mechanical engineering and related vibration control study branches, since usually mechanical system's contained scale allows for monitoring both the impressed input signal and the output structural response. Considering the mechanical engineering field, first attempts were represented by condition monitoring of rotating machines during in-service life, i.e. normally excluding the transient periods of start-up and shut-down [7]. Typically accelerometer sensors are employed, but also velocity sensors and laser contact-less displacement transducers. On the other hand, despite OMA methods sharing and deriving mostly its theoretical background from EMA, OMA refers to output-only methodologies attempting to characterize the entire system only knowing the structural response. Therefore, it is named “operational” because it refers to the unmeasured random loads acting on the structure during its in-service operational life. This was a crucial factor for the success of OMA over the EMA for civil engineering systems, since the scale of buildings and infrastructure is excessively large to be able to artificially induce a proper excitation to activate the entire dynamics of the structure, and it is also impracticable to accurately measure input random forces such as traffic and wind loads. As illustrated in Fig. 2.1, a typical fundamental assumption is formulated to generally describe the nature of the unknown inputs. A white noise input signal is considered in origin, feeding a loading excitation filter which generates the actual unknown random forces acting on the structure under investigation in operating conditions (e.g. wind, traffic, etc.) resulting in the vibration response actually monitored. This led to the OMA key concept of identifying the “the whole system” (or combined system [96]), encompassing both the actual structural system and the loading excitation system [95]. Dealing with civil structures, since generally the acceleration response is in the order

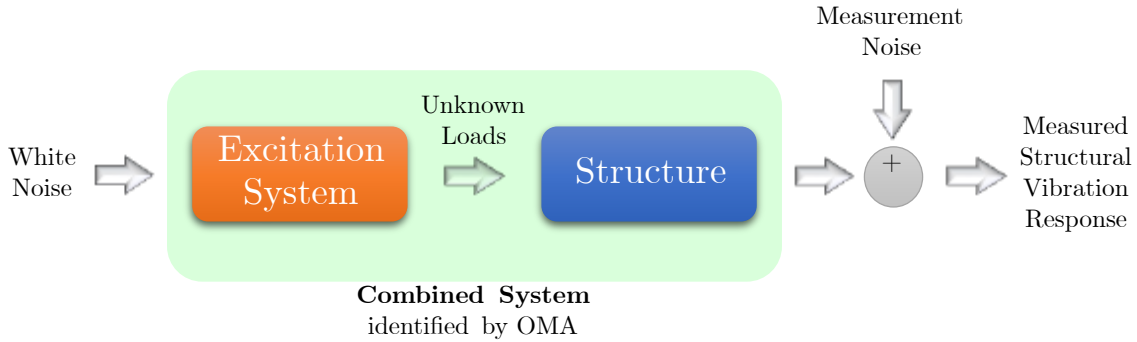


Figure 2.1: Combined system identified within the OMA context.

of magnitude of mg, very sensitive, high performance, and low noise piezoelectric accelerometers are required [96], but also other typologies are commonly adopted such as force-balance accelerometers and, due to recent advancements in micro-electronics, the micro-electro-mechanical systems (MEMS), electric-resistance ones or vibrating wire strain gauges have been also widely adopted [7]. Therefore, the main difference between EMA and OMA is the nature of the input, which is measured and known in EMA whilst completely unknown in OMA [96]. Another reason for the popularity and success of OMA over EMA among researchers, engineers, and practitioners can be ascribed to the relatively low cost and speed of the experimental campaigns, jointly with the recent advancement of the computational methods [95]. For instance, referring e.g. to a bridge, it is not strictly required to shut the traffic down, since it is of interest to capture a representative vibration response during usual in-service operating conditions. Modern OMA properly formalized as a research field started at the beginning of last century [96], even though literature is well documented from around 1930s-1960s, especially regarding earthquake conditions and ambient vibration tests on buildings [95], and later on fostered by new computational capabilities of modern calculators and because of the introduction of efficient numerical methods such as the Fast Fourier Transform in 1965 [97]. Nevertheless, the theoretical background was mature enough to foster practical implementations of vibration-based damage assessment systems for civil structures starting around the 1980s [7], and as extensively discussed in the previous chapter of the present document, national and international regulations began enacting mandatory rules for periodically or continuously monitoring the health state of strategic structure and infrastructures mainly for public safety reasons [7].

2.1.2 Signal processing basics for OMA

In general, a signal is any function of multiple independent variables which carry information about a physical system. Considering time as an independent variable, it is possible to distinguish between continuous-time signals, $x(t)$, and discrete-time

ones, $x(t_k)$, being t_k a k -th time instant [97]. Another fundamental distinction is based on the nature of the amplitude of the signal (the dependent variable), which discriminates between analogical signals, when both time and amplitude are continuous, and numerical or digital signals in which time and amplitude are discrete sequences. Analogical sensing instrumentations have been progressively replaced by electronic circuits and calculators, imposing a conceptual transition toward the digital signal processing field. As previously mentioned, the theoretical bases owe their ancient origins to the 1600s with groundbreaking improvements in the 17th and 18th, further revolutionized around the 1940s-1960s due to the computational capabilities of modern calculators and the development of specific electronics or computing algorithms. Therefore, since then every monitored physical quantity has been sampled at discrete time and stored in a finite arithmetic calculator, imposing the evolution of theoretical and mathematical backgrounds from a continuous domain to a discrete one. Signal processing is the transformation of signals to convey intrinsically incorporated information in a more direct interpretable way [97].

The Fourier theorem represents the fundamental starting point of the signal processing area, allowing to decomposition of any signal in a linear combination of sinusoidal components at different frequencies called harmonics. Originally developed for periodic signals only, it was extended to non-periodic signals as well, assuming that period is infinite. In continuous time, the direct and inverse Fourier transform appear as follows [96]:

$$X(f) = \int_{-\infty}^{\infty} x(t)e^{-i2\pi ft} dt \quad ; \quad x(t) = \int_{-\infty}^{\infty} X(f)e^{i2\pi ft} df, \quad (2.1)$$

in which i is the imaginary unit, f denotes continuous frequency and t indicates continuous time. The Fourier transforms exhibit interesting properties such as linearity, time shift, integral and differentiation, and convolution properties [96]. The latter one synthetically states that a convolution operation in the time domain translates into a simple multiplication operation in the Fourier frequency domain. Dealing with finite length $T = N\Delta t$ digital signals $x_n = x(n\Delta t)$ with $n = 0, \dots, N-1$, sampled with a sampling frequency $f_s = 1/\Delta t$, being $\Delta t = t_{n+1} - t_n$ the sampling period, the discrete Fourier transform (DFT) and its inverse form have been formalized, considering a discrete frequency domain described by $f_k = k/T$ with $k = 0, \dots, N-1$:

$$X_k = X(f_k) = \sum_{n=0}^{N-1} x_n e^{-\frac{i2\pi kn}{N}} \quad ; \quad x_n = \frac{1}{N} \sum_{k=0}^{N-1} X_k e^{\frac{i2\pi kn}{N}}. \quad (2.2)$$

According to the Shannon-Nyquist theorem [96, 7], the highest frequency that can be represented in the discrete Fourier domain is denoted Nyquist frequency and it

is given by the half of the sampling frequency:

$$f_{\max} = \frac{f_s}{2}. \quad (2.3)$$

The physical quantities monitored in OMA generally appear as a random (stochastic) process, being the collection of all the realization of random variables over a certain time duration. A random process can be characterized according to some descriptors and descriptive statistics such as probability density functions, mean, variance, auto-correlation and cross-correlation functions, auto-spectral and cross-spectral density functions, and coherence functions. Due to the basic hypothesis of conventional OMA, signals are usually considered stationary stochastic ergodic random processes. Stationarity implies that the properties characterizing the signals, e.g. mean μ_X and the autocorrelation R_{XX} , do not change over time [96]. Ergodicity of a finite length stationary stochastic process (finite-energy signals) means that the time average statistic is a finite constant value and it can be obtained by the discrete estimator of average overall arbitrary sample sequences [7, 97], instead of using the ensemble average expectation operation which supposes using infinite realizations of random variables over time (infinite-energy signals) [97]. Indeed, since dealing with random variables, this should imply considering a collection of signals covering all possible realizations at every time instant, thus characterizing the random process through ensemble averages or expectations. However, if the time window of observation is infinitely long, a single digital signal can be used to estimate the characteristics of the entire random process:

$$\mu_X = \mathbb{E}[x(t_k)] = \lim_{N \rightarrow \infty} \frac{1}{N} \sum_{k=1}^N x(t_k), \quad (2.4)$$

$$R_{XX}(\tau) = \mathbb{E}[x(t_k)x(t_k + \tau)] = \lim_{N \rightarrow \infty} \frac{1}{N} \sum_{k=1}^N x(t_k)x(t_k + \tau). \quad (2.5)$$

in which τ is the time lag. In practice, the autocorrelation function quantifies how much a signal is similar to itself to inspect regularities in the signal [7], by computing the product of the finite digital signal with itself translated in all possible positions in the time domain, controlled by the time lag parameter. The second-order statistics covariance function is connected with the correlation function

$$C_{XY}(\tau) = \mathbb{E}[(x(t_k) - \mu_X)(x(t_k + \tau) - \mu_X)] = R_{XY}(\tau) - \mu_X^2, \quad (2.6)$$

and they coincide when the process is zero-mean. Considering a second signal $y(t_k)$, the cross-correlation represents a measure of similarity between the two signals, and it is defined as

$$\begin{aligned} C_{XY}(\tau) &= \mathbb{E}[(x(t_k) - \mu_X)(y(t_k + \tau) - \mu_Y)] \\ &= \mathbb{E}[(x(t_k))(y(t_k + \tau))] - \mu_X\mu_Y = R_{XY}(\tau) - \mu_X\mu_Y. \end{aligned} \quad (2.7)$$

If two processes are uncorrelated, $C_{XY}(\tau) = 0, \forall \tau$ implying that $R_{XY}(\tau) = \mu_X \mu_Y$. Noticing that $|C_{XY}(\tau)|^2 \leq C_{XX}(0)C_{YY}(0)$ (and equivalently for correlation functions), this implies that the maximum values of the covariance and correlation functions are obtained for zero-lag.

Another fundamental tool to characterize finite duration T stationary stochastic processes is the power spectral density (PSD) functions, also named simply spectra, which are defined as the auto- and cross-correlations of the complex conjugate of the Fourier transform and the Fourier transform of the signal itself. Since input signals in OMA are modeled as a Gaussian zero-mean white noise random process, they are completely determined by the auto-spectral density which is directly connected to the variance of the stochastic process. The two-side auto-PSD (real-valued functions) and cross-PSD (complex-valued function) are defined as [96]

$$S_{XX}(f) = \lim_{T \rightarrow \infty} \mathbb{E} \left[\frac{1}{T} X_k^* X_k \right] = \lim_{T \rightarrow \infty} \mathbb{E} \left[\frac{1}{T} |X_k|^2 \right], \quad (2.8)$$

$$S_{YY}(f) = \lim_{T \rightarrow \infty} \mathbb{E} \left[\frac{1}{T} Y_k^* Y_k \right] = \lim_{T \rightarrow \infty} \mathbb{E} \left[\frac{1}{T} |Y_k|^2 \right], \quad (2.9)$$

$$S_{XY}(f) = \lim_{T \rightarrow \infty} \mathbb{E} \left[\frac{1}{T} X_k^* Y_k \right], \quad (2.10)$$

whereas the typically used one-side version is given by doubling the amplitude but preserving the phase:

$$G_{XX}(f) = 2S_{XX}(f), \quad (2.11)$$

$$G_{YY}(f) = 2S_{YY}(f), \quad (2.12)$$

$$G_{XY}(f) = 2S_{XY}(f). \quad (2.13)$$

It is worth noting that PSD and correlation functions are Fourier transform pairs (Wiener-Khinchin relations [96]), meaning that it is possible to obtain the PSD from the Fourier transform of the correlation functions:

$$S_{XX}(f) = \int_{-\infty}^{+\infty} R_{XX}(\tau) e^{-i2\pi f\tau} d\tau, \quad (2.14)$$

$$S_{YY}(f) = \int_{-\infty}^{+\infty} R_{YY}(\tau) e^{-i2\pi f\tau} d\tau, \quad (2.15)$$

$$S_{XY}(f) = \int_{-\infty}^{+\infty} R_{XY}(\tau) e^{-i2\pi f\tau} d\tau. \quad (2.16)$$

The coherence function $\gamma_{XY}^2(f)$ is defined as the ratio between the squared cross-PSD and the product of the auto-PSD. It varies between 0 and 1 and determines the degree of linear dependency of two signals, thus helping to detect nonlinearities, since it formally resembles the linear correlation coefficient (Pearson coefficient)

[42]:

$$\gamma_{XY}^2(f) = \frac{|G_{XY}(f)|^2}{G_{XX}(f)G_{YY}(f)} = \frac{|S_{XY}(f)|^2}{S_{XX}(f)S_{YY}(f)} \quad (2.17)$$

In practice, according to the Blackman-Tukey procedure [96], for finite and long enough stationary ergodic processes, it is possible to estimate the correlation function from a direct computation procedure as below, see e.g. Fig. 2.2,

$$\hat{R}_{XX}(r\Delta t) = \frac{1}{(N-r)\sigma_X^2} \sum_{n=1}^{N-r} (x_n - \mu_X)(x_{n+r} - \mu_X), \quad r = 0, 1, \dots, m \quad (2.18)$$

denoting r as the lag number, m as the maximum possible lag, μ_X , and σ_X the sample mean and sample variance of the signal, and thereafter computing the PSD through its Fourier transform. However, the introduction of the efficient Fast Fourier Transform (FFT) algorithm permitted a direct computation of the PSD according to the acknowledged Welch procedure [96]. To improve the accuracy, the one-side PSD estimator is computed by splitting the signal into a number of segments with duration T and then averaging the spectra obtained by performing the Fourier transform on every single segment. It is worth reminding that the Fourier transform was formulated specifically for periodic signals, therefore performing the FFT on a non-periodic segment of the signal will generate errors and inaccuracies in the spectra. As illustrated in the example of Fig. 2.3, this problem known as leakage leads to a dispersion of the energy content associated with every frequency line which spreads on a wider frequency bandwidth. This problem can not be avoided, but it can be attenuated by considering a proper windowing procedure, i.e. imposing the signal to be zero at the beginning and the end of the considered window. Rectangular windows $w_{\text{rectangular}}(t_k)$ have been adopted initially, i.e. the new signal is given by $x(t_k)w_{\text{rectangular}}(t_k)$, being

$$w_{\text{rectangular}}(t_k) = \begin{cases} 1 & \text{if } 0 \leq t_k \leq T, \\ 0 & \text{otherwise.} \end{cases} \quad (2.19)$$

The rectangular window narrows the leakage frequency bandwidth, but the energy is still quite dispersed in the nearby of every frequency line. To quantify this latter aspect, it is important to define the side-lobe attenuation, expressed in decibels (dB), which represents the magnitude amplitude difference in the spectrum between the highest lobe and the first side lobe. As demonstrated in Fig. 2.4, rectangular window is characterized by a side-lobe reduction of 13 dB, however it is preferred to adopt the Hanning or cosine window $w_{\text{hanning}}(t_k)$ which is characterized by a greater side-lobe reduction of 32 dB, but with a broader bandwidth dispersion:

$$w_{\text{hanning}}(t_k) = \begin{cases} \sqrt{\frac{8}{3}} \left[\frac{1}{2} - \frac{1}{2} \cos\left(\frac{2\pi t}{T}\right) \right] & \text{if } 0 \leq t_k \leq T, \\ 0 & \text{otherwise.} \end{cases} \quad (2.20)$$

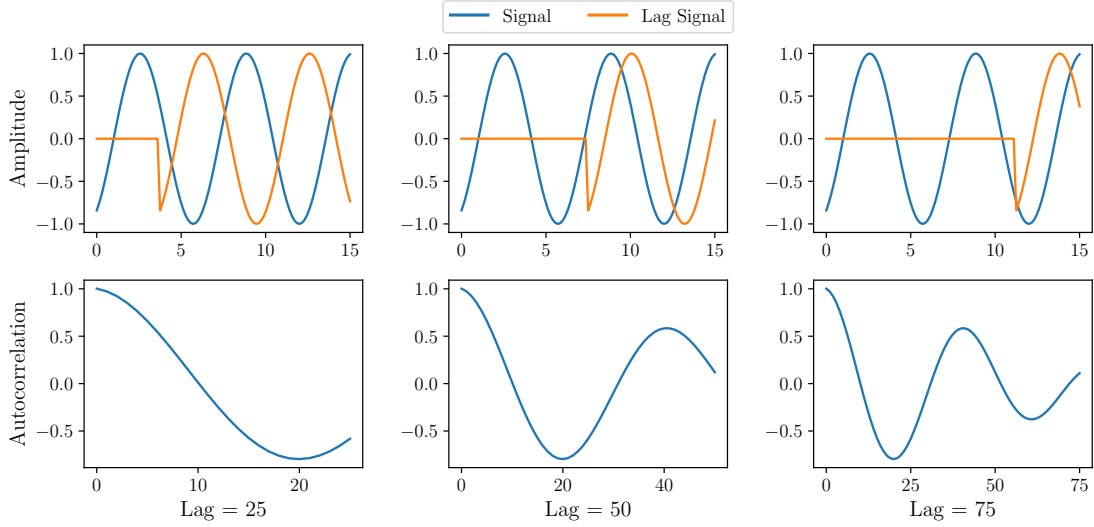


Figure 2.2: Direct computation of auto-correlation function according to Eq. (2.18) on a sinusoidal signal.

Windowing sometimes needs the introduction of some correction factor to adjust frequency spectra amplitude to maintain the signal's energy equivalence, as demonstrated by the $\sqrt{\frac{8}{3}}$ factor in Eq. (2.20) [96].

Besides the Shannon-Nyquist theorem, another important aspect must be accounted for when dealing with sampled digital signals. The aliasing issue is related to the sampling frequency which undersamples all those high-frequency components greater than the Nyquist frequency, which may erroneously appear in the range of observable frequencies. Therefore, the only way to avoid the aliasing problem is to apply an anti-aliasing filter which is an analog low-pass filter, which cancels out all those high-frequency components before storing the digital signal [96]. Since a real filter is characterized by a certain transition band, consequently, the Nyquist frequency is further reduced by about 20%.

The Laplace transform represents the generalization of the Fourier transform [95] since the foremost converts a signal to a general complex plane in the variable s , whereas the second one maps a signal to the frequency complex plane if , so implying that $s = if$. However, when dealing with sampled signals of structural response the vibration response is typically damped over time because civil structures are normally underdamped systems [98]. Therefore, the related digital signal is better treated in the Z-domain, being the z-transform a sort of discrete version of the Laplace transform being able to capture also the negative exponential decay part. Indeed, the z complex variable is defined in polar form as

$$z = re^{i\omega}, \quad (2.21)$$

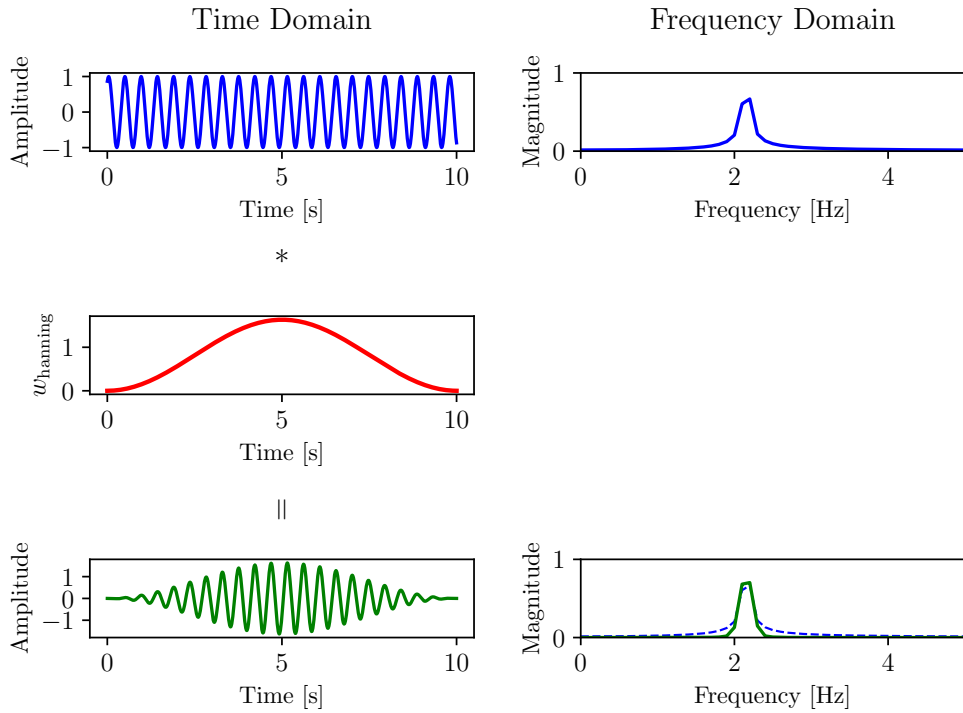


Figure 2.3: Spectral leakage attenuation through the windowing procedure.

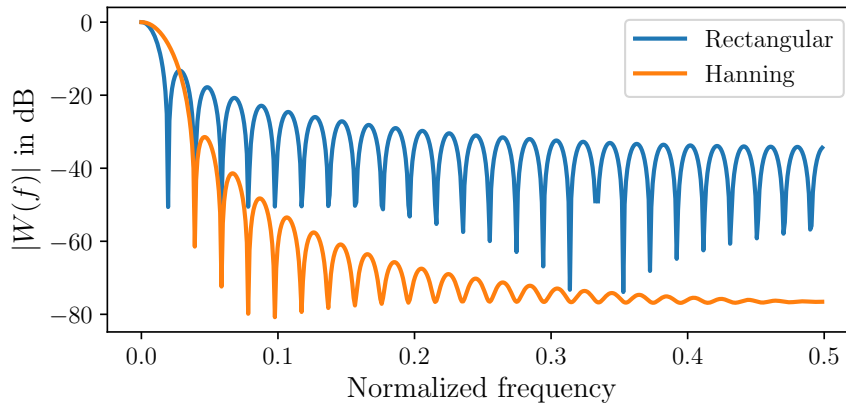


Figure 2.4: Fourier transform of rectangular and Hanning windows to show side-lobe attenuation.

being ω the circular frequency, $\omega = 2\pi f_k$, and the Z-transform of a digital signal x_n is given by the Fourier transform of the signal multiplied for an exponential

sequence [97]

$$X(z) = \sum_{n=-\infty}^{\infty} x_n z^{-n} \Rightarrow X(re^{i\omega}) = \sum_{n=-\infty}^{\infty} x_n (re^{i\omega})^{-n} = X(\mathbf{f}_k) r^{-n}. \quad (2.22)$$

The general equation of the motion for any LTI multi-degree of freedom (MDOF) system is given by a set of N second-order ordinary differential equations (ODEs) written according to the acknowledged D’Alembert principle of dynamic equilibrium [98]:

$$\mathbf{M}\ddot{\mathbf{y}}(t) + \mathbf{C}\dot{\mathbf{y}}(t) + \mathbf{K}\mathbf{y}(t) = \mathbf{f}(t), \quad (2.23)$$

in which the symbols \mathbf{M} , \mathbf{C} and \mathbf{K} denotes respectively the mass, the damping and the stiffness matrices, whereas $\mathbf{y}(t)$ and its temporal derivatives indicates the DOFs displacement, velocity and acceleration, whilst $\mathbf{f}(t)$ denotes the input forces vector. The system is defined as stable if it produces finite outputs as a consequence of bounded input excitation. The system is defined as causal or physical realizable [96], when it depends only on past inputs with respect to the current time instant, implying that the response is zero for time instants before the zero instant, so that the moment from which the system started being observed [97]. Under the proportional damping hypothesis, in the OMA context is the typical assumption of monitoring LTI systems, i.e. in elastic conditions [95]. In this way, it is possible to characterize the modal response according to the modal decoupling of the set of coupled ODEs into a set of N decoupled first-order ODEs. Moreover, one of the main hypotheses of LTI systems is based on the superposition principle validity, so that the response of the system to an arbitrary load sequence, can be obtained according to the discretization of the input into a sequence of unitary impulse (Dirac’s delta function $\delta(t_k - \tau)$) excitation, and the Duhamel’s convolution integral of the unitary impulse response function (IRF) $h(t_k)$ convoluted with the arbitrary discretized input signal [98]. Through the superposition principle, the solution delivers natural frequencies, damping factors, and mode shapes of every natural mode of vibration. The concept of characteristic mode shape describes in practice the spatial distribution of movement of a structure. Reminding the concept of identification of the whole combined system, the early dynamic identification methods delivered “operating deflection shape” (ODS) instead of mode shapes, defined as the macroscopic deflection exhibited from a structure being excited at a certain frequency value [95]. It is worth underlining that the mode shape is a different concept from the ODS because the latter is defined for any frequency value, whereas a mode shape is specifically defined for a certain natural frequency, presenting an infinite number of equivalent numerical representations [95]. Theoretically speaking, mode shapes are obtained for LTI systems in stationary conditions, whereas ODS can be defined also in nonlinear conditions. According to the modal superposition principle, the dynamic response of a linear structure can be reconstructed by superposing the harmonics which do not depend on any external force or load but only depend

intrinsically on the stiffness and mass properties (eigenvalue analysis). Conversely, ODS is in a direct dependence relationship with the applied loads. Among all non-unique and infinite possible descriptions, the mode shapes are usually reported as normalized vectors, whereas only a single unique version with certain values and units exists for the ODS. Despite all the above-mentioned conceptual differences, at natural frequencies, the ODS can be confused with the mode shapes being numerically equivalent [95].

Considering the Fourier transform (or in general the Z-transform) of the motion Eq. (2.23), the set of differential equations translates to a system of algebraic equations. Furthermore, it is possible to define the frequency response function (FRF) $H(\omega)$ which merely represents the ratio between the transform of the output signal $Y(\omega)$ and the transform of the input forces $F(\omega)$:

$$\mathbf{Y}(\omega) = \mathbf{H}(\omega)\mathbf{F}(\omega). \quad (2.24)$$

The FRF contains information on the structural system of interest. Indeed, expressing the FRF with a polynomial partial fraction expansion form [95], i.e.

$$\mathbf{H}(\omega) = \sum_{n=1}^N \left(\frac{\mathbf{A}_n}{i\omega - \lambda_n} + \frac{\mathbf{A}_n^*}{i\omega - \lambda_n^*} \right). \quad (2.25)$$

denoting $\mathbf{A}_n = \boldsymbol{\phi}_n \boldsymbol{\gamma}_n^T$ as the residue matrices consisting of mode shape vector $\boldsymbol{\phi}_n$ and modal participation vector $\boldsymbol{\gamma}_n^T$ [99], and the superscript $(\bullet)^*$ indicating the complex conjugate operator, the poles λ_n of the system contains the modal parameter of interest, i.e. natural frequencies, damping ratios, and it would be possible to obtain also the mode shapes. It is worth recalling that, if a function can be expressed by the ratio of two polynomials, the solutions of the numerators are called roots or zeros, whereas the solutions of the denominator are denoted as poles. It is worth noting that IRF and FRF are also Fourier pairs, since it is possible to convert the convolution Duhamel's integral in a simple product in the transformed domain, thus obtaining the FRF from the transform of the IRF:

$$\mathbf{h}(t) = \sum_{n=1}^N (\mathbf{A}_n e^{\lambda_n t} + \mathbf{A}_n^* e^{\lambda_n^* t}). \quad (2.26)$$

The PSD of the response in Eq. (2.24) carries the same information as the FRF, considering that if the hypothesis of input white noise holds, the spectrum of the input forces should be constant. The poles of the system present a four-quadrant symmetry, thus delivering four complex conjugate pairs of the same mode, two referred to stable solutions (negative real parts), and two referred to unstable solutions (positive real parts).

However, in the OMA context, the input is not measured, therefore this path is not a feasible procedure. Nevertheless, it is worth noting that, besides that FRF

and IRF are Fourier transform pairs, and PSD and correlation functions are also Fourier transform pairs, it is possible to observe that IRF and correlation functions are also Fourier transform pairs in the OMA field [96]. Therefore, this observation allows to consider that second-order statistics of the output response signals should contain those structural modal information of interest. Referring to the only causal part of the solution, the poles will appear as complex conjugate pairs [96], i.e. with a two-quadrant symmetry. To obtain only half of the poles of interest, it is possible to compute the positive PSD (PSD⁺), considering only positive time lags, i.e.

$$S_{YY}^+(\omega) = \text{DFT}(R_{YY}(\tau)|_{\tau \geq 0}), \Rightarrow S_{YY}(\omega) = S_{YY}^+(\omega) + [S_{YY}^+(\omega)]^H, \quad (2.27)$$

being $\text{DFT}(\bullet)$ the operator of the discrete Fourier transform, and the superscript $(\bullet)^H$ the Hermitian operator, which means delivering the complex conjugate transpose of a matrix. Therefore, as extensively discussed in [95], the vibration response data of LTI systems can be decomposed in the time domain according to the following modal decomposition

$$\mathbf{y}(t) = \mathbf{\Phi} \mathbf{p}(t) \quad (2.28)$$

being $\mathbf{\Phi}$ the modal shape matrix and the column vector $\mathbf{p}(t)$ the modal coordinates of the response obtained from solving the Duhamel's integral of the modal load of each n -th mode. From this definition, an analytical procedure explains the correlation function in terms of the causal part of the response in polynomial residual partial fractional form, thus showing the poles in the discrete time domain [95]. As reported in [96], in the output-only case, the correlation function of the output measurements can thus be expressed as a sum of complex exponentials, and the causal part only (positive time lags) associated with the N pairs of only stable poles (λ_n, λ_n^*) is given by

$$\mathbf{R}_{YY}(\tau \geq 0) = \sum_{n=1}^N (\phi_n \gamma_n^T e^{\lambda_n \tau} + \phi_n^* \gamma_n^H e^{\lambda_n^* \tau}), \quad (2.29)$$

in which γ_n^T are the modal participation vectors [99] of the n -th mode shape ϕ_n . On the other hand, also the PSD can be decomposed accordingly, leveraging the fact that it is a Fourier pair of the correlation function, allowing the expression of the PSD in partial fractional terms, making explicit the four complex conjugate pairs discrete-domain poles, related to both causal and non-causal parts [95].

Traditional input-output methods have been reformulated to cope with output-only conditions, e.g. referring to the readjusted version of FRF as spectrum-driven methods, or IRF used with correlation functions [95]. Therefore, different output-only techniques have been developed and derived from the historical reasoning of the FRF able to work with response-only data to characterize always multiple-input and multiple-output (MIMO) systems, the only subjects of OMA procedures [96]. The system is defined as observable when a layout of several sensors is properly designed to capture vibration information able to reconstruct (estimate) with reverse

procedure the entire dynamics of the system. Since working with digital signals in the Z -domain, the found poles $\lambda_n = z_n$ which carry modal information of actual interest has to be converted back to the continuous time Laplace domain with the complex variable s_n in order to obtain the real values of modal parameters. Therefore, the following transformation should be performed:

$$\lambda_n = z_n = e^{s_n \Delta t}, \quad \Rightarrow \quad s_n = \frac{\ln(\lambda_n)}{\Delta t} \quad (2.30)$$

$$f_n = \frac{|s_n|}{2\pi} \quad (2.31)$$

$$f_{d,n} = \frac{\Im(s_n)}{2\pi} \quad (2.32)$$

$$\xi_n = -\frac{\Re(s_n)}{|s_n|} \quad (2.33)$$

$$(2.34)$$

in which, referring to the n -th mode, f_n and $f_{n,d}$ indicate the natural frequency and the damped natural frequency respectively, whereas ξ_n is the damping ratio of the system.

2.1.3 Vibration tests and experimental campaigns

Mathematical models are usually employed to describe the dynamic properties of the structure. Nonetheless, to be representative, any model should undergo a careful calibration process, i.e. conditioning it on real vibration data responses collected with experimental tests campaign [95]. Due to historical origins within the EMA field, the first vibration testing methods were the forced-type ones. During forced tests, an artificially controlled excitation is imposed on a small/medium scale structure using basically the following different methodologies:

- *Mechanical shakers*: These devices allow imparting sufficiently large dynamic forces in a sweep frequency range of interest and even adjusting the sinusoidal waveform. For instance, considering large bridge structures the first natural frequencies of interest are below 1 Hz, however, it is still challenging to produce large forces at low frequencies without incurring prohibitive direct and indirect costs, i.e. for equipment, transportation, and mounting. Common adopted devices are of the type electro-magnetic, eccentric mass, or hydraulic (even including laboratories shaking tables) [95].
- *Transient loads*: this technique involves two main strategies. The foremost is denoted as the impact test, based on an impact hammer equipped with a force traducer. This is mainly devoted to studying small-size structures likewise mechanical ones. Secondly, another widespread technique is denoted as pull

back or quick release test. The method imposes a certain static displacement far enough from its static equilibrium point and suddenly releases it. In this way, the structure exhibits a free decaying vibration response [95].

- *Man-excited motions*: in this technique walking or jumping patterns of a number of people knowing all individual masses represent the known artificially induced excitation.
- *Induced ground-motion*: this method is based on adopting shaking table devices programmed to reproduce ground-shaking recordings time histories.

Nonetheless, when dealing with large-scale civil structures, the main difficulties of forced vibration tests are related to adequately exciting all the modes which mainly contributes to the actual response of a structure in-service conditions without inducing any damage due to an excessive excitation [95]. Therefore, this challenging task fostered the output-only methods based on *ambient vibration tests*, i.e. recording the vibrational response under natural or environmental excitation levels. This led to challenges in the mathematical framework requiring it to be able to extract the modal information of interest working with a low level of vibration close to the background noise. Typically, the order of magnitude of the recorded accelerations sweeps from tens to hundreds of milli-g's (mg) under pure ambient vibration without traffic and strong wind actions, and it can be considerably different considering e.g. a truck passage. In order to capture such vibration levels, good-quality sensors are needed. For instance, for recording accelerations piezoelectric sensors represent the best option in terms of frequency resolution and bandwidth and easy installation procedures, however their are expensive, fragile, and it is not able to catch the zero-frequency (DC) band [96]. Another cost-effective widely used accelerometer typology is the force-balance type which is characterized by low noise floor and is able to capture DC frequency, however, the frequency range is upper bounded at a few hundred Hz, so that much lower than piezoelectric ones [96]. Nowadays a very low-cost cost sensing solution is related to lately advancements of micro-electronics represented by MEMS sensors. Moreover, another challenging aspect is using a limited number of sensors which may capture noisy data periodically during the structure's lifetime in a continuous monitoring scenario. In summary, OMA methods must deal with statistical uncertainties both aleatory and epistemic ones, arising e.g. from random measurement errors due to also electrical noise of sensors themselves, as shown in Fig. 2.1. On the contrary, the main success factors of this kind of ambient test are the rapidity of the experimental campaign and generally lower costs than the forced tests. It is worth noting that besides the above-mentioned difficulties, a series of assumptions are conducted when dealing with large civil structures, thus crucially affecting the identification process [95]. For instance, simplified assumptions are usually performed considering e.g. soil-structures interaction, and in general the surrounding environment. In fact, during

operating conditions, structures are actually subjected to wind loads, traffic excitation on or beneath the structure, walking or jumping of people and occupants, operating mechanical systems, micro-tremors, etc. Therefore, the basic assumption of white noise input actually derives from statistical considerations inspired by the central limit theorem [100]. Indeed, the results of many additive random sources tend toward a Gaussian white noise process. A consequence of this assumption is that every single natural frequency is not biased or driven in any particular way by the unknown input source since all the energy spectra are constant and thus equally and broadly distributed in the entire frequency domain. However, considering real in-service conditions the complete respectfulness of this basic assumption is a utopia because every single kind of input is not an ideal white noise process, therefore the input disturbances will activate natural frequencies in more or less different ways [95]. It is worth reminding that the stiffness properties of e.g. a bridge structure may vary with temperature both daily and seasonally. Therefore, this variation can be recorded as a damage alert if not properly accounted for, whereas a data normalization procedure should aim to avoid false positives due to known environmental changes [7]. Similarly, different traffic conditions may produce varying operational conditions, which need some other source of information in order to mitigate their adverse effects. Furthermore, when multiple kinds of sensors are adopted, it could be useful to adopt a data-fusion method to get a deeper and more reliable insight into the real modal properties and actual health state of the structure [7].

2.2 Conventional OMA stationary methods

2.2.1 Several potential classifications of OMA methods

The various OMA techniques share a common root since they historically derive from the previously discussed reasoning about the IRF, FRF, correlation functions, and spectral functions. As noticed in [96], the many different methods can be theoretically reconducted in a unified matrix polynomial approach to modal analysis (UMPA). However, for historical reasons, the various OMA methods are normally distinguished according to different criteria, as synthetically schematized in Fig. 2.5. The most important distinction, and usually the most adopted generally, is based on the domain of analysis, discriminating between time-domain methods and frequency-domain ones. The foremost is usually preferred since the mathematical backgrounds ensure better conditioning of methods (avoiding intrinsic spectral leakage issue) and an improved behavior dealing with noisy data, sometimes with proper noise rejection techniques [96]. On the other hand, frequency-domain methods are worse conditioned due to e.g. spectral leakage issues, but it has been improved using windowing and Z-domain equations, whilst noise reduction has been improved through averaging approach, e.g. referring to partial overlapping of windows during

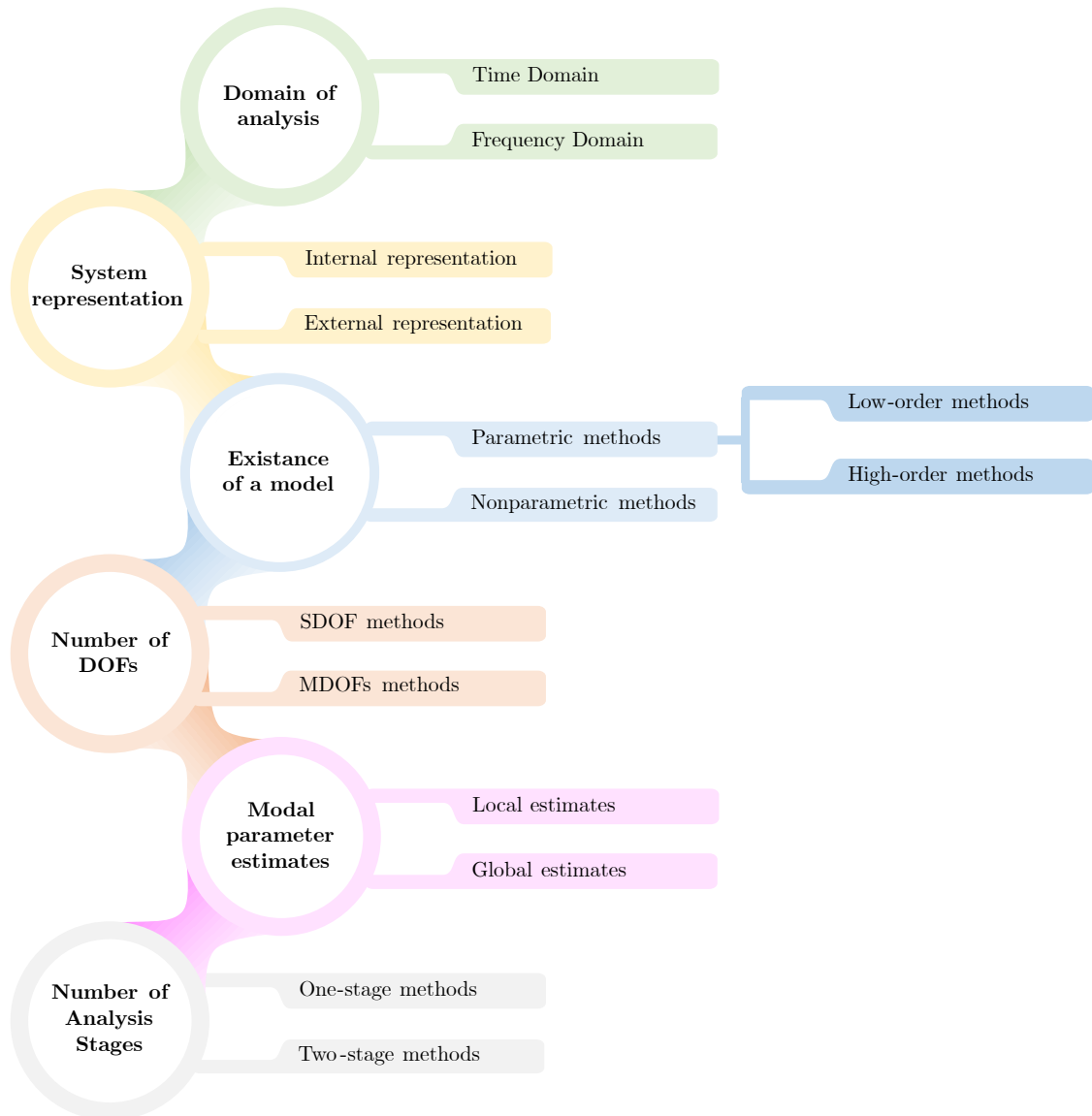


Figure 2.5: Several potential classifications of OMA methods.

windowing operations. Some OMA joint time-frequency domain analysis methods convey results in terms of periodogram or spectrogram, i.e. a combined frequency and temporal graphical representation [95].

Another possible criterion to rearrange OMA methods is based on the type of representation of the dynamical model of the system. It is distinguished between internal representation methods, the ones that provide a detailed description of the dynamical model, and external representation methods, the approaches based on a set of equations which not directly reflect the physics of the vibration phenomena but are just best fitted to the measured response [96]. If a mathematical model is

adopted, characterized by a certain number of parameters to be calibrated according to the experimental vibration data, the methods are denoted as parametric, otherwise, they are called non-parametric ones. For instance, parametric time-domain models are further distinguished between covariance-driven and data-driven methods. The foremost requires a pre-processing step to estimate the correlation functions of data, whereas the latter deals directly with raw vibration sequences. OMA parametric methods are further classified according to the number of parameters to be calibrated, discriminating between low-order models and high-order ones. In analogy to this definition, non-parametric models can be referred to as zero-order methods. Despite the modal decomposition, the dynamics of a structural system depend on the effects superposition of all modes together. However, at resonance, it is possible to assume that only the mode characterized by the single natural frequency mainly exhibits. Therefore, when a single mode is dominant and can be separately identified, the OMA method is defined as an SDOF approach, whereas when dealing with closely-spaced modes the OMA method is defined as MDOFs technique [96]. It is worth noting that the natural frequencies and damping ratios can be identified based on local estimates, i.e. since they are inherently contained in every single vibration response signal and theoretically do not depend on the specific sensor spatial layout, which instead is fundamental for reconstructing mode shapes and avoiding spatial aliasing post-processing problems. Therefore, when modal parameters can be obtained from every single vibration sequence, the OMA method is denoted as a local estimate, whereas it is denoted as a global method when the modal parameter estimates depend on processing all the time-histories sequence altogether. OMA techniques are classified as one-stage methods when directly delivering all modal information, whereas two-stage approaches indicate that natural frequencies and damping ratios are obtained at first, and then, afterward selecting every specific mode of interest according to the found natural frequencies, the related mode shape can be obtained accordingly [96].

2.2.2 Frequency domain methods

2.2.2.1 Peak-peaking method

The peak-peaking method, also acknowledged as the basic frequency domain method, is one of the earliest and simplest OMA algorithms developed, and nowadays is mainly used as a stand-alone procedure for a rapid in-situ assessment of the preliminary effectiveness of the ambient vibration testing experimental campaign [96]. It could be defined as an SDOF method since it is based on the hypothesis to identify every single mode separately, which hardly ever naturally happens in reality. Therefore, to fulfill the starting assumption of the method, it works fine with well-separated modes characterized by low damping ratios. An r -th mode is considered well-separated in the spectral domain if the minimum distance from any other

mode is greater than the bandwidth B of that mode, determined as $B = 2\xi_r f_r$, being ξ_r its damping ratio and f_r its natural frequency [95]. The modal parameters are obtained as a local estimate, i.e. it is based on the analysis of every vibration signal coming from every sensor channel separately. It is worth underlining that the method delivers only the ODS and not the proper mode shapes.

As its name suggests, it is based on identifying the peaks on the PSD matrix graph, which is characterized also by a certain degree of subjectivity, being the main drawback of this technique. When the r -th mode is dominant, the modal decomposition of Eq. (2.28) simplifies by considering only the r -th modal coordinate $p(t)$ and mode shape ϕ_r , i.e.

$$\mathbf{y}(t) = \phi_r p(t). \quad (2.35)$$

The correlation function matrix of the output signal $\mathbf{R}_{YY}(\tau)$ can be obtained by considering the autocorrelation of the modal coordinate $R_{p_r p_r}(\tau)$, i.e.

$$\mathbf{R}_{YY}(\tau) = \mathbb{E}[\mathbf{y}(t + \tau)\mathbf{y}^T(t)] = R_{p_r p_r}(\tau)\phi_r\phi_r^T. \quad (2.36)$$

Using the Fourier transform pair property, the one-side PSD matrix can be obtained by considering the spectral density of the modal coordinate $G_{p_r p_r}(f)$, i.e.

$$\mathbf{G}_{YY}(f) = G_{p_r p_r}(f)\phi_r\phi_r^H. \quad (2.37)$$

The latter equation demonstrated that the PSD $G_{YY}(f) = [\mathbf{g}_1, \mathbf{g}_2 \dots]$ of the response signal $\mathbf{y}(t)$ contain the modal information of interest, being \mathbf{g}_i the generic column vector composing the PSD. Moreover, at the resonance frequency, the system can be approximated as an SDOF system characterized only by the r -th mode. This implies that the PSD matrix is rank 1, and any column or row is proportional to the mode shape vector ϕ_r and can be assumed as an estimate of it as

$$\hat{\phi}_r = \mathbf{g}_i. \quad (2.38)$$

Normally, to better discriminate among structural modes of real interest, the PSD graph is analyzed in conjunction with the coherence function (Eq. (2.17)), since when it goes to 1 it implies a high signal-to-noise ratio (SNR). Usually expressed in dB, the SNR represents a measure of how much a superimposed undesired noise contaminates the signal of actual interest and it is defined as the base-10 logarithm of the square ratio between the signal amplitude A_y and the noise amplitude A_n , i.e.

$$\text{SNR} = \log_{10} \left(\frac{A_y}{A_n} \right)^2. \quad (2.39)$$

Despite its simplicity, the peak-peaking method is not reliable if used stand-alone, and more reliable and systematic procedures have been developed accordingly.

2.2.2.2 Frequency domain decomposition

The Frequency domain decomposition (FDD) method generalizes the peak-peaking method since it overcomes the limitation of well-separated modes, and centralizes all the evaluation in a single graph based on the singular value decomposition of the PSD matrix. This time, the response signal can be decomposed according to the modal decomposition expressed in Eq. (2.28), and the correlation function matrix $\mathbf{R}_{YY}(\tau)$ of the output signal can be obtained considering the autocorrelation matrix of the modal coordinates $\mathbf{R}_{PP}(\tau)$, i.e.

$$\mathbf{R}_{YY}(\tau) = \mathbb{E}[\mathbf{y}(t + \tau)\mathbf{y}^T(t)] = \mathbf{\Phi}\mathbf{R}_{PP}(\tau)\mathbf{\Phi}^T. \quad (2.40)$$

Leveraging the Fourier transform pair property, the one-side PSD matrix can be obtained by considering the spectral density of the modal coordinate $\mathbf{G}_{PP}(f)$, i.e.

$$\mathbf{G}_{YY}(f) = \mathbf{\Phi}\mathbf{G}_{PP}(f)\mathbf{\Phi}^H. \quad (2.41)$$

The response PSD matrix can be decomposed according to the linear algebra tool named singular value decomposition, which is a generalization of the diagonalization procedure [7]. The matrix $\mathbf{G}_{YY}(f)$ is thus decomposed into a diagonal matrix $\mathbf{\Sigma} = \text{diag}(\sigma_1, \sigma_2, \dots)$ containing the singular values (SVs) sorted in descending order and two orthogonal and unitary matrices $\mathbf{U} = [\mathbf{u}_1, \mathbf{u}_2, \dots]$ and \mathbf{V} , meaning that $\mathbf{U}^H\mathbf{U} = \mathbf{U}\mathbf{U}^H$ are equal to the identity matrix \mathbf{I} . Since the PSD is a positive definite Hermitian matrix, it holds that $\mathbf{U} = \mathbf{V}$, therefore:

$$\mathbf{G}_{YY}(f) = \mathbf{U}\mathbf{\Sigma}\mathbf{V}^H = \mathbf{U}\mathbf{\Sigma}\mathbf{U}^H. \quad (2.42)$$

Comparing Eqs. (2.41) and (2.42), it is possible to observe that $\mathbf{G}_{PP}(f)$ is diagonal if and only if the modal coordinates are uncorrelated each other, thus reinterpreting the SVs as the auto spectral densities of the modal coordinates [95]. In this case, it is possible to establish a relationship between the estimated PSD matrix from the output monitored signals and its SVD matrix, permitting reducing PSD at rank 1 for a selected frequency f_k , i.e.

$$\mathbf{G}_{YY}(f_r) = \sigma_r \mathbf{u}_r(f_r) \mathbf{u}_r^H(f_r). \quad (2.43)$$

and defining the number of mode shapes according to the rank of SVs matrix (non-zeros SVs), and estimating every r -th mode shape according to the columns of left eigenvectors \mathbf{U} , i.e.

$$\hat{\phi}_r = \mathbf{u}_r(f_r). \quad (2.44)$$

However, if the uncorrelated modal coordinate assumption does not hold, the mode shape estimates are biased and should not be used for physical interpretations [95]. Anyway, mode shapes are inherently biased within FDD since SVD decomposition imposes singular vector to be orthogonal. Therefore, in [95] it is suggested that

the best estimate of mode shape is obtained considering only the first singular vector at a frequency line being the dominant one, i.e. imposing σ_1 in Eq. (2.43). However, due to noise presence, the estimate of natural frequencies and mode shapes is uncertain if only the peak value of the first SV is considered at a frequency line f_k . Therefore, in the Enhanced Frequency Domain Decomposition (EFDD) method also information around the peaks is exploited. In fact, this led to the concept of extracting an SDOF bell around the peaks, considering a set of SVs around the mode of interest. To determine the SVs of interest to retain, the correlation among the mode shape estimates in the nearby peak is evaluated according to a quantitative metric denoted as the Modal Assurance Criterion (MAC). Considering two general mode shapes ϕ_a and ϕ_b , the MAC is defined as

$$\text{MAC}(\phi_a, \phi_b) = \frac{|\phi_a^H \phi_b|^2}{(\phi_a^H \phi_a)(\phi_b^H \phi_b)} \quad , \quad 0 \leq \text{MAC}(\phi_a, \phi_b) \leq 1. \quad (2.45)$$

When MAC is equal to one means that two vectors are perfectly correlated, on the contrary when it is 0 the two vectors are completely uncorrelated [99]. Therefore, considering the mode shape estimate at the peak $\hat{\phi}_r$ and any closer mode shape, the retained SVs are characterized by a MAC value greater than the threshold, usually imposed to 80%. The SDOF bell in the PSD extracted around the peak can be converted back to the time domain with the inverse transform. The resulting correlation function can be interpreted as a free decay response of a corresponding SDOF structural system. Therefore, besides the natural frequency and mode shape, the EFDD method allows estimating also the damping ratio ξ_r associated with the r -th mode [95], e.g. adopting the logarithm decrement technique which is a linear regression of the number of zero-crossing or extremes of the free decay correlation function graph [96, 98]. The damped natural frequency is thus given by

$$f_{r,d} = f_r \sqrt{1 - \xi_r^2}. \quad (2.46)$$

Toward the idea of an assisted or automatic selection of structural modal peaks of actual interest rather than noise peaks on the SVD graph of the PSD matrix, the modal coherence indicator function $d_1(f_k)$ can be used [99]. This is basically a correlation measure between the first singular vector at a selected frequency f_k and the other neighbor frequencies f :

$$d_1(f_k) = \mathbf{u}_1^T(f) \mathbf{u}_1(f_k). \quad (2.47)$$

It is worth noting that another advantage of FDD is its intrinsic noise separation effect provided by the adoption of the SVD tool. For instance, referring to the illustrative example using synthetic data, the SVD graph of the PSD matrix from the FDD method points out that the system is excited from a sinusoidal excitation

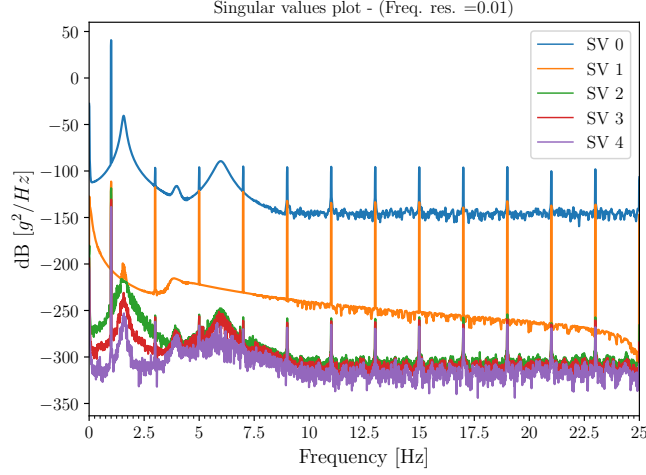


Figure 2.6: SVD graph of the PSD within the FDD method, showing the intrinsic noise separation effect provided by the SVD method.

with constant peaks appearing in the SV lines, but, without considering them, it is possible to notice that the real peaks of the first SV are related to the natural frequencies of the system, i.e. at 1.57 Hz, 3.97 Hz, and 5.98 Hz. Moreover, without special noise excitation exciting particular frequencies, the SV graph allows highlighting peaks related to structural modes of interest which significantly rise in amplitude, especially from the first SV line above the noise floor level.

2.2.3 Time domain methods

2.2.3.1 Stochastic state-space models

The time-domain description of the dynamics of a structural system can be done using a parametric model with a physical basis denoted as a state-space model [96]. The main idea is to rewrite the general second-order ODEs of the motion, Eq. (2.23), into two separate ODEs of the first order denoted as state equation and observation equation, by expressing them according to a new variable called state vector $\mathbf{s}(t)$:

$$\mathbf{s}(t) = \begin{bmatrix} \mathbf{y}(t) \\ \dot{\mathbf{y}}(t) \end{bmatrix}. \quad (2.48)$$

The state variables are sometimes also denoted as hidden variables because they characterize the internal representation of the model which is unmeasurable, and to study the dynamics of the system, only the response of the structure is the actually observed quantity. Focusing on the continuous-time domain firstly, the forcing vector in Eq. (2.23) is rewritten as $\mathbf{f}(t) = \mathbf{P}\mathbf{u}(t)$ according to an input location matrix $\mathbf{P} \in \mathbb{R}^{n \times N_{in}}$ and a function $\mathbf{u}(t)$ describing the variations of input actions

over time, being n the number of DOFs and N_{in} the number of inputs. The specific definition of these two latter terms \mathbf{P} and $\mathbf{u}(t)$ depend on the intrinsic nature of the input actions, i.e. on which DOFs the input is acting on. For instance, in earthquake engineering, the input is usually represented by an acceleration ground input indicated as $\ddot{\mathbf{u}}_g(t)$ acting only at the base DOFs of the structure. Nevertheless, Eq. (2.23) is reformulated as

$$\mathbf{M}\ddot{\mathbf{y}}(t) + \mathbf{C}\dot{\mathbf{y}}(t) + \mathbf{K}\mathbf{y}(t) = \mathbf{P}\mathbf{u}(t), \quad (2.49)$$

The first derivatives of the state vector are given by

$$\dot{\mathbf{s}}(t) = \begin{bmatrix} \dot{\mathbf{y}}(t) \\ \ddot{\mathbf{y}}(t) \end{bmatrix}, \quad (2.50)$$

The first component $\dot{\mathbf{s}}_1(t)$ of Eq. (2.50) is directly given by

$$\dot{\mathbf{s}}_2(t) = [\mathbf{0} \quad \mathbf{I}] \mathbf{s}(t) + [\mathbf{0}] \mathbf{u}(t), \quad (2.51)$$

whereas the second component $\dot{\mathbf{s}}_1(t)$ of Eq. (2.50) is directly derived by making explicit the response acceleration vector of Eq. (2.49)

$$\dot{\mathbf{s}}_2(t) = [-\mathbf{M}^{-1}\mathbf{K} \quad -\mathbf{M}^{-1}\mathbf{C}] \mathbf{s}(t) + [-\mathbf{M}^{-1}] \mathbf{P}\mathbf{u}(t), \quad (2.52)$$

eventually obtaining the state equation

$$\begin{aligned} \dot{\mathbf{s}}(t) &= \begin{bmatrix} \mathbf{0} & \mathbf{I} \\ -\mathbf{M}^{-1}\mathbf{K} & -\mathbf{M}^{-1}\mathbf{C} \end{bmatrix} \mathbf{s}(t) + \begin{bmatrix} \mathbf{0} \\ -\mathbf{M}^{-1} \end{bmatrix} \mathbf{P}\mathbf{u}(t) \quad \Leftrightarrow \\ \dot{\mathbf{s}}(t) &= \mathbf{A}_c \mathbf{s}(t) + \mathbf{B}_c \mathbf{u}(t), \end{aligned} \quad (2.53)$$

in which $\mathbf{A}_c \in \mathbb{R}^{2n \times 2n}$ is the state transition matrix, or simply the state matrix, which transforms the current state into the next state representation, and $\mathbf{B}_c \in \mathbb{R}^{2n \times n}$ is the input influence matrix, the subscript c denotes the continuous time domain. The observation equation depends on the number l and the type of sensors used to monitor the physical quantities characterizing the response of the structure gathered in $\mathbf{y}_l(t)$. Ideally, monitoring both accelerations, velocities, and displacements at all n DOFs, the response vector $\mathbf{y}_l(t)$ belongs to $\mathbb{R}^{3n \times 1}$, gathering on the column dimensions the displacements $\mathbf{y}(t)$, velocities $\dot{\mathbf{y}}(t)$, and accelerations $\ddot{\mathbf{y}}(t)$. It could be theoretically expressed as a function of the state vector, and accordingly decomposed accounting for the relative output location matrices \mathbf{C}_a , \mathbf{C}_v , and \mathbf{C}_d belonging to $\mathbb{R}^{n \times n}$, i.e.

$$\mathbf{y}_l(t) = \mathbf{C}_a \ddot{\mathbf{y}}(t) + \mathbf{C}_v \dot{\mathbf{y}}(t) + \mathbf{C}_d \mathbf{y}(t) \quad (2.54)$$

and substituting the acceleration $\ddot{\mathbf{y}}(t)$ made explicit from Eq. (2.49), it becomes

$$\tilde{\mathbf{y}}_l(t) = [\mathbf{C}_d - \mathbf{C}_a \mathbf{M}^{-1} \mathbf{K} \quad \mathbf{C}_v - \mathbf{C}_a \mathbf{M}^{-1} \mathbf{C}] \begin{bmatrix} \mathbf{y}(t) \\ \dot{\mathbf{y}}(t) \end{bmatrix} + \mathbf{C}_a \mathbf{M}^{-1} \mathbf{B} \mathbf{u}(t) \quad (2.55)$$

It is worth noting that the latter equation provides only those part of the response vector $\mathbf{y}_l(t)$ referred to the accelerations, thus indicated as $\tilde{\mathbf{y}}_l(t)$. Furthermore, this demonstrated that, since the state space formulation, the accelerations measurements in observation equations explicitly depends on the state variables, which are displacements and velocities respectively. Conversely, the displacement and velocity measurements can be considered independently provided by the state variables, and are possibly affected only by direct input. Therefore, considering a plausible and general scenario in which, for every single DOF, both displacements, velocities, and accelerations are measured, observation equations which express response vector $\mathbf{y}_l(t)$ in Eq. (2.54) as a function of state variables $\mathbf{s}(t)$ becomes

$$\mathbf{y}_l(t) = \begin{bmatrix} \mathbf{C}_d & \mathbf{0} \\ \mathbf{0} & \mathbf{C}_v \\ \mathbf{C}_d - \mathbf{C}_a \mathbf{M}^{-1} \mathbf{K} & \mathbf{C}_v - \mathbf{C}_a \mathbf{M}^{-1} \mathbf{C} \end{bmatrix} \mathbf{s}(t) + \begin{bmatrix} \mathbf{0} \\ \mathbf{0} \\ \mathbf{C}_a \mathbf{M}^{-1} \end{bmatrix} \mathbf{P} \mathbf{u}(t) \quad \Leftrightarrow$$

$$\mathbf{y}_l(t) = \mathbf{C}_c \mathbf{s}(t) + \mathbf{D}_c \mathbf{u}(t), \quad (2.56)$$

In latter equation, $\mathbf{C}_c \in \mathbb{R}^{3n \times 2n}$ is called the output influence matrix and $\mathbf{D}_c \in \mathbb{R}^{3n \times 2n}$ is the direct transmission matrix, which explains how an input directly reflects in the output response. In structural dynamics, it is worth noting that for the mathematical framework herein analyzed, the input directly affects the acceleration measurements. Beside, the above mentioned general case, considering a realistic scenario for SHM, in which only accelerometer sensors are deployed on the structure under investigation, the observation equations can be restricted only to Eq. (2.55), with an obvious consequent reformulation of \mathbf{C}_c and \mathbf{D}_c .

All the previous mathematical elaborations permitted to rewriting of the motion equation according to the deterministic continuous-time state-space model according to the state equation and observation equation respectively, i.e.

$$\dot{\mathbf{s}}(t) = \mathbf{A}_c \mathbf{s}(t) + \mathbf{B}_c \mathbf{u}(t), \quad (2.57)$$

$$\mathbf{y}_l(t) = \mathbf{C}_c \mathbf{s}(t) + \mathbf{D}_c \mathbf{u}(t). \quad (2.58)$$

This model is called deterministic since the input excitation is considered deterministic, and the modal information that characterizes the structural system is contained in the eigenvalues of state matrix \mathbf{A}_c . Infinite equivalent state space model representations, called realizations, can be defined for a certain system. Indeed, when a similarity transformation matrix with an arbitrary non-singular square matrix \mathbf{T} is applied to the state vector, the resulting state space model changes, but the eigenvalues of the state matrix preserved modal information of interest since the eigenvalues do not vary. Therefore, with a vibration experimental test, the idea is to use the monitored response to find one specific realization among the infinite possible realizations of the same system.

Considering the discrete time-domain, with time instants $t_r = r \cdot \Delta t$ described according to a sampling period Δt , with $r \in \mathbb{N}$, and discrete state vector $\mathbf{s}_r(t_r) =$

$\mathbf{s}(r \cdot \Delta t)$ with dimensionality n characterizing the order of the system, under the zero-order hold sampling assumption (input is piecewise-constant on every sampling period), and a total number N of l channels measurements $\mathbf{y}_r \in \mathbb{R}^l$, the discrete version of the deterministic state space model can be derived

$$\mathbf{s}_{r+1}(t_{r+1}) = \mathbf{A}\mathbf{s}_r(t_r) + \mathbf{B}\mathbf{u}_r(t_r), \quad (2.59)$$

$$\mathbf{y}_r(t_r) = \mathbf{C}\mathbf{s}_r(t_r) + \mathbf{D}\mathbf{u}_r(t_r), \quad (2.60)$$

in which the state space matrices are defined as

$$\mathbf{A} = e^{\mathbf{A}_c \Delta t}, \quad (2.61)$$

$$\mathbf{B} = (\mathbf{A} - \mathbf{I})\mathbf{A}_c^{-1}\mathbf{B}_c, \quad (2.62)$$

$$\mathbf{C} = \mathbf{C}_c, \quad (2.63)$$

$$\mathbf{D} = \mathbf{D}_c. \quad (2.64)$$

In order to take into account unmeasurable noise sequences, two random processes are introduced. The process noise \mathbf{w}_r encompasses disturbances and the so-called modeling errors, due to inaccuracies of the state space model to capture the actual dynamics of the physical system. The measurement noise \mathbf{v}_r is instead due to the electronics of sensors, which convert physical analog signals into finite-arithmetic and finite-memory digital equipment. These two noise processes are considered additive components, as already evidenced by the measurement noise process in Fig. 2.1, and they are assumed zero-mean Gaussian white noise processes, thus unequivocally determined by the second-order statistics. Therefore, considering any couple of time instants p and q , the variance is given by

$$\mathbb{E} \left[\begin{pmatrix} \mathbf{w}_p \\ \mathbf{v}_p \end{pmatrix} \begin{pmatrix} \mathbf{w}_q & \mathbf{v}_q \end{pmatrix} \right] = \begin{cases} \begin{bmatrix} \mathbf{Q}^{ww} & \mathbf{S}^{wv} \\ (\mathbf{S}^{wv})^T & \mathbf{R}^{vv} \end{bmatrix} & \text{if } p = q \\ \mathbf{0} & \text{if } p \neq q, \end{cases} \quad (2.65)$$

The matrices $\mathbf{Q}^{ww} \in \mathbb{R}^{n \times n}$, $\mathbf{S}^{wv} \in \mathbb{R}^{n \times l}$, and $\mathbf{R}^{vv} \in \mathbb{R}^{l \times l}$ are the covariance matrices of the noise processes \mathbf{w}_r and \mathbf{v}_r [101]. Accordingly, dropping the explicit dependence from the discrete-time instants, the discrete-time deterministic (input) stochastic state space model is given by

$$\mathbf{s}_{r+1} = \mathbf{A}\mathbf{s}_r + \mathbf{B}\mathbf{u}_r + \mathbf{w}_r, \quad (2.66)$$

$$\mathbf{y}_r = \mathbf{C}\mathbf{s}_r + \mathbf{D}\mathbf{u}_r + \mathbf{v}_r, \quad (2.67)$$

In the OMA context, the input excitation is generally unknown and modeled as a Gaussian white noise process. Therefore, it is possible to simply define the pure stochastic state space model by incorporating the unmeasurable input into the process and measurement noise sequences, i.e.

$$\mathbf{s}_{r+1} = \mathbf{A}\mathbf{s}_r + \mathbf{w}_r, \quad (2.68)$$

$$\mathbf{y}_r = \mathbf{C}\mathbf{s}_r + \mathbf{v}_r, \quad (2.69)$$

Therefore, the process noise directly becomes the unmeasurable input excitation action of the system, whereas the measurement process represents a direct disturbance which is reflected in the measured output. Indeed, the measured response is thus split into an observable part of the system and a direct unobservable disturbance. This is in accordance with the concept of a combined system (see Fig. 2.1). This fact is also reflected in the eigenvalues of the state matrix which will encompass both poles related to the structural system and ones related to the input noise excitation process. Therefore, the main objective in OMA when adopting stochastic state space time-domain parametric models is to determine at least one realization of matrices $\mathbf{A} \in \mathbb{R}^{n \times n}$ and $\mathbf{C} \in \mathbb{R}^{l \times n}$ in order to retrieve the modal information of interest. The matrix pairs \mathbf{A} and \mathbf{C} are considered observable, implying that all modes are observable in the output measurements \mathbf{y}_r [101]. Furthermore, the order of the system n is still unknown, thus it has to be also defined within the OMA procedure, as well as the second-order statistics of the output of the model and of the given output which are equal [101].

2.2.3.2 Covariance-equivalent representation of stochastic state space model

In agreement with the OMA framework, the stochastic state space model system's response is represented by a zero-mean Gaussian process, and thus the output covariance conveys all significant information to describe this random process. Hence, it is possible to define a covariance equivalent model as an estimated state space model characterized by an optimal unbiased estimator, i.e. the correct output covariance able to describe the statistical properties of the output process [96]. Assuming an LTI stationary stochastic process, the state vector is also a zero-mean Gaussian process characterized by the following state covariance matrix Σ_{s_r} which is independent of the time and uncorrelated with noise processes [101]:

$$\Sigma_{s_r} = \mathbb{E} [\mathbf{s}_r \mathbf{s}_r^T] \quad , \quad \mathbb{E} [\mathbf{s}_r \mathbf{w}_r^T] = \mathbb{E} [\mathbf{s}_r \mathbf{v}_r^T] = \mathbf{0}. \quad (2.70)$$

The Lyapunov equation provides an alternative definition for the state covariance matrix Σ_{s_r} considering the next state \mathbf{s}_{k+1} [101]

$$\begin{aligned} \Sigma_{s_r} &= \mathbb{E} [\mathbf{s}_{k+1} \mathbf{s}_{k+1}^T] = \mathbb{E} [(\mathbf{A} \mathbf{s}_k + \mathbf{w}_r) (\mathbf{A} \mathbf{s}_k + \mathbf{w}_r)^T] \\ &= \mathbf{A} \mathbb{E} [\mathbf{s}_r \mathbf{s}_r^T] \mathbf{A}^T + \mathbb{E} [\mathbf{w}_r \mathbf{w}_r^T] \\ &= \mathbf{A} \Sigma_{s_r} \mathbf{A}^T + \mathbf{Q}^{ww}. \end{aligned} \quad (2.71)$$

The output covariance matrix, i.e. the cross-correlation matrix of the measured output response from all sensors' channels for sample r and with finite time lag i , is defined in general as

$$\mathbf{R}_i = \mathbb{E} [\mathbf{y}_{r+i} \mathbf{y}_r^T] \quad (2.72)$$

from which it is possible to derive the initial output covariance matrix \mathbf{R}_0 for lag $i = 0$,

$$\begin{aligned}\mathbf{R}_0 &= \mathbb{E}[\mathbf{y}_r \mathbf{y}_r^T] = \mathbb{E}[(\mathbf{C} \mathbf{s}_k + \mathbf{v}_r)(\mathbf{C} \mathbf{s}_k + \mathbf{v}_r)^T] \\ &= \mathbf{C} \mathbb{E}[\mathbf{s}_r \mathbf{s}_r^T] \mathbf{C}^T + \mathbb{E}[\mathbf{v}_r \mathbf{v}_r^T] \\ &= \mathbf{C} \boldsymbol{\Sigma}_{s_r} \mathbf{C}^T + \mathbf{R}^{vv}.\end{aligned}\quad (2.73)$$

It is possible to define the next state-output covariance matrix \mathbf{G} which represents the covariance between the response of the system \mathbf{y}_r and the updated state vector \mathbf{s}_{r+1}

$$\begin{aligned}\mathbf{G} &= \mathbb{E}[\mathbf{s}_{r+1} \mathbf{y}_r^T] = \mathbb{E}[(\mathbf{A} \mathbf{s}_k + \mathbf{w}_r)(\mathbf{C} \mathbf{s}_k + \mathbf{v}_r)^T] \\ &= \mathbf{A} \mathbb{E}[\mathbf{s}_r \mathbf{s}_r^T] \mathbf{C}^T + \mathbb{E}[\mathbf{w}_r \mathbf{v}_r^T] \\ &= \mathbf{A} \boldsymbol{\Sigma}_{s_r} \mathbf{C}^T + \mathbf{S}^{wv}.\end{aligned}\quad (2.74)$$

from which it is possible to obtain an alternative definition for the output covariance matrix sequence \mathbf{R}_i , so that

$$\mathbf{R}_i = \mathbf{C} \mathbf{A}^{i-1} \mathbf{G} \quad , \quad \mathbf{R}_{-i} = \mathbf{G}^T (\mathbf{A}^{i-1})^T \mathbf{C}^T. \quad (2.75)$$

The Eq. (2.75) has fundamental consequences which are at the base of stochastic subspace identification algorithms, being that output covariance can be considered as Markov parameters of an LTI system defined by state space matrices \mathbf{A} , \mathbf{C} , \mathbf{G} , and \mathbf{R}_0 . In general, Markov parameters describe the input-output relationship of a discrete-time model with sampled response according to a pulse response function to a unit pulse input [102]. This implies that \mathbf{R}_i can be estimated directly from the measured data, viz. from \mathbf{G} , and the decomposition of the output covariance matrices permits to retrieve the state matrix \mathbf{A} whose poles represent the sought solution of the dynamic identification problem when employing a parametric stochastic state space time-domain method based on a covariance-driven approach.

2.2.3.3 Kalman filter representation of stochastic state space model

The stochastic state space model in Eqs. (2.68)-(2.69) can be expressed in an alternative form according to the Kalman filter approach [96]. Henceforth, it is assumed that the system matrices \mathbf{A} , \mathbf{C} , \mathbf{Q}^{ww} , \mathbf{R}^{vv} and \mathbf{S}^{wv} are already known. All the measurements beforehand r -th time instant can be gathered according to the following measurements matrix

$$\mathbf{Y}_{r-1} = [\mathbf{y}_0 \quad \mathbf{y}_1 \quad \dots \quad \mathbf{y}_{r-1}]^T. \quad (2.76)$$

The best state space model estimate should minimize the prediction error between the estimated response $\hat{\mathbf{y}}_r$ at r -th time instant and the measured one \mathbf{y}_r denoted as innovation error \mathbf{e}_r [96]:

$$\mathbf{e}_r = \mathbf{y}_r - \hat{\mathbf{y}}_r, \quad (2.77)$$

noting that \mathbf{e}_r is a zero-mean Gaussian white noise process because also \mathbf{y}_r is assumed of this type. The estimated response can be statistically defined as the conditional expectation of the ideal response \mathbf{y}_r at time t_r conditioned on past measured ones \mathbf{Y}_{r-1} , and assuming no correlation holds with the measurement noise process \mathbf{v}_r , i.e.

$$\hat{\mathbf{y}}_r = \mathbb{E}[\mathbf{y}_r | \mathbf{Y}_{r-1}] = \mathbb{E}[\mathbf{C}\mathbf{s}_r + \mathbf{v}_r | \mathbf{Y}_{r-1}] = \mathbf{C}\mathbf{s}_r. \quad (2.78)$$

The minimization of the innovation error can be obtained if the optimal state estimate $\hat{\mathbf{s}}_r$ at every r -th time instant can be found, which is statistically defined as the conditional expectation of the ideal current state conditioned from the past responses [96]:

$$\hat{\mathbf{s}}_r = \mathbb{E}[\mathbf{s}_k | \mathbf{Y}_{r-1}]. \quad (2.79)$$

The state prediction error $\boldsymbol{\varepsilon}_r$ is the difference between the ideal state \mathbf{s}_k and the predicted state $\hat{\mathbf{s}}_k$, thus representing the error part which cannot be estimated from one step ahead of the state vector [96], i.e.

$$\boldsymbol{\varepsilon}_r = \mathbf{s}_k - \hat{\mathbf{s}}_k. \quad (2.80)$$

The nonsteady state stochastic state space model adopting the Kalman filter for the LTI system is called the forward innovation model and it is based on the state predictors $\hat{\mathbf{s}}_r$ and output response predictor $\hat{\mathbf{y}}_r$, i.e

$$\hat{\mathbf{s}}_{r+1} = \mathbf{A}\hat{\mathbf{s}}_r + \mathbf{K}_r \mathbf{e}_r, \quad (2.81)$$

$$\mathbf{e}_r = \mathbf{y}_r - \mathbf{C}\hat{\mathbf{s}}_r, \quad (2.82)$$

in which \mathbf{K}_r is denoted as nonsteady Kalman gain. The model in Eqs. (2.81) and (2.82) assumes that the initial state estimate is zero $\hat{\mathbf{s}}_0 = \mathbf{0}$. Moreover, denoting with $\mathbf{P}_r = \mathbb{E}[\hat{\mathbf{s}}_r \hat{\mathbf{s}}_r^T]$ the Kalman state covariance matrix, the initial covariance matrix of Kalman state estimate is given by

$$\mathbf{P}_0 = \mathbb{E}[\hat{\mathbf{s}}_0 \hat{\mathbf{s}}_0^T] = \mathbf{0}. \quad (2.83)$$

The covariance of the innovation error is given by [101]:

$$\mathbb{E}[\mathbf{e}_r \mathbf{e}_r^T] = \mathbf{R}_0 - \mathbf{C}\mathbf{P}_k \mathbf{C}^T, \quad (2.84)$$

in which \mathbf{R}_0 is the initial output covariance matrix defined in Eq. (2.73). The general idea behind the stochastic state space Kalman formulation is that at the r -th time instant, the nonsteady Kalman state estimates $\hat{\mathbf{s}}_r$ substitute the state \mathbf{s}_r in stochastic state space formulation in Eqs. (2.68)-(2.69), and both equations the two noise processes \mathbf{w}_r and \mathbf{v}_r are condensed in a single term, i.e. the innovation error \mathbf{e}_r . The nonsteady Kalman state estimate $\hat{\mathbf{s}}_r$ is found by solving a series of recursive formulas depending only on previous Kalman state estimates and

past output measures [96], thus finally delivering the state estimate, the nonsteady Kalman gain, the Kalman state covariance, i.e.

$$\hat{\mathbf{s}}_r = \mathbf{A}\hat{\mathbf{s}}_{r-1} + \mathbf{K}_{r-1}(\mathbf{y}_r - \mathbf{C}\mathbf{s}_r), \quad (2.85)$$

$$\mathbf{K}_{r-1} = (\mathbf{G} - \mathbf{A}\mathbf{P}_{r-1}\mathbf{C}^T)(\mathbf{R}_0 - \mathbf{C}\mathbf{P}_{r-1}\mathbf{C}^T)^{-1}, \quad (2.86)$$

$$\mathbf{P}_r = \mathbf{A}\mathbf{P}_{r-1}\mathbf{A}^T + (\mathbf{G} - \mathbf{A}\mathbf{P}_{r-1}\mathbf{C}^T)(\mathbf{R}_0 - \mathbf{C}\mathbf{P}_{r-1}\mathbf{C}^T)^{-1}(\mathbf{G} - \mathbf{A}\mathbf{P}_{r-1}\mathbf{C}^T)^T. \quad (2.87)$$

The Eq. (2.87) is acknowledged as the Riccati equation. Theoretically, the forward innovation model is denoted as nonsteady because Kalman state covariance is nonsteady for a transient period at the beginning of the recursive process. Nevertheless, under the assumption of stable state matrix \mathbf{A} , meaning that at a finite input excitation the response is limited as well, which translates in mathematical terms in evaluating that all eigenvalues of the matrix have negative real parts (see section 2.1.2), both Kalman state covariance and Kalman gain are constant and independent from time instants, i.e.

$$\mathbf{P}_r = \mathbf{P}, \quad \mathbf{K}_r = \mathbf{K} \quad (2.88)$$

Therefore, the steady-state Kalman filter stochastic state space formulation is given by

$$\hat{\mathbf{s}}_{r+1} = \mathbf{A}\hat{\mathbf{s}}_r + \mathbf{K}\mathbf{e}_r, \quad (2.89)$$

$$\mathbf{e}_r = \mathbf{y}_r - \mathbf{C}\hat{\mathbf{s}}_r, \quad (2.90)$$

in which the Kalman gain

$$\mathbf{K} = (\mathbf{G} - \mathbf{A}\mathbf{P}\mathbf{C}^T)(\mathbf{R}_0 - \mathbf{C}\mathbf{P}\mathbf{C}^T)^{-1} \quad (2.91)$$

can be found by the resolution of the Riccati equation

$$\mathbf{P} = \mathbf{A}\mathbf{P}\mathbf{A}^T + (\mathbf{G} - \mathbf{A}\mathbf{P}\mathbf{C}^T)(\mathbf{R}_0 - \mathbf{C}\mathbf{P}\mathbf{C}^T)^{-1}(\mathbf{G} - \mathbf{A}\mathbf{P}\mathbf{C}^T)^T \quad (2.92)$$

solved through a generalized eigenvalue problem as described in detail in [101]. Rearranging (2.90) to explicit the response estimate vector $\hat{\mathbf{y}}_r$, the steady state Kalman filter forward innovation model of Eqs. (2.89)-(2.90) is directly comparable with stochastic state space formulation in Eqs. (2.68)-(2.69):

$$\begin{array}{l|l} \hat{\mathbf{s}}_{r+1} = \mathbf{A}\hat{\mathbf{s}}_r + \mathbf{K}\mathbf{e}_r & \mathbf{s}_{r+1} = \mathbf{A}\mathbf{s}_r + \mathbf{w}_r \\ \mathbf{y}_r = \mathbf{C}\hat{\mathbf{s}}_r + \mathbf{e}_r & \mathbf{y}_r = \mathbf{C}\mathbf{s}_r + \mathbf{v}_r \end{array} \quad (2.93)$$

Despite the well-posed theoretical framework, within the OMA context the basic assumption hypothesis of already knowing the system matrices \mathbf{A} , \mathbf{C} , \mathbf{Q}^{ww} , \mathbf{R}^{vv} and \mathbf{S}^{wv} does not hold. Therefore, the modal identification strategies based on the Kalman filter formulation are denoted as data-driven time-domain parametric methods, because they must rely solely on the output measurement data to estimate the state sequences, thus avoiding analytically solving the Riccati equation [96].

2.2.3.4 Covariance-based stochastic-subspace identification

Several time-domain methods have been developed for OMA in the last decades, based on the analysis of correlation functions of vibration output responses under natural excitation conditions, which progressively replaced forced vibration tests as discussed in section 2.1.3. Therefore, the related output-only OMA methods have been denoted as Natural Excitation Techniques (NExT), and it is worth mentioning at least three distinguished approaches, i.e. the least square complex exponential (LSCE) algorithm, the Ibrahim time domain (ITD) method and the eigenvalue realization algorithm (ERA), which is very similar to subspace-based identification approaches. The interested reader about LSCE, ITD, and ERA can refer to [103, 104, 105] respectively. The NExT OMA procedures were very popular at the beginning but they were progressively abandoned for several limitations and/or drawbacks [96], preferring stochastic subspace identification strategies.

The covariance-based stochastic-subspace identification (SSI-cov) is a parametric time-domain algorithm based on the Ho-Kalman realization algorithm [106], which estimates states' realizations using only output measured data. The SSI-cov algorithm is based on the stochastic state space model Eqs. (2.68)-(2.69), characterized by a certain order n of the model, a number l of monitored DOFs with a finite number N_d of measured output data samples in total, with $\mathbf{s}_r \in \mathbb{R}^n$, $\mathbf{y}_r \in \mathbb{R}^l$, $\mathbf{A} \in \mathbb{R}^{n \times n}$ and $\mathbf{C} \in \mathbb{R}^{l \times n}$, under the hypothesis that all the states of the system are controllable and observable. A state is defined as controllable if it can be obtained from any previous initial state with certain control actions, whereas it is defined as observable when the state at a certain time instant is completely determined by knowing both the input and output of the system. Similarly to Eq. (2.18), the output correlation matrices $\hat{\mathbf{R}}_i \in \mathbb{R}^{l \times l}$ are estimated according to a user-defined finite integer lag parameter $i \in \mathbb{N}$, called time shift or number of block rows within the context of stochastic-subspace identification approaches [96], i.e.

$$\hat{\mathbf{R}}_i = \frac{1}{N_d - i} \mathbf{Y}_{1:N_d-i} \mathbf{Y}_{i:N_d}^T, \quad (2.94)$$

in which matrices $\mathbf{Y}_{1:N_d-i} = [\mathbf{y}_0 \ \mathbf{y}_1 \ \dots \ \mathbf{y}_{N_d-i}]^T \in \mathbb{R}^{l \times N_d}$ and $\mathbf{Y}_{i:N_d} \in \mathbb{R}^{N_d \times l}$ represent the output measurements time histories obtained from l sensors gathered and rearranged in a similar manner as Eq. (2.76). All correlation estimates, which assume the meaning of output covariance matrices in the SSI-cov context, are computed for time lags from i to $2i - 1$ and they are rearranged into a block Toeplitz matrix $\mathbf{T}_{1|i} \in \mathbb{R}^{il \times il}$ (viz. a matrix with constant diagonals) as follows:

$$\mathbf{T}_{1|i} = \begin{bmatrix} \mathbf{R}_i & \mathbf{R}_{i-1} & \dots & \mathbf{R}_2 & \mathbf{R}_1 \\ \mathbf{R}_{i+1} & \mathbf{R}_i & \ddots & \ddots & \mathbf{R}_2 \\ \vdots & \ddots & \ddots & \ddots & \vdots \\ \vdots & \ddots & \ddots & \ddots & \mathbf{R}_{i-1} \\ \mathbf{R}_{2i-1} & \mathbf{R}_{2i-2} & \dots & \mathbf{R}_{i+1} & \mathbf{R}_i \end{bmatrix}. \quad (2.95)$$

The subscript in $\mathbf{T}_{1|i}$ indicates the indices of the first column of the matrix [101]. The derivation of the Toeplitz matrix of output correlations starting from the output vibration measured data is extensively discussed in the Appendix A. The use of the Toeplitz matrix of output covariance matrices can reduce the computational effort during the modal identification, thereby improving the efficiency of the elaboration. For a system of order n , the choice of the number of block rows parameter i must fulfill the following condition [96]

$$li \geq n. \quad (2.96)$$

The real order n of the state-space model is unknown. The Ho-Kalman realization algorithm is based on the minimal realization concept, meaning that the results of the algorithm attempt to deliver also the minimum order n which ensures that the system is fully controllable and observable. Nevertheless, at the beginning of the SSI-cov procedure, a preliminary rough estimate of n can be obtained by exploring the rank of the PSD of the output response measurements or of the SVD of the PSD, such as according to the FDD method. This latter rough estimate permits a proper choice of the time shift parameter by fulfilling the condition $i \geq n/l$. When the system is fully controllable and observable, the Toeplitz matrix can be factorized into the product of two matrices denoted as observability matrix $\mathbf{O}_i \in \mathbb{R}^{li \times n}$, which only depends on the state matrix \mathbf{A} and the output influence matrix \mathbf{C} , and reversed controllability matrix $\mathbf{\Gamma}_i \in \mathbb{R}^{n \times li}$, which depends solely on the state matrix \mathbf{A} and the next state output covariance matrix \mathbf{G} , i.e.

$$\mathbf{T}_{1|i} = \begin{bmatrix} \mathbf{C} \\ \mathbf{CA} \\ \vdots \\ \mathbf{CA}^{i-1} \end{bmatrix} [\mathbf{A}^{i-1}\mathbf{G} \quad \dots \quad \mathbf{AG} \quad \mathbf{G}] = \mathbf{O}_i \mathbf{\Gamma}_i. \quad (2.97)$$

Therefore, matrix \mathbf{C} can be readily extracted from the first l rows of \mathbf{O}_i , whereas matrix \mathbf{G} can be obtained from the last l columns of $\mathbf{\Gamma}_i$. In order to obtain the observability and controllability matrices separately, the SVD decomposition of the Toeplitz matrix is employed, i.e.

$$\mathbf{T}_{1|i} = \mathbf{U} \mathbf{\Sigma} \mathbf{V}^T = [\mathbf{U}_1 \quad \mathbf{U}_2] \begin{bmatrix} \mathbf{\Sigma}_1 & \mathbf{0} \\ \mathbf{0} & \mathbf{0} \end{bmatrix} \begin{bmatrix} \mathbf{V}_1 \\ \mathbf{V}_2 \end{bmatrix} \approx \mathbf{U}_1 \mathbf{\Sigma}_1 \mathbf{V}_1^T \quad (2.98)$$

in which the dimension of the SV matrix $\mathbf{\Sigma}$ is approximately reduced to its actual rank n by excluding all the near-zero SVs in the $\mathbf{\Sigma}_1 \in \mathbb{R}^{n \times n}$, and with $\mathbf{U}_1 \in \mathbb{R}^{li \times n}$ and $\mathbf{V}_1^T \in \mathbb{R}^{n \times li}$. Therefore, the observability and controllability matrices are obtained as follows

$$\mathbf{T}_{1|i} = \mathbf{U}_1 \mathbf{\Sigma}_1 \mathbf{V}_1^T = \mathbf{U}_1 (\mathbf{\Sigma}_1^{1/2} \mathbf{\Sigma}_1^{1/2}) \mathbf{V}_1^T = (\mathbf{U}_1 \mathbf{\Sigma}_1^{1/2}) (\mathbf{\Sigma}_1^{1/2} \mathbf{V}_1^T) = \mathbf{O}_i \mathbf{\Gamma}_i, \quad (2.99)$$

$$\mathbf{O}_i = \mathbf{U}_1 \mathbf{\Sigma}_1^{1/2} \mathbf{T}, \quad (2.100)$$

$$\mathbf{\Gamma}_i = \mathbf{T}^{-1} \mathbf{\Sigma}_1^{1/2} \mathbf{V}_1^T, \quad (2.101)$$

noting that in the Eqs. (2.100)-(2.101) a similarity non-singular transformation matrix have been included since the method formally identifies one specific realization from the measured data among the infinite equivalent state-space realizations, but it generally simplifies assuming an identity matrix $\mathbf{T} = \mathbf{I}$.

Once the observability and controllability matrix is known, the second part of the SSI-cov method deals with finding the state matrix \mathbf{A} , and with an output influence matrix \mathbf{C} estimate the modal parameters of actual interest. As already above-mentioned, matrix \mathbf{C} can be readily extracted from the first l rows of \mathbf{O}_i , whereas matrix \mathbf{G} can be obtained from the last l columns of $\mathbf{\Gamma}_i$. For estimating matrix \mathbf{A} at least two main different procedures are available in the literature [96]. The first method is based on the NExT-ERA approach, which requires defining a new one-time lag Toeplitz matrix of the output covariances $\mathbf{T}_{2|i+1}$, and noting that in its factorization \mathbf{A} readily appears besides observability and controllability matrices:

$$\mathbf{T}_{2|i+1} = \begin{bmatrix} \mathbf{R}_{i+1} & \mathbf{R}_i & \cdots & \mathbf{R}_3 & \mathbf{R}_2 \\ \mathbf{R}_{i+2} & \mathbf{R}_{i+1} & \ddots & \ddots & \mathbf{R}_3 \\ \vdots & \ddots & \ddots & \ddots & \vdots \\ \vdots & \ddots & \ddots & \ddots & \mathbf{R}_{i-1} \\ \mathbf{R}_{2i} & \mathbf{R}_{2i-1} & \cdots & \mathbf{R}_{i+2} & \mathbf{R}_{i+1} \end{bmatrix} = \mathbf{O}_i \mathbf{A} \mathbf{\Gamma}_i. \quad (2.102)$$

Therefore, considering Eqs. (2.100)-(2.101) obtained from SVD decomposition of the original output covariance Toeplitz matrix Eq. (2.95), the state matrix \mathbf{A} estimate is given by

$$\mathbf{A} = \mathbf{O}_i^\dagger \mathbf{T}_{2|i+1} \mathbf{\Gamma}_i^\dagger = \left(\mathbf{\Sigma}_1^{-1/2} \mathbf{U}_1^T \right) \mathbf{T}_{2|i+1} \left(\mathbf{V}_1 \mathbf{\Sigma}_1^{-1/2} \right). \quad (2.103)$$

where the \dagger superscript indicates the Moore–Penrose pseudo-inverse operation [96].

The second method to estimate state matrix \mathbf{A} has been initially formulated by Yi and Yun [107, 96]. It is based on pre- and post- multiplying the output covariance Toeplitz matrix Eq. (2.95) by two invertible matrices \mathbf{W}_1 and \mathbf{W}_2 , i.e. $\mathbf{W}_1 \mathbf{T}_{1|i} \mathbf{W}_2$, thus delivering after SVD decomposition, the following alternative definition for the observability matrix:

$$\mathbf{O}_i = \mathbf{W}_1^{-1} \mathbf{U}_1 \mathbf{\Sigma}_1^{1/2} \mathbf{T}. \quad (2.104)$$

In the literature, two different weighting schemes have been proposed, denoted as balanced realization (BR) and canonical variate analysis (CVA) weighting [108]. In the BR procedure, if the weight matrices are equal to the identity matrix, viz. $\mathbf{W}_1 = \mathbf{W}_2 = \mathbf{I}$. In this case, it is possible to demonstrate that $\mathbf{O}_i^T \mathbf{O}_i = \mathbf{\Gamma}_i \mathbf{\Gamma}_i^T = \mathbf{\Sigma}_1$ (Gram matrices), and the term balanced in BR refers to the fact that the input excitation transfers to the state in a similar and balanced way as well as the state transfers to the output response [96]. Leveraging the shift-invariance property of \mathbf{O}_i [109], it is possible to further decompose the observability matrix to make explicit

obtaining state matrix \mathbf{A} by defining a matrix \mathbf{O}_i^\uparrow , obtained by removing the last l lines from \mathbf{O}_i , and a matrix \mathbf{O}_i^\downarrow , retrieved by removing the first l rows of \mathbf{O}_i [110, 111], i.e.

$$\mathbf{O}_i = \begin{bmatrix} \mathbf{C} \\ \mathbf{CA} \\ \vdots \\ \mathbf{CA}^{i-1} \end{bmatrix} = \begin{bmatrix} \mathbf{O}_i^\uparrow \\ \mathbf{CA}^{i-1} \end{bmatrix} = \begin{bmatrix} \mathbf{C} \\ \mathbf{O}_i^\downarrow \end{bmatrix} \Rightarrow \mathbf{O}_i^\uparrow = \begin{bmatrix} \mathbf{C} \\ \mathbf{CA} \\ \vdots \\ \mathbf{CA}^{i-2} \end{bmatrix}, \mathbf{O}_i^\downarrow = \begin{bmatrix} \mathbf{CA} \\ \mathbf{CA}^2 \\ \vdots \\ \mathbf{CA}^{i-1} \end{bmatrix} \quad (2.105)$$

$$\Rightarrow \mathbf{O}_i^\uparrow \mathbf{A} = \mathbf{O}_i^\downarrow \Rightarrow \mathbf{A} = \mathbf{O}_i^{\uparrow \dagger} \mathbf{O}_i^\downarrow \quad (2.106)$$

On the other hand, the CVA weighting is based on ensuring balanced energy levels among all the system's modes and it adopts the Cholesky decomposition of two new Toeplitz matrices to retrieve the weighting matrices [108]. \mathbf{W}_1 is given by the inverse of the lower triangular matrix $[\mathbf{L}^+]^{-1}$ obtained from the Cholesky factorization of a reversed one-time lag Toeplitz matrix of the output covariances $\mathbf{T}_{0|i-1}^+$ in which the upper triangle is transposed, i.e.

$$\mathbf{T}_{0|i-1} = \begin{bmatrix} \mathbf{R}_0 & \mathbf{R}_1^T & \dots & \mathbf{R}_{i-2}^T & \mathbf{R}_{i-1}^T \\ \mathbf{R}_1 & \mathbf{R}_0 & \ddots & \ddots & \mathbf{R}_{i-2}^T \\ \vdots & \ddots & \ddots & \ddots & \vdots \\ \vdots & \ddots & \ddots & \ddots & \mathbf{R}_{i-1}^T \\ \mathbf{R}_{i-1} & \mathbf{R}_{i-2} & \dots & \mathbf{R}_1 & \mathbf{R}_0 \end{bmatrix} = \mathbf{L}^+ [\mathbf{L}^+]^T \Rightarrow \mathbf{W}_1 = [\mathbf{L}^+]^{-1}. \quad (2.107)$$

\mathbf{W}_2 is given by the inverse of the lower triangular matrix $[\mathbf{L}^-]^{-1}$ obtained from the Cholesky factorization of a reversed one-time lag Toeplitz matrix of the output covariances $\mathbf{T}_{0|i-1}^-$ in which, instead, the lower triangle is transposed, i.e.

$$\mathbf{T}_{0|i-1} = \begin{bmatrix} \mathbf{R}_0 & \mathbf{R}_1 & \dots & \mathbf{R}_{i-2} & \mathbf{R}_{i-1} \\ \mathbf{R}_1^T & \mathbf{R}_0 & \ddots & \ddots & \mathbf{R}_{i-2} \\ \vdots & \ddots & \ddots & \ddots & \vdots \\ \vdots & \ddots & \ddots & \ddots & \mathbf{R}_{i-1} \\ \mathbf{R}_{i-1}^T & \mathbf{R}_{i-2}^T & \dots & \mathbf{R}_1^T & \mathbf{R}_0 \end{bmatrix} = \mathbf{L}^- [\mathbf{L}^-]^T \Rightarrow \mathbf{W}_2 = [\mathbf{L}^-]^{-1}. \quad (2.108)$$

Therefore, the eigenvalues of the weighted Toeplitz matrix in Eq. (2.95), i.e. $\mathbf{W}_1 \mathbf{T}_{1|i} \mathbf{W}_2$, can be geometrically interpreted as canonical angles between two subspaces which ensure balanced energy levels among all the system's modes [96, 108].

The OMA identification solution, i.e. the modal parameter estimates of interest (natural frequencies, damping ratios, and mode shapes), can be obtained once state matrix \mathbf{A} and output influence matrix \mathbf{C} have been determined. The eigenvalue decomposition (EVD) of matrix \mathbf{A} leads to the diagonal matrix $\mathbf{\Lambda} = \text{diag}([\lambda_1, \dots, \lambda_u, \dots, \lambda_m]) \in \mathbb{R}^{n \times n}$ of discrete-time complex conjugate system poles

pairs λ_u, λ_u^* (two-quadrant symmetry) and corresponding right eigenvectors ψ_u :

$$\mathbf{A} = \mathbf{\Psi} \mathbf{\Lambda} \mathbf{\Psi}^{-1} \quad , \quad \mathbf{A} \psi_u = \lambda_u \psi_u, \quad (2.109)$$

where $1 \leq u \leq m$, being $m = n/2$ the total number of eigenvalues of actual interest. The motivation of this latter aspect is due to the fact that only modes with positive damping, i.e. with positive imaginary parts, are of actual interest among the n complex conjugate poles, implying that for physical reasons the number of modes of interest is half of the system's order [96, 112]. The undamped and damped natural frequencies and damping ratios are finally determined through the conversion back from Z-domain discrete time to Laplace-domain continuous time, i.e. according to Eqs. (2.30)-(2.33), reported also here for simplicity:

$$s_u = \frac{\ln(\lambda_u)}{\Delta t} \quad , \quad f_u = \frac{|s_u|}{2\pi} \quad , \quad \xi_u = -100 \frac{\Re(s_u)}{|s_u|},$$

where s_u are the continuous-time system poles, Δt is the sampling interval, $|\cdot|$ denotes the complex modulus and $\Re(s_u)$ is the real part of s_u . The real part of the eigenvectors ψ_u instead leads to the experimental mode shapes ϕ_u , given by

$$\phi_u = \Re(\mathbf{C} \psi_u), \quad (2.110)$$

with $\mathbf{\Phi} = [\phi_1, \dots, \phi_u, \dots, \phi_m] \in \mathbb{R}^{l \times m}$.

It is worth mentioning that the entire SSI-cov procedure can be equivalently performed by using a block-Hankel matrix (a matrix with constant anti-diagonals) of the output measurements' covariance estimates instead of the Toeplitz matrix in Eq. (2.95), as summarized in the Appendix A. Furthermore, it is necessary to point out that the entire theoretical framework is based on estimated quantities (e.g. output covariances Eq. (2.94)), since the measurement data are composed of a finite number of data. Moreover, considering additive noise source due to the state space modeling inaccuracies, and sensors' hardware measurement noise, jointly with computational noise due to finite precision arithmetic of computers, the rank of the estimated Toeplitz matrix is not able to exactly deliver the real theoretical order of the system, even because due to noise the Toeplitz factorization is not mathematically exact. The Toeplitz matrix rank can be theoretically highlighted by the greatest relative difference exhibited in its SVs sorted in decreasing order. Nevertheless, since in the OMA context, the real goal is achieving reliable modal parameters' estimates rather than finding a very accurate dynamics description through a state space model, a conservative overestimation approach for the system order is normally adopted, resulting in the acknowledged stabilization diagram (SD) approach [96]. In practice, the system order n is imposed from low values and progressively increased to higher over-specification values until reaching a user-defined threshold. Therefore, the Toeplitz output covariance matrix dimensions are initially restricted to low dimensions and, according to the SSI-cov, poles are then

computed. This procedure is repeated imposing the sizes of the Toeplitz matrix for all progressively increasing orders. Reminding that the obtained poles of interest are only half of the system order in the subspace-based identification field because of retaining only poles with positive imaginary parts, the system order grows up by twos. The over-specification of the model order n reveals new spurious poles along with the physical ones of interest. The spurious ones are denoted noise poles, when they are associated with real physical basis because of the identification of the excitation system beside the structural system (see combined system concept in Fig. 2.1). On the other hand, they are called mathematical modes when they arise due to all the other inaccuracies and noise sources mentioned before. As depicted in the example Fig. 2.7, the stabilization diagram is a bi-dimensional graph showing the poles of the system for a certain order on the ordinate axis with respect to the natural frequency reported on the abscissa axis. The SD provides a simple yet powerful tool to clearly separate stable physical modes from unstable spurious ones, by tracking the stable poles' alignments for progressively increasing orders of the system. Stability checks are performed to discriminate between stable and unstable poles in terms of frequency, damping ratio, and mode shapes, and they are configured into two classes. Hard validation criteria (HVC) are based on rigorous physical principles and they apply to all poles singularly, whereas soft validation criteria (SVC) establish relative thresholds between pole pairs at two different orders [113, 114]. The HVC defines spurious poles as those that do not appear as complex conjugate pairs, modes with natural frequencies greater than maximum Nyquist frequency (also considering possible decimation), and those with negative or unrealistic excessive positive damping ratios (usually set at 10%) [113]:

$$\xi_u \leq 0.1, \quad (2.111)$$

$$f_u \leq \frac{f_s}{2}. \quad (2.112)$$

Assuming that a is a pole identified at model order n , the SVC define spurious poles by comparing pole a with any other pole b at the model orders $2, 4, \dots, n/2$ according to the following relative stability criteria [96]:

$$\Delta\xi = \frac{\xi_a - \xi_b}{\xi_a} \leq 0.05, \quad (2.113)$$

$$\Delta f = \frac{f_a - f_b}{f_a} \leq 0.01, \quad (2.114)$$

$$1 - \text{MAC}(\phi_a, \phi_b) \leq 0.02. \quad (2.115)$$

In general, stabilization diagram representation can be adapted for any parametric OMA method. This graphical tool permits a quite clear separation of physical models rather than spurious ones. Moreover, as depicted in the example Fig. 2.8, the stabilization diagram is often combined with at least the first SV graph of the PSD

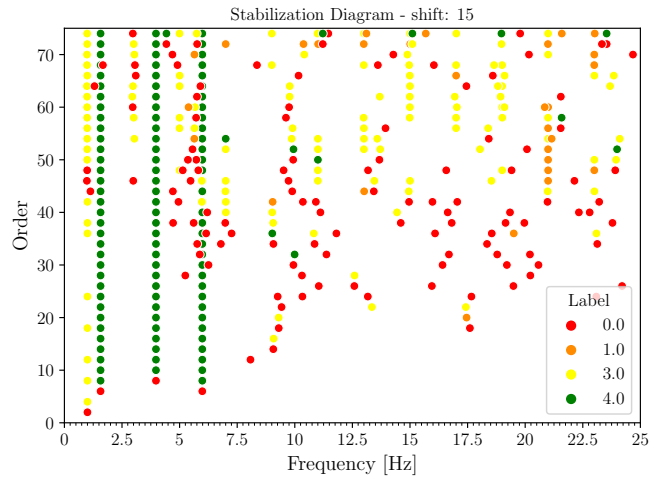


Figure 2.7: Stabilization diagram. The colors of the poles, identified by the numbers 0.0 to 4.0 in the legend, indicate respectively: unstable, stable in frequency, stable in frequency and mode shape, stable in frequency and damping, stable in frequency damping and mode shape.

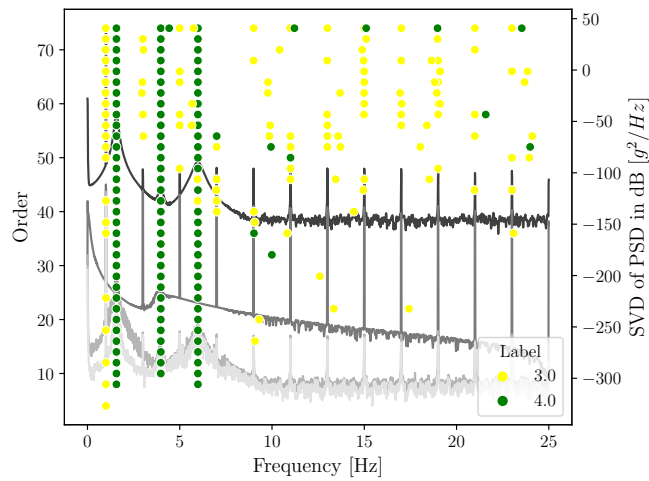


Figure 2.8: Stabilization diagram with overlapped SVD graph of the PSD, from synthetic data used in the example shown in Fig. 2.6.

matrix, for double checking that the stable pole alignments are in correspondence of the peaks of the SV lines of the PSD identified by the FDD method.

2.2.3.5 Data-driven-based stochastic-subspace identification

The Data-driven SSI (SSI-dat) is based on the Kalman filter formulation of the stochastic state space modeling, stemming the issue of solving the Riccati equation (see Eq. (2.92)) because it estimates the Kalman states sequence directly from available data. The SSI-dat starts with the rearrangement of the measured data from l sensors, gathered in vectors $\mathbf{y}_r \in \mathbb{R}^l$ for every r -th time instant, with $r = 0, 1, \dots, N_t$, in a Hankel matrix (a matrix with constant anti-diagonals) $\mathbf{Y}_{0|2i-1}$ with a predefined number of block-rows according to an integer time lag parameter i . Therefore, the Hankel matrix has a fixed number of block rows equal to $2li$ and consequently, considering a total number of data equal to $N_d = N_t + 1$, the number of columns is directly given by $j = N_d - 2i + 1$, see also Appendix A.

$$\mathbf{Y}_{0|2i-1} = \frac{1}{\sqrt{j}} \begin{bmatrix} \mathbf{y}_0 & \mathbf{y}_1 & \mathbf{y}_2 & \cdots & \cdots & \mathbf{y}_{N_t-2i+1} \\ \mathbf{y}_1 & \mathbf{y}_2 & \mathbf{y}_3 & \ddots & \ddots & \mathbf{y}_{N_t-2i+2} \\ \mathbf{y}_2 & \mathbf{y}_3 & \ddots & \ddots & \ddots & \mathbf{y}_{N_t-2i+3} \\ \vdots & \ddots & \ddots & \ddots & \ddots & \vdots \\ \vdots & \ddots & \ddots & \ddots & \ddots & \mathbf{y}_{N_t-i-1} \\ \mathbf{y}_{i-1} & \mathbf{y}_i & \ddots & \ddots & \ddots & \mathbf{y}_{N_t-i} \\ \mathbf{y}_i & \mathbf{y}_{i+1} & \ddots & \ddots & \ddots & \mathbf{y}_{N_t-i+1} \\ \mathbf{y}_{i+1} & \mathbf{y}_{i+2} & \ddots & \ddots & \ddots & \mathbf{y}_{N_t-i+2} \\ \vdots & \ddots & \ddots & \ddots & \ddots & \vdots \\ \mathbf{y}_{2i-2} & \mathbf{y}_{2i-1} & \ddots & \ddots & \ddots & \mathbf{y}_{N_t-1} \\ \mathbf{y}_{2i-1} & \mathbf{y}_{2i} & \cdots & \cdots & \mathbf{y}_{N_t-1} & \mathbf{y}_{N_t} \end{bmatrix} = \begin{bmatrix} \mathbf{Y}_p \\ \mathbf{Y}_f \end{bmatrix}. \quad (2.116)$$

The Hankel matrix can be subdivided into two submatrices denoted as past data matrix \mathbf{Y}_p and future data matrix \mathbf{Y}_f , both with dimensions $li \times j$. Within the SSI-dat context, the Kalman states vector \mathbf{s}_r obtained from output observation up to instant $r-1$ are gathered in a Kalman state sequence matrix $\mathbf{S}_i = [\mathbf{s}_i, \mathbf{s}_{i+1}, \dots, \mathbf{s}_{i+j-1}]$ [96, 101]. This latter matrix is estimated according to $\hat{\mathbf{S}}_i$, obtained by linear algebra geometric orthogonal projection operations of the row space of future data matrix \mathbf{Y}_f toward the row space of past data matrix \mathbf{Y}_p , mathematically expressed according to a projection matrix $\mathbf{\Pi}_i$:

$$\mathbf{\Pi}_i = \mathbf{Y}_f / \underline{\mathbf{Y}_p} = \mathbf{Y}_f \mathbf{Y}_p^T (\mathbf{Y}_p \mathbf{Y}_p^T)^\dagger \mathbf{Y}_p, \quad (2.117)$$

in which the symbol $\underline{\mathbf{Y}_p}$ underlines that the projection result lies in the past data matrix row space. It is worth noting that the product $\mathbf{Y}_f \mathbf{Y}_p^T$ holds the output autocorrelation of the data used for constructing the Toeplitz matrix in the SSI-cov method, demonstrating that this orthogonal projection and output covariances are strongly interconnected, see Appendix A. Under the assumption of a fully controllable and observable system [96], and if the time lag parameter i is fulfilling the

condition in Eq. (2.96), the main theorem of stochastic subspace identification state that the projection matrix $\mathbf{\Pi}_i$ can be decomposed as the product of the extended observability matrix \mathbf{O}_i and the Kalman filter state sequence $\hat{\mathbf{S}}_i$ [101], i.e.

$$\mathbf{\Pi}_i = \mathbf{O}_i \hat{\mathbf{S}}_i = \begin{bmatrix} \mathbf{C} \\ \mathbf{CA} \\ \vdots \\ \mathbf{CA}^{i-1} \end{bmatrix} [\hat{\mathbf{s}}_i \quad \hat{\mathbf{s}}_{i+1} \quad \cdots \quad \hat{\mathbf{s}}_{i+j-1}]. \quad (2.118)$$

The Hankel matrix of output data can be decomposed according to linear algebra LQ decomposition, which delivers a lower triangular matrix \mathbf{L} and an orthogonal matrix \mathbf{Q} ($\mathbf{Q}\mathbf{Q}^T = \mathbf{Q}^T\mathbf{Q} = \mathbf{I}$). Considering the block-row nature of the output data Hankel matrix, the lower triangular matrix can be actually decomposed into block sub-matrices, where $\mathbf{L}_{11} \in \mathbb{R}^{li \times li}$, $\mathbf{L}_{21} \in \mathbb{R}^{l \times li}$, $\mathbf{L}_{22} \in \mathbb{R}^{l \times l}$, $\mathbf{L}_{31} \in \mathbb{R}^{l(i-1) \times li}$, $\mathbf{L}_{32} \in \mathbb{R}^{l(i-1) \times l}$, and $\mathbf{L}_{33} \in \mathbb{R}^{l(i-1) \times l(i-1)}$, and consequently also the orthogonal matrix is decomposed into block sub-matrices $\mathbf{Q}_1 \in \mathbb{R}^{j \times li}$, $\mathbf{Q}_2 \in \mathbb{R}^{j \times l}$, and $\mathbf{Q}_3 \in \mathbb{R}^{j \times l(i-1)}$, so that

$$\mathbf{Y}_{0|2i-1} = \mathbf{L}\mathbf{Q} = \begin{bmatrix} \mathbf{L}_{11} & \mathbf{0} & \mathbf{0} \\ \mathbf{L}_{21} & \mathbf{L}_{22} & \mathbf{0} \\ \mathbf{L}_{31} & \mathbf{L}_{32} & \mathbf{L}_{33} \end{bmatrix} \begin{bmatrix} \mathbf{Q}_1^T \\ \mathbf{Q}_2^T \\ \mathbf{Q}_3^T \end{bmatrix}. \quad (2.119)$$

Therefore, the projection matrix can be numerically obtained directly from the LQ decomposition of the output data Hankel matrix as follows

$$\mathbf{\Pi}_i = \mathbf{Y}_f / \underline{\mathbf{Y}}_p = \begin{bmatrix} \mathbf{L}_{21} \\ \mathbf{L}_{31} \end{bmatrix} [\mathbf{Q}_1^T]. \quad (2.120)$$

Reminding Eq. (2.118) it is possible to obtain the extended observability matrix \mathbf{O}_i and the Kalman filter state sequence matrix $\hat{\mathbf{S}}_i$ using the SVD of the numerically estimated projection matrix (2.120), resembling in someway the SSI-cov Toeplitz matrix decomposition (refer to Eq. (2.98)):

$$\mathbf{\Pi}_i = \mathbf{U}\mathbf{\Sigma}\mathbf{V}^T = [\mathbf{U}_1 \quad \mathbf{U}_2] \begin{bmatrix} \mathbf{\Sigma}_1 & \mathbf{0} \\ \mathbf{0} & \mathbf{0} \end{bmatrix} \begin{bmatrix} \mathbf{V}_1 \\ \mathbf{V}_2 \end{bmatrix} \approx \mathbf{U}_1 \mathbf{\Sigma}_1 \mathbf{V}_1^T, \quad (2.121)$$

thus obtaining

$$\mathbf{O}_i = \mathbf{U}_1 \mathbf{\Sigma}_1^{1/2} \mathbf{T}, \quad (2.122)$$

$$\hat{\mathbf{S}}_i = \mathbf{O}_i^\dagger \mathbf{\Pi}_i, \quad (2.123)$$

where \mathbf{T} is a transformation matrix that can be considered as an identity matrix. Now it is possible to estimate the state matrices \mathbf{A} and \mathbf{C} to get the modal parameter of interest.

Alternatively, the output data Hankel matrix can be decomposed considering the following rearrangement with past output matrix with a block row added \mathbf{Y}_p^+ and future matrix with first block row removed \mathbf{Y}_f^- :

$$\mathbf{Y}_{0|2i-1} = \frac{1}{\sqrt{j}} \begin{bmatrix} \mathbf{y}_0 & \mathbf{y}_1 & \mathbf{y}_2 & \cdots & \cdots & \mathbf{y}_{N_t-2i+1} \\ \mathbf{y}_1 & \mathbf{y}_2 & \mathbf{y}_3 & \ddots & \ddots & \mathbf{y}_{N_t-2i+2} \\ \mathbf{y}_2 & \mathbf{y}_3 & \ddots & \ddots & \ddots & \mathbf{y}_{N_t-2i+3} \\ \vdots & \ddots & \ddots & \ddots & \ddots & \vdots \\ \vdots & \ddots & \ddots & \ddots & \ddots & \mathbf{y}_{N_t-i-1} \\ \mathbf{y}_{i-1} & \mathbf{y}_i & \ddots & \ddots & \ddots & \mathbf{y}_{N_t-i} \\ \mathbf{y}_i & \mathbf{y}_{i+1} & \ddots & \ddots & \ddots & \mathbf{y}_{N_t-i+1} \\ \mathbf{y}_{i+1} & \mathbf{y}_{i+2} & \ddots & \ddots & \ddots & \mathbf{y}_{N_t-i+2} \\ \vdots & \ddots & \ddots & \ddots & \ddots & \vdots \\ \mathbf{y}_{2i-2} & \mathbf{y}_{2i-1} & \ddots & \ddots & \ddots & \mathbf{y}_{N_t-1} \\ \mathbf{y}_{2i-1} & \mathbf{y}_{2i} & \cdots & \cdots & \mathbf{y}_{N_t-1} & \mathbf{y}_{N_t} \end{bmatrix} = \begin{bmatrix} \mathbf{Y}_{0|i-1} \\ \mathbf{Y}_{i|i} \\ \mathbf{Y}_{i+1|2i-1} \end{bmatrix} = \begin{bmatrix} \mathbf{Y}_p^+ \\ \mathbf{Y}_f^- \end{bmatrix}. \quad (2.124)$$

Therefore, considering the LQ decomposition in Eq. (2.119), the projection matrix and the output matrix $\mathbf{Y}_{i|i}$ can be obtained as follows:

$$\mathbf{\Pi}_{i-1} = \mathbf{Y}_f^- / \mathbf{Y}_p^+ = [\mathbf{L}_{31} \quad \mathbf{L}_{32}] \begin{bmatrix} \mathbf{Q}_1^T \\ \mathbf{Q}_2^T \end{bmatrix} \quad (2.125)$$

$$\mathbf{Y}_{i|i} = [\mathbf{L}_{21} \quad \mathbf{L}_{22}] \begin{bmatrix} \mathbf{Q}_1^T \\ \mathbf{Q}_2^T \end{bmatrix} \quad (2.126)$$

Reversed controllability matrix $\mathbf{\Gamma}_i$ can be obtained from Eq. (2.97) as follows

$$\mathbf{\Gamma}_i = \mathbf{O}_i^\dagger \mathbf{T}_{1|i}, \quad (2.127)$$

from which \mathbf{G} matrix can be obtained extracting the last l columns. The initial output covariance \mathbf{R}_0 can be obtained as

$$\mathbf{R}_0 = \frac{1}{j} \mathbf{Y}_{i|i} \mathbf{Y}_{i|i}^T, \quad (2.128)$$

According to [96], three methods are available to estimate state matrices \mathbf{A} and \mathbf{C} . The first method is based on solving a least square problem on a set of overdetermined equations according to the Kalman states sequence $\hat{\mathbf{S}}_i = [\hat{\mathbf{s}}_i, \hat{\mathbf{s}}_{i+1}, \dots, \hat{\mathbf{s}}_{i+j-1}]$ from the time instant i until $i+j-1$ [96], being $\boldsymbol{\rho}_w$ and $\boldsymbol{\rho}_v$ the residuals which are uncorrelated with regressors $\hat{\mathbf{S}}_j$:

$$\begin{bmatrix} \hat{\mathbf{S}}_{i+1} \\ \mathbf{Y}_{i|i} \end{bmatrix} = \begin{bmatrix} \mathbf{A} \\ \mathbf{C} \end{bmatrix} \hat{\mathbf{S}}_i + \begin{bmatrix} \boldsymbol{\rho}_w \\ \boldsymbol{\rho}_v \end{bmatrix}, \quad (2.129)$$

$$\begin{bmatrix} \mathbf{A} \\ \mathbf{C} \end{bmatrix} = \begin{bmatrix} \hat{\mathbf{S}}_{i+1} \\ \mathbf{Y}_{i|i} \end{bmatrix} \hat{\mathbf{S}}_i^\dagger. \quad (2.130)$$

All terms in Eq. (2.130) are numerically obtained by LQ decomposition.

The second method to estimate state matrices leverages the shifting nature of the observability matrix, identical to the SSI-cov method described in Eqs. (2.105)-(2.106).

$$\begin{aligned} \mathbf{O}_i &= \begin{bmatrix} \mathbf{C} \\ \mathbf{CA} \\ \vdots \\ \mathbf{CA}^{i-1} \end{bmatrix} = \begin{bmatrix} \mathbf{O}_i^\uparrow \\ \mathbf{CA}^{i-1} \end{bmatrix} = \begin{bmatrix} \mathbf{C} \\ \mathbf{O}_i^\downarrow \end{bmatrix} \Rightarrow \mathbf{O}_i^\uparrow = \begin{bmatrix} \mathbf{C} \\ \mathbf{CA} \\ \vdots \\ \mathbf{CA}^{i-2} \end{bmatrix}, \mathbf{O}_i^\downarrow = \begin{bmatrix} \mathbf{CA} \\ \mathbf{CA}^2 \\ \vdots \\ \mathbf{CA}^{i-1} \end{bmatrix} \\ &\Rightarrow \mathbf{O}_i^\uparrow \mathbf{A} = \mathbf{O}_i^\downarrow \Rightarrow \mathbf{A} = \mathbf{O}_i^{\uparrow\dagger} \mathbf{O}_i^\downarrow \end{aligned}$$

Alternatively, it is possible to decompose with SVD the linear combination of \mathbf{O}_i^\uparrow and \mathbf{O}_i^\downarrow matrices, i.e.

$$\begin{bmatrix} \mathbf{O}_i^\downarrow - \mathbf{O}_i^\uparrow \end{bmatrix} = \mathbf{U} \mathbf{\Sigma} \mathbf{V}^T \Rightarrow \mathbf{V} = \begin{bmatrix} \mathbf{V}_{11} & \mathbf{V}_{12} \\ \mathbf{V}_{21} & \mathbf{V}_{22} \end{bmatrix}, \quad (2.131)$$

$$\mathbf{A} = \mathbf{V}_{22} \mathbf{V}_{12}^{-1} \quad (2.132)$$

with $\mathbf{V}_{11}, \mathbf{V}_{12}, \mathbf{V}_{21}, \mathbf{V}_{22} \in \mathbb{R}^{n \times n}$.

At this point, it is noteworthy to remind that these first two methods are not able to mathematically guarantee positive realness of state sequence estimates, and therefore this holds also for SSI-cov algorithm, which is based on this second approach (Eqs. (2.105)-(2.106)) [96, 101]. Indeed, the noise covariance estimates, and matrices \mathbf{G} and \mathbf{R}_0 are unbiased estimates under the assumption of infinitely long monitored data sequence. However, dealing with finite duration vibration response data, these estimates occasionally lead to a state space model whose states are not real and nor positive. This fact translates in the frequency domain into a synthesized spectrum which is not positive at every frequency line, which is meaningless from a mathematical point of view. Theoretically, in this case, any forward innovation model cannot be obtained [96, 101], even if it is worth underlining that in the OMA context we are more interested in providing reliable estimates of modal parameters of the structure under investigation rather than provide a very accurate state space model [96]. Nevertheless, when positive realness is a stringent requirement, the third method to estimate state matrices must be adopted. This approach adopts the same least square problem on the first method, i.e. Eq. (2.129), but uses the residuals to estimate the nonsteady state covariance matrices of the noise process affecting the states, viz. the innovation, in Kalman filter state space formulation, so that

$$\frac{1}{j} \begin{bmatrix} \boldsymbol{\rho}_w \\ \boldsymbol{\rho}_v \end{bmatrix} \begin{bmatrix} \boldsymbol{\rho}_w^T & \boldsymbol{\rho}_v^T \end{bmatrix} = \begin{bmatrix} \mathbf{Q}_i^{ww} & \mathbf{S}_i^{wv} \\ [\mathbf{S}_i^{wv}]^T & \mathbf{R}_i^{vv} \end{bmatrix} \hat{\mathbf{S}}_i^\dagger. \quad (2.133)$$

Since the Kalman filter converges unbiased with infinite data, the approximation for finite data introduces a bias but still ensures the positive realness of the states because the noise process covariance matrix in Eq. (2.133) is a positive-definite matrix for construction (all its eigenvalues are positive), i.e.

$$\mathbf{Q}^{ww} = \mathbf{Q}_i^{ww} \quad , \quad \mathbf{S}^{wv} = \mathbf{S}_i^{wv} \quad , \quad \mathbf{R}^{vv} = \mathbf{R}_i^{vv}. \quad (2.134)$$

The steady-state approximation ensures the validity of Eqs. (2.71)-(2.75), thus permitting to directly numerically solving the Riccati equation (2.92) in order to obtain the forward innovation model [96].

Once state matrices \mathbf{A} and \mathbf{C} are known, the modal parameters can be obtained as aforementioned in SSI-cov method in Eq. (2.109), i.e. by solving the EVD problem of state transition matrix \mathbf{A} in order to find Z-domain eigenvalues, which converted back to continuous Laplace domain, deliver modal parameters in terms of natural frequencies, damped natural frequencies, and damping ratios according to Eqs. (2.30)-(2.33), whilst mode shapes are estimated according to Eq. (2.110). Also in SSI-dat, despite the actual model order n can be theoretically estimated by the rank of the projection matrix, it is unknown in reality due to noise and often not evident from missing large relative scatter in SVs. Therefore, a conservative approach based on a stabilization diagram is commonly adopted also in this case, in order to find the stable pole alignments characterizing the real modes of the structure. The stability checks are the same as expressed in HVC Eqs. (2.111)-(2.112) and SVC Eqs. (2.113)-(2.115).

Some SSI-dat variants have been proposed in literature according to weighting procedures with matrices $\mathbf{W}_1 \in \mathbb{R}^{li \times li}$ and $\mathbf{W}_2 \in \mathbb{R}^{j \times j}$ pre- and post- multiplied to the projection matrix $\mathbf{W}_1 \mathbf{\Pi}_i \mathbf{W}_2$ beforehand the LQ decomposition [96]. The unweighted principal components (UPC) method is the one that has been discussed so far, i.e. considering identity matrices for both \mathbf{W}_1 and \mathbf{W}_2 matrices. The UPC SSI-dat is normally used with well and equally excited modes, and with good SNR data [96]. Instead, the canonical variate analysis (CVA) SSI-dat is preferred with non-uniformly excited modes and with noisy response data [96]. It employs the following weighting matrices:

$$\mathbf{W}_1 = \left(\frac{1}{j} \mathbf{Y}_p \mathbf{Y}_p^T \right)^{-1/2} \quad , \quad \mathbf{W}_2 = \mathbf{I}_{j \times j}. \quad (2.135)$$

Similarly to CVA SSI-cov, the SV of the weighted projection matrix can be interpreted as principal cosine angles between past output matrix row subspace and future output matrix row subspace [96]. Eventually, the principal component (PC) SSI-dat represents a compromise between CVA SSI-dat and UPC SSI-dat, so using the following weighting matrices:

$$\mathbf{W}_1 = \mathbf{I}_{li \times li} \quad , \quad \mathbf{W}_2 = \mathbf{Y}_p^T \left(\frac{1}{j} \mathbf{Y}_p \mathbf{Y}_p^T \right)^{-1/2} \mathbf{Y}_p. \quad (2.136)$$

Despite UPC, PC, and CVA having slightly different physical meanings, no significant differences in modal parameter estimate accuracy have been evidenced in the literature [96].

2.2.3.6 Quality assessment of the dynamic identification results

Afterward, the modal identification in the OMA context, assessing the quality of the outcomes is fundamental to ensure the reliability and representativeness of the obtained modal results. For instance, considering time-domain parametric SSI methods, the stochastic state space model attempts to describe the dynamic behavior of the system under a white noise excitation, therefore a synthetic response spectrum can be associated to this state space model which can be directly compared with the spectrum directly obtained from the vibration response measurements, or from the first SV from the SVD of the PSD (FDD method). An analytical closed-form of the synthetic spectrum associated with a discrete-time stochastic state space model can be found in [115], depending only on the state matrices \mathbf{A} , \mathbf{C} , \mathbf{G} , and \mathbf{R}_0 :

$$\mathbf{S}_{YY}(z) = \mathbf{C}(z\mathbf{I} - \mathbf{A})^{-1} \mathbf{G} + \mathbf{R}_0 + \mathbf{G}^T (z^{-1}\mathbf{I} - \mathbf{A}^T)^{-1} \mathbf{C}^T \Big|_{z=e^{i\omega\Delta t}}, \quad (2.137)$$

being ω the circular frequency, $\omega = 2\pi f_k$. This spectral comparison permits to assessment of the frequency-domain performance of the time-domain parametric SSI methods [115].

To ensure better reliability of OMA results, several different algorithms are usually employed alongside for mutual validation of the modal estimates outcomes. Furthermore, a fundamental aspect of assessing the quality of modal results lies in deeply analyzing the mode shape estimates. Foremost, from a mathematical point of view, the mode shapes usually appear as complex vectors since the real-world case studies are normally affected by noise (measurement and process noise), but sometimes also from other physical phenomena such as nonlinearities, aerodynamics interactions, non-proportional damping effects, gyroscopic effects, and so on. Therefore, the analysis of their degree of complexity is crucial. Visual inspecting the mode shape components in the Argand-Gauss complex plane, real mode shape results should be characterized by a phase angle close to 0° or to 180° . Therefore, the real to complex conversion in Eq. (2.110) could be potentially done without any loss of information only for those modes whose components have phase angle $0^\circ \pm 10^\circ$ or to $180^\circ \pm 10^\circ$. In practice, the complex to real conversion is done anyway, despite the analysis of this aspect could be important to evidence if some of the aforementioned physical phenomena are occurring on the structure under investigation. To quantitatively evaluate the degree of complexity of mode shape, two indicators have been proposed in the literature named modal phase collinearity (MPC) and mean phase deviation (MPD), and the interested reader can refer to [96] for further details. OMA mode shapes results are normally unscaled, and the

user generally scales them according to the maximum component or according to a fixed DOF, e.g. the highest point at the top of the building, acting as a sort of control point.

Consistency checks should be pursued both among different concurrent OMA algorithms used for mutual validation, but also concerning the modal results obtained from numerical finite element (FE) models. These latter are initially implemented with undamped models and nominal values for structural materials, however, they must be calibrated according to experimental results, in order to capture the actual dynamic behavior of the real-world structure through a numerical FE model. This fitting procedure is known as model updating and it configures an optimization problem [116]. A crucial aspect is the mode pairing process, i.e. finding the right estimates of the mode shapes for each natural frequency value. For instance, in the stabilization diagram, the stable pole alignments permit identifying the natural frequency, however, any pole associated with a specific alignment is associated with a certain complex mode shape vector. The modal parameter pairing can be visually inspected from a tabular representation, highlighting their relative difference, or on a Cartesian plane, expecting a good pairing if the modal parameter associated with two different sets lies the closest possible to the bisector line. During the pairing procedure, to better characterize closed modes, it could be useful to account also for the frequency separation, referring to the modal overlap factor (MOF) index, which instead considers natural frequency and damping ratio of a reference mode n with respect to a close pole $n - 1$:

$$\text{MOF}_n = \frac{f_n \xi_n}{f_n - f_{n-1}}. \quad (2.138)$$

The MAC index in Eq. (2.45) is a metric to characterize the degree of similarity (correlation) between mode shape pairs, merely based on vector components. From a linear algebra point of view, the MAC index represents the squared cosine angle between two vectors, and it could be interpreted as a squared linear regression coefficient. If MAC is greater than 0.8, the two modes can be considered highly correlated, conversely, when it is lower than 0.2 the two modes are practically uncorrelated. MAC values are organized in the MAC matrix, and it can be used also to define AutoMAC values, when checking the effectiveness of sensors layout evidencing the possible presence of a spatial aliasing problem, or CrossMAC values, when used to compare results derived from different OMA techniques. Despite MAC is probably the widest adopted indicator, the main drawbacks of MAC are its insensitivity to small changes in modal displacements (due to e.g. systematic deviations or either random aleatory errors), and the fact that no information about scatter for each DOF is preserved [96]. Another indicator that can be used alongside MAC is the modal scale factor (MSF) used only to highlight if any difference in the scale factor between two modes holds [96]. To overcome the drawback of MAC insensitivity to small changes, the normalized modal difference (NMD) indicator

has been proposed, and it was demonstrated to work well, especially with highly correlated modes:

$$\text{NMD}(\phi_a, \phi_b) = \sqrt{\frac{1 - \text{MAC}(\phi_a, \phi_b)}{\text{MAC}(\phi_a, \phi_b)}}. \quad (2.139)$$

To overcome the MAC issue of not considering DOF spatial information, two other indicators have been proposed in the literature, i.e. the coordinate modal assurance criterion (COMAC) and its enhanced version (ECOMAC) to avoid errors due to different mode scaling [96].

2.2.4 Notes about other OMA methods

As already before mentioned, several time-domain methods have been developed for OMA in the last decades, based on the analysis of correlation functions of vibration output responses under natural excitation conditions, which progressively replaced forced vibration tests as discussed in section 2.1.3. Therefore, the related output-only OMA methods have been denoted as Natural Excitation Techniques (NExT), and it is worth mentioning at least three distinguished approaches, i.e. the least square complex exponential (LSCE) algorithm, the Ibrahim time domain (ITD) method and the eigenvalue realization algorithm (ERA), which is very similar to subspace-based identification approaches. The interested reader about LSCE, ITD, and ERA can refer to [103, 104, 105] respectively. The NExT OMA procedures were very popular at the beginning but they were progressively abandoned for several limitations and/or drawbacks [96], preferring stochastic subspace identification (SSI) strategies. Some other topical and quite popular OMA techniques are related to wavelet analysis or cepstral analysis [7], transmissibility functions [96], random decrement techniques [96], or yet the poly-reference versions (commercially known as polymax) of the frequency domain and time domain SSI techniques [96]. Furthermore, the nonparametric techniques are taking place such as the second-order blind identification method [96].

In the beginning of OMA, the autoregressive moving average (ARMA) models were also another very popular and widely used technique, which have been progressively abandoned due to their convergence issues and excessive computational burden, besides the high number of spurious modes not trivially separable from the structural ones [96]. In practice, the ARMA models do not rely on a physical internal representation as the state space modeling, but they only set a fitting problem of a polynomial function able to reproduce the measured data. As the name suggests, the polynomial model is based on two parts, one related to autoregressive (AR) coefficients, whose calibration delivers the modal parameters of actual interest, and the second one is the moving average (MA) nonlinear part, which instead ensures a good statistical description of the vibration response. Therefore, ARMA

models attempt to analytically replicate the vibration response random process, therefore modeling both the actual response of the structure and also the noise and disturbances, thus requiring very high-order models which consequently deliver a huge number of spurious modes.

2.3 PyOMA: a Python package for operational modal analysis

Within the structural health monitoring (SHM) field, the operational modal analysis (OMA) gained special attention in recent years becoming the most acknowledged and standard approach for mechanical, civil, and aerospace engineering to inspect the actual state of a structural system during its in-service conditions. The OMA comprises an ensemble of algorithms capable of identifying the dynamic characteristics of a structure (i.e., eigenfrequencies, mode shapes, and damping ratios) leveraging information contained in output-only vibration response measurements. Frequency domain decomposition and stochastic subspace identification (SSI) algorithms among others form the most acknowledged and well-established techniques employed nowadays. As delineated in Fig. 2.9, the PyOMA module has been developed within a research project conducted within the current Ph.D. program and supported by the [ArtIStE](#) (artificial intelligence in structural engineering) research team in Politecnico di Torino University. The PyOMA project was born from the collaboration among three institutions: the University of L'Aquila (Italy), the Norsk Treteknisk Institutt (Norwegian Institute of Wood Technology) in Oslo (Norway), and the Politecnico di Torino University (Italy). For the first time, an open-source Python OMA module has been implemented to provide an effective, versatile, and free-to-use OMA framework oriented both for researchers and practitioners. Especially for this latter category, the authors also provided a more familiar graphical user interface (GUI) of the same OMA python framework denoted as `PyOMA_GUI`, to further increase the usability of the above-mentioned implementation to everyone, without requiring any specific Python coding skills. In the current section of this Thesis, the main features of the PyOMA module and its GUI-based counterpart are illustrated. The PyOMA source code in the released version 1.5 and the `PyOMA_GUI` software in the released version 1.1 are made freely available by the authors at the following [GitHub repository \(https://github.com/dagghe/PyOMA\)](https://github.com/dagghe/PyOMA). For a complete and detailed overview of the PyOMA software functionalities, the reader can also refer to [117]. In detail, the current released version 1.5 of the PyOMA package implements the following six acknowledged techniques, the first three based on frequency domain approaches, and the last three according to time domain methods, whose theoretical frameworks have been already extensively discussed in the previous sections:

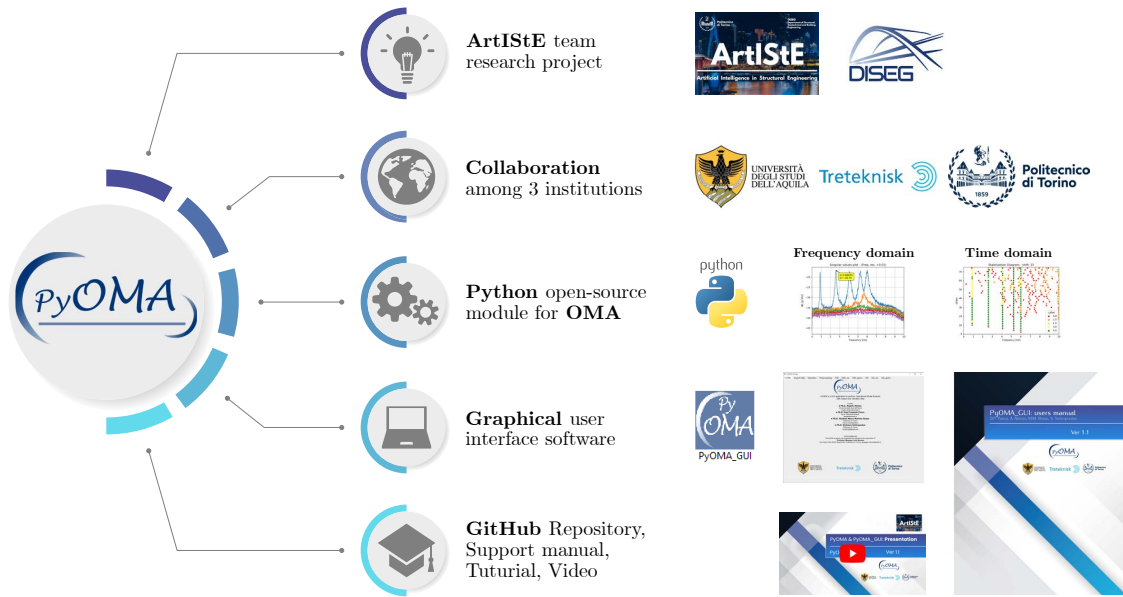


Figure 2.9: PyOMA research project overview.

1. frequency domain decomposition (FDD) [118];
2. enhanced frequency domain decomposition (EFDD) [119];
3. frequency spatial domain decomposition (FSDD) [120];
4. covariance driven stochastic subspace identification (Cov-SSI) [115, 96];
5. data-driven stochastic subspace identification (DD-SSI) [101];
6. natural excitation technique eigensystem realization algorithm (NExT-ERA) [96, 105];

PyOMA module is therefore an open-source Python module that implements a complete output-only OMA suite for researchers, engineers, and practitioners [117]. As depicted in the flowchart of Fig. 2.10, after importing the vibration data, the user may estimate the modal parameters using the implemented functions both for frequency (FDD-based variants) and/or time (SSI-based variants) domain analyses.

The PyOMA implementation delivers the first Python-based OMA package for researchers and practitioners. The authors further equipped their tool with a Python-based graphical user interface (GUI) called PyOMA_GUI software. This additional available option clearly enhanced the user-friendly and immediate usage of this software. PyOMA_GUI has been developed in PyQt5, which implements in a single integrated tool the operational modal analysis of civil structures with output-only measurement data. A general overview of the software functionalities

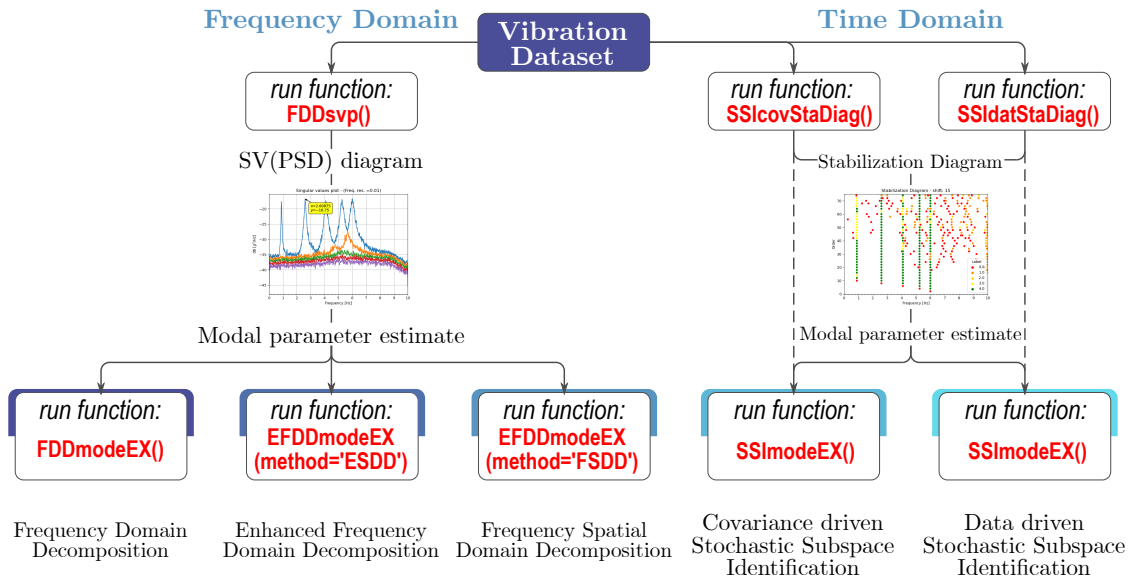


Figure 2.10: PyOMA implemented algorithms.

is depicted in Fig. 2.11. This software employs the functionalities mentioned above offered by the `PyOMA` python module. Therefore, `PyOMA_GUI` provides an exceptionally user-friendly interface to improve the accessibility of the `PyOMA` module, ensuring widespread usage for scientists, researchers, and applied civil and structural engineers. The main features `PyOMA_GUI` provides are listed below:

- Importing data tab;
- Definition of the geometry of the structure and the monitoring system (channels and degrees of freedom, DOFs);
- Pre-processing of the acquired signals with detrending and decimation options;
- Dynamic identification algorithms with visualization of the results (graphs, modal shapes);
- Post-processing tabs and output export functionalities.

Recently, our multi-institutional research team is currently working to release a completely renewed version of the `PyOMA` module denoted as `PyOMA2`, as shown in the new logo shown in Fig. 2.12. This new implementation transforms `PyOMA` from a basic function library into a sophisticated module, fully leveraging Python’s class capabilities, thus improving its usability and functionality in the OMA field. A notable addition is interactive plotting, enabling users to directly

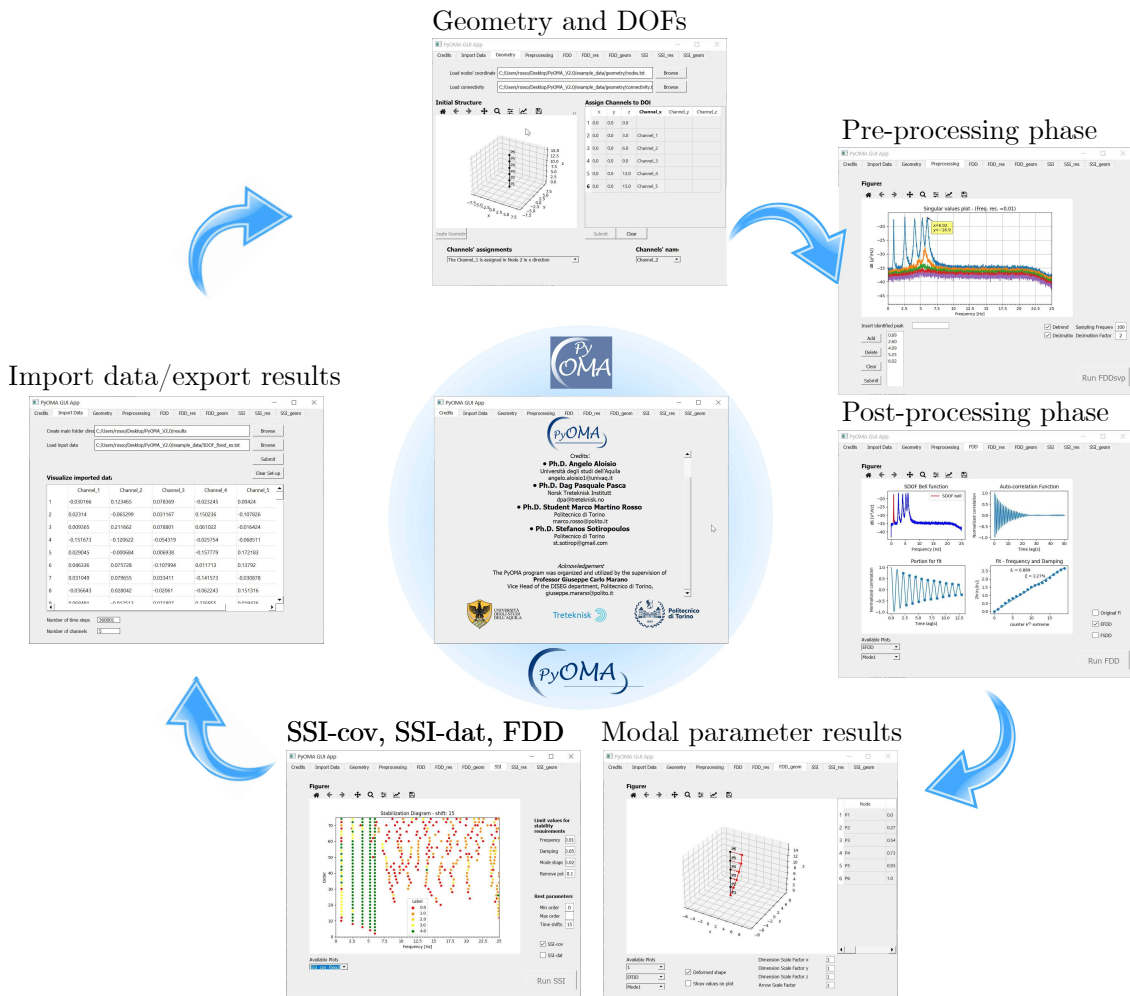


Figure 2.11: “PyOMA_GUI” graphical user interface software general overview.

select modes for extraction from algorithm-generated plots. This was mainly inspired by the open-source module PyEMA (<https://github.com/ladisk/pyEMA>). Furthermore, a novel feature allows users to define the geometry of the structures under analysis, enhancing the visualization of mode shapes post-analysis. The new source code is accessible from the following GitHub repository (<https://github.com/dagghe/PyOMA2>). In detail, the new PyOMA2 module is structured into three primary levels of Python classes. At the first level are the setup classes: users instantiate these classes by providing a data array and the sampling frequency for a single setup scenario, or a list of data arrays and their respective sampling frequencies for a multi-setup scenario. The second level comprises the algorithm classes: users can instantiate the algorithms they wish to run and then add them to the setup class. The third level contains the support classes, which serve as auxiliary components to the first two levels. This level includes various

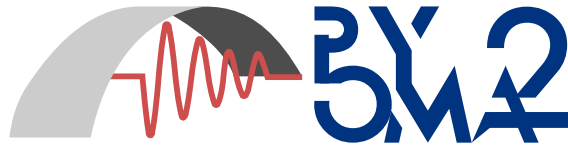


Figure 2.12: The new PyOMA2 logo.

specialized classes, i.e. the result classes, where outcomes are stored, the geometry classes, for storing geometric data, the run parameters classes, where parameters used for running the algorithms are kept, and dedicated classes for animating mode shapes and interacting with plots generated by the algorithm classes. In addition, there is a further level that includes the set of functions internally called by the class methods, which represents an updated version of those functions available in our previous release PyOMA. For users interested in a more direct approach, it is still possible to import only the functions and execute them sequentially to obtain the results. However, this approach precludes the use of interactive plots and the animation capabilities provided by the dedicated classes. Collectively, all these layers work together to create a robust and comprehensive framework, facilitating efficient module operation and data processing. PyOMA2 expands its scope to support both single and multi-setup data measurements, effectively managing multiple acquisitions involving a combination of reference and roving sensors [109]. This includes the SSI-dat versions illustrated in [121], denoted as Post Separate Estimation Re-scaling (PoSER) and Pre-Global Estimation Re-scaling (PreGER). Moreover, besides retaining the previous algorithms found in its predecessor, PyOMA2 introduces the multi-setup versions of SSI algorithms and also the poly-reference Least Square Frequency Domain (pLSCF) method, also known as Polymax [96].

2.4 PyOMA for model-updating-related studies

Our PyOMA module revealed practical advantages, especially in the automatic OMA and SHM perspectives. Moreover, the scientific soundness of using our Python-based code for OMA has been already successfully demonstrated in some recent research studies and applications. Hereinafter, some research studies conducted during the current Ph.D. program are presented united by the adoption of PyOMA for pursuing the model updating procedure on the case studies analyzed. In summary, the parametric model updating defines those optimization procedures to find the best estimates of the N_p parameters $\theta \subset \Omega \in \mathbb{R}^{N_p}$ of a numerical finite element model which governs its dynamic behavior in order to cope with the experimental vibration data collected from vibration test [116, 122]. Therefore, the model updating process is nothing more than an optimization problem, i.e. from a mathematical point of view, it is the minimization of a function called objective or merit

function (OF) $\mathcal{F}(\boldsymbol{\theta})$ which depends on a certain choice of design or decision variables $\boldsymbol{\theta}$. In general, for solving optimization problems, the branch of mathematics called operational research formalized starting from World War II on several mathematical programming techniques, which configures gradient-based methods [123]. Afterward, new heuristic approaches were developed to solve complex optimization problems in which classical methods failed or required prohibitive computational costs. These new methodologies were mainly inspired by Nature, mimicking intelligent behavior and survival strategies of animals [123]. These paradigms were also introduced to the Artificial Intelligence field (AI) and were mathematically formalized under the category of methods called meta-heuristic algorithms to solve optimization problems. During the current Ph.D. program, some innovative hybrid meta-heuristic methods have been proposed, and the interested reader can refer to [46, 124, 48, 50, 125] for further details.

In control engineering, the model updating procedure is normally conducted as an on-line procedure, whereas in the civil engineering field, it is typically done off-line. Indeed, for civil structures, the main goal of model updating is not simply numerically replicating the physical test data, but calibrating the numerical model in order to be more representative of the actual conditions of the real-world structural system by using its dynamic footprint obtained from signal processing dynamic identification methods, and use the calibrated model to make predictions for alternative loading conditions, estimate residual life, SHM, damage detection procedure and digital twin, etc. [122]. The model updating procedure configures as an optimization problem based on minimizing the following objective function accounting for the relative difference of every u -th natural frequencies and mode shapes' MAC index between the experimental results denoted by superscript (e) and the numerical multi-modal model denoted by superscript (c), with $1 \leq u \leq m$ being m the maximum number of modes of interest [126, 116]:

$$\min_{\boldsymbol{\theta} \in \Omega} \mathcal{F}(\boldsymbol{\theta}) = \sum_{u=1}^m \gamma_u \left(\frac{f_u^{(e)} - f_u^{(c)}(\boldsymbol{\theta})}{f_u^{(e)}} \right) + \sum_{u=1}^m \beta_u \left[1 - \text{MAC}(\boldsymbol{\phi}_u^{(e)}, \boldsymbol{\phi}_u^{(c)}(\boldsymbol{\theta})) \right], \quad (2.140)$$

in which γ_u and β_u are two set of weighting factors. For instance, in [126], when there is major confidence in lower modes, the weighting factors can be trivially assumed as inversely proportional to the natural frequency value. The modeling parameters are generally configured as the geometric and material properties of a structure, since they directly affect its modal response. However, since the geometric properties come from a direct survey and they are generally known with good confidence, model updating often reduces to mainly assess the stiffness-related parameters only [127]. Model updating problems are inverse problems since the objective is to obtain the parameters that produce a given output. Nevertheless, this optimization problem is often prone to ill-posedness and ill-conditioning, meaning that the existence, uniqueness, and stability of a solution to the inverse problem

cannot be guaranteed [127]. Indeed, OMA methods provide only mode shapes unscaled with respect to the mass matrix. Therefore, the mass and the stiffness matrices cannot be both unknowns simultaneously. The mass matrix is often assumed as known because it derives from materials' specific weights and geometric properties, which can be usually known with good confidence, and consequently, the optimization strategy may only focus on stiffness parameters. Deterministic model updating aims to find the optimal parameters associated with the best fit between the model output and the observed data, generally solving a constrained optimization problem under the assumption of the existence of an optimal solution characterized by a deterministic set of design variables. In contrast, probabilistic model updating procedures assume that the design vector is composed of random variables, and the goal is defining the entire distribution of the modeling parameters, often pursued in a Bayesian way. The main challenges in finding the agreement between experimental and numerical mode shapes depended on the chosen arrangement of the accelerometers, which can lead to spatial aliasing problems. Furthermore, the choice of updating parameters is determinant since the numerical predictions of modal parameters should be sensitive to small changes in parameters. In addition, the modeling process often requires accounting for factors and specific parametrizations of inaccurate parts, such as boundary conditions, that normally are not considered in a regular finite element model [116]. Therefore, sensitivity analyses are often required to select which parameters greatly affect the dynamic response rather than others that can be not considered during the optimization process, thus reducing the complexity and computational burden of the model updating problem. Anyway, it is worth reminding you that the updating process will never be a perfect fit, since experimental data are inherently affected by some noise sources, both aleatory and systematic. Additionally, due to the Nyquist-Shannon sampling theorem, the sampling frequency of measured data directly limits the maximum number m of numerical modes which can be considered when solving the optimization problem in Eq. (2.140) [116]. Eventually, to assess the quality of the updating process outcome, it is necessary to evaluate that the mass, stiffness, and damping ratios of the updated model are still based on physically meaningful parameters [116].

2.4.1 Indirect estimate of concrete strength: The Corvara Bridge case study

The current section discusses our research study [127], which proposed a methodology to estimate the concrete strength of a structure based on an ambient vibration test and leveraging the Young's modulus value retrieved by a FE model updating process. The optimization problem of deterministic FE model updating leads to an optimal set of N_{θ_M} model parameters $\hat{\theta}_M \in \mathcal{D} \subseteq \mathbb{R}^{N_{\theta_M}}$ which minimizes a

cost function \mathcal{F} , defined as the discrepancy of the operational response from dynamic vibration experimental data, denoted as \mathbf{y} , and model predictions denoted as $\mathbf{G}_M(\boldsymbol{\theta}_M)$ [116]:

$$\hat{\boldsymbol{\theta}}_M = \arg \min_{\boldsymbol{\theta}_M} \mathcal{F} \left(\mathbf{G}_M(\boldsymbol{\theta}_M) - \mathbf{y} \right) \Big|_{\boldsymbol{\theta}_M} \quad (2.141)$$

The modeling parameters ($\hat{\boldsymbol{\theta}}_M$) generally configure as the geometric and material features, which directly affect the modal response of the structure. Since the geometric properties come from a direct survey and they are generally known with good confidence, model updating reduces to mainly assess the stiffness parameters only. Therefore, the FE model updating using the modal parameters can only estimate the stiffness parameters, but not the strength of the material, which is generally assessed from additional experimental tests, e.g. destructive tests on concrete specimens. Nevertheless, these two variables are in general correlated and [128] attempted to estimate material properties from the FE model updating stiffness parameters. In our research study [127], the proposed indirect method for estimation of the concrete resistance from ambient vibration data has been formalized in five steps:

1. **Initial FE model.** With first-attempt estimates or nominal values of the parameters, an initial FE model allows to perform of the modal analysis, helpful to optimal sensor placement.
2. **Experimental campaign and OMA.** Modal parameters are estimated with the OMA methods from vibration response measurements collected under operational conditions.
3. **FE model updating.** The resolution of the optimization problem leads to the optimal set estimate of model parameters. Their prior admissible variability range depends on the user experience and knowledge of the existing structure. Since the geometric features are known, then the mass matrix is assumed to be known, and the model updating optimization considers only the stiffness properties. The variance matrix of the optimal parameters $\boldsymbol{\Sigma}_{\hat{\boldsymbol{\theta}}_M}$ can be estimated by propagating the variance with a first-order approximation of the OF in the minimum point.

$$\boldsymbol{\Sigma}_{\hat{\boldsymbol{\theta}}_M} = \left(\mathbf{J}_{\hat{\boldsymbol{\theta}}_M, \mathcal{F}} \right)^\dagger \sigma_{\mathcal{F}}^2 \left(\mathbf{J}_{\hat{\boldsymbol{\theta}}_M, \mathcal{F}}^T \right)^\dagger \quad (2.142)$$

where $\sigma_{\mathcal{F}}^2$ is the variance of the OF at the minimum, $\mathbf{J}_{\hat{\boldsymbol{\theta}}_M, \mathcal{F}} = \frac{\partial \mathcal{F}}{\partial \boldsymbol{\theta}_M} \Big|_{\boldsymbol{\theta}_M = \hat{\boldsymbol{\theta}}_M}$ is the Jacobian matrix of the OF at the optimum $\hat{\boldsymbol{\theta}}_M$.

4. **Indirect estimation of the material strength.** Empirical relationships hold between the concrete strength \mathbf{R} and the modeling parameters $\mathbf{R} =$

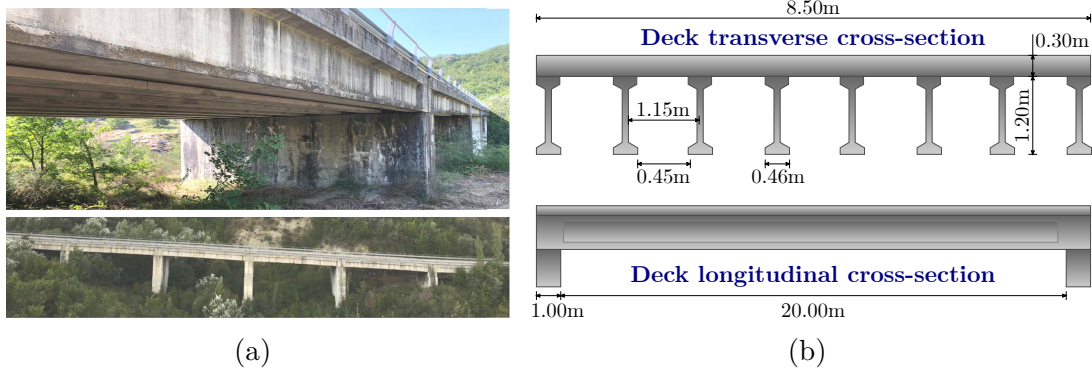


Figure 2.13: Corvara bridge case study: (a) Global and side view of the; (b) Transverse and longitudinal cross-section of the bridge.

$\mathbf{R}(\boldsymbol{\theta}_M)$, therefore its estimate $\hat{\mathbf{R}}$ can be obtained by evaluating these empirical relationships in the optimum $\hat{\boldsymbol{\theta}}_M$. The covariance matrix of the estimated resistance ($\boldsymbol{\Sigma}_{\hat{\mathbf{R}}}$) can be obtained from the first-order approximation of these empirical relationships as

$$\boldsymbol{\Sigma}_{\hat{\mathbf{R}}} = \left(\mathbf{J}_{\hat{\boldsymbol{\theta}}_M, \mathbf{R}} \right) \boldsymbol{\Sigma}_{\hat{\boldsymbol{\theta}}_M} \left(\mathbf{J}_{\hat{\boldsymbol{\theta}}_M, \mathbf{R}}^T \right) \quad (2.143)$$

where $\mathbf{J}_{\hat{\boldsymbol{\theta}}_M, \mathbf{R}} = \frac{\partial \mathbf{R}}{\partial \boldsymbol{\theta}_M} \Big|_{\boldsymbol{\theta}_M = \hat{\boldsymbol{\theta}}_M}$ is the Jacobian matrix of the empirical relationships evaluated by the optimum values of the parameters.

The proposed procedure has been applied to a multi-span prestressed concrete bridge located in Corvara (Pescara, Italy), illustrated in Fig. 2.13. The bridge consists of seven equal spans 20.00 m long, each of these composed of eight prestressed concrete girders (PSC) of the type TAS-PN 120/46, and a reinforced concrete (RC) deck. The bridge presented an overall good conservation state, despite the lack of a proper rainwater drainage system. Additionally, the deck lacks bearings: the piers support the bridge without any load transfer device [127]. On 4th August 2020, the authors measured the response of the bridge to ambient excitation, recording the one-hour structural vibration sampled at 200 Hz for each span separately, obtaining seven different measurement datasets. Ten bi-axial Force-Balance accelerometers (FBA) were arranged equally spaced in two symmetric measurement chains, placed at 1.30 m from the lateral edges and with the extremal ones in correspondence of the span edges, as depicted in Fig. 2.14. Due to the bridge traffic closure during the experimental campaign, shallow levels of vibration have been recorded with root-mean-square values below 0.1 mg. The experimental modal parameters have been obtained by processing the experimental data employing both EFDD and SSI-cov algorithms for mutual validation, both provided in the PyOMA module. Despite the low level of the excitation, the stabilization diagram in Fig. 2.14 permitted identifying four stable modes in the frequency range 0-20 Hz, whose results are

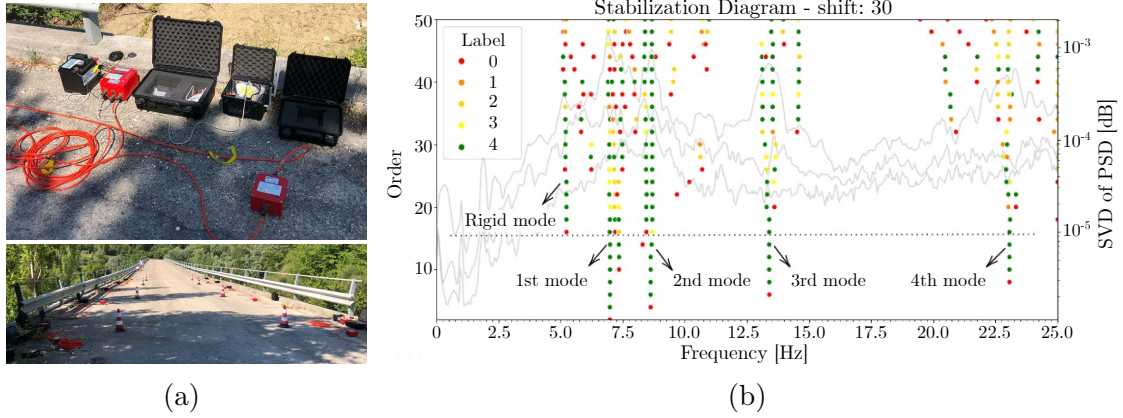


Figure 2.14: Corvara bridge case study: (a) experimental setup overview; (b) stabilization diagram.

Table 2.1: Corvara case study: OMA results of the seven spans: f_i and ξ_i are the natural frequency and damping ratio of the i -th mode.

Span num.	f_1 [Hz]	ξ_1 [%]	f_2 [Hz]	ξ_2 [%]	f_3 [Hz]	ξ_3 [%]	f_4 [Hz]	ξ_4 [%]
1	7.38	1.58%	9.15	1.29%	14.20	1.70%	-	-
2	7.17	1.55%	8.68	1.93%	14.10	1.33%	23.53	1.22%
3	7.33	1.64%	8.87	1.12%	13.45	1.34%	-	-
4	6.98	1.13%	8.62	1.26%	13.39	1.58%	23.06	2.05%
5	6.95	1.95%	8.44	1.34%	13.42	1.58%	22.89	1.10%
6	7.15	1.81%	8.53	1.09%	14.14	1.50%	23.73	1.15%
7	7.17	1.69%	8.55	1.17%	14.60	1.42%	-	-

reported in Tab. 2.1 for the seven spans, and the experimental mode shapes are illustrated in Fig. 2.15. It is noteworthy that the very first alignment of poles in the stabilization diagram has been identified as a rigid translational mode, therefore the actual modes of interest started at nearly 7 Hz. In a different set of identical PSC girders, the first mode shapes tend to be very similar to each other ($\text{MAC} > 0.99$), confirming that there is no substantial difference in boundary restraint conditions among the spans [129]. On the other hand, the respective natural frequencies may reveal more scattered values, probably due to the dispersion of the concrete Young's modulus due to different degradation levels among the spans. The second mode is the first torsional mode. Since the lack of bearing devices, displacement by the supports is nearly zero due to the mono-lateral nature of the constraint. Due to the sensor setup, it is not possible to unambiguously distinguish the mode shape of the first and third modes (in which bending seems coupled with horizontal deformation); nevertheless FE model allows us to make such a distinction. Despite it was not possible to identify the fourth mode in all the tested spans, when it was possible, the mode shape clearly resembles the second mode of a beam-like structure. The damping ratios between 1.5 and 2% are consistent with reasonable

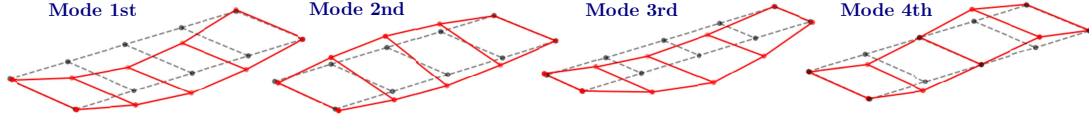


Figure 2.15: Corvara case study: visualization of the experimental mode shapes of a sample bridge span.

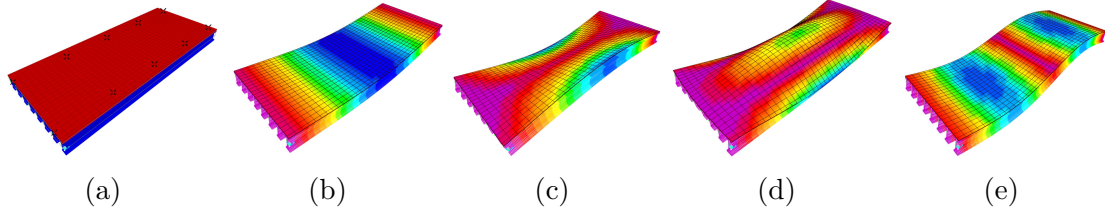


Figure 2.16: Corvara case study: (a) FE model view with marked accelerometers positions; (b)-(e) first four FE mode shapes corresponding to the experimental ones.

physical values.

In order to perform the model updating procedure according to Eq. (2.140), a FE model of a single span has been implemented in CSI SAP2000 commercial software [130], adopting beam and shell elements with pinned-pinned boundary restraints. Due to mode updating intrinsic ill-posedness and ill-conditioning, sensitivity analysis provided a quantitative assessment of the goodness of choice of the model parameter to be considered in the OF. The unknown model parameters are the longitudinal Young's moduli of the girder and the deck, denoted as E_b and E_d respectively. The two Young's moduli were the base of a variance-based sensitivity analysis which consisted of decomposing the variance of the model output into fractions attributed to the chosen mechanical parameters. After setting the inputs sampling range with a standard deviation of 30% (see Tab. 2.2), model parameters were generated with Saltelli's sampling scheme [131, 132]. Total, ($N_s \cdot (2D_\theta + 2)$) models were generated (where $N_s = 100$ is the number of samples, and $D_\theta = 2$ is the number of input parameters) and the related first-order (S_1) and total-order (S_T) sensitivity indices are reported Tab. 2.3. They measure, respectively, the effect of varying a single parameter alone and the output variance caused by all the varying parameters. Both the OF in Eq. (2.140) and the first three natural frequencies appeared more sensitive to Young's modulus of the deck. Conversely, f_4 is more affected by Young's modulus of the supporting girders, which is consistent with the observed torsional mode shape behavior which involves a greater deformation of girders. The sensitivity analysis demonstrated the good choice of unknown modal parameters in the FE model updating.

Table 2.2: Corvara case study: nominal values in MPa of concrete mechanical parameters, being f_k the characteristic nominal strength.

Structure	f_k	σ_f	E	σ_E
Girder	55.00	4.88	36688.63	194.78
Deck	30.00	4.88	30588.56	297.73

Table 2.3: Variance-based sensitivity analysis results (Sobol Indicators).

Parameters	OF		f_1		f_2		f_3		f_4	
	S_1	S_T	S_1	S_T	S_1	S_T	S_1	S_T	S_1	S_T
E_b	28.8%	37.0%	30.8%	29.8%	21.5%	20.5%	17.9%	17.1%	87.5%	87.1%
E_d	63.8%	72.1%	71.2%	69.5%	80.5%	79.0%	84.0%	82.6%	13.6%	12.4%

For solving the modal updating optimization problem, two optimization algorithms were adopted for mutual validation of the results, i.e. the Differential Evolution (DE) [133] and the Particle Swarm Optimization (PSO) [134, 46]. However, since the outcomes were nearly coincident, only the results of the DE algorithm are reported hereafter. The relative tolerance for convergence was set to 0.01, then OF variance ($\sigma_{\mathcal{F}}$) is approximately $\sigma_{\mathcal{F}} \approx \mathcal{F}(\hat{\theta}_M) \cdot 0.01$. The results are reported in Tab. 2.4 which also illustrates the relative error between experimental and optimal frequency is approximately below 15%. Still, the correspondence is very satisfactory and the FE model achieves a good matching with the experimental data. According to the Italian Building Code (NTC18), the empirical correlation between Young's modulus and the compression strength of concrete can be written as:

$$E = 22000 \cdot \left(\frac{f}{10} \right)^{0.3} \quad (2.144)$$

where E is the mean value of Young's modulus and f is the mean value of the compression strength, which is related to characteristic compressive strength f_k , according to Eurocode EN 1992, as $f = f_k + 8$. Assuming a normal distribution, and knowing that the characteristic value lies at 5% percentile of the distribution, the standard deviation σ is:

$$f_k = f - 1.64\sigma \quad \Rightarrow \quad \sigma = \frac{8}{1.64} = 4.878 \quad (2.145)$$

The results reported in Tab. 2.5, provided the estimate of mean values of the concrete mechanical properties coming from Eq. (2.144) and the relative variances calculated with Eqs. (2.142)-(2.143). Young's moduli results highlight the different concrete classes of the girders (33000 - 48000 MPa) and the deck (24000 - 28000 MPa), which even reflects on the strengths (deck: 15 - 20 MPa; girders: 35 - 105 MPa). The deck resistance is lower than the nominal value (30 MPa), conversely, it is higher for girders (55 MPa), probably due to the different pouring and curing conditions. Because of the low tolerance in OF convergence, the variances of the

Table 2.4: Comparison between experimental and optimized numerical natural frequencies [Hz].

Span No 1				Span No 5			
f_n	$f^{(e)}$	$f^{(c)}$	$(f^{(e)}-f^{(c)})/f^{(e)}$	f_n	$f^{(e)}$	$f^{(c)}$	$(f^{(e)}-f^{(c)})/f^{(e)}$
f_1	8.01	7.34	8.35%	f_1	6.95	6.97	-0.30%
f_2	9.15	8.56	6.42%	f_2	8.44	7.37	12.67%
f_3	14.20	14.48	-1.95%	f_3	13.42	14.88	-10.86%
f_4	-	22.88	-	f_4	22.89	22.65	1.02%
Span No 2				Span No 6			
f_n	$f^{(e)}$	$f^{(c)}$	$(f^{(e)}-f^{(c)})/f^{(e)}$	f_n	$f^{(e)}$	$f^{(c)}$	$(f^{(e)}-f^{(c)})/f^{(e)}$
f_1	7.17	7.28	-1.55%	f_1	7.15	7.21	-0.84%
f_2	8.68	7.74	10.81%	f_2	8.53	7.63	10.55%
f_3	14.10	15.69	-11.25%	f_3	14.14	15.41	-9.02%
f_4	23.53	22.88	2.76%	f_4	23.73	23.31	1.77%
Span No 3				Span No 7			
f_n	$f^{(e)}$	$f^{(c)}$	$(f^{(e)}-f^{(c)})/f^{(e)}$	f_n	$f^{(e)}$	$f^{(c)}$	$(f^{(e)}-f^{(c)})/f^{(e)}$
f_1	7.5	7.18	4.27%	f_1	8.27	7.84	5.20%
f_2	8.85	7.56	14.59%	f_2	9.3	8.24	11.40%
f_3	13.45	15.18	-12.84%	f_3	14.6	16.44	-12.60%
f_4	-	23.93	-	f_4	-	23.45	-
Span No 4							
f_n	$f^{(e)}$	$f^{(c)}$	$(f^{(e)}-f^{(c)})/f^{(e)}$				
f_1	6.98	7.00	-0.31%				
f_2	8.62	7.41	14.02%				
f_3	13.39	14.97	-11.83%				
f_4	23.06	22.61	1.97%				

Table 2.5: Estimated mechanical parameters and related variances.

Parameters	Span No 1	Span No 2	Span No 3	Span No 4	Span No 5	Span No 6	Span No 7
E_b [MPa]	44234.63	33754.20	41530.07	34622.50	35227.49	36909.78	48203.66
E_d [MPa]	27323.36	29599.20	24647.76	25638.10	24981.85	27088.64	28427.66
σ_{E_b} [MPa]	27.41	28.92	23.14	87.38	62.01	66.18	28.21
σ_{E_d} [MPa]	55.98	125.07	8.12	128.77	16.80	149.79	35.96
$\sigma_{E_b E_d}$ [MPa]	31.85	60.14	13.71	59.46	32.27	99.56	31.85
f_b [MPa]	81.29	36.12	67.27	38.98	41.06	47.22	105.19
f_d [MPa]	19.16	24.35	14.06	15.83	14.64	18.67	21.58
σ_{f_b} [MPa]	0.15	0.09	0.11	0.30	0.22	0.25	0.18
σ_{f_d} [MPa]	0.12	0.31	0.01	0.24	0.03	0.31	0.08

estimates are quite low. Tab. 2.6 lists the estimated values of Young’s moduli and concrete resistance averaged over the seven spans. As anticipated, the concrete resistance of the deck exhibits a significantly lower resistance compared to the reference values in Tab. 2.2, on average equal to 63.70%, while that of the girders showed a slight improvement, on average equal to 7.70%. The reference variances of E and f , estimated from Eq. (2.145) are significantly higher than the tolerances of the estimates. The above indirect procedure for estimating the concrete resistance from Young’s moduli has been validated against the values of the concrete resistance evaluated from 3 concrete specimens extracted from each span. Unfortunately, the authors could not extract the specimens from the deck and had to limit the validation to the sole resistance of the girders. Tab. 2.7 compares the values of Young’s moduli and resistance of the girders from concrete specimens (superscript d) with those evaluated from the indirect method (superscript i), reporting the mean value $f_b^{(i)}$ and the variance $\sigma_{f_b}^{(i)}$ calculated for each specimen set

Table 2.6: Averaged parameters among the spans.

Parameters	Estimated	Reference	Percentage difference
E_b [Mpa]	39211.76	36688.63	6.43%
E_d [Mpa]	26815.22	30588.56	-14.07%
σ_{Eb} [Mpa]	5119.68	194.78	96.20%
σ_{Ed} [Mpa]	1695.72	297.73	82.44%
f_b [Mpa]	59.59	55.00	7.70%
f_d [Mpa]	18.33	30.00	-63.70%
σ_{fb} [Mpa]	26.39	4.88	81.52%
σ_{fd} [Mpa]	24.15	4.88	79.80%

Table 2.7: Comparison between the concrete resistance estimated from the FE model updating (indirect) and that estimated from concrete samples (direct).

Span No	Indirect Estimation		Direct Estimation		Percentage difference	
	$f_b^{(i)}$ [Mpa]	$\sigma_{fb}^{(i)}$ [Mpa]	$f_b^{(d)}$ [Mpa]	$\sigma_{fb}^{(d)}$ [Mpa]	$\frac{f_b^{(i)} - f_b^{(d)}}{f_b^{(d)}}$	$\frac{\sigma_{fb}^{(i)} - \sigma_{fb}^{(d)}}{\sigma_{fb}^{(d)}}$
1	81.29	0.15	67.80	3.20	19.89%	-95.28%
2	36.12	0.09	29.40	1.20	22.85%	-92.26%
3	67.27	0.11	54.40	3.40	23.66%	-96.69%
4	38.98	0.30	42.10	4.50	-7.42%	-93.44%
5	41.06	0.22	38.30	3.10	7.20%	-93.01%
6	47.22	0.25	45.50	2.50	3.79%	-89.84%
7	105.19	0.18	60.20	1.70	74.73%	-89.14%

for each span. Except for span 7, where the indirect strength estimate is quite far from the actual value, the percentage error of each set varies between 3%-23%. The obtained results demonstrated the validity of the proposed indirect method as a valid alternative to direct destructive tests. Moreover, the indirect method provides a global evaluation of the health of the structures and it allows the possibility of tracking the values of interest over time when coupled with a permanent monitoring system. Conversely, the extraction of concrete samples is limited mainly because of uneconomic and local evaluation. The percentage differences of the two variances are approximately 100%. Thus, the reference variance is far higher than that obtained by propagating the variance of the OF. The two variances are not comparable and derive from two different sources of uncertainties. First, the variance determined from the FE model updating expresses a modeling error. Instead, the one from concrete samples represents the spatial variability of the concrete resistance, which can not be estimated with an FE model in which Young's modulus is constant along the girder. In a real structure, Young's modulus of concrete can vary from point to point, exhibiting significant scatter in its mechanical properties. Therefore, effectively dealing with damage localization may require to develop of a refined FE model, with a more refined mesh with a varying Young's modulus among the FEs. However, this approach is virtually computationally expensive and hardly ever applicable in practice. In summary, destructive tests on concrete specimens are the common practice nowadays to evaluate the strength of concrete

structures. However, the current study provided a valid alternative and less invasive indirect framework for strength estimation from Young’s moduli estimated through OMA and FE model updating. With a permanent monitoring system, this approach may virtually track the mechanical parameters for potential nearly real-time assessment of the structural capacity. However, estimating the variance of the concrete strength is not always possible and it strongly depends on the level of detail of the FE model. When the FE model can address the spatial variability of the Young’s moduli along the girders, the proposed framework may be virtually able to even capture the strength uncertainty.

In conclusion, the combined FE model updating with modal data and empirical correlation between Young’s modulus and concrete may represent a valid alternative to destructive tests, especially if continuous monitoring of the concrete state is required. Focusing on the specific Corvara bridge case study, the estimated resistance of the deck and the girders differed from the reference values assumed in the design. After almost 30 years of life, the deck’s concrete resistance exhibited an average 60% decrement, while the girders’ resistance had an approximate 7% increment. The outcomes of the proposed indirect method for estimating the compressive strength of concrete are entirely confirmed by the resistances of the concrete specimens extracted from each span. The percentage error between the compressive strengths obtained from the two methods is approximately 20%. The indirect estimates are generally associated with an overestimation of Young’s moduli.

2.4.2 Cables force estimate in cable-stayed bridges: The Marghera Bridge case study

The current section is dedicated to our research study [135] which discusses the feasibility of complete model updating of cable-stayed bridges using experimental estimates of the cable forces and modal parameters. Since OMA techniques provide mass-unscaled mode shapes, the model updating optimization of both stiffness and mass matrix simultaneously turns into an ill-posed problem [96]. Thus, current traditional vibration-based finite element (FE) parametric model updating procedures fail on large-scale structures [116]. Nevertheless, in cable-stayed bridges, it is possible to experimentally determine both the deck’s modal parameters and cables’ natural frequencies, which may also provide an indirect estimate of cable forces [136]. In this bridge typology, a well-posed FE model updating may be obtained by estimating both mass mode shape scaling factors and cable forces by using a step-wise FE updating procedure illustrated in Fig. 2.17. In the first step, the mass matrix is determined from the cable forces, in turn, estimated from the natural frequencies of the cables. Then, the unscaled mode shapes and natural frequencies are used to tune the stiffness matrix in a second step. The validity of uncoupling the updating procedure has been demonstrated by two variance-based sensitivity analyses [131, 132], used also to select which parameters affect at most the two unknowns,

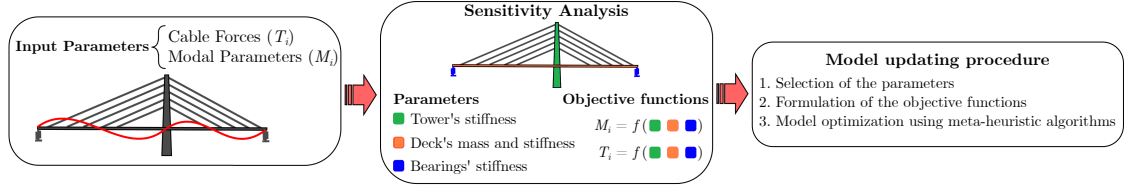


Figure 2.17: Marghera bridge case study: proposed step-wise model updating procedure for cable-stayed bridges.

i.e. the cable forces and the modal parameters. The former is the sensitivity of the cable forces to the specific mass and bearing deformability. The latter is the sensitivity of the natural frequencies to Young's moduli. This approach, thus requires splitting and regrouping bridge components which mainly affect cable forces and modal parameters. Anyway, this procedure can be fairly generalized since bridges belonging to this cable-stayed category are commonly characterized by three main parts: the deck, the bearings, and the tower. Therefore, the stiffness of the deck, bearings, and tower, jointly with the deck's mass may influence both cable forces and modal parameters. Consequently, the model updating optimization problem in Eq. (2.140) is modified accordingly for accounting for two functions containing the squared difference between the two types of input parameters:

$$\min_{\theta \in \Omega} \{ \mathcal{F}(\theta) \} \quad (2.146)$$

$$\mathcal{F}(\theta) = \begin{cases} \sum_{i=1}^{n_c} \left(\frac{T_i^{(e)} - T_i^{(c)}}{T_i^{(e)}} \right)^2, & \text{Cable forces} \\ \sum_{i=2}^{n_m} \left(\frac{\omega_i^{(e)} - \omega_i^{(c)}}{\omega_i^{(e)}} \right)^2 + \sum_{i=2}^{n_m} [1 - \text{MAC}(\phi_i^{(e)}, \phi_i^{(c)})], & \text{Modal parameters} \end{cases}$$

in which θ refers to all the involved bridge parameters defined in an input design variable space Ω . The superscript e refers to measured parameters, whereas c to the calculated ones. T are the cables forces, ω the angular frequencies, and Φ denotes the mode shapes.

The proposed methodology has been tested on the iconic curved cable-stayed case study bridge located in Venice (Italy) at the Marghera harbor, see Fig. 2.18. With a total length of 387m, it is divided into six spans (42 m + 105 m + 126 m + 30 m + 42 m + 42 m), in which the first spans present a straight alignment, and the others a curved one with a 175m radius. The deck consists of a composite concrete-steel continuous girder embracing all six spans, supported by a set of cables flowing into an inclined L-shape prestressed concrete tower. The cables are progressively numbered from 1 to 9 starting from the tower symmetrically both toward the two opposite directions, i.e. Mestre and Venice, as depicted in Fig. 2.18. A more detailed description of the Marghera bridge can be found in [135, 137]. During two ambient vibration tests performed in Autumn 2010 and Spring 2011 [138], the



Figure 2.18: Marghera bridge case study: global overview.

Laboratory of Vibrations and Dynamic Monitoring of Structures from Politecnico di Milano University (Milan, Italy) carried out the dynamic identification of the Marghera bridge identifying about 11 modes in the 0-6 Hz dynamic range for both the bridge and the cable stays, as reported in Fig. 2.19. Ambient vibration tests were carried out using a 16-channel data acquisition system with 14 uniaxial piezoelectric accelerometers (WR model 731A). Each sensor was connected to a power unit acting also as an amplifier providing the needed power supply and selective filtering. The sampling frequency was 200 Hz. The duration of each acquisition was 60 min. Three different sensor layout configurations were adopted for a total of about 50 points of measurement [137]. The dynamic characterization through the PyOMA module confirmed the modal results obtained in other studies, as extensively discussed in [137]. On the other hand, each cable stay was instrumented with a single sensor as evidenced in Fig. 2.18, placed at approximately nine meters above the road surface, permitting to estimate their natural frequencies as reported in Fig. 2.19. The cable forces reported in Tab. 2.8 have been derived by adopting the simplified mechanical model of a fixed-fixed vibrating string and knowing its experimental natural frequencies from the 2011 vibration test campaign, i.e.:

$$f_n = \frac{1}{2L} \left(\frac{T}{\rho} \right)^{0.5} \Rightarrow T = \rho \left[2L \left(\frac{\partial f_n}{\partial n} \right) \right]^2 \quad (2.147)$$

Each cable force T is related to the n -th natural frequency f_n of the cable, its length L , and its density ρ , and as demonstrated by Eq. (2.147), it may be obtained by the derivative of the interpolating law n - f_n . It is worth noting that factors like sag

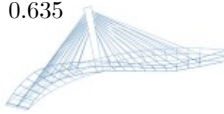
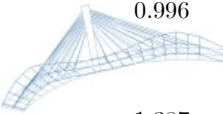
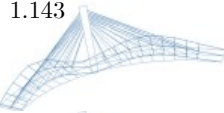
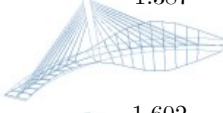


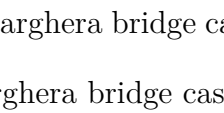
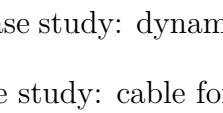
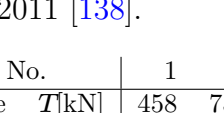
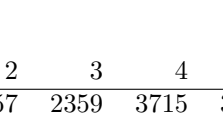
DECK		STAY CABLES					
Mode	f [Hz]	Mode shapes visualization [Hz]:		Cable num.	f [Hz] Mestreside	f [Hz] Veniceside	
1	0.635	0.635		0.996	1	1.230	1.406
2	0.996				0.996		2
3	1.143	1.143		1.387			3
4	1.387				1.387		4
5	1.523	1.523		1.602			5
6	1.602				1.602		6
7	1.963	1.523		1.602			7
8	2.646				1.602		8
9	4.072	1.523		1.602			9
10	4.951				1.602		9
11	5.625	9	0.977	0.938			

Figure 2.19: Marghera bridge case study: dynamic identification results from [138].

Table 2.8: Marghera bridge case study: cable forces identified from vibration data in the tests of 2011 [138].

Cable No.		1	2	3	4	5	6	7	8	9
Mestreside	T [kN]	458	757	2359	3715	3842	4199	4828	5289	4771
Veniceside	T [kN]	614	860	2381	3704	3961	4352	4698	5310	4655

extensibility, cable bending stiffness, and intermediate springs do not play a significant role in affecting the cable forces [137]. However, a remarkable discrepancy of the cable forces between the two tower sides has been evidenced in Tab. 2.8.

A linear FE model of the Marghera bridge not reproducing any geometrical or mechanical nonlinearity has been implemented in SAP2000, which is configured in 8014 nodes and 6600 elements (namely 2946 beams, 18 trusses, and 3636 solid elements), using four-nodes shell elements for the concrete slab and solid elements for the tower. Initial values have been assumed for concrete Poisson’s ratio (0.2) and Young’s modulus (25.0 kN/m^3), and for the steel’s specific weight (78.5 kN/m^3) and Young’s modulus (205 GPa). Using these nominal values for structural materials, the initial modal parameters before performing the updating procedure showed already an acceptable agreement with the experimental value despite a certain gap still exists, but conversely, the cable forces are enormously biased and far from the experimental values. Therefore, a sensitivity analysis of the modeling parameters and cable forces was strictly required to understand which parameters need to be updated while also capturing the relative influences of the modeling parameters affecting the modal properties and the OF in Eq. (2.146). An error function \mathcal{F}_1 was set as the first part of Eq. (2.146), accounting for the 18 force values discrepancy

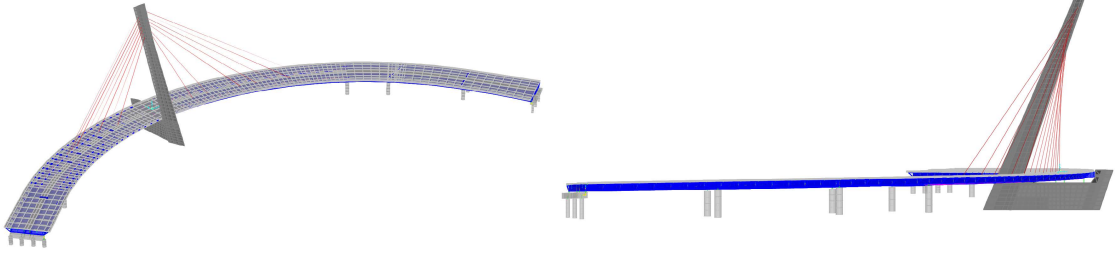


Figure 2.20: Marghera bridge case study: SAP2000 FE model overview.

 Table 2.9: Marghera bridge case study: sensitivity indicators S_1 for the error function Eq. (2.148) and for the cable forces.

	S_1 on Eq. (2.148) [%]	Mestre Side cables S_1 [%]								
		1	2	3	4	5	6	7	8	9
$E_{c,t}$	5.14	87.13	38.14	9.06	1.32	0.01	0.27	0.97	2.10	4.22
ρ_s	0.34	0.08	0.25	0.27	0.23	0.17	0.12	0.07	0.05	0.03
ρ_c	4.13	12.57	61.29	86.05	78.93	55.23	31.74	16.75	9.23	6.82
$E_{c,d}$	1.21	0.51	1.37	1.35	1.12	0.79	0.47	0.24	0.11	0.07
k_a	93.14	0.48	0.69	4.79	19.18	43.59	66.41	80.52	86.86	87.17
		Venice side cables S_1 [%]								
		1	2	3	4	5	6	7	8	9
$E_{c,t}$		82.85	30.49	6.76	1.18	0.12	0.00	0.08	0.21	0.44
ρ_s		0.18	0.39	0.41	0.36	0.29	0.20	0.12	0.05	0.01
ρ_c		17.14	68.93	93.46	94.99	78.15	48.68	22.88	8.28	2.06
$E_{c,d}$		0.22	0.95	1.32	1.44	1.28	0.91	0.48	0.15	0.02
k_a		0.19	0.83	0.01	3.79	21.13	50.04	75.34	89.66	95.70

between the estimated $T_i^{(e)}$ and the numerical $T_i^{(c)}$ values:

$$\mathcal{F}_1 = \sum_{i=1}^{n_c} \left(\frac{T_i^{(e)} - T_i^{(c)}}{T_i^{(e)}} \right)^2 \quad (2.148)$$

From mechanical considerations, the authors identified that the most reasonable influencing parameters of cable forces and their domain space Ω may be: the stiffness of the tower $E_{c,t} \in [30, 50]$ GPa, the abutments supports' stiffness $k_a \in [10, 500]$ kN/mm, the steel mass $\rho_s \in [75, 80]$ kN/m³ and concrete mass $\rho_c \in [24, 30]$ kN/m³ of the deck, and its stiffness $E_{c,d} \in [30, 50]$ GPa. The cables' geometry and material properties are accurately known, thus they were excluded from the sensitivity analysis assessment. This sensitivity analysis permitted decomposing the model output variance into fractions related to each analyzed mechanical parameter [139]. Saltelli's sampling scheme has been adopted [131] to define the total number of simulations required. The variance-based sensitivity analysis provides the first-order (not accounting for input variables' interactions) Sobol sensitivity indicators S_1 , which have been reported in Tab. 2.9 and also visually depicted in Fig. 2.21. These outcomes proved that k_a mainly affects the cable forces estimated by Eq.

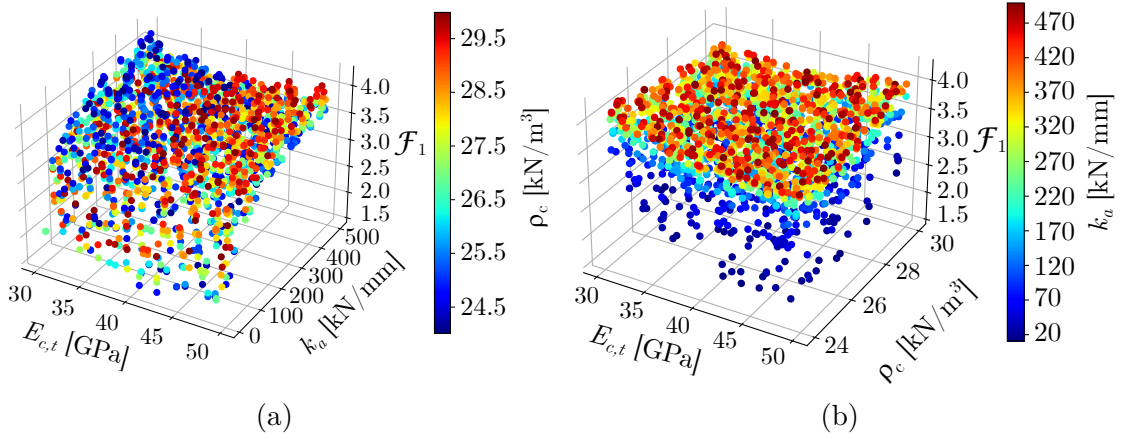


Figure 2.21: Marghera bridge case study: graphical representation of the sensitivity of the objective functions in Eq. (2.148) with two different views (a)-(b) according to the concrete Young's modulus of the tower ($E_{c,t}$), the vertical stiffness of the bearings (k_a) and the mass of the concrete deck (ρ_c).

(2.148), thus being the most influential parameter in the subsequent FE model updating procedure. $E_{c,t}$ and ρ_c also fairly affects the cable forces in Eq. (2.148). From the cable forces point of view, three main trends may be evidenced from the sensitivity analysis results. k_a affects at the most the extreme cables (cable No. 6-9), whereas $E_{c,t}$ plays a significant role for cables closer to the tower (cable No. 1-2). The intermediate cables (cable No. 3-5) appeared to be mainly affected by ρ_c . In summary, the sensitivity analysis results aided in defining the optimal set of parameters to be considered in the FE model updating procedure, and it was also possible to restrict the parameter space domain as follows to speed up the optimization process: $E_{c,t} > 30$ MPa, $\rho_c < 25$ kN/m³, and $k_a < 100$ kN/mm.

On the other hand, the sensitivity analysis has been also conducted considering the modal parameters influence according to the second term of Eq. (2.146), since numerical modal parameters ($\omega^{(c)}, \phi^{(c)}$) are functions of modeling parameters θ . The second term of Eq. (2.146) denoted as $\mathcal{F}_2(\theta)$ can be synthetically rewritten as $\mathcal{F}_2(\theta) = f_1(\theta) + f_2(\theta)$. $f_1(\theta)$ denotes the part depending on the angular frequencies, whereas the $f_2(\theta)$ is the MAC-related part. The Sobol sensitivity indicators have been reported in Tab. 2.10-2.11. Inspecting Tab. 2.11, ρ_c generally appears as the most influential parameter in terms of natural frequency, immediately followed by k_a . Conversely, inspecting Tab. 2.10, k_a appears to be the most influential with respect to mode shapes. As expected both mass and stiffness parameters play a crucial role in the modal-based part of the FE model updating problem. Focusing on mode 2, it is the only case where the sensitivity indicators showed a strong influence of $E_{c,t}$ in terms of frequencies. With deeper insights, modes 2-4 in Tab. 2.11 reported comparable values of $E_{c,t}$, ρ_c , and k_a , and in modes 4 and 6 also ρ_s

Table 2.10: Sensitivity indicators S_1 for $\mathcal{F}_2(\boldsymbol{\theta})$, $f_1(\boldsymbol{\theta})$ and $f_2(\boldsymbol{\theta})$, and for the frequency of each modes (see Fig. 2.19).

	S_1 on		
	$\mathcal{F}_2(\boldsymbol{\theta})$ [%]	$f_1(\boldsymbol{\theta})$ [%]	$f_2(\boldsymbol{\theta})$ [%]
$E_{c,t}$	0.30	0.60	0.40
ρ_s	0.50	0.90	0.70
ρ_c	3.70	61.40	1.30
$E_{c,d}$	0.00	0.10	0.00
k_a	94.60	41.60	97.20

	S_1 on each frequency mode [%]										
	1	2	3	4	5	6	7	8	9	10	11
$E_{c,t}$	3.20	94.40	17.00	3.80	0.10	0.00	0.00	1.40	0.00	1.90	0.00
ρ_s	0.30	0.00	5.30	17.80	0.70	1.20	0.50	3.90	5.30	4.30	2.00
ρ_c	42.20	4.40	75.40	52.90	48.90	65.40	49.30	65.80	60.20	54.80	52.00
$E_{c,d}$	0.10	0.00	0.60	0.70	0.10	0.10	0.10	0.10	0.60	0.00	0.80
k_a	54.60	4.40	23.30	39.20	53.20	33.80	51.00	34.10	52.30	48.30	51.90

 Table 2.11: Sensitivity indicators S_1 for for the MAC of each modes (see Fig. 2.19).

	S_1 on MAC of each mode [%]										
	1	2	3	4	5	6	7	8	9	10	11
$E_{c,t}$	2.80	49.60	41.50	24.30	1.40	1.60	0.00	1.60	0.00	0.60	0.00
ρ_s	2.60	0.20	16.30	58.30	3.80	48.80	0.00	0.60	0.90	0.60	0.60
ρ_c	2.20	25.40	57.70	41.60	11.60	24.20	0.40	4.80	1.60	0.70	1.70
$E_{c,d}$	0.00	0.00	0.20	0.40	0.00	0.10	0.00	0.20	0.00	0.00	0.00
k_a	95.70	74.10	30.20	36.30	97.90	87.20	99.60	98.50	99.40	98.40	96.90

is quite influential. In conclusion, on average, the sensitivity analysis provided a ranking from the most to the least influential selected parameters according to k_a , ρ_c , $E_{c,t}$, $E_{c,d}$, ρ_s respectively.

It is worth mentioning that the preliminary model already approaches the agreement with experimental modal information, thus any model updating process only driven by modal parameters may produce an identity of the updated parameters. On the contrary, considering both mass and stiffness parameters an indeterminate problem is encountered. Moreover, the possible discontinuities in the natural frequency or mode shape parameters' subspaces, may prevent an effective metaheuristic-based optimization process. Therefore, the FE model updating driven by both cable forces and modal characteristics would be beneficial compensating for the above-mentioned adverse effects. Specifically, due to the uncorrelation of the above-selected parameters with respect to the cable forces (see Tab. 2.10-2.11), a lower number of parameters may be considered for FE model updating, i.e.:

1. Assuming an $E_{c,t}$, the optimization refers only to ρ_c and k_a for cables from 3 to 9, using the OF in Eq. (2.146).
2. Assuming ρ_c and k_a from the previous step, the optimization is limited to $E_{c,t}$ for cables 1-2 and mode shape 2, using the OF in Eq. (2.146) limited to the just mentioned conditions.
3. Assuming ρ_c , k_a , and $E_{c,d}$ from the previous steps, a final optimization involving deck's $E_{c,d}$, using the general OF statement of Eq. (2.146).

Table 2.12: Cable forces and modal parameters associated with the optimum set of parameters and percentage error before and after the updating. In the bottom right part of the table, the optimum parameters are listed with the upper (U.B) and lower (L.B.) bounds. In the cable notation, M indicates the Mestre side, whereas V is the Venice side. Instead, in the mode labels, letters V, M, and T indicate the prevalent mode nature, i.e. Bending, Mixed, or Torsional respectively.

Cable Label	Exp. [kN]	Num. [kN]	Error	Initial error	Mode Label	Exp. [Hz]	Num. [Hz]	MAC	Freq. error	Initial MAC	Initial freq. error
M1	458	408	11%	52%	V1	0.635	0.699	97.10%	-10.1%	97.41%	-6.5%
M2	757	1228	-62%	-77%	V2	0.996	0.975	93.79%	2.1%	93.06%	2.1%
M3	2359	2372	-1%	-2%	V3	1.143	1.226	82.41%	-7.3%	85.58%	-7.3%
M4	3715	3852	-4%	5%	T1	1.387	1.395	95.03%	-0.6%	95.26%	-0.5%
M5	3842	4271	-11%	12%	M1	1.523	1.650	78.13%	-8.3%	80.01%	-8.1%
M6	4199	4453	-6%	29%	T2	1.602	1.513	75.38%	5.5%	75.56%	5.7%
M7	4828	4540	6%	48%	V4	1.963	2.073	97.04%	-5.6%	96.91%	-5.5%
M8	5289	5041	5%	56%	T3	2.646	2.559	94.04%	3.3%	94.19%	3.3%
M9	4771	4618	3%	58%	T5	4.072	3.995	89.03%	1.9%	89.10%	1.9%
V1	614	530	14%	43%	T6	4.951	4.826	93.29%	2.5%	91.61%	2.2%
V2	860	1279	-49%	-86%	T7	5.625	5.539	94.48%	1.5%	94.48%	1.5%
V3	2381	2460	-3%	-19%							
V4	3704	3872	-5%	-10%							
Optimized parameters											
V5	3961	4284	-8%	0%	Param.	Unit	L.B.	U.B.	Optimum		
V6	4352	4563	-5%	18%	ρ_c	kN/m ³	23	30	24		
V7	4698	4573	3%	40%	k_a	kN/mm	100	10000	1350		
V8	5310	5229	2%	57%	$E_{c,d}$	GPa	30	1	40		
V9	4655	4791	-3%	76%	$E_{c,t}$	GPa	30	70	51.1		

Further details about the above step-wise optimization procedure can be found in [135]. Two meta-heuristic global optimization algorithms have been employed for mutual validation, specifically the PSO method [134] and the differential evolution (DE) [133] by their Python implementations, and leveraging the SAP2000-OAPI [130]. No significant discrepancies were obtained between the two algorithms, thus the authors reported only PSO results in this case. The three above-mentioned step-wise optimizations led to the final values of the OF respectively of 0.4306, 0.0347, and 1.0296, and the final optimal modeling parameters values have been reported in Tab. 2.12.

The optimum values are still consistent with the engineering judgment, except for the tower stiffness which appears slightly overstated than usual values. However, it is worth noting that beyond its physical meaning, Young’s modulus acts as a modeling parameter in FE model updating procedures, governing global dynamic properties, and thus it is affected by a high level of uncertainties [140]. These uncertainties may be mainly related to modeling errors, due to complex structure simplifications or even meshes discretization, or to modeling parameters intrinsic errors due to material and geometric properties uncertainties. Furthermore, the FE model updating results are consistent with the ones discussed in [137]. It is worth noting that the analyses also revealed that the agreement between modal

parameters does not improve significantly, since the average percentage error remains almost equal before and after the updating. Conversely, the cable forces exhibited a significant consistent improvement, and the key to this improvement has been identified in the introduction of the bearing stiffness in the sensitivity and optimization procedure. The bearings consist of layered neoprene pads with an estimated vertical stiffness equal to 1350 kN/mm, consistent with the vertical stiffness of these structural devices.

In summary, the almost complete FE model updating optimization problem of cable-stayed bridges using modal parameters and cable forces estimates is particularly challenging when dealing with large-scale structures with numerous degrees of freedom using traditional parametric model updating methods. However, in [135] it was demonstrated that if an in-depth preliminary sensitivity analysis is carried out to support the mindful formulation of the objective functions, the traditional model updating based on meta-heuristic optimization algorithms still represents a feasible approach, on the condition that the optimization problem must be solved in a step-wise approach. Indeed, in the Marghera bridge case study, the availability of the cable forces estimates allowed updating the inertial and stiffness features, compared to more conventional FE updating where the sole modal parameters usually deliver ill-posedness and indeterminacy of the optimization problem, imposing the updating of only the mass or stiffness matrix to avoid this indeterminacy.

2.4.3 Train-track-bridge-interaction model in railway bridges: The Orte-Falconara bridge case study

Another case study in which PyOMA was successfully adopted by our research group for the dynamic characterization of a bridge structure can be found in [141]. This latter document is dedicated to the analysis of the dynamic characterization of ballasted railway bridges using a non-proportional damping analytical finite difference model. Ballasted track is the most widespread railway typology, consisting of the superstructure part (rails) and substructure one (ballast). Ballast is composed of natural or crushed coarse-sized, angular, crushed hard stone and rock uniformly graded. Some of the most important functions accomplished by the ballast among others are retaining the tracks and sleepers, ensuring stress propagation from tracks to subgrade and bearing functions, providing water drainage properties to the deck, etc. The presence of the ballast produces changes in the boundary conditions and damping of the structure of medium-length span railway bridges. Recent studies in this field investigated the dynamic response characterization of railway bridges under moving trains. Many of them focused only on the train-bridge interaction modeling, concerning only about the type of trainload model (moving load, moving mass, and/or moving spring-damper), or track mathematical model. Despite some simplified modeling techniques that have been initially proposed in the literature based on beam or shell elements for both the bridge and track, nowadays

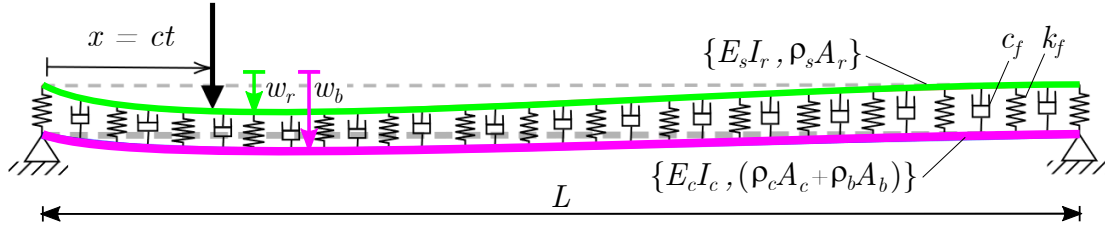


Figure 2.22: Orte-Falconara bridge case study: TTBI model illustration.

research trends go towards increasing the model complexity attempting to capture even more complex mechanical phenomena. Nevertheless, this normally involves a high computational burden, with associated modeling errors and convergence issues, with an overall impactful uncertainty level. These latter aspects motivate our research group to investigate a simplified train-track-bridge interaction (TTBI) model, thus reducing model complexity and still maintaining the agreement with experimental data through an appropriate model updating validation procedure. Specifically, as illustrated in Fig. 2.22, the bridge and the track are modeled both as Euler-Bernoulli beams coupled through a distributed spring-dashpot layer to simulate the ballast, subjected to moving loads and solved by a Runge-Kutta finite difference scheme with spatial and temporal discretization.

In detail, for the track modeling strategy, an Euler-Bernoulli beam model has been employed, denoting its deflection as $w_r(x, t)$, being $\rho_s A_r$ its constant mass per unit length, ρ_s indicating the steel specific mass, being A_r the rails cross-section area, characterized by constant bending stiffness $E_s I_r$, with E_s denoting the steel Young's modulus and I_r the moment of inertia of rails. Therefore, the track-beam equation of motion can be written as [142]:

$$\rho_s A_r \ddot{w}_r(x, t) + E_s I_r w_{r,xxxx}(x, t) = q_r(x, t) + f_r(x, t), \quad (2.149)$$

in which the symbols \ddot{w}_r and $w_{r,xxxx}$ denote, respectively, the second time derivative and the fourth spatial coordinate x derivative of w_r . The distributed load $q_r(x, t)$ arises from the contact restraint to the track displacement provided by the ballast modeled through spring-dashpot bedding:

$$q_r(x, t) = q_b(x, t) = k_f [w_r(x, t) - w_b(x, t)] + c_f [\dot{w}_r(x, t) - \dot{w}_b(x, t)], \quad (2.150)$$

in which w_b indicates the bridge substructure deflection, while k_f and c_f denote the stiffness and damping of the viscous-elastic Winkler spring-dashpot bedding. $f_r(x, t)$ represents the effect of the interaction forces between the rails and the vehicles. As depicted in Fig. 2.23, the train loads have been modeled as moving concentrated uniformly spaced forces with span L_v and being L_t is the train full length, in which each car is modeled by a single force distributed on two axes. In a such way that a train of N_v cars presents $N_v + 1$ moving forces, labeled

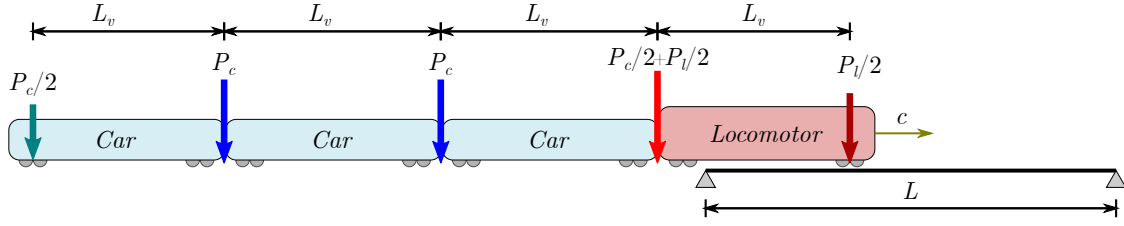


Figure 2.23: Orte-Falconara bridge case study: moving train loading model.

as P_k with $k = 1, 2, \dots, N_v + 1$. Considering that the locomotive has a different weight P_l with respect to the other cars P_c , then P_k can be expressed as $P = \left\{ \frac{P_l}{2}, \left(\frac{P_l}{2} + \frac{P_c}{2} \right), P_c, \dots, P_c, \dots, P_c, \frac{P_c}{2} \right\}$. Assuming the first force enters the bridge at the initial time instant $k = 0$, the time of the k -th load entering the bridge can be expressed as $t_k = (k - 1)L_v/c$.

$$f_r(x, t) = \sum_{k=1}^{N_v} P_k \delta [x - c(t - t_k)] \quad (2.151)$$

Denoting L as the bridge length, the boundary conditions are expressed as follows for a pinned-pinned track:

$$w_r(0, t) = 0 \quad ; \quad w_{r,xx}(0, t) = 0 \quad ; \quad w_r(L, t) = 0 \quad ; \quad w_{r,xx}(L, t) = 0 \quad (2.152)$$

The bridge has been also modeled by Euler–Bernoulli beam, denoting $(\rho_c A_c + \rho_b A_b)$ as mass per unit length, ρ_c as the concrete specific mass of concrete, A_c as the cross-section area of the beam, ρ_b as the ballast specific mass, A_b as the ballast cross-section area, $E_c I_c$ constant bending stiffness, with E_c as concrete Young’s modulus and I_c as the beam cross-section inertia. The following partial differential equation describe the vertical bridge deflection $w_b(x, t)$ [143]:

$$(\rho_c A_c + \rho_b A_b) \ddot{w}_b(x, t) + E_c I_c w_{r,xxxx}(x, t) = q_b(x, t) \quad (2.153)$$

where $q_b(x, t)$ is the force that is transferred to the bridge via the springs bedding, defined as

$$q_b(x, t) = k_f [w_b(x, t) - w_r(x, t)] + c_f [\dot{w}_b(x, t) - \dot{w}_r(x, t)] \quad (2.154)$$

Since the bridge has a pinned-pinned scheme, the boundary conditions are the same as Eq. (2.152). The TTBI model outlined in Fig. 2.22 can be rewritten in matrix form by adopting the finite difference method considering the Eqs. (2.149)-(2.150), and Eqs. (2.153)-(2.154):

$$\begin{aligned} & \begin{bmatrix} (\rho_c A_c + \rho_b A_b) & 0 \\ 0 & \rho_s A_r \end{bmatrix} \begin{Bmatrix} \ddot{w}_b(x, t) \\ \ddot{w}_r(x, t) \end{Bmatrix} + \begin{bmatrix} E_c I_c & 0 \\ 0 & E_s I_r \end{bmatrix} \begin{Bmatrix} w_{b,xxxx}(x, t) \\ \ddot{w}_{r,xxxx}(x, t) \end{Bmatrix} + \\ & + \begin{bmatrix} -k_f & k_f \\ k_f & -k_f \end{bmatrix} \begin{Bmatrix} w_b(x, t) \\ w_r(x, t) \end{Bmatrix} + \begin{bmatrix} -c_f & c_f \\ c_f & -c_f \end{bmatrix} \begin{Bmatrix} \dot{w}_b(x, t) \\ \dot{w}_r(x, t) \end{Bmatrix} + \begin{Bmatrix} 0 \\ f_r \end{Bmatrix} \end{aligned} \quad (2.155)$$

Therefore, the spatial discretization requires subdividing into n intervals of Δx length each of the entire beam domain and consequently approximating the fourth derivative. Denoting $\mathbf{I} \in \mathbb{R}^{n \times n}$ and $\mathbf{0} \in \mathbb{R}^{n \times n}$ as the identity and null matrices, $\mathbf{D}_4 \in \mathbb{R}^{n \times n}$ as the approximate fourth matrix derivative which satisfies the specific boundary conditions (2.152), $\mathbf{w}_b(t) \in \mathbb{R}^{n \times 1}$ and $\mathbf{w}_r(t) \in \mathbb{R}^{n \times 1}$ as the vertical deflection field of the bridge and track $\mathbf{f}_r \in \mathbb{R}^{n \times 1}$ as the discretization moving force vector described in Eq. (2.151), one obtains

$$\begin{aligned}
 & \left[\begin{array}{cc} (\rho_c A_c + \rho_b A_b) \Delta x \mathbf{I} & \mathbf{0} \\ \mathbf{0} & \rho_s A_r \Delta x \mathbf{I} \end{array} \right] \left\{ \begin{array}{c} \ddot{\mathbf{w}}_b(t) \\ \ddot{\mathbf{w}}_r(t) \end{array} \right\} + \\
 & \left[\begin{array}{cc} E_c I_c \mathbf{D}_4 - k_f \Delta x \mathbf{I} & k_f \Delta x \mathbf{I} \\ k_f \Delta x \mathbf{I} & E_s I_r \mathbf{D}_4 - k_f \Delta x \mathbf{I} \end{array} \right] \left\{ \begin{array}{c} \mathbf{w}_b(t) \\ \mathbf{w}_r(t) \end{array} \right\} + \\
 & + \left[\begin{array}{cc} -c_f \Delta x \mathbf{I} & c_f \Delta x \mathbf{I} \\ c_f \Delta x \mathbf{I} & -c_f \Delta x \mathbf{I} \end{array} \right] \left\{ \begin{array}{c} \dot{\mathbf{w}}_b(t) \\ \dot{\mathbf{w}}_r(t) \end{array} \right\} + \left\{ \begin{array}{c} \mathbf{0} \\ \mathbf{f}_r \end{array} \right\} = 0
 \end{aligned} \tag{2.156}$$

which, in compact form, is formally identical to the classical conventional dynamic problem in Eq. (2.23), in which $\mathbf{M} \in \mathbb{R}^{2n \times 2n}$, $\mathbf{C} \in \mathbb{R}^{2n \times 2n}$ and $\mathbf{K} \in \mathbb{R}^{2n \times 2n}$ denotes the mass, damping, and stiffness matrices, $\mathbf{f}(t)$ is the generalized forcing term, and finally the generalized displacement field contains both bridge and track vertical deflections $\mathbf{y}(t) = [\mathbf{w}_b(t)^T, \mathbf{w}_r(t)^T]^T \in \mathbb{R}^{2n \times 1}$. The $\mathbf{D}_4 \in \mathbb{R}^{n \times n}$ matrix is a four-banded matrix, in which the boundary conditions of the considered simply supported beam have been imposed by replacing the coefficients in bold which yield to nullify the bending moment and displacement in both the extremes of the beam:

$$\mathbf{D}_4 = \frac{1}{\Delta x^4} \begin{bmatrix} \mathbf{4} & -4 & 1 & 0 & 0 & 0 & 0 & 0 & \vdots & 0 \\ \mathbf{-7/2} & 6 & -4 & 1 & 0 & 0 & 0 & 0 & \vdots & 0 \\ 1 & -4 & 6 & -4 & 1 & 0 & 0 & 0 & \vdots & 0 \\ 0 & 1 & -4 & 6 & -4 & 1 & 0 & 0 & \vdots & 0 \\ & & \ddots & \ddots & \ddots & \ddots & \ddots & & & \\ 0 & \vdots & 0 & 0 & 1 & -4 & 6 & -4 & 1 & 0 \\ 0 & \vdots & 0 & 0 & 0 & 1 & -4 & 6 & -4 & 1 \\ 0 & \vdots & 0 & 0 & 0 & 0 & 1 & -4 & -4 & \mathbf{-7/2} \\ 0 & \vdots & 0 & 0 & 0 & 0 & 0 & 1 & -4 & \mathbf{2} \end{bmatrix} \tag{2.157}$$

On the other hand, the following continuous-time state-space model allowed performing the time domain discretization of the generalized equation of the motion Eq. (2.23):

$$\dot{\mathbf{x}}(t) = \mathbf{A}(t)\mathbf{x}(t) + \mathbf{B}\mathbf{u}(t) \tag{2.158}$$

in which $\mathbf{x}(t)$, $\mathbf{A}(t)$ and \mathbf{B} and $\mathbf{u}(t)$ are defined in [144] as a function of the generalized mass, damping and stiffness matrices, and the forcing term. Thereafter, the Tustin Approximation method from Matlab System Identification Toolbox provided the discrete-time form of Eq. (2.158), denoting k as the time step, which has



Figure 2.24: Orte-Falconara bridge case study: viaduct overview and ambient vibration testing.

been solved using the Dormand-Prince method based on an explicit Runge-Kutta temporal discretization [145].

$$\dot{\mathbf{x}}_k = \mathbf{A}_k \mathbf{x}_k + \mathbf{B} \mathbf{u}_k \quad (2.159)$$

The proposed analytical model has been employed for the Orte-Falconara railway bridge case study, located in the municipality of Trevi (Italy), and illustrated in Fig. 2.24. The viaduct consists of 46 spans of about 20 m lengths and the planimetric route of the piers identifies a curve with a radius equal to about 2232 m. As indicated in Fig. 2.25, each span consists of 8 PSC beams 1.40 m high and thickness varying from 16 to 33 cm. The prestressing reinforcement is arranged in the lower wing, and, according to the design drawings of the time, it consists of 29 cables arranged in 3 rows, sheathed at the support. In every span, four cross-beams with rectangular cross-sections are present, consisting of a 40cm width and a height equal to the beams. Above the beams, there is a 20 cm thick reinforced concrete slab with 1.40 cantilevered elements, which support the side walkways to the railway line and the parapets. The total width of the deck is about 12.40 m and bears two running high-speed train tracks. A complete description of the bridge can be found in [141].

The vibration testing experimental layout illustrated in Fig. 2.24 consisted of two rows of seven equally-spaced FBA accelerometers with a mutual spacing equal to 3.30 m, and the two extreme accelerometers were placed in correspondence of the supports. Specifically, the accelerometers were arranged into two measurement chains, each one driven by a master recording unit connected to a wireless access point and synchronized by GPS receivers. The dynamic tests were carried out under ambient excitation, acquiring 20-minute long signals sampled at a rate of 200 Hz, despite finally a cut-off frequency of the anti-aliasing filter was set to 40 Hz. The modal parameters were estimated using the SSI-cov method implemented in PyOMA, specifically setting a block-row parameter equal to 7 and a maximum model order equal to 70. The OMA results have been reported in Fig. 2.26,

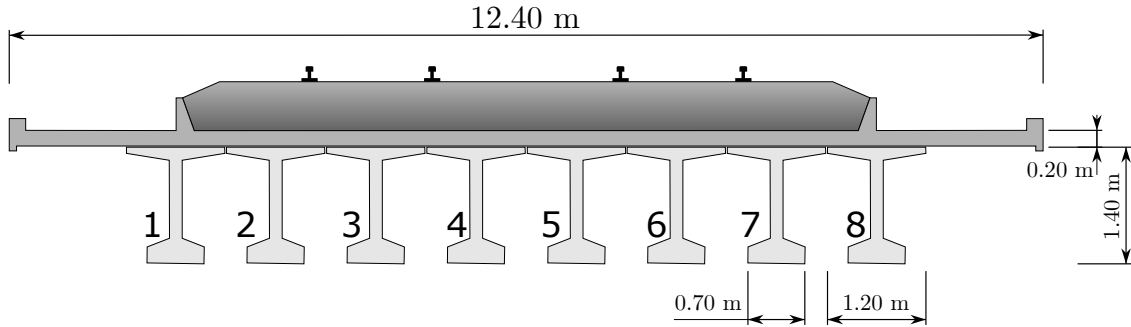


Figure 2.25: Orte-Falconara bridge case study: cross-section details with beams numbering.

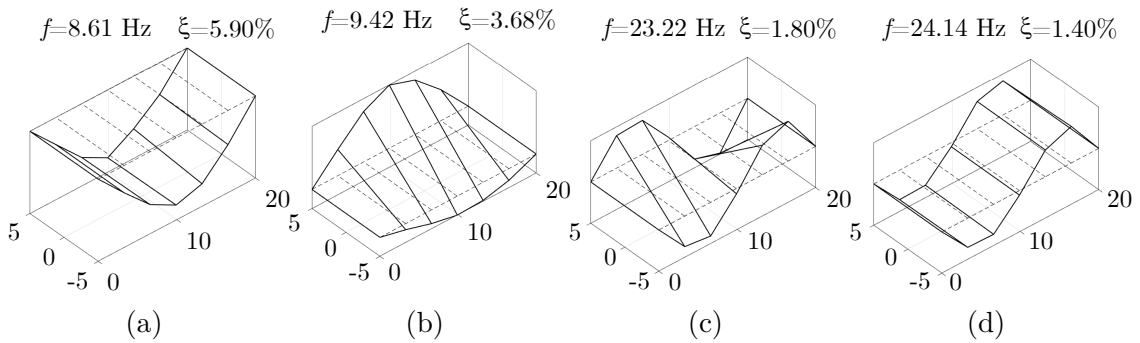


Figure 2.26: Orte-Falconara bridge case study: modal parameter estimates obtained with PyOMA software.

evidencing that the first bending and torsional modes are at approximately 8 Hz and 9 Hz respectively.

Considering the above coupled TTBI model, in our research study [141], two different excitation scenarios of the bridge were considered, i.e. ambient vibration and train transit. In the former scenario, the ambient vibration measurements permitted to estimate of the modal parameters, highlighting that the bridge exhibits both bending and torsional modes. However, it is evident from the first two modes illustrated in Fig. 2.26 that bending modes are not coupled with the torsional ones. Specifically, the first mode closely resembles that of a pinned-pinned beam, and the modal components by the supports are almost null, proving that the bearing deformation can be considered negligible in the current case study. Additionally, the modal components of the first mode associated with the two rows of accelerometers are almost coincident, proving prevalent bending rather than torsional modal deformation. These considerations proved that the first bending mode was negligibly influenced by the track due to its minimal stiffness contribution compared to the bridge cross-section. Therefore, the first bending mode obtained by ambient OMA

Table 2.13: Input parameters of the deterministic model updating optimization algorithm.

Description	Label	Value	Unit
Beam length	L	19.85	m
Discretization step	Δx	0.5	m
Concrete specific mass	ρ_c	2500	kg/m ³
Cross-section area of the bridge	A_c	6.67	m ²
Ballast specific mass	ρ_b	2000	kg/m ³
Cross-section area of the rails	A_r	0.01	m ²
Steel specific mass	ρ_s	2000	kg/m ³
Cross-section area of the ballast	A_b	5.67	m ²
Bending stiffness of the bridge	$E_c I_c$	12600	kN·mm ²
Young's modulus of steel	E_s	210000	Mpa
Cross section area of the rails	I_r	$833 \cdot 10^4$	mm ⁴
Velocity of the train	c	110	km/h
Locomotive's length	L_v	5	m
Car's length	L_v	22	m
Locomotive weight	P_l	300	kN
Car's weight	P_c	600	kN
Number of locomotives		2	
Number of cars		7	

in terms of mode shapes and natural frequencies could be reasonably used to estimate the bending stiffness $E_c I_c$ of the bridge model in Eq. (2.156) according to a simplified equivalent beam model. Thus, a deterministic model updating process has been performed using the parameters in Tab. 2.13. Specifically, the theoretical natural frequencies and mode shapes of a pinned-pinned Euler-Bernoulli beam are given by:

$$f_i = \left(\frac{i^2 \pi}{2L^2} \right) \sqrt{\frac{E_c I_c}{\rho_c A_c}} \quad , \quad \phi_i = \sin \left(\frac{i\pi}{L} x \right) \quad (2.160)$$

where n is the mode number, f_n the n -th natural frequency, ϕ_n the n -th mode shape. The following nonlinear least-squares problem has been solved to perform the deterministic model updating process for estimating the bridge model bending stiffness $E_c I_c$ included in design vector $\boldsymbol{\theta}$ of the model parameters to be optimized [146, 147]:

$$\hat{\boldsymbol{\theta}} = \arg \min_{\boldsymbol{\theta}} J(\boldsymbol{\theta}) = \arg \min_{\boldsymbol{\theta}} \sum_i w_{\varepsilon_i} \cdot [\varepsilon_{z_i}(\boldsymbol{\theta})]^2 \quad , \quad (2.161)$$

where w_{ε_i} is the weighting factor (assumed as unity in this case), and ε_{z_i} denotes the residuals between the experimental and numerical modal data z . In detail, only the undamped eigenvalue $z_i = \lambda_i$ was adopted, considering $\lambda_i = (2\pi f_i)^2$ where f_i indicating the natural frequency:

$$\varepsilon_{\lambda_i}(\boldsymbol{\theta}) = \frac{\lambda_i(\boldsymbol{\theta}) - \tilde{\lambda}_i}{\tilde{\lambda}_i} \quad , \quad (2.162)$$

where the upper tilde denotes the experimental values. The global minimum of the objective function has been found in the correspondence of $E_c I_c \approx 12,600 \text{ kN} \cdot \text{mm}^2$.

On the other hand, in the latter excitation scenario considered, the train transit exhibits the effect of the track. Indeed, as previously mentioned, the effect of the track was negligible in the ambient OMA modal parameters due to its low bending stiffness compared to the bridge cross-section. Nevertheless, the track's role showed up during the train transit due to the load redistribution caused by the track-ballast interaction. Therefore, the track-ballast-bridge model is considered in the train transit case and optimized using experimental train transit data. These data were represented by the vertical displacement history of the bridge collected during train transit by using Micro-epsilon optoNCDT 1420 laser sensors with a sampling rate of 1000Hz. The second part of the study [141] led to the determination of the non-proportional damping coefficient associated with the ballast according to the proposed Euler-Beroulli TTBI model. However, this discussion using displacement data for model updating of the ballast parameters is out of the scope of the present Thesis document, and the interested reader can refer to [141] for further details. In addition, another research study has been investigated leveraging the same optimized TTBI model which can be found in [148]. This latter study is dedicated to the topic of the fragility estimate of railway bridges due to concrete fatigue under repetitive loading cycles due to train transits by knowing the annual train transit scheduling.

2.5 Conventional OMA conclusive remarks

In the present chapter, the main historical highlights on the theoretical background of traditional operational modal analysis (OMA) techniques have been presented. Afterward, the discussion moved to the PyOMA module, the first Python open-source software for OMA, implementing and including those presented frequency-domain-based and time-domain-based methods. This module provides both a suite of user-friendly Python commands included in a single library and, additionally, a first Graphical User Interface version for further improving the usability of the PyOMA package also to practitioners without requiring specific coding knowledge. In the final part of the chapter, some model-updating case studies analyzed during the current Ph.D. program have been discussed, in which PyOMA was successfully used to perform the modal parameters' estimates.

Concluding this chapter, it is noteworthy to stress and point out some of the main drawbacks and limitations of traditional OMA methods. All the basic assumptions of traditional OMA (combined system, input white noise excitation, stationarity and ergodicity) permit to clearly identify the validity scope of the presented OMA algorithms, which mainly address dynamic identification of linear-time-invariant (LTI) structures under stationary and unknown input signals during

operating life conditions. This suggests that a completely different branch of study is instead devoted to nonstationary and/or nonlinear OMA procedures because it requires a completely different mathematical framework. Besides these aspects, two apparent limitations can be noticed within traditional OMA. The first is represented by the absence of mass scaling of the mode shapes, thus mainly affecting the damage detection strategies that analyze mass-normalized mode shapes such as in flexibility-based methods [95]. Furthermore, despite input excitation is not directly controlled in OMA, many concerns still normally arise when no adequate excitation level is induced. Indeed, since the real input conditions are often quite far from the theoretical white noise signals, a certain lack of sufficient excitation of some modes of interest may occur, resulting in non-completely identifiable vibration response data. In [95] some interesting considerations are presented about heuristically checking if the loading conditions could be considered adequate. The first consideration is about concentrated loads and it applies specifically to bridge structures. Specifically, this first aspect concerns a large enough moving load when it involves a large part of the structure under study. In this case, likewise, a car or truck crossing a bridge, the load will excite the structure in an infinite number of points, producing punctual effects that are propagated and overlapped along the structure. Furthermore, this kind of load will excite precisely the vertical modes of major interest. Instead, always in [95], a second aspect is discussed when involving distributed loads and checking if the correlation length is significantly smaller than the global structural scale. For instance, this is the case of wind load conditions because the acting loads are random forces both in time and space dimensions. Nevertheless, if the correlation length at a fixed time is smaller than the size of the structure under investigation, this ensures a random nature of the loading model, thus falling into the hypothesis of having a multiple-inputs dynamic excitation. Similar observations can be made also for traffic on a road in the nearby urban context in which the building under study is located. Indeed, the external traffic induces multiple random inputs exciting the structure, but if the road is far enough, a single car may induce a single input loading source, resulting in a non-representative modal result. In [95], two gold rules are finally remarked within the OMA field. The first relates to carefully checking about a proper random multiple input excitation able to activate the modes of major interest. The second rule is actually a fundamental common sense consideration remarking the garbage-in-garbage-out (GIGO) principle. Accordingly, it is necessary to record good quality output-only vibration response data in order to attempt to achieve reliable modal estimates. Practically speaking, this means also checking the signal-to-noise ratio, checking the presence of outliers and dropouts, the presence of spikes in measured signals, employing an adequate sensing system, avoiding spatial aliasing using a sufficient number of sensors, etc.

Nowadays topical research trends prompted by the use of machine learning and artificial intelligence tools can offer the possibility to improve conventional OMA

methods, especially in the field of automatic OMA (AOMA) or in the damage detection field. In the following chapters, these latter topics are thus extensively discussed. Specifically, the next chapter is dedicated to the development of an effective introduction of the machine learning technologies within the stochastic subspace identification algorithm to overcome existing arbitrary and subjectivity of the existing method, while delivering a novel, intelligent-based, and automatic operational modal analysis framework.

Chapter 3

Machine-learning-aided operational modal analysis

As addressed so far in the previous Chapter 2, OMA methods have been proven effective in identifying dynamic properties of existing structures and infrastructures under operational conditions. Nevertheless, the provision and installation of continuous monitoring systems for long-term SHM purposes potentially applicable to the entire infrastructure network require significant economic planning efforts. As previously discussed in Chapter 1 in Figs. 1.5-1.6 countries all around the whole world are still actively working in that direction to permit a transition at a large regional scale of a widespread, real-time, and continuous SHM-based safety assessment. Therefore, this specific transnational background context has lately motivated for earmarking significant research efforts toward a novel design of lower-cost but still reliable monitoring sensing systems and seeking for the improvement, and automation of the available OMA methods. Indeed, the present Chapter introduces a new paradigm for the automatic output-only modal identification of linear structures under ambient vibrations developed during the current Ph.D. program, namely the intelligent automatic operational modal analysis (i-AOMA). In summary, this new framework leverages the SSI-cov algorithm, but it can be easily extended also to the alternative SSI-dat method. The i-AOMA workflow consists of two main phases. Initially, quasi-random samples of the control parameters for the SSI-cov algorithm are generated. Once the SSI-cov algorithm is performed for each sample, the corresponding stabilization diagrams are overlapped and processed in order to set up a database for training the intelligent core of the i-AOMA method. This latter is represented by the machine learning random forest (RF) technique. The RF is demanded to predict which combination of the SSI-cov governing parameters is able to provide mostly good modal estimates and simultaneously with the least possible spurious noisy information. Afterward, the second main step of the iAOMA method starts, and new quasi-random samples of the control parameters for the SSI-cov algorithm are generated repeatedly until a statistical convergence

criterion on modal estimates is achieved. If the generic sample is classified as feasible by the intelligent core of the i-AOMA method, then the SSI-cov algorithm is performed, thus saving computational resources when the RF predicts a poorly informative governing parameters set. Finally, stable modal results are distilled from gathering all the computed stabilization diagrams and relevant statistics are computed to provide an uncertainty measure of the modal estimates due to the variability of the SSI-cov control parameters.

The present chapter is organized as follows. In the next section 3.1, the iAOMA method is described in detail. Afterward, in section 3.3 the potentials of iAOMA are demonstrated on a synthetic numerical benchmark represented by an MDOF system which simulates a five-story bi-dimensional shear type frame.

In section 3.4, the proposed i-AOMA method has been applied to identify the modal features of a 1380 m long-span suspension bridge located in Norway, i.e. the Hardanger bridge. Another real-world iconic case study is addressed in section 3.5 by considering the Al-Hamra Firduos Tower, a 412.6 m high twisted tall building located in Kuwait City (Kuwait). In the real-world case studies herein discussed, the final results provide extraordinary agreement with the previous experimental literature studies, demonstrating the effectiveness of the iAOMA method in dealing with large-scale civil engineering structures. It is noteworthy to remark that the implemented iAOMA open-source Python code has been made freely available at the following GitHub repository <https://github.com/marco-rosso-m/i-AOMA> for contributing to an Open-Science perspective philosophy.

3.1 Automatic Operational Modal Analysis

The growing use of SHM requires efficient solutions that aim at automatizing the extraction of the modal parameters (viz., natural frequencies, mode shapes, and damping ratios) from the recorded dynamic response of the structures. This need originated the development of some strategies able to facilitate the identification of the modal parameters under free or ambient vibrations, in such a way to mitigate the influence of analyst's decisions on the whole elaboration process [149, 150]. Within this framework, the SSI algorithm [96, 117] is often considered for the automatic operational modal analysis (AOMA) of linear structures subjected to ambient vibrations. Specifically, the automatic identification via SSI algorithm is commonly performed either from the covariances of the outputs (SSI-cov) [151, 152, 153, 154, 155, 156, 114, 157, 158] or directly from time series collected at the tested structure by means of projections (SSI-dat) [159, 160, 161, 162, 163, 164]. Regardless the specific version, the implementation of proper strategies is required to make fully automatic each elaboration phase of the general workflow of the SSI algorithm, namely:

- definition of the set of control parameters;

- estimation of the system poles by means of the SSI algorithm;
- interpretation of the stabilization diagram (SD);
- confidence level assessment of the results.

Although the proper operation of the SSI algorithm largely depends on several control parameters, few efforts have been spent hitherto to avoid a manual selection. In fact, these control parameters are often fixed a priori as constant values or are obtained after a sensitivity analysis within given intervals, and their definition is ultimately based on subjective evaluations or personal experiences [e.g. 152, 153, 154, 159, 165, 166, 167, 168, 141]. However, there are also some recent works that attempted to provide rationale guidelines for tuning automatically the control parameters of the SSI algorithm. For example, Priori et al. [169] proposed some rules to select the optimal values of the number of block rows and columns of the Hankel matrix collecting the output data as well as those for the number of block rows of the past output subpartition and the number of block rows of the future output subpartition in the SSI-dat algorithm. Particularly, the minimum number of block rows of the Hankel matrix has been related to the number of cycles of the fundamental frequency. Next, the minimum number of block rows of the future output subpartition is associated with the modal characteristics of the structure and the sampling frequency. The proper setting of the lower bounds of the remaining control parameters is finally based on the amount of information that the algorithm takes into account for identifying the system (upper and lower bounds of the model order are instead assigned a priori, and the final value is defined as the minimum order at which the largest number of modes appear to be stable). Recently, Zini et al. [114] proposed a procedure to define the number of block rows in the Hankel matrix gathering all the output data and the range of variation of the model order in the SSI-cov algorithm. Herein, the minimum model order is first assumed as twice the number of modes estimated from a preliminary spectral analysis, and further increased by means of an amplifying coefficient. The maximum model order is calculated as the product between the minimum model order and an overmodelling coefficient. The maximum model order is then employed to estimate the upper and lower bounds of the number of block rows of the Hankel matrix. The final number of block rows in the Hankel matrix is obtained from a sensitivity analysis, and the maximum model order is also validated.

Once the control parameters are selected, the poles of the identified linear system are computed for each model order using the SSI algorithm (e.g., either SSI-cov or SSI-dat). The estimated poles of the system are usually presented in a stabilization diagram (SD). Some poles will represent stable (i.e., physical) modes while others will correspond to spurious (i.e., numerical) modes. Indeed, spurious modes will inevitably appear owing to the fact that parametric models attempt to fit the noisy data as best as possible for an imposed conservative over-specification of the

model order [96]. Since the amount of collected data from continuous monitoring can be very large, the manual interpretation of estimated poles is unfeasible and automatic procedures are required. Most of the recent approaches for the automated interpretation of the SD are mainly based on a clustering technique that joints together stable poles with similar properties. This is by far the most investigated aspect within AOMA. Hierarchical clustering and partition clustering methods are the most common in the current literature. The hierarchical clustering technique considers all stable modes as separate clusters, and then groups two adjacent clusters in order to produce a new one. This procedure is repeated until the distances between the rest clusters are larger than a user-specified threshold. Partition clustering techniques tend to divide the stable modes into several clusters [170]. On the one hand, a critical issue in the application of hierarchical clustering methods is the selection of the threshold value of the distances between the rest clusters for which the iterative procedure is stopped. On the other hand, a critical issue in the application of partition clustering techniques is attributable to the fact that the number of clusters must be assigned in advance.

For instance, the clustering-based approach proposed by Reynders et al. [153] for the automated interpretation of the SD consists of the following steps: 1. a pre-cleaning stage by means of a classification of all the identified modes as possible physically or certainly spurious; 2. hierarchical clustering of the possible physical modes for the automatic detection of vertical lines in the SD; 3. final classification of the formed clusters. Some applications of the hierarchical clustering method for the automatic interpretation of the SD have been reported by Magalhaes et al. [152], de Almeida Cardoso et al. [161], Zonno et al. [171], and Garcia-Macias and Ubertini [172], among the others. Zini et al. [114] also proposed a statistical approach to define the cut-off threshold in the hierarchical clustering technique. As regards the partition clustering techniques, the k -means clustering (where the clusters are mutually exclusive) [153] and the fuzzy c -means clustering (where the clusters overlap) [173, 174, 151, 155, 164] have been adopted. For the sake of completeness, it is pointed out that hybrid clustering approaches have been also proposed [175, 156]. For example, Mugnaini et al. [176] proposed the application of the k -means clustering to separate the poles that exhibit high stability from those that show low stability. Subsequently, hierarchical clustering was used to create clusters of poles with similar features. The k -means clustering was then applied once again to discern between highly and sparsely populated clusters, and the latter are discarded. Short reviews about clustering techniques for AOMA have been presented by Hasan et al. [177] as well as Chauhan and Tcherniak [178]. As a matter of fact, all these works that implement a clustering algorithm are instances of machine learning applications in AOMA. A different way to integrate machine learning and AOMA has been presented recently by Liu et al. [179]. It is based on two neural networks [94]: while the first neural network is employed to determine the model order, the second one is used to identify the modal parameters.

Whichever way the identification is performed, the uncertainties at the origin propagate throughout the workflow and affect the final evaluation of the modal parameters as pointed out by Reynders et al. [180], who also provided a partial list of the sources of uncertainty. Some uncertainties are somehow irreducible, such as those due to nonlinearities and nonstationarity. The uncertainties due to the control parameters setting are reducible, but cannot be removed at all. Since the identification of the exact modal parameters is utopistic, it is thus important to assess the confidence in the final estimates (e.g., in terms of bounds, distributions, or statistical moments). Pintelon et al. [181] as well as Reynders et al. [180, 182] are among the few who addressed this issue. To this end, they employ the first-order perturbation analysis to quantify how uncertainties propagate into the final results of the output-only modal analysis of structures. These studies, however, are not intended for automated applications. In this regard, because of the high influence of the control parameters on the final modal estimates, it would be especially important to also evaluate how the uncertainty inherent to their definition propagates in the AOMA.

During the current Ph.D. program, a new paradigm have been proposed for the automatic output-only identification of the modal features of structures and infrastructures subjected to ambient vibrations, called the intelligent operational modal analysis (i-AOMA). The proposed methodology is extensively illustrated in the next sections and it implements the SSI-cov algorithm for modal identification and the overall procedure is basically divided into two steps. Quasi-random samples of the control parameters for the SSI-cov algorithm are generated during the first Phase 1 of i-AOMA. The SSI-cov algorithm is then performed for each sample and the corresponding SDs are elaborated in order to prepare a database for training the intelligent core of the i-AOMA method. This is a machine learning technique, specifically a random forest (RF) classifier, that predicts which combination of the control parameters for the SSI-cov algorithm is able to provide good modal estimates. In the second Phase 2 of the i-AOMA, new quasi-random samples of the control parameters for the SSI-cov algorithm are generated repeatedly. If the generic sample is classified as feasible by the intelligent core of the i-AOMA method, then the SSI-cov algorithm is performed. Once a convergence criterion is achieved, final stable modal results of interest are distilled from the SDs, and relevant statistics are computed to evaluate their confidence level.

3.2 Intelligent automatic operational modal analysis

The survey about the SSI-cov algorithm discussed in Chapter 2 section 2.2.3.4, highlighted that it is governed by the following control parameters:

- the number of block rows i (also known as time shift);
- the length of the data time windows j ;
- the model order n .

Ultimately, the efficiency and accuracy of the SSI-cov algorithm depend on the proper selection of i , j , and n . Furthermore, it is noted that these control parameters are not independent of each other. Particularly, recalling Eq.2.96, below reported for the sake of clearness, a feasible system of order n can be identified as far as the following condition is fulfilled [96]:

$$il \geq n.$$

Moreover, it has been shown [183] that the variance of the estimates initially decreases when i increases because a larger amount of noise is rejected. Conversely, splitting phenomena occur for too high values of i , and the resulting mathematical modes lead to a bias in the physical pole estimates. Such evidence implies that the value of i cannot be set as large as possible. Finally, it is theoretically required that $j \rightarrow \infty$. In reality, this requirement can be only approximated since the output signals are always finite in length. Indeed, the reliable and efficient execution of the SSI-cov algorithm requires that i and j are fixed consistently with n by taking also into account computational effort and memory usage. A machine-learning-based strategy has been conceived in the present work to deal with the output-only automatic modal identification of linear structures under ambient vibrations via SSI-cov.

The proposed approach for the intelligent automatic operational modal analysis (i-AOMA) moves from a recent study by Zhou et al. [184, 185], who introduced a Monte Carlo (MC) simulations-based construction of the SD for SSI algorithms. Specifically, MC simulations are performed by sampling randomly the length of the data time window $j \in [j_{min}, j_{max}]$ and the maximum model order $n \in [n_{min}, n_{max}]$. The time window j is centered symmetrically with respect to a randomly generated time instant $t \in [0, j_{max}]$. The underlying assumption by Zhou et al. [184, 185] is that, in a statistical sense, spurious modes occur occasionally while physical modes occur recurrently. Accordingly, a stability check is performed in order to discriminate the poles denoting the physical modes from those representing spurious modes over s simulations (it is noted that each simulation corresponds to one application of the SSI-cov algorithm). The resulting SD is finally processed via the k -means clustering technique to determine the structural modal parameters.

The methodology proposed by Zhou et al. [184, 185] is attractive, but the following issues can also be recognized.

- The time shift i is still considered a user-defined parameter. Given the relevance of such control parameter, the manual tuning of its value is an impediment towards accurate automatic applications.

- The number of MC simulations s is a new user-defined parameter that plays a somehow important role. However, neither motivations nor guidelines are given about its selection.
- The intervals of the control parameters for Monte Carlo simulations must be defined carefully. Otherwise, several random samplings might result into an ill-conditioned application of the SSI algorithm, also leading to numerical failures or excessive elaboration time. This, in turn, also reflects on the final results, which can actually be carried out from a too low number of samples.
- The MC simulations-based construction of the SD is analyzed in order to derive a deterministic estimation of the modal parameters. So doing, any information about the confidence level of the final estimates due to the different combinations of the control parameters is lost.

The proposed novel approach relies on the MC simulations-based construction of the SD for SSI algorithms presented by Zhou et al. [184, 185], which is largely revised by means of a machine-learning-driven strategy designed to overcome all these limitations. In its essence, it is organized as follows.

- *Database preparation and training of the intelligent core (i-AOMA Phase 1).* Quasi-random samples of the control parameters for the SSI-cov algorithm are generated. The SSI-cov algorithm is then performed for each sample and the corresponding SDs are elaborated in order to prepare a database for training the intelligent core of the i-AOMA method. This is a machine learning technique that predicts which combination of the control parameters for the SSI-cov algorithm is able to provide good modal estimates.
- *Machine-learning-driven automatic identification and uncertainty propagation (i-AOMA Phase 2).* New quasi-random samples of the control parameters for the SSI-cov algorithm are generated repeatedly. If the generic sample is classified as feasible by the intelligent core of the i-AOMA method, then the SSI-cov algorithm is performed. Once a convergence criterion is achieved, final stable modal results of interest are distilled from the SDs, and relevant statistics are computed to evaluate their confidence level.

3.2.1 i-AOMA Phase 1a: stabilization diagram processing through kernel density estimation

The Halton technique [186, 187] is adopted to generate quasi-random samples of the control parameters for the SSI-cov algorithm within the corresponding ranges. They are the maximum model order n , the time window length j , the time target t with respect to which the time window is centered [185], and the time shift

parameter i . Taking into consideration the existing literature [185, 188, 183], the bounded ranges for $\{n, j, t, i\}$ are defined as follows:

$$n \in [n_{min}, n_{max}] = [2 \cdot l, i_{max} \cdot l], \quad (3.1)$$

$$j \in [j_{min}, j_{max}] = \left[\left\lfloor \frac{2}{\max\{f_{f,1}\}} \right\rfloor, j_{max} \cdot l \right], \quad (3.2)$$

$$t \in [t_{min}; t_{max}] = [0, j_{max}], \quad (3.3)$$

$$i \in [i_{min}, i_{max}] = \left[\left\lfloor \frac{f_s}{2 \max\{f_{f,1}\}} \right\rfloor, 10 \left\lfloor \frac{f_s}{2 \max\{f_{f,1}\}} \right\rfloor \right], \quad (3.4)$$

where $\lfloor \cdot \rfloor$ is the rounding operation to the nearest integer, l is the number of monitored degrees of freedom (DOFs), and f_f the fundamental frequency (which is estimated by means of the singular value decomposition of the power spectral density as suggested by Zhou and Li [185]).

A database is then prepared for training the intelligent core of i-AOMA. To this end, s successful quasi-MC simulations are performed: each simulation corresponds to an application of the SSI-cov algorithm using a sample of control parameters generated according to the bounds listed in Eqs. (3.1)-(3.4) by means of the Halton technique. This database is prepared by assuming $s \geq 100$ as suggested by Zhou and Li [185]. It is pointed out that the user's intervention is limited to roughly defining the ranges of the control parameters $\{n, j, t, i\}$, even if their reasonable definition as per Eqs. (3.1)-(3.4) is useful to enhance the efficiency of the i-AOMA. After the training stage, in fact, the intelligent core of i-AOMA will detect the combinations of the control parameters $\{n, j, t, i\}$ that are likely to produce satisfactory results by means of the SSI-cov algorithm. Similarly, the combinations of the control parameters that cause the premature stop of the SSI-cov algorithm because of numerical failure or excessive elaboration time (herein assumed equal to 30 s) are not discarded since they will serve to train the intelligent core of i-AOMA in recognizing unuseful combinations of the control parameters $\{n, j, t, i\}$. Furthermore, only a reasonable value for s is required in such a way to properly train the intelligent core of i-AOMA, but an automatic procedure will be introduced to determine how many quasi-MC simulations must be carried out in order to get the final modal estimates and to calculate the corresponding confidence level.

The SDs resulting from the s successful quasi-Monte Carlo simulations are then overlapped. So doing, a single comprehensive SD is obtained and, for each pole, a stability check is performed in terms of frequency, damping ratio, and mode shapes, in such a way to identify those corresponding to possibly physical modes. Specifically, the HVC and SVC stability criteria illustrated in Eqs.(2.111)-(2.115) have been herein considered. The extraction of certainly physical poles (i.e., the identification of the most recurrent modes having physical meaning) from possibly stable poles (i.e., the poles that fulfill all stability criteria in Eqs. (2.111)-(2.115))

is not performed as most common by means of a traditional clustering procedure. Instead, this is accomplished via Kernel Density Estimation (KDE).

The KDE aims at providing a nonparametric estimation of probability density functions (PDFs) directly from data [189]. Specifically, the KDE is an evolution of any naive estimator because it is based on a symmetric kernel function $K(-z) = K(z)$ that satisfies the following conditions [190, 51]:

$$\int_{-\infty}^{+\infty} K(z)dz = 1, \quad (3.5)$$

$$K(z) \geq 0. \quad (3.6)$$

The most common kernel is the Gaussian one [190, 51]. In this context, the data consists of all the possible stable poles N_p within the comprehensive SD, which are considered as a univariate dataset along the frequency axis only. Therefore, the univariate KDE based on a Gaussian kernel can be written as follows:

$$\hat{\varphi} = \frac{1}{N_p h} \sum_{p=1}^{N_p} K\left(\frac{z - z_p}{h}\right), \quad (3.7)$$

where

$$K\left(\frac{z - z_p}{h}\right) = \frac{1}{\sqrt{2\pi}h} e^{-\frac{(z - z_p)^2}{2h}}. \quad (3.8)$$

The parameter h in Eqs. (3.7)-(3.8) is known as bandwidth (BW) or smoothing parameter, and it is normally fixed across the entire sample [190]. The optimal choice of the BW is challenging because it rules the spread of the kernel, and thus the complexity of the resultant density estimate. Its optimal value represents a variance-bias trade-off between over-smoothed densities at high values of BW (which are not able to capture multi-modality properties) and excessively noisy densities at low values of BW (which present useless spurious fine structures [190, 191]). Since the BW definition has a significant impact, a user-dependent definition of its value should be avoided in automatic applications. Therefore, the improved Sheather-Jones (ISJ) algorithm [191, 192] is performed to facilitate the automatic definition of the BW. This method is especially suitable when data are expected to be multimodal and far from Gaussian normality. Moreover, in order to analyze the performance of any KDE, error criteria are usually set to verify both punctual and global convergence to the real density $\varphi(\cdot)$ of the density estimation $\hat{\varphi}(\cdot; h)$. An appropriate global indicator of their \mathcal{L}_2 distance is represented by the mean integrated squared error (MISE), which is defined as follows [191]:

$$\text{MISE} [\hat{\varphi}(\cdot, h)] = \mathbb{E} \int (\hat{\varphi}(z; h) - \varphi(z))^2 dz, \quad (3.9)$$

where \mathbb{E} denotes the expected value.

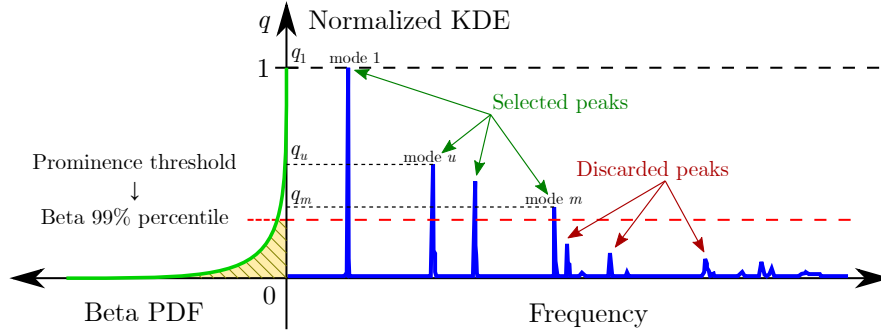


Figure 3.1: Statistical-based criterion for the automatic definition of the prominence threshold and the detection of significant peaks from the normalized KDE.

The ISJ algorithm is mainly based on the minimization of the asymptotic MISE, which recursively produces sequences of BW estimates [192]. It is highlighted that the direct implementations of the KDE algorithms might be computationally expensive in the magnitude of $\mathcal{O}(N_p^2)$ or even larger [189]. This evidence motivated the development of some approximated implementations in the past years. Specifically, the adopted KDE algorithm relies on the discrete convolution workflow provided by the Fast Fourier Transform (FFT-KDE). This is implemented by exploiting the symmetry of the chosen Gaussian kernel function to reduce the computational effort [193]. Particularly, a uniform discrete grid of M points is used to bin the N_p stable poles, thus achieving an overall complexity of $\mathcal{O}(N_p 2^1 + M \log M)$ [191]. For better controlling the granularity of the grid, in the current study, M is set equal to $\lceil 1000 \cdot f_s / 2 \rceil$, being f_s the sampling frequency of the signals.

The KDE plays a crucial role in post-processing the overlapped SDs. In fact, it allows detecting recurrent and significant patterns of stable poles' alignments only (i.e., certainly physical modes) from possibly stable poles, thus acting as a filter for the actual modal parameters. Indeed, the actual natural frequencies are located at the m peaks of interest in the normalized KDE (which is obtained by scaling the KDE in such a way that its largest value is equal to one). In order to automatize the extraction of certainly physical modes, only those stable poles around the m peaks of the normalized KDE within a distance equal to b_w times the BW h are retained, being b_w a factor governing the severity of the filtering effect of the poles of interest. The retaining bands are thus defined as follows:

$$[f_u - b_w \cdot h, f_u + b_w \cdot h]_u \quad (\text{with } u = 1, \dots, m), \quad (3.10)$$

where m is the total number of peaks of interest and f_u is the natural frequency associated with the u -th peak. The value of b_w is the minimum integer number for which all the m groups of certainly stable poles are not empty.

A prominence-based criterion is employed to detect the m peaks of interest

within the normalized KDE. Specifically, only the peaks above a prominence threshold are considered because they are attributable to physical modes. Conversely, the peaks below the prominence threshold are discarded. A statistical approach is proposed to setup automatically the prominence threshold value. By observing that the values of the normalized KDE lie within the bounded range $[0,1]$, all the peak values are fitted through the Beta distribution with parameters α and β , denoted as $\mathcal{B}(\alpha, \beta)$. The maximum likelihood estimation algorithm is here employed for this task. It is noted that the normalized KDE will exhibit a few spiky peaks due to highly recurrent physical modes while it is equal to or close to zero otherwise: therefore, the fitted $\mathcal{B}(\alpha, \beta)$ is expected to be very squashed towards the zero of the normalized KDE (i.e. $\alpha \ll \beta$). The adopted statistical-based criterion for the selection of the prominence threshold is illustrated in Fig. 3.1.

It is worth highlighting that such prominence-based criterion implies a statistically-based discrimination between physical modes and spurious modes. In fact, let q be the generic peak value of the normalized KDE and q_u the corresponding value associated to a certainly physical mode u (where $1, \dots, m$ is the set of all the labels associated to the physical modes of interest of the structure). Then, the proposed prominence-based criterion is equivalent to the application of the following condition:

$$u(q_u) \in \{1, \dots, m\} \iff \int_0^{q_u} f_{\mathcal{B}}(q; \alpha, \beta) dq \geq 1 - p_f, \quad (3.11)$$

where $f_{\mathcal{B}}$ denotes the Beta distribution probability density function. The prominence threshold is ruled by p_f , which defines the threshold probability of failure (i.e., the acceptable probability of extracting a spurious mode rather than a physical mode). In the present work, it is assumed $p_f = 1\%$, which means that the prominence threshold is the value corresponding to the 99th percentile in the fitted Beta distribution. This, in turn, implies that the chance of considering a spurious mode within the final set of the physical modes of interest $\{1, \dots, m\}$ is required to be no larger than 1%. It is evident that the larger p_f , the larger is m , but the larger is also the probability of considering spurious modes within the final set of m modes. The vice versa holds for low values of p_f .

3.2.2 i-AOMA Phase 1b: the random forest intelligent core

The number of successful quasi-MC simulations s has been defined arbitrarily. Although this value can be assumed very large to achieve a predefined convergence criterion, this strategy would be a waste of computational effort because some combinations of the control parameters are likely to produce poor results. Hence, the outcomes of all the previous simulations (i.e., successful and aborted simulations) are considered to fill a training database for a random forest (RF) algorithm, which acts as an intelligent core of the proposed i-AOMA method. Specifically, the RF algorithm will be required to predict whether a new combination of the control

parameters is able to provide enough useful modal information by producing as many certainly stable poles as possible within the retaining bands defined in Eq. (3.10).

A suitable metric must be associated with each previous k -tuple of the control parameters within the database in order to quantify objectively its goodness. To this end, an information content index IC is thus computed for each previous k -tuple of the control parameters $\{n, j, t, i\}_k$. It is defined as the ratio between the number of certainly stable poles $N_{p,k}^*$ (i.e., the number of stable poles falling within the retaining bands in Eq. (3.10)) and the total number of stable poles of the k -th SD $N_{p,k}$, that is:

$$\text{IC}_k = \frac{N_{p,k}^*}{N_{p,k}}. \quad (3.12)$$

So doing, it is possible to associate a quality index IC_k to each previous k -tuple of the control parameters $\{n, j, t, i\}_k$. In fact, IC_k is equal to one if the k -th set of control parameters provides a SD where all the stable poles are retained because they fall within the KDE-based retaining bands in Eq. (3.10). Conversely, it is equal to zero if the set of k -th control parameters provides a SD where no stable pole falls within the KDE-based retaining bands in Eq. (3.10) (IC_k is also equal to zero by default for the combinations of the control parameters that lead to a numerical failure or an excessive elaboration time). The main advantage of the metric in Eq. (3.12) is attributable to its simplicity since the implementation does not require further control parameters and is based on a simple counting procedure. This avoids growing the computational burden. However, other metrics (or a combination thereof) can possibly be adopted.

It is evident that the optimum computational effort is achieved when the analysis is performed for those combinations of the control parameters $\{n, j, t, i\}_k$ that corresponds to a high value of IC_k while those for which $\text{IC}_k \approx 0$ are almost useless. It is assumed that if IC_k is less than a threshold value $\text{IC}_{th} = 0.10$, then the corresponding set of control parameters $\{n, j, t, i\}_k$ is unfeasible because it is non-informative of the actual modal properties of the structure. Conversely, if IC_k is equal to or larger than a threshold value $\text{IC}_{th} = 0.10$, then the corresponding set of control parameters $\{n, j, t, i\}_k$ is feasible because it provides enough information about the actual modal properties of the structure. The RF algorithm is thus trained to classify each freshly generated set of the control parameters $\{n, j, t, i\}_k$ as either feasible or unfeasible, without performing the SSI-cov algorithm. Boolean discrimination is adopted such that the k -tuple of the control parameters $\{n, j, t, i\}_k$ is labeled with 1 if $\text{IC}_k > \text{IC}_{th}$ (feasible set of control parameters) and 0 otherwise (unfeasible set of control parameters). Boolean labeling improves the diversity among the most and the less informative sets of control parameters. The RF algorithm is one of the most powerful and robust, yet simple, machine learning algorithms for classification problems [43]. Briefly, RF is an ensemble machine learning

technique based on the simultaneous training of a group of various decision trees (weak learners), whose predictions are finally aggregated with a majority voting method [61]. The RF algorithm adopts an initial bagging procedure (also known as bootstrap), which is performed by randomly drawing a number of samples with replacements from the training set. A subset of input features is then used to train each decision tree component [43]. The usual size of this subset is \sqrt{d} , where d is the dimension of the features vector. Each decision tree component is trained in order to maximize the information gain [61], in such a way to look for the best features among the selected subset, thereby improving the tree diversity. The greatest advantage of any ensemble method is based on the adoption of a final majority voting system, which ensures a consistent level of accuracy and robustness in contrast to any single weak learner alone. The aggregation provides, in general, better results and reduces both bias and variance. This, in turn, improves the generalization capabilities and drastically mitigates any possible overfitting issue [43]. The use of the RF is especially attractive to enhance the automation level of the i-AOMA because it does not require careful tuning of its hyperparameters value by virtue of the intrinsic robustness due to its ensemble nature [61]. The only significant control parameter of the RF algorithm is the number of decision trees composing the forest: if it is high, then it would provide better results, with the side-effect of increasing the computation cost. In the present study, the RF algorithm is implemented by considering 100 trees, an information gain measure based on the Gini impurity index, no depth tree pruning, and a maximum number of features for the bootstrap subset equal to $\sqrt{d} = 2$ (being $d = 4$ the size of the each k -tuple of the control parameters $\{n, j, t, i\}_k$).

3.2.3 i-AOMA Phase 2: intelligent-guided automatic modal identification and uncertainty propagation

The Halton technique is employed to sample new k -tuples of the control parameters $\{n, j, t, i\}_k$ within the bounds listed in Eqs. (3.1)-(3.4). Then, the trained RF applies as an intelligent core in order to classify the newly generated k -tuple of the control parameters $\{n, j, t, i\}_k$: if it is classified as unfeasible, then the SSI-cov does not apply and a new set is considered. This allows to save elaboration time since only feasible k -tuples of the control parameters $\{n, j, t, i\}_k$ are processed henceforth. This intelligence-driven procedure is reaped until a suitable convergence criterion is achieved. The convergence check is performed periodically considering a batch size of successful quasi-MC simulations b (i.e., convergence check of i-AOMA is performed every successful b runs of the SSI-cov algorithm). The selected convergence criterion depends on the uncertainty associated with the estimated mode shapes $\phi_u = [\phi_{u,1} \ \dots \ \phi_{u,l}]^\top$, which are carried out for $u = 1, \dots, m$ from the selected poles within the retaining bands defined in Eq. (3.10) on the basis of the

normalized KDE. The mode shape vectors ϕ_u are thus considered as multivariate random vectors, and the overall uncertainty is assessed by means of the generalized sample variance matrix \mathbf{S}_u (i.e, a covariance matrix of the components of the u -th mode shape vector ϕ_u), which is defined as follows [194]:

$$\mathbf{S}_u = \begin{bmatrix} \text{Var}[\phi_{u,1}] & \text{Cov}[\phi_{u,1}, \phi_{u,2}] & \dots & \text{Cov}[\phi_{u,1}, \phi_{u,l}] \\ & \text{Var}[\phi_{u,2}] & \dots & \vdots \\ & & \ddots & \text{Cov}[\phi_{u,l-1}, \phi_{u,l}] \\ \text{Sym.} & & & \text{Var}[\phi_{u,l}] \end{bmatrix}. \quad (3.13)$$

This is a symmetric matrix collecting the sample variances ($\text{Var}[\cdot]$) of the ϕ_u 's components on the main diagonal, whereas the sample covariances ($\text{Cov}[\cdot, \cdot]$) outside of the main diagonal are computed among pairs of ϕ_u 's components. A suitable measure of the overall variability of a multivariate random vector is the total sample variance, which corresponds to the trace of the matrix \mathbf{S}_u [194], namely $\text{tr}(\mathbf{S}_u)$. Hence, the traces of the sample covariance matrices given by Eq. (3.13) for $u = 1, \dots, m$ are computed, and the acceptable shifting convergence band rule (ASCBR) [195, 196] is employed to limit the subjective judgment of the convergence condition. The batch size is taken $b = 50$ [196] whereas the intelligence-driven procedure is stopped (i.e., new samples of the control parameters are no longer generated) once the relative total sample variance for each mode of interest $\{\Delta \text{tr}(\mathbf{S}_u)\}_{u=1}^m$ is restricted to $\pm 2\%$ [197].

Once the convergence is achieved, the SDs carried out from all the applications of the SSI-cov algorithm are overlapped, and the stability criteria in Eqs. (2.111)-(2.115) apply to identify possibly physical modes. Thereafter, the normalized KDE-based filtering procedure is performed once again to retrieve the final estimates of the modal parameters, and basic statistics are determined. These statistics allow quantifying the epistemic uncertainty in the final modal estimates due to the variability of the control parameters. As far as the uncertainty quantification for the estimated mode shapes, a boxplot-based representation is recommended [198, 199]. So doing, the boxplot's whiskers represent the distance between the first quartile or the third quartile of the modal displacement with respect to the lower and upper fence, respectively. The fences, in turn, are located at an additional distance of 1.5 times the interquartile range. The whiskers-based representation is deemed appropriate since it provides a robust and not necessarily symmetric measure of the uncertainty level.

3.2.4 i-AOMA recap and Python implementation

The workflows recap for both Phase 1 and Phase 2 of the i-AOMA method are depicted in Fig. 3.2.

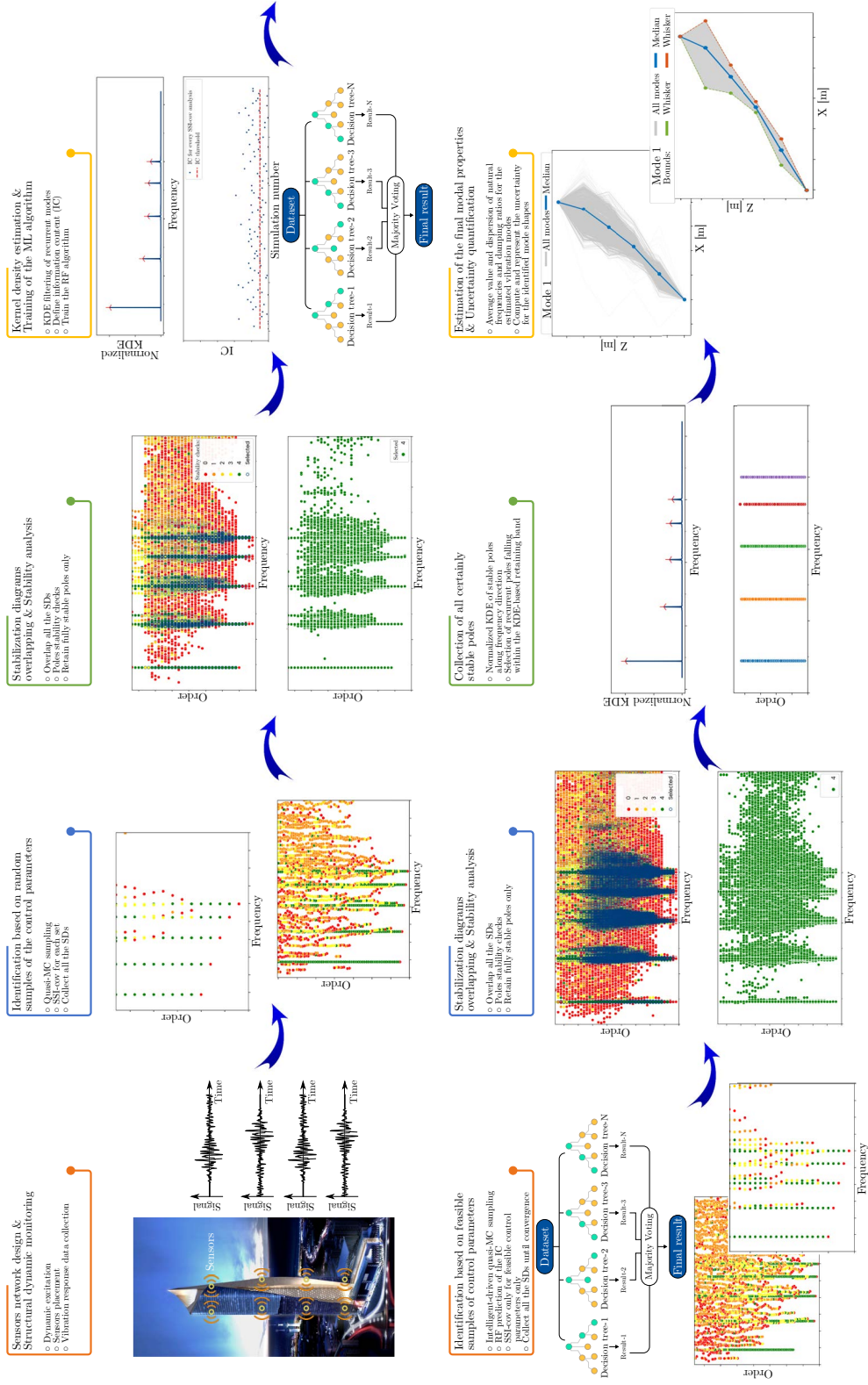


Figure 3.2: The i-AOMA workflow: i-AOMA Phase 1 (top row) and i-AOMA Phase 2 (bottom row).

Algorithm 1 Pseudocode of i-AOMA Phase 1 – Database preparation and training of the intelligent core

```

Define  $s$                                 ▷ Successful runs of the SSI-cov for training the RF algorithm
Define  $n_{max}, j_{min}, j_{max}, i_{min}, i_{max}$     ▷ Reasonable control parameters bounds
Generate quasi-random samples of the control parameters  $\{n, j, t, i\}_{k=1, \dots}$ 
while  $s$  successful runs of SSI-COV are not completed do
  try
    @check execution time  $\leq 30$  s          ▷ Admissible elaboration time
    SSI-cov( $\{n, j, t, i\}_k$ )                ▷ Compute the SD via SSI-cov
    Normalize mode shapes
  except                                     ▷ Numerical failure, execution time larger than 30 s
    Set  $IC_k = 0$                              ▷ Unfeasible set of control parameters
end while
Overlap all the SDs
Check the poles stability                    ▷ Detect possibly stable poles
Perform KDE                                  ▷ Perform FFT-KDE with ISJ algorithm
Recognize certainly stable poles from the normalized KDE
Calculate  $IC_k$ 
Set IC threshold  $IC_{th}$ , if  $IC_k \geq IC_{th}$  then  $IC_k = 1$  else  $IC_k = 0$ 
Classifier training  $RF.fit(inputs = \{n, j, t, i\}_{k=1, \dots}, targets = \{IC_k\}_{k=1, \dots})$ 

```

Algorithm 1 and Algorithm 2 provides the pseudocode for Phase 1 and Phase 2 of the i-AOMA method, respectively. The proposed i-AOMA method has been implemented by means of the Python programming language. Particularly, the implementation of i-AOMA relies on PyOMA [117], which is a suite of Python libraries for standard output-only modal identification of linear structures. The code implementation is based on the extensive use of the object-oriented programming paradigm in order to make the elaboration as fast as possible. The elaboration time can be dramatically reduced by means of a suitable parallelization of the elaboration tasks. The code is available at the following Google Colab notebook link: <https://colab.research.google.com/drive/1D6z1zM71qJavI6yyMCI8BMnEqV9zw7kW?usp=sharing>. It can also be freely downloaded from the following GitHub repository: <https://github.com/marco-rosso-m/i-AOMA>.

3.3 i-AOMA validation: numerical shear-type planar frame benchmark case study

The proposed i-AOMA method is initially tested on a numerical benchmark problem following Pasca et al. [117]. A five degrees-of-freedom (DOF) shear-type planar frame under white noise excitation is considered, with lumped mass at each floor

Algorithm 2 Pseudocode of i-AOMA Phase 2 – Machine-learning-driven automatic identification and uncertainty propagation

```

Set the batch size  $b = 50$            ▷ Convergence check every 50 runs of the SSI-cov
Set a large number  $s_{max}$ 
Generate quasi-random samples of the control parameters  $\{n, j, t, i\}_{k=1}^{s_{max}}$ 
while  $k \leq s_{max}$  and  $\{\Delta \text{tr}(\mathbf{S}_u)\}_{u=1}^m \geq \pm 2\%$  do
  try
    if RF.predict(inputs=  $\{n, j, t, i\}_k$ ) = 1 then           ▷ RF classification
      @check execution time  $\leq 30$  s           ▷ Admissible elaboration time
      SSI-cov( $\{n, j, t, i\}_k$ )           ▷ Compute the SD via SSI-cov
      Normalize mode shapes
      if  $k$  reaches multiples of  $b$  then
        Overlap all the SDs up to  $k$  runs
        Check the poles stability           ▷ Detect possibly stable poles
        Perform KDE           ▷ Perform FFT-KDE with ISJ algorithm
      end if
    else
      Set  $\text{IC}_k = 0$            ▷ Unfeasible set of control parameters
    end if
  except           ▷ Numerical failure, execution time larger than 30 s
    Set  $\text{IC}_k = 0$            ▷ Unfeasible set of control parameters
end while
Overlap all the SDs
Check the poles stability           ▷ Detect possibly stable poles
Perform KDE           ▷ Perform FFT-KDE with ISJ algorithm
Select certainly stable poles from the normalized KDE
Compute basic statistics of the physical modal parameters of interest

```

equal to 25.91 Ns²/mm and story stiffness equal to 10,000 N/mm for every floor level. The damping matrix is computed by assuming a constant damping ratio equal to 2% for every mode. System frequencies and mode shapes (normalized with respect to the largest value) are the following:

$$\mathbf{f} = \begin{bmatrix} f_1 \\ f_2 \\ f_3 \\ f_4 \\ f_5 \end{bmatrix} = \begin{bmatrix} 0.88995 \\ 2.59776 \\ 4.09511 \\ 5.2607 \\ 6.0001 \end{bmatrix} \text{ Hz}, \quad (3.14)$$

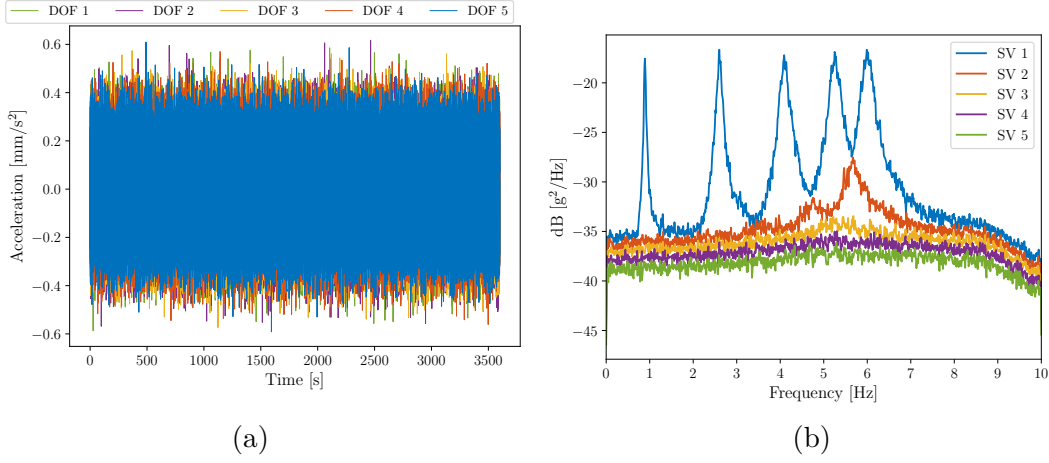
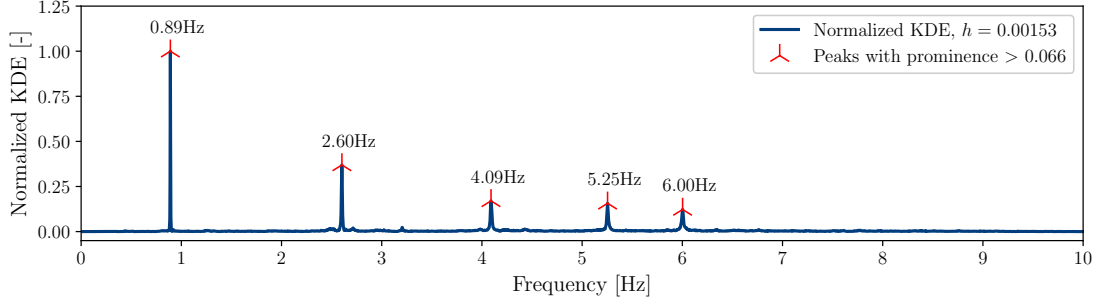


Figure 3.3: Numerical benchmark case: synthetic monitoring data (a) and singular value decomposition of the power spectral density (b).

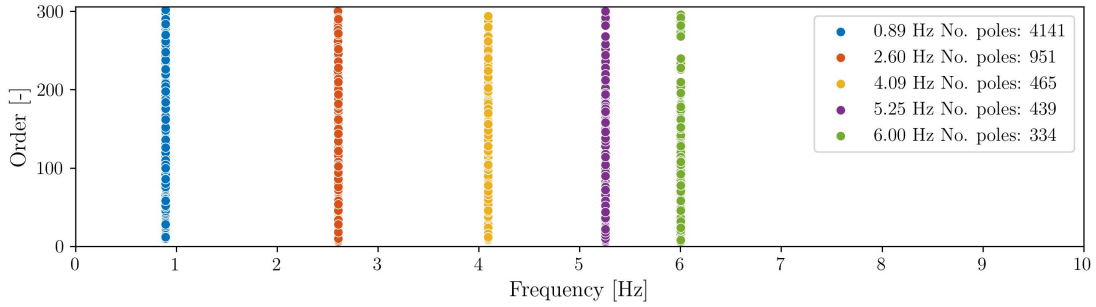
$$\begin{aligned}
 \Phi &= [\phi_1 \ \phi_2 \ \phi_3 \ \phi_4 \ \phi_5] \\
 &= \begin{bmatrix} 0.28463 & -0.763521 & 1 & 0.918986 & -0.5462 \\ 0.5462 & -1 & 0.28463 & -0.763521 & 0.918986 \\ 0.763521 & -0.5462 & -0.918986 & -0.28463 & -1 \\ 0.918986 & 0.28463 & -0.5462 & 1 & 0.763521 \\ 1 & 0.918986 & 0.763521 & -0.5462 & -0.28463 \end{bmatrix}. \quad (3.15)
 \end{aligned}$$

Vibration response data at every DOF corresponding to 1 h recordings have been generated with a sampling frequency of $f_s = 100$ Hz. The response data have been polluted by adding a white noise with a signal-to-noise ratio equal to 10% in order to reproduce real-world monitoring conditions. Following Pasca et al. [117], synthetic monitoring data have been decimated with a factor equal to 5 after the application of a finite impulse response anti-aliasing low-pass filter with a 30 points Hamming window. Fig. 3.3 illustrates synthetic monitoring data and the singular value decomposition of the power spectral density.

The singular value decomposition of the power spectral density shows that the fundamental frequency is $f_f = 0.890$ Hz. Hence, the bounds of the control parameters are roughly defined according to Eqs. (3.1)-(3.4). A total of $s = 100$ quasi-random samples of the control parameters have been generated according to the Halton technique for the present benchmark case during the i-AOMA Phase 1. To this end, 220 sets of control parameters have been sampled to gather $s = 100$ successful applications of the SSI-cov algorithm, thus resulting in a success rate of about 45%. Numerical failure or excessive elaboration time occurred for the remaining 120 samples. Once the SDs corresponding to $s = 100$ successful applications of the SSI-cov algorithm have been overlapped, stability checks have been performed according to Eqs. (2.111)-(2.115) and possibly stable poles are then



(a)



(b)

Figure 3.4: Numerical benchmark case *i*-AOMA Phase 1: normalized KDE together with the identified peaks (a) and certainly stable poles falling within the retaining bands (b) obtained from the sets of control parameters generated for training the intelligent core of *i*-AOMA.

identified. The FFT-KDE algorithm has been next applied on these possibly stable poles, delivering an estimate of the BW equal to 0.0015 Hz with the ISJ algorithm. The statistical value of the prominence threshold for the peaks' identification from the normalized KDE (99th percentile in the fitted Beta distribution) is equal to 0.066. A factor of $b_w = 1$ has been automatically identified to successfully collect non-empty groups of stable poles around the peaks of the normalized KDE according to Eq. (3.10). Subsequently, the database consisting of all the generated control parameters and the corresponding IC values is prepared in order to train the intelligent core of the *i*-AOMA method, i.e. the RF algorithm. Figs. 3.4-3.5 illustrate the main results obtained from the $s = 100$ sets of control parameters generated during the *i*-AOMA Phase 1.

Henceforth, new quasi-random samples of the control parameters are generated with the Halton technique. However, the SSI-cov analysis is now performed only for those samples that are classified as feasible by the RF algorithm. In total, the algorithm generated new 2,105 samples, but only 600 new samples were actually

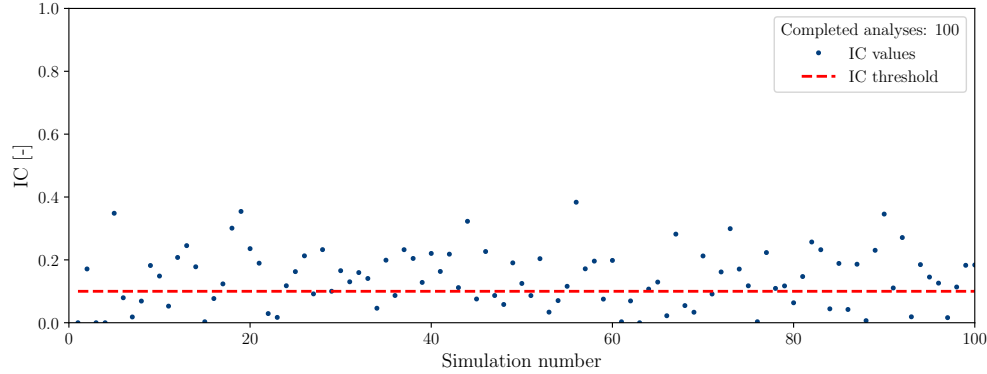


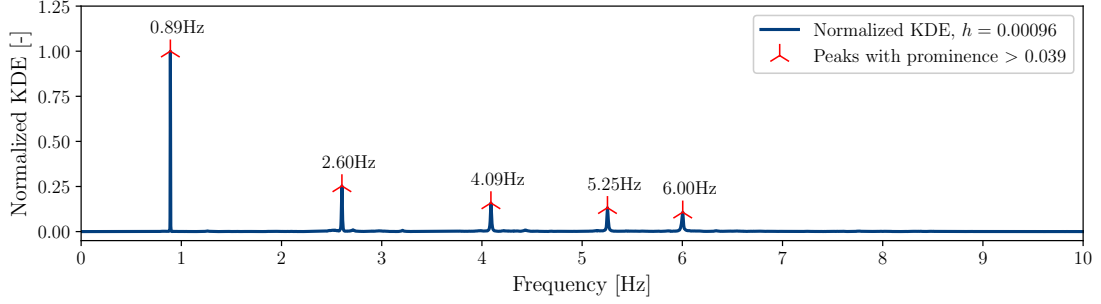
Figure 3.5: Numerical benchmark case: numerical values of IC obtained from the sets of control parameters generated for training the intelligent core of i-AOMA.

analyzed with the SSI-cov algorithm, demonstrating the filtering effect provided by the i-AOMA intelligent core based on the RF algorithm. Therefore, after collecting 600 new SDs, the convergence criterion based on Eq. (3.13) has been fulfilled. Figs. 3.6-3.8 illustrate the final results of the i-AOMA.

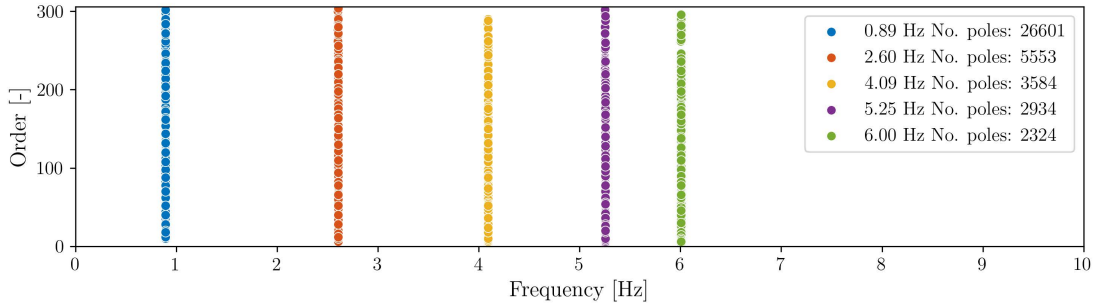
It is worth noting in Fig. 3.6 that a lower estimate of the BW equal to 0.00096 Hz has been obtained with the ISJ algorithm. The reduction of the BW value in the i-AOMA Phase 2 is due to the selection pressure provided by the RF algorithm, which reduces the uncertainty of the modal estimates attributable to the control parameters by driving the selection of their most appropriate values. Furthermore, Fig. 3.8 demonstrates that the trained RF algorithm drives intelligently the control parameters sampling, since most of the points are above the IC threshold value. Fig. 3.9 illustrates the joint (bidimensional) probability density functions of the control parameters that have been classified as feasible from the intelligent core of i-AOMA. These plots provide interesting interpretative maps that illustrate where the best values of the control parameters were actually sampled for this benchmark case study.

The estimates of the natural frequencies for the present benchmark case are 0.89 Hz, 2.60 Hz, 4.09 Hz, 5.25 Hz, and 6.00 Hz. The corresponding estimates of the damping ratios are 1.97%, 1.99%, 2.12%, 2.13%, and 1.95%. The identified mode shapes are shown in Fig. 3.10. By resorting to a boxplot-type representation, this figure also highlights the uncertainty level related to the selected poles in Fig. 3.6, as it emerges from the corresponding combinations of the control parameters adopted for the SSI-cov algorithm.

Although the final stable poles are relatively close to each other, it is worth noting in Fig. 3.10 that the uncertainty due to the control parameter values propagates and possibly amplifies through the identification procedure. Notably, the uncertainty level in the final mode shapes is not constant. On the contrary, it is



(a)



(b)

Figure 3.6: Numerical benchmark case i-AOMA Phase 2: the normalized KDE together with the identified peaks (a) and certainly stable poles falling within the retaining bands (b) obtained at the end of the i-AOMA.

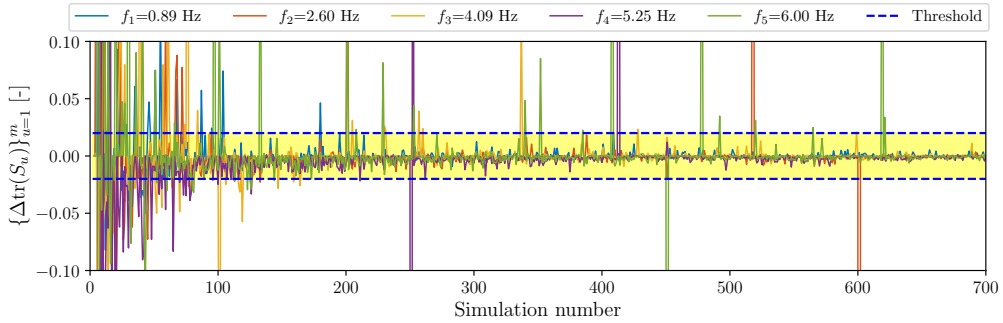


Figure 3.7: Numerical benchmark case: convergence analysis of the relative total sample variance for each mode.

very low in some cases but it can be also quite large, depending on the considered DOF and the mode number.

Eventually, Figs. 3.11-3.12 illustrate the convergence of average and standard

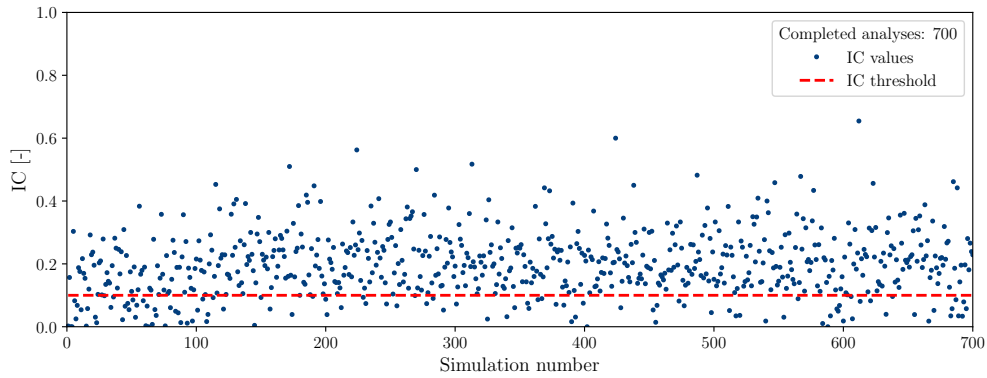


Figure 3.8: Numerical benchmark case: numerical values of IC obtained from all the feasible sets of control parameters generated during i-AOMA.

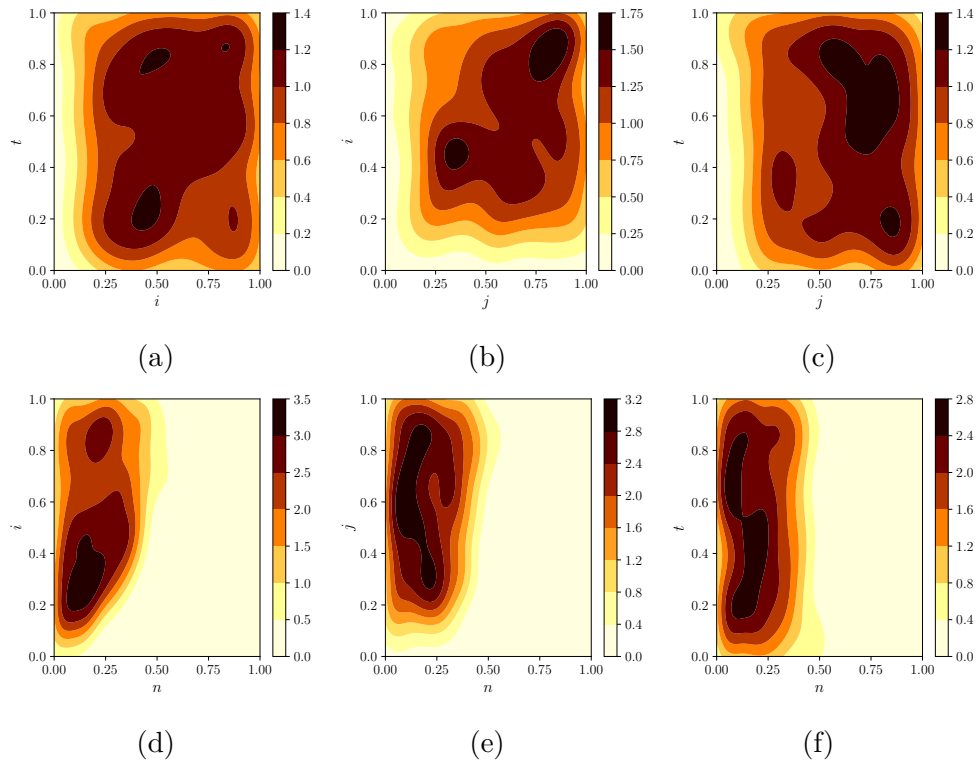


Figure 3.9: Numerical benchmark case: joint probability density functions of the control parameters samples that have been classified as feasible from the intelligent core of i-AOMA.

deviation for natural frequencies and damping ratios, respectively, over all the feasible samples of the control parameters. The final standard deviation values in Figs. 3.11-3.12 show that the uncertainty level about the natural frequencies due to the

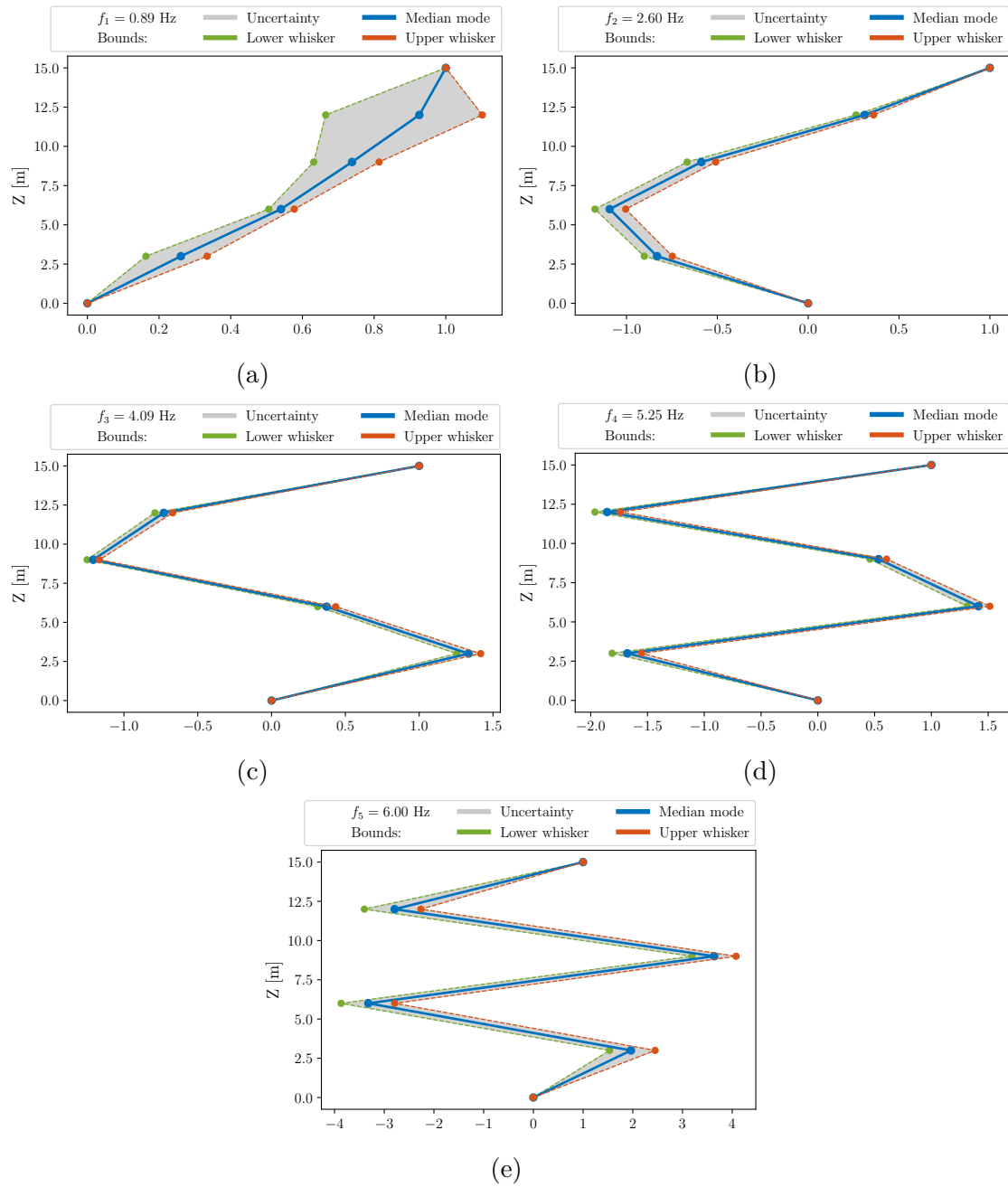


Figure 3.10: Numerical benchmark case: median mode shapes and corresponding uncertainty level in terms of boxplot’s whiskers.

variability of the control parameters is generally lower than that observed for the mode shapes. A significant uncertainty level is also observed for the estimation of the modal damping ratios.

It is pointed out that the original MC simulations-based construction of the

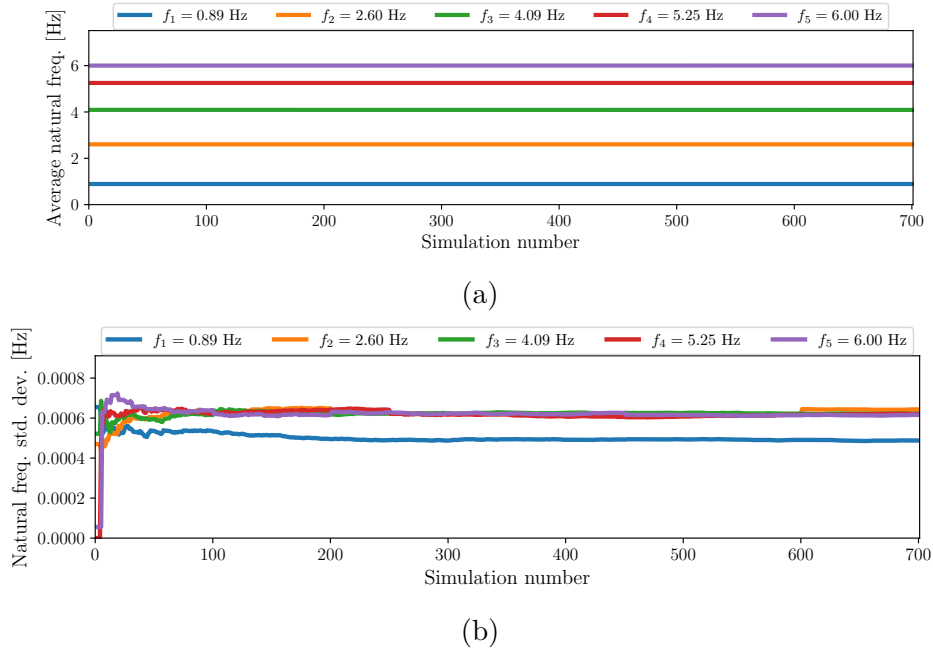


Figure 3.11: Numerical benchmark case: average (a) and standard deviation (b) of natural frequencies over the feasible samples of the control parameters.

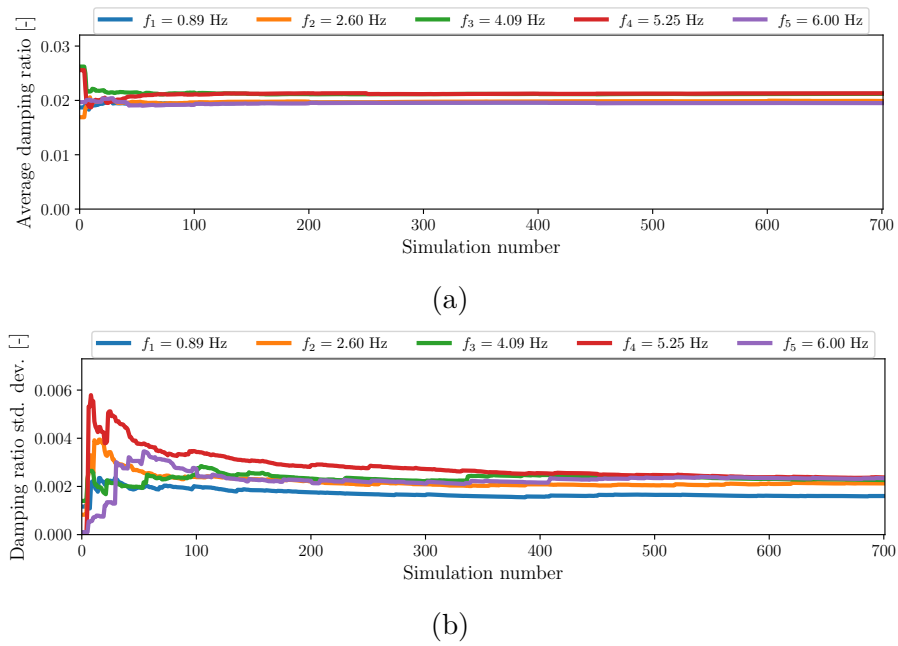


Figure 3.12: Numerical benchmark case: average (a) and standard deviation (b) of damping ratios over the feasible samples of the control parameters.

SD has been applied for the sake of validation by considering all the quasi-random samples of the control parameters (i.e., without restricting the application of the SSI-cov algorithm to those control parameters that have been classified as feasible from the intelligent core of the *i-AOMA*). So doing, practically identical results have been obtained on average whereas narrow confidence bounds are obtained by means of the proposed *i-AOMA*. This is attributable to the selection pressure exerted by the RF algorithm, which allows reducing the uncertainties related to the variability of the control parameters. This demonstrates that the proposed *i-AOMA* methods allow for achieving more accurate results with no significant influence of the analyst’s decisions while dramatically reducing the whole computational effort.

3.4 *i-AOMA* application: the Hardanger Bridge case study in Norway

3.4.1 Long-term monitoring system description and open database

SHM is one of the main critical aspects of bridge engineering among others, since it aims to ensure the safety and longevity of these vital communication infrastructures. This is particularly important for less common typologies such as slender, long-span, and relatively lightweight steel-made suspended bridges. Unlike other more conventional bridges, which often have bulkier designs and shorter spans, suspended bridges feature streamlined configurations with expansive lengths, often surpassing a kilometer. These strong dissimilarities in the stiffness-to-weight ratio pose unique challenges for dynamic monitoring, demanding specialized attention. To begin with, even in still air and default ambient conditions, their dynamic behavior is markedly different, with much lower natural frequencies. Furthermore, this inherent slenderness introduces complexities in their behavior under varying operational and environmental conditions, including wind, traffic, and thermal loads. Consequently, monitoring systems for these bridges must adapt to account for their sensitivity to dynamic forces, ensuring precision in detecting potential structural changes. Therefore, the application of ambient vibration testing by OMA and AOMA systems is particularly challenging for these infrastructures. Many techniques that can be considered a viable option for RC bridges being scarcely affected by wind and other conditions, besides their relatively high and well-spaced natural frequencies, could not probably withstand these increased difficulties.

The real-world compelling case study herein analyzed to test the effectiveness of the *i-AOMA* method is the Hardanger Bridge [200, 201, 202, 203]. As illustrated in Fig. 3.13, it is located in Norway, precisely in the Eidfjorden branch off of the main Hardangerfjorden in Vestland county, about 120 km inland from the open North Sea. This position is peculiar for its strong winds blowing from European

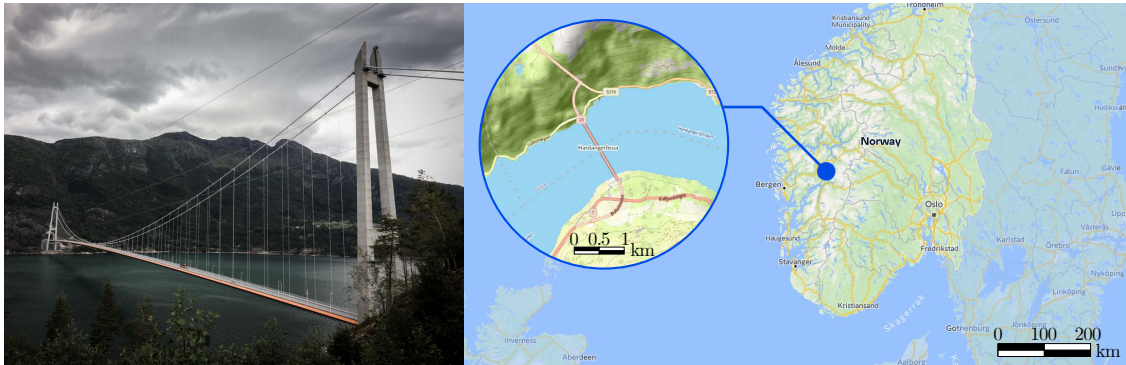


Figure 3.13: The Hardanger Bridge (Norway), picture courtesy of Sami Haidar (CC BY-NC 2.0).

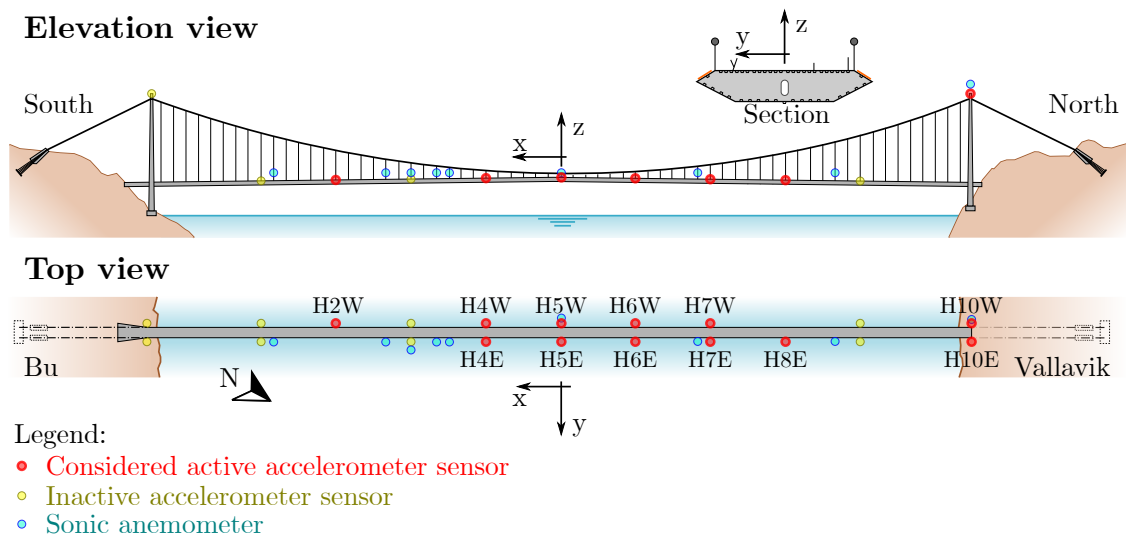


Figure 3.14: Illustration of the Hardanger Bridge and its long term monitoring sensors layout.

windstorms. Indeed, the surrounding orographic landscape with mountains up to 1,000÷1,600 m altitude contributes to generating complex wind patterns around the bridge, affecting the dynamic response of this very slender case study bridge. The Hardanger Bridge represents Norway's longest suspension bridge, spanning 1,308 meters with short spans on both sides. The road continues over the bridges with two road tunnels crossing surrounding mountains on both sides of the bridge. Despite the slender design of the steel box deck, the bridge was designed for carrying two traffic lanes and a lateral cycle lane (bikeway). The girder is supported by 130 hangers with lengths ranging between 2÷128 m, connected to two main cables hanging to two extreme 200-meter-high pylons.

Table 3.1: Hardanger Bridge: location of the accelerometers.

Accelerometer	X [m]	Y [m]	Z [m]
H1E/H1W	480.00	6.33/-6.64	-8.38
H2W	360.00	-6.64	-6.41
H3E/H3W	240.00	6.33/-6.64	-4.45
H4E/H4W	120.00	6.33/-6.64	-2.48
H5E/H5W	-7.00	6.33/-6.64	-0.4
H6E/H6W	-120.00	6.33/-6.64	-2.25
H7E/H7W	-240.00	6.33/-6.64	-4.22
H8E	-360.00	6.33	-6.18
H9E/H9W	-480.00	6.33/-6.64	-8.15
H10E/H10W	-655.00	4.50/-4.50	120.50
H11E/H11W	655.00	4.50/-4.50	120.50

Afterward its construction, thus since 2013, the bridge is equipped with a continuous long-term monitoring system depicted in Fig. 3.14. Implemented by the Norwegian University of Science and Technology (NTNU), the SHM system is composed of 20 triaxial accelerometers with a sampling rate of 200 Hz placed on the deck and pylons, together with 9 sonic anemometers. These latter are placed 8 meters from the girder to avoid disrupting wind flow. For all sensors, the channel orientations followed the global reference frame, with the x-axis oriented longitudinally along the bridge (positive direction from Vallavik to Bu), the y-axis being transversal to the bridge (positive towards East), and the z-axis following the positive upwards vertical direction. The accelerometer positions are detailed in Tab. 3.1. However, in September 2018, wind speed monitoring ceased at the tower tops following the removal of one sensor from the Vallavik tower. The local geographical context involves strong wind loads whose effects make the dynamic identification process challenging [200, 201]. Both raw and organized long-term wind and acceleration data for SHM purposes have been published in an open-access repository by [202] which can be accessed and downloaded freely. Thanks to this openly accessible database, this case study suspension bridge has been already studied in depth in the existing scientific literature, e.g. referring to [200, 201, 202, 203], and therefore it represents a very compelling experimental benchmark, both for structural and environmental reasons. On the one hand, its fundamental vibrational modes of main interest are all very closely-spaced and clustered at very low frequencies (below 1 Hz). On the other hand, its specific building material, structural configuration, and location make it very susceptible to environmental effects (wind speed and pattern, specifically).

All these concomitant aspects further emphasize that this case study choice is a very interesting stress test for the *i-AOMA* proposed procedure having the possibility to compare the modal results with the ones already published and validated in existing literature. Nevertheless, in order to produce results directly comparable to [200, 201, 202, 203, 204], the following precautions have been followed for the

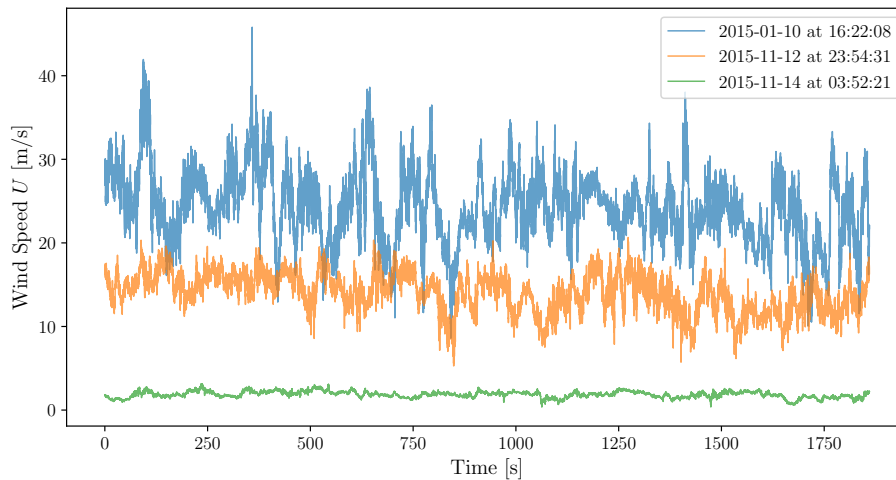


Figure 3.15: Wind speed recordings of the A6 anemometer located in the midspan for the three selected cases under investigation.

sake of consistency during the i-AOMA analyses: 1. The original data, sampled at $f_s = 200$ Hz, have been used; 2. The acceleration data have been decimated by a factor of 20, thus focusing only on the 0÷10 Hz range, further reduced to 5 Hz because of Nyquist’s theorem; 3. All natural frequencies appearing higher than 5 Hz have been discarded; 4. In order to further speed up the i-AOMA algorithm and for a more consistent stabilization diagram overview with the existing literature studies, the range of model orders n has been limited from 20 to 200, thus not making use of the first relation proposed in (3.1).

3.4.2 Dynamic identification under sustained wind conditions

The case study represents a compelling experimental benchmark for the i-AOMA method, both for structural and environmental reasons. It is noteworthy that most of the literature modal results on the Hardanger Bridge [201, 205, 206, 207] are referred to a sustained wind environmental condition, being a condition in which the wind speed exceeds the level of 15 m/s at any of the deployed anemometers. Indeed, referring to these sustained wind conditions is reasonable because this operational load situation is able to adequately excite all modes of the bridge, especially the lateral ones, thus making them much easier to identify. Therefore, in [206] the authors explicitly explained that the measurement system was set for both periodic and event recordings, the latter triggered when a wind speed of at least 15 m/s is exceeded at any of the anemometers.

Consequently, to ensure fair comparability between the current i-AOMA analysis and the literature works [201, 205, 206, 207], similar wind conditions must be

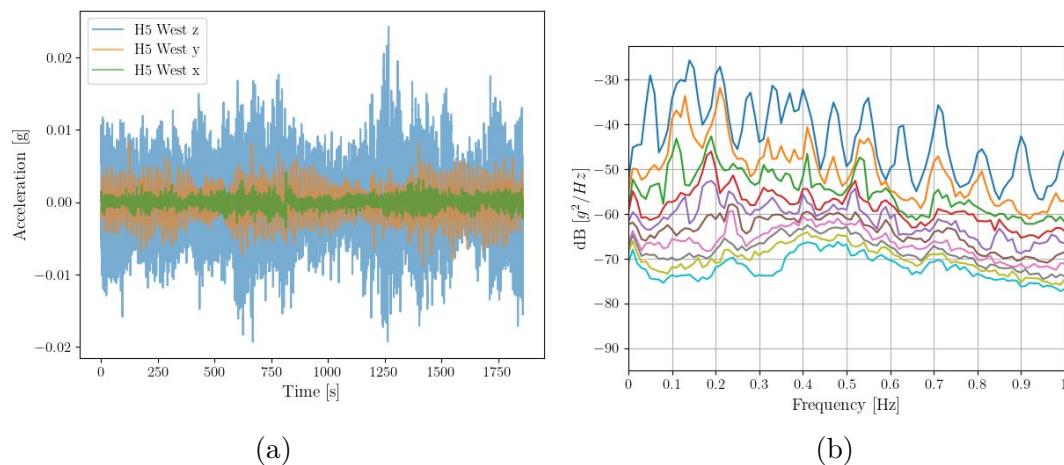


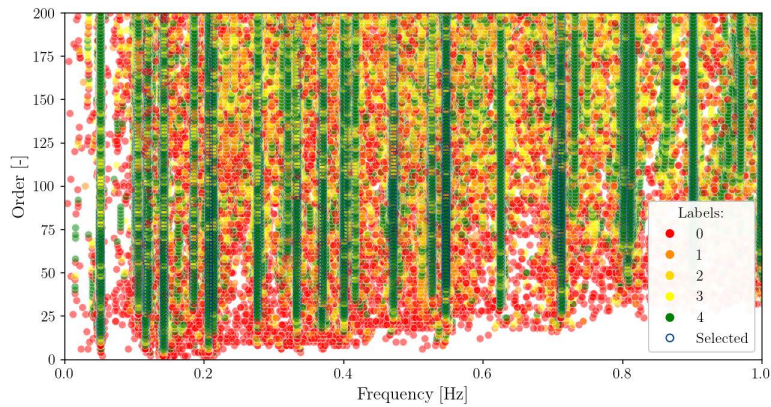
Figure 3.16: Hardanger Bridge: accelerations recorded on November 12th, 2015 at midspan accelerometer on the west side H5W (a) and singular value decomposition of the power spectral density limited to the first ten singular values (b).

considered, with an average speed of 15 m/s. Nonetheless, in order to further investigate the main remarkable different scenarios among the well-documented effects of wind speed on the modal parameters of this structure [201, 205, 206, 200, 202, 203, 204, 207], the following three wind conditions have been herein considered:

- case 1, an almost still air condition (very low wind speed, below 2 m/s), referring to recordings on November 14th, 2015 (2015-11-14 at 03:52:21 local time) characterized by a wind speed of 1.86 ± 0.38 m/s;
- case 2, a sustained wind condition representing the average typical situation considering the recording on November 12th, 2015 (2015-11-12 at 23:54:31 local time) characterized by a wind speed of 14.02 ± 2.28 m/s;
- case 3, an extreme sustained wind storm situation (Tina storm event of January 2015), referring to the recording on January 10th, 2015 (2015-01-10 at 16:22:08 local time) characterized by a wind speed of 24.26 ± 4.27 m/s.

To visualize these three wind speed conditions, Fig. 3.15 reported wind speed recordings obtained from the sonic anemometer sensor A6 located in the midspan of the bridge.

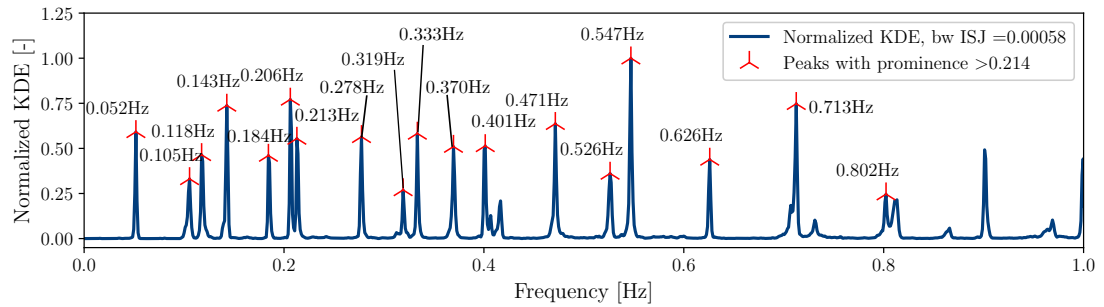
It is worth underlining that during the extreme Tina storm event case 3, only 12 accelerometers (namely, H2W, H4E, H4W, H5E, H5W, H6E, H6W, H7E, H7W, H8E, H10E, and H10W, with E indicating east side and W for west side) out of the all 20 deployed sensors on the bridge were active. Therefore, to uniform the results and make them consistent and fully comparable among the three analyzed cases, only those 12 accelerometers for a total of 36 output channels have been considered even in cases 1 and 2, as already depicted in Fig. 3.14.



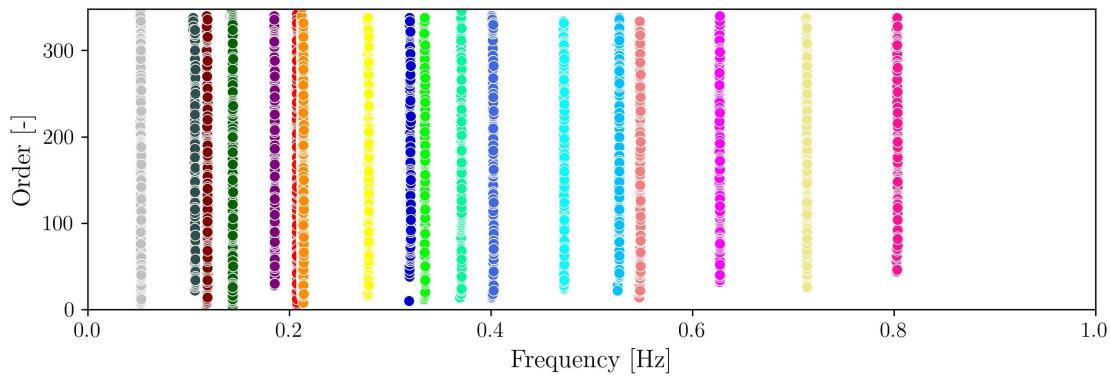
(a)

Figure 3.17: Hardanger Bridge: overlapped stabilization diagram at the end of Phase 1 of the i-AOMA method.

The results demonstrated that the i-AOMA resulted in similar findings in all three analyzed cases, therefore only the average sustained wind speed case 2 has been hereafter reported and extensively discussed, whilst details are omitted to conserve space for cases 1 and 3. Specifically, the case 2 acceleration data for the 12 considered accelerometers were downloaded from the open database [202], referring to an event of duration 31 min sampled at 200Hz under the environmental conditions of sustained wind recorded on November 12th, 2015 at 23:54:31 with a wind speed of 14.02 ± 2.28 m/s. The data have been decimated with a factor of 20, and following Nyquist's theorem, the maximum observable natural frequency reaches 5 Hz, determining a dynamic range of investigation in the 0-5 Hz frequency interval.



(a)



- | | |
|--------------------------------------|---------------------------------------|
| ● Mode 1: 0.052 Hz; Num. Poles: 2600 | ● Mode 10: 0.333 Hz; Num. Poles: 2545 |
| ● Mode 2: 0.105 Hz; Num. Poles: 1558 | ● Mode 11: 0.370 Hz; Num. Poles: 2393 |
| ● Mode 3: 0.118 Hz; Num. Poles: 2337 | ● Mode 12: 0.401 Hz; Num. Poles: 2678 |
| ● Mode 4: 0.143 Hz; Num. Poles: 3949 | ● Mode 13: 0.471 Hz; Num. Poles: 2961 |
| ● Mode 5: 0.185 Hz; Num. Poles: 2245 | ● Mode 14: 0.526 Hz; Num. Poles: 1782 |
| ● Mode 6: 0.207 Hz; Num. Poles: 3936 | ● Mode 15: 0.547 Hz; Num. Poles: 4715 |
| ● Mode 7: 0.213 Hz; Num. Poles: 2741 | ● Mode 16: 0.626 Hz; Num. Poles: 2217 |
| ● Mode 8: 0.277 Hz; Num. Poles: 2664 | ● Mode 17: 0.712 Hz; Num. Poles: 3496 |
| ● Mode 9: 0.319 Hz; Num. Poles: 1313 | ● Mode 18: 0.802 Hz; Num. Poles: 1267 |

(b)

Figure 3.18: Hardanger Bridge: *i*-AOMA Phase 1, normalized KDE together with the identified peaks (a) and certainly stable poles falling within the retaining bands (b) obtained from the sets of control parameters generated for training the intelligent core of *i*-AOMA.

It is preliminary interesting to visualize the recorded data both to become aware of the order of magnitude involved, evidencing the presence of any measurement error, and even to qualitatively assess the stationarity hypothesis at the basic foundations of traditional OMA methods. Therefore, the three directions accelerations recorded in the midspan accelerometer on the west side H5W have been reported in Fig. 3.16 (a). Furthermore, the SVD of the PSD of the recorded signals for the 12 accelerometers considered have been computed delivering the graph reported in

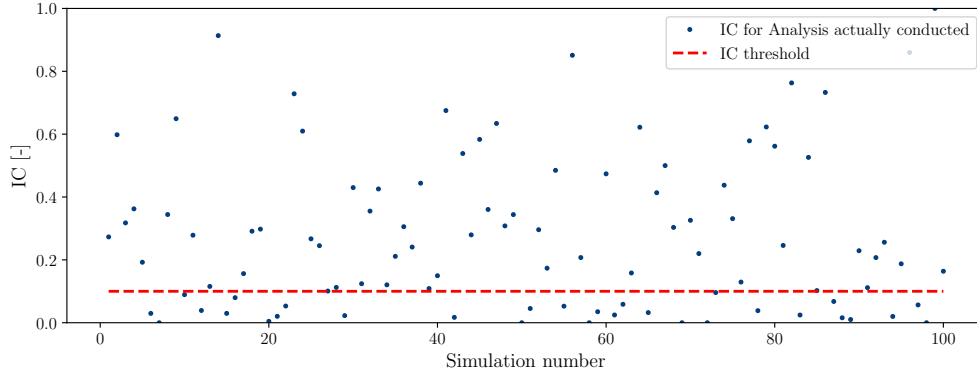


Figure 3.19: Hardanger Bridge: i-AOMA Phase 1, numerical values of IC obtained from the sets of control parameters generated for training the intelligent core of i-AOMA.

Fig. 3.16 (b). From the analysis of the latter graph, the fundamental frequency appears very low, below 0.1 Hz, therefore the bounds of the control parameters are roughly defined according to Eqs. (3.1)-(3.4) setting $f_f = 1$ Hz. Nevertheless, in order to further speed up the i-AOMA algorithm and for a more consistent stabilization diagram overview with the existing literature studies, the range of model orders n has been limited from 20 to 200, thus not making use of the first relation proposed in Eq. (3.1).

The i-AOMA method started with Phase 1 until a total number of feasible control parameters set equal to $s = 100$ have been collected. Specifically, through the quasi-Monte Carlo Halton sampling technique, only 3 out of the total 103 generated samples have not been completed with the SSI-cov algorithm execution, showing that a properly imposed tailored limitation of the model order space can actually provide substantial improvements in the algorithm's initial sampling exploration phase. This case is particularly important when the fundamental frequency is considerably lower than 1 Hz, because the suggested automatic range relationship in Eq. (3.1) may provide an unrealistic excessive upper bound and thus possibly dispersing the search for most informative control parameters sets. Anyway, the automatic choice in Eq. (3.1) is always a viable option, but paying attention that it may require increasing the number of arbitrary feasible simulations to collect in order to guarantee enough exploration of the search space. The overlapped SD obtained at the end of Phase 1 afterward the stability checks according to Eqs. (2.111)-(2.115) has been reported in Fig. 3.17. Stable poles only have been retained, and the FFT-KDE algorithm has been executed and reported in Fig. 3.18 (a) delivering an estimate of the BW equal to 0.00058 Hz by means of the ISJ algorithm.

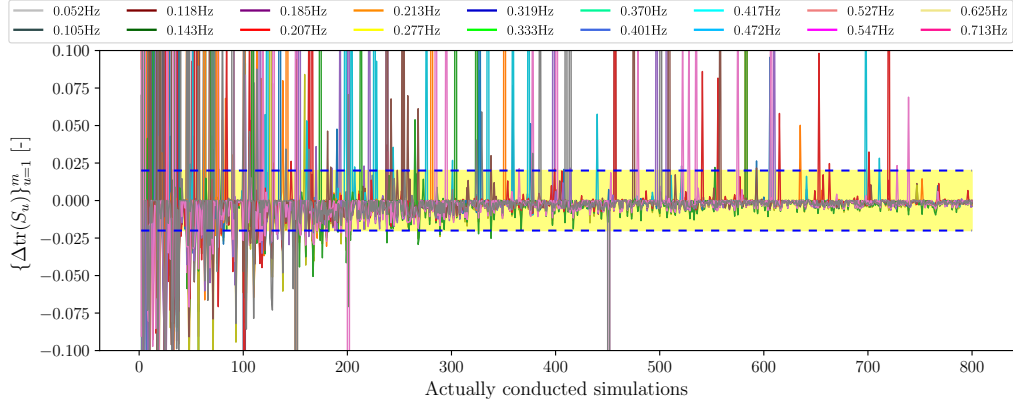


Figure 3.20: Hardanger Bridge: convergence analysis of the relative total sample variance for each mode.

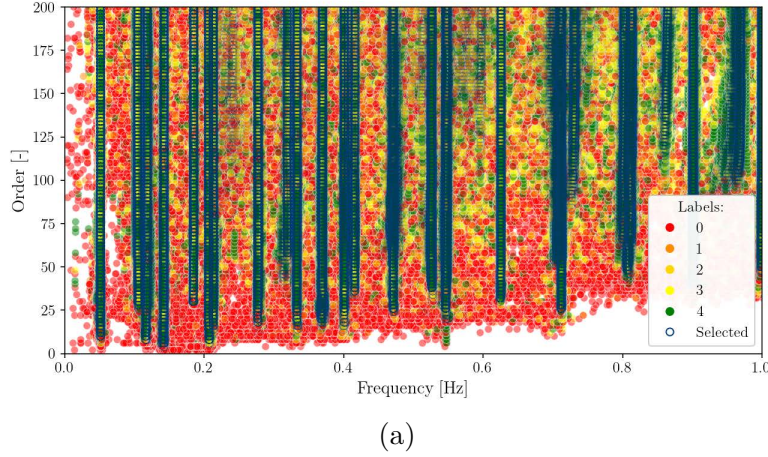
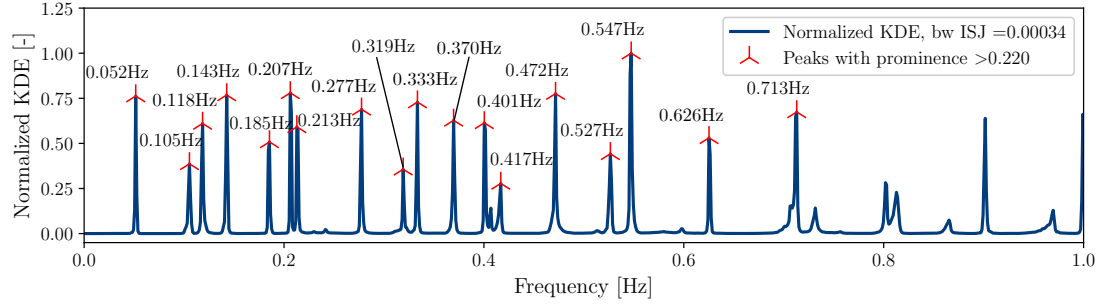
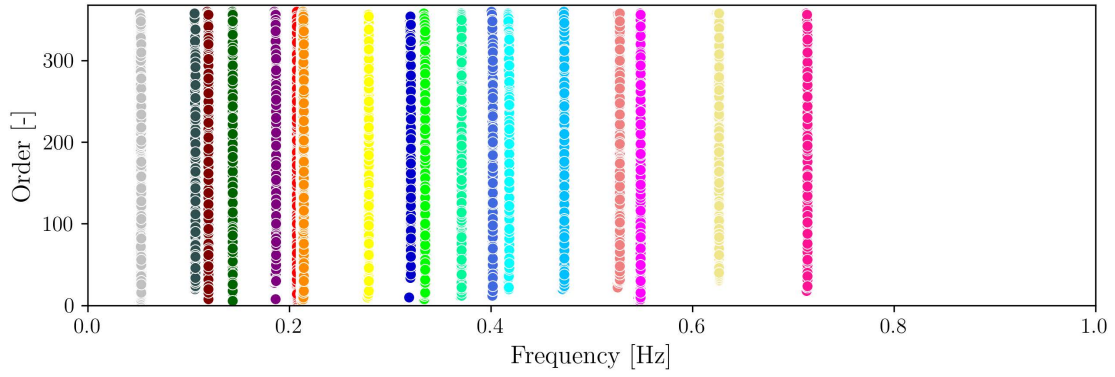


Figure 3.21: Hardanger Bridge: overlapped stabilization diagram at the end of Phase 2 of the *i*-AOMA method.

The statistical value of the prominence threshold for the peaks' identification from the normalized KDE (99th percentile in the fitted Beta distribution) is equal to 0.2139, and $b_w = 1$ has been determined. In total, about 29 modes have been identified by the *i*-AOMA method within the observable dynamic frequency range of 0-5 Hz. Nevertheless, for further improving the convergence of the next Phase 2, and even considering the modal results regarding the Hardanger Bridge observed in the existing literature with proven physical evidence, the authors limited the retained modes focusing only on the already consistent number of modes lying below 1 Hz, in particular limiting the results extraction to only the first 18 *i*-AOMA founded modes. Afterward, the database consisting of all the generated control parameters and the corresponding IC values is prepared in order to train the RF algorithm.



(a)



● Mode 1: 0.052 Hz; Num. Poles: 33892	● Mode 10: 0.333 Hz; Num. Poles: 35453
● Mode 2: 0.105 Hz; Num. Poles: 22510	● Mode 11: 0.370 Hz; Num. Poles: 31831
● Mode 3: 0.118 Hz; Num. Poles: 32539	● Mode 12: 0.401 Hz; Num. Poles: 37614
● Mode 4: 0.143 Hz; Num. Poles: 44557	● Mode 13: 0.417 Hz; Num. Poles: 14186
● Mode 5: 0.185 Hz; Num. Poles: 31274	● Mode 14: 0.472 Hz; Num. Poles: 39186
● Mode 6: 0.207 Hz; Num. Poles: 46887	● Mode 15: 0.527 Hz; Num. Poles: 25392
● Mode 7: 0.213 Hz; Num. Poles: 35500	● Mode 16: 0.547 Hz; Num. Poles: 61803
● Mode 8: 0.277 Hz; Num. Poles: 35717	● Mode 17: 0.626 Hz; Num. Poles: 28575
● Mode 9: 0.319 Hz; Num. Poles: 17467	● Mode 18: 0.713 Hz; Num. Poles: 40070

(b)

Figure 3.22: Hardanger Bridge: i-AOMA Phase 2, normalized KDE together with the identified peaks (a) and certainly stable poles falling within the retaining bands (b) obtained from the sets of control parameters generated for training the intelligent core of i-AOMA.

Figs. 3.18-3.19 illustrate the main results obtained from the $s = 100$ feasible sets of control parameters generated for training the intelligent core of i-AOMA.

Subsequent to the training of the RF intelligent core, the i-AOMA Phase 2 started by generating new quasi-random samples of the control parameters generated by means of the Halton technique, and the SSI-cov algorithm is performed only for those that are classified as feasible from the trained RF intelligent core. The convergence criterion based on Eq. (3.13) has been fulfilled after generating

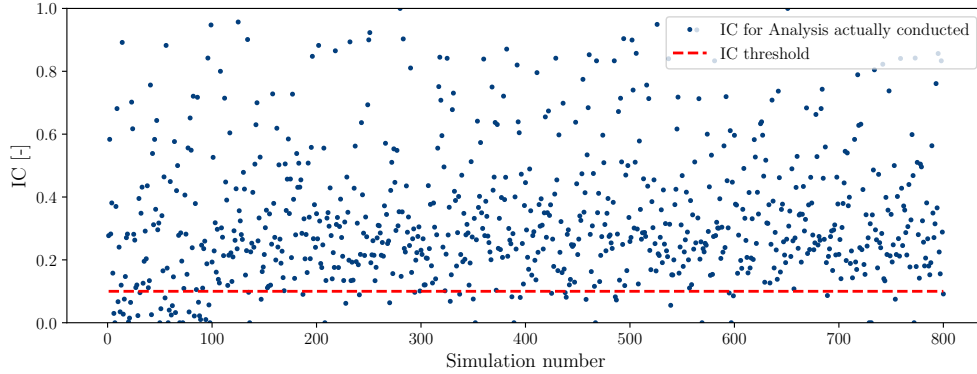


Figure 3.23: Hardanger Bridge: i-AOMA Phase 2, numerical values of IC obtained from the sets of control parameters generated for training the intelligent core of i-AOMA.

961 further simulations, thus collecting a total of 800 useful results and intelligently discarding 261 control parameters set, whereof 700 newly control parameters sets from Phase 2 only. Therefore, the RF algorithm discarded about 27% of newly generated simulations because they were predicted to be poorly informative. The convergence graph which testifies the ASCBR criterion fulfilled on the mode shape estimates of the 18 considered modes is reported in Fig. 3.20.

Stability checks according to Eqs. (2.111)-(2.115) has been performed on the overlapped SD obtained at the end of Phase 2, as depicted in Fig. 3.21. Retaining only fully stable poles, the results of the FFT-KDE algorithm have been reported in Fig. 3.18 (a) evidencing a reduction of one order of magnitude of the estimate of the BW obtained through the ISJ algorithm, i.e. becoming equal to 0.00034 Hz. The 99th percentile in the fitted Beta distribution defines the value of the prominence threshold for the peaks' identification from the normalized KDE, becoming now equal to 0.2202. A factor $b_w = 2$ has been determined in order to avoid empty clusters of stable poles within the 18 natural frequencies of interest. The final results regarding the stable poles' alignments of the 18 founded modes obtained through the i-AOMA method for wind case 2 are reported in Figs. 3.22 3.23. In the latter graph of the ICs, it is worth noting that after the first 100 explorative simulations of Phase 1, the IC values under the IC threshold of 0.10 have been substantially reduced, confirming the effectiveness of the i-AOMA RF intelligent core in discarding those control parameter sets predicted to be poorly informative.

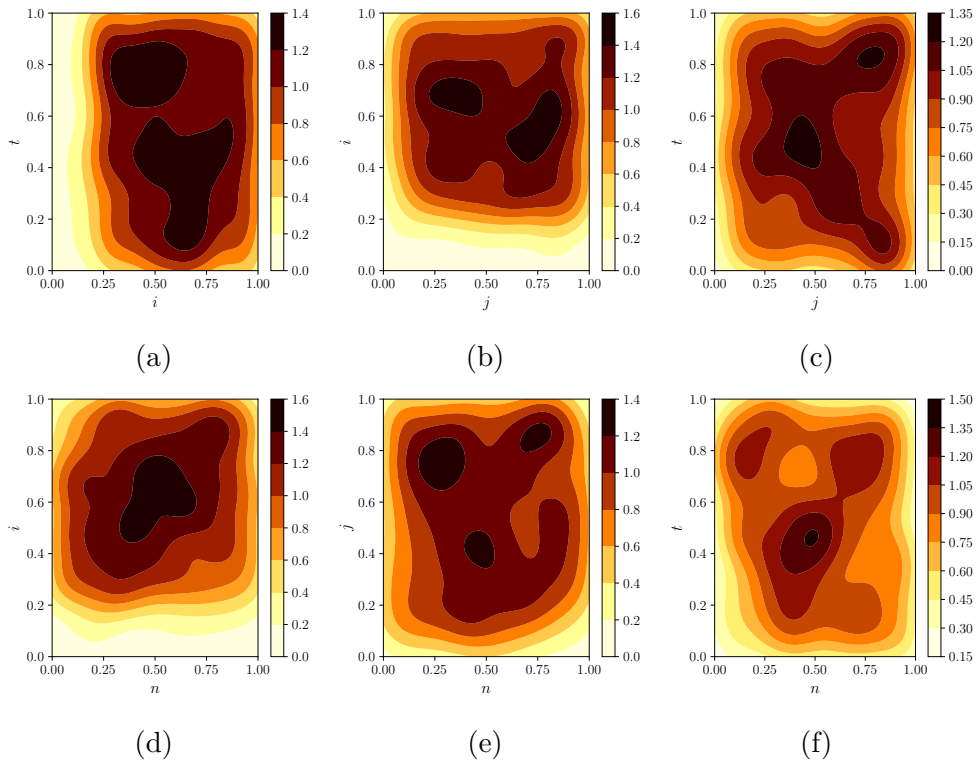


Figure 3.24: Hardanger Bridge: joint probability density functions of the control parameters that have been classified as feasible from the intelligent core of i-AOMA.

Even in this case study, the joint (bidimensional) probability density functions of the sampled control parameters set that have been classified as feasible from the intelligent core of i-AOMA have been computed and depicted in Fig. 3.24. Once again, the interpretation of these bidimensional density maps evidences the need for an automatic procedure for the selection of the SSI-cov control parameters because all of these different combinations together contributed to identifying the same modal results of actual interest. Since the optimal tuning of a unique control parameter always valid set is hardly achievable, an automatic exploration of different combinations of them likewise in the i-AOMA is advisable for obtaining more reliable physical modal results whilst attenuating the spurious solutions due to the random nature of the dynamic excitation.

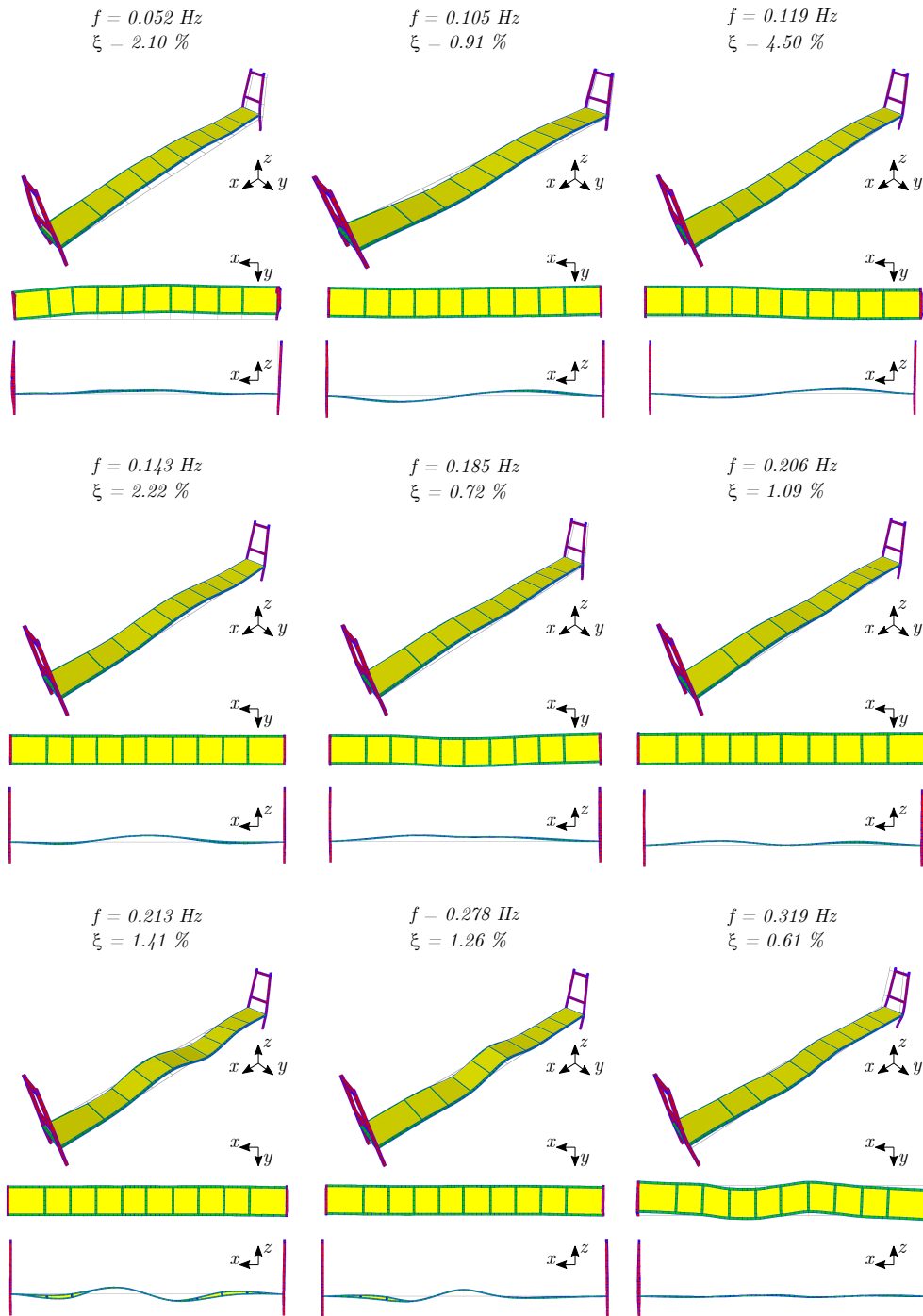


Figure 3.25: Hardanger Bridge: i-AOMA Phase 2, simplified geometrical mode shape visualization for modes from 1 to 9.

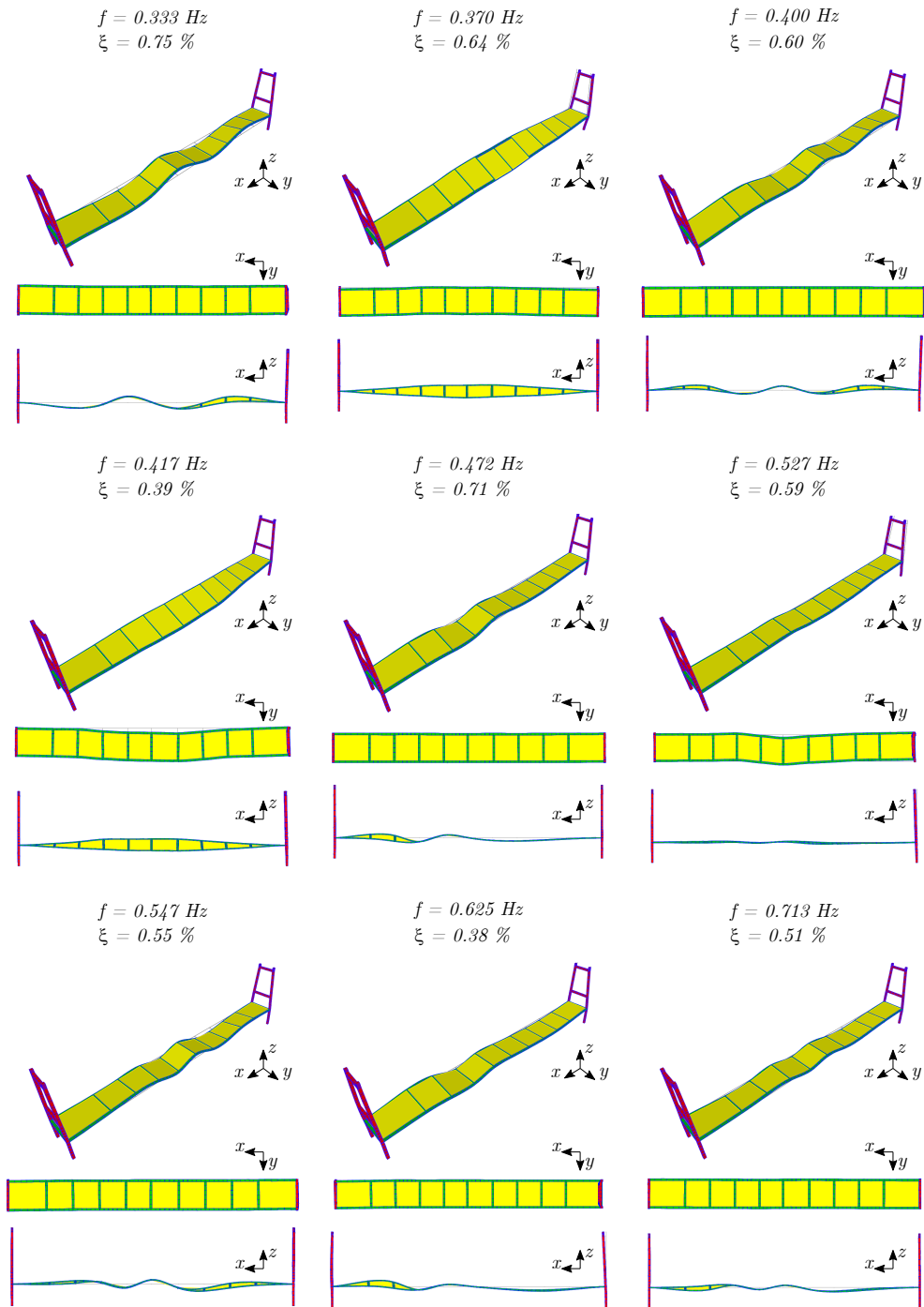


Figure 3.26: Hardanger Bridge: i-AOMA Phase 2, simplified geometrical mode shape visualization for modes from 10 to 18.

The 18 modes of the Hardanger Bridge founded for the sustained wind case 2 have been identified corresponding to natural frequencies value equal respectively to 0.052 Hz, 0.105 Hz, 0.119 Hz, 0.143 Hz, 0.185 Hz, 0.206 Hz, 0.213 Hz, 0.278 Hz, 0.319 Hz, 0.333 Hz, 0.370 Hz, 0.400 Hz, 0.417 Hz, 0.472 Hz, 0.527 Hz, 0.547 Hz, 0.625 Hz, 0.713 Hz. The related estimates of the damping ratios are 2.10%, 0.91%, 4.50%, 2.22%, 0.72%, 1.09%, 1.41%, 1.26%, 0.61%, 0.75%, 0.64%, 0.60%, 0.39%, 0.71%, 0.59%, 0.55%, 0.38%, and 0.51%. The corresponding mode shapes are shown in Figs. 3.25-3.26, which are depicted considering a simplified geometrical model derived from the sensor network layout by imposing mode shapes displacements as imposed deformation in the monitored nodes whilst interpolating the deformed shape elsewhere. The i-AOMA delivered modal results which exhibit a very good agreement with the literature results in terms of natural frequencies as reported in Tab. 3.2, but apparently overestimating the damping ratios. Nevertheless, it is worth noting that the damping ratios retrieved from [205, 201] have been computed from a numerical model in still-air conditions, therefore in weakly dynamic excitation environment, more consistent with wind case 1 (November 14th, 2015 at 03:52:21 local time characterized by a wind speed of 1.86 ± 0.38 m/s) rather than current sustained wind case 2. Besides the evident damping ratios differences on which it is normal in the literature evidencing such uncertain values [208], it is worth noting that the most complete modal identification results through SSI were reported in [207] providing the first 30 observed modes. Relative differences, expressed in percentages, have been computed for both natural frequencies and damping ratios, computed as

$$\Delta f = \frac{f_{\text{ref},k} - f_{\text{i-AOMA},k}}{f_{\text{ref},k}} \cdot 100, \quad \Delta \xi = \frac{\xi_{\text{ref},k} - \xi_{\text{i-AOMA},k}}{\xi_{\text{ref},k}} \cdot 100, \quad (3.16)$$

in which $f_{\text{ref},k}$ and $\xi_{\text{ref},k}$ are the k -th natural frequencies and damping ratios respectively referred to literature references by Petersen et al. [207, 205, 201], whilst the symbols $f_{\text{i-AOMA},k}$ and $\xi_{\text{i-AOMA},k}$ indicate respectively the k -th natural frequencies and damping ratios retrieved from i-AOMA algorithm. With a deeper overview of the Tab. 3.2, mode 8 indicated as cable/horizontal in [207] unfortunately didn't have any match in the other literature references [205, 201], and on the other hand modes 15 and 19 were not founded by the i-AOMA method. Nonetheless, these modes have less physical interest with respect to the first modes, which generally mainly govern the dynamic behavior of the system under investigation. Furthermore, the lack of evidence of mode 17 in the current i-AOMA results is actually reasonable on a physical basis, since no sensors have been considered on the pylon on the southern Bu side because of the restriction to only 12 sensors out of 20 in this specific analysis (for being fully consistent with wind case 3).

Furthermore, the similarity among the founded median mode shapes have been analyzed using the cross-MAC matrix. Fig. 3.27 illustrates the MAC indicators among the first 11 modes obtained by the i-AOMA. Generally, all the mode shapes

Table 3.2: Hardanger Bridge: comparison between the modal results reported by Petersen et al. [207, 205, 201] and those obtained in the present study by means of the i-AOMA algorithm for sustained wind case 2 (November 12th, 2015 at 23:54:31 with a wind speed of 14.02 ± 2.28 m/s). Note that f is the natural frequency, whereas ξ indicates the damping ratio.

Mode	Mode	Ref. [207]	Ref. [205, 201]	i-AOMA		Relative Diff.	
No	Type	f [Hz]	ξ [%]	f [Hz]	ξ [%]	Δf [%]	$\Delta \xi$ [%]
1	Horizontal	0.052	0.65	0.052	2.10	0.73	-223.08
2	Vertical	0.105	0.77	0.105	0.91	-0.35	-18.18
3	Vertical	0.119	1.77	0.119	4.50	0.40	-154.24
4	Vertical	0.142	0.65	0.143	2.22	-0.46	-241.54
5	Mixed vertical/horizontal	0.183	0.77	0.185	0.72	-1.33	6.49
6	Vertical	0.206	0.27	0.206	1.09	-0.13	-303.70
7	Mixed vertical/torsion	0.212	0.35	0.213	1.41	-0.40	-302.86
8	Cable/horizontal	0.230	-	-	-	-	-
9	Mixed vertical/torsion	0.276	0.26	0.278	1.26	-0.56	-384.62
10	Horizontal	0.318	0.63	0.319	0.61	-0.39	3.17
11	Mixed vertical/torsion	0.333	0.25	0.333	0.75	-0.15	-200.00
12	Torsion	0.374	0.41	0.370	0.64	1.15	-56.10
13	Mixed vertical/torsion	0.401	0.24	0.400	0.60	0.15	-150.00
14	Mixed horizontal/torsion	0.418	0.15	0.417	0.39	0.28	-160.00
15	Horizontal	0.464	1.56	-	-	-	-
16	Mixed vertical/torsion	0.471	0.26	0.472	0.71	-0.14	-173.08
17	Pylon	0.516	0.16	-	-	-	-
18	Mixed horizontal/pylon	0.529	0.22	0.527	0.59	0.47	-168.18
19	Mixed vertical/torsion	0.547	0.31	0.547	0.55	-0.07	-77.42
20	Torsion	0.560	0.65	-	-	-	-
21	Mixed vertical/torsion	0.628	-	0.625	0.38	0.44	-
22	Mixed vertical/torsion	0.715	-	0.713	0.51	0.28	-

appear to be uncorrelated (MAC below 20%, as reported in section 2.2.3.6) or with a weak correlation (MAC below or around 50%), except for the vertical mode shapes 2 (0.105 Hz) and 3 (0.119 Hz) showing a MAC of 71%, or considering modes 5 (0.185 Hz) and 6 (0.206 Hz) with a MAC of 66%. These evidenced similarities are reflected in the mode shapes illustrations of Figs. 3.25-3.26.

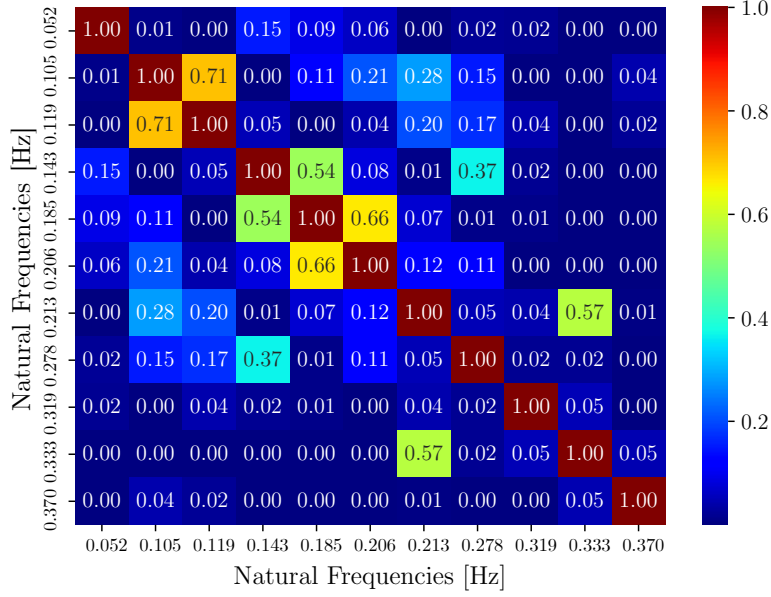


Figure 3.27: Hardanger Bridge: MAC matrix of the median mode shapes finally retrieved by i-AOMA, with a special focus on the first 11 modes.

In order to graphically visualize the uncertainty associated with the mode shape based on the use of various control parameters sets explored in the i-AOMA method, Fig. 3.28 depicts the uncertainties around the median components $\bar{\phi}_i$ of three mode shapes based on the boxplot’s whiskers definition. Specifically, the Fig. 3.28 illustrate separately the longitudinal ($\bar{\phi}_{i,x}$), transversal ($\bar{\phi}_{i,y}$), and vertical ($\bar{\phi}_{i,z}$) components of median modes and their respectively uncertain regions for every monitored DOF separating between the active sensors located on the west side of the bridge (H2W, H4W, H5W, H6W, H7W, H10W) and the active sensors placed on the east side of the bridge (H4E, H5E, H6E, H7E, H8E, H10E), whose longitudinal coordinates were reported in Tab. 3.1. It is noteworthy that these shaded regions reflect how uncertainty due to different control parameters propagates and sometimes it is amplified throughout the output-only identification process, despite the final stable poles’ alignments distilled from the final overlapped SD appearing relatively close to each other. Moreover, it has been also proven that the uncertainty level is not constant. While it is very low in some cases, it results very large in others. Indeed, the uncertainty degree depends on which DOF and mode number is the current focus. For instance, considering that mode 1 is mainly horizontal, the uncertainties associated with transversal components exhibited a significantly greater region rather than vertical or longitudinal ones, similar conclusions can be drawn from the other depicted modes’ uncertainties.

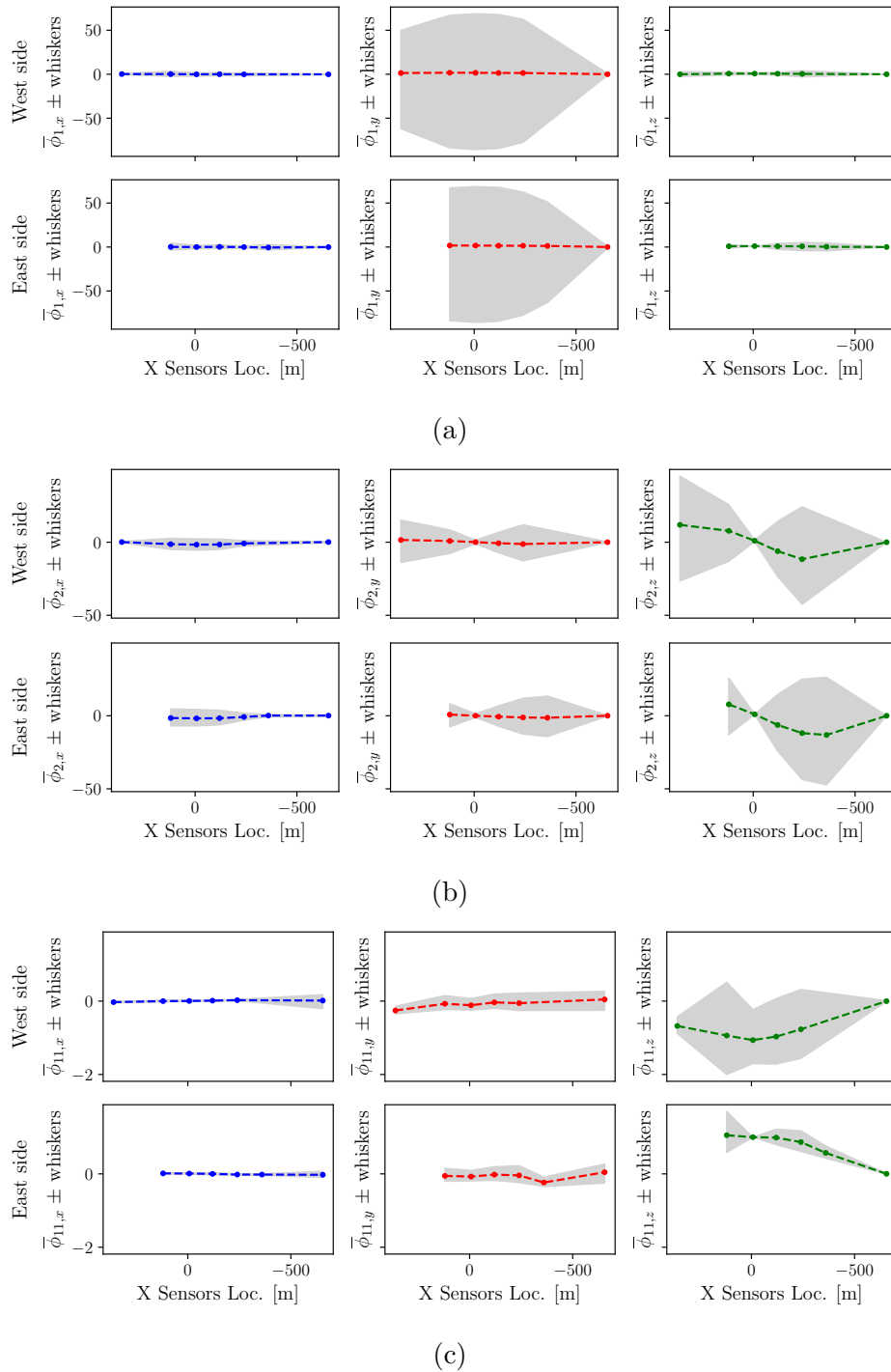
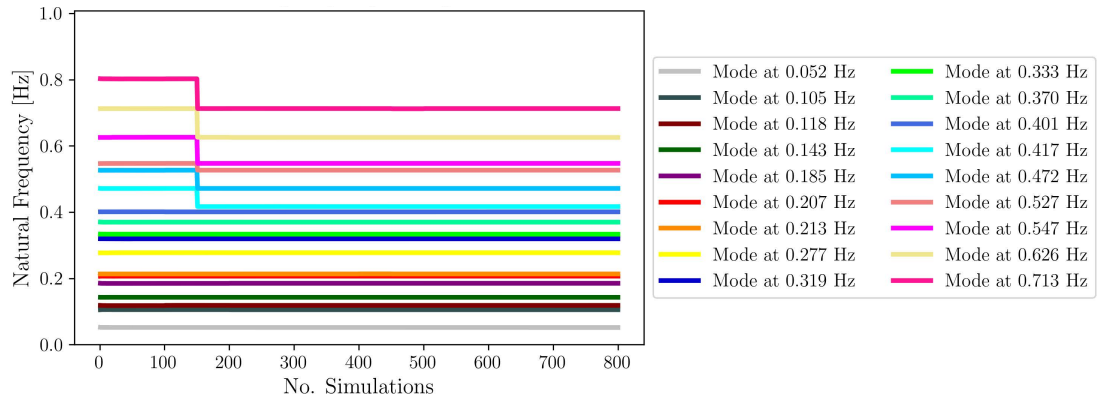
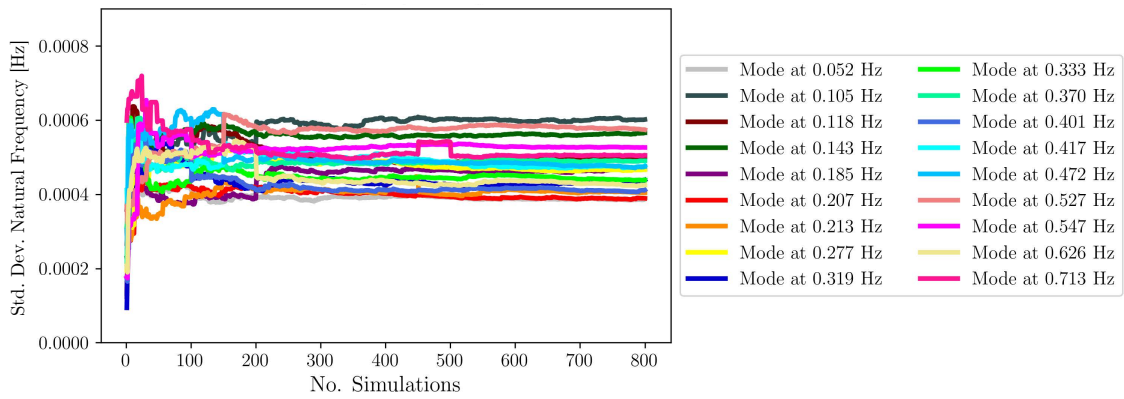


Figure 3.28: Hardanger Bridge: i-AOMA uncertainty level in terms of boxplot's median components and whiskers for the horizontal mode 1 (a), for the vertical mode 2 (b), and for the torsion mode 11 (c) of the bridge.



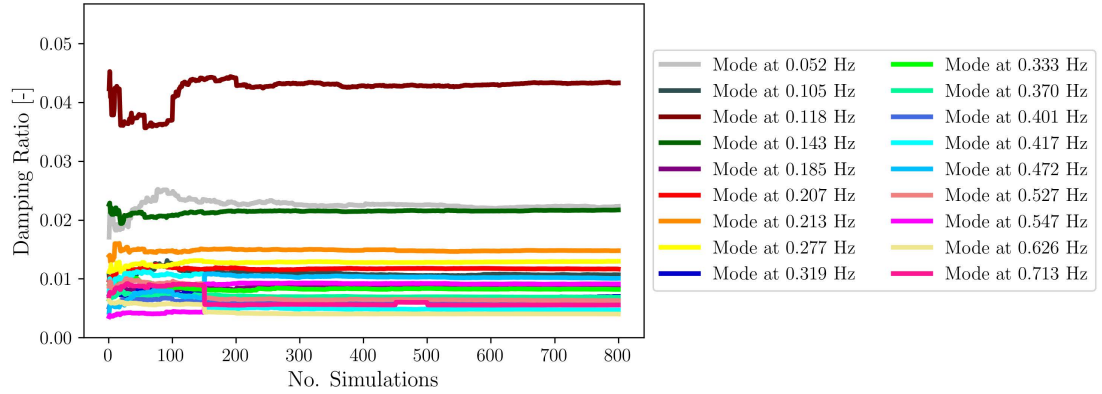
(a)



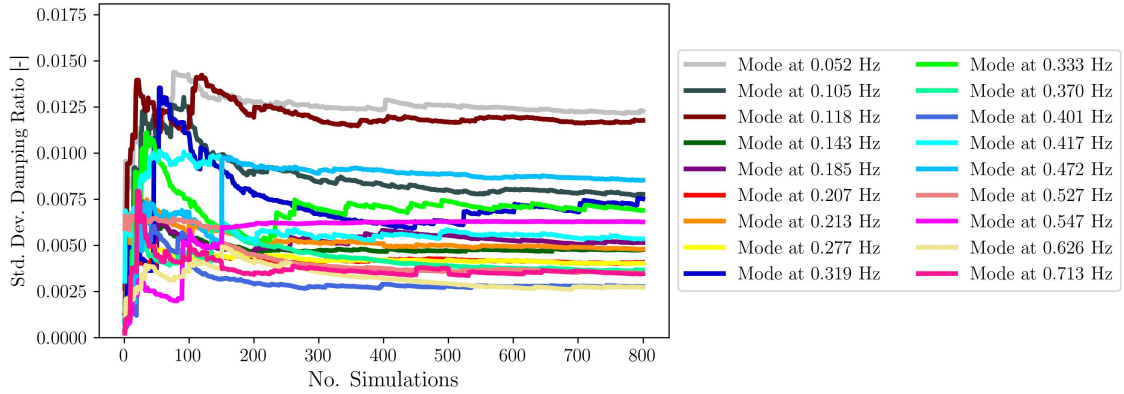
(b)

Figure 3.29: Hardanger Bridge: *i*-AOMA average (a) and standard deviation (b) of natural frequencies over the feasible samples of the control parameters.

The convergence of average and standard deviation for natural frequencies and damping ratios over all the feasible samples of the control parameters are reported in Figs. 3.29-3.30, respectively.



(a)



(b)

Figure 3.30: Hardanger Bridge: i-AOMA average (a) and standard deviation (b) of damping ratios over the feasible samples of the control parameters.

The entire so-far conducted discussion for sustained wind case 2 could be potentially repeated for wind cases 1 and 3 since these analyses delivered similar findings. However, all the i-AOMA cases 1 and 3 steps, details, and graphs have been omitted to conserve space, and only the final Phase 2 modal results have been summarized in Tab. 3.3. From this final comparison, it is worth noting that the case most close to still air condition, i.e. weak wind case 1, was the most difficult case since fewer modes were found rather than the other cases within the first 22, following the same numbering used in Tab. 3.2. This outcome appears very sensible from a physical standpoint. Indeed, this is probably due to the vibration response which derives from the low dynamic excitation level associated with wind case 1, likely able to adequately excite fewer structural modes rather than the other considered sustained wind scenarios. Furthermore, it is worth noting that in this

Table 3.3: Hardanger Bridge: comparison between the modal results of the i-AOMA method for wind cases 1, 2 and 3. Note that f is the natural frequency, whereas ξ indicates the damping ratio.

Mode	Mode	i-AOMA wind case 1		i-AOMA wind case 2		i-AOMA wind case 3	
No	Type	f [Hz]	ξ [%]	f [Hz]	ξ [%]	f [Hz]	ξ [%]
1	Horizontal	-	-	0.052	2.10	0.052	3.32
2	Vertical	0.108	0.78	0.105	0.91	0.106	1.38
3	Vertical	0.125	1.31	0.119	4.50	0.112	8.21
4	Vertical	0.142	0.25	0.143	2.22	0.146	4.01
5	Mixed vertical/horizontal	-	-	0.185	0.72	0.184	1.00
6	Vertical	0.206	0.10	0.206	1.09	0.207	3.00
7	Mixed vertical/torsion	0.213	0.25	0.213	1.41	0.215	2.46
8	Cable/horizontal	-	-	-	-	-	-
9	Mixed vertical/torsion	0.276	0.14	0.278	1.26	0.279	1.97
10	Horizontal	-	-	0.319	0.61	0.320	0.91
11	Mixed vertical/torsion	0.334	0.15	0.333	0.75	0.338	1.39
12	Torsion	-	-	0.370	0.64	0.367	1.10
13	Mixed vertical/torsion	0.401	0.26	0.400	0.60	0.405	1.34
14	Torsion	-	-	0.417	0.39	-	-
15	Horizontal	-	-	-	-	-	-
16	Mixed vertical/torsion	0.472	0.30	0.472	0.71	0.477	1.18
17	Pylon	-	-	-	-	-	-
18	Mixed horizontal/pylon	-	-	0.527	0.59	0.538	1.91
19	Mixed vertical/torsion	0.549	0.55	0.547	0.55	0.552	1.22
20	Torsion	-	-	-	-	-	-
21	Mixed vertical/torsion	0.627	0.35	0.625	0.38	-	-
22	Mixed vertical/torsion	0.690	0.48	0.713	0.51	0.717	1.25

weak wind, case 1 the damping ratios seem more in agreement with the literature numerical reference values, reminding that those latter have been retrieved from model updating procedures of the still air bridge model. On the other hand, strong wind case 3 is in good agreement with wind case 2 in terms of natural frequencies, but it generally exhibits a further increase in damping ratios. These results lead to the assumption that, for strong excitation wind conditions, the bridge tends to activate higher damping ratios. Indeed, for wind-sensitive structures likewise long-span suspension bridges, the preponderant part of damping ratios is mainly related to aeroelastic effects, as reported in [209]. Indeed, it was demonstrated in [210] that the higher values of damping ratios found by output-only OMA procedures for Hardanger bridge during strong wind conditions such as in a storm reached peak values around 6.77%, thus in accordance or with a slight over-estimation comparing with the damping ratios founded in wind case 2 and 3 herein analyzed and reported in Tab. 3.3.

3.5 i-AOMA application: the Al-Hamra Firduos Tower case study in Kuwait

3.5.1 General description, sensor network for dynamic monitoring and finite element analysis

The proposed i-AOMA is finally applied to perform the modal identification of the Al-Hamra Firduos Tower (hereafter named Al-Hamra Tower for the sake of compactness), which is a sculptured skyscraper located in the center of Kuwait City, Kuwait. Started in 2005 and completed in 2011, this iconic high-rise building is composed of about 80 floors with a total height of 412.6 m, thus resulting the tallest building in Kuwait [211, 212, 213]. The skyscraper mainly hosts offices, whereas the first five floors are devoted to commercial uses. This commercial area extends beyond the planar footprint of the tower and merges with a multi-level car park area. However, this latter portion is structurally independent from the tower due to the presence of a decoupling expansion joint [211, 212], and thus it is neglected in the current analysis.

From the architectural standpoint, the tower presents an approximately square sectional plan from the top view, with a removed slice on the southern edge and with an internal open void that creates a counter-clockwise facade twisting movement along the full height as shown in Fig. 3.31. The south-faced wall is made of concrete and has numerous openings with glass windows. East, west, and north-faced walls are made of glass curtain walls. Several technical challenges were faced during construction works, such as pumping concrete at high elevations. The concrete grade varies from C40 (toward top levels) to C70 (at low levels) [211]. The average inter-storey height is 4 m high, and the typical floor is entirely built with reinforced concrete beams and slabs.

From a structural standpoint, starting from the base, the Al-Hamra Tower is connected to the foundation level with a web-like concrete lamella structure visible at the lobby entrance level [211, 212] in order to avoid buckling of the base columns. A 4 m depth raft foundation is placed above 289 cast-in-situ bored piles, which have a diameter equal to 1.2 m and extend up to 27 m inside the ground [212]. The high-rise building internal structural system relies on core shear walls with thicknesses varying between 1.20 m and 0.30 m along the height [212]. On the southern side of the building, perimeter curved shear walls provide further stability to the structural system [211]. Due to its twisting shape and thus variable floor plan shape, the center of mass shifts for each floor diaphragm along the height [211].

The Al-Hamra Tower was equipped with a sensor network consisting of 24 bi-axial force balance accelerometers to record its horizontal dynamic response in the north and east directions, which are labelled as X and Y directions, respectively, as illustrated in Fig. 3.32. Particularly, Fig. 3.32 shows that the typical instrumented

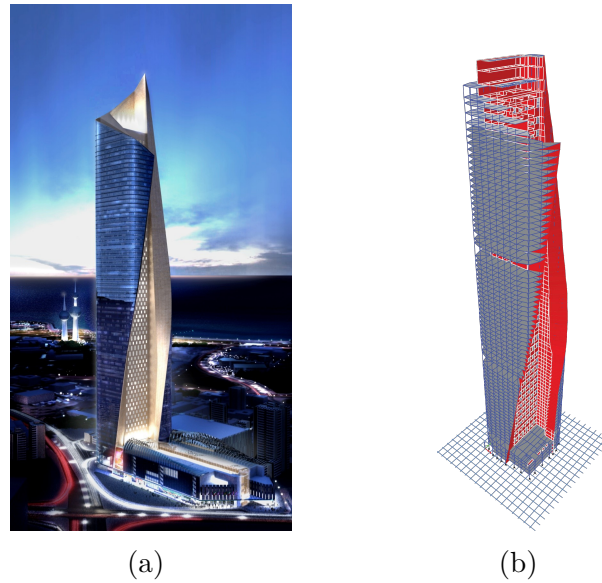


Figure 3.31: Al-Hamra Tower: general view (a) and finite element model adopted for the modal analysis (b).

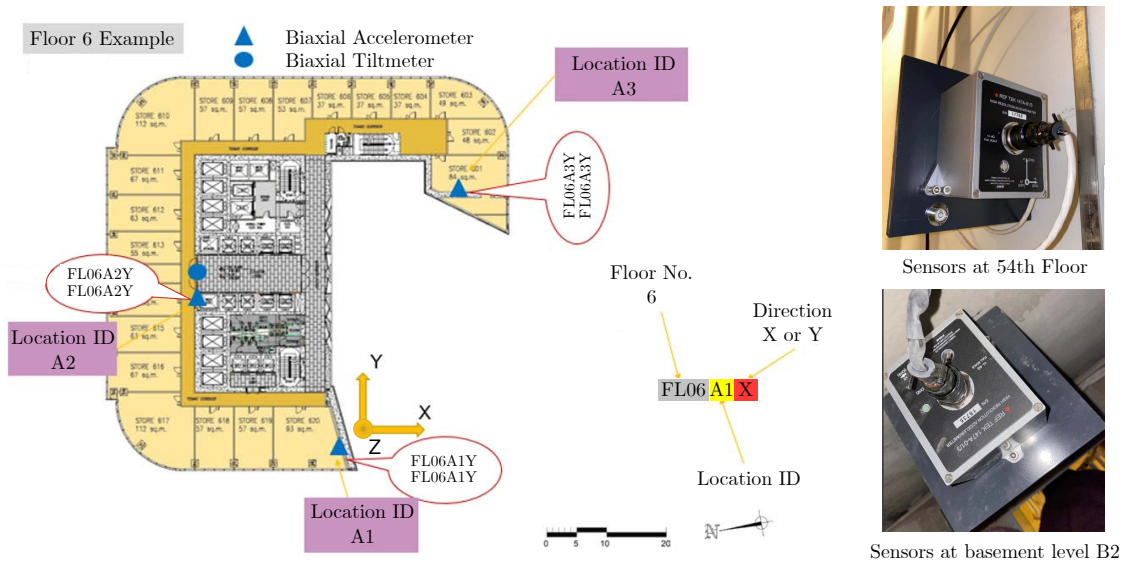


Figure 3.32: Al-Hamra Tower: typical monitored floor of the Al-Hamra Tower (left) and view of the biaxial accelerometers (right).

floor is monitored by means of three accelerometers placed at three extreme corners, so as to capture the torsional motion of the tower. The full-scale range of the accelerometers is ± 4 g, the dynamic range is larger than 155 dB (DC to 10 Hz), and the sensitivity is 2.5 V/g. The sensors' position is detailed in Tab. 3.4. It is worth

Table 3.4: Al-Hamra Tower: location of the accelerometers.

Sensor ID	X [mm]	Y [mm]	Z [mm]	Floor number
FL76A1	15,150	1,320		
FL76A2	-700	19,935	344,000	76
FL76A3	15,150	34,050		
FL65A1	7,955	-600		
FL65A2	-700	12,835	295,075	65
FL65A3	16,295	35,300		
FL54A1	40,475	2,645		
FL54A2	-800	20,975	246,602	54
FL54A3	16,525	46,125		
FL42A1	15,450	-800		
FL42A2	-900	14,235	194,375	42
FL42A3	20,390	35,250		
FL29A1	36,018	-9,247		
FL29A2	-900	14,575	137,360	29
FL29A3	32,332	35,360		
FL16A1	15,385	-800		
FL16A2	-900	13,865	80,975	16
FL16A3	29,685	35,350		
FL06A1	22,235	-11,870		
FL06A2	-900	13,775	38,975	6
FL06A3	38,600	29,675		
FLB2A1	45,100	-12,050	-4,400	
FLB2A2	-1,200	14,200	-6,220	B2
FLB2A3	35,285	45,480	-7,090	

noting that the sensors at the B2 floor are actually located at slightly different elevations due to technical installation reasons [211]. However, the elevation change within the B2 level compared to the elevation variations between the monitored floors is negligible. All the sensors are connected to the data loggers by means of cables. The multi-channel centralized data loggers are installed in the refuge area located on the 54th floor. The sensors are synchronized by a GPS installed on the top of the roof.

Modal properties of the tower have been preliminarily obtained from the high-fidelity finite element model [211] illustrated in Fig. 3.31. Details about the finite element model of the tower can be found in the paper by Sun et al. [211]. Numerical results of the modal analysis for the first 15 modes are reported in Tab. 3.5. It is evident from Tab. 3.5 that the first 15 modes mobilize almost the entire cumulative mass participating ratio (about 90%), except for the rotational mass in X and Y directions (about 82%). The first five modes are characterized by very close natural frequencies and are lower than 1 Hz.

Table 3.5: Al-Hamra Tower: numerical values of the modal properties estimated from finite element analysis (T is the natural period; f is the natural frequency; UX and UY represent the participating mass ratio along X direction and Y direction, respectively; RX, RY and RZ denote the participating rotational mass ratio along X direction, Y direction and vertical direction, respectively; the symbol Σ stands for cumulative sum of the participating mass ratios up to that mode number).

Mode	T [s]	f [Hz]	UX [-]	UY [-]	RX [-]	RY [-]	RZ [-]
1	6.441	0.155	0.467	0.152	0.091	0.285	0.020
2	4.705	0.213	0.141	0.483	0.280	0.101	3.54E-05
3	2.761	0.362	0.009	0.004	2.00E-04	0.002	0.686
4	1.459	0.685	0.173	0.003	0.016	0.199	0.001
5	1.178	0.849	0.010	0.156	0.217	0.009	6.00E-04
6	0.938	1.066	0.001	8.00E-04	0.003	4.00E-04	0.114
7	0.692	1.446	0.062	0.003	0.002	0.097	1.00E-04
8	0.559	1.789	0.003	0.004	0.006	0.005	0.047
9	0.535	1.870	0.002	0.054	0.082	0.005	0.003
10	0.399	2.509	0.038	0.001	0.002	0.076	2.00E-04
11	0.355	2.814	2.00E-04	2.53E-05	1.00E-04	3.00E-04	0.035
12	0.33	3.026	0.001	0.036	0.067	0.003	2.95E-05
13	0.264	3.784	0.018	3.00E-04	4.00E-04	0.040	0.003
14	0.256	3.911	0.004	1.00E-04	1.00E-04	0.009	0.023
15	0.228	4.392	1.08E-05	0.028	0.055	1.61E-05	1.00E-04
Mode	T [s]	f [Hz]	Σ UX [-]	Σ UY [-]	Σ RX [-]	Σ RY [-]	Σ RZ [-]
1	6.441	0.155	0.467	0.152	0.091	0.285	0.020
2	4.705	0.213	0.609	0.634	0.370	0.385	0.020
3	2.761	0.362	0.617	0.639	0.370	0.388	0.706
4	1.459	0.685	0.791	0.642	0.386	0.586	0.707
5	1.178	0.849	0.800	0.798	0.603	0.595	0.708
6	0.938	1.066	0.802	0.799	0.606	0.596	0.821
7	0.692	1.446	0.864	0.802	0.608	0.693	0.821
8	0.559	1.789	0.867	0.806	0.614	0.698	0.868
9	0.535	1.870	0.869	0.860	0.695	0.702	0.871
10	0.399	2.509	0.907	0.861	0.698	0.778	0.871
11	0.355	2.814	0.908	0.861	0.698	0.778	0.905
12	0.33	3.026	0.909	0.897	0.765	0.781	0.905
13	0.264	3.784	0.927	0.898	0.765	0.820	0.908
14	0.256	3.911	0.931	0.898	0.765	0.829	0.931
15	0.228	4.392	0.931	0.925	0.820	0.829	0.931

3.5.2 Identification under ambient vibrations

The experimental data for the present application were collected from the sensor network on May 2, 2022. One-hour monitoring data with a sampling frequency $f_s = 200$ Hz are analyzed. The monitored data were decimated with a factor equal to 40 in order to investigate accurately the low frequency modes of the structure. According to the Nyquist’s theorem, the upper bound of the observable frequency

range is thus equal to 2.50 Hz. Fig. 3.33 illustrates the time-histories of the recorded accelerations at three different floors and the singular value decomposition of the power spectral density limited to the first six higher singular values. The Welch's method has been adopted by setting the Hann window length and the overlap percentage equal to 500 points and 50%, respectively [214]. Furthermore, the stationarity of the recorded dynamic responses have been verified through the augmented Dickey-Fuller test [215, 216].

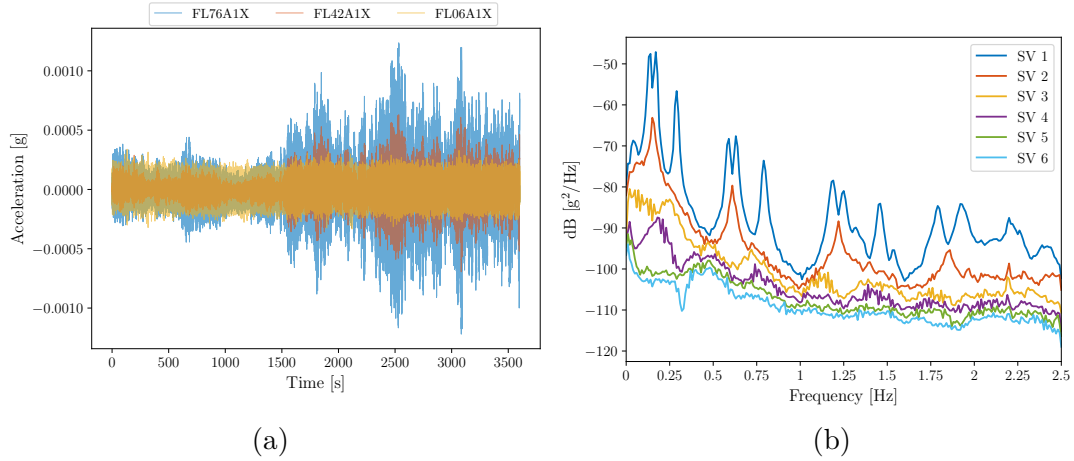
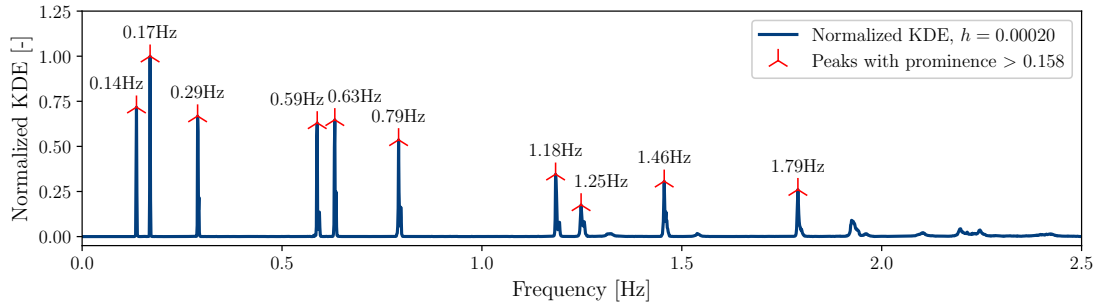
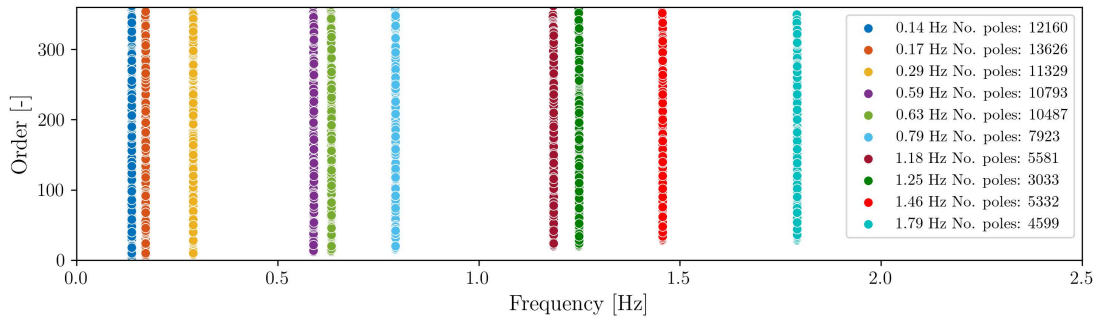


Figure 3.33: Al-Hamra Tower: accelerations recorded on May 2, 2022 at 6th, 42th, and 76th floor (a) and singular value decomposition of the power spectral density limited to the first six singular values (b).

The inspection of the singular value decomposition of the power spectral density shows that $f_f = 0.16$ Hz. Hence, the bounds of the control parameters are roughly defined according to Eqs. (3.1)-(3.4). The number of quasi-random samples of the control parameters generated by means of the Halton technique for the present case study is set to $s = 200$. Specifically, 631 applications of the SSI-cov algorithm out of 831 total generated samples have not been completed because of numerical failure or excessive elaboration time (success rate about 24%). Once the SDs corresponding to $s = 200$ successful applications of the SSI-cov algorithm have been overlapped, stability checks have been performed according to Eqs. (2.111)-(2.115) and possibly stable poles are then identified. The FFT-KDE algorithm has been next performed considering these possibly stable poles. So doing, an estimate of the BW equal to 0.0002 Hz is obtained by means of the ISJ algorithm. The statistical value of the prominence threshold for the peaks' identification from the normalized KDE (99th percentile in the fitted Beta distribution) is equal to 0.1585, and $b_w = 3$ has been calculated. Next, the database consisting of all the generated control parameters and the corresponding IC values is prepared in order to train the RF algorithm. Figs. 3.34-3.35 illustrate the main results obtained from the $s = 200$ sets of control



(a)



(b)

Figure 3.34: Al-Hamra Tower: normalized KDE together with the identified peaks (a) and certainly stable poles falling within the retaining bands (b) obtained from the sets of control parameters generated for training the intelligent core of *i*-AOMA.

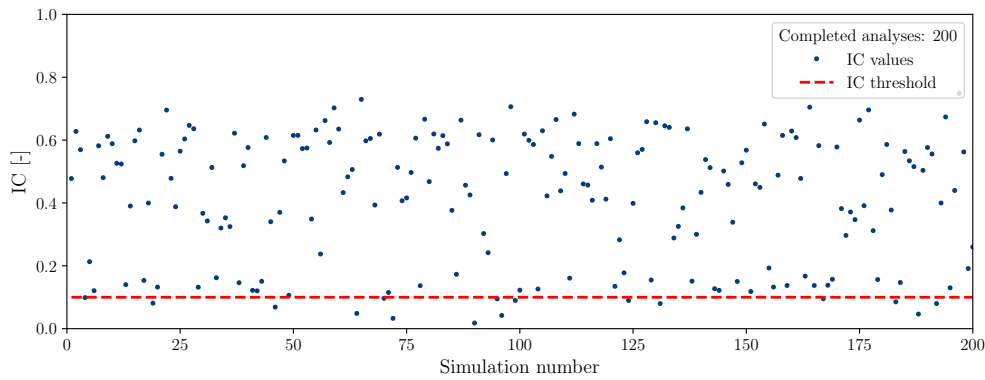
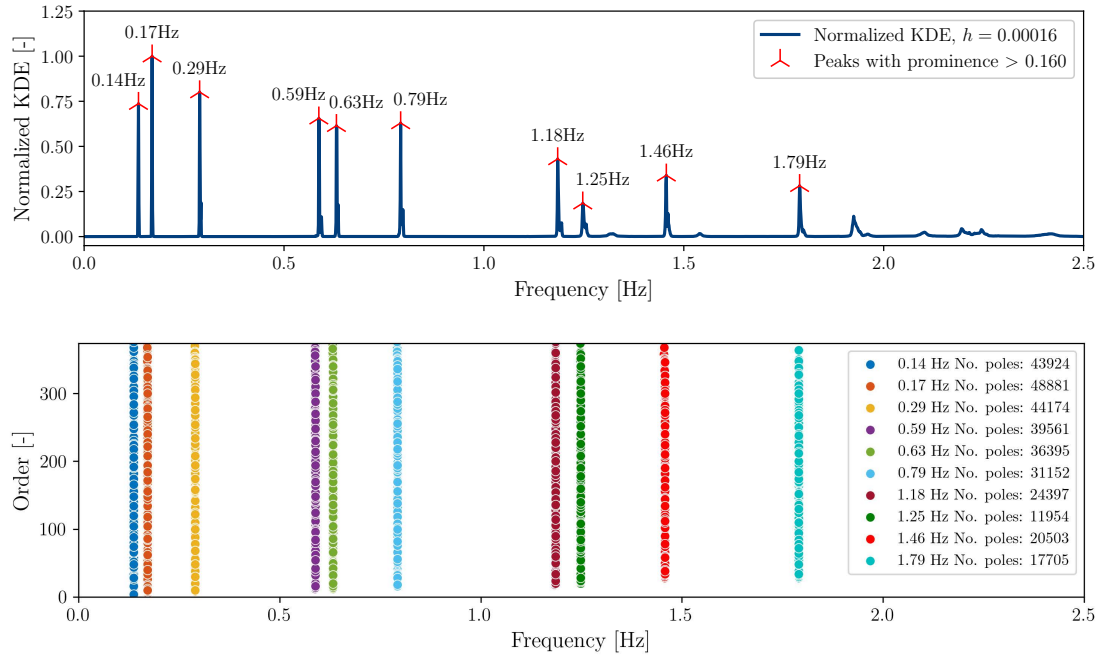


Figure 3.35: Al-Hamra Tower: numerical values of IC obtained from the sets of control parameters generated for training the intelligent core of *i*-AOMA.

parameters generated for training the intelligent core of *i*-AOMA.

Afterward, new quasi-random samples of the control parameters are generated



(a)

Figure 3.36: Al-Hamra Tower: the normalized KDE together with the identified peaks (a) and certainly stable poles falling within the retaining bands (b) obtained at the end of the i-AOMA.

by means of the Halton technique and the SSI-cov algorithm is performed only for those that are classified as feasible. The convergence criterion based on Eq. (3.13) has been fulfilled when the trained RF algorithm has enabled the application of the SSI-cov algorithm for 500 newly samples out of 2,311 quasi-random combinations of the control parameters. Figs. 3.36-3.38 illustrate the final results of the i-AOMA.

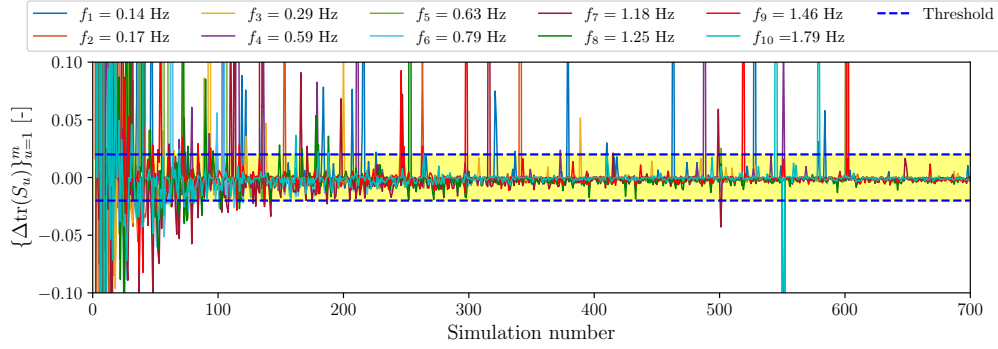


Figure 3.37: Al-Hamra Tower: convergence analysis of the relative total sample variance for each mode.

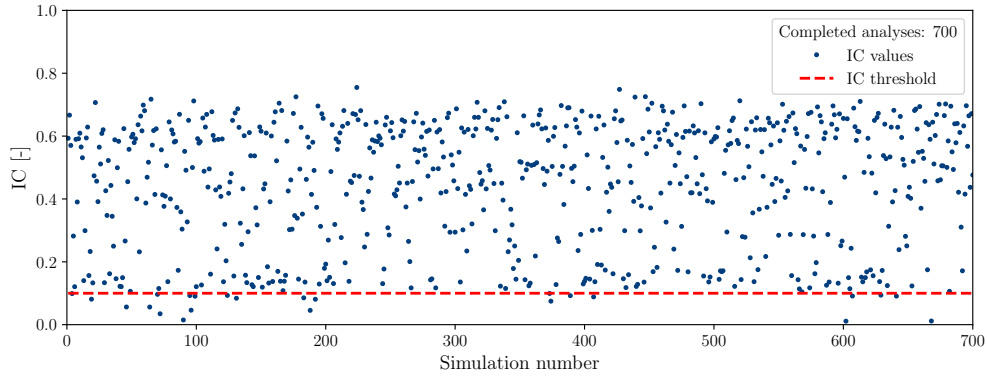


Figure 3.38: Al-Hamra Tower: numerical values of IC obtained from all the feasible sets of control parameters generated during *i*-AOMA.

It is noted in Fig. 3.36 that the ISJ algorithm now provides an estimate of the BW equal to 0.00016 Hz whereas it results in $b_w = 4$. Therefore, the BW has reduced while b_w increased. Once again, therefore, the selection pressure provided by the RF algorithm has reduced the dispersion of the final certainly stable poles, thereby lowering the uncertainty level about the modal estimates attributable to the control parameters. Moreover, Fig. 3.38 confirms the effectiveness of the trained RF algorithm in selecting feasible sets of control parameters for modal identification, given the small number of events for which the IC value is lower than the threshold.

Fig. 3.39 illustrates the joint (bidimensional) probability density functions of the control parameters that have been classified as feasible from the intelligent core of *i*-AOMA. The comparison between Fig. 3.39 and Fig. 3.9 demonstrates, as expected, that the most appropriate combinations of the control parameters of the SSI-cov algorithm change on a case-by-case basis. This, in turn, confirms the need for an automatic procedure for their optimal tuning.

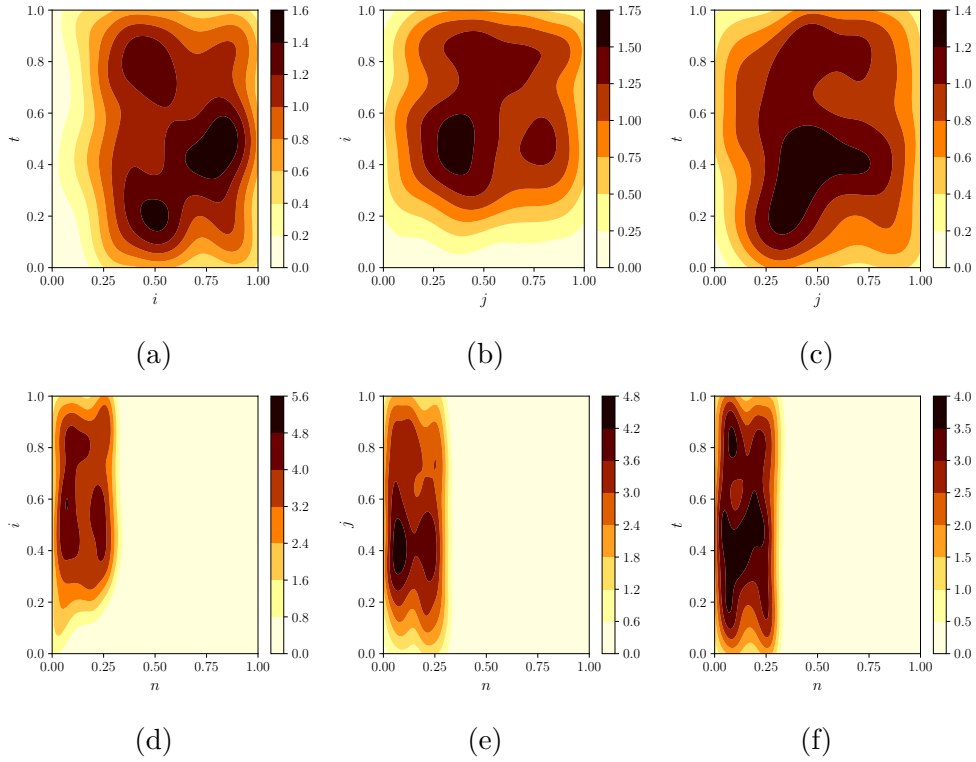


Figure 3.39: Al-Hamra Tower: joint probability density functions of the control parameters that have been classified as feasible from the intelligent core of i-AOMA.

Ten modes of the tower have been identified corresponding to natural frequencies value equal to 0.14 Hz, 0.17 Hz, 0.29 Hz, 0.59 Hz, 0.63 Hz, 0.79 Hz, 1.18 Hz, 1.25 Hz, 1.46 Hz, and 1.79 Hz. The related estimates of the damping ratios are 1.08%, 0.54%, 0.66%, 0.76%, 0.58%, 0.62%, 0.82%, 1.11%, 0.75%, and 1.05%. The corresponding mode shapes are shown in Figs. 3.40-3.49, which are depicted considering a simplified wireframe geometrical model derived from the sensor network layout. The uncertainty level of the mode shapes due to the variability of the control parameters adopted for the SSI-cov algorithm is highlighted by means of a boxplot-type representation. Numerical mode shapes obtained from the finite element analysis are also shown in Figs. 3.40-3.49.

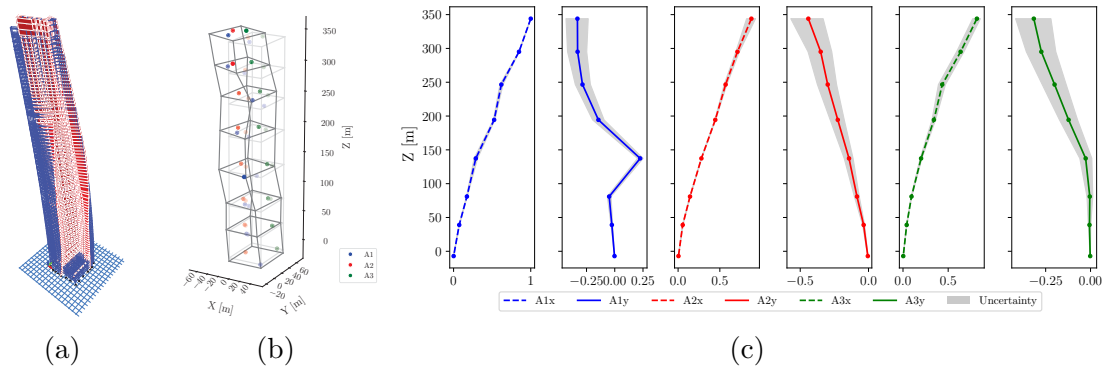


Figure 3.40: Al-Hamra Tower: numerical mode shape (a), median experimental mode shape (b) and corresponding uncertainty level in terms of boxplot's whiskers (c) for the first mode of the tower.

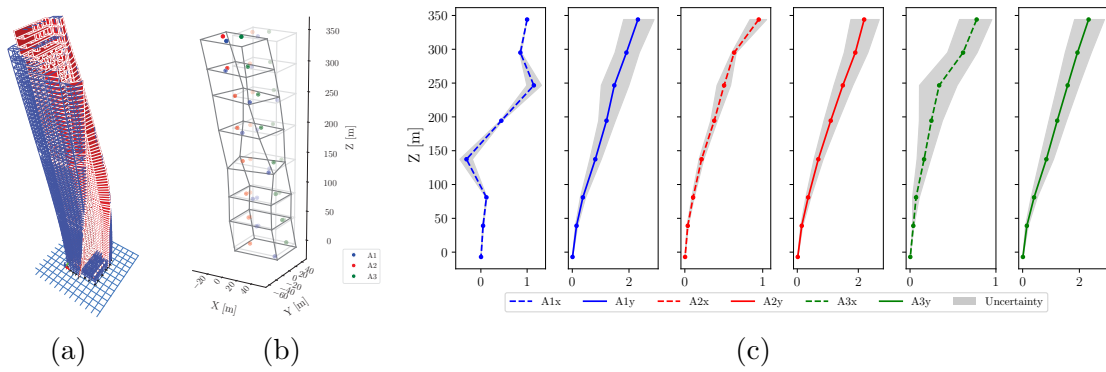


Figure 3.41: Al-Hamra Tower: numerical mode shape (a), median experimental mode shape (b) and corresponding uncertainty level in terms of boxplot's whiskers (c) for the second mode of the tower.

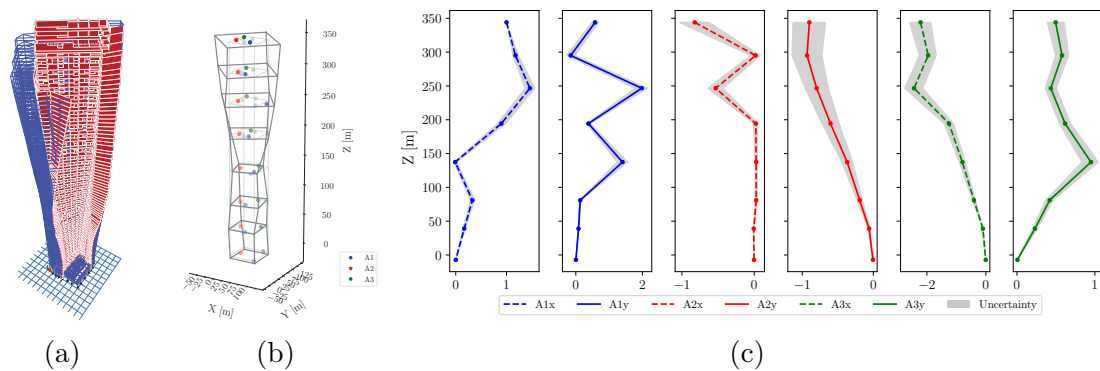


Figure 3.42: Al-Hamra Tower: numerical mode shape (a), median experimental mode shape (b) and corresponding uncertainty level in terms of boxplot's whiskers (c) for the third mode of the tower.

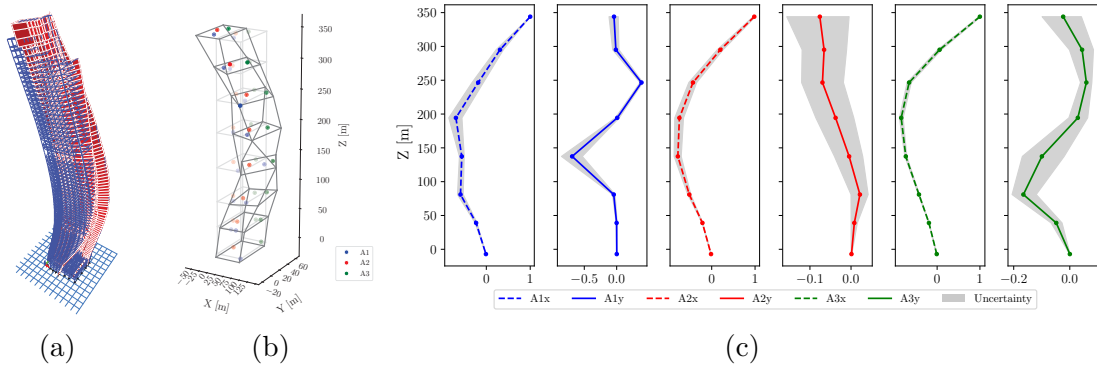


Figure 3.43: Al-Hamra Tower: numerical mode shape (a), median experimental mode shape (b) and corresponding uncertainty level in terms of boxplot's whiskers (c) for the fourth mode of the tower.

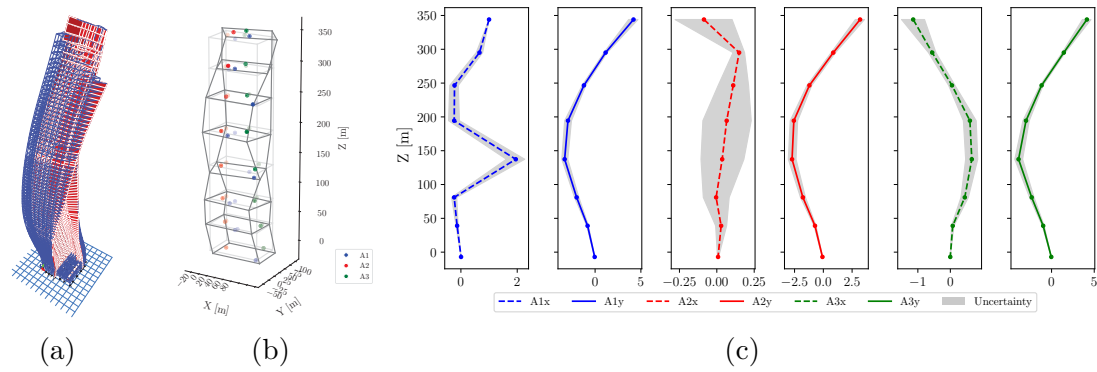


Figure 3.44: Al-Hamra Tower: numerical mode shape (a), median experimental mode shape (b) and corresponding uncertainty level in terms of boxplot's whiskers (c) for the fifth mode of the tower.

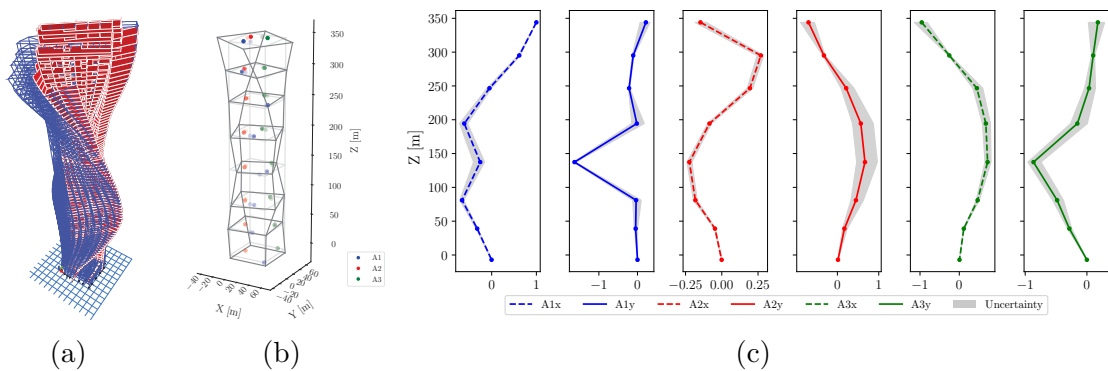


Figure 3.45: Al-Hamra Tower: numerical mode shape (a), median experimental mode shape (b) and corresponding uncertainty level in terms of boxplot's whiskers (c) for the sixth mode of the tower.

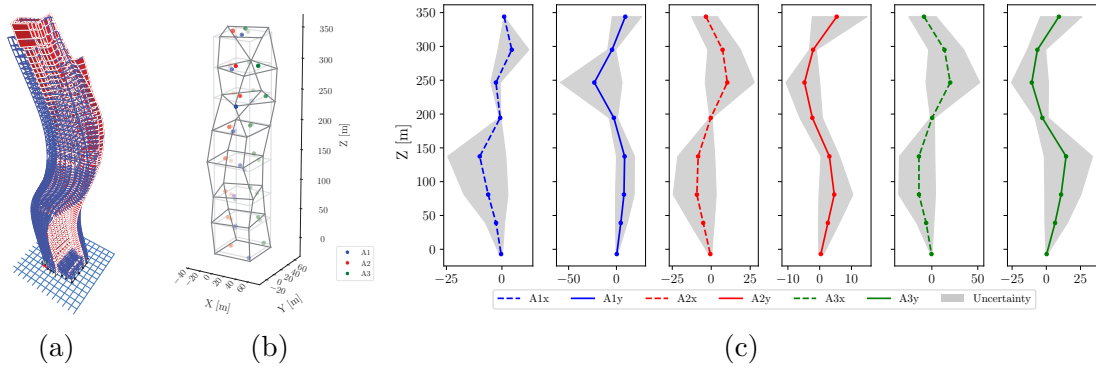


Figure 3.46: Al-Hamra Tower: numerical mode shape (a), median experimental mode shape (b) and corresponding uncertainty level in terms of boxplot's whiskers (c) for the seventh mode of the tower.

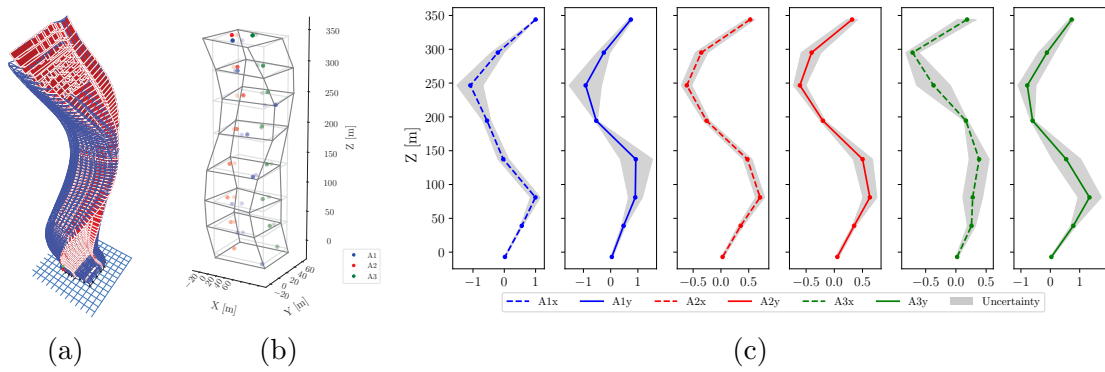


Figure 3.47: Al-Hamra Tower: numerical mode shape (a), median experimental mode shape (b) and corresponding uncertainty level in terms of boxplot's whiskers (c) for the eighth mode of the tower.

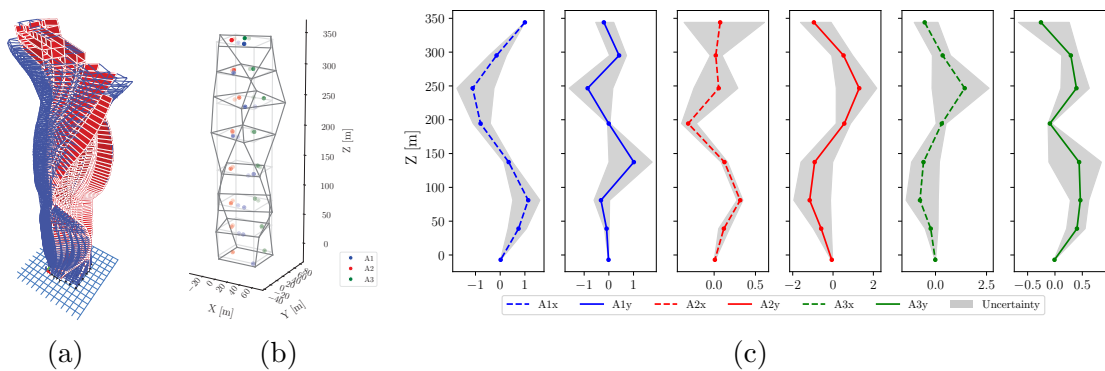


Figure 3.48: Al-Hamra Tower: numerical mode shape (a), median experimental mode shape (b) and corresponding uncertainty level in terms of boxplot's whiskers (c) for the ninth mode of the tower.

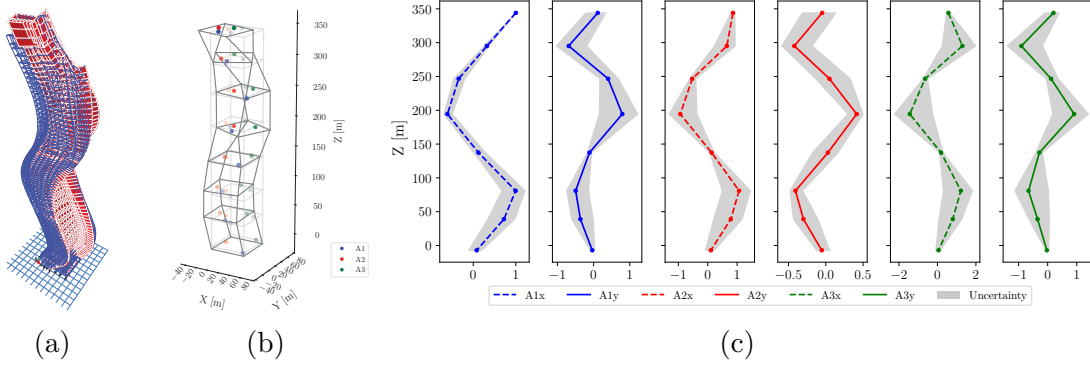


Figure 3.49: Al-Hamra Tower: numerical mode shape (a), median experimental mode shape (b) and corresponding uncertainty level in terms of boxplot's whiskers (c) for the tenth mode of the tower.

A satisfactory matching can be observed between the estimated mode shapes and the corresponding numerical predictions. The first eight modes are also in very good agreement with previous experimental results reported by Sun et al. [211]. The last two modes shapes identified in the present study were never detected before, and they are in good agreement with numerical predictions obtained from the finite element model (modes number 9 and 10 in Tab. 3.5). Table 3.6 provides a synthetic comparative assessment between the results reported by Sun et al. [211] and those obtained in the present study.

Table 3.6: Al-Hamra Tower: comparison between the results reported by Sun et al. [211] and those obtained in the present study by means of the i-AOMA algorithm (f is the natural frequency, whereas ξ indicates the damping ratio).

Mode No.	Mode type	Sun et al. [211]	This study	
		f [Hz]	f [Hz]	ξ [%]
1	NS flexural (1)	0.14	0.14	1.08
2	EW flexural (1)	0.18	0.17	0.54
3	Torsional (1)	0.31	0.29	0.66
4	NS flexural (2)	0.61	0.59	0.76
5	EW flexural (2)	0.66	0.63	0.58
6	Torsional (2)	0.84	0.79	0.62
7	NS flexural (3)	1.24	1.18	0.82
8	EW flexural (3)	1.30	1.25	1.11
9	Torsional (3)	-	1.46	0.75
10	NS flexural (4)	-	1.79	1.05

Once again, it is evident from Figs. 3.40-3.49 that the uncertainty due to the control parameter values propagates and possibly amplifies through the identification procedure, even if the final stable poles are relatively close each other. It is also confirmed that the uncertainty level is not constant. While it is very low in some

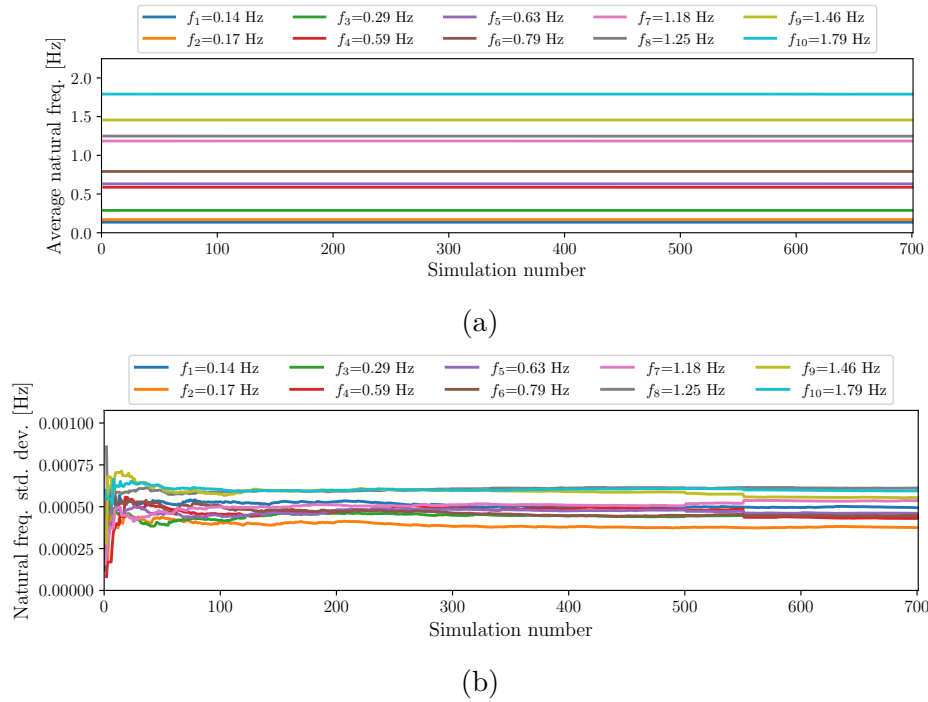


Figure 3.50: Al-Hamra Tower: average (a) and standard deviation (b) of natural frequencies over the feasible samples of the control parameters.

cases, it results very large in others. The uncertainty level depends on which DOF and mode number is considered, and, as expected, higher modes are often associated with a higher uncertainty.

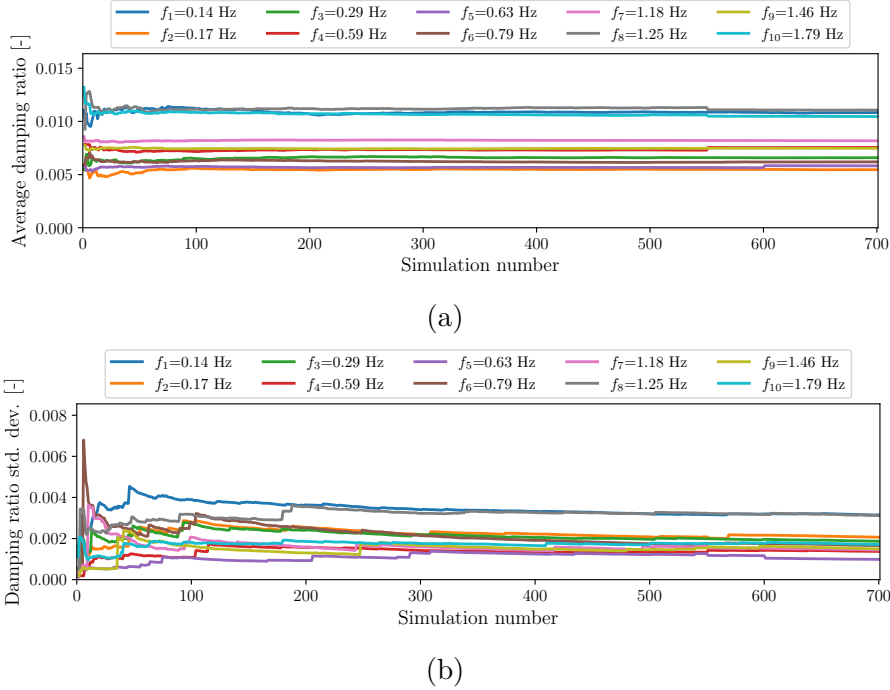


Figure 3.51: Al-Hamra Tower: average (a) and standard deviation (b) of damping ratios over the feasible samples of the control parameters.

Finally, the convergence of average and standard deviation for natural frequencies and damping ratios over all the feasible samples of the control parameters are reported in Figs. 3.50-3.51, respectively.

3.6 i-AOMA conclusive remarks

The present chapter mainly focused on automatic operational modal analysis (AOMA) systems for output-only vibration analysis, especially useful for continuous structural health monitoring (SHM). Specifically, the limitations of the existing AOMA methods have been identified, and during the current Ph.D. program, a new data-driven and artificial-intelligent-based framework has been formulated to attempting overcoming some of the main issues still existing in the automatic covariance-driven stochastic state-space identification (SSI-cov). Therefore, the intelligent automatic operational modal analysis (i-AOMA) attempted to overcome the arbitrary choice of the SSI-cov control parameters, permitting the exploration of various sets in reasonable ranges via a quasi-Monte Carlo sampling scheme. Moreover, the machine learning (ML) part has been effectively integrated within the proposed framework to save the computational burden traditionally associated with a Monte Carlo

scheme in order to guess the quality of the modal results associated with a specific set of SSI-cov control parameters. This permitted discarding in advance those sets that were predicted to be poorly informative, and just earmarking computational resources on those likely informative ones. Furthermore, all the stabilization diagrams associated with the various SSI-cov analyses are overlapped and comprehensively processed in one step. The nonparametric kernel density estimation (KDE) algorithm in the automatic version based on the improved Sheather-Jones (ISJ) algorithm and Fast Fourier Transform (FFT-KDE) has been consequently adopted to process the overlapped stabilization diagram for distilling those most recurrent stable poles' alignments associated with physical modes of actual interest. The use of KDE appeared quite attractive, especially for the lower computational burden of the current FFT-KDE implementation rather than standard clustering techniques nowadays adopted in the AOMA field, and even for its proven precision in automatically locating the most recurrent stable poles' alignments. In summary, the proposed *i-AOMA* framework has been formulated to increase the actual automation level of the existing AOMA methods, requiring a minimum intervention for the user to only setup the procedure the first time, and leveraging the AI and ML learning process, the system is able to autonomously recursively execute analysis automatically choosing the SSI-cov control parameters afterward this initial training phase. It is noteworthy that considering all the modal results associated with all the conducted analysis it is possible to compute statistical indicators to evaluate how the uncertainty on the control parameters propagates in the final modal estimates. The effectiveness of the proposed *i-AOMA* approach has been herein validated on a numerical benchmark case, and two compelling real-world case studies, i.e. the long-span Hardanger suspension bridge in Norway, and the Al-Hamra Firdus Tower in Kuwait City in Kuwait.

The output-only dynamic identification problem has been discussed hitherto, both referred to the traditional OMA strategies incorporated in the PyOMA software, and to the AI-based ones with the release of the *i-AOMA*. The focus in the next chapter of the present Thesis document moves toward the damage detection field, with special emphasis on the research studies conducted during the current Ph.D. program, also discussing other indirect non-destructive testing (NDT) methods besides the vibration-based ones, both with a certain degree of machine learning integration.

Chapter 4

Machine-learning-aided damage detection strategies for civil structures

Existing structural heritage is nowadays widely approaching the end of its nominal life, and often the emergence of critical degradation phenomena further reduces their safety levels and threatens their structural integrity. However, a complete replacement with their demolition and reconstruction is often not economically sustainable and/or a viable option. This practical consideration promoted the adoption of continuous monitoring systems such as SHM paradigms to evaluate the long-term degradation process and provide an uninterrupted evaluation of structural safety and performance. This aids structural prevention mindset, i.e. timely prioritizing maintenance interventions to optimally intervene on existing structures and infrastructures heritage in order to diffusely extend their nominal life [7]. The term *prevention* means that via continuous monitoring it should be theoretically possible to identify any damage in its initial stages, and therefore restore it with light and economic interventions before damage becomes seriously critical or irreversible, thus when instead it requires significantly expensive restoration costs [15]. Intuitively, the very first imperative step to accomplish these goals is understanding if any structural damage is emerging or not in the structure under investigation. The term *damage* generally refers to any defect or imperfection that may occur in a structure, potentially harming its functionality or performances [217]. Referring to the combined system schematically represented in Fig. 2.1 belonging to the system analysis field, damage can be modeled as an additional excitation resulting in energy dissipation flow modifying the expected output response signal [217]. This definition reveals inverse problem nature of the damage detection procedure, which translates in identifying the changes to structural physical parameters such as material properties that unfavorably affect the output response during operational loading conditions.

The present chapter is therefore dedicated to the research studies conducted during the current Ph.D. program in the direction of damage detection strategies, combining the potentials offered by visionary artificial intelligence and machine learning tools with traditional existing methodologies. Specifically, the herein conducted studies have examined not only OMA-related and vibration-based methods, but also some other indirect and non-destructive testing (NDT) methodologies, most appropriate and effective for some specific structural typologies. The next section starts by introducing the damage detection approach, and how it configures within the SHM paradigm, also mentioning the related maintenance philosophies existing within our engineering sector.

4.1 Structural damage detection

Structural damage can be defined as any change occurring in material, geometric properties, boundary conditions, mass, stiffness, energy dissipation characteristics, etc. producing negative effects on current or future safety levels or structural performances [7]. Different terminology is adopted according to length scale, i.e. cracks, defects, imperfections, or failure, and it can be denoted as accumulated damage when referring to the time scale, e.g. involving fatigue or corrosion phenomena. In the context of the current Thesis, the damage detection (DD) procedure is the inverse problem of identifying the modifications that are occurring in the structural system due to degradation effects by analyzing the output response of the structure [217]. This absolute definition of DD task is an ends-in-itself formula, unless it is expressed in relative terms [7]. Indeed, the occurring damage can be revealed and quantified when a comparison among two or more structural health states is performed and evaluated in different moments of the operational in-service life. Two main paradigms have been identified in the DD field. Model-based DD strategies grounded in using various mathematical models or representations of the behavior of the structural system under investigation. Afterward an update procedure [116], it is possible to identify the differences in the response output or in the model's parameter to evidence with the residues the degradation effects occurred, viz. the level of damage relevant to the model's changes. To achieve more representative and accurate modeling, this approach sometimes also requires information from measuring the input acting loads [217]. On the other hand, data-driven signal-based DD strategy inspects the output response signals accounting for e.g. structural response vibrations, noise signals, etc. Features are therefore extracted from these signals, attempting to establish some relationship connecting them to the possible damaging scenario. In any case, both procedures leverage various signal processing tools. For instance, as reported in [217], the signature analysis is based on processing information obtained by simple features which are e.g. statistical indicators of the monitored output response and/or physical/modal parameters. Instead,

advanced signature procedures leverage multi-dimensional vectors or matrices of features collectively, attempting to evidence more complex hidden patterns and relationships useful for fulfilling DD tasks. The observations about signature methods highlighted the pattern recognition nature of the DD problem [7]. Pattern recognition (PR) is a machine learning branch dealing with mathematical and statistical concepts for automatic classification tasks and possibly considering the involved uncertainties. For instance, in the current civil structures monitoring context, the PR task should learn and distinguish between healthy and damaged states. ML procedures are indeed expected to learn the hidden existing relationships or establish new ones between damage-sensitive features extracted from vibration data and the various health states. A statistical PR framework is usually structured in the following steps [7]: 1. Evaluation of in-service operational conditions; 2. Vibration data acquisition, cleansing, and pre-processing; 3. Damage-sensitive feature selection and extraction; 4. Statistical PR phase with ML model training and testing. At the early beginning of this workflow, a feasibility study is required involving all the necessary preliminary evaluations, such as defining a proper monitoring plan, i.e. choosing the type of sensing solution by understanding operational and/or environmental loading conditions [95]. From an SHM perspective, besides the life-safety concerns of the monitored structure, the social functions and the importance aspects are also non-negligible factors to justify the economical effort of implementing an integrated SHM system which must be maintained functional over the years. Last but not least, the monitoring system can be locally optimized if delimiting it to the most likely occurring damaged parts only. For instance, monitoring systems can be placed in half-joint bridges focusing specifically on the most critical parts, i.e. usually the dapped end parts of the supporting girders [218]. In the optics of a bridge assessment management system, an SHM system can be designed to aim toward different goals as stated in [36], one of them is the early identification of damage for operational safety purposes. It is worth reminding that the DD task represents the very first phase of the subsequent steps of an ideal SHM framework. Specifically, Rytter in 1993 initially proposed five different levels for classifying the various SHM paradigms, based on the knowledge depth of the entire damage identification process [219]. These five levels soon become the formalization of the SHM paradigms [7, 217, 219]. As illustrated in Fig. 4.1, Level 0 is represented by the SHM implementation with the data collection and feature extraction phases. Subsequently, Level 1 is the DD problem to understand if any structural damage has emerged and become physically identifiable or not. When any damage has emerged, Level 2 of inspection aims to localize its position, e.g. for virtually permitting a direct visual inspection of the damaged area. Level 3 deals with the assessment of the type of damage that is occurring, whilst Level 4 is related to an evaluation of the extent and size of damage, related to its severity with respect to the induced safety level reduction. These latter three levels (Levels 2-4) are usually denoted as the damage diagnosis phase of the monitored structure, adopting a nomenclature

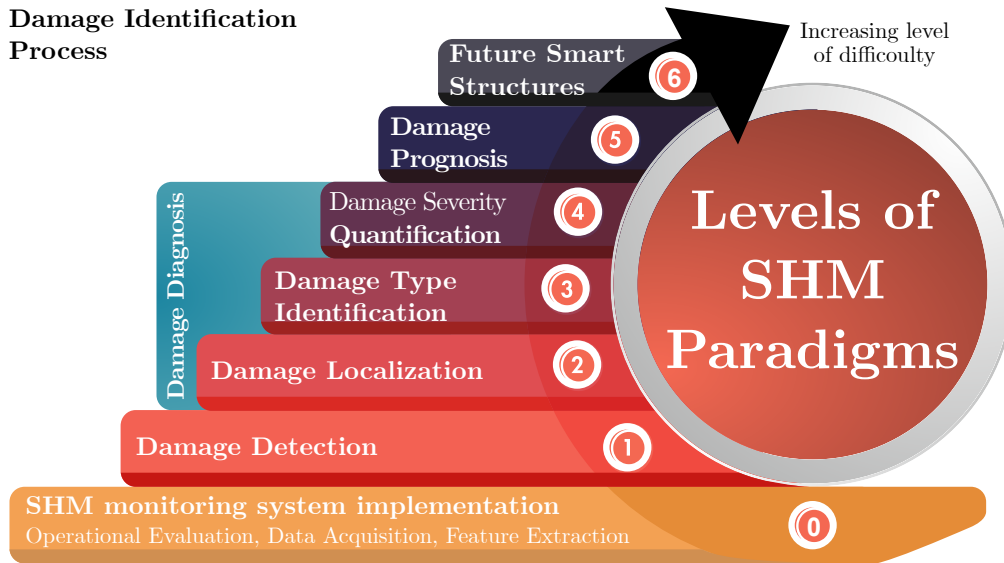


Figure 4.1: Levels of SHM paradigms based on the knowledge depth of damage identification process, with Levels 1-5 based on Rytter (1993) [219].

borrowed from the medical field. The last Level 5 instead is mainly related to estimating the remaining life in operation of the structure given the current health state, i.e. aiming to perform a prognosis evaluation of the structural system. This last level can be associated with reliability analysis, fracture mechanics, fatigue life estimation, and statistical analyses, because it also requires a careful prediction of the degradation velocity over time. Considering nowadays existing built heritage, this latter phase is mainly a prerogative of smart structures with self-diagnostic and self-evaluating systems, even with some additional control capacities through actuators [217]. Nevertheless, to this day, no market-ready solutions are commercially available, and this is still relegated to the research field, which is actively working especially on data fusion and heterogeneous information processing leveraging modern AI-based solutions. Next-future monitored smart structures may possibly identify a new Level 6 of the SHM paradigms, for better distinguishing between the traditional-knowledge-based prognosis scenarios (Level 5) and the innovative smart structure with AI-assisted prognosis predictions. According to [220], reliable and efficient damage prognosis in practical applications still requires extensive and multidisciplinary research efforts to mature enough the current approaches. As stated in [7], the monitoring system may also functioning as a protective setup for the structural systems, because it may trigger a warning alert to possibly avoid catastrophic and unsafe failures before they happen, e.g. with immediate traffic closure considering a strategic bridge infrastructure. These triggers should activate when damage sensitive features reaches some predefined threshold levels. Furthermore, in a prevention mindfulness, these triggers give the possibility to restore the safety

levels with appropriate and dedicated maintenance interventions before any critical failure occur.

4.1.1 Maintenance philosophies

As illustrated in [36], an SHM system may aim toward fulfilling different goals. Foremost, it could be able to detect the emergence of structural damage in its early stages, thus making a prevention-based approach with light and economic maintenance interventions, rather than extraordinary maintenance actions and expensive restoration operations with severe damage conditions. In addition, an SHM system could be useful to validate design assumptions and verify the actual structural performances under operating conditions. Furthermore, when natural extreme events occur, a still-operating SHM system may provide real-time monitoring in immediate post-disaster scenarios. OMA and SHM can be used also afterward extreme events, such as earthquakes, to provide relatively rapid screening of the residual health state and the integrity of the non-collapsed structures [7]. In this regards, SHM play a crucial role in post-earthquake damage assessment with both economics and social impacts, e.g. focusing on the reoccupation of buildings or for gather enough reconstruction funding required in post-emergency conditions. In addition, the near-future smart infrastructures would possibly provide reliable estimations of their prognosis, i.e. information regarding the remaining useful in-service life and the residual loading-carrying capacities. A deeper knowledge of the evolution of the health state in time may foster optimal decision tools for effective maintenance, periodical inspection, and rehabilitation planning. In addition, prospecting a diffuse network of monitored smart infrastructures in the future, the SHM paradigm may also provide a collection of massive databases of structural information for developing novel artificial-intelligence-based research to improve data management and infrastructural decision process, from the design specifications to management guidelines [36].

Despite these visionary goals, nowadays, the actual limitations to a widespread SHM installation are mainly still related to the relatively high installation and management costs, requiring periodic maintenance to ensure the sensing system is working for the entire service life [36]. To progressively shift toward a diffuse SHM network system at a regional or national scale can be promoted by quantifying the real benefits of SHM massive installation, e.g. by evaluating the earmarked capitals and associated costs shifting from time-based maintenance programs toward an SHM-related condition-based maintenance strategy. Indeed, different maintenance philosophies have evolved over the years [7]. In origins, engineering systems were kept in service until any failure of a critical component was reached, denoting the so-called run-to-failure perspective. No maintenance plans were established in order to guarantee the functionality of the structure, without any anticipated warning

alert system and without spending any resources until failure was reached. However, besides the high costs suddenly required at the failure moment, this approach is unreasonable when life-safety aspects are involved. For instance, especially in aeronautic fields, a time-based maintenance philosophy took place. Every strategic component is totally replaced at a predefined moment regardless of its actual condition. This more proactive strategy replaces every component before any critical degradation failure occurs due to its normal operating life. Nonetheless, it requires higher costs and a pre-defined maintenance plan actuated during the nominal life of the system. Since this latter maintenance philosophy ensures higher safety levels, its integration with SHM delivered the new condition-based maintenance philosophy. Therefore, the maintenance interventions are prioritized by periodically inspecting through SHM the actual evolution of the health state and the degradation levels of the structure, allowing a better relocation of the economic resources both in time and on the territorial scale. Warning systems can be jointly implemented to preserve life-safety conditions when serious adverse deviations toward unsafe conditions occur.

Predicting the degradation evolution during the entire life-cycle is essential for optimizing the rationale behind aging structures' successful management plans. This is especially crucial considering the limited financial resources that can be earmarked yearly, insufficient to improve the safety levels of all structures and infrastructures heritage simultaneously. Nevertheless, the degradation evolution predictions for damage prognosis can not be performed deterministically, because of the high levels of epistemic uncertainties associated with the multidisciplinary nature of damage and degradation evolution phenomena over the entire life-cycle assessment [220]. The reliability of a structure can be expressed according to a state function $g(\mathbf{X})$, being $\mathbf{X} = \mathbf{X}(t)$ a vector of multi-variate random variables involved in the degradation evolution phenomena over time t . This state function is defined as the limit state function when $g(\mathbf{X}) = 0$, because it represents the separation frontier between a safe state ($g(\mathbf{X}) > 0$) and an unsafe one ($g(\mathbf{X}) < 0$). As illustrated in Fig. 4.2 (a), the structural reliability can be virtually observed over time according to a performance index, e.g. defined as the expected value calculated for $g(\mathbf{X}) > 0$ of the joint probability density function $f_{\mathbf{X}}[x(t)]$ associated to the random variables \mathbf{X} [220]. The performance index is practically constant after the construction era until structural damages may occur at an uncertain time instant, setting off the degradation initiation point with the progressive deterioration of its reliability level. If no maintenance interventions are performed over time, the reliability will decrease with a degradation rate until reaching the last acceptable limit threshold of the structural reliability, i.e. associated with the failure probability of the limit state function. This latter point denotes the service life of the structure $t_{\text{life},0}$. However, maintenance actions can improve the structural performance, and therefore its reliability, thus extending its service life. The quantification of the reliability improvement depends on the type and the time instant of maintenance

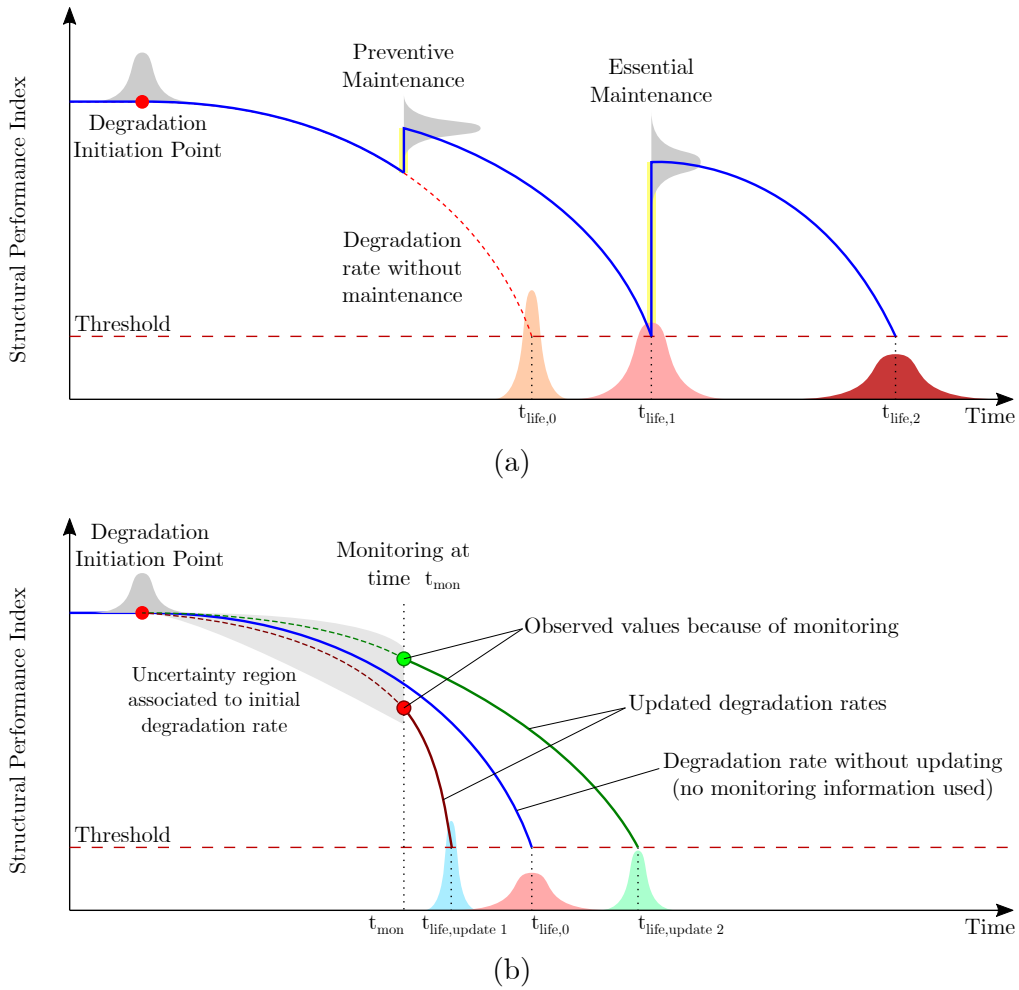


Figure 4.2: Schematic visualization of the time-dependent behavior of a performance index (such as the reliability index) during the life-cycle of a structure, evidencing preventive and essential maintenance interventions effects on extending the in-service lifetime (a); illustration of the two possible updating cases for time-dependent behavior of a performance index leveraging SHM monitoring data (b).

intervention. Two kinds of maintenance interventions can roughly be distinguished. Preventive maintenance involves light and economic interventions, thus occurring with early stages of structural damage evolution, i.e. prior to reaching the performance index threshold. Conversely, essential maintenance involves urgent, heavy, and typically expensive restoration actions because it occurs with advanced damaged conditions, i.e. being in proximity to the reliability threshold value. For instance, in the schematic representation of Fig. 4.2 (a), following a preventive maintenance action, the performance index increased to a certain mean value due to its uncertain nature. Therefore, starting from this new value, the degradation

rate mean law could possibly change, but it is expected that the new service life value $t_{\text{life},1}$ is greater than the initial one without any maintenance intervention $t_{\text{life},0}$. Furthermore, conceiving to virtually reaching the threshold level at $t_{\text{life},1}$, an essential maintenance intervention has been depicted in the graph, which extended one more time the service life to the new value $t_{\text{life},2}$. It is noteworthy to observe the shapes of the uncertain distributions associated with the service life predictions $t_{\text{life},0}$, $t_{\text{life},1}$, and $t_{\text{life},2}$, which are progressively more dispersed around their mean value. This is mainly due to the obvious increasing uncertainties over time for progressively farther future forecasts with respect to the current time of analysis. In summary, considering the general schematization proposed in Fig. 4.2 (a), an optimization procedure should be performed to identify the optimum types and acting time instants minimizing the expected life-cycle total cost c_{ET} , formalized in [220] as below:

$$c_{ET} = c_{INI} + c_{INS} + c_M + c_{FAIL}, \quad (4.1)$$

in which c_{INI} is the initial design and construction cost, c_{INS} indicates the periodic inspections cost, c_M denotes the maintenance intervention cost. The expected cost of failure, denoted as c_{FAIL} , is defined as the product of the expected monetary loss due to structural failure c_{failure} and the associated probability of failure p_F computed as the cumulative density function of the joint probability density function $f_{\mathbf{X}}[x(t)]$ when $g(\mathbf{X}) < 0$ [220].

So far, only the maintenance effects have been considered on the reliability evolution over time due to degradation effects, but the presence of an SHM system can be advantageous for various aspects. Considering the levels of SHM paradigms of Fig. 4.1, the damage diagnosis phase should provide periodically or continuously updated information about the health status of the monitored structure, therefore this information should help in reducing the high levels of uncertainties associated with the degradation rate predictions. Furthermore, identifying critical locations for damage initiations at its early stages should permit preventive maintenance action planning, with optimized management of the financial resources. These aspects could potentially represent valid evaluation elements for the decision process at the design phase, for assessing the actual benefits provided by implementing or not an SHM system and justifying its initial high implementation costs. Focusing on Fig. 4.2 (b), after the degradation initiation point, the performance index decreasing law is uncertain, evidenced by its gray shadowed region. Considering a periodic monitoring SHM system, at a time instant t_{mon} the performance index is directly observed thanks to the collected monitoring data. Considering the blue line the expected value of the performance index at time instant t_{mon} , two possible cases can be potentially observed after the monitoring session. In the worst-case scenario, the mean observed performance value is lower than the one initially predicted with the blue line, therefore the updated degradation law may probably deliver an estimated service life $t_{\text{life,update } 1}$ lower than $t_{\text{life},0}$. On the other hand, the mean observed

performance index may be greater than the one initially predicted with the blue line and, in this second case, the updated degradation law may probably deliver an estimated service life $t_{\text{life,update 2}}$ greater than $t_{\text{life,0}}$. In any case, it is worth noting that the shape of the distributions associated with the service life instants $t_{\text{life,update 1}}$ and $t_{\text{life,update 2}}$ are basically sharper than the one associated to $t_{\text{life,0}}$, because they are conditioned on the new observed information at t_{mon} delineating a new and less uncertain situation at an intermediate time period. Instead, the information used for computing the blue line was referred to as the initial zero time instant in this case. This clarifies why the monitoring-based maintenance programs are denoted as condition-based maintenance strategies, in contrast with the obsolete run-to-failure time-based maintenance approach (the one used for the blue line). Therefore, the expected life-cycle total cost in Eq. (4.1) can be accordingly modified considering the presence of an SHM system [220]:

$$c'_{ET} = c'_{INI} + c'_{INS} + c'_M + c'_{FAIL} + c_{MON}. \quad (4.2)$$

The new term c_{MON} stands for the monitoring costs, whilst the other terms remain the same of Eq. (4.1), but they assume different values than before, thus indicated with the apostrophe superscript. As already mentioned, these aspects could potentially represent valid elements for assessing the real benefits of implementing or not an SHM system on a specific structure. From a simple economic consideration, for justifying the SHM initial high implementation costs, it should be demonstrated that the SHM benefits computed as $B_{\text{SHM}} = c_{ET} - c'_{ET}$ is a positive quantity [220]. These aspects should aid in evidencing the economic feasibility of asset management strategies at regional or national scale, providing tangible evaluations for justifying high capital investments for progressively transitioning from a time-based maintenance approach toward a condition-based maintenance strategy, with a damage-tolerance design concept [217]. Indeed, despite the economical aspects, the nowadays modern technologies adopted for the SHM systems may provide overwhelming advantages to the condition-based maintenance method. For instance, today's continuous and almost real-time health monitoring may support asset management board in the decision-making process with always new and updated information. The quality of this information will improve in the next years thanks to the current research activities for collecting and inspecting heterogeneous data, and creating integrated and more sophisticated monitoring systems with data science and AI-assisted tools. This may virtually reduce the uncertainties associated with the structural performance evaluations and damage prognosis predictions, with a virtual elimination of over-maintenance useless interventions, or lack of structural maintenance when urgently required [36].

4.1.2 Nondestructive Testing and Evaluation, SHM, and OMA for damage detection

As illustrated in Fig. 4.1, SHM paradigms' deeper levels are progressively oriented toward a full understanding of the structural damage from its identification, moving through its diagnosis, and potentially delivering some prognosis information [219]. To pursue this aim, a structure is observed over time by monitoring certain physical quantities of interest, in order to periodically extract and statistically analyze damage-sensitive features, and perform effective damage detection policies, e.g. for timely acting repairing interventions for preserving structural integrity [7]. The long-term SHM indicates an automatic continuous or periodic monitoring of the structural performance during its entire operating lifetime, similar to the AOMA context, but mainly focusing on the damage accumulation perspective rather than the solely dynamic identification task.

Damage detection and SHM are often confused and misunderstood as synonyms in engineering scenarios, despite DD involves many specialist areas, and one of them is the SHM itself [217]. Several other disciplines strongly related to the SHM field can be mentioned. For instance, condition monitoring (CM) is the name assumed by the SHM strategies in the mechanical field, i.e. when rotating machinery is involved [7, 217]. In the CM, since the monitored structures are at the laboratory scale, DD is an approximately well-established topic, in which also the influence of environmental conditions on measured data has been well investigated. Therefore, CM procedures posed the basis for many worldwide standards of monitoring of rotating machines [217]. Statistical process control (SPC) is another discipline mainly derived from the industry field [7, 217]. The main goals are not only detecting the emergence of any structural damage, but also processing its diagnostic, recognizing how the structural performance process variations are within normal conditions over time or when reaches some warning upper or lower control limits. Direct testing (DT) approach is another discipline useful for DD tasks. It involves the study of mechanical properties of in-situ structural materials by extracting specimens that are subsequently analyzed in the laboratory via destructive tests. The characteristic cylindrical compression strength of concrete specimens or tensile strength tests for steel reinforced bars are examples of direct tests for RC existing structures. Furthermore, specific laboratory tests can be also performed to characterize the aging conditions, e.g. the carbonation tests for concrete specimens with a phenolphthalein-based solution. Despite the higher quality of retrieved information useful for DD purposes, the high costs in terms of both monetary and spent time often limit a widespread direct testing campaign. Moreover, their local and punctual nature limits the mechanical or aging results to a quite restricted area surrounding the specimen extraction locations, rarely directly expandable to the entire structural system. Therefore, another key specialist field involved in DD and often

preferred or used in conjunction with some direct tests is related to nondestructive evaluation (NDE), also denoted as nondestructive testing (NDT). NDT/NDE indirect techniques have been successfully included in cost-effective diagnosis and maintenance plans to reduce existing structures surveying costs. Likewise, for all the indirect testing methods, their main shortcoming is the need for an accurate calibration to rely on their outcomes entirely. Therefore, the indirect approaches are not a substitute for the direct ones. Still, they support direct investigations, mainly when these latter are limited in number due to budget restrictions [59]. Not all the NDT techniques are only limited to single point measurements [217], but some of them may allow for scanning large areas of the structure, virtually giving a global evaluation of the mechanical properties. For instance, vibration-based OMA techniques are comprised within the NDT methods. Vibration-based NDE and SHM evaluate incipient damage at the macro or global scale of the structure, differentiating its scope from e.g. the fracture mechanics which relates to the micro-scale on the contrary. Continuous SHM is often carried out online during the operational life, delivering a global overview of the structural system, whereas NDT is often carried out offline, and based on the specific technique can be both a local or global method. As suggested in [217], global SHM can be useful to understand the presence and a rough location of an emerging structural damage, and thereafter NDT can be efficiently adopted to better characterize the precise location and its severity without requiring disassembly or sacrificing some parts of the structural system as a direct testing approach would require. Another difference between SHM and NDT can be found in the hardware architectures [217]. Indeed, SHM sensors and actuators can be directly integrated into the design before the construction of new buildings and infrastructures, thus providing an embedded electronic system e.g. with power supply already connected to the external power grid lines. Conversely, NDT usually adopts an external sensing system independent from the specific structure under investigation.

As affirmed by [7], some fundamental axioms should be reminded when dealing with SHM for DD strategies. Foremost, structural materials are not perfect and have intrinsic flaws that can trigger the beginning of damage at that point, e.g. due to stress concentration phenomena or crack coalescence. DD should be expressed always in relative terms, e.g. establishing a comparison between various health states of the system in different moments of the in-service life. DD can be performed by choosing appropriate damage-sensitive features, which can be extracted using a proper sensing system. An optimized SHM system plan should be designed and tailored for the specific damage length and time scale. However, sensors themselves hardly ever directly measure the defects, but the discriminating capabilities of the chosen damage-sensitive features also depend on the algorithm's sensitivity or noise rejection capabilities. Anyway, generally speaking, the presence of any damage and its localization can be usually performed in a successful way. However, a full understanding of the damage type and its severity may require much deeper insights, thus

requiring special expeditions with direct visual inspections or proper NDT/direct testing campaigns. Indeed, a typical problem for acquiring specific SHM data from a damaged structure is the limited accessibility of its damaged components during operation [217], e.g. directly inspecting the status of bearing systems in a bridge when missing a proper accessible way. To overcome this issue, the understanding the damaged structure's behavior require detailed multiscale and multi-physics modeling and simulation strategies. Nevertheless, damage growth phenomena may involve nonlinear effects, which in turn increase the complexity of the physical problem. SHM for DD can be executed with a physics-informed model-based approach or a data-driven-based method. The foremost mainly regards the finite element model-updating procedure [116]. However, a critical aspect is the necessity of reliable information to establish the best initial conditions of the model update step which governs the entire exploration and the effectiveness of the optimization procedure. A misconception regarding the second data-driven method is the absence of any model, when in reality a sort of statistical model is always established for damage diagnosis purposes [7, 221]. It is noteworthy to underline that the main advantage of vibration-based SHM for DD is its global evaluation nature which monitors the whole structure without requiring placing accelerometer sensors immediately close to the actually damaged area. However, the main disadvantage of this approach is the structural vibration wavelength and amplitude are close to the background noise level, determining its relatively low sensitivity to detecting small damages, especially for lower vibration modes [217].

Besides the vibration-based approaches, in the field of NDT, acoustic emission (AE) represents a well-established technique used for damage detection, especially for concrete structures among others. Introduced in the early 1990s, it is based on ultrasonic elastic wave propagation with wavelength in the order of kHz or MHz [222]. For instance, in RC structures, it can be used with two antennas, one emitter, and one receiver to characterize the presence of cracks that modify the ultrasonic wave flows in the material. However, AE can be adopted as indirect and passive monitoring methods for structures that emit ultrasonic elastic waves during cracks and micro-cracks formation [223]. During the current Ph.D. program, some starting applications have been investigated using a publicly available dataset collected by a pencil lead break (PLB) test on the external faces of a monitored concrete bulk element. The PLB, also known as the Hsu-Nielsen source, is an artificial method of generating AE signals in a concrete mean knowing the position of the source of AE damage, i.e. the pencil lead breaking point. In this latter research work conducted during the current Ph.D. program, AE passive monitoring has been studied with an interesting application of the DL model for sound event detection (SED) problems. Indeed, AE signals have been interpreted similarly to acoustic audio data in clangorous environments with multiple but recognizable sound sources. Temporal-sequence-based DL models for SED tasks are demanded to recognize and classify different sounds from the audio data recording, defining the source that produced

that sound and in which time instants occur. This latter research work has not been reported in this Thesis document, but for further information, the interested reader can refer to [224].

Another NDT technique investigated during the current Ph.D program besides the vibration-based methods is the ground-penetrating radar (GPR) for tunnel linings' flaws detection. GPR is a geophysical technique [225] that involves transmitting high-frequency electromagnetic wave impulses inside the material under study using an antenna with a frequency of 10 to 2600 MHz. The dielectric characteristics of the material influence the propagation of such an impulse. A receiver antenna collects the reflected signals to inspect the material in-depth [225]. The GPR provides, therefore, an image as output, evidencing the presence of anomalies, defects, fractures, etc., overcoming the drawbacks of a direct visual inspection. A GPR inspection output is an image that presents the progressive longitudinal distance from the beginning of the tunnel. Three profiles are usually inspected with two-lane roads to characterize the single tunnel better. In contrast, five profiles are generally examined for three-lane roads. As shown, notwithstanding two different GPR testing profile configurations, in both cases, the attention is mainly focused on the critical segment of the top crown area, which comprises the two lateral haunches (shoulder joints). This area represents the most dangerous zone for road drivers if some concrete chunks from the primary concrete layer detachments fall on the road.

The rest of the current chapter is organized as follows. Section 4.2 is dedicated to the research studies conducted in the current Ph.D. program integrating deep learning strategies with GPR monitoring of tunnel linings for automatically detecting lining flaws [59, 226]. Section 4.3 is instead dedicated to the vibration-based methods for the DD task with an AI-based application using the subspace-based damage indicators, i.e. damage-sensitive features extracted from subspaces formulated by the SSI algorithms during the formalization of the Hankel matrices.

4.2 Tunnel linings damage detection with ground penetrating radar

Tunnels are essential underground or underwater infrastructure for setting up new communication routes and overcoming significant orographic obstacles and/or geomorphological constraints [227]. Focusing on underground tunnels, the lining part represents the perimetral structural supporting elements that stabilize the excavation hole and the surrounding ground. Linings can be continuous elements when crossing unstable ground formations, whereas they can also be constituted of limited supports in stable rock conditions. Generally made of RC, linings are often equipped with bolts and anchors for surrounding ground stabilization purposes, besides grouting concrete injections. Linings constitute primary structural supports

for tunnels, aiming to stabilize the opening in the ground excavation, denoted as permanent support when they are demanded to carry long-term linings design loads, or temporary support when installed only for short periods of time [228, 227]. Furthermore, linings can be composed of different layers. The design of permanent linings needs to fulfill the main structural requirements given by ground loading conditions and underground water flow control, e.g. for waterproofing layers [227]. Moreover, linings should meet operational requirements such as durability, functionality, and appearance, such as deformation control, cracking opening limitations, surface textures, etc. Moreover, it is worth reminding that lining design is not only a structural problem, but it is mainly a geotechnical and structure-ground interaction four-dimensional problem. Indeed, both transverse and longitudinal arching systems concur to define the tunnel's stability, considering both time-dependent effects and even the uncertain nature of acting loads, completely governed by the surrounding ground [227]. Different technologies are available nowadays for tunnel lining construction. Sprayed concrete (shotcrete) is conveyed to the ground surface via nozzles with high pressure, which immediately ensures also its compaction. The double shell of sprayed concrete with a two-pass lining method is generally used for building permanent linings in a wide range of ground or profile conditions, i.e. forming a first sacrificial layer followed by the actual permanent secondary lining layer. Another technology used for linings is combining steel ribs around the circumference of the excavated tunnel placed at a certain interval with e.g. sprayed concrete. The gap between steel ribs should be suitably wedged to prevent excessive deformation, e.g. with steel bar meshes. Segmental linings use a number of prefabricated interlocking structural blocks for creating the continuous lining surface, which can be connected with dowels or bolts, or without a physical connection. Segmental linings are typically used in soft ground conditions, and can constitute both permanent or temporary linings. This is the typical solution used when tunnel boring machines (TBM) are used for excavating and immediately erecting the tunnel. Prefabricated blocks can be made up of unreinforced concrete, steel or fiber RC, steel, or even spheroidal graphite cast iron. Another alternative technology for lining erection is the traditional cast in situ method, typically used in self-supporting rock conditions, or used as a secondary lining layer when a temporary lining is stabilizing the excavated tunnel.

A complete risk analysis of road tunnels involves several parameters and careful evaluations. At least the following aspects should be considered: traffic conditions, management procedures, surroundings, structural plant equipment, and the structural elements. The nowadays diagnosis paradigm for the health assessment of road tunnels requires an initial knowledge phase based on original drawings and documentation. This foremost step characterizes the declared project requirements, the initial structural testing reports, and the material. This information is usually combined with the results of periodical visual inspections to know the actual as-built state. Periodic direct testing of specimens (e.g. concrete core drilling) is a reliable

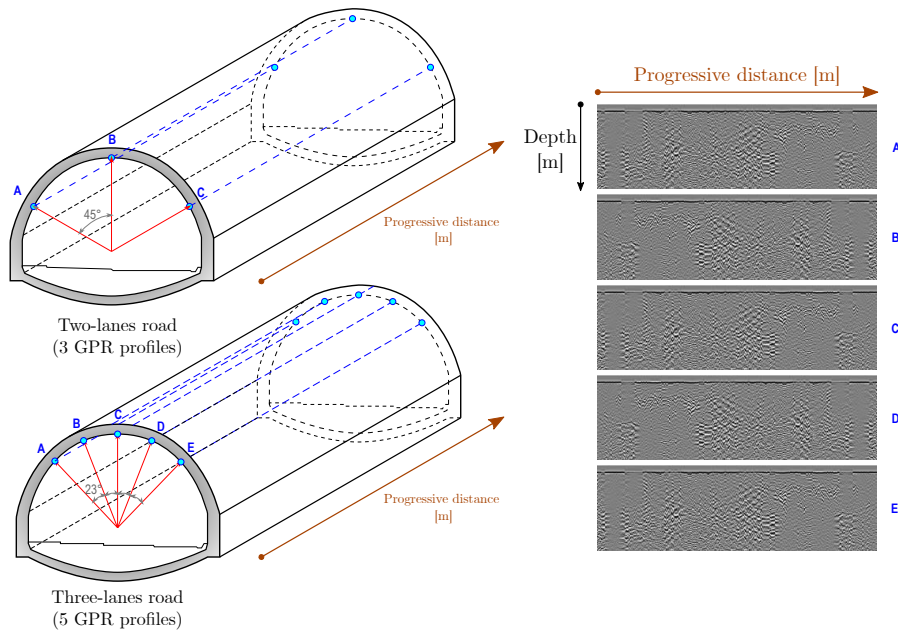


Figure 4.3: Illustration of the typically surveyed GPR tunnel lining profiles for different tunnel’s widths (different number of road lanes).

solution to directly assess the quality, mechanical properties, and temporal changes of the in-situ constitutive structural materials. However, these tests provide punctual, albeit detailed, information, which does not always reflect the actual state of the entire structure [229]. Moreover, the overall involved direct testing procedures are often lengthy and costly. Therefore, to increase the productivity and quickness of periodical inspections, NDE/NDT have become more prominent, reliable, and adopted methods. Focusing on SHM for road tunnels structures [230], some of the most adopted NDT techniques are e.g. rebound hammer testing, rebar scanning with pachometer device, ultrasonic pulse testing, AE passive monitoring for micro-cracks detection, concrete resistivity, thermal imaging thermography with infrared cameras, laser scanner and lidar devices to monitoring tunnel linings deformations. During the current Ph.D. program, research on DD for tunnel linings predominantly focused on indirect testing with ground penetrating radar (GPR) devices for concrete linings flaws detection and annotation [231], even if, in the literature, GPR was often adopted in the past to reveal tunnel lining concrete layer thickness only. The contents herein reported in the current section are taken from [59, 226], and the interested reader can refer to them for further deeper insights.

Similarly to other geophysical methods, the GPR device probes the tunnel linings by propagating high-frequency electromagnetic wave impulses (10-2600 MHz) and analyzing the reflected signals. The impulses’ penetration level or reflection rate depends on the dielectric features of the inspected material and the possible

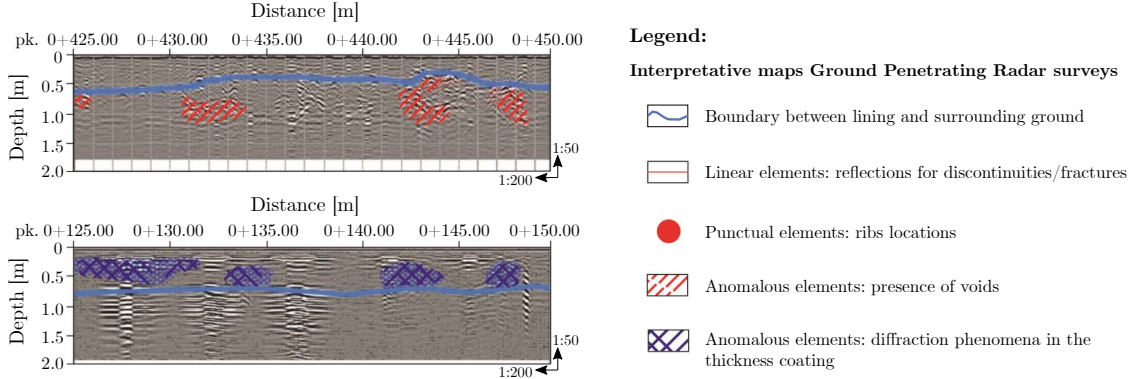


Figure 4.4: Human interpretation of GPR tunnel lining profiles' defects.

presence of certain agents (e.g. water, reinforcement bars, the interface between concrete linings and surrounding ground, linings defects). The architecture of a GPR system is composed of emitting and receiver units, a single or dual frequency antenna, display, control, and storage unit. The GPR provides images as output named profiles, where the abscissa represents the progressive distance from the beginning of the probing (i.e. progressive kilometer, pk, from the beginning of the tunnel), whereas the ordinate axis represents the GPR examined lining depth. Three profiles are usually inspected with two-lane roads to characterize the single tunnel better. In contrast, five profiles are generally examined for three-lane roads, as illustrated in Fig. 4.3. As depicted in Fig. 4.4, in a traditional GPR indirect testing pipeline, specialist staff decodes linings defects from the surveyed profiles with a manual, lengthy and costly post-processing phase [232]. To improve the efficiency, reliability, and productivity of the traditional GPR monitoring process, AI and DL offer innovative tools to accomplish the above-mentioned task by leveraging computer vision and image processing-based methods. Therefore, a novel hierarchical multi-level road tunnel linings defects classification scheme has been herein proposed. This scheme formalization was effective for implementing a DL-based automatic flaws classification task, improving the efficiency, reliability, and productivity of the traditional GPR monitoring process, besides overcoming the actual existing limitations of the traditional manual GPR profiles interpretation. The dataset herein adopted is based on a series of NDT campaigns conducted on several tunnel linings with the GPR device, as illustrated in Fig. 4.5. The data have been collected on tunnels spread throughout Italy, whose construction era is between the 1960s and 1980s. To provide a proper dataset to feed a subsequent DL classifier, some basic data preparations were needed after collecting GPR profiles. Firstly, every long output image generated by the GPR testing was interpreted by specialist staff to decode linings defects as the current traditional GPR post-processing workflow [232]. The long images were subsequently cropped with constant pixels

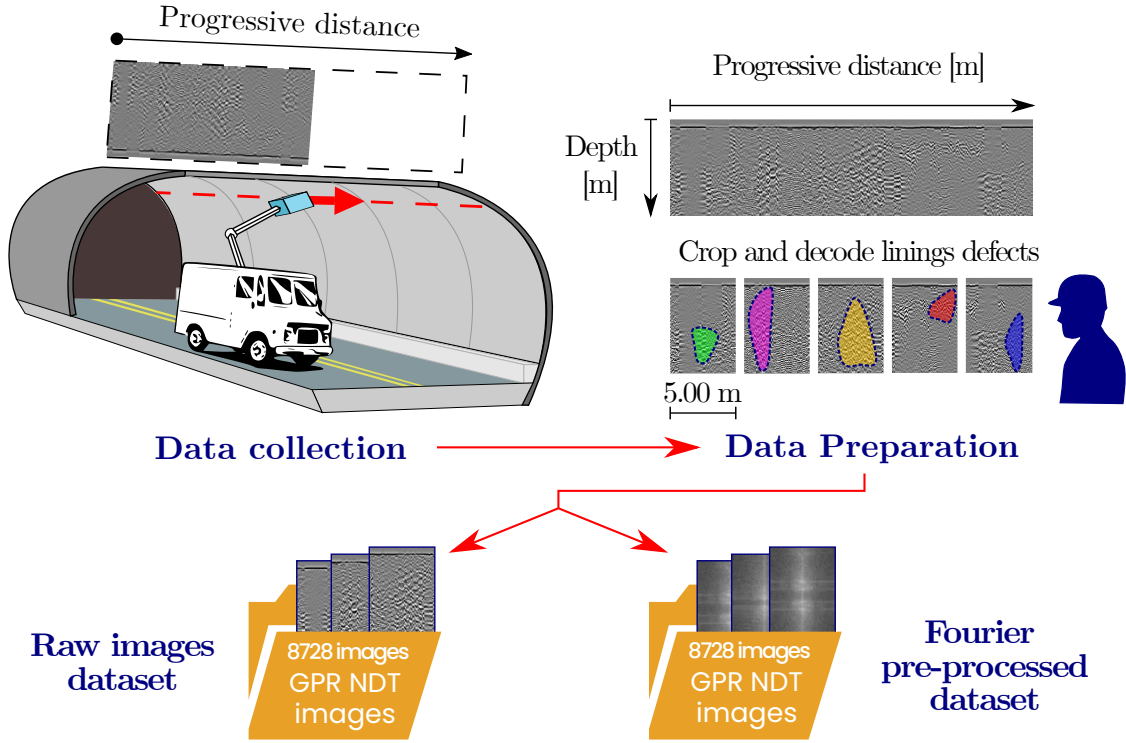


Figure 4.5: Data collection, preliminary preparations and the final obtained dataset with and without Fourier pre-processing.

step along the abscissa, which represents the progressive distance from the beginning to the end of the tunnel lining profile. This constant pixels step was calibrated in order to provide that each image sample width generally corresponds to about five meters on the real scale length of the tunnel progressive distance. However, in order to avoid some defects that were only placed across the cropping line and consequently end up on different images, the cropping line was occasionally manually adjusted. This latter operation was done on occasion with the minimum invasive intervention, providing a new defect-centered sample image, acting as a sort of local data augmentation. Nevertheless, all the sample images will be subjected to a resizing operation to homogeneously feed the DL models always with the same resolution images. In this way, a total number of 8728 GPR sample images were obtained for the subsequent innovative AI-based paradigm based on DL tunnel lining defects hierarchical classifiers. To develop this automatic DL-based classification, a hierarchical classification tree has been defined as represented in Fig. 4.6. It is based on a classification pattern in which a single defect may be classified, adopting a binary approach at each node of the hierarchical graph. This method resembles the human expert’s mental process while recognizing and classifying each defect in the GPR profile. In total, 14 classes have been considered, denoted as C_i

with $i = 1, 2, \dots, 14$, spread over 6 main levels: Level 1 (C1, C2 folders), Level 2a (C3, C4 folders), Level 2b (C5, C6 folders), Level 3 (C7, C8 folders), Level 4 (C9, C10 folders), Level 5 (C11, C12 folders), and Level 6 (C13, C14 folders). Level 1 is devoted to locating the completely healthy samples (C1) from the ones with generic flaws (C2). Level 2a deals with healthy samples (C3) to potentially locate the ones with the presence of reinforcement bars (C4), characterized by distinctive narrow hyperbolas patterns. Level 2b, performs an initial defects classification by a generic warning mix (C5) which may not easily be categorized from other more specific flaws (C6). The class C6 is further analyzed to locate cracks (C7) in level 3 from other flaws (C8). This latter is further investigated in level 4, to characterize the anomalies in the concrete linings (C9) from the voids defects (C10). In level 5, a more detailed classification provides the image categorization with simple voids (C11) from the others (C12). Finally, this latter class is further analyzed in level 6 to categorize the excavation problems (C13) and the concrete-rock detachments issues (C14). Therefore, seven DL classification models have been trained and tested to accomplish the GPR tunnel defects classification tasks for SHM purposes.

Furthermore, as illustrated in Fig. 4.5, for the sake of completeness, in an attempt to improve the current basic technique, a preprocessing phase has been performed, adopting the bi-dimensional Fourier transform to the GPR sample images. The generality of the Fourier analysis provides the ability to analyze and decompose also higher dimensional signals. Any digital image can be interpreted as a discrete ordered spatial bi-dimensional distribution of tensors of pixels [233]. Considering a digital image in the spatial domain A of size $n \times m$ with components a_{rs} , with $0 \leq r \leq n - 1$, $0 \leq s \leq m - 1$, the bi-dimensional discrete Fourier transform (2D-DFT) is a matrix F in the Fourier domain of size $n \times m$ with components [234]:

$$f(k, l) = \sum_{r=0}^{n-1} \sum_{s=0}^{m-1} a(r, s) e^{-2\pi i (\frac{kr}{m} + \frac{ls}{n})} \quad (4.3)$$

where: $0 \leq k \leq n - 1$, $0 \leq l \leq m - 1$. Consequently, the 2D-DFT provides a new representation of the digital image as a double sum of the products of the input spatial image and the sinusoidal basis waveform. The average brightness of the input image is summarized by the DC component $f(0,0)$ in the Fourier domain [235]. On the other hand, the last realization $f(n - 1, m - 1)$ corresponds to the highest retrievable frequency component according to the Nyquist-Shannon theorem [235]. The inverse mapping is carried out through the bi-dimensional discrete Fourier transform (2D-IDFT):

$$a(r, s) = \frac{1}{n \cdot m} \sum_{k=0}^{n-1} \sum_{l=0}^{m-1} f(k, l) e^{2\pi i (\frac{kr}{m} + \frac{ls}{n})} \quad (4.4)$$

The outcomes of digital image Fourier analysis are assembled into a complex matrix, whose components are usually expressed in terms of phase ($\phi_{k,l}$) and modulus

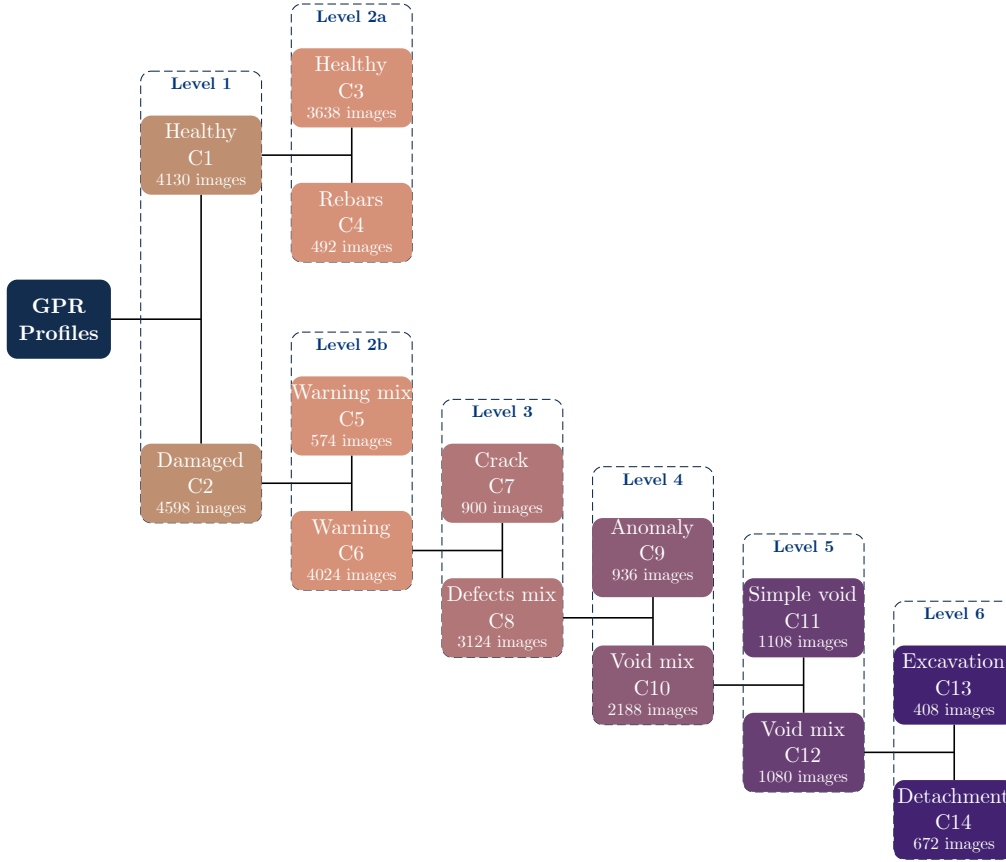


Figure 4.6: Hierarchical framework for the multi-level tunnel defects GPR profiles classification.

magnitude ($M_{k,l}$). Since, this latter assumes extremely dispersed values of several orders of magnitude, the following logarithmic manipulation is employed:

$$\tilde{f}(k, l) = c \cdot \log(1 + |M_{k,l}|) \quad (4.5)$$

in which

$$M_{k,l} = \sqrt{\Re(f(k, l))^2 + \Im(f(k, l))^2} \quad (4.6)$$

The factor c of equation (4.5) is a scale parameter, set the to unity in the present study. Since in many practical applications, the phase $\phi_{k,l}$ is apparently useless, only the information contained in the magnitude is often retained. However, to guarantee a successful inverse 2D-IDFT mapping, this information is mandatory to avoid a corrupted image [235]. Computing the 2D-DFT as a series of $2 \cdot n$ one-dimensional DFTs considerably helped to save computational effort leading to an overall complexity of $O(N^2)$ [235], being N the number of operations to compute computational complexity. To further improve the convergence speed of discrete bi-dimensional signals Fourier analyses, the efficient fast Fourier transform (2D-FFT)

algorithm drastically reduces the computational complexity to $O(N \cdot \log_2(N))$ [235].

The DL models denoted as CNN are essentially based on convolution, correlation, and in general filtering operations. A thorough understating of these operations within Fourier analysis of digital images revealed the possible advantages of adopting the bi-dimensional Fourier pre-processing technique. The convolution theorem states that convolving two functions $h(t) * x(t)$ in the input (time or spatial) domain, this becomes a simple product in the Fourier domain:

$$h(t) * x(t) = \int_{-\infty}^{+\infty} x(\tau)h(t - \tau)d\tau \Leftrightarrow H(\omega)X(\omega) \quad (4.7)$$

Since the correlation operation is closely related to the convolutional one, a correlation theorem holds:

$$\int_{-\infty}^{+\infty} x(\tau)h(t + \tau)d\tau \Leftrightarrow H(\omega)X^*(\omega) \quad (4.8)$$

being X^* the transform complex conjugate of $x(t)$. The convolution operation is employed for image filtering [235], e.g. to detect edges, smoothing operations, etc. Digital filter kernel transfer function $h(r, s)$ correlates with the image $a(r, s)$ on a certain receptive field:

$$g(r, s) = h(r, s) * a(r, s) \quad (4.9)$$

For the duality property, the convolution operation is substantially a correlation in which the filter mask is rotated with a straight angle, i.e. using a flipped kernel $h(-r, -s)$. Fundamentally, since the CNNs make extensive use of the discrete convolution operations during the initial feature extraction part, the prior adoption of the bi-dimensional Fourier analysis as an image pre-processing technique may provide a more efficient convolution operation. As a matter of fact, the Fourier domain mapping delivers a synthesized and more compact version of the information contained in the original image, as illustrated in Fig. 4.7. On the contrary, a possible drawback may virtually be excessive information compression, which delivers overly similar images, thus threatening the global accuracy of a data-driven classifier. Moreover, since the Fourier domain enhances the components with the higher frequency content, the Fourier pre-processing method permits actually removing the periodic and non-periodic noise or disturbance patterns in the GPR profiles, which are inherent in the heterogeneous reflectivity properties of the inspected material mean with GPR tool.

Therefore, the hierarchical multi-level tunnel lining flaws automatic classification have been trained adopting four DL models, as depicted in Fig. 4.8 for the sake of a more complete classification performance evaluation and a mutual validation purpose of the generalization capabilities. Another main goal of this investigation was to compare the effects on the classification performances of the four DL analyzed models with and without a prior pre-processing phase of the

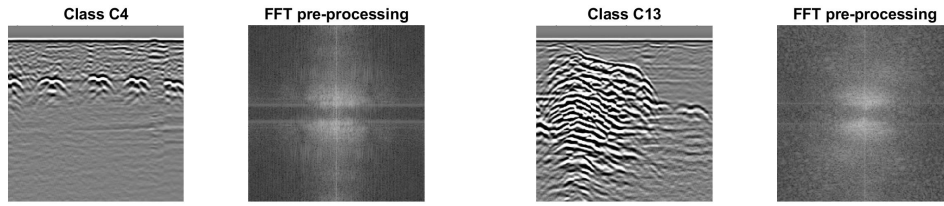


Figure 4.7: Resulting magnitude pre-processed images with bi-dimensional Fourier transform of two samples belonging to class C4 (reinforcement bars) and C13 (excavation) respectively.

GPR image dataset through the bi-dimensional Fourier transform. Two state-of-art convolutional architectures have been compared, i.e. ResNet-50 model [236] and the EfficientNet-B0 model [237]. On the other hand, two state-of-art transformer models in the version suited for working with image data, i.e. Vision Transformer (ViT) [238] and Compact Convolutional Transformer (CCT) [239] have been herein adopted. The chosen hyperparameters reported in Fig. 4.8 for every analyzed DL model have been obtained by a trial-and-error approach to achieving the best possible results [59, 226]. A brief description of the four DL adopted models is detailed below.

The ResNet-50 architecture was developed in 2015 by He et al. [236] and it is pre-trained on the ImageNet Large Scale Visual Recognition Challenge (ILSVRC) dataset. The main feature of the ResNet model is the presence of skip or residual connections, see Chapter 1 section 1.2.2. ResNet-50 is composed of 50 layers (only counting the convolutional layers and the fully connected layers). It comprises a stack of residual units, each composed of two convolutional layers, without pooling layers, batch normalization, and rectified linear unit (ReLU) activation function, using 3x3 kernels with stride 1. Input images are 224x224x3 tensors, considering the common RGB for coloured image codification. The initial pre-trained ResNet-50 was able to classify images into 1000 different object categories, but the final fully connected layer has been modified to accomplish the binary classification tasks for each hierarchical level presented in Fig. 4.6. Since every level of the hierarchical classification tree presents an unbalanced number of images, to train a good classification model, the class forced a balanced approach with the minimum number of samples.

Firstly presented in 2019 [237], EfficientNet model effectively incorporated multiple techniques and previous existing strategies in an innovative way. A still ongoing widespread methodology to achieve the best accuracy results and contain the required computational effort in CNN is the depth network scaling, i.e. varying the number of layers. Depth network scaling means varying the number of layers. For instance, the ResNet-152 base model was initially developed with 152 layers, and then it was scaled to other variants such as ResNet-50, using 50 layers only.

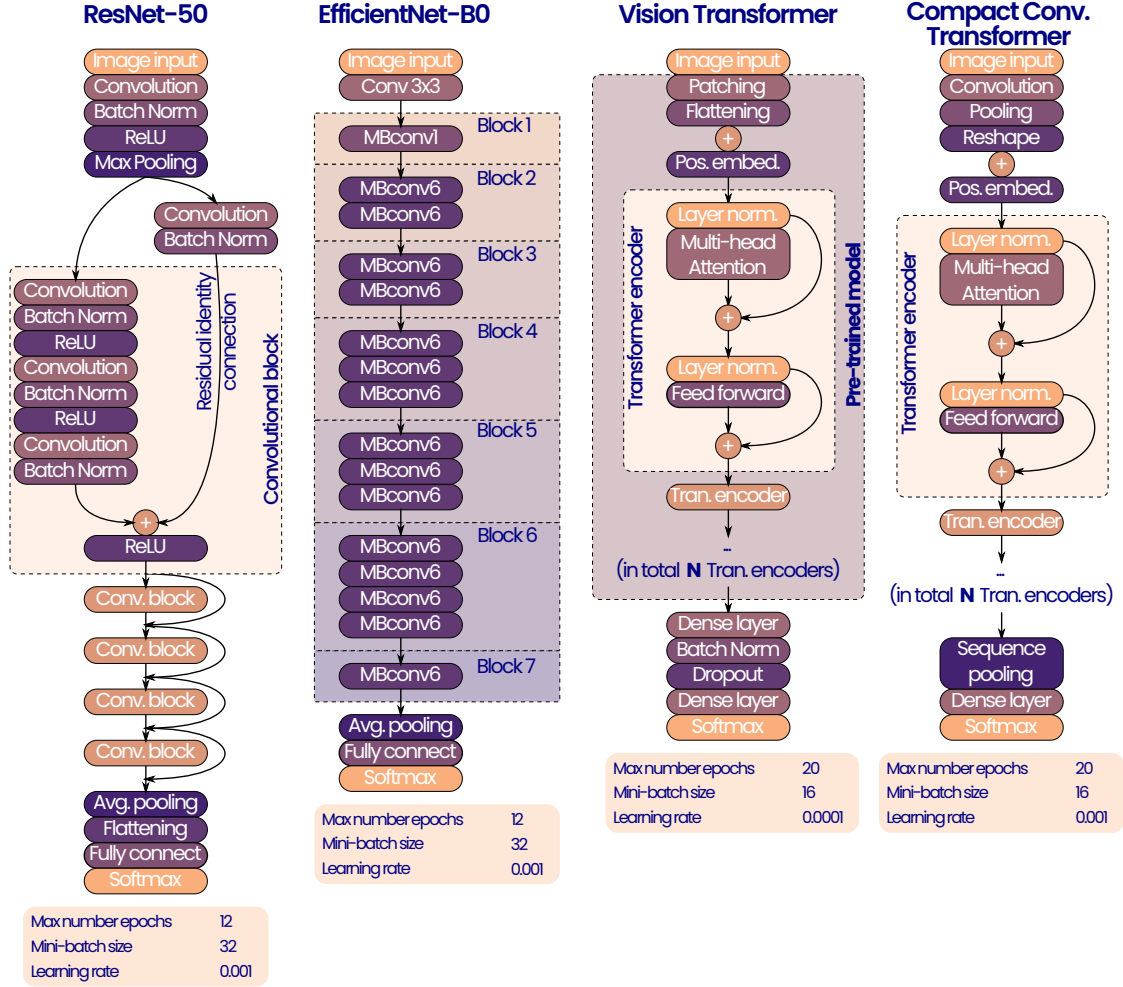


Figure 4.8: Illustrative representation of the neural models with hyperparameters herein adopted.

Moreover, scaling up CNN models means enlarging the receptive field of convolutional layers. Alternative possible scaling approaches that aim to capture more fine-grained features are width scaling, i.e. varying the number of channels, especially for smaller models, or even scaling the input image resolution. In [237], it was noticed that the different scaling dimensions are not completely independent, and the best models were obtained by a compound scaling method, i.e. uniformly scaling and balancing simultaneously both depth, width, and image resolution according to constant scaling factors. Herein adopted EfficientNet-B0 relies on 7 building blocks which employs the inverted residual blocks of mobile inverted bottleneck convolutional building blocks (MobileNetV2) [237], resulting in a less connected network than ResNet models. Indeed, the residual shortcuts connect only those layers in which the number of inputs and outputs are the same.

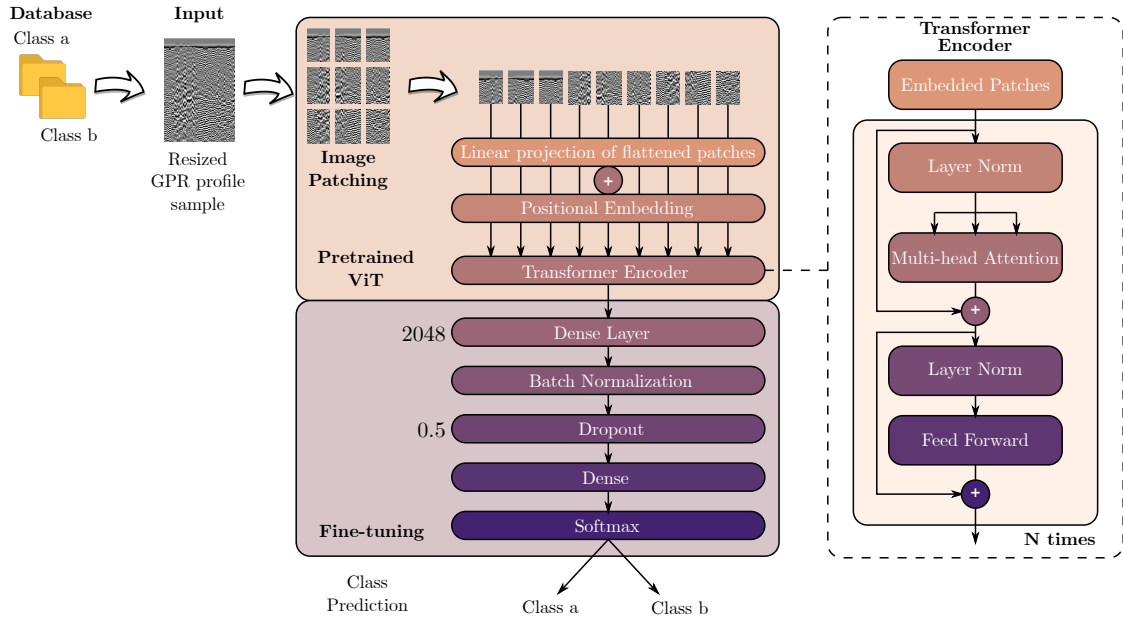


Figure 4.9: ViT-L16 model architecture visualization, highlighting the pre-trained part and the fine-tuned part.

Neural transformers in 2017 echoed as a revolution in DL, with their first applications to Natural Language Processing (NLP) tasks [91]. This DL architecture was born to overcome the problematic of dealing with long data sequences with DL. Its main peculiarity is the total confidence into the self-attention mechanism, which provides the network with short and even very long-range relationships among every element with the others composing the data sequence. With this hidden information, the network can extract deep knowledge from data and produce noticeably promising results for machine learning tasks, e.g. classification problems. Moreover, due to their nature, every block of the transformer may be parallelized to improve computational efficiency. However, since these models are remarkably computational demanding due to the massive number of learnable parameters, it is not easy to train a transformer from scratch without possessing a considerably extended dataset and allocating computational resources for days or, more probably, for weeks. For this reason, transfer learning approaches have proved to be the most promising way to exploit them effectively. Recently, impactful and fruitful studies have been conducted, such as, e.g., the introduction of Bidirectional Encoder Representations from Transformers (BERT) model which exploits only the encoder part of the transformers, or the adaptation of neural transformers to deal with images data types. In 2020, in [238], a novel architecture to deal with image data, i.e. the Vision Transformer (ViT), was released. ViT is based solely on the neural transformer architecture’s encoder network part, similarly to the BERT model for natural language processing [91]. The model architecture of the ViT adopted for

the current automatic defects classification for road tunnel GPR indirect testing is depicted in Fig. 4.9. To deal with image data, it was necessary to rethink the image data as a sequence of data. This was realized by producing a partitioning of the input image, which is subdivided into a finite number n of patches. These patches may overlap or not, and each one is a tensor with shape $d_1 \times d_2 \times d_3$, this latter corresponding to the RGB digital colored image encoding. However, it is always required to define an exact and suitable finite number n of resulting patches considering the resolution of the starting image. To treat these patches as an ordered sequence of elements, a vectorization procedure involves each i -th patch provide a column vector \mathbf{x}_i , with $i = 1, 2, \dots, n$, of dimension $d_1 d_2 d_3 \times 1$, resulting at the end into n vectors. These vectors of flattened patches are fed into a dense layer with shared parameters and linear activation function, producing the hidden embedded representation typical of the transformer architectures denoted as \mathbf{z}_i . The shared weights of this dense layer, which are learned from training data during the training phase, act as the flattening operation using a linear projection matrix [238]. Since in a sequence, the comparison ordering is extremely important, to maintain the information of the actual position of each patch within the initial image, a positional encoding [91] should be applied. The positional encoding is usually referred to sine and cosine functions at high frequency, which adds spatial information into the network. Then, they are simply summed to the embedding representations \mathbf{z}_i . In this way, the new representation of the input information \mathbf{z}_i captures both the content and the position of the i -th patch. Similar to BERT-based architecture, the ViT relies only on the transformer encoder block, which is repeated N times, and the current transformer encoder block is repeated $N = 16$ times denoting name ViT-L16 model. However, in order to accomplish the classification task, BERT introduced an additional token denoted as [CLASS] token. Similarly, also in the ViT model, the [CLASS] token for classification is fed to an embedding layer producing the vector \mathbf{z}_0 of the same shape as other embeddings. The sequence of vectors $\{\mathbf{z}_i\}_{i=0}^n$ are subsequently fed to the neural transformer encoder block, composed of a stack of a multi-head self-attention and dense fully-connected layer blocks, actually employing normalization and skip connections, as depicted in detail in Fig. 4.9. The output of the neural transformer encoder is a new representation of the input vectors $\{\mathbf{z}_i\}_{i=0}^n$ mapped to a new representations $\{\mathbf{c}_i\}_{i=0}^n$ which integrates the scaled dot-product attention (the self-attention) [91]. In any case, only the \mathbf{c}_0 is considered for the classification task, the one referred to the [CLASS] token, and the others may usually be neglected. This vector represents the feature vector from the input image. This vector is thus normally fed to a final multi-layer perceptron followed by a softmax classifier. This last layer results in a column vector \mathbf{p} of size equal to the number of output classes, representing a probability to belong to each output class.

The last herein DL adopted model is the Compact Convolutional Transformer (CCT). This model was developed in [239], starting from the baseline model of ViT

and introducing some substantial modifications. In literature, the transformers deserved the title of data-hungry models because of their main drawback of almost prohibitive computational effort for training from scratch in applications with a limited dataset size. Therefore, the CCT model was developed to alleviate this issue. In CCT, a convolutional tokenization procedure has been set in place of the ViT patching method. In this way, it is no more strictly required to set the specific image resolution size and an appropriate and arbitrary fixed number of patches. Adopting the right number of conventional convolutional blocks, it is possible to realize an embedding input to properly feed the subsequent transformer encoder blocks. This procedure is expected to provide a more efficient compact image embedding representation [239]. Indeed, on one side, this new embedding process reflects the desirable properties of CNNs, i.e. hierarchical feature extractor with local information preservation, weight sharing, and efficiency. On the other hand, the CCT permits the adoption of the powerful framework of the self-attention mechanism to process long-range and global dependencies. Another key difference between CCT and ViT is related to the dropping of the BERT-based class token while promoting a sequence pooling approach. This latter method leverages the information of the entire scored output sequence and it does not refer only to a single class token as in the ViT. The sequence pooling method helped to enhance the efficiency of the final dense layers accountable for the classification task [239]. The herein CCT model architecture is composed of two convolutional layers and $N = 2$ number of transformer encoder blocks.

The current implementations for CNNs architectures were trained in Matlab environment, whereas neural transformers relies on the implementations provided in the Keras python environment [240]. The GPR images dataset at every level of hierarchical multi-class classification tree have been split with a proportion of 80% for the training set and 20% for the test set for the CNN-based models, and adopting the k-fold cross-validation method with $k = 10$ folds, representing a good choice to avoid both significant variance and biased values. Conversely, due to the greater computational time when dealing with the transformer-based models, this time the splitting has been set equal to 90%-10% respectively for training and test set without performing any cross-validation.

Tab. 4.1 reports the confusion matrices of the averaged classification results expressed in percentages for the models trained with the raw GPR samples dataset. The table also illustrates the level of overall accuracy values and the class metrics precision, recall, and f1-score. It is worth noting that every level has revealed a good accuracy above 90% in all the cases, reaching a peak of 98.30% in level 5 and a minimum value of 90.40% in level 2b. Averaging all the levels of accuracy, the ResNet-50 model trained with the raw dataset, i.e. without any Fourier pre-processing, reached a global classification accuracy of 94.51%. On the other hand, Tab. 4.2 reports the confusion matrices of the averaged classification results expressed in percentages

Table 4.1: Confusion matrices and classification metrics for ResNet-50 model trained with raw image data.

Level 1	Predicted		Accuracy	92.60%		
True	C1	C2	Class	Precision	Recall	f1-score
C1	93.30%	6.70%	C1	92.01%	93.30%	92.65%
C2	8.10%	91.90%	C2	93.20%	91.90%	92.55%
Level 2a	Predicted		Accuracy	97.25%		
True	C3	C4	Class	Precision	Recall	f1-score
C3	98.40%	1.60%	C3	96.19%	98.40%	97.28%
C4	3.90%	96.10%	C4	98.36%	96.10%	97.22%
Level 2b	Predicted		Accuracy	90.40%		
True	C5	C6	Class	Precision	Recall	f1-score
C5	90.90%	9.10%	C5	90.00%	90.90%	90.45%
C6	10.10%	89.90%	C6	90.81%	89.90%	90.35%
Level 3	Predicted		Accuracy	95.90%		
True	C7	C8	Class	Precision	Recall	f1-score
C7	92.70%	7.30%	C7	99.04%	92.70%	95.76%
C8	0.90%	99.10%	C8	93.14%	99.10%	96.03%
Level 4	Predicted		Accuracy	91.80%		
True	C9	C10	Class	Precision	Recall	f1-score
C9	94.90%	5.10%	C9	89.36%	94.90%	92.05%
C10	11.30%	88.70%	C10	94.56%	88.70%	91.54%
Level 5	Predicted		Accuracy	98.30%		
True	C11	C12	Class	Precision	Recall	f1-score
C11	98.80%	1.20%	C11	97.82%	98.80%	98.31%
C12	2.20%	97.80%	C12	98.79%	97.80%	98.29%
Level 6	Predicted		Accuracy	95.35%		
True	C13	C14	Class	Precision	Recall	f1-score
C13	96.60%	3.40%	C13	94.24%	96.60%	95.41%
C14	5.90%	94.10%	C14	96.51%	94.10%	95.29%

for the models trained with the bi-dimensional Fourier pre-processed GPR samples dataset. In this circumstance, level 2b stands out for its worst accuracy value stacked to 76.30%. However, in the other levels, the ResNet-50 has revealed a good accuracy above 85% in virtually all the cases, reaching a peak value of 90.55% in level 6. Averaging all the levels of accuracies, the ResNet-50 model trained with the bi-dimensional Fourier pre-processed dataset reached a global classification accuracy of 85.60%, about 8.91% below the global accuracy of the ResNet-50 model trained with the raw dataset. These results demonstrated that, notwithstanding the envisaged advantages of adopting the Fourier pre-processing technique on the GPR sample images for the convolution operation, the ResNet-50 model is not able to reach the accuracy levels of the previous case, i.e. trained with the raw GPR dataset. Downstream of the obtained results, it is reasonable supposing that the Fourier pre-processing probably introduced an exaggerated information compression, thus providing too similar images with such detrimental effects on the classification accuracy. In an effort to demonstrate the contingent presence of overfitting during the training phase of all the ResNet-50 trained models with and without the Fourier pre-processed dataset, the convergence curves have been reported in the Appendix B.1. These graphs show the trend of the loss, the accuracy, the validation loss, and the validation accuracy during the training epochs or iterations. Since each

Table 4.2: Confusion matrices and classification metrics for ResNet-50 model trained with bi-dimensional Fourier pre-processed image data.

Level 1	Predicted		Accuracy	88.25%		
True	C1	C2	Class	Precision	Recall	f1-score
C1	87.90%	12.10%	C1	88.52%	87.90%	88.21%
C2	11.40%	88.60%	C2	87.98%	88.60%	88.29%
Level 2a	Predicted		Accuracy	83.15%		
True	C3	C4	Class	Precision	Recall	f1-score
C3	79.30%	20.70%	C3	85.92%	79.30%	82.48%
C4	13.00%	87.00%	C4	80.78%	87.00%	83.77%
Level 2b	Predicted		Accuracy	76.30%		
True	C5	C6	Class	Precision	Recall	f1-score
C5	73.50%	26.50%	C5	77.86%	73.50%	75.62%
C6	20.90%	79.10%	C6	74.91%	79.10%	76.95%
Level 3	Predicted		Accuracy	85.90%		
True	C7	C8	Class	Precision	Recall	f1-score
C7	97.80%	22.00%	C7	91.57%	81.64%	86.32%
C8	9.00%	91.00%	C8	80.53%	91.00%	85.45%
Level 4	Predicted		Accuracy	85.15%		
True	C9	C10	Class	Precision	Recall	f1-score
C9	83.90%	16.10%	C9	86.05%	83.90%	84.96%
C10	13.60%	86.40%	C10	84.29%	86.40%	85.33%
Level 5	Predicted		Accuracy	89.90%		
True	C11	C12	Class	Precision	Recall	f1-score
C11	85.70%	14.30%	C11	93.56%	85.70%	89.46%
C12	5.90%	94.10%	C12	86.81%	94.10%	90.31%
Level 6	Predicted		Accuracy	90.55%		
True	C13	C14	Class	Precision	Recall	f1-score
C13	92.40%	7.60%	C13	89.10%	92.40%	90.72%
C14	11.30%	88.70%	C14	92.11%	88.70%	90.37%

level accounts for 10 different trained models because of the k-fold cross-validation procedure, the average curves have been depicted among the 10 considered models. However, for the purpose of not losing the variability information among the ten different models, the shaded area around the average curve represents the envelope among the maximum and minimum curves among the 10 considered models. Excluding level 1 in which a slightly increasing trend of the average validation loss manifests around iteration 400, the ResNet-50 with raw dataset presents a comprehensive excellent behavior without any evidence of overfitting issues. Concerning the convergence curves of the ResNet-50 model with Fourier pre-processed GPR images dataset, a noticeable overfitting problem is evidenced in the level 2b from iteration around 50, thus explaining the poor classification accuracy of that level, as illustrated in table 4.2. Moreover, slightly overfitting phenomena are tangible in levels 1 from iteration around 400 and level 4 from iteration around 80.

Tab. 4.3 reports the confusion matrices of the averaged classification results expressed in percentages of the EfficientNet-B0 models trained with the raw GPR samples dataset for each binary classification level of Fig. 4.6. As before, the table also illustrates the level of overall accuracies and the class metrics precision, recall, and f1-score. It is worth noting that every level has revealed a fairly good accuracy above 90% in virtually all the cases, except for level 2b in which the worst value of

Table 4.3: Confusion matrices and classification metrics for EfficientNet model trained with raw image data.

Level 1	Predicted		Accuracy	94.55%		
True	C1	C2	Class	Precision	Recall	f1-score
C1	95.50%	4.50%	C1	93.73%	95.50%	94.60%
C2	6.39%	93.61%	C2	95.41%	93.61%	94.50%
Level 2a	Predicted		Accuracy	91.07%		
True	C3	C4	Class	Precision	Recall	f1-score
C3	89.24%	10.76%	C3	92.63%	89.24%	90.91%
C4	7.10%	92.90%	C4	89.62%	92.90%	91.23%
Level 2b	Predicted		Accuracy	81.01%		
True	C5	C6	Class	Precision	Recall	f1-score
C5	81.71%	18.29%	C5	80.58%	81.71%	81.14%
C6	19.69%	80.31%	C6	81.45%	80.31%	80.87%
Level 3	Predicted		Accuracy	94.94%		
True	C7	C8	Class	Precision	Recall	f1-score
C7	99.00%	1.00%	C7	91.57%	99.00%	95.14%
C8	9.11%	90.89%	C8	98.91%	90.89%	94.73%
Level 4	Predicted		Accuracy	90.70%		
True	C9	C10	Class	Precision	Recall	f1-score
C9	88.56%	11.44%	C9	92.52%	88.56%	90.50%
C10	7.16%	92.84%	C10	89.03%	92.84%	90.90%
Level 5	Predicted		Accuracy	93.47%		
True	C11	C12	Class	Precision	Recall	f1-score
C11	90.65%	9.35%	C11	96.07%	90.65%	93.28%
C12	3.70%	96.30%	C12	91.15%	96.30%	93.65%
Level 6	Predicted		Accuracy	96.08%		
True	C13	C14	Class	Precision	Recall	f1-score
C13	96.33%	3.67%	C13	95.85%	96.33%	96.09%
C14	4.17%	95.83%	C14	96.31%	95.83%	96.07%

81.01% is reported. Level 2b was likewise observed with the lowest accuracy also for The ResNet-50 model. On the contrary, the best accuracy of 96.08% was obtained in level 6. Averaging all the levels of accuracies, the EfficientNet-B0 model trained with the raw dataset, i.e. without any Fourier pre-processing, reached a global classification accuracy of 91.69%. Conversely, Tab. 4.4 reports the confusion matrices of the averaged classification results expressed in percentages for the EfficientNet-B0 models trained with the bi-dimensional Fourier pre-processed GPR samples dataset. In the present case, level 2b pointed out, once again, the worst accuracy value stacked to 73.87%, i.e. 7.14% below than the counterpart EfficientNet-B0 trained with the raw dataset. However, in the other levels, the EfficientNet-B0 has revealed a good accuracy above 80% in virtually all the cases, except for level 2b, with an average reduction of 5.75% with respect to the counterpart EfficientNet-B0 trained with the raw dataset. The maximum accuracy value of 93.06% was realized in level 3. Averaging all the levels of accuracies, the EfficientNet-B0 model trained with the bi-dimensional Fourier pre-processed dataset reached a global classification accuracy of 85.94%, about 5.75% below the global accuracy of the same models trained with the raw dataset. Even in these circumstances, the obtained results proved that the bi-dimensional Fourier pre-processing provided detrimental effects

Table 4.4: Confusion matrices and classification metrics for EfficientNet model trained with bi-dimensional Fourier pre-processed image data.

Level 1	Predicted		Accuracy	87.43%		
True	C1	C2	Class	Precision	Recall	f1-score
C1	87.65%	12.35%	C1	87.27%	87.65%	87.46%
C2	12.78%	87.22%	C2	87.60%	87.22%	87.41%
Level 2a	Predicted		Accuracy	84.15%		
True	C3	C4	Class	Precision	Recall	f1-score
C3	82.75%	17.25%	C3	85.14%	82.75%	83.93%
C4	14.44%	85.56%	C4	83.22%	85.56%	84.37%
Level 2b	Predicted		Accuracy	73.87%		
True	C5	C6	Class	Precision	Recall	f1-score
C5	72.47%	27.53%	C5	74.55%	72.47%	73.50%
C6	24.73%	75.27%	C6	73.22%	75.27%	74.23%
Level 3	Predicted		Accuracy	93.06%		
True	C7	C8	Class	Precision	Recall	f1-score
C7	98.78%	1.22%	C7	88.63%	98.78%	93.43%
C8	12.67%	87.33%	C8	98.62%	87.33%	92.63%
Level 4	Predicted		Accuracy	0.8215		
True	C9	C10	Class	Precision	Recall	f1-score
C9	81.95%	18.05%	C9	82.29%	81.95%	82.12%
C10	17.64%	82.36%	C10	82.02%	82.36%	82.19%
Level 5	Predicted		Accuracy	88.66%		
True	C11	C12	Class	Precision	Recall	f1-score
C11	83.70%	16.30%	C11	92.91%	83.70%	88.07%
C12	6.39%	93.61%	C12	85.17%	93.61%	89.19%
Level 6	Predicted		Accuracy	92.28%		
True	C13	C14	Class	Precision	Recall	f1-score
C13	94.85%	5.15%	C13	90.21%	94.85%	92.47%
C14	10.29%	89.71%	C14	94.57%	89.71%	92.07%

in terms of classification accuracy. Both ResNet-50 and EfficientNet-B0 models exhibit a worse classification behavior with the bi-dimensional Fourier pre-processed dataset despite the envisaged beneficial effects in computing the convolution operation. To demonstrate any potential presence of overfitting during the training phase of all the EfficientNet-B0 trained models with and without the Fourier pre-processed dataset, the convergence curves during the training iterations have been reported in the Appendix B.1. Although the EfficientNet-B0 models trained with raw dataset apparently do not manifest any sign of overfitting issue presence, level 2b revealed a barely noticeable slightly increasing trend of the average validation loss manifests around iteration 100. Concerning the convergence curves of the EfficientNet-B0 model with the Fourier pre-processed GPR images dataset, slightly overfitting issues are evidenced in level 1 from iteration around 400, in level 2b from iteration around 80, and in level 4 from iteration around 150.

Tab. 4.5 reports the confusion matrices of the averaged classification results expressed in absolute terms, i.e. the number of samples from the test set of the raw GPR samples dataset which has been predicted for each class. The table illustrates the level of overall accuracies and the class metrics precision, recall, and f1-score. It is worth noting that every level has revealed excellent accuracy results above 94% in all the cases, even reaching a peak value of 100.00% in level 3 and with

Table 4.5: Confusion matrices and classification metrics for ViT model trained with raw image data.

Level 1	Predicted		Accuracy			95.42%		
True	C1	C2	Class	Nr img/class	Test support	Precision	Recall	f1-score
C1	380	21	C1	408	401	95.24%	94.76%	95.00%
C2	19	453	C2	672	472	95.57%	95.97%	95.77%
Level 2a	Predicted		Accuracy			99.03%		
True	C3	C4	Class	Nr img/class	Test support	Precision	Recall	f1-score
C3	359	0	C3	408	359	98.90%	100.00%	99.45%
C4	4	50	C4	672	54	100.00%	92.59%	96.15%
Level 2b	Predicted		Accuracy			94.57%		
True	C5	C6	Class	Nr img/class	Test support	Precision	Recall	f1-score
C5	45	11	C5	408	56	76.27%	80.36%	78.26%
C6	14	390	C6	672	404	97.26%	96.53%	96.89%
Level 3	Predicted		Accuracy			100.00%		
True	C7	C8	Class	Nr img/class	Test support	Precision	Recall	f1-score
C7	95	0	C7	408	95	100.00%	100.00%	100.00%
C8	0	308	C8	672	308	100.00%	100.00%	100.00%
Level 4	Predicted		Accuracy			99.04%		
True	C9	C10	Class	Nr img/class	Test support	Precision	Recall	f1-score
C9	94	2	C9	408	96	98.95%	97.92%	98.43%
C10	1	216	C10	672	217	99.08%	99.54%	99.31%
Level 5	Predicted		Accuracy			99.54%		
True	C11	C12	Class	Nr img/class	Test support	Precision	Recall	f1-score
C11	115	0	C11	408	115	99.14%	100.00%	99.57%
C12	1	103	C12	672	104	100.00%	99.04%	99.52%
Level 6	Predicted		Accuracy			99.07%		
True	C13	C14	Class	Nr img/class	Test support	Precision	Recall	f1-score
C13	52	1	C13	408	53	100.00%	98.11%	99.05%
C14	0	55	C14	672	55	98.21%	100.00%	99.10%

a minimum accuracy value of 95.42% in correspondence of level 2b, just like the worst levels of the above-mentioned convolutional models. Averaging all the levels of accuracies, the ViT model trained with the raw dataset, i.e. without any Fourier pre-processing, reached a global classification accuracy of 98.10%. On the other hand, Tab. 4.6 reports the confusion matrices of the averaged classification results expressed in percentages for the ViT models trained with the bi-dimensional Fourier pre-processed GPR samples dataset. In this case, the worst level is the first one, presenting the worst accuracy value of 86.14%. In the other levels, the ViT has still revealed a good accuracy greater than 90% in virtually all the cases nonetheless, still reaching a noticeable maximum accuracy value of 99.07% in level 6. However, averaging all the levels of accuracies, the ViT model trained with the bi-dimensional Fourier pre-processed dataset reached a less global classification accuracy of 93.65%, with an average reduction of 4.45% with respect to the counterpart ViT trained with the raw dataset. Again, the above-mentioned results demonstrated that, notwithstanding the envisaged advantages of adopting the Fourier pre-processing technique on the GPR sample images, also the ViT model is not able to reach the accuracy levels of the training with the raw GPR dataset. Since ViT is not essentially based on the convolution operation likewise CNNs, the obtained results strengthen the hypothesis of an excessive information compression

Table 4.6: Confusion matrices and classification metrics for ViT model trained with bi-dimensional Fourier pre-processed image data.

Level 1	Predicted		Accuracy					86.14%
True	C1	C2	Class	Nr img/class	Test support	Precision	Recall	f1-score
C1	302	99	C1	408	401	93.21%	75.31%	83.31%
C2	22	450	C2	672	472	81.97%	95.34%	88.15%
Level 2a	Predicted		Accuracy					92.98%
True	C3	C4	Class	Nr img/class	Test support	Precision	Recall	f1-score
C3	358	1	C3	408	359	92.75%	99.72%	96.11%
C4	28	26	C4	672	54	96.30%	48.15%	64.20%
Level 2b	Predicted		Accuracy					90.87%
True	C5	C6	Class	Nr img/class	Test support	Precision	Recall	f1-score
C5	29	27	C5	408	56	65.91%	51.79%	58.00%
C6	15	389	C6	672	404	93.51%	96.29%	94.88%
Level 3	Predicted		Accuracy					98.76%
True	C7	C8	Class	Nr img/class	Test support	Precision	Recall	f1-score
C7	95	0	C7	408	95	95.00%	100.00%	97.44%
C8	5	303	C8	672	308	100.00%	98.38%	99.18%
Level 4	Predicted		Accuracy					94.57%
True	C9	C10	Class	Nr img/class	Test support	Precision	Recall	f1-score
C9	85	11	C9	408	96	93.41%	88.54%	90.91%
C10	6	211	C10	672	217	95.05%	97.24%	96.13%
Level 5	Predicted		Accuracy					93.15%
True	C11	C12	Class	Nr img/class	Test support	Precision	Recall	f1-score
C11	103	12	C11	408	115	97.17%	89.57%	93.21%
C12	3	101	C12	672	104	89.38%	97.12%	93.09%
Level 6	Predicted		Accuracy					99.07%
True	C13	C14	Class	Nr img/class	Test support	Precision	Recall	f1-score
C13	52	1	C13	408	53	100.00%	98.11%	99.05%
C14	0	55	C14	672	55	98.21%	100.00%	99.10%

produced with the Fourier pre-processing procedure, resulting in fairly deleterious effects on the classification capacity of the analyzed DL models. For the purpose of demonstrating a possible presence of overfitting during the training phase of all the ViT trained models with and without the Fourier pre-processed dataset, the convergence curves have been reported in the Appendix B.1. These graphs show the trend of the loss, the accuracy, the validation loss, and the validation accuracy during the training epochs. The convergence curves do not always reach the maximum of 20 epochs because of the adoption of the early-stopping criterion. This means that the training phase is early interrupted when no further improvements occur to both save computational resources and avoid overfitting training. Despite the validation loss curves appearing quite noisy during the training epochs, their global descending trends proved that ViT model trained with raw GPR images dataset does not incur any overfitting phenomena at every level. Focusing on the ViT models trained with the Fourier pre-processed dataset, the validation curve trends revealed overfitting occurrence in level 1, level 4, and slight evidence in level 3, besides they appeared to be noisier than the previous case.

Tab. 4.7 reports the confusion matrices of the averaged classification results expressed in absolute terms, i.e. the number of samples from the test set of the raw GPR samples dataset which has been predicted for each class. The table illustrates

Table 4.7: Confusion matrices and classification metrics for CCT model trained with raw image data.

Level 1	Predicted	Accuracy 85.22%						
True	C1 C2	Class	Nr img/class	Test support	Precision	Recall	f1-score	
C1	324 77	C1	408	401	86.17%	80.80%	83.40%	
C2	52 420	C2	672	472	84.51%	88.98%	86.69%	
Level 2a	Predicted	Accuracy 92.74%						
True	C3 C4	Class	Nr img/class	Test support	Precision	Recall	f1-score	
C3	355 4	C3	408	359	93.18%	98.89%	95.95%	
C4	26 28	C4	672	54	87.50%	51.85%	65.12%	
Level 2b	Predicted	Accuracy 89.13%						
True	C5 C6	Class	Nr img/class	Test support	Precision	Recall	f1-score	
C5	35 21	C5	408	56	54.69%	62.50%	58.33%	
C6	29 375	C6	672	404	94.70%	92.82%	93.75%	
Level 3	Predicted	Accuracy 87.59%						
True	C7 C8	Class	Nr img/class	Test support	Precision	Recall	f1-score	
C7	64 31	C7	408	95	77.11%	67.37%	71.91%	
C8	19 289	C8	672	308	90.31%	93.83%	92.04%	
Level 4	Predicted	Accuracy 85.62%						
True	C9 C10	Class	Nr img/class	Test support	Precision	Recall	f1-score	
C9	72 24	C9	408	96	77.42%	75.00%	76.19%	
C10	21 196	C10	672	217	89.09%	90.32%	89.70%	
Level 5	Predicted	Accuracy 75.34%						
True	C11 C12	Class	Nr img/class	Test support	Precision	Recall	f1-score	
C11	91 24	C11	408	115	75.21%	79.13%	77.12%	
C12	30 74	C12	672	104	75.51%	71.15%	73.27%	
Level 6	Predicted	Accuracy 76.85%						
True	C13 C14	Class	Nr img/class	Test support	Precision	Recall	f1-score	
C13	32 21	C13	408	53	88.89%	60.38%	71.91%	
C14	4 51	C14	672	55	70.83%	92.73%	80.31%	

the level of overall accuracies and the class metrics precision, recall, and f1-score. Notwithstanding the training conditions may appear limited for training the CCT from scratch, the results in Tab. 4.7 have revealed still fairly good behavior with accuracy values above 75% in all the cases. The worst accuracy value of 75.34% has been reached in level 5 whereas the best accuracy value of 92.74% has been recorded in correspondence of level 2a. Averaging all the levels of accuracies, the CCT model trained with the raw dataset, i.e. without any Fourier pre-processing, reached a global classification accuracy of 84.64%. By contrast, Tab. 4.8 reports the confusion matrices of the averaged classification results expressed in percentages for the CCT models trained with the bi-dimensional Fourier pre-processed GPR samples dataset. In this case, the worst level is the last one, presenting the worst accuracy value of 50.93%. Observing in detail the absolute number of predicted samples, it is evident how the CCT biased learned to classify every sample only toward class C14. However, the number of images per class and even the test set supports seem fairly balanced in size. Therefore, it is reasonable to believe that one of the more probable reasons for this dreadful result may be a consequence of a severely negative effect of the Fourier pre-processing in level 6, even probably combined with the under-training of the CCT model. The same explanation could be stated for level 5 in which the accuracy stacked only to 65.30%. In the other remaining levels, the

Table 4.8: Confusion matrices and classification metrics for CCT model trained with bi-dimensional Fourier pre-processed image data.

Level 1	Predicted		Accuracy					79.84%
True	C1	C2	Class	Nr img/class	Test support	Precision	Recall	f1-score
C1	317	84	C1	408	401	77.51%	79.05%	78.27%
C2	92	380	C2	672	472	81.90%	80.51%	81.20%
Level 2a	Predicted		Accuracy					88.62%
True	C3	C4	Class	Nr img/class	Test support	Precision	Recall	f1-score
C3	354	5	C3	408	359	89.39%	98.61%	93.77%
C4	42	12	C4	672	54	70.59%	22.22%	33.80%
Level 2b	Predicted		Accuracy					87.83%
True	C5	C6	Class	Nr img/class	Test support	Precision	Recall	f1-score
C5	0	56	C5	408	56	-	0.00%	-
C6	0	404	C6	672	404	87.83%	100.00%	93.52%
Level 3	Predicted		Accuracy					84.86%
True	C7	C8	Class	Nr img/class	Test support	Precision	Recall	f1-score
C7	41	54	C7	408	95	85.42%	43.16%	57.34%
C8	7	301	C8	672	308	84.79%	97.73%	90.80%
Level 4	Predicted		Accuracy					81.15%
True	C9	C10	Class	Nr img/class	Test support	Precision	Recall	f1-score
C9	55	41	C9	408	96	75.34%	57.29%	65.09%
C10	18	199	C10	672	217	82.92%	91.71%	87.09%
Level 5	Predicted		Accuracy					65.30%
True	C11	C12	Class	Nr img/class	Test support	Precision	Recall	f1-score
C11	89	26	C11	408	115	64.03%	77.39%	70.08%
C12	50	54	C12	672	104	67.50%	51.92%	58.70%
Level 6	Predicted		Accuracy					50.93%
True	C13	C14	Class	Nr img/class	Test support	Precision	Recall	f1-score
C13	1	52	C13	408	53	50.00%	1.89%	3.64%
C14	1	54	C14	672	55	50.94%	98.18%	67.08%

CCT has still revealed a good accuracy greater than 79% nonetheless, still reaching an appreciable maximum accuracy value of 88.62% in level 2a. Despite level 2b presenting an interesting accuracy value of 87.83%, observing in detail the absolute number of predicted samples, or to the precision, recall, and f1-score metrics of class C5, also, in this case, the CCT has miserably failed to correctly classify the samples, with a biased tendency toward the class C6 only. However, in this circumstance, it appears quite evident that the most probable reason is related to the unbalanced size of the two classes, and consequently even the test set. For future studies, a possible solution could be forcing a balanced training approach by the class with the minimum number of samples. However, averaging all the levels of accuracies, the CCT model trained with the bi-dimensional Fourier pre-processed dataset reached a less global classification accuracy of 76.93%, with an average reduction of 7.71% with respect to the counterpart CCT trained with the raw dataset. Again, the above-mentioned results demonstrated that, notwithstanding the envisaged advantages of adopting the Fourier pre-processing technique on the GPR sample images, also the ViT model is not able to reach the accuracy levels of the training with the raw GPR dataset. In summary, even in the case of CCT models, the Fourier pre-processing procedure resulted in nefarious effects on the classifiers' ability. This is also virtually exacerbated by a combination of underfitting issues, under-trained

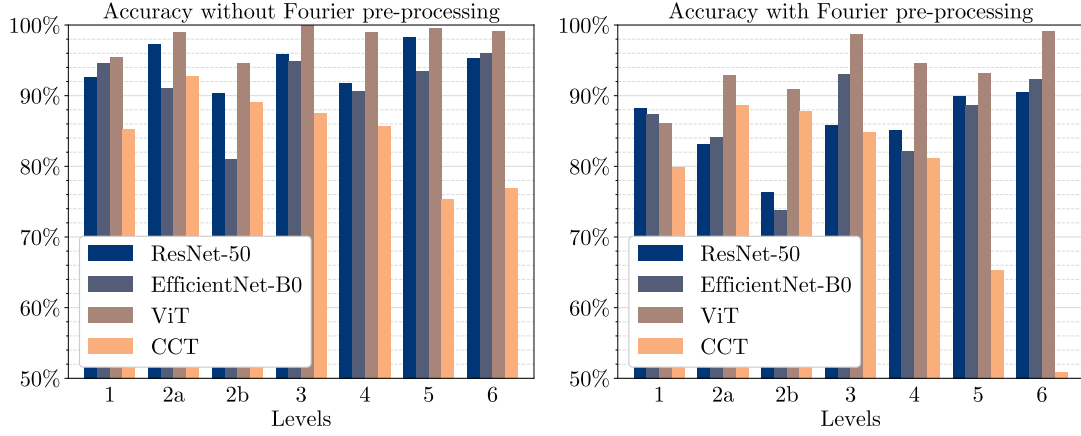


Figure 4.10: Comparative analysis of the various DL models' classification accuracy with and without Fourier pre-processing among the classification levels.

Table 4.9: Global average accuracy for the three analyzed neural models.

Neural model	Without Fourier	With Fourier
ResNet-50	94.51%	85.60%
EfficientNet-B0	91.69%	85.94%
ViT	98.10%	93.65%

models, and even an excessive trivial or compact architecture such as the CCT base model. Lastly, in order to demonstrate a possible presence of overfitting or underfitting issues during the training phase of all the CCT trained models with and without the Fourier pre-processed dataset, the convergence curves have been reported in the Appendix B.1. These graphs show the trend of the loss, the accuracy, the validation loss, and the validation accuracy during the training epochs. Focusing on the CCT model trained with raw GPR images dataset, the validation loss curves exhibit global descending trends in all the levels, proving the absence of any overfitting phenomena. However, these curves manifested a possible underfitting, testifying to the under-training of the CCT models which virtually required an increase in the training epochs. Conversely, for the CCT models trained with the Fourier pre-processed dataset, the validation curve trends revealed the total absence of overfitting occurrences, whilst testifying serious underfitting issues in virtually all the cases, especially in level 2b, level 5, and level 6.

The results among the various DL trained models. Fig. 4.10 provides a comparative overview of the obtained accuracy results. The classification outcomes have been organized for the various GPR defects classification levels. The graph is arranged according to the four DL analyzed models, and depicted in two juxtaposed histogram representations related to the training phase with the raw dataset

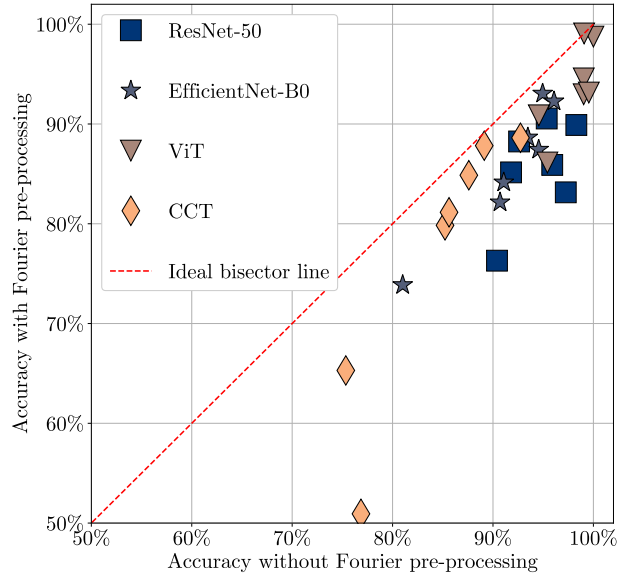


Figure 4.11: Scatter plot of classification accuracy with and without Fourier pre-processing among the classification levels.

and with the bi-dimensional Fourier pre-processed dataset. At first sight of the diagram, among the various DL models, the ViT architecture delivered the highest accuracy values for virtually all the levels of both cases with and without Fourier pre-processing. However, the ResNet-50 provided an accuracy result of 88.25% with the Fourier pre-processed dataset, thus providing a higher result than ViT model. On the contrary, as already anticipated, the CCT model produced the worst results among all the levels for both two cases under comparison. However, especially in the case of Fourier pre-processing, the CCT base models were severely affected by under-fitting issues. These training problems probably arose due to the under-training of the model or because of the adoption of an excessively simple and compact architecture. It is worth mentioning that all four DL models struggled to reach high accuracy value in level 2b. With a deeper inspection of the various convergence curves reported in the appendix, overfitting issues emerged in ResNet-50 with Fourier pre-processed dataset, in EfficientNet-B0 in both the two analyzed cases, and in the ViT model with Fourier pre-processed dataset. The difficulties in level 2b may be related to the critical unbalance in the amount of GPR images samples between classes C5 and C6. In addition, another possible reason could also be a quite critical similarity degree among the images of these two specific classes C5 and C6. This may be plausible especially in the Fourier case, which may produce overly similar images due to excessive data information compression. Fig. 4.11

illustrates a dispersion graph of the accuracy levels for the four DL models between the cases with and without Fourier pre-processing. The ViT model appears the least scattered and even the most concentrated around the best ideal point, located in the upper-right corner. Similarly, the ResNet-50 model and EfficientNet-B0 are fairly little dispersed, except for one point, i.e. related to level 2b, and farther from the ideal point than the ViT model, whereas the CCT model exhibits the most dispersed behavior. Additionally, considering an ideal bisector diagonal line of the present graph, the points that belong to the upper diagonal region are positively affected by the Fourier pre-processing technique, conversely, the lower diagonal area collects the points for which the Fourier pre-processing induced negative accuracy reduction effects. Therefore, this graph evidences a global detrimental effect on the classification accuracy of the analyzed models, because all the points belong to the lower diagonal region, except for the ViT in level 6 which barely belongs to the upper diagonal region. Eventually, Tab. 4.9 reports the global average accuracy results among the various levels. It is worth noting the average accuracy reductions for the four DL models between the raw dataset case and Fourier pre-processed dataset. The ViT model recorded the lowest average accuracy reduction equal to 4.45%, whereas the EfficientNet-B0 exhibited a reduction value of 5.75%. The CCT architecture delivered an average reduction of 7.71%, and the highest reduction of 8.91% was suffered from the ResNet-50 model. Despite the second-best model in terms of accuracy is the ResNet-50 with the raw dataset, it appeared the least robust architecture with respect to the induced effects of the Fourier pre-processed dataset, thus delivering the most consistent average accuracy reduction.

In summary, it is worth noting that in virtually all the analyzed cases, the dataset with Fourier pre-processed GPR sample images provided a final accuracy reduction with respect to the raw images dataset. Therefore, despite the possible envisaged advantages of the Fourier pre-processing technique, it is reasonable concluding that in this case, the Fourier pre-processing procedure may introduce an exaggerated data information compression. This information loss led to overly similar images, with resultant detrimental effects on the final classification accuracy. Focusing instead on a different perspective, considering the total number of learnable parameters of the implemented models, the ResNet-50 contains 25,583,592 parameters whereas the EfficientNet-B0 provided a mobile version characterized by totally 5,309,556 parameters. On the other hand, virtually training the current ViT from scratch would require optimizing 305,413,122 parameters, whereas the current base CCT model presents only 407,107 parameters. Although the base CCT model implementation provided the worst accuracy levels with the raw GPR images dataset, it was able to still reach comparable accuracy levels of the same order of magnitude with respect to the other extremely heavy models. This suggests that in future studies, proper tuning and adjustments of e.g. the CCT model may represent a very promising solution for real-time applications of the proposed NDT with the

GPR device. Since CCT is a powerful and compact model, it may effectively revolutionize the nowadays GPR traditional pipeline with real-time implementations and innovative integrations with internet of things (IoT) edge devices.

During the last decades, with the widespread adoption of evermore sophisticated DL network architectures, in scientific community concerns about interpretability of the neural models arose, exacerbating the idea of neural networks as merely black boxes. In fact, it became fairly challenging to provide a clear explanation of what the network learned to classify an image in a specific certain class rather than another one. Thus, in [241], the authors pointed out that, leveraging the global average pooling layer in a certain manner, it is possible to highlight the powerful localization capabilities of CNN models, even when trained for classification purposes only and not specifically for e.g. object detection tasks. They introduced the concept of class activation maps (CAM), i.e. a visual representation of those portions of input images that mainly contributes to the classification score for a given class. Since the final classification output score is in practice a weighted sum operation performed by a fully connected layer, similarly, the CAM is actually the representation of the activation maps following the last convolutional layer weighted by the weights of the final fully connected layer. Thereafter, other researchers e.g. [242] formalized a gradient-weighted CAM or e.g. the most recent gradient-free Score-CAM method [243]. Adopting the Matlab implementation of [244], in B.2 it has been provided a visual inspection of CAM for an example image of the test set belonging to every single class of the proposed GPR defects' classification tree. The CAM are reported both for the models ResNet-50, EfficientNet, and ResNet-50 with Fourier pre-processing technique. The CAM visually pointed out a quite impressive successful learning of the ResNet-50 model with original images to focus on the more characteristic pattern of the GPR images. On the contrary, EfficientNet performed moderately worse than ResNet-50, presenting in general more dispersed activation maps. At first sight, the CAM for ResNet-50 on Fourier pre-processed images may appear as well quite dispersed, without any apparent consideration of the main frequency component pattern. However, considering two classes level by level, e.g. comparing C3 and C4 in level 2a, it seems that the network mainly focuses on central regions of the image belonging to class C4 and, in a complementary manner, it focuses on extremum areas of the images for class C3. A similar pattern of CAM is more evident in C5 and C6 in level 2b, in C7 and C8 in level 3, and in C9 and C10 in level 4. On the other side, another merit that distinguishes the neural transformers-based architecture, such as the herein analysed ViT model, is the adoption of the attention mechanism. Therefore, the transformers models have already intrinsically incorporated an essential interpretability tool to give the user the possibility to inspect what the network learned, without requiring any further post-processing procedure as before, sometimes time and resources-consuming. Thus, in the B.2, the attention maps for ViT reveal tremendous localization capabilities for those parts of the input images which mainly contributed to defining

the right output classes, crowning the neural transformers models as one of the nowadays more naturally and reliably interpretable DL models.

4.3 Neural-based damage detection with subspace features and statistical indicators

The damage detection tasks could be virtually performed by monitoring any change over time of some meaningful quantities retrieved from the measured output response. For instance, experimental modal parameters retrieved from OMA are representative of the dynamics of the structure under study. However, several researchers proved that OMA results are not the most informative elements to directly and unambiguously solve DD tasks effectively [245], since OMA results also encapsulate uncertainties from unmeasured inputs, as already mentioned referring to in the combined system concept of Fig. 2.1. Therefore, some most informative damage indicators (DIs) were proposed and formalized lately, which do not strictly require OMA. In [246], at least two main advantages of adopting non-parametric damage detection procedures have been illustrated. Indeed, these procedures avoid manipulating vibration data, thus no further modeling errors are introduced. Additionally, these DIs could be easily integrated into automated monitoring systems, such as AOMA or continuous SHM approaches. In particular, some of these DIs denoted as subspace-based [247, 248], rely on residues calculated by covariance changes between two different situations: an initial reference condition and a current, possibly damaged, one [249]. Despite the excitation covariance may be significantly different among the two acquisition moments, these indicators are quite robust because they rely on the simple orthonormal factorization property among different subspaces, i.e. the active space in the reference state and the null space in the current situation [246]. Their robustness bestows them the capacity to effectively detect damages and not variations due to very different excitation inputs. Some scholars even attempted adopting the subspace-based DI to perform the damage localization [250], i.e. the level 2 of an ideal SHM paradigm. During the current Ph.D. program, some starting research studies were conducted on vibration-based subspace DIs combined with artificial neural networks (ANN) in a supervised classification learning scheme, mainly exploring the potentialities of AI with these DIs with numerically simulated damaged scenarios and some simple real-world validation tests. The contents reported in the current section are inspired from [251, 252] and the interested reader can refer to these related full papers.

The currently adopted subspace-based DIs definition plunges its roots in [247, 248], and, specifically, the current implementation is mainly referred to the DIs formulation retrieved from the SSI-cov algorithm approach. It is worth reminding that, as illustrated in the Appendix , the theoretical output covariance estimates

$\hat{\mathbf{R}}_i$ from Eq. (2.94) [96] can be equivalently used for setting up a block Hankel matrix \mathbf{H}_R of the output covariance matrices defined in Eq. (A.9), instead of the typical Toeplitz matrix of SSI-cov algorithm [111, 108]. As reported in Eq. (A.9), in this Hankel-based version of the SSI-cov algorithm, the modal structural intrinsic properties are still retrieved via the factorization property of the Hankel matrix which allows decomposing it in an observability matrix \mathbf{O}_i and a controllability matrix \mathbf{L}_i , given a user-defined time shift (number of block rows) parameter i . The observability matrix can be numerically estimated adopting the linear algebra SVD method applied to the output covariances Hankel matrix \mathbf{H}_R :

$$\mathbf{H}_R = \mathbf{U} \mathbf{\Sigma} \mathbf{V}^T = [\mathbf{U}_1 \quad \mathbf{U}_2] \begin{bmatrix} \mathbf{\Sigma}_1 & \mathbf{0} \\ \mathbf{0} & \mathbf{0} \end{bmatrix} \begin{bmatrix} \mathbf{V}_1 \\ \mathbf{V}_2 \end{bmatrix} \approx \mathbf{U}_1 \mathbf{\Sigma}_1 \mathbf{V}_1^T \quad (4.10)$$

In the above equation, $\mathbf{\Sigma}_1$ collects the non-neglectable singular values in a diagonal matrix sorted in descending order. \mathbf{U}_1 represents the left active subspace of the independent column vectors of the Hankel matrix, whereas \mathbf{U}_2 denotes the null subspace of the independent column vectors of the Hankel matrix. Similar definitions are provided for \mathbf{V}_1 and \mathbf{V}_2 for row vectors of the Hankel matrix. These singular vector matrices maintain orthonormal properties, of key importance in the subspace-based DIs definition. Therefore, similarly to the approximation $\mathbf{\Sigma}_1 \approx \mathbf{U}_1^T \mathbf{H}_R \mathbf{V}_1$, an exact zero matrix should be theoretically obtained when considering $\mathbf{0} \approx \mathbf{U}_2^T \mathbf{H}_R \mathbf{V}_2$. Furthermore, considering the orthonormal property of singular vector matrices, multiplying the Hankel matrix on the right by the row singular vectors of the null space, or multiplying the Hankel matrix on the left by the column singular vectors of the null space, should theoretically deliver exact zero matrices. However, the results of these products are residues denoted as $\boldsymbol{\varepsilon}_V$ and $\boldsymbol{\varepsilon}_U$ respectively.

$$\mathbf{H}_R \mathbf{V}_2 \approx \boldsymbol{\varepsilon}_V \quad (4.11)$$

$$\mathbf{U}_2^T \mathbf{H}_R \approx \boldsymbol{\varepsilon}_U \quad (4.12)$$

These residual matrices can be significantly different from zero vectors because of noise effect or neglected weakly excited high modes. Therefore, the singular vector are not the ideal candidates for tracking relative changes for damage detection purposes [253]. The amplitude of the residues, resulting from the definition of the system order or the amplitude excitation, may mask the residues variation due to minor structural damages. Instead, the above property can be exploited by comparing two different states, since Basseville et al. [254] originally proposed a residual function obtained by comparing the system reference state (undamaged) with the current one (damaged or undamaged):

$$\mathbf{H}_{R,\text{ref}} \approx \mathbf{U}_{1,\text{ref}} \mathbf{\Sigma}_{1,\text{ref}} \mathbf{V}_{1,\text{ref}}^T \quad (4.13)$$

$$\mathbf{H}_{R,\text{cur}} \approx \mathbf{U}_{1,\text{cur}} \mathbf{\Sigma}_{1,\text{cur}} \mathbf{V}_{1,\text{cur}}^T \quad (4.14)$$

In practice, the above orthonormal property can be exploited when comparing two different states. Instead of using the null space on the parameterized observability matrix, an empirical (nonparametric) null space and active subspaces are computed via SVD on an estimated block Hankel matrix from data in both reference and current states. Therefore, the conventional residue $\hat{\boldsymbol{\epsilon}}_c$ between two different state can be expressed as the product of an empirical non-parametric null subspace $\mathbf{U}_{2,\text{ref}}$ in the reference state and the Hankel matrix $\mathbf{H}_{\mathbf{R},\text{cur}}$ in the current state [254, 255]:

$$\hat{\boldsymbol{\epsilon}}_c = \mathbf{U}_{2,\text{ref}}^T \mathbf{H}_{\mathbf{R},\text{cur}} \quad (4.15)$$

However, the excitation covariance may vary between different measurement sessions of the system because of random environmental factors. Therefore, in [253, 256], a new residue definition robust to variations of excitation $\hat{\boldsymbol{\epsilon}}_r$ was formulated, i.e. considering the product of the null subspace $\mathbf{U}_{2,\text{ref}}$ in the reference state and the active subspace $\mathbf{U}_{1,\text{cur}}$ in the current state, thus leveraging the noise attenuation properties of SVD:

$$\hat{\boldsymbol{\epsilon}}_r = \mathbf{U}_{2,\text{ref}}^T \mathbf{U}_{1,\text{cur}} \quad (4.16)$$

These subspace-based DIs definitions allow geometrical interpretations of the residue matrix concept, such as the expression of a loss of orthonormality between reference subspace and another current state [253]. Therefore, these kind of DIs are related to the rotation angle arising between the two subspaces when any structural damage occurs. Despite based on the same theoretical framework, different practical alternatives were proposed in the literature for computing the DI value [254]. In the current implementation, the work of Yan et al. [253] have been considered, in which the DI has been established as the spectral norm of the conventional or robust residue matrix:

$$\text{DI}_{c,\text{Yan}} = \text{norm}(\hat{\boldsymbol{\epsilon}}_c) \quad , \quad \text{DI}_{r,\text{Yan}} = \text{norm}(\hat{\boldsymbol{\epsilon}}_r) \quad (4.17)$$

where $\text{norm}(\cdot) : \mathbb{R}^{m \times n} \rightarrow \mathbb{R}$ is the matrix spectral norm operator, i.e. the maximum singular value of the residual matrices.

To leverage at most all the potentialities of AI-based techniques, particular care must be dedicated to the dataset collection, which plays a crucial role in determining accurate and reliable final results. Therefore, after placing the accelerometer sensors on the structure under investigation, the first critical phase is collecting output-only vibration data response. Specifically, as discussed in the previous section, the subspace-based damage indicators rely on comparing two different states. Indeed, the very first measurement session is assumed as the reference state. On the other hand, any subsequent measurement session should be considered as a current state (undamaged or potentially damaged). Since the availability of real-world recorded data may be strongly limited in general, the current method relies on a data augmentation procedure based on numerical simulations. Specifically, a FE

model calibrated on the reference state measurements may be dynamically excited imposing various damage conditions in order to collect a sufficiently comprehensive dataset of vibration responses related to different and likely damaged current states. After collecting these structural responses dataset, three different methodologies respectively named (A), (B), and (C) have been proposed as schematically illustrated in Fig. 4.12. Precisely, these three methods share a common artificial intelligence core, i.e. an ANN model with a MLP architecture, and thereafter also tested with a 1D-CNN model. A classification task is entrusted to the neural model with the final goal of recognizing the health status of the current state of the structure under investigation. Nevertheless, to fulfill this task, the authors have identified three possible different sets of input features to feed the MLP model, thus formalizing three different methodologies.

Some previous attempts have been conducted by in Finotti et al. [257], in which both a support vector machine model and an MLP architecture have been trained on a numerical pinned-pinned beam model to perform the damage classification task. The ANN has been trained on statistical parameters directly calculated on the raw time series vibration data. Therefore, inspired by Finotti et al. [257], method (A) involves a supervised damage classification scheme based on statistical features only. Specifically, some basic statistics have been computed directly on the raw time-histories vibration response data. These synthetic descriptors are used to feed the MLP model since they represent potentially time-domain discriminating indicators between the undamaged reference state and a damaged current state. In particular, only the most significant and discriminative statistical features have been herein considered according to results retrieved in [257]. Specifically, the computed statistical features are the peak value, the mean square value, the root mean square, the variance, the standard deviation, and the K-factor.

Nonetheless, despite the promising idea of method (A), in [257] the accuracy classification performance was demonstrated being decent but not outstanding. The reasons may be probably lie in the limited scattering interval of some statistics even though passing from an healthy status to a very seriously damaged one. Therefore, the latter consideration was the main motivation to attempt further improvements of the method (A) thus investigating another set of more discriminating input features. As depicted in Fig. 4.12, in method (B), the MLP network is fed with the previous statistical features jointly with the most discriminative Yan's et al. [253] subspace-based damage-sensitive feature $DI_{r,Yan}$, see Eq. (4.17). It is worth noting that some previous attempts have been already conducted by Saeed et al. [258], in which a MLP has been adopted in a supervised learning scheme combined with subspace DIs to perform classification tasks among a healthy and two other damage states. Despite their promising results, they evidence how the main subspace-based DIs drawback is related to the arbitrary choice of the time shift considered in the construction of the Hankel matrix and the truncation order to define the active and null subspaces, to detect damage and not the excitation variation noise effectively.

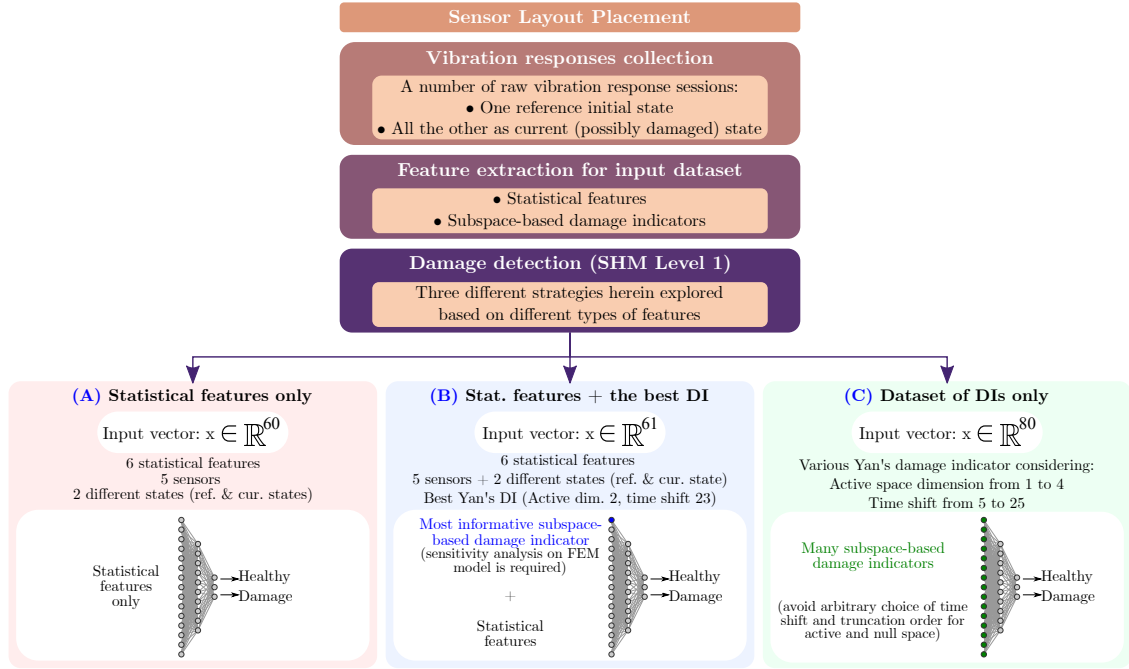


Figure 4.12: Flowchart of the various data-driven damage detection proposed strategies based on statistical information and subspace-based DIs.

Therefore, to overcome this limitation of these two governing parameters, a possible more reliable and systematic method to define the most informative, and thus the most discriminative subspace-based feature, can be handled with an empirical sensitivity analysis. The final aim of the latter is to detect the optimal combination of these two governing parameters in order to achieve the most damage-sensitive subspace-based indicator. However, this kind of analysis may be sometimes quite tricky, depending on the specific modal identification problem, and rather computationally expensive. Nevertheless, a certain degree of arbitrary still remains within the choice of these two governing parameters. Consequently, a third method (C) has been proposed, as illustrated in Fig. 4.12. In this latter case, to fully leveraging the potentialities offered by the AI solutions, the MLP network has been fed with a set of input features entirely represented by the solely Yan's et al. [253] subspace-based damage-sensitive features $DI_{r,Yan}$, see Eq. (4.17). The objective of method (C) is thus removing the remaining user's arbitrary degree in the choice of the governing parameters affecting the computation of the subspace-based indicators, i.e. the time shift and the truncation order. Indeed, an entire set of Yan's et al. DIs only can be computed by varying both the time shift and the truncation order values within certain reasonable intervals respectively. Each time shift and truncation order pair determines a specific Yan's et al. DI value. In this way, in addition to the advantage of reducing the arbitrary level of the previously proposed methods,

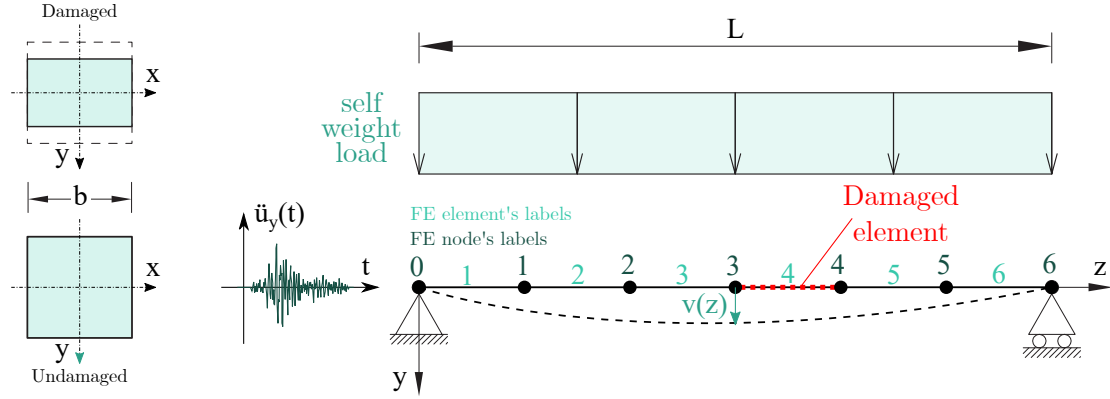


Figure 4.13: Numerical beam model studied for testing damage detection procedures proposed in Fig. 4.12.

method (C) allows considering those hidden patterns of the various subspace-based indicators given by the governing parameters for the same raw time series. Moreover, this third method is expected to be associated with a higher classification accuracy due to the higher sensitivity of these indicators to structural damages.

An initial numerical beam problem presented in Fig. 4.13 have been analyzed for testing the classification scheme proposed in Fig. 4.12. Specifically, the numerical model involves a planar simply supported beam with x, y, z denoting the Cartesian global coordinates reference system under the gravity action of its self-weight producing a static deflection $v(z)$. The symbol b in Fig. 4.13 indicates the square cross section side, whilst L is the span length. A Gaussian white noise acceleration input ($\ddot{u}_y(t)$) is adopted as dynamic input to the simply supported beam. The output-only vibration dataset has been obtained by a FE modeling implemented with OpenSeesPy software [259], using elasticBeamColumn elements a square cross-section of 0.10 m and a span length of 2.00m. The structural uniaxialMaterial properties is steel characterized by Young's modulus $E = 210$ GPa and a mass density of $\rho = 7850$ kg/m³. This structural model has been chosen as simply as possible for the main purpose of avoiding some uncontrolled modeling errors will affect the outcomes. This permitted both testing and analyzing in depth the proposed procedures, and also studying the effects of the sensors' noise on the entire classification procedure. As illustrated in Fig. 4.13, the beam element has been discretized with a uniform mesh by assuming to divide the beam domain into six finite elements. In this way, seven nodes labelled from 0 to 6 are identified in the model. The constraint conditions of the hinged beam are applied to the extremity nodes 0 and 6, which are thus considered fixed in the vertical direction. In the central nodes, 1 to 5, the time history acceleration responses have been collected, simulating a realistic monitoring system with accelerometers placed in correspondence with the nodes. Although there are several ways to model structural damage,

Table 4.10: Modes in the undamaged case of the numerical beam under study retrieved from an eigenvalue analysis and an OMA analysis conducted with the PyOMA module.

Mode	Undamaged		
	OMA	Eigenvalue	An.
	f [Hz]	ξ [%]	f [Hz]
1	1.871	0.44	1.872
2	7.501	1.46	7.479
3	16.440	3.71	16.722
4	28.031	3.69	20.583

in the present study the damage has been introduced in the model as a percentage reduction of the cross-section area corresponding to the damaged elements. The completely undamaged situation has been set as a reference state. The natural frequencies of the undamaged beam model computed by an eigenvalue analysis and by an OMA method using the PyOMA module have been reported in Tab. 4.10. Then, the current damage state has been represented by considering three possible different situations. In the foremost current state, the structure may be still completely undamaged, thus the current state corresponds to the reference state. In the second case, a slight damage is introduced by reducing the cross-sectional area by 25%. Finally, in the last case, a 50% reduction of the cross-sectional area is introduced to represent a sever damage condition. It is worth noting that in real-world scenarios with conventional standard environmental exposure conditions, severe damages have been reported reaching up to 30% of cross section losses at the end of the structure's nominal life [260, 261]. Nonetheless, with specific environmental exposure conditions, chloride attacks, pitting corrosion, and crevice corrosion may lead to dramatic cross section losses of up to 50% [262, 263]. Therefore, in the current preliminary study, the authors analyzed cross section losses up to 50%, still representing a sort of reasonable boundary thus reflecting real-world advanced corrosion scenarios. Although the herein introduced damage may appear far higher than the actual values measured on real structures, e.g. for real-world corrosion attacks, at this stage it was decided to study extreme damage cases on a simplified model. Nevertheless, the presented method can be applied to configurations characterized by different levels of damage without loss of generality. For the sake of generality, the number of damaged sections and their location on the beam domain has been randomly selected. The dynamic analysis was carried out by exciting one support of the structure by a Gaussian random white noise acceleration with a sampling frequency of 50 Hz. The white noise process has been generated by a random sampling of a standard normalized zero-mean normal distribution $\mathcal{N}(0, 1)$, and rescaled up to $0.01g$ of peak acceleration. The input acceleration has been limited to the vertical direction since a plane beam model is considered. The time

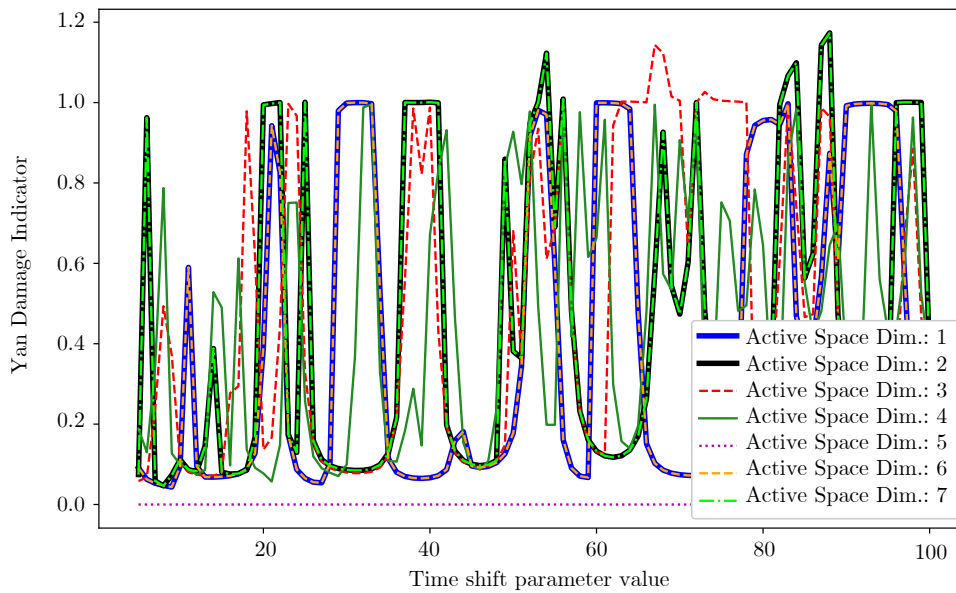


Figure 4.14: Sensitivity analysis on active space dimensions and, consequently the complementary null space dimensions, compared with the time shift user's defined choice.

history analyses have been conducted with OpenSeesPy python module. The collected acceleration histories response data simulate a monitoring setup composed of accelerometers with a sampling frequency of 500 Hz. Five-minute acquisition duration sessions have been performed on damaged and undamaged models. Because of the randomness of Gaussian distribution, to ensure that all data can be obtained repeatedly, the authors controlled the random seeds. In particular, to improve the result's accuracy and ensure that enough data is generated to train the DL models, the seed of the random sampling was set from 1 to 5000 to obtain 5000 time history runs.

As already mentioned, one of the main advantage of working with subspace-based DIs is not strictly requiring to perform a prior OMA. However, to further explore the potentials of the proposed DD methods, specifically focusing on method (C), an empirical sensitivity analysis was conducted to build a numerical dataset of damage-sensitive features that will consider many different damage situations and different white noise Gaussian random processes as input. This latter aided defining the user's choice parameters to get the most informative subspace-based DI features, permitting to study in detail the influence of the choice of the active space dimension, and consequently the null space dimension, combined with the entirely arbitrary user's selection of the time shift. As depicted in Fig. 4.14, there

is a great variation among the Yan et al. subspace-based DIs with different choices of both active subspace dimension and time shift. Focusing on the first aspect, the active space dimension is related to the space whose base is represented by the left singular column vectors associated with the singular values which are quite different from zero. Since the singular values decomposition provides a diagonal matrix with singular values in ascending order, it is quite easy to evidence where there is a great relative difference between the first singular values and the last ones. As a matter of fact, a consistent discontinuous step between singular values and orders of magnitude has been recorded at the fifth singular value (passing from 10^{-6} to 10^{-16}). Nevertheless, Fig. 4.14, demonstrated that, with a constant time shift, even with different subspace dimensions the Yan et al. DIs presented quite scattered values. Specifically, with an active space dimension equal to five which corresponds to the watershed among the DIs' order of magnitude, the Yan et al. DI does not provide any information. On the other hand, regarding the choice of the time shift, this is related to the block rows considered in the block Toeplitz matrix assembling. According to [96], for identification of a system of order n , the time shift i , i.e. the number of block rows, must respect the condition in Eq. (2.96), i.e. $li \geq n$, where l is the number of monitoring sensors applied on the structure. Since for practical applications on continuous systems, the n is theoretically infinite and, in practice, unknown, different rules of thumb and practical approaches have been proposed in the literature to identify a good choice for the time shift, often based on power spectral density matrix [96]. Trying to provide a quite concrete interpretation of this user-defined parameter, the longer the time shift is, the greater time window inter-dependencies will be considered in the correlation matrices of the raw data but in the face of a greater computational effort. Therefore, when dealing with SSI-cov, the time shift is chosen in an empirical way until e.g. the stabilization diagram provides a good resolution to a first-sight identification of the vertical alignments related to stable poles with progressively increasing system's order. It is worth noting that Fig. 4.14 pointed out that results related to active space dimension 1 were virtually the same as active space dimension 6, whereas results associated with dimension 2 were coincident with dimension 7, and these latter reached Yan DI maximum absolute values around time shift equal to 88. Indeed, the results of this initial sensitivity analysis suggested adopting in this case an active space dimension equal to two which is consistent with the higher non-zero singular values, and, in order to mitigate the computational effort, employing a time shift equal to 23. Thereafter the above-mentioned parameters have been identified, in [251], another subsequent sensitivity analysis has been conducted in order to show the influence of the damage level percentage on the Yan et al. DI value considering increasing discrete damaged conditions from 0% to 50% of cross-section reduction with 5% constant step size. Results in [251] evidenced that even for low levels of damage after the undamaged case, Yan et al. DIs assume non-zero values, highlighting the presence of structural performance degradation. The indicators

Table 4.11: Summary of the properties of the implemented MLP. None means variable dimension, depending on the batch chosen size (in this case empirically set to 200). In this case, input units are referred to method (B).

Layer	Output Shape	Activation Function	Parameters Number
Input Layer	[(None, 61)]	-	0
Hidden Layer	(None, 10)	ReLU	620
Output Dense Layer	(None, 3)	Softmax	33

Total Trainable parameters: 653
 Epochs: 1000 (also with Early Stopping)
 Loss: Categorical Cross-entropy (Optimizer: Adam)

assume a monotonic behavior with progressively increasing values for a higher level of damage, showing a virtually constant state around 0.8 when approaching 50% cross-section reduction. Further empirical sensitivity analysis were conducted in [251], regarding the acquisition time duration demonstrating that 5 minutes of acquisition time represented the best trade-off between computational efficiency effort and damage identification resolution, and even representing a critical case in which Yan et al. DIs presented a significant scattered behavior, whilst for longer acquisition up to 30 minutes Yan’s et al. DIs seem to be no more influenced by the measurement session duration.

Afterward, the empirical sensitivity analysis has been performed, the numerical test was carried out considering two main situations: the reference undamaged state and a current, possibly damaged, one. For this latter, the algorithm was able to randomly choose among three possible cases: a further undamaged situation which, in combination with the reference one, it would virtually lead to a nil Yan et al. DI value; a low damage situation, considering a cross-section reduction percentage of 25%; an high damage situation, characterized by a cross-section reduction percentage of 50%. In order to further increase the generality of the results of the present study, for every run, the algorithm randomly selected how many and which elements are considered damaged with the three above-mentioned possible damaged statuses. Under these conditions, 5000 numerical simulations were executed, collecting 5 minutes long acceleration time history acquisitions for each structural node of the FE model which simulates the presence of a realistic monitoring system placed on that beam. For each acceleration record, the statistical features were computed. Since the number of accelerometers inside the beam domain is 5 (excluding the extreme support restraint points), for each simulation acquisition, 6 statistical features have been extracted from each accelerometer producing, in total, 30 extracted features. Recalling that for each simulation, two cases have been considered (undamaged status and a possible damaged one), altogether, 60 features have been produced from each algorithm run in method (A). Method (A) presented in Fig. 4.12, adopts as input these 60 features. Furthermore, these 60 features, in addition to the most informative Yan et al. DI, have been considered as the input to the MLP method (B) as illustrated in Fig. 4.12. The most informative

subspace-based DI was defined through the previous sensitivity analysis by setting a time shift of 23 and an active space dimension of 2. Finally, method (C) of Fig. 4.12 has also been implemented with the same MLP architecture but considering in input many Yan's et al. DIs only. They have been calculated considering all the time shifts from 5 to 25 and truncation orders which define active space dimensions from 1 to 4, collecting in total 80 input features for every one of the 5000 simulations. The first MLP adopted in the current study presents a single hidden layer, with 10 units, which have been empirically found to be the best trade-off between accuracy performances and computational effort avoiding typical machine learning issues such as overfitting and underfitting [60, 61]. The summary of the current MLP properties model is reported in Tab. 4.11. It is worth noting that the trainable weights are not usually considered in the input layer because it only transmits the information to the next layer [60]. The activation function for the hidden layer is the ReLu function in order to avoid negative values reaching the output layer, which instead incorporates a softmax activation function suitable for classification tasks [60, 61]. The multiclass classification MLP adopts the strategy one-versus-the-rest, or also acknowledged as one-versus-all [61], since after collecting the probability of belonging to one of the three output classes, the one which presents the highest score is denoted as the selected class [43]. The loss adopted in the current problem is the categorical cross-entropy which has been solved by the Adam optimizer algorithm [60, 61].

To assess the performance of the AI-based models for the proposed multi-class classification methods, the dataset has been subdivided into a training and test set with 80% and 20% proportions respectively. Moreover, a validation set with 10% of the training set have been used for constructing training curves and evaluating the performances during training. For instance, Fig. 4.15 (a) depicts the (A) proposed method MLP performances during the training phase. In particular, the loss function both for the training and the validation sets is depicted over the epochs, reporting also on the same graph the accuracy for both sets. It is worth noting that when the validation loss starts to increase after a monotonic decreasing behavior, at that point the overfitting of the model is reached. In the current plot, the validation loss is still decreasing and only in the very last epochs start to flatten out, without reaching yet the overfitting point and evidencing also a constant overall accuracy from epoch 600 until the end. The performance of the trained model (A) has been validated with the test set, whose classification results have been condensed in the confusion matrix illustrated in Fig. 4.15 (b). The overall accuracy obtained is about 92.20% and it measures the portion of the validation set which has been correctly classified (the sum of main diagonal terms) out of the entire validation set size (1000 samples). Two other metrics are presented in the confusion matrix: precision and recall. The precision measures the number of samples correctly classified in a certain class over the total number of samples which have been associated with that class, whereas the recall represents the number of

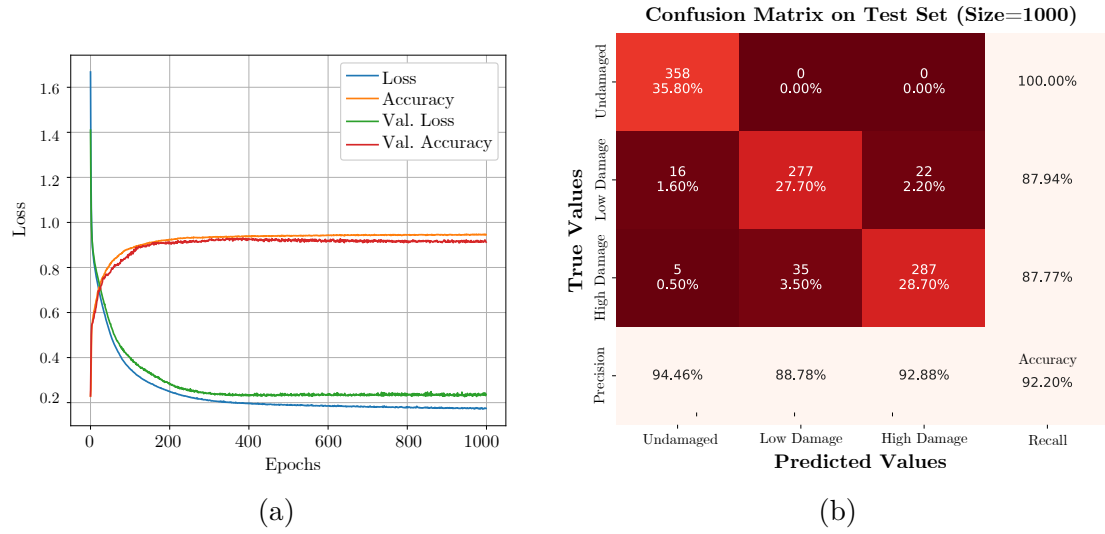


Figure 4.15: MLP multiclass classification results for method (A). (a) MLP convergence curves; (b) MLP confusion matrix on the test set.

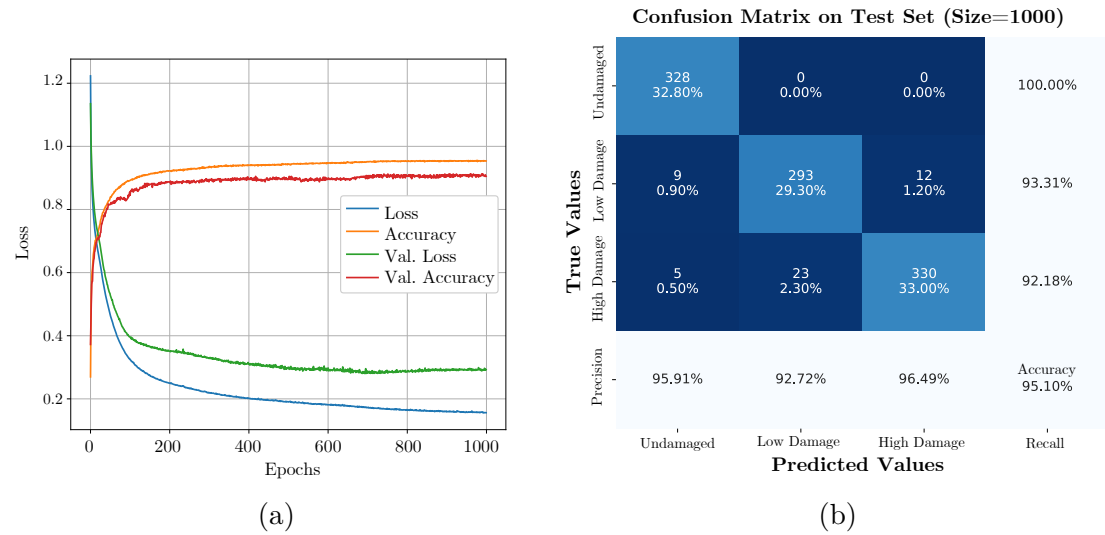


Figure 4.16: MLP multiclass classification results for method (B). (a) MLP convergence curves; (b) MLP confusion matrix on the test set.

samples correctly classified to a certain class over the number of samples which actually belongs to that class [61]. Therefore, considering the position of the true values along the vertical axis and the predicted values along with the horizontal one, summing the elements of the confusion matrix along the rows for a certain column, it is possible to get the number of samples associated with that column. On the other hand, by summing the elements of the confusion matrix along the column

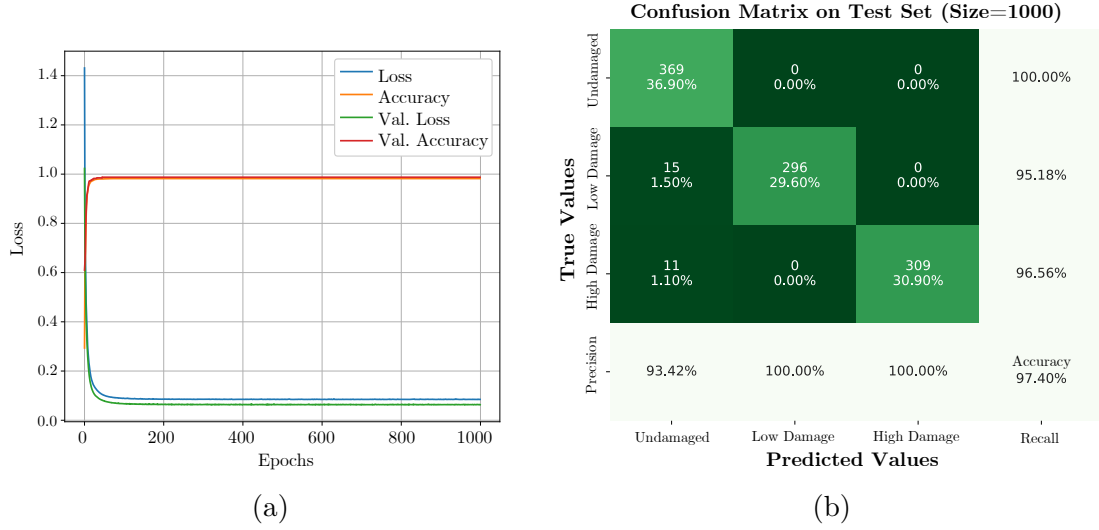


Figure 4.17: MLP multiclass classification results for method (C). (a) MLP convergence curves; (b) MLP confusion matrix on the test set.

for a certain row, it is possible to get the number of samples that actually belong to that row. In other words, focusing on a certain class (column), the precision evaluates how the predictor performs well, concerning when it associates always that class even if in reality the true class was another one (false positives). Instead, focusing on a certain true class (row), the recall evaluates the predictor performance in terms of correctness of classification with respect to the ground truth, i.e. the actual number of elements which have supposed to belong to that class and even considering the so-called false negative. In this case, both the precision values and the recall values are quite high, above 87% for all the classification possible outcomes. Fig. 4.16 (a) depicts the (B) proposed method MLP performances during the training phase, evidencing the absence of overfitting issues. From a deeper insight into the loss and accuracy trends, it would virtually be possible to stop the training to epoch 850, in order to save computational cost and obtain almost the same performances. The performance of the trained model (B) has been validated with the test set, whose classification results have been condensed in the confusion matrix illustrated in Fig. 4.16 (b). The overall accuracy obtained is about 95.10% and it measures the portion of the validation set which has been correctly classified (the sum of main diagonal terms) out of the entire validation set size (1000 samples). As expected, the presence of the most informative Yan's et al. DI with the statistical feature inputs provides better classification performance to the trained model. The higher classification of method (B) with respect to method (A) proves that this most informative subspace-based feature improves the classification performances of the ANN model in Level 1 of the SHM task. Afterward, Fig. 4.17 (a) depicts the (C) proposed method MLP performances during the training

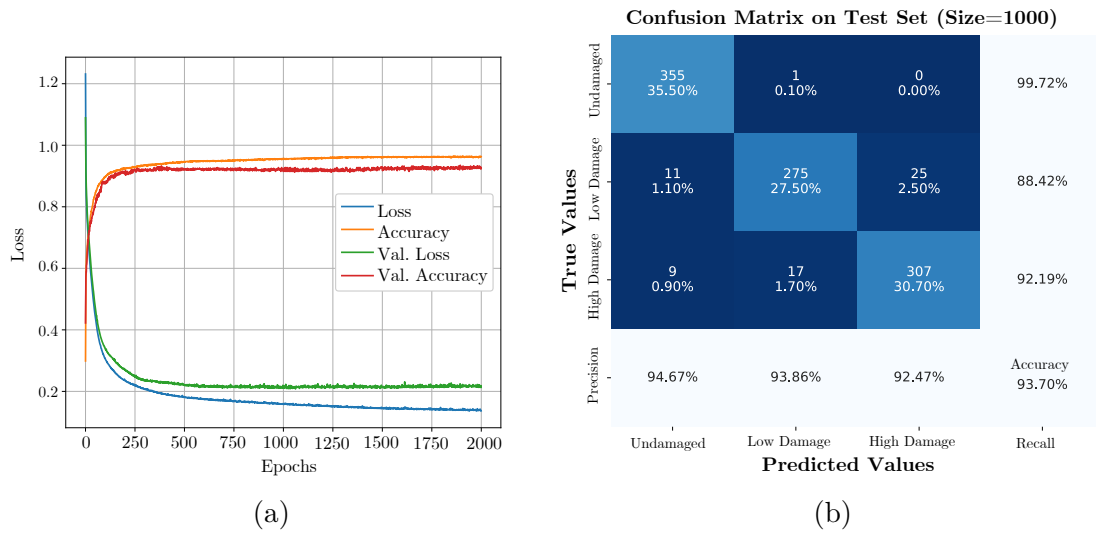


Figure 4.18: MLP with dropout regularization multiclass classification results for method (B). (a) MLP convergence curves; (b) MLP confusion matrix on the test set.

phase, evidencing, even in this case, the absence of any overfitting issues. From a deeper insight into the loss and accuracy trends, it would virtually be possible to stop the training downright to epoch 150, in order to greatly save computational cost and obtain almost the same performances. The performance of the trained model (C) has been validated with the test set, whose classification results have been condensed in the confusion matrix illustrated in Fig. 4.17 (b). The overall accuracy obtained is about 97.40% and it measures the portion of the validation set which has been correctly classified (the sum of main diagonal terms) out of the entire validation set size (1000 samples). As expected, the presence of Yan’s et al. DIs only provides better classification performance to the trained model with respect to the previous cases. The outstanding higher classification performance of method (C) with respect to methods (A) and (B) proves that considering an entire set of informative subspace-based features remarkably improves the classification performances of the ANN model for the damage detection task. Furthermore, the advantage of method (C) is that removes the arbitrary choice of the user about governing parameters in the subspace-based DI calculations.

Some further regularization techniques have also been adopted in method (B) of Fig. 4.12, attempting to improve the model accuracy and reduce the computational effort. The early stopping criterion may even be regarded as a form of regularization because it stops the algorithm when the error on a part of the training set begins to rise. Thus, it may actually restrict the parameter search space [60]. A dropout regularization has been even applied to the hidden layer in an attempt to improve the performance of the MLP, with a dropout probability of each unit of

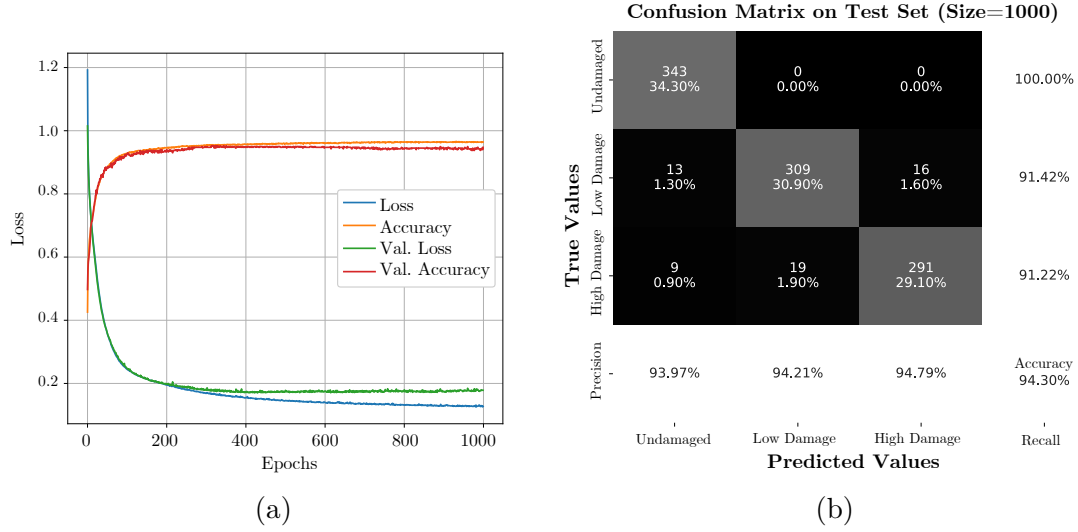


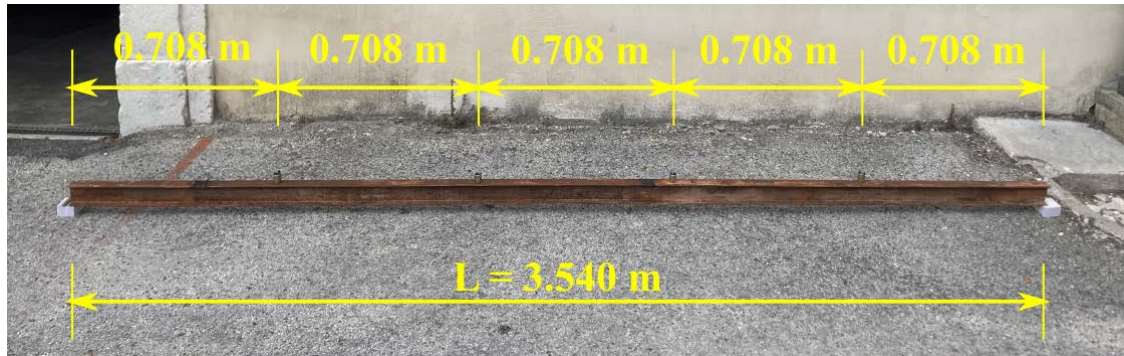
Figure 4.19: MLP multiclass classification results for method (B)-worsened. (a) MLP convergence curves; (b) MLP confusion matrix on the test set.

40% [43]. However, as shown in Fig. 4.18 (a), it required a greater computational effort and a longer training phase (2000 epoch) to reach barely 93.70% of overall accuracy, as reported in the confusion matrix depicted in Fig. 4.18 (b). Focusing on the history diagram, it is possible to see that the main effect of the dropout regularization is slowing the learning rate, but this reflects a more regular training behavior considering both the loss and the accuracy trends compared with Fig. 4.16. Furthermore, the random dropout of some units provides a more resilient ANN model, in which the weights are learned to work even when some neurons are completely ignored [43].

Finally, another variant of method (B) has been implemented, denoted as (B)-worsened. In this case, the (B)-worsened method adopts as input the statistical features joined with a bad choice of subspace-based DI governing parameters, which leads to a poorly informative Yan’s et al. indicator. In particular, considering all previously calculated DIs for method (C), it has been empirically identified that a bad choice could be virtually associated with a time shift equal to 10 for an active space of dimension 1 for all of the 5000 simulations. Fig. 4.19 (a) depicts the variant (B)-worsened method MLP performances during the training phase, evidencing also here the absence of overfitting issues. From a deeper insight into the loss and accuracy trends, it would be virtually possible to stop the training to epoch 400, in order to save computational cost and obtain almost the same performances. The performance of the trained model (B)-worsened have been validated with the test set, whose classification results have been condensed in the confusion matrix illustrated in Fig. 4.19 (b). The overall accuracy obtained is about 94.30% and it measures the portion of the validation set which has been correctly classified (the

sum of main diagonal terms) out of the entire validation set size (1000 samples). As demonstrated in this last example, even with a poor choice of a less informative subspace-based DI, since it is still more sensitive to structural damage, this always improves the classification accuracy performances with respect to method (A), which relies on statistical features only. This demonstrates the robustness of the proposed method because, even considering a less informative but still more sensitive DI, this further improves the model capacities to effectively fulfill the Level 1 of SHM. In conclusion, the current MLP is able to provide quite interesting multiclass classification results considering the statistical time series features coupled with Yan's et al. subspace DI, extending the capabilities of the MLP model trained in [257]. Furthermore, a good generalization of the current deep learning model is related to the fact that the 5000 numerical simulations randomly considered both how many damaged elements to take into account (even none) and the level of damage to associate with those selected elements. This produced time-series signals which cover many different cases, which were anyway successfully traced back to three possible classification results: undamaged situation, low damage status (cross-section reduction of about 25%), and high damage condition (cross-section reduction of about 50%).

To further testing the effectiveness of proposed methods, a real-world monitoring setup was arranged, being composed of a simply supported steel I-beam with a span length of $L = 3.540$ m. The cross section is characterized by a depth equal to 80mm and a base width of 40mm, with a flange width of 5mm and a web width of 4mm. As illustrated in Fig. 4.20, four uni-axial velocimeter sensors have been adopted in the current case, placed every 0.708 m on the beam length, in order to collect the vertical vibration response of the beam. The acquisition system of the measured signals was composed of an oscilloscope with 200 MHz of bandwidth (-3 dB) at 50 Ω input impedance and 4 analog channels. The velocimeter sensors consist of a spring-suspended wire coil moving inside a magnetic field, thus capturing voltage deviations with respect to their baseline response. This latter is defined by the sensor's natural frequency, in this case, equal to $10 \pm 3.5\%$ Hz. This kind of sensor represents the ideal cost-effective and high-sensitivity solution for SHM able to capture the natural frequency of structures above the sensor natural frequency [95]. Thus, before adopting the proposed MLP-based damage detection methodologies, the authors conducted the OMA analysis on the signals acquired with 1000 Hz of sampling frequency from the steel I-beam for undamaged conditions, to verify that the first vertical mode of the experimental beam was greater than 10 Hz. Since the natural environmental vibration excitation alone was not enough to identify any modal parameter, the authors caused environmental excitation able to activate at least the first four vertical modes of the beam by indirectly exciting the surrounding ground with a rubber-headed hammer. Fig. 4.21 (a) demonstrated that the rubber-headed permitted to avoid spikes in the acquired vibration signals, and avoided excessive deviations from the output-only OMA base hypotheses. Fig. 4.21 (b)



(a)



(b)

(c)

(d)

Figure 4.20: Experimental steel beam case study. (a) Beam monitoring setup with measures; (b) Beam cross section dimensions; (c) Damage induced with a localized cross section reduction. (d) Velocimeter sensors.

illustrates the relative stabilization diagram, computed with time shift equal to 15, in which apparently five alignments of stable poles are evidenced. All the pole alignments at 16.92 Hz, 74.27 Hz, 139.05 Hz, and 248.05 Hz appear stables from lower orders up to higher orders, whereas the alignment around 43 Hz appears noisier along the orders. To validate the OMA results, a FEM modal analysis with OpenSeesPy software has been conducted. With a preliminary FEM modal analysis, the authors were able to exclude the alignment around 43 Hz, since it does not represent an actual vertical mode of the structural system. However, the existing steel beam needs a calibration of the flexural rigidity parameter EI , which can be conducted by solving an unconstrained optimization problem leveraging the OMA results according to objective function in Eq. (2.140) [126, 116], but limiting to only the first part of equation and performing the square operation to magnify

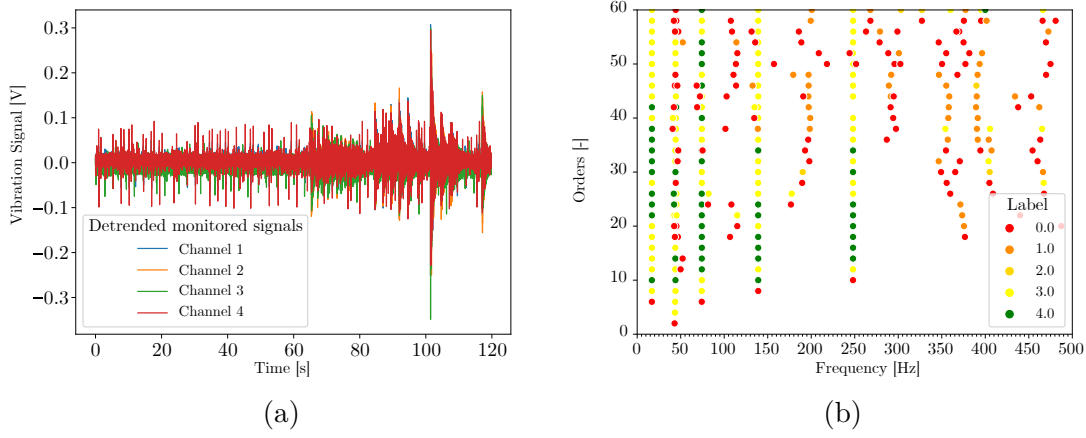


Figure 4.21: OMA analysis for undamaged conditions of the experimental beam. (a) Monitored signals expressed in Volt [V]; (b) Resulting stabilization diagram.

the relative differences, i.e.:

$$\min_{\theta \in \Omega} \mathcal{F}(\theta = EI) = \sum_{u=1}^m \gamma_u \left(\frac{f_u^{(e)} - f_u^{(c)}(\theta = EI)}{f_u^{(e)}} \right)^2 \quad (4.18)$$

where $m = 4$ is the number of considered modes, $\gamma_u = 1$ factors have been all set to unity, $f_u^{(e)}$ are the experimental frequency obtained from the OMA and the $f_u^{(c)}$ are obtained analytically based on the dynamics formulation of a continuous simply supported beam [264]:

$$f_u^{(c)}(\theta = EI) = \frac{m^2 \pi}{2L^2} \sqrt{\frac{EI}{\rho A}} \quad (4.19)$$

in which ρ is the material density equal to 7850 kg/m³ for structural steel, and A is the cross-section area of the steel I-beam, whose dimensions are reported in Fig. 4.20 (b). The FEM mode shapes retrieved from OpenSeesPy modal analysis evidenced a good agreement with the experimental ones. Afterward, the numerical FEM model in OpenSeesPy was adjusted with the OMA-calibrated flexural rigidity in order to simulate five-minutes time-histories vibration responses database under various white noise Gaussian excitation with PGA of 0.01 g and with different damage scenarios. To collect the vibration response of the simulated I-beam, the nodes of the model have been placed accordingly to the actual sensors' placement along the beam, see Fig. 4.20 (a). As depicted in Fig. 4.20 (c), in this realistic scenario, the damage has been introduced as punctual damage, by locally reducing the cross-section. Therefore, in total 5000 FEM simulations have been conducted

Table 4.12: Summary of the properties of the implemented MLP for the experimental case study. None means variable dimension, depending on the batch chosen size (in this case empirically set to 200). In this case, input units are referred to method (A).

Layer	Output Shape	Activation Function	Parameters Number
Input Layer	[(None, 48)]	-	0
Hidden Layer	(None, 10)	ReLU	490
Output Dense Layer	(None, 2)	Softmax	22

Total Trainable parameters: 512
 Epochs: 300
 Loss: Categorical Cross-entropy (Optimizer: Adam)

both in a reference (undamaged) state and in a current (possibly damaged) state, with different punctual damages randomly located along the beam and with a possible entity of 0%, 5%, 10%, 15%, or 20% of cross section reduction. With a deeper insight into these 5000 FEM simulations, it was possible to notice an unbalanced number of undamaged scenarios, randomly occurring only in 965 simulations. Despite the unbalance between the two healthy and damaged classes may produce biased training toward the damage scenario with respect to the undamaged one, the authors leveraged this fact to show if the damage-sensitive features are effective and discriminative enough to ensure a good training of the MLP models even with a biased dataset, a condition which usually occurs in real-world situations. In order to show a realistic application of the three proposed intelligent damage detection methods, the authors trained the neural models with only two output classes, i.e. healthy or damaged, acting therefore as an anomaly detection procedure. The numerical FEM model of the experimental beam permitted training the neural models, which have been finally tested on real vibration acquisitions from the experimental setup thereafter. The MLP has been chosen with a hidden layer with 10 units as reported in Table 4.12. As before, to effectively train the MLP models, datasets of damage-sensitive features have been collected from the 5000 simulated time history responses for each of the three proposed methods (A), (B), and (C). Afterward, every dataset of features has been subdivided into two parts: the 80% composed the training set, whereas the remaining 20% is the test set. The validation set size has been set equal to 10% of the training set.

Six statistical features are computed for Method (A) for both reference and current state, and considering the adoption of four velocimeter sensors on the steel experimental I-beam setup, the input vector has a dimension of 48. The results of the training of the MLP for method (A) are reported in Fig. 4.22. The convergence curves over 300 epochs highlighted overfitting issues occurring from around epoch number 20 due to the increasing trend of validation loss. Therefore, the early stopping procedure was employed by limiting the training over 20 epochs, as reported in Fig. 4.22 (a). Nevertheless, with punctual damage, statistical features of the

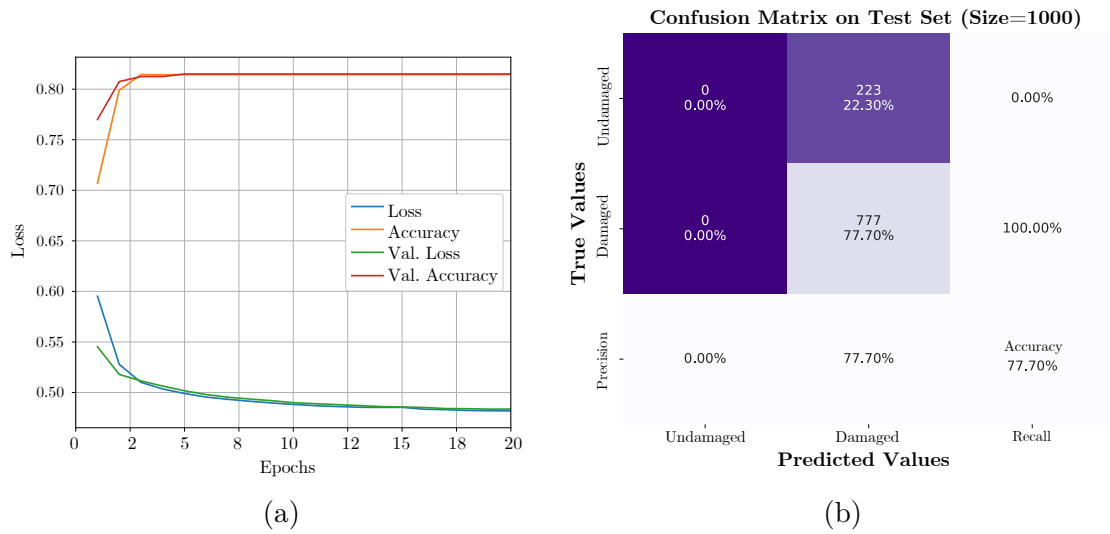


Figure 4.22: MLP training performances for method (A) on simulated I-beam. (a) 20 epochs due to early stopping to avoid overfitting; (b) Confusion matrix on the test set.

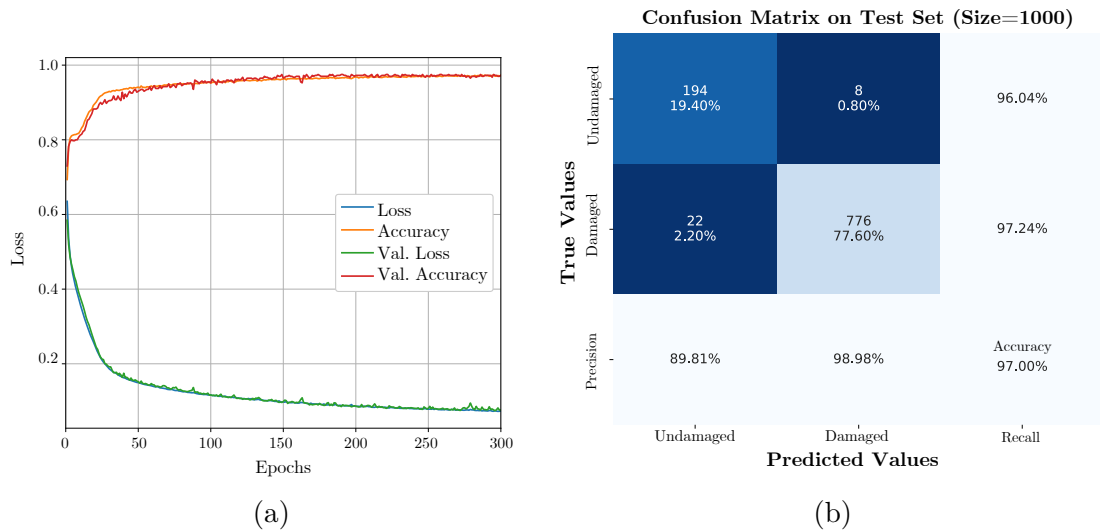


Figure 4.23: MLP training performances for method (B) on simulated I-beam. (a) 300 epochs without any evidence of overfitting; (b) Confusion matrix on the test set.

time series responses were not sufficiently discriminative between damaged and undamaged cases. Indeed, as depicted in Fig. 4.22 (b), the confusion matrix on the test set revealed a biased behavior of the MLP for method (A) toward the damaged class, reflecting the biased unbalance of the 5000 simulations. Method (B) relies

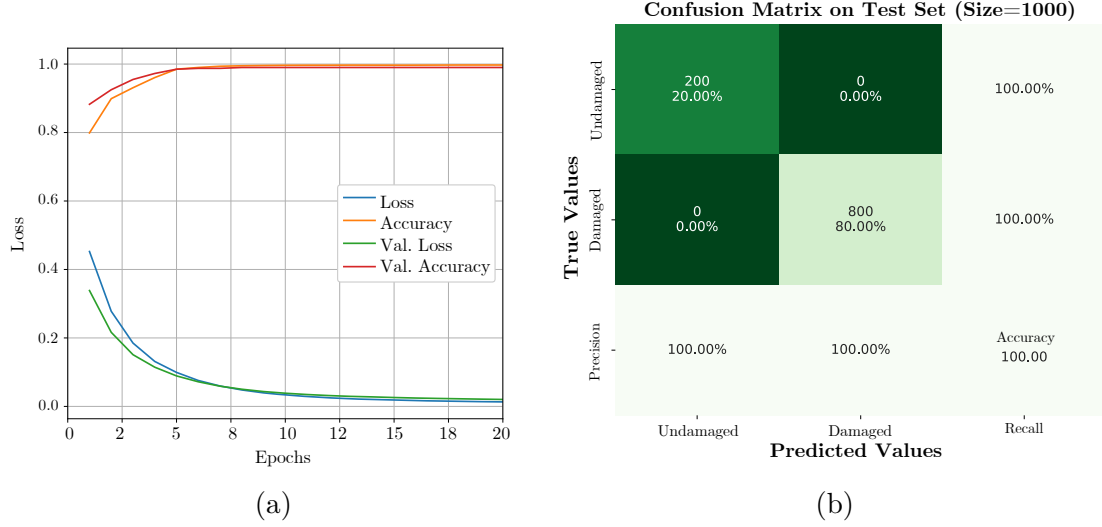


Figure 4.24: MLP training performances for method (C) on simulated I-beam. (a) 20 epochs due to early stopping to avoid overfitting; (b) Confusion matrix on the test set.

on the calculation of the same six features of method (A) for every sensor for both reference and current states, whilst additionally considering the most informative subspace-based Yan's et al. [253] DI feature, delivering an input features vector with dimension of 49. The results of the training of the MLP for method (B) are reported in Fig. 4.23. The convergence curves over 300 epochs evidenced that no overfitting issues occurred because of a monotonic decreasing trend of the validation loss. Therefore, the confusion matrix on the test set for method (B) reported in Fig. 4.23 (b) demonstrated the benefits of considering a subspace-based DI in addition to the statistical features. Actually, the additional information carried with Yan's et al. DI substantially improved the training performance of method (A), and now the trained MLP for method (B) does not reflect anymore the biased unbalance of the 5000 simulations. The Yan's et al. subspace indicator thus provided more discriminative features which substantially helped the MLP model to correctly classify damaged and undamaged samples. Eventually, method (C) relies on the calculation of an entire dataset composed of subspace-based Yan's et al. damage sensitive feature only. In accordance with the previous numerical case study analyzed, these DIs have been calculated considering all the time shifts from 5 to 25 and truncation orders which define active space dimensions from 1 to 4. Thus, the input feature vector to the MLP for method (C) has a dimension of 80. The results of the training of the MLP for method (C) are reported in Fig. 4.24. Again, the convergence curves over 300 epochs highlighted overfitting issues occurring from around epoch number 20 due to the increasing trend of validation loss. Therefore, the early stopping procedure was employed by limiting the training

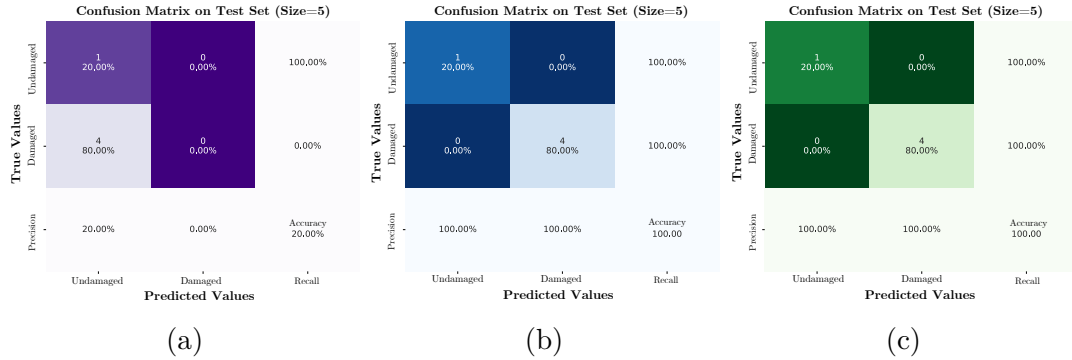


Figure 4.25: After training MLP predictions on experimental measurements collected from the steel-I beam for one undamaged and four damaged scenarios. (a) predictions of MLP trained with method (A); (b) predictions of MLP trained with method (B); (c) Predictions of MLP trained with method (C).

over 20 epochs, as reported in Fig. 4.24 (a). Since the benefits of Yan’s et al DIs have been already demonstrated before, even with small and punctual damages their informative content is very effective and discriminative between damaged and undamaged cases. Fig. 4.24 (b) illustrates that the confusion matrix on the test set revealed the outstanding behavior of the MLP for method (C) by correctly classifying all the samples of the so far unseen simulated test set.

In conclusion, the authors tested the numerically trained MLP for the three methods (A), (B), and (C) with vibration responses collected from the experimental setup in five different scenarios, denoted as 1 to 5. The first scenario is referred to as the undamaged situation and was identified as the reference situation, whereas all the scenarios from 1 to 5 taken individually have been considered as the current state. The scenarios from 2 to 5 represent the steel I-beam with induced punctual damage introduced in the midspan, as depicted in Fig. 4.20 (c). Specifically, the scenarios from 2 to 5 represent progressively increasing damage level situations with a local cross-section reduction of about 5.9%, 11.8% 23.5% 25.7% respectively. In each of the 5 experimental scenarios, the authors collected a few minutes of vibration responses from the four velocimeter sensors placed on the steel I-beam and calculated the input features vector to feed the after-training MLP neural models for the three proposed methods. The prediction results of the trained MLP models have been reported in terms of the confusion matrix in Fig. 4.25. As shown in Fig. 4.25 (a), the poor training performances on numerical simulations of method (A) reflected also on the experimental measurements, whereas methods (B) and (C), Figs. 4.25 (b)-(c) respectively, provided outstanding results correctly classifying the four damage scenarios and the remaining undamaged one. Obviously, it is worth noting that due to the very reduced number of samples, these results serve as an initial validation of the proposed method. However, the current results should

be deeply extended with more data, and further future studies and extensions to understanding the robustness of the proposed DD methods to more complex structural systems, aiming to further generalize and also simplify the adoption of our approach. Indeed, the main limitation of our proposed model is requiring the implementation of a FEM of the structure to accurately train the AI-based models, which can be probably unfeasible when dealing with very complex structural systems.

4.3.1 Effects of noise on the proposed subspace-based damage detection strategies

Regardless of the methodology, the quality of SHM outcomes is strongly affected by the characteristics of the sensors employed to collect the vibration response of the structural system of interest. Different factors and the noise source may affect and corrupt the structural response, e.g. changes in the input excitation (e.g. stochastic nature of traffic load conditions), environmental and climatic agents such as wind, temperature, or even humidity and moisture which may cause sensors damaging and failures, and imperfect intrinsic nature of the sensing system e.g. reading or calibration errors (systematic effects). Furthermore, when dealing with output-only OMA, operational conditions deliver very low amplitude vibrations and a reliable modal estimation requires high-quality and low-noise sensors [96]. Therefore, to further analyze the robustness of the previously proposed DD strategies, the simulated numerical beam system have been studied to realistically simulate real-world accelerometer sensors. Many types of sensors are used for SHM purposes [265, 252], and today's most common tendencies are fiber optic sensors (FOS), piezoelectric sensors (PZT), micro-electro-mechanical systems sensors (MEMS). To plausibly simulate noise coming from a real-world sensors array, an additive random noise process usually contaminates the structural time series response collected from each sensor, whose level is quantified by the SNR in dB [96]. The SNR values were herein calibrated attempting to faithfully reproduce MEMS accelerometers available on the market, whose characteristics have been retrieved from a market survey and a literature review conducted by the authors of the most widely adopted sensors for SHM purposes. For instance, considering the Italian context, the ANAS agency has recently fixed some rules for new SHM monitoring system design, totally embracing the MEMS technology for its low costs, but setting some minimum requirements imposing to use only some good-quality MEMS models and avoiding extremely low-cost devices typically associated with noisy or low-quality measures, insufficient for the SHM purposes. Specifically, allowed MEMS accelerometers should present an output signal of 4-20 mA direct current or differential voltage signal, able to recording with a full-scale range of at least ± 2 g and a dynamic range bandwidth of 0-500 Hz, characterized by a noise floor lower than $25 \mu\text{g}/(\text{Hz}^{0.5})$ and a standard sensitivity of at least 2000 mV/g, guaranteeing an environmental protection at least with IP67 class for hardware components, with a temperature operative range of

Table 4.13: Summary of the properties of the implemented 1D-CNN for studying noise effects.

Layer	Output Shape	Activation Function	Parameters Number
Input and reshape layer	[(None,80,1)]	-	0
Conv1D_1	(None,77,15)	ReLU	75
Conv1D_2	(None,74,15)	Batch Normalization +ReLU	(915+60)
Max Pooling	(None,24,15)	-	0
Conv1D_3	(None,21,40)	Batch Normalization +ReLU	(2440+160)
Global Average Pooling	(None,40)	Drop out	0
Output Dense Layer	(None,3)	Softmax	123

Total Trainable parameters: 3773
Trainable parameters:3663
Epochs: 1000
Loss: Categorical Cross-entropy (Optimizer: Adam)

Table 4.14: Summary of the properties of the implemented MLP for studying noise effects.

Layer	Output Shape	Activation Function	Parameters Number
Input and reshape layer	[(None,80)]	-	0
Hidden layer	(None,15)	ReLU	930
Output Dense Layer	(None,3)	Softmax	48

Total Trainable parameters: 3773
Trainable parameters:3663
Epochs: 1000
Loss: Categorical Cross-entropy (Optimizer: Adam)

-20 ÷ +60 °C and temperature stability lower than 0.01 %/°C, and a phase angle variation lower than 15° in the 0-50 Hz domain. In typical real-case data acquisition scenarios, recorded signals are characterized by the presence of background noise. The noise effect in SHM is also related to intrinsic sensor errors, including sampling frequency, time, and systematic errors of calibration. All these errors can be eliminated to a certain degree [266]. However, some noise components cannot be removed but only attenuated. According to Rahaman [267], the current state-of-the-art MEMS sensors can guarantee an SNR that ranges between 27dB and 67dB under real-world working conditions. Therefore, three different level of SNR are herein chosen to simulate MEMS performance on real-case data collecting: 20dB (low quality), 40dB (medium quality), and 60dB (good quality). Considering the previously methods (A), (B), and (C), illustrated in Fig. 4.12, and the three SNR values, two ANN architecture have been adopted this time on the simulated beam case study illustrated in Fig. 4.13. In particular, a 1D-CNN and an MLP have been trained, whose architecture and hyperparameters information are reported in Tabs. 4.13-4.14 respectively, in which input dimensions are referred to the method (C). The 1D-CNNs are used in this work because of their effectiveness in obtaining

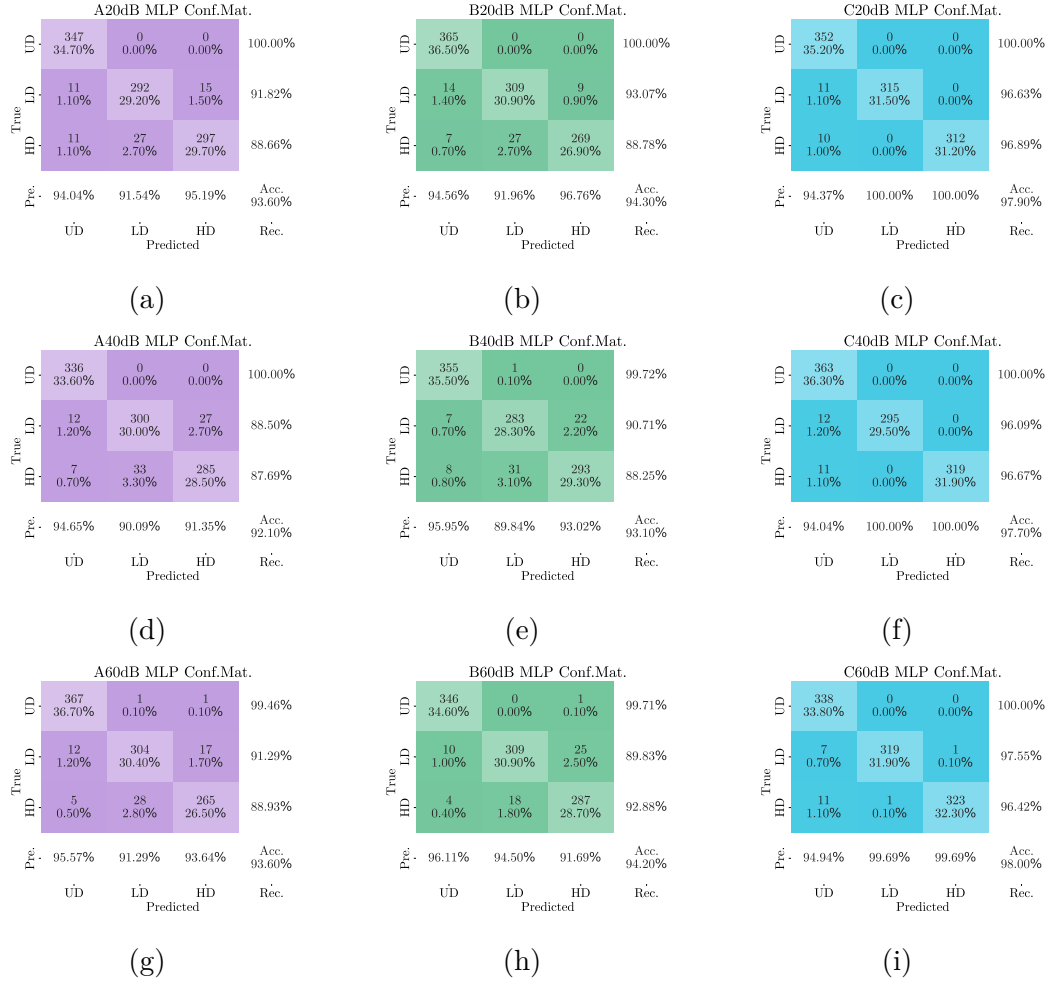


Figure 4.26: Classification results of the MLP models exploring varying noise effects.

a feature maps from a short segment of the overall dataset, especially in the case in which the feature’s location in that data segment is not highly correlated. The CNN model has been implemented in python through the TensorFlow module with the Keras front-end. Before training the neural models, the dataset is divided into two parts: a training set and a test set, with proportions of 80% (4000 simulations) and 20% (1000 simulations) respectively, and a further partition of 10% inside the training set defined the validation set for assessing accuracy performance online during the training phase among the epochs.

The performance of the best trained MLP model on different SNR levels has been validated with the test set, whose classification results have been condensed in the confusion matrix illustrated in Fig. 4.26. On the other hand, Fig. 4.27 shows the results from the best CNN model on the same datasets. The accuracy levels

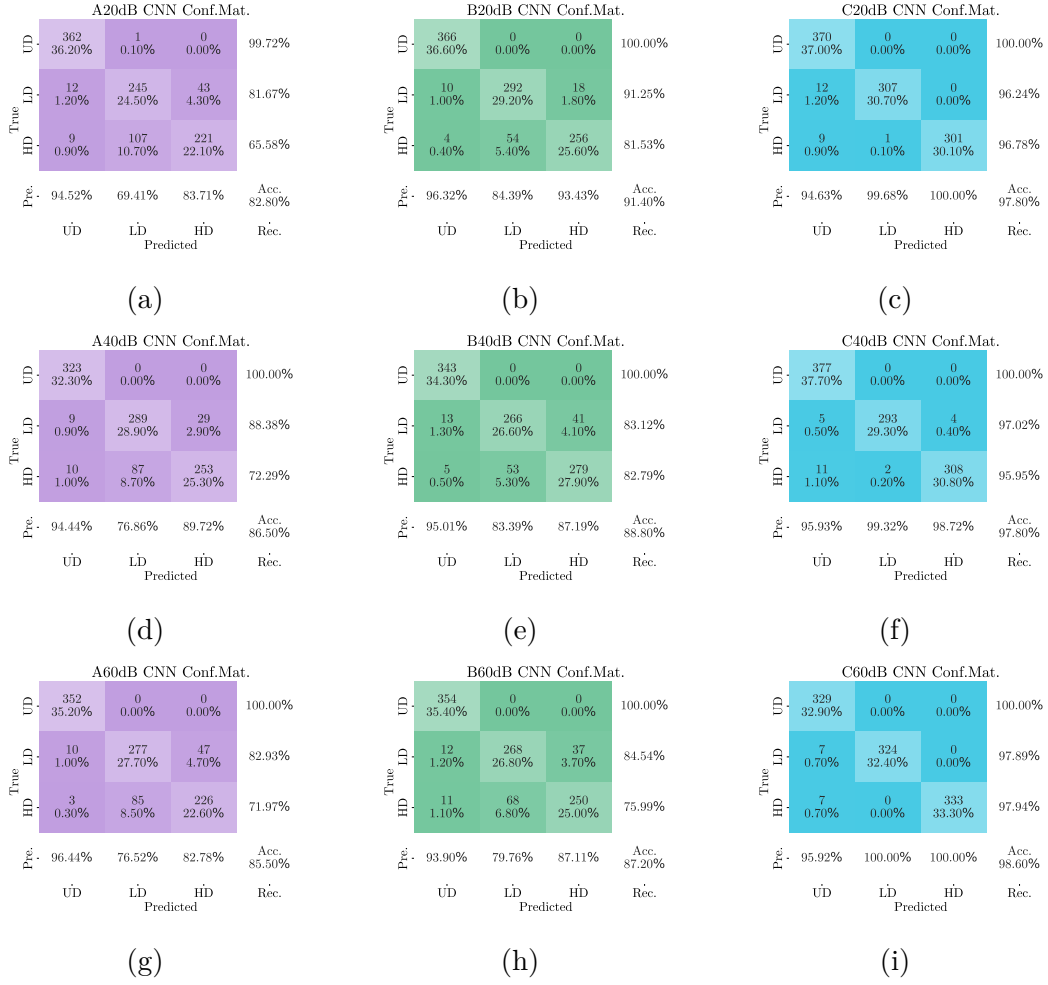


Figure 4.27: Classification results of the CNN models exploring varying noise effects..

are all above 90% for MLP models but decrease to 82.80% for CNN models in the cases (A) and (B). Accuracy measures the portion of the test set which has been correctly classified.

The precision measures the number of samples correctly classified in a particular class over the total number of samples which have been associated with that class. In contrast, the recall represents the number of samples correctly classified into a specific class over the number of samples which belongs to that class [61]. The precision and recall values are quite high, being above the 87.69% for all the classification possible outcomes in MLP models. Instead, there is a significant decrease on CNN, even to 65.58%. Considering CNN models in 60dB SNR levels, in Fig. 4.27 (g), the overall accuracy for method (A) is 85.50%. Fig. 4.27 (h) shows that the accuracy for method (C) is around 87.20%, and the higher classification

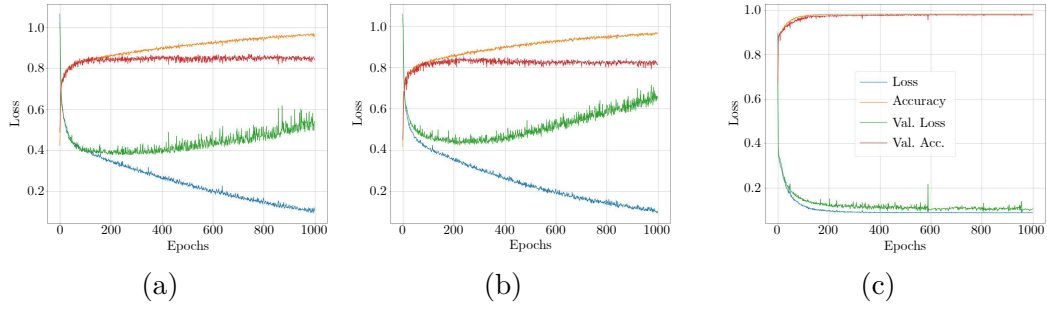


Figure 4.28: 60-dB noise level CNN training performances history during the epochs.

of the method (B) with respect to method (A) proves that this most informative subspace-based feature improves the classification performances of both CNN and ANN model for every noise levels. In Fig. 4.27 (i), the final accuracy for the trained model in method (C) is 98.60%. The outstanding higher classification performance of method (C) to methods (A) and (B) proves that considering an entire set of informative subspace-based features improves the classification performances of the DL models for the damage detection task.

Best weights and models should be saved for prediction. The loss function both for the training and the validation sets is depicted over the epochs, for the CNN model in 60dB SNR levels is reported in Fig. 4.28. When the validation loss starts to increase after a monotonic decreasing behavior, the overfitting of the model is reached. In Fig. 4.28 (a), the validation loss increases gradually while the loss on the training set decreases, reaching the overfitting point at around 400 epochs. The same situation appears in Fig. 4.28 (b), while the overfitting point is around 450 epochs. The validation accuracy continues to increase a little even when the overfitting point is reached. In Fig. 4.28 (c), the loss is relatively low. From a deeper insight into the loss and accuracy trends, it would virtually be possible to stop the training to epoch 150 to save computational cost and obtain almost the same performances.

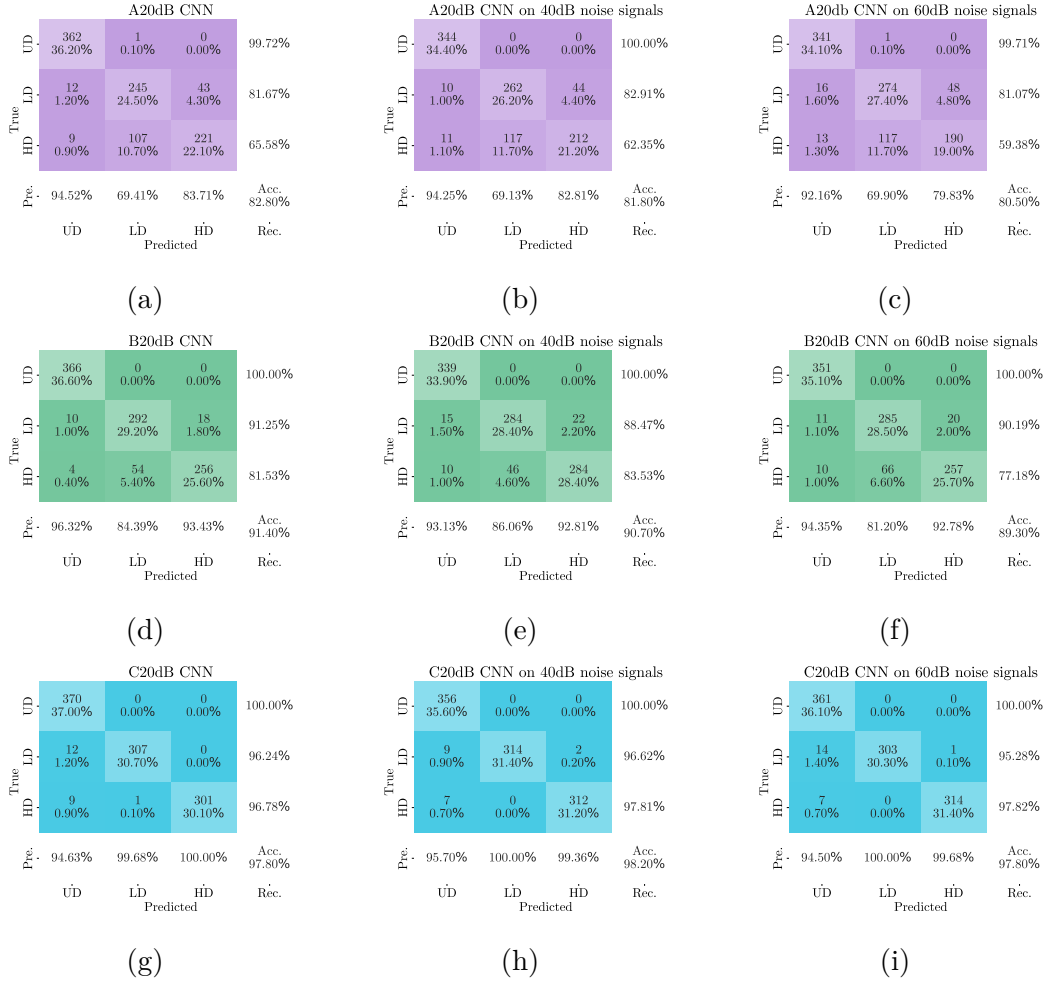


Figure 4.29: Classification results of the 20dB CNN models on other SNR levels in all three methods.

The robustness of the deep-learning is affected by the noise. Figure 4.29 (a), (d), and (g) respectively show the performance of the best CNN models in methods (A), (B), and (C). In method (A), the performances of the CNN model trained with the 20dB SNR level have been validated with the test set from 40dB SNR level, as illustrated in Figure 4.29 (b). The overall accuracy obtained results to be 81.80%. In Figure 4.29 (c), accuracy is 80.50% for the test set with the 60dB SNR level. The same outcomes can be drawn even for methods (B), and (C). Figure 4.30 shows the results for 60dB noise levels. Even if the noise level has changed significantly, the previously trained model gives good predictions.

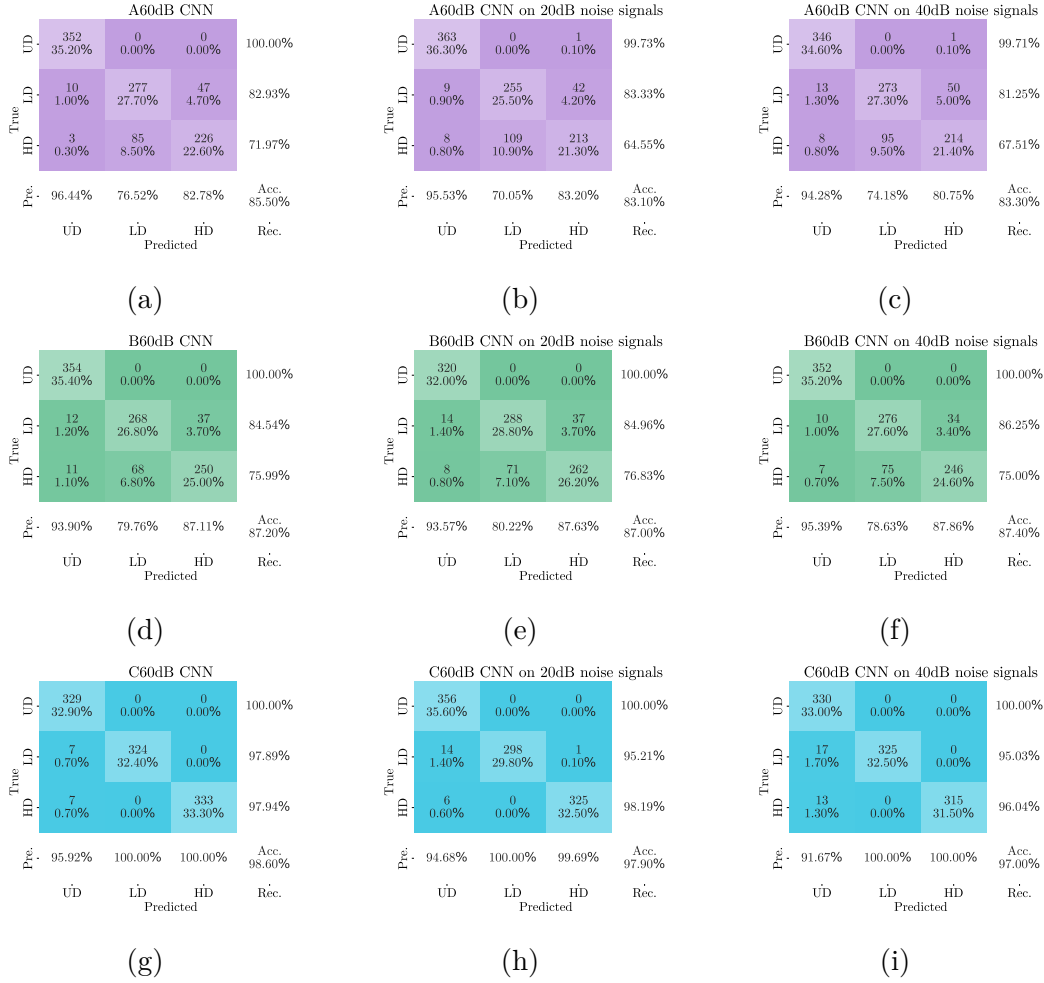


Figure 4.30: Classification results of the 60dB CNN models on other SNR levels in all three methods.

The current MLP and CNN models can provide quite interesting multiclass classification results considering the statistical time series features coupled with the Yan et al. subspace damage indicator [253]. This allows extending the capabilities of the MLP model. Furthermore, a good generalization of the current DL models is related to the fact that the 5000 numerical simulations randomly considered both how many damaged elements to consider and the level of damage to associate with those selected elements. This produced a time-series signal which covers many different cases, which was anyway successfully traced back to the three possible classification results: undamaged situation, low damage status (cross-section reduction of about 25%) and high damage condition (cross-section reduction of about 50%). The influence of noise is further reduced. DL models are robust to noise.

4.4 Damage detection conclusive remarks

In the present chapter, the studies conducted during the current Ph.D. program within the damage detection (DD) field were reported and discussed. Specifically, the DD represents the starting point in the study of how structural damage occurs and evolves under operating and in-service conditions. DD is indicated as the level 1 of the structural health monitoring (SHM) paradigm initially formalized by Rytter et al. [219]. For the sake of completeness, two further levels have been herein added to the SHM ideal paradigm, as reported in Fig. 4.1. Level 0 is a necessary condition because it refers to all the operations of the design and installation of any SHM monitoring system. On the other hand, the prognosis level 5 has been further detailed adding a new level 6 for adjusting this last level to the innovations and trends of the latest periods. Indeed, the novel emerging sensing technologies combined with artificial-intelligence-based solutions are paving a new road for rethinking smart structures of the next future, configuring new and intelligent structures within the smart city concept and environments with auto-diagnosis features, integrated early warning alert systems, and even with auto-prognosis predictions features. Therefore, for the crucial importance of the identification of structural damage, in the current Ph.D. program, the research studies were mainly focused on level 1 of the SHM paradigm, proposing some effective integration of AI solutions to improve existing methodologies. Besides vibration-based DD strategies, other nondestructive testing or evaluation (NDT/NDE) alternatives have been also studied. Specifically, some starting efforts were dedicated to acoustic emission (AE) passive monitoring strategies for crack identification and localization, see e.g. [224]. Another AI-based integration with NDT has been herein addressed focusing on tunnel linings' flaws detection via ground penetrating radar (GPR) monitoring systems. The current proposed approach for GPR indirect tunnel monitoring principally treated the problem as a multi-class defects classification problem arranged as a set of hierarchical binary classification schemes, as illustrated in Fig. 4.6. Immediate future research efforts should be geared towards the other three SHM paradigm remaining levels, i.e. the damage localization task, the damage severity quantification, and the actual safety health state assessment. The main purpose of all deeper levels formalized in the ideal SHM paradigm is to provide a reliable and exhaustive diagnosis, of existing structures and infrastructures, and possibly also with prognosis insights [219]. A promising research path for continuing the current research studies in that direction may be leveraging the deep learning (DL) model's interpretability tools in innovative ways, for instance exploiting attention maps which are naturally provided by the outputs of transformer models for defects' localization and severity assessment.

On the other hand, mainly focusing on the vibration-based approaches, during the current Ph.D. program special attention was dedicated to subspace-based damage indicators. Their definition is derived from the theoretical background of

the stochastic subspace identification (SSI) algorithm. In particular, the Yan et al. subspace-based DIs [253] herein adopted are formalized from the SSI-cov version based on the Hankel formulation of the output covariance estimates, see Appendix . The greatest advantage of dealing with subspace-based DIs is not strictly requiring to perform a prior complete OMA, and damage can be evidenced when comparing a reference state and a current, possibly damaged one. However, these indicators may exhibit poor informative value if their governing parameters are not properly selected. Therefore, to fully leverage all the potentials offered by innovative AI-based solutions, and even attempting reducing the arbitrary choice of governing parameters, and potentially poorly informative, an artificial neural network (ANN) solution was proposed to learn hidden patterns in a bunch of damage indicators computed for a reasonable range of values of governing parameters. The validations herein conducted on a numerical simple beam problem are promising, and an initial experimental real-world beam laboratory test appears as an encouraging assessment of the proposed methodology. Nonetheless, this initial study presents some limitations, such as requiring a representative finite element model to create the training database, which plays a crucial role in the effectiveness of the entire procedure. However, with very complex structural systems this approach seems quite unfeasible. Therefore, future studies should be mainly oriented on overcoming these limitations, rethinking the AI-assisted methodology whilst further exploring the potentialities offered by the subspace-based signature methods for all the levels in an ideal SHM paradigm [219].

Chapter 5

Future developments and conclusions

The main research topics conducted during the current Ph.D. program and discussed hitherto in the present Thesis document were mainly dedicated to the world of output-only vibration-based operational modal analysis (OMA) for structural health monitoring (SHM) purposes. Special attention was deserved to their branches of automatic operational modal analysis (AOMA) and damage detection (DD), pursuing the main goal of integrating artificial intelligence (AI), data-driven machine learning (ML), and deep learning (DL) solutions for further improving the conventional approaches, attempting to overcome some of the still existing limitations of the traditional methods.

It is worth reminding that one of the main fundamental underlining assumptions of conventional output-only OMA techniques is that the subject of the dynamic identification process is the whole combined system, as illustrated in Fig. 2.1. This implies the characterization of modal parameters, viz. natural frequencies, damping ratios, and mode shapes, related not only to the actual structural system of interest, but also to those harmonic components inherently present in the unmeasured input excitation [96]. In particular, the actual random operating loads causing vibration responses are conceived as the results of a loading filter fed with a stationary Gaussian white noise process in origin. This basic assumption actually restricted the OMA methods' validity scope to linear-time-invariant (LTI) structures under operating conditions in which their input vibration can be assumed as stationary and ergodic zero mean Gaussian white noise processes. In detail, the LTI property implies that the parameters governing the dynamic behavior of the structure under investigation are constant over time. Another advantage of vibration analysis of LTI systems is the validity of the modal superposition principle which allows reconstructing the dynamic response of a linear structure by superposing the harmonics which do not depend on any external force or load but only depend intrinsically on the stiffness and mass properties (eigenvalue analysis). On

the other hand, the acting in-service loads can be quite far from stationary conditions, reflecting their effects in the monitored vibration response. Therefore, this latter observation justifies the usual adoption of long vibration measurement acquisition duration in OMA. Indeed, the final goal is to mitigate instantaneous random effects of input excitation by averaging them over long observation time windows, thus approaching the stationary condition hypothesis [95]. Nevertheless, acquiring very long acquisitions to average the nonstationary effects is not always a feasible option. For instance, considering a structure under earthquake excitation or a bridge under very low traffic conditions (e.g. few train passages per day), the monitored vibration responses are typically short in time due to the very short duration of input excitation. The recorded time series usually exhibit an initial transient period in which nonstationary loads are acting, usually followed by a quite short free-decay response. Therefore, the impossibility of acquiring in-situ long vibration measurements being representative of these quite short input excitations typically prevents the adoption of conventional OMA methods, since they are often significantly far from their validity scope. Furthermore, in these latter special cases, it is not uncommon that structural systems are damaged during strong excitations like earthquakes. This implies the variation of their modal parameters during the transient period, especially with stiffness reductions, without respecting anymore the LTI condition. Another example in which the LTI hypothesis is lost is with mass-varying systems. Especially, focusing on civil engineering systems, in [7] it was mentioned that vibration-based monitoring of off-shore platforms can exhibit mass variation for various possible causes. For instance, salinity jointly with continuous dry and wet cycles at sea level may induce both corrosion on one side or marine growth on the other side. Moreover, even a simple water ingress may vary mass and damping dissipating properties of the off-shore platform. A further different example of a civil structure with mass-varying properties can be represented by cables of suspension or stayed bridges in arctic regions, which undergo ice accretion issues [268, 269].

All the above observations suggested that a completely different branch of study is instead devoted to nonstationary and/or nonlinear OMA procedures since a completely different mathematical framework is required. In this last chapter, a possible future promising research path is briefly mentioned dedicated to nonstationary OMA methods for analyzing time-varying structural systems. This specific subject represents frontier research within the civil engineering SHM-broad-range solutions. This is especially true from the perspective of effectively integrating innovative AI-aided tools aiming to overcome the still-existing analytical or methodological limitations in this field. This research area represents the most natural attaining for the topics currently addressed in the present Thesis document. Only some basic aspects of nonstationary OMA are mentioned in the remaining part of the chapter whilst progressively moving to the final conclusion section, unpretentious of being

completely exhaustive of this wide multidisciplinary discipline. It is worth underlining that no new case studies and/or new author's research papers are reported in the current and following sections. Indeed, the material herein reported should be interpreted as a brief literature review conducted in the last weeks of the current Ph.D. program. The final aim of this last chapter is therefore highlight some promising future research paths regarding the nonstationary OMA methods, which will be developed after the end of the current Ph.D. program, being probably the most natural research topic continuation.

5.1 Notes about nonstationary operational modal analysis

The structural system's nonlinearities may arise from several different sources [270], such as friction, gyroscopic effects, kinematic effects such as backlash phenomena [271], structural materials hysteresis, geometric constraints, and second-order deformation effects. These nonlinear effects further increase the difficulties of the dynamic behavior characterization due to the rise of multiple equilibrium points, bifurcation phenomena, resonance jump, and chaos among others [270]. Moreover, it is worth reminding that in dynamics and vibration control, it is fundamental to analyze stability conditions, thus investigating if the system returns to the same equilibrium point or if it maintains its original steady state of motion under small oscillations and perturbations. The most complete approach for the study of stability can be found in the study entitled "*The General Problem of the Stability of Motion*" by the Russian mathematician Lyapunov in the late 1900s [270]. Its direct method states that a system is in a stable equilibrium state if it is possible to formulate a positive-definite function of the state coordinates, called the Lyapunov function, and it is always negative or zero for small perturbations around the equilibrium point. Since its specific formulation depends on the analyzed system, the Lyapunov function has been studied for a number of classes of nonlinear dynamical systems, and it serves as a generalized norm of the dynamical system solution. Another popular method to study nonlinear random vibrations is to approximate the solutions of nonlinear systems according to statistical linearization or equivalent linearization techniques [272]. Besides nonlinearities, the nonstationarity of vibration responses of a system means that their statistical moments are time-dependent [272], and consequently their governing modal parameters are time-varying quantities [273]. The vibration solution can still be approximated to be Gaussian if the system is weakly nonlinear. In this case, the Duhamel integral equivalent to linear impulse response function still holds [272]. Otherwise, modal parameters exhibit time-varying properties, and an acknowledged method to visualize their changes over time is representing them according to time-frequency analysis methods [273].

Despite the concepts of amplitude and frequency spectrum being intuitive in stationary conditions, when dealing with nonstationary signals it is necessary to introduce the concept of instantaneous amplitude (IAs) and instantaneous frequencies (IFs), due to the intrinsic difficulties of characterizing these time-varying properties. Indeed, due to the nonperiodic nature of nonstationary involved signals, spectral base Fourier methods are inadequate. Therefore, a new starting technique was initially developed moving from Fourier transform concepts, called short-time Fourier transform (STFT) [273]. In STFT, nonstationary or transient signals are studied simultaneously in the time and frequency domain. This method relies on dividing the signal $x(t)$ into several short time blocks, separated or overlapped, according to a family of translating windowing functions $w(t - \tau)$ formulated for ensuring a certain frequency modulation, see e.g. Eqs. (2.19)-(2.20), and finally performing FT on each block:

$$X(\tau, f) = \int_{-\infty}^{\infty} x(t)w(t - \tau)e^{-i2\pi ft} dt, \quad (5.1)$$

Analyzing the time-frequency spectrogram, i.e. a graphical representation of the magnitude spectrum $|X(\tau, f)|^2$ versus time instants, the STFT is able to identify when and which frequencies are varying over time. However, the quality of spectral information retrievable is determined by the window length size. Being this latter the same for every frequency, in STFT it is important to choose the window size as a trade-off between computational efficiency and frequency resolution quality.

Adaptive STFT and multi-resolution STFT have been also formulated, i.e. when certain frequency bands are of special interest rather than others [273]. However, to systematically overcome the window limitation definition of the STFT method, the continuous wavelet transform (CWT) technique [7, 273] was developed, establishing its success in dealing with non-stationary signal analysis. CWT of a signal $x(t)$ can be expressed as follows:

$$X(a, b) = \int_{-\infty}^{\infty} x(t)\bar{\psi}_{a,b}(t)dt, \quad \text{where} \quad \bar{\psi}_{a,b}(t) = \frac{1}{\sqrt{a}}\bar{\psi}\left(\frac{t-b}{a}\right) \quad (5.2)$$

in which the symbol $\bar{\psi}(t)$ represents a prototype of window called mother wavelet, and the scaling factor $\frac{1}{\sqrt{a}}$ ensures energy normalization. The main advantage of CWT is determining correlations of the signal $x(t)$ at any time and scale changes, for a given mother wavelet function [273]. Therefore, CWT is able to detect chaotic behavior, and the resulting frequency resolution varies based on the window adopted with respect to the center frequency.

Another example of a most recent and widespread approach to studying the IFs is the Hilbert-Huang transform (HHT) technique. HHT adopts a two-step method. The foremost part is denoted as the empirical mode decomposition (EMD), also acknowledged as the sifting process. In this first part, the signal is decomposed into

n intrinsic mode functions (IMFs) $c_j(t)$, representing a set of base functions [274, 275, 276]:

$$x(t) = \sum_{j=1}^n c_j(t) + r_n, \quad (5.3)$$

being r_n the residue. The IMFs are narrow-band time signals extracted from the mother signal and are respectful of two conditions. Firstly, the number of zero crossings and its extremes must be the same, or at a limit different by one in all data. The second condition claims that the envelope delineated by the local minimum and maximum, usually interpolated by a cubic spline, must be symmetrical, thus delivering a zero average everywhere. Iterative repeating this sifting procedure, all the IMFs are found until an ending condition is met, e.g. based on a deviation limit between two consecutive IMFs [273]. Thereafter, the second part of the HHT algorithm relies on the adoption of the Hilbert transform (HT) technique for obtaining the time-frequency domain representation for each IMF in terms of time-dependent IAs and IFs. Denoted by the operator $H[\bullet]$, the Hilbert transform $d_j(t)$ of the j -th IMF $c_j(t)$ is given by

$$d_j(t) = H[c_j(t)] = \frac{1}{\pi} \text{P} \left[\int_{-\infty}^{\infty} \frac{c_j(\tau)}{t - \tau} d\tau \right], \quad (5.4)$$

in which $\text{P}[\bullet]$ denotes the Cauchy principal value, since this convolution integral of a function type $(1/t)$ does not always converge being not integrable in zero [276]. It was observed that the results of the HT method and the original signal given as the input argument of the HT are complex conjugate pairs. Therefore, leveraging this aspect in the HHT method, an analytic complex form $z_j(t)$ can be reconstructed by combining the IMFs acting as the real part and interpreting its HT as the imaginary part, i.e.

$$z_j(t) = c_j(t) + i d_j(t) = a_j(t) e^{i\theta_j(t)}. \quad (5.5)$$

As highlighted in Eq. (5.5), the analytical signal can be expressed in polar form according to an IA function $a_j(t)$ and an instantaneous phase angle function $\theta_j(t)$, from which obtaining the IFs $f_j(t)$ for the j -th IMF component:

$$a_j(t) = \sqrt{[c_j(t)]^2 + [d_j(t)]^2}, \quad \theta_j(t) = \arctan \left[\frac{d_j(t)}{c_j(t)} \right], \quad f_j(t) = \frac{d\theta_j(t)}{dt}. \quad (5.6)$$

After performing the HT part for all IMFs, it is possible to substitute the results in Eq. (5.3). Specifically, maintaining only the real parts and dropping the residue term r_n , the original signal $x(t)$ can be approximated as

$$x(t) = \Re \left\{ \sum_{j=1}^n a_j(t) e^{[i \int_0^t f_j(\tau) d\tau]} \right\}, \quad (5.7)$$

The residue term r_n has been left out on purpose, since this term is usually a constant or a monotonic term [275]. Indeed, despite HT can also simply treat constant or monotonic terms as a component for longer oscillation, the energy involved in the residual trend represents a mere mean offset, but its uncertainty over a longer trend is not of actual interest when the main focus is on oscillatory components. Comparing Eq. (5.7) with the classical Fourier Transform in Eq. (2.1) it is clear that HT represents a generalization of the classical FT. Indeed, whilst the FT allows decomposing any signal in a linear combination of sinusoidal components at different frequencies called harmonics, the amplitude coefficients are constant over time. On the other hand, HT permits overcoming this limitation allowing to account for time-varying IAs and IFs, enabling the analysis of nonlinear and nonstationary vibration signals. Specifically, the frequency-time distribution of the amplitude $H(f, t)$ is called Hilbert amplitude spectrum, or simply Hilbert spectrum. If the IAs are squared, this quantity is energy-related, thus denoting the so-called Hilbert energy spectrum. The marginal Hilbert spectrum $h(f)$ is given by integrating the Hilbert spectrum $H(f, t)$ over time, similar to the marginalization operation in joint probability distributions. $h(f)$ provides the accumulated amplitude over time in the probabilistic sense, representing a measure of the total energy contribution from each frequency value [275]. Similarly, instantaneous energy $IE(t)$ can be defined as the integral of the Hilbert spectrum over frequency variable, giving information about the time-variation of energy.

The HHT validity and superiority to other methods for time-frequency analysis dealing with nonstationary and nonlinear data have been demonstrated in literature [275], confirming its adaptive basis, i.e. do not require using additional spurious harmonics to represent non-stationary and nonlinear components [273]. Despite the gained recognition in the scientific and engineering community in the last decades, the HHT theoretical basis is still controversial and debated nowadays, motivating the topical frontier research perspective. The greater concerns are especially related to the definition of meaningful IFs, which often require imposing restrictive conditions otherwise negative IAs may appear as an outcome of the HT process [276]. Moreover, regarding system identification tasks, time-frequency analysis methods like HHT have been adapted to the cases where both input and output data are known, e.g. in the vibration control engineering sector. Conversely, dealing with unknown systems typical of civil engineering structures and just focusing on output-only data may provide very complex and possibly ill-posed problems. A priori knowledge of the skeleton of the mathematical framework involved in the physical process that generated the nonlinear vibration (e.g. damaging structure under extreme loading conditions such as seismic scenarios) may aid in setting up an identification framework based on the HHT method [275].

Finally, as observed in STFT or CWT, nonstationary vibration analysis often involves local analysis methods over small time windows. This permits tracking

the time-varying modal properties of interest. In contrast, in LTI and stationary systems spectral analyses are typically global methods, acting on the entire vibration duration. Starting from this locality consideration usually involved in nonstationary vibration analysis methods, some attempts have been proposed in the literature to re-adapt the conventional OMA approaches, such as the SSI-dat method for dealing with nonstationary signals. In particular, as the conclusions of the present chapter, and even of the current Ph.D. program, a brief description of the recursive SSI (RSSI) algorithm have been discussed in the next subsection.

5.1.1 Recursive stochastic subspace identification

Among the first attempts to re-adapt conventional OMA techniques for nonstationary output-only vibration analysis, some scholars attempted to use SSI algorithms by imposing a recursive analysis framework over short time sliding windows [277, 278, 279, 280]. The main goal they aspired to was developing an online modal parameters tracking system, e.g. serving for damage detection (DD) purposes in the civil engineering sector, for instance under earthquake shaking conditions. In the existing literature, two main different subspace identification branches were delineated for nonstationary data. The recursive subspace identification (RSI) identifies those methods based on the input-output state space formulation, thus with the disadvantage of requiring acquiring also the input excitation. One of the most recurrent solving algorithms for RSI in the literature is defined as the Multivariable Output-Error State Space (MOESP) algorithm. On the other hand, the recursive stochastic subspace identification (RSSI) method is based on output-only measurements, thus being of greater interest in the current Thesis document and for OMA purposes. Its mathematical framework directly moves from SSI formulations previously discussed in Chapter 2. Specifically, the attention is herein mainly focused on the RSSI mainly provided by Weng et al. [277] and Loh et al. [278, 279]. The scholars derived the RSSI formalization starting from the SSI-dat framework, implying the basic assumption that all input sources are white noise processes. To truly attempting approaching this stringent assumption even for nonstationary systems, it is necessary to avoid a one-batch analysis of the entire vibration time history recordings. Instead, it is necessary to make a recursive calculation over very short sliding time windows of analysis. Indeed, besides abrupt changes in structural stiffness and/or mass properties suddenly occurring, the system can be reasonably still approximated to an instantly LTI structure in every short time window separately.

As illustrated both in Chapter 2 and in Appendix A, the measured data from l sensors with a sampling frequency f_s are gathered in vectors $\mathbf{y}_r \in \mathbb{R}^l$ for every r -th time instant, with $r = 0, 1, \dots, N_t$. According to the SSI-dat formulation, the output measurement vectors are then arranged in a Hankel matrix $\mathbf{Y}_{0|2i-1} \in \mathbb{R}^{2li \times j}$ according to Eq. (2.116), given a user-defined integer number of block-rows called time shift parameter i . Consequently, the resulting Hankel matrix

is characterized by a fixed number of block rows equal to $2li$ and, considering all output-only measurement data equal to $N_d = N_t + 1$, a resulting number of columns equal to $j = N_d - 2i + 1$. This Hankel matrix $\mathbf{Y}_{0|2i-1}$ can be partitioned into two submatrices denoted as past data matrix \mathbf{Y}_p and future data matrix \mathbf{Y}_f , both with dimensions $li \times j$. The Kalman state sequence matrix \mathbf{S}_i can be estimated according to linear algebra geometric orthogonal projection of the row space of future data matrix \mathbf{Y}_f toward the row space of past data matrix \mathbf{Y}_p , defining the so-called projection matrix $\mathbf{\Pi}_i$, see Eq. (2.117): The SSI fundamental theorem states that when the system is fully controllable and observable [96], and if the chosen time shift parameter i is fulfilling the condition in Eq. (2.96), $\mathbf{\Pi}_i$ can be decomposed as the product of the extended observability matrix \mathbf{O}_i and the Kalman filter state sequence estimates $\hat{\mathbf{S}}_i$ [101], as in Eq. (2.118).

$$\mathbf{Y}_{0|2i-1} = \begin{bmatrix} \mathbf{Y}_p \\ \mathbf{Y}_f \end{bmatrix}, \quad \mathbf{\Pi}_i = \mathbf{Y}_f / \mathbf{Y}_p = \mathbf{O}_i \hat{\mathbf{S}}_i = \begin{bmatrix} \mathbf{C} \\ \mathbf{CA} \\ \vdots \\ \mathbf{CA}^{i-1} \end{bmatrix} [\hat{\mathbf{s}}_i \quad \hat{\mathbf{s}}_{i+1} \quad \dots \quad \hat{\mathbf{s}}_{i+j-1}].$$

To avoid the expensive direct computation of the projection matrix according to Eq. (2.117) requiring the matrix inversion operation, alternatively, $\mathbf{\Pi}_i$ can be numerically estimated more efficiently starting from the LQ decomposition of the output measurement Hankel matrix, thus delivering a lower triangular matrix \mathbf{L} and an orthogonal matrix \mathbf{Q} ($\mathbf{Q}\mathbf{Q}^T = \mathbf{Q}^T\mathbf{Q} = \mathbf{I}$). It is worth reminding that, the LQ decomposition of a long rectangular matrix likewise the output measurement Hankel matrix $\mathbf{Y}_{0|2i-1} \in \mathbb{R}^{2li \times j}$ with $j > 2li$, generally deliver a long lower triangular matrix $\mathbf{L} \in \mathbb{R}^{2li \times j}$ which present the right $j - 2li$ columns of entire zeros, whereas it has an orthogonal matrix $\mathbf{Q} \in \mathbb{R}^{j \times j}$. Therefore, it is possible to further simply the LQ decomposition of the $\mathbf{Y}_{0|2i-1}$ matrix with the approach denoted *thin LQ decomposition*, i.e. defining a lower triangular partition $\mathbf{L}_1 \in \mathbb{R}^{2li \times 2li}$ and the related sub-matrices derived from the orthogonal one, being $\mathbf{Q}_{L_1} \in \mathbb{R}^{2li \times j}$ and $\mathbf{Q}_{L_2} \in \mathbb{R}^{(j-2li) \times j}$, still having orthogonal rows:

$$\mathbf{Y}_{0|2i-1} = [\mathbf{L}_1 \quad \mathbf{0}] \begin{bmatrix} \mathbf{Q}_{L_1} \\ \mathbf{Q}_{L_2} \end{bmatrix} = \mathbf{L}_1 \mathbf{Q}_{L_1} \quad (5.8)$$

When output measures Hankel matrix has full rank $2li$, then the matrices \mathbf{L}_1 and \mathbf{Q}_{L_1} are unique matrix, but not \mathbf{Q}_{L_2} in general [277]. Therefore, similarly to Eq. (2.119), thereafter performing the thin LQ decomposition of Eq. (5.8), the block-row nature of the output data Hankel matrix permits a further partitioning of the square lower triangular matrix \mathbf{L}_1 into block sub-matrices, i.e. partitioning $\mathbf{L}_1 \in \mathbb{R}^{2li \times 2li}$ into $\mathbf{L}_{11}, \mathbf{L}_{21}, \mathbf{L}_{22} \in \mathbb{R}^{li \times li}$ and splitting the related $\mathbf{Q}_{L_1} \in \mathbb{R}^{2li \times j}$

into $\mathbf{Q}_{11}, \mathbf{Q}_{22} \in \mathbb{R}^{j \times li}$, finally obtaining [277]:

$$\mathbf{Y}_{0|2i-1} = \begin{bmatrix} \mathbf{Y}_p \\ \mathbf{Y}_f \end{bmatrix} = \mathbf{L}_1 \mathbf{Q}_{L_1} = \begin{bmatrix} \mathbf{L}_{11} & \mathbf{0} \\ \mathbf{L}_{21} & \mathbf{L}_{22} \end{bmatrix} \begin{bmatrix} \mathbf{Q}_{11}^T \\ \mathbf{Q}_{22}^T \end{bmatrix} \Rightarrow \mathbf{\Pi}_i = \mathbf{Y}_f / \mathbf{Y}_p = \mathbf{L}_{21} \mathbf{Q}_{11}^T \quad (5.9)$$

The extended observability matrix \mathbf{O}_i is of special interest because it provides the chased modal properties, encoded in the state transition matrix \mathbf{A} and the output influence matrix \mathbf{C} . In the traditional SSI-dat version, the matrix \mathbf{O}_i can be retrieved using the SVD of the projection matrix $\mathbf{\Pi}_i$, see Eq. (2.121).

$$\mathbf{\Pi}_i = \mathbf{O}_i \hat{\mathbf{S}}_i = \mathbf{U} \mathbf{\Sigma} \mathbf{V}^T \approx \mathbf{U}_1 \mathbf{\Sigma}_1 \mathbf{V}_1^T, \Rightarrow \mathbf{O}_i = \mathbf{U}_1 \mathbf{\Sigma}_1^{1/2} \mathbf{T},$$

where \mathbf{T} is a transformation matrix that can be considered as an identity matrix. Nevertheless, as demonstrated in Eq. (5.9), the columns space of \mathbf{O}_i can be obtained directly from the columns space of the matrix \mathbf{L}_{21} , demonstrating that only \mathbf{L}_{21} is needed for system identification purposes. Therefore, as evidenced in [277], it is possible to deal with an economic matrix size rather than computing the complete projection matrix by Eq. (2.117), directly obtaining the extended observability matrix \mathbf{O}_i from the left singular vectors of matrix \mathbf{L}_{21} :

$$\mathbf{L}_{21} = \mathbf{U}_{L_{21}} \mathbf{\Sigma}_{L_{21}} \mathbf{V}_{L_{21}}^T = [\mathbf{U}_{1,L_{21}} \quad \mathbf{U}_{2,L_{21}}] \begin{bmatrix} \mathbf{\Sigma}_{1,L_{21}} & \mathbf{0} \\ \mathbf{0} & \mathbf{0} \end{bmatrix} \begin{bmatrix} \mathbf{V}_{1,L_{21}}^T \\ \mathbf{V}_{2,L_{21}}^T \end{bmatrix} \quad (5.10)$$

$$\approx \mathbf{U}_{1,L_{21}} \mathbf{\Sigma}_{1,L_{21}} \mathbf{V}_{1,L_{21}}^T, \Rightarrow \mathbf{O}_i = \mathbf{U}_{1,L_{21}}. \quad (5.11)$$

Now it would be virtually possible to estimate the state matrices \mathbf{A} and \mathbf{C} , e.g. according to Eqs. (2.105)-(2.106), to get the modal parameter of interest by solving the EVD problem of state transition matrix \mathbf{A} using Eq. (2.109), and making use of Eqs. (2.30)-(2.33), and Eq. (2.110) to get natural frequencies, damping ratios, and mode shape respectively.

However, these latter observations have not solved yet the recursive problem of using SSI-dat on different sliding time windows of analysis. Indeed, an efficient procedure almost real-time has been formulated in Weng et al. [277] and Loh et al. [278, 279], conceived as a two-step procedure attempting to avoid recursively executing the computational demanding SVD decomposition process. Considering overlapping time windows, there is a part of shared data in common between two consecutive time windows of analysis. Therefore the first step of the two-step RSSI procedure is updating the LQ decomposition by dropping a portion of old data and adding an equivalent portion of new data, whilst leveraging already processed information of remaining data to efficiently perform this updating step. The second step of the RSSI procedure instead is demanded to update the column space of the extended observability matrix, again for providing a more efficient estimation of modal parameters of interest.

Preliminary observations on the LQ decomposition of the Hankel matrix in Eq. (5.9) permit to deal with an “economic-size” of the output measurement Hankel matrix. Indeed, Hankel matrix $\mathbf{Y}_{0|2i-1}$ is generally a rectangular matrix belonging to $\mathbb{R}^{2li \times j}$, however, as evidenced in Eq. (5.9) only li columns of the LQ decomposition are necessary, since the key information of interest for estimating the projection matrix are carried only by $\mathbf{L}_{21} \in \mathbb{R}^{li \times li}$ and $\mathbf{Q}_{22}^T \in \mathbb{R}^{j \times li}$. Therefore, the Hankel matrix $\mathbf{Y}_{0|2i-1}$ can be truncated to a square matrix $\mathbf{Y}_{1|j} \in \mathbb{R}^{j \times j}$, thus imposing a block column number j being equal to the total number of block rows $2li$, and indicating each column of this matrix as \mathbf{h}_k with $k = 1, 2, \dots, j$. It is worth noting that truncating the Hankel matrix to this square dimension implies that the sliding time window of analysis for every recursive step of the RSSI has a fixed length of $w = j + 2i - 1$ in terms of number of considered samples of the measured data, or equivalently $W = w/fs$ if expressed in seconds. Therefore, the choice of time shift parameter i plays a crucial role in imposing the resolution of the analysis signal, directly affecting the dimension of the time window length of analysis [279]. The LQ decomposition of this new square matrix $\mathbf{Y}_{1|j}$ is denoted as

$$\mathbf{Y}_{1|j} = [\mathbf{h}_1 \ \mathbf{h}_2 \ \dots \ \mathbf{h}_k \ \dots \ \mathbf{h}_j] = \mathbf{L}_1 \mathbf{Q}_1 \quad \text{with } \mathbf{L}_1, \mathbf{Q}_1 \in \mathbb{R}^{j \times j} \quad (5.12)$$

In the recursive step, a user-defined time window shifting time Δt should be defined, or equivalently the number of samples p to be considered as the stride parameter of the sliding window. For ensuring overlapping sliding windows, p must be chosen lower than j , i.e. $p < j$ [277]. Therefore, in the first initial window dataset of samples in the range $[1, j]$, the squared Hankel matrix can be partitioned in the first p data that will be dropped $\mathbf{Y}_{1|p}$ and in the remaining $j - p$ data which will be useful for estimating the next window of analysis. Compute the next window LQ decomposition $\mathbf{L}_2 \mathbf{Q}_2$ leveraging information in the remaining $j - p$ data is crucial for the success of the RSSI algorithm. The method of the Givens rotations has been adopted to compute the LQ decomposition of a matrix. Indeed, as reported in [277], to better understand the recursive passage a deeper insight into how LQ decomposition is computed is necessary. Indeed, one of the methods that can be used for computing LQ decomposition is using the Givens rotations transformation method. A Givens rotation is a square transformation matrix $m \times m$ defined as an identity unitary diagonal matrix with zeros elsewhere, except for four elements at position respectively (a, a) , (a, b) , (b, a) , (b, b) , with $a, b \leq m$, $a \neq b$:

$$\mathbf{g}(a, b, \theta) = \begin{bmatrix} 1 & \dots & 0 & \dots & 0 & \dots & 0 \\ \vdots & \ddots & \vdots & & & & \vdots \\ 0 & \dots & \cos(\theta) & \dots & \sin(\theta) & \dots & 0 \\ \vdots & \ddots & \vdots & & & & \vdots \\ 0 & \dots & -\sin(\theta) & \dots & \cos(\theta) & \dots & 0 \\ \vdots & \ddots & \vdots & & & & \vdots \\ 0 & \dots & 0 & \dots & 0 & \dots & 1 \end{bmatrix} \quad (5.13)$$

A Givens rotation is an orthogonal matrix since $\mathbf{g}(a, b, \theta)[\mathbf{g}(a, b, \theta)]^T = \mathbf{I}$. When the Givens rotation is multiplied to a column vector $\mathbf{z} \in \mathbb{R}^{m \times 1}$, it performs a counterclockwise rotation of θ radians in the (a, b) coordinate plane. Therefore, with a suitable definition of the θ angle, the Givens rotation can be used for zeroing the z_b entry when multiplied to the column vector \mathbf{z} , i.e.

$$\mathbf{g}(a, b, \theta) \begin{bmatrix} z_1 \\ z_2 \\ \vdots \\ z_a \\ \vdots \\ z_b \\ \vdots \\ z_m \end{bmatrix} = \begin{bmatrix} z_1 \\ z_2 \\ \vdots \\ \bar{z}_a \\ \vdots \\ 0 \\ \vdots \\ z_m \end{bmatrix}, \quad \text{with } \cos(\theta) = \frac{z_a}{\bar{z}_a}, \sin(\theta) = \frac{z_b}{\bar{z}_a}, \bar{z}_a = \sqrt{z_a^2 + z_b^2}. \quad (5.14)$$

Indeed, applying series of appropriate Givens rotations $\mathbf{g}_1 \mathbf{g}_2 \dots \mathbf{g}_t$ with $\mathbf{g}_k \in \mathbb{R}^{n \times n}$ to the right side of a generic rectangular matrix $\mathbf{M} \in \mathbb{R}^{m \times n}$ with $n > m$, it is possible to transform it into a lower triangular matrix $\mathbf{L} \in \mathbb{R}^{m \times n}$ coherent with the LQ decomposition method. Since every \mathbf{g}_k component has the same dimensions of the number of columns n , the same reasoning of Eq. (5.14) should be applied to deliver a lower triangular matrix, but the column vector \mathbf{z} should represent the generic row of the matrix \mathbf{M} . The resulting right product of the Givens rotations $\mathbf{g}_1 \mathbf{g}_2 \dots \mathbf{g}_t$ is denoted as \mathbf{G}^T . Therefore, the LQ decomposition is thus obtained as in Eq. (5.15), noting that \mathbf{G} is equal to the orthogonal matrix \mathbf{Q} . From Eq. (5.15), the same reasoning of thin LQ decomposition in Eq. (5.8) can be done once again.

$$\mathbf{M} = (\mathbf{M}\mathbf{G}^T)\mathbf{G} = \mathbf{L}\mathbf{G} = \mathbf{L}\mathbf{Q}. \quad (5.15)$$

Recalling the Eq. (5.12), the Givens rotations method is used to transform the first p columns of \mathbf{Q}_1 of squared output measurement Hankel matrix $\mathbf{Y}_{1|j}$ into an upper triangular matrix by multiplying \mathbf{G}_1 to the left of \mathbf{Q}_1 . In [277] it was demonstrated that this upper triangular matrix in reality appears as a block diagonal matrix as follows:

$$\mathbf{G}_1 \mathbf{Q}_1 = \begin{bmatrix} \mathbf{I}_p & \mathbf{0} \\ \mathbf{0} & \bar{\mathbf{Q}}_1 \end{bmatrix}, \quad (5.16)$$

in which the identity matrix associated to the first p columns is $\mathbf{I}_p \in \mathbb{R}^{p \times p}$, whereas the matrix $\bar{\mathbf{Q}}_1 \in \mathbb{R}^{(j-p) \times (j-p)}$ is an orthogonal matrix. Therefore, in the first dataset time window, leveraging the Givens rotation \mathbf{G}_1 , it is possible to rewrite Eq. (5.12) partitioning Hankel matrix columns associated with the first p data which will be dropped and the remaining data after the window sliding process:

$$\begin{aligned} \mathbf{Y}_{1|j} &= \mathbf{L}_1 \mathbf{Q}_1 = (\mathbf{L}_1 \mathbf{G}_1^T)(\mathbf{G}_1 \mathbf{Q}_1) = [\mathbf{Y}_{1|p} \quad \bar{\mathbf{L}}_1] \begin{bmatrix} \mathbf{I}_p & \mathbf{0} \\ \mathbf{0} & \bar{\mathbf{Q}}_1 \end{bmatrix} \\ &= [\mathbf{Y}_{1|p} \quad \bar{\mathbf{L}}_1 \bar{\mathbf{Q}}_1] = [\mathbf{Y}_{1|p} \quad \mathbf{Y}_{p+1|j}], \end{aligned} \quad (5.17)$$

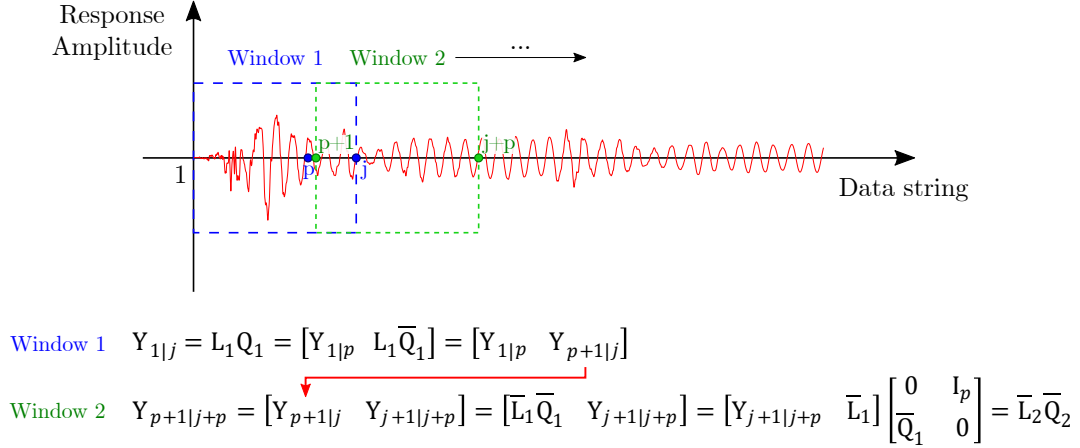


Figure 5.1: RSSI recursive updating procedure with sliding windows of analysis.

in which matrices $\bar{\mathbf{L}}_1$ and $\bar{\mathbf{Q}}_1$ can be estimated via the first Givens rotations of \mathbf{L}_1 and \mathbf{Q}_1 . $\bar{\mathbf{L}}_1$ is an almost lower triangular matrix, resulting from the first Givens rotations of this quasi-LQ decomposition, also denoted as temporary decomposition [279].

After the first window sliding, the situation is the one illustrated in Fig. 5.1. New $p < j$ columns of the complete Hankel matrix $\mathbf{Y}_{0|2i-1}$ should be added to $\mathbf{Y}_{1|j}$. However, in order to maintain the same square size of the Hankel matrix, the first p columns of the squared Hankel matrix $\mathbf{Y}_{1|j}$ must be dropped. This delivers a new LQ decomposition of the updated block Hankel matrix:

$$\mathbf{Y}_{1+p|j+p} = \mathbf{L}_2 \mathbf{Q}_2 \quad \text{with } \mathbf{L}_2, \mathbf{Q}_2 \in \mathbb{R}^{j \times j} \quad (5.18)$$

The goal is to compute this new LQ decomposition efficiently, i.e. using new incoming data and leveraging the already computed information on the overlapped part of past $(j - p)$ data, reminding that from Eq. (5.17) it was demonstrated that $\bar{\mathbf{L}}_1 \bar{\mathbf{Q}}_1 = \mathbf{Y}_{p+1|j} \in \mathbb{R}^{j \times (j-p)}$. Appending the new data of the current window of analysis, it is possible to obtain a second temporary decomposition as follows:

$$\begin{aligned} \mathbf{Y}_{1+p|j+p} &= [\mathbf{Y}_{1+p|j} \quad \mathbf{Y}_{j+1|j+p}] = [\bar{\mathbf{L}}_1 \bar{\mathbf{Q}}_1 \quad \mathbf{Y}_{j+1|j+p}] \\ &= [\mathbf{Y}_{j+1|j+p} \quad \bar{\mathbf{L}}_1] \begin{bmatrix} \mathbf{0} & \mathbf{I}_p \\ \bar{\mathbf{Q}}_1 & \mathbf{0} \end{bmatrix} = \bar{\mathbf{L}}_2 \bar{\mathbf{Q}}_2, \end{aligned} \quad (5.19)$$

in which the resulting block matrix $\bar{\mathbf{L}}_2$ is almost a lower triangular matrix defined as

$$\bar{\mathbf{L}}_2 = [\mathbf{Y}_{j+1|j+p} \quad \bar{\mathbf{L}}_1] \quad (5.20)$$

whereas $\bar{\mathbf{Q}}_2$ is an orthogonal matrix defined as

$$\bar{\mathbf{Q}}_2 = \begin{bmatrix} \mathbf{0} & \mathbf{I}_p \\ \bar{\mathbf{Q}}_1 & \mathbf{0} \end{bmatrix} \quad (5.21)$$

Starting from this quasi-LQ decomposition estimate, in order to retrieve the complete decomposition of Eq. 5.18, a second Givens rotations method is adopted to transform the almost lower triangular matrix $\bar{\mathbf{L}}_2$ into the chased \mathbf{L}_2 matrix:

$$\mathbf{Y}_{1+p|j+p} = (\bar{\mathbf{L}}_2 \mathbf{G}_2)(\mathbf{G}_2^T \bar{\mathbf{Q}}_2) = \mathbf{L}_2 \mathbf{Q}_2 \quad (5.22)$$

In conclusion, the Givens rotations transformation is thus recursively used twice for every RSSI sliding window. The first Givens rotations \mathbf{G}_1 are used for decoupling the old LQ decomposition in order to drop the old p columns. The second Givens rotation \mathbf{G}_2 is instead used after new p data columns have been added for transforming back the temporary decomposition into a complete LQ decomposition. The advantage is that the terms $\bar{\mathbf{L}}_1$ and $\bar{\mathbf{Q}}_1$ are not computed again, thus reducing the overall computational burden [277]. Some adjustments have been proposed to further reduce the influence of older data whilst giving greater importance to newly appended data. Indeed, in Eq. (5.20), it is possible to consider a forgetting factor μ acting on the $\bar{\mathbf{L}}_1$ term, which can aid to better detect sudden abrupt changes in modal parameters tracking over the sliding time windows of analysis [277].

5.2 Final remarks

The current Ph.D. program has been primarily dedicated to analyzing and improving the conventional operational modal analysis (OMA) framework and procedures, integrating innovative artificial intelligence solutions. The PyOMA module, and its graphical user interface (GUI) version, are the first main achievements of the current research program referring to the study of traditional and well-established OMA methods. Gratefully to an international collaboration with other two institutions, i.e. the University of L'Aquila (Italy) and the Norwegian Institute of Wood Technology in Oslo (Norway), this new Python-based package provided both researchers and practitioners worldwide with an all-in-one convenient tool for the dynamic identification of civil structures and infrastructures. PyOMA encompasses a quite complete suite of the most widespread techniques, working both in time and in frequency domains, fundamental instruments for anyone working in the sector of dynamic identification of systems.

Furthermore, considering the advances within the digital revolution of the last decades, artificial intelligence (AI) and machine learning (ML) tools are significantly opening new ground-breaking frontiers and innovations in all the scientific and engineering disciplines. Therefore, the greatest efforts of the current Ph.D. program research studies were mainly devoted to understanding existing limitations in conventional OMA approaches, and effectively integrating AI-assisted solutions for attempting to overcome some of those still existing shortcomings. In particular, the current most remarkable research achievement was the formulation of a novel intelligent automatic operational modal analysis (i-AOMA) framework. Perfectly

contextualized within the current growing demand for continuous and automatic structural health monitoring (SHM) systems, the proposed i-AOMA attempted to increase the automation level of the existing OMA alternatives, whilst combining in an original way some ML-based techniques for improving the reliability of dynamic identification results. Just to mention some of the main features offered, the i-AOMA method combines quasi-Monte Carlo sampling to reduce the impacts of the user's arbitrary choice of OMA control parameters, and postprocessing the identification results with effective ML-based data-driven solutions. This methodology can reliably identify actual physical recurrent modal properties whilst discarding those spurious ones. Moreover, it also provides an uncertainty evaluation of the modal parameter results.

Moving to a broader perspective besides the output-only vibration-based dynamic identification of modal parameters, many research efforts have been also dedicated during the current Ph.D. program to the damage detection problem. Indeed, a comprehensive SHM ideal paradigm can be formalized into different levels based on the level of detail and depth of understanding of the occurring structural damage diagnosis and prognosis. The damage detection task represents the first level of the ideal SHM paradigm, playing a crucial role in determining the amount of economic and time resources to be earmarked for further deeper damage diagnosis and/or prognosis evaluations, and even for optimizing and prioritizing maintenance activities and safety restoration interventions at regional or even national scale. In particular, the herein-conducted research investigations aimed to introduce ML and deep learning (DL) data-driven methods for supporting the identification of flaws and structural damages based on indirect nondestructive testing and evaluation (NDT/NDE) approaches. Computer vision applications for tunnel lining monitoring and vibration-based damage indicators for bridges derived from the mathematical OMA framework have been explored. Nevertheless, considerable research work should be still spent in this field to provide in future for further deeper insights into the above-mentioned aspects.

In conclusion, this last chapter presented a mini-review of the topic that can be probably considered the most natural progression of the currently analyzed topics. Specifically, since the scope of applicability of conventional OMA approaches is limited to linear time-invariant (LTI) structures under operational stationary white noise excitation, future promising research paths should additionally explore the field of nonlinear and nonstationary OMA methods. For instance, exploring vibration-based identification methods even transient under earthquake conditions, especially with a progressively damaging of the structural system during the analysis, it is still challenging nowadays and requires a more sophisticated mathematical framework to adapt the OMA method to nonstationary scenarios. Therefore, a promising future research path may be the analysis of time-varying structural systems and their SHM-oriented techniques for tracking the evolution of dynamic behavior governing modal parameters. In particular, for continuously growing and

expanding the nowadays research boundaries, pioneering novel cutting-edge integrations with AI-assisted tools may represent an essential step for overcoming existing analytical or numerical limitations. This must be achieved always without forgetting about the knowledge and already gained experience from the existing scientific literature and past studies, as well as considering already available information and physics-based considerations, for better controlling growing complex AI-based smart systems.

Bibliography

- [1] Micelli, F., D. Perrone, and M. A. Aiello. “Influence of strengthening interventions on the structural performance of a Maillart-type arch bridge: the case of “Ciolo Bridge” in the South of Italy.” In: vol. 6. 5. Wiley Online Library, 2023, pp. 89–98. DOI: <https://doi.org/10.1002/cepa.2205>.
- [2] Deng, L., W. Wang, and Y. Yu. “State-of-the-art review on the causes and mechanisms of bridge collapse.” In: *Journal of Performance of Constructed Facilities* 30.2 (2016), p. 04015005. DOI: [https://doi.org/10.1061/\(ASCE\)CF.1943-5509.0000731](https://doi.org/10.1061/(ASCE)CF.1943-5509.0000731).
- [3] Nuti, C., B. Briseghella, A. Chen, D. Lavorato, T. Iori, and I. Vanzi. “Relevant outcomes from the history of Polcevera Viaduct in Genova, from design to nowadays failure.” In: *Journal of Civil Structural Health Monitoring* 10 (2020), pp. 87–107. DOI: <https://doi.org/10.1007/s13349-019-00371-6>.
- [4] Brencich, A. “Collapse of an industrial steel shed: A case study for basic errors in computational structural engineering and control procedures.” In: *Engineering Failure Analysis* 17.1 (2010), pp. 213–225. DOI: <https://doi.org/10.1016/j.engfailanal.2009.06.015>.
- [5] American Society of Civil Engineers, A. *2021 Report Card for America’s Infrastructure*. https://infrastructurereportcard.org/wp-content/uploads/2020/12/National_IRC_2021-report.pdf, <https://books.google.it/books?id=1J0JzgEACAAJ>, ASCE, 2021.
- [6] Di Prisco, M. et al. “Critical infrastructures in Italy: State of the art, case studies, rational approaches to select the intervention priorities.” In: *Proceedings of the fib Symposium 2019: Concrete-Innovations in Materials, Design and Structures*. International Federation for Structural Concrete. 2019, pp. 49–58. URL: <https://re.public.polimi.it/handle/11311/960608>.
- [7] Farrar, C. R. and K. Worden. *Structural health monitoring: a machine learning perspective*. John Wiley & Sons, 2012. DOI: <https://doi.org/10.1002/9781118443118>.
- [8] Saleh, J. H. and C. C. Pendley. “From learning from accidents to teaching about accident causation and prevention: Multidisciplinary education and safety literacy for all engineering students.” In: *Reliability Engineering & System Safety* 99 (2012), pp. 105–113. DOI: <https://doi.org/10.1016/j.res.2011.10.016>.
- [9] Billah, K. Y. and R. H. Scanlan. “Resonance, Tacoma Narrows bridge failure, and undergraduate physics textbooks.” In: *American Journal of Physics* 59.2 (1991), pp. 118–124. DOI: <https://doi.org/10.1119/1.16590>.
- [10] Feldman, B. J. “The Collapse of the I-35W Bridge in Minneapolis.” In: *The Physics Teacher* 48.8 (2010), pp. 541–542. DOI: <https://doi.org/10.1119/1.3502509>.

- [11] Mimmi, L. M. “Italy in Front of the Challenge of Infrastructure Maintenance: Existing Issues and Promising Responses.” In: *Public Works Management & Policy* (2023), p. 1087724X231164648. DOI: <https://doi.org/10.1177/1087724X231164648>.
- [12] Lu, X., H. Guan, H. Sun, Y. Li, Z. Zheng, Y. Fei, Z. Yang, and L. Zuo. “A preliminary analysis and discussion of the condominium building collapse in surfside, Florida, US, June 24, 2021.” In: *Frontiers of structural and civil engineering* 15 (2021), pp. 1097–1110. DOI: <https://doi.org/10.1007/s11709-021-0766-0>.
- [13] Pellecchia, C., A. Cardoni, G. P. Cimellaro, M. Domaneschi, F. Ansari, and A. A. Khalil. “Progressive Collapse Analysis of the Champlain Towers South in Surfside, Florida.” In: *Journal of Structural Engineering* 150.1 (2024), p. 04023211. DOI: <https://doi.org/10.1061/JSENDH.STENG-12485>.
- [14] Potenza, F., C. Rinaldi, E. Ottaviano, and V. Gattulli. “A robotics and computer-aided procedure for defect evaluation in bridge inspection.” In: *Journal of Civil Structural Health Monitoring* 10 (2020), pp. 471–484. DOI: <https://doi.org/10.1007/s13349-020-00395-3>.
- [15] Clemente, P. “Monitoring and evaluation of bridges: Lessons from the Polcevera Viaduct collapse in Italy.” In: *Journal of civil structural health monitoring* 10.2 (2020), pp. 177–182. DOI: <https://doi.org/10.1007/s13349-020-00384-6>.
- [16] Martucci, D., M. Civera, and C. Surace. “Bridge monitoring: Application of the extreme function theory for damage detection on the I-40 case study.” In: *Engineering Structures* 279 (2023), p. 115573. DOI: <https://doi.org/10.1016/j.engstruct.2022.115573>.
- [17] Bazzucchi, F. and G. A. Ferro. “The anatomy of a collapse: Forensic analyses, monitoring and restoration attempts of the Fossano Bridge.” In: *Advances in Engineering Materials, Structures and Systems: Innovations, Mechanics and Applications*. CRC Press, 2019, pp. 2131–2135. DOI: <http://dx.doi.org/10.1201/9780429426506-367>.
- [18] Bazzucchi, F., L. Restuccia, and G. A. Ferro. “Considerations over the Italian road bridge infrastructure safety after the Polcevera viaduct collapse: past errors and future perspectives.” In: *Frattura e Integrità Strutturale* 12 (2018). DOI: <https://doi.org/10.3221/IGF-ESIS.46.37>.
- [19] Losanno, D., S. Galano, F. Parisi, M. R. Pecce, and E. Cosenza. “Experimental Investigation on Nonlinear Flexural Behavior of Post-Tensioned Concrete Bridge Girders with Different Grouting Conditions and Prestress Levels.” In: *Journal of Bridge Engineering* 29.3 (2024), p. 04023121. DOI: <https://doi.org/10.1061/JBENF2.BEENG-6466>.
- [20] Prisco, M. di, M. Colombo, and P. Martinelli. “Structural Aspects of the Collapse of a RC Half-Joint Bridge: Case of the Annone Overpass.” In: *Journal of Bridge Engineering* 28.11 (2023), p. 05023007. DOI: <https://doi.org/10.1061/JBENF2.BEENG-6063>.
- [21] Scattarreggia, N., R. Salomone, M. Moratti, D. Malomo, R. Pinho, and G. M. Calvi. “Collapse analysis of the multi-span reinforced concrete arch bridge of Capriogliola, Italy.” In: *Engineering Structures* 251 (2022), p. 113375. DOI: <https://doi.org/10.1016/j.engstruct.2021.113375>.
- [22] Ministero delle Infrastrutture e dei Trasporti, M. and C. S. dei Lavori Pubblici. *Linee guida per la classificazione e gestione del rischio, la valutazione della sicurezza ed il monitoraggio dei ponti esistenti*. Ministero delle Infrastrutture e dei Trasporti, Consiglio Superiore dei Lavori Pubblici: Roma, Italy, 2020. URL: https://www.mit.gov.it/sites/default/files/media/notizia/2020-05/1_Testo_Linee_Guida_ponti.pdf.

- [23] Pieraccini, L., M. Palermo, T. Trombetti, and F. Baroni. “The role of ductility in the collapse of a long-span steel roof in North Italy.” In: *Engineering Failure Analysis* 82 (2017), pp. 243–265. DOI: <https://doi.org/10.1016/j.engfailanal.2017.07.012>.
- [24] Campione, G. and G. Giambanco. “Influence of design mistakes and material degradation on the collapse of a long-span RC roof in South Italy.” In: *Engineering Failure Analysis* 111 (2020), p. 104257. DOI: <https://doi.org/10.1016/j.engfailanal.2019.104257>.
- [25] Strollo, A., D. Smiraglia, R. Bruno, F. Assennato, L. Congedo, P. De Fioravante, C. Giuliani, I. Marinosci, N. Riitano, and M. Munafò. “Land consumption in Italy.” In: *Journal of Maps* 16.1 (2020), pp. 113–123. DOI: <https://doi.org/10.1080/17445647.2020.1758808>.
- [26] Oxoli, D., M. Molinari, M. Brovelli, et al. “Hotspot Analysis, an open source GIS tool for exploratory spatial data analysis: application to the study of soil consumption in Italy.” In: *Rendiconti Online della Societ Geologica Italiana* 46 (2018), p. 82. DOI: <http://dx.doi.org/10.3301/ROL.2018.56>.
- [27] Istituto Superiore per la Protezione e la Ricerca Ambientale, I. *Consumo di suolo, dinamiche territoriali e servizi ecosistemici. Edizione 2023*. 2023. URL: <https://www.snambiente.it/snpa/consumo-di-suolo-dinamiche-territoriali-e-servizi-ecosistemici-edizione-2023/>.
- [28] Micelli, E. and P. Pellegrini. “Wasting heritage. The slow abandonment of the Italian Historic Centers.” In: *Journal of Cultural Heritage* 31 (2018), pp. 180–188. DOI: <https://doi.org/10.1016/j.culher.2017.11.011>.
- [29] Cavalagli, N., A. Kita, V. Castaldo, A. Pisello, and F. Ubertini. “Hierarchical environmental risk mapping of material degradation in historic masonry buildings: An integrated approach considering climate change and structural damage.” In: *Construction and Building Materials* 215 (2019), pp. 998–1014. DOI: <https://doi.org/10.1016/j.conbuildmat.2019.04.204>.
- [30] Lenticchia, E., R. Ceravolo, and C. Chiorino. “Damage scenario-driven strategies for the seismic monitoring of XX century spatial structures with application to Pier Luigi Nervi’s Turin Exhibition Centre.” In: *Engineering Structures* 137 (2017), pp. 256–267. DOI: <http://dx.doi.org/10.1016/j.engstruct.2017.01.067>.
- [31] Cresciani, M. and J. Forth. “Three Resilient Megastructures by Pier Luigi Nervi.” In: *International Journal of Architectural Heritage* 8.1 (2014), pp. 49–73. DOI: <https://doi.org/10.1080/15583058.2012.669023>.
- [32] Kanda, K., M. Nakashima, Y. Suzuki, and S. Ogasawara. ““q-NAVI”: A case of market-based implementation of structural health monitoring in Japan.” In: *Earthquake Spectra* 37.1 (2021), pp. 160–179. DOI: <https://doi.org/10.1177/8755293020935884>.
- [33] Bhowmik, B., B. Hazra, and V. Pakrashi. *Real-time Structural Health Monitoring of Vibrating Systems*. CRC Press, 2022. DOI: <https://doi.org/10.1201/9780429351341>.
- [34] United States of America, U. *Infrastructure Investment and Jobs Act*. Public Law 117–58 - NOV. 15, 2021 - 117th Congress. 2021. URL: <https://www.congress.gov/117/plaws/publ58/PLAW-117publ58.pdf>.
- [35] Commission, E., D.-G. for Mobility, Transport, R. Monden, K. El Beyrouty, M. Gatto, H. Kramer, L. Wijngaarden, A. Schrotten, M. Brambilla, V. Lambla, F. Trosky, S. Amaral, M. Killer, D. Bertschmann, and S. Maffii. *Overview of transport infrastructure expenditures and costs*. Publications Office, 2019. DOI: <https://doi.org/10.2832/853267>.

- [36] AlBanwan, A., A. AlFoudari, and R. AlBehbehani. “Infrastructure asset management and the role of structural health monitoring.” In: CRC Press, 2023, pp. 3404–3411. DOI: <https://doi.org/10.1201/9781003323020-416>.
- [37] Carrión, F. J., J. A. Quintana, and S. E. Crespo. “Techno-economical and practical considerations for SHM systems.” In: *Journal of Civil Structural Health Monitoring* 7.2 (2017), pp. 207–215. DOI: <https://doi.org/10.1007/s13349-017-0215-x>.
- [38] Gkoumas, K., M. Galassi, D. Allaix, A. Anthoine, S. Argyroudis, G. Baldini, L. Benedetti, F. Bono, J. Brownjohn, E. Caetano, G. Camata, D. Cantero, G. Cimellaro, M. Cutini, S. Escriba, U. Fugiglando, K. Gkoktsi, R. Horvath, M. Limongelli, A. Malekjarfarian, E. O'Brien, M. Petracca, F. Petrini, A. Sextos, C. Stoura, D. Tirelli, and G. Tsionis. *Indirect structural health monitoring (iSHM) of transport infrastructure in the digital age*. KJ-04-23-036-EN-N (online), KJ-04-23-036-EN-C (print). Luxembourg (Luxembourg): Publications Office of the European Union, 2023. ISBN: 9789276619772. DOI: <https://dx.doi.org/10.2760/364830>.
- [39] Ullah, A., S. M. Anwar, J. Li, L. Nadeem, T. Mahmood, A. Rehman, and T. Saba. “Smart cities: The role of Internet of Things and machine learning in realizing a data-centric smart environment.” In: *Complex & Intelligent Systems* (2023), pp. 1–31. DOI: <https://doi.org/10.1007/s40747-023-01175-4>.
- [40] Zinno, R., S. S. Haghshenas, G. Guido, and A. Vitale. “Artificial intelligence and structural health monitoring of bridges: A review of the state-of-the-art.” In: *IEEE Access* 10 (2022), pp. 88058–88078. DOI: <https://doi.org/10.1109/ACCESS.2022.3199443>.
- [41] Tapeh, A. T. G. and M. Naser. “Artificial intelligence, machine learning, and deep learning in structural engineering: a scientometrics review of trends and best practices.” In: *Archives of Computational Methods in Engineering* 30.1 (2023), pp. 115–159. DOI: <https://doi.org/10.1007/s11831-022-09793-w>.
- [42] Goulet, J.-A. *Probabilistic machine learning for civil engineers*. MIT Press Ltd, 2020. ISBN: 9780262538701. URL: https://profs.polymtl.ca/jagoulet/Site/Goulet_web_page_B00K.html.
- [43] Géron, A. *Hands-on machine learning with Scikit-Learn*. Vol. 1. O’Reilly Media, 2019. ISBN: 9781492032649. URL: <https://www.oreilly.com/library/view/hands-on-machine-learning/9781492032632/>.
- [44] Kalita, J. K., D. K. Bhattacharyya, and S. Roy. *Fundamentals of Data Science: Theory and Practice*. Academic Press, Elsevier, Dec. 2023, p. 336. ISBN: 9780323917780. URL: <https://shop.elsevier.com/books/fundamentals-of-data-science/kalita/978-0-323-91778-0>.
- [45] Quaranta, G., W. Lacarbonara, and S. F. Masri. “A review on computational intelligence for identification of nonlinear dynamical systems.” In: *Nonlinear Dynamics* 99.2 (2020), pp. 1709–1761. DOI: <https://doi.org/10.1007/s11071-019-05430-7>.
- [46] Rosso, M. M., R. Cucuzza, F. Di Trapani, and G. C. Marano. “Nonpenalty machine learning constraint handling using PSO-SVM for structural optimization.” In: *Advances in Civil Engineering* 2021 (2021), pp. 1–17. DOI: <https://doi.org/10.1155/2021/6617750>.
- [47] Cucuzza, R., M. M. Rosso, and G. C. Marano. “Optimal preliminary design of variable section beams criterion.” In: *SN Applied Sciences* 3.8 (2021), p. 745. DOI: <https://doi.org/10.1007/s42452-021-04702-5>.

- [48] Rosso, M. M., R. Cucuzza, A. Aloisio, and G. C. Marano. “Enhanced Multi-Strategy Particle Swarm Optimization for Constrained Problems with an Evolutionary-Strategies-Based Unfeasible Local Search Operator.” In: *Applied Sciences* 12.5 (2022), p. 2285. DOI: <https://doi.org/10.3390/app12052285>.
- [49] Cucuzza, R., M. M. Rosso, A. Aloisio, J. Melchiorre, M. L. Giudice, and G. C. Marano. “Size and Shape Optimization of a Guyed Mast Structure under Wind, Ice and Seismic Loading.” In: *Applied Sciences* 12.10 (2022), p. 4875. DOI: <https://doi.org/10.3390/app12104875>.
- [50] Rosso, M. M., J. Melchiorre, R. Cucuzza, A. Manuello, and G. C. Marano. “Estimation of Distribution Algorithm for Constrained Optimization in Structural Design.” In: *WCCM-APCOM 2022, Yokohama, July 31 to August 5, 2022*. 2022. DOI: <http://dx.doi.org/10.23967/wccm-apcom.2022.048>.
- [51] Bishop, C. M. and N. M. Nasrabadi. *Pattern recognition and machine learning*. Vol. 4. 4. Springer, 2006. ISBN: 9780387310732. URL: <https://link.springer.com/book/9780387310732>.
- [52] Sutton, R. S. and A. G. Barto. *Reinforcement learning: An introduction*. MIT press, 2018. ISBN: 9780262039246. URL: <https://mitpress.ubliish.com/ebook/reinforcement-learning-an-introduction-2-preview/2351/Cover>.
- [53] Cerda, P. and G. Varoquaux. “Encoding high-cardinality string categorical variables.” In: *IEEE Transactions on Knowledge and Data Engineering* 34.3 (2020), pp. 1164–1176. DOI: <https://doi.org/10.1109/TKDE.2020.2992529>.
- [54] Takayama, K. “Encoding Categorical Variables with Ambiguity.” In: *Proceedings of the International Workshop NFMCP in conjunction with ECML-PKDD, Tokyo, Japan*. Vol. 16. 2019. URL: <https://api.semanticscholar.org/CorpusID:231717086>.
- [55] Stone, M. “Cross-validatory choice and assessment of statistical predictions.” In: *Journal of the royal statistical society: Series B (Methodological)* 36.2 (1974), pp. 111–133. DOI: <https://doi.org/10.1111/j.2517-6161.1974.tb00994.x>.
- [56] He, H. and E. A. Garcia. “Learning from imbalanced data.” In: *IEEE Transactions on knowledge and data engineering* 21.9 (2009), pp. 1263–1284. DOI: <https://doi.org/10.1109/TKDE.2008.239>.
- [57] He, H. and Y. Ma. *Imbalanced learning: foundations, algorithms, and applications*. John Wiley & Sons, 2013. DOI: <https://doi.org/10.1002/9781118646106>.
- [58] Wolpert, D. H. and W. G. Macready. “No free lunch theorems for optimization.” In: *IEEE transactions on evolutionary computation* 1.1 (1997), pp. 67–82. DOI: <https://doi.org/10.1109/4235.585893>.
- [59] Rosso, M. M., G. Marasco, S. Aiello, A. Aloisio, B. Chiaia, and G. C. Marano. “Convolutional networks and transformers for intelligent road tunnel investigations.” In: *Computers & Structures* 275 (2023), p. 106918. DOI: <https://doi.org/10.1016/j.compstruc.2022.106918>.
- [60] Aggarwal, C. C. et al. *Neural networks and deep learning*. Vol. 10. 978. Springer, 2018, p. 3. DOI: <https://doi.org/10.1007/978-3-319-94463-0>.
- [61] Raschka, S. and V. Mirjalili. *Python machine learning: Machine learning and deep learning with Python, scikit-learn, and TensorFlow 2*. Packt Publishing Ltd, 2017. ISBN: 9781787126022. DOI: https://books.google.it/books?id=_pLGDwAAQBAJ.

- [62] Kohavi, R. et al. “A study of cross-validation and bootstrap for accuracy estimation and model selection.” In: *Proceedings of the Fourteenth International Joint Conference on Artificial Intelligence (IJCAI 1995)*. Vol. 14. 2. Montreal, Canada. 1995, pp. 1137–1145. URL: <http://robotics.stanford.edu/%7Eronnyk/accEst.pdf>.
- [63] Cernezel, A., I. Rozman, and B. Brumen. “Comparisons between Three Cross-Validation Methods for Measuring Learners’ Performances.” In: *Information Modelling and Knowledge Bases XXVI, 24th International Conference on Information Modelling and Knowledge Bases (EJC 2014), Kiel, Germany, June 3-6, 2014*. Ed. by Thalheim, B., H. Jaakkola, Y. Kiyoki, and N. Yoshida. Vol. 272. Frontiers in Artificial Intelligence and Applications. IOS Press, 2014, pp. 77–87. ISBN: 978-1-61499-472-5. DOI: [10.3233/978-1-61499-472-5-77](https://doi.org/10.3233/978-1-61499-472-5-77). URL: <http://dx.doi.org/10.3233/978-1-61499-472-5-77>.
- [64] Ferri, C., J. Hernández-Orallo, and R. Modroiu. “An experimental comparison of performance measures for classification.” In: *Pattern recognition letters* 30.1 (2009), pp. 27–38. DOI: <https://doi.org/10.1016/j.patrec.2008.08.010>.
- [65] Kohavi, R., D. H. Wolpert, et al. “Bias plus variance decomposition for zero-one loss functions.” In: *ICML*. Vol. 96. 1996, pp. 275–283. URL: <http://robotics.stanford.edu/~ronnyk/biasVar.pdf>.
- [66] Hastie, T., R. Tibshirani, J. H. Friedman, and J. H. Friedman. *The elements of statistical learning: data mining, inference, and prediction*. Vol. 2. Springer, 2009. DOI: <https://doi.org/10.1007/978-0-387-21606-5>.
- [67] Vapnik, V. N. *The nature of statistical learning theory*. Springer Science & Business Media, 1995. DOI: <https://doi.org/10.1007/978-1-4757-3264-1>.
- [68] Cristianini, N. and J. Shawe-Taylor. *An introduction to support vector machines and other kernel-based learning methods*. Cambridge university press, 2000. DOI: <https://doi.org/10.1017/CB09780511801389>.
- [69] Breiman, L., J. H. Friedman, R. A. Olshen, and C. J. Stone. *Classification and regression trees*. CRC press, 1984. DOI: <https://doi.org/10.1201/9781315139470>.
- [70] Breiman, L. “Random forests.” In: *Machine Learning* 45.1 (2001), pp. 5–32. DOI: <https://doi.org/10.1023/A:1010933404324>.
- [71] LeCun, Y., Y. Bengio, and G. Hinton. “Deep learning.” In: *Nature* 521.7553 (2015), pp. 436–444. DOI: <https://doi.org/10.1038/nature14539>.
- [72] Freund, Y. and R. E. Schapire. “A decision-theoretic generalization of on-line learning and an application to boosting.” In: *Journal of computer and system sciences* 55.1 (1997), pp. 119–139. DOI: <https://doi.org/10.1006/jcss.1997.1504>.
- [73] McCallum, A., K. Nigam, et al. “A comparison of event models for naive bayes text classification.” In: *AAAI-98 workshop on learning for text categorization*. Vol. 752. 1. Madison, WI. 1998, pp. 41–48. URL: <http://citeseerx.ist.psu.edu/viewdoc/summary?doi=10.1.1.46.1529>.
- [74] Cramer, J. “The origins of logistic regression.” In: 119.4 (2002). DOI: <https://dx.doi.org/10.2139/ssrn.360300>.
- [75] Fisher, R. A. “The use of multiple measurements in taxonomic problems.” In: *Annals of eugenics* 7.2 (1936), pp. 179–188. DOI: <https://doi.org/10.1111/j.1469-1809.1936.tb02137.x>.
- [76] Hennig, C., M. Meila, F. Murtagh, and R. Rocci. *Handbook of cluster analysis*. CRC press, 2015. ISBN: 9780429185472. DOI: <https://doi.org/10.1201/b19706>.

- [77] Sreedhar, C., N. Kasiviswanath, and P. Chenna Reddy. “Clustering large datasets using K-means modified inter and intra clustering (KM-I2C) in Hadoop.” In: *Journal of Big Data* 4.1 (2017), p. 27. DOI: <https://doi.org/10.1186/s40537-017-0087-2>.
- [78] Kassambara, A. *Practical guide to cluster analysis in R: Unsupervised machine learning*. Vol. 1. Multivariate Analysis. STHDA, 2017. ISBN: 9781542462709. URL: <https://books.google.it/books?id=plEyDwAAQBAJ>.
- [79] Bonaccorso, G. *Mastering Machine Learning Algorithms: Expert techniques for implementing popular machine learning algorithms, fine-tuning your models, and understanding how they work, 2nd Edition*. Expert insight. Packt Publishing, Limited, 2020. ISBN: 9781838820299. URL: <https://books.google.it/books?id=ustHzQEACAAJ>.
- [80] Wold, S., K. Esbensen, and P. Geladi. “Principal component analysis.” In: *Chemometrics and intelligent laboratory systems* 2.1-3 (1987), pp. 37–52. DOI: [https://doi.org/10.1016/0169-7439\(87\)80084-9](https://doi.org/10.1016/0169-7439(87)80084-9).
- [81] Rosso, M. M., R. Cucuzza, G. C. Marano, A. Aloisio, and G. Cirrincione. “Review on deep learning in structural health monitoring.” In: *Bridge Safety, Maintenance, Management, Life-Cycle, Resilience and Sustainability*. CRC Press, 2022, pp. 309–315. DOI: <http://dx.doi.org/10.1201/9781003322641-34>.
- [82] Rosenblatt, F. “The Perceptron, a Perceiving and Recognizing Automaton (Project Para).” In: Report: Cornell Aeronautical Laboratory (1957). URL: https://books.google.it/books?id=P_XGPgAACAAJ.
- [83] McCulloch, W. S. and W. Pitts. “A logical calculus of the ideas immanent in nervous activity.” In: *The bulletin of mathematical biophysics* 5.4 (1943), pp. 115–133. DOI: <https://doi.org/10.1007/BF02478259>.
- [84] Aloisio, A., M. M. Rosso, A. M. De Leo, M. Fragiaco, and M. Basi. “Damage classification after the 2009 L’Aquila earthquake using multinomial logistic regression and neural networks.” In: *International Journal of Disaster Risk Reduction* 96 (2023), p. 103959. DOI: <https://doi.org/10.1016/j.ijdr.2023.103959>.
- [85] Rumelhart, D. E., G. E. Hinton, R. J. Williams, et al. “Learning internal representations by error propagation.” In: (1985). URL: <https://apps.dtic.mil/sti/pdfs/ADA164453.pdf>.
- [86] Goodfellow, I., Y. Bengio, and A. Courville. *Deep learning*. Adaptive Computation and Machine Learning series. MIT Press, 2016. ISBN: 9780262035613. URL: <https://books.google.it/books?id=Np9SDQAAQBAJ>.
- [87] Rosebrock, A. *Deep Learning for Computer Vision with Python: Starter Bundle*. PyImageSearch, 2017. URL: <https://books.google.it/books?id=9U1-tgEACAAJ>.
- [88] Hubel, D. H. “Single unit activity in striate cortex of unrestrained cats.” In: *The Journal of physiology* 147.2 (1959), p. 226. DOI: <https://doi.org/10.1113%2Fjphysiol.1959.sp006238>.
- [89] LeCun, Y., L. Bottou, Y. Bengio, and P. Haffner. “Gradient-based learning applied to document recognition.” In: *Proceedings of the IEEE* 86.11 (1998), pp. 2278–2324. DOI: <https://doi.org/10.1109/5.726791>.
- [90] Gonzalez, R. C., R. E. Woods, and S. L. Eddins. *Digital image processing using MATLAB*. Pearson Prentice-Hall, Inc., 2004. ISBN: 9780130085191. URL: <https://books.google.it/books?id=YYuJQgAACAAJ>.

-
- [91] Vaswani, A., N. Shazeer, N. Parmar, J. Uszkoreit, L. Jones, A. N. Gomez, Ł. Kaiser, and I. Polosukhin. “Attention is all you need.” In: *Advances in neural information processing systems* 30 (2017). DOI: <https://doi.org/10.48550/arXiv.1706.03762>.
- [92] Foster, D. *Generative deep learning*. O’Reilly Media, 2019. ISBN: 9781492041894. URL: <https://books.google.it/books?id=RqegDwAAQBAJ>.
- [93] Goodfellow, I., J. Pouget-Abadie, M. Mirza, B. Xu, D. Warde-Farley, S. Ozair, A. Courville, and Y. Bengio. “Generative adversarial nets.” In: *Advances in neural information processing systems* 27 (2014). DOI: <https://doi.org/10.48550/arXiv.1406.2661>.
- [94] Marano, G. C., M. M. Rosso, A. Aloisio, and G. Cirrincione. “Generative adversarial networks review in earthquake-related engineering fields.” In: *Bulletin of Earthquake Engineering* (2023), pp. 1–52. DOI: <https://doi.org/10.1007/s10518-023-01645-7>.
- [95] Brincker, R. and C. Ventura. *Introduction to operational modal analysis*. John Wiley & Sons, 2015. DOI: <https://doi.org/10.1002/9781118535141>.
- [96] Rainieri, C. and G. Fabbrocino. *Operational modal analysis of civil engineering structures*. Vol. 142. Springer, 2014, p. 143. DOI: <https://doi.org/10.1007/978-1-4939-0767-0>.
- [97] Oppenheim, A. and R. Schaffer. *Digital Signal Processing*. MIT video course. Prentice-Hall, 1975. ISBN: 9780132146357. URL: <https://books.google.it/books?id=vfdSAAAAMAAJ>.
- [98] Chopra, A. *Dynamics of Structures, in SI units V Edition*. Pearson Education, 2019. ISBN: 9781292249209. URL: <https://books.google.it/books?id=Z76GEAAAQBAJ>.
- [99] Greiner, B. *Operational modal analysis and its application for SOFIA telescope assembly vibration measurements*. Ph.D. Thesis at University of Stuttgart, Jan. 2009. DOI: <https://doi.org/10.18419/opus-3826>.
- [100] Ang, A. and W. Tang. *Probability Concepts in Engineering: Emphasis on Applications in Civil & Environmental Engineering*. Wiley, 2014. ISBN: 9788126540594. URL: <https://books.google.it/books?id=q6HXzgEACAAJ>.
- [101] Van Overschee, P. and B. De Moor. *Subspace identification for linear systems: Theory—Implementation—Applications*. Springer Science & Business Media, 2012. DOI: <https://doi.org/10.1007/978-1-4613-0465-4>.
- [102] Phan, M., J.-N. Juang, and R. W. Longman. *On Markov parameters in system identification*. Tech. rep. 1991. URL: <https://ntrs.nasa.gov/api/citations/19920004241/downloads/19920004241.pdf>.
- [103] Mohanty, P. and D. J. Rixen. “Operational modal analysis in the presence of harmonic excitation.” In: *Journal of sound and vibration* 270.1-2 (2004), pp. 93–109. DOI: [https://doi.org/10.1016/S0022-460X\(03\)00485-1](https://doi.org/10.1016/S0022-460X(03)00485-1).
- [104] Ibrahim, S. R. and E. Mikulcik. “A method for the direct identification of vibration parameters from the free response.” In: *The Shock and Vibration Inform. Ctr. Shock and Vibration Bull. Part. 4: Sep. 1977* (1977). DOI: <https://ntrs.nasa.gov/citations/19800070016>.
- [105] Juang, J.-N. and R. S. Pappa. “An eigensystem realization algorithm for modal parameter identification and model reduction.” In: *Journal of guidance, control, and dynamics* 8.5 (1985), pp. 620–627. DOI: <https://doi.org/10.2514/3.20031>.
- [106] Ho, B. and R. E. Kálmán. “Effective construction of linear state-variable models from input/output functions: Die Konstruktion von linearen Modellen in der Darstellung durch Zustandsvariable aus den Beziehungen für Ein-und Ausgangsgrößen.” In: *at-Automatisierungstechnik* 14.1-12 (1966), pp. 545–548. DOI: <https://doi.org/10.1524/auto.1966.14.112.545>.

-
- [107] Yi, J.-H. and C.-B. Yun. “Comparative study on modal identification methods using output-only information.” In: *Structural engineering and mechanics: An international journal* 17.3 (2004), pp. 445–466. DOI: http://dx.doi.org/10.12989/sem.2004.17.3_4.445.
- [108] Kvåle, K. A., O. Øiseth, and A. Rönquist. “Covariance-driven stochastic subspace identification of an end-supported pontoon bridge under varying environmental conditions.” In: *Dynamics of Civil Structures, Volume 2: Proceedings of the 35th IMAC, A Conference and Exposition on Structural Dynamics 2017*. Springer. 2017, pp. 107–115. DOI: https://doi.org/10.1007/978-3-319-54777-0_14.
- [109] Döhler, M. and L. Mevel. “Modular subspace-based system identification from multi-setup measurements.” In: *IEEE Transactions on Automatic Control* 57.11 (2012), pp. 2951–2956. DOI: <https://doi.org/10.1109/TAC.2012.2193711>.
- [110] Yeny, V. A. A., I. D. G. Araújo, J. D. Villalba-Morales, and L. A. A. Aracayo. “Validation of the uncertainty bounds on modal parameters identified with the SSI-COV method.” In: *Latin American Journal of Solids and Structures* 18 (2021). DOI: <https://doi.org/10.1590/1679-78256725>.
- [111] Lardiès, J. “Modal parameter identification from output data only.” In: *MATEC Web of Conferences*. Vol. 20. EDP Sciences. 2015, p. 01002. DOI: <http://dx.doi.org/10.1051/mateconf/20152001002>.
- [112] Li, S., J.-T. Wang, A.-Y. Jin, and G.-H. Luo. “Parametric analysis of SSI algorithm in modal identification of high arch dams.” In: *Soil Dynamics and Earthquake Engineering* 129 (2020), p. 105929. DOI: <https://doi.org/10.1016/j.soildyn.2019.105929>.
- [113] Ardila, Y., I. Gómez-Araújo, and J. Villalba-Morales. “An Automated Procedure for Continuous Dynamic Monitoring of Structures: Theory and Validation.” In: *Journal of Vibration Engineering & Technologies* (2023), pp. 1–21. DOI: <https://doi.org/10.1007/s42417-023-01121-1>.
- [114] Zini, G., M. Betti, and G. Bartoli. “A quality-based automated procedure for operational modal analysis.” In: *Mechanical Systems and Signal Processing* 164 (2022), p. 108173. DOI: <https://doi.org/10.1016/j.ymsp.2021.108173>.
- [115] Peeters, B. *System identification and damage detection in civil engineering*. Ph.D. Thesis at Katholieke Universiteit te Leuven, 2000. URL: <https://lirias.kuleuven.be/1725571&lang=en>.
- [116] Friswell, M. and J. E. Mottershead. *Finite element model updating in structural dynamics*. Vol. 38. Springer Science & Business Media, 1995. DOI: <https://doi.org/10.1007/978-94-015-8508-8>.
- [117] Pasca, D. P., A. Aloisio, M. M. Rosso, and S. Sotiropoulos. “PyOMA and PyOMA_GUI: A Python module and software for Operational Modal Analysis.” In: *SoftwareX* 20 (2022), p. 101216. DOI: <https://doi.org/10.1016/j.softx.2022.101216>.
- [118] Brincker, R., L. Zhang, and P. Andersen. “Modal identification of output-only systems using frequency domain decomposition.” In: *Smart materials and structures* 10.3 (2001), p. 441. DOI: <https://doi.org/10.1088/0964-1726/10/3/303>.
- [119] Brincker, R., C. E. Ventura, and P. Andersen. “Damping estimation by frequency domain decomposition.” In: *Proceedings of IMAC 19: A Conference on Structural Dynamics: februar 5-8, 2001, Hyatt Orlando, Kissimmee, Florida, 2001*. Society for Experimental Mechanics. 2001, pp. 698–703. URL: <https://vbn.aau.dk/en/publications/2bcee690-9c2e-11db-8ed6-000ea68e967b>.

- [120] Zhang, L., T. Wang, and Y. Tamura. “A frequency–spatial domain decomposition (FSDD) method for operational modal analysis.” In: *Mechanical systems and signal processing* 24.5 (2010), pp. 1227–1239. DOI: <https://doi.org/10.1016/j.ymsp.2009.10.024>.
- [121] Döhler, M., P. Andersen, and L. Mevel. “Data merging for multi-setup operational modal analysis with data-driven SSI.” In: *Structural Dynamics, Volume 3: Proceedings of the 28th IMAC, A Conference on Structural Dynamics, 2010*. Springer. 2011, pp. 443–452. DOI: https://doi.org/10.1007/978-1-4419-9834-7_42.
- [122] Marwala, T. *Finite element model updating using computational intelligence techniques: applications to structural dynamics*. Springer Science & Business Media, 2010. DOI: <https://doi.org/10.1007/978-1-84996-323-7>.
- [123] Rao, S. S. *Engineering optimization: theory and practice*. John Wiley & Sons, 2019. DOI: <https://doi.org/10.1002/9781119454816>.
- [124] Rosso, M. M., A. Aloisio, R. Cucuzza, R. Asso, and G. C. Marano. “Structural Optimization With the Multistrategy PSO-ES Unfeasible Local Search Operator.” In: *Proceedings of International Conference on Data Science and Applications: ICDSA 2022, Volume 1*. Springer. 2023, pp. 215–229. DOI: https://doi.org/10.1007/978-981-19-6631-6_16.
- [125] Marano, G. C., M. M. Rosso, and J. Melchiorre. “Optimization as a Tool for Seismic Protection of Structures.” In: *World Conference on Seismic Isolation*. Springer International Publishing Cham. 2022, pp. 100–113.
- [126] Zhang, W. and O. Postolache. “Parametric model updating with frequency and MAC combined objective function of port crane structure based on operational modal analysis.” In: *Open Physics* 17.1 (2019), pp. 69–76. DOI: <https://doi.org/10.1515/phys-2019-0008>.
- [127] Aloisio, A., D. P. Pasca, L. Di Battista, M. M. Rosso, R. Cucuzza, G. C. Marano, and R. Alaggio. “Indirect assessment of concrete resistance from FE model updating and Young’s modulus estimation of a multi-span PSC viaduct: Experimental tests and validation.” In: 37 (2022), pp. 686–697. DOI: <https://doi.org/10.1016/j.istruc.2022.01.045>.
- [128] Jurowski, K. and S. Grzeszczyk. “The influence of concrete composition on Young’s modulus.” In: *Procedia Engineering* 108 (2015), pp. 584–591. DOI: <https://doi.org/10.1016/j.proeng.2015.06.181>.
- [129] Aloisio, A., D. P. Pasca, R. Alaggio, and M. Fragiacomò. “Bayesian estimate of the elastic modulus of concrete box girders from dynamic identification: a statistical framework for the A24 motorway in Italy.” In: *Structure and Infrastructure Engineering* 17.12 (2020), pp. 1–13. DOI: <https://doi.org/10.1080/15732479.2020.1819343>.
- [130] Inc, C. *CSI Analysis Reference Manual for Sap2000, Etabs and Safe*. Berkeley, California. URL: <https://books.google.it/books?id=WBRrQwAACAAJ>.
- [131] Saisana, M., A. Saltelli, and S. Tarantola. “Uncertainty and sensitivity analysis techniques as tools for the quality assessment of composite indicators.” In: *Journal of the Royal Statistical Society: Series A (Statistics in Society)* 168.2 (2005), pp. 307–323. DOI: <https://doi.org/10.1111/j.1467-985X.2005.00350.x>.
- [132] Saltelli, A. and I. M. Sobol’. “Sensitivity analysis for nonlinear mathematical models: numerical experience.” In: *Matematicheskoe Modelirovanie* 7.11 (1995), pp. 16–28. URL: <https://publications.jrc.ec.europa.eu/repository/handle/JRC11279>.
- [133] Storn, R. and K. Price. “Differential evolution—a simple and efficient heuristic for global optimization over continuous spaces.” In: *Journal of global optimization* 11.4 (1997), pp. 341–359. DOI: <https://doi.org/10.1023/A:1008202821328>.

- [134] Eberhart, R. and J. Kennedy. “Particle swarm optimization.” In: *Proceedings of the IEEE - ICNN'95 - International Conference on Neural Networks*. Vol. 4. 1995. DOI: <https://doi.org/10.1109/ICNN.1995.488968>.
- [135] Aloisio, A., D. P. Pasca, M. M. Rosso, and B. Briseghella. “Role of Cable Forces in the Model Updating of Cable-Stayed Bridges.” In: *Journal of Bridge Engineering* 28.7 (2023), p. 05023002. DOI: <https://doi.org/10.1061/JBENF2.BEENG-6168>.
- [136] Zhao, W., G. Zhang, and J. Zhang. “Cable force estimation of a long-span cable-stayed bridge with microwave interferometric radar.” In: *Computer-Aided Civil and Infrastructure Engineering* 35.12 (2020), pp. 1419–1433. DOI: <https://doi.org/10.1111/mice.12557>.
- [137] Briseghella, B., G. Fa, A. Aloisio, D. Pasca, L. He, L. Fenu, and C. Gentile. “Dynamic characteristics of a curved steel–concrete composite cable-stayed bridge and effects of different design choices.” In: 34 (2021), pp. 4669–4681. DOI: <https://doi.org/10.1016/j.istruc.2021.10.060>.
- [138] Talebinejad, I., C. Fischer, and F. Ansari. “Numerical evaluation of vibration-based methods for damage assessment of cable-stayed bridges.” In: *Computer-Aided Civil and Infrastructure Engineering* 26.3 (2011), pp. 239–251. DOI: <https://doi.org/10.1111/j.1467-8667.2010.00684.x>.
- [139] Pasca, D. P., A. Aloisio, M. Fragiacomio, and R. Tomasi. “Dynamic Characterization of Timber Floor Subassemblies: Sensitivity Analysis and Modeling Issues.” In: *Journal of Structural Engineering* 147.12 (2021), p. 05021008. DOI: [https://doi.org/10.1061/\(ASCE\)ST.1943-541X.0003179](https://doi.org/10.1061/(ASCE)ST.1943-541X.0003179).
- [140] Schlune, H., M. Plos, and K. Gylltoft. “Improved bridge evaluation through finite element model updating using static and dynamic measurements.” In: *Engineering structures* 31.7 (2009), pp. 1477–1485. DOI: <http://dx.doi.org/10.1016/j.engstruct.2009.02.011>.
- [141] Aloisio, A., M. M. Rosso, and R. Alaggio. “Experimental and Analytical Investigation into the Effect of Ballasted Track on the Dynamic Response of Railway Bridges under Moving Loads.” In: *Journal of Bridge Engineering* 27.10 (2022), p. 04022085. DOI: [https://doi.org/10.1061/\(ASCE\)BE.1943-5592.0001934](https://doi.org/10.1061/(ASCE)BE.1943-5592.0001934).
- [142] Di Lorenzo, S., M. Di Paola, G. Failla, and A. Pirrotta. “On the moving load problem in Euler–Bernoulli uniform beams with viscoelastic supports and joints.” In: *Acta Mechanica* 228.3 (2017), pp. 805–821. DOI: <https://doi.org/10.1007/s00707-016-1739-6>.
- [143] Fryba, L. *Vibration of solids and structures under moving loads*. Vol. 1. Springer Science & Business Media, 2013. DOI: <https://doi.org/10.1007/978-94-011-9685-7>.
- [144] Craig Jr, R. R. and A. J. Kurdila. *Fundamentals of structural dynamics*. John Wiley & Sons, 2011. ISBN: 9781118174449. URL: <https://books.google.it/books?id=RM6MYkiF-mAC>.
- [145] Dormand, J. R. and P. J. Prince. “A family of embedded Runge-Kutta formulae.” In: *Journal of computational and applied mathematics* 6.1 (1980), pp. 19–26. DOI: [https://doi.org/10.1016/0771-050X\(80\)90013-3](https://doi.org/10.1016/0771-050X(80)90013-3).
- [146] Mottershead, J. E., M. Link, and M. I. Friswell. “The sensitivity method in finite element model updating: A tutorial.” In: *Mechanical systems and signal processing* 25.7 (2011), pp. 2275–2296. DOI: <http://dx.doi.org/10.1016/j.ymsp.2010.10.012>.

- [147] He, L., C. Castoro, A. Aloisio, Z. Zhang, G. C. Marano, A. Gregori, C. Deng, and B. Briseghella. “Dynamic assessment, FE modelling and parametric updating of a butterfly-arch stress-ribbon pedestrian bridge.” In: *Structure and Infrastructure Engineering* (2021), pp. 1–12. DOI: <https://doi.org/10.1080/15732479.2021.1995444>.
- [148] Aloisio, A., M. M. Rosso, M. Fragiaco, and R. Alaggio. “Fragility estimate of railway bridges due to concrete fatigue.” In: 49 (2023), pp. 70–87. DOI: https://doi.org/10.1007/978-3-031-21187-4_8.
- [149] Magalhães, F., Á. Cunha, and E. Caetano. “Vibration based structural health monitoring of an arch bridge: From automated OMA to damage detection.” In: *Mechanical Systems and signal processing* 28 (2012), pp. 212–228. DOI: <https://doi.org/10.1016/j.ymsp.2011.06.011>.
- [150] Mazzeo, M., D. De Domenico, G. Quaranta, and R. Santoro. “Automatic modal identification of bridges based on free vibration response and variational mode decomposition technique.” In: *Engineering Structures* 280 (2023), p. 115665. DOI: <https://doi.org/10.1016/j.engstruct.2023.115665>.
- [151] Carden, E. P. and J. M. Brownjohn. “Fuzzy clustering of stability diagrams for vibration-based structural health monitoring.” In: *Computer-Aided Civil and Infrastructure Engineering* 23.5 (2008), pp. 360–372. DOI: <http://dx.doi.org/10.1111/j.1467-8667.2008.00543.x>.
- [152] Magalhaes, F., A. Cunha, and E. Caetano. “Online automatic identification of the modal parameters of a long span arch bridge.” In: *Mechanical Systems and Signal Processing* 23.2 (2009). cited By 365, pp. 316–329. DOI: <http://doi.org/10.1016/j.ymsp.2008.05.003>.
- [153] Reynders, E., J. Houbrechts, and G. De Roeck. “Fully automated (operational) modal analysis.” In: *Mechanical Systems and Signal Processing* 29 (2012). cited By 311, pp. 228–250. DOI: <http://doi.org/10.1016/j.ymsp.2012.01.007>.
- [154] Cabboi, A., F. Magalhaes, C. Gentile, and A. Cunha. “Automated modal identification and tracking: Application to an iron arch bridge.” In: *Structural Control and Health Monitoring* 24.1 (2017). DOI: <http://doi.org/10.1002/stc.1854>.
- [155] He, M., P. Liang, J. Li, Y. Zhang, and Y. Liu. “Fully automated precise operational modal identification.” In: *Engineering Structures* 234 (2021), p. 111988. DOI: <https://doi.org/10.1016/j.engstruct.2021.111988>.
- [156] He, M., P. Liang, E. OBrien, X. Sun, and Y. Zhang. “Continuous modal identification and tracking of a long-span suspension bridge using a robust mixed-clustering method.” In: *Journal of Bridge Engineering* 27.3 (2021), p. 05022001. DOI: [https://doi.org/10.1061/\(ASCE\)BE.1943-5592.0001836](https://doi.org/10.1061/(ASCE)BE.1943-5592.0001836).
- [157] He, Y., J. P. Yang, and X.-F. Li. “A three-stage automated modal identification framework for bridge parameters based on frequency uncertainty and density clustering.” In: *Engineering Structures* 255 (2022), p. 113891. DOI: <https://doi.org/10.1016/j.engstruct.2022.113891>.
- [158] Zhong, Q.-M., S.-Z. Chen, Z. Sun, and L.-C. Tian. “Fully automatic operational modal analysis method based on statistical rule enhanced adaptive clustering method.” In: *Engineering Structures* 274 (2023), p. 115216. DOI: <https://doi.org/10.1016/j.engstruct.2022.115216>.

- [159] Ubertini, F., C. Gentile, and A. Materazzi. “Automated modal identification in operational conditions and its application to bridges.” In: *Engineering Structures* 46 (2013). cited By 190, pp. 264–278. DOI: <https://doi.org/10.1016/j.engstruct.2012.07.031>.
- [160] Cardoso, R., A. Cury, and F. Barbosa. “A robust methodology for modal parameters estimation applied to SHM.” In: *Mechanical Systems and Signal Processing* 95 (2017), pp. 24–41. DOI: <https://doi.org/10.1016/j.ymsp.2017.03.021>.
- [161] Almeida Cardoso, R. de, A. Cury, and F. Barbosa. “A clustering-based strategy for automated structural modal identification.” In: *Structural Health Monitoring* 17.2 (2018), pp. 201–217. DOI: <https://doi.org/10.1177/1475921716689239>.
- [162] Mao, J.-X., H. Wang, Y.-G. Fu, and B. F. Spencer Jr. “Automated modal identification using principal component and cluster analysis: Application to a long-span cable-stayed bridge.” In: *Structural Control and Health Monitoring* 26.10 (2019), e2430. DOI: <https://doi.org/10.1002/stc.2430>.
- [163] Fan, G., J. Li, and H. Hao. “Improved automated operational modal identification of structures based on clustering.” In: *Structural Control and Health Monitoring* 26.12 (2019), e2450. DOI: <https://doi.org/10.1002/stc.2450>.
- [164] Mostafaei, H., M. Ghamami, and P. Aghabozorgi. “Modal identification of concrete arch dam by fully automated operational modal identification.” In: *Structures* 32 (2021), pp. 228–236. DOI: <https://doi.org/10.1016/j.istruc.2021.03.028>.
- [165] Rainieri, C. and G. Fabbrocino. “Development and validation of an automated operational modal analysis algorithm for vibration-based monitoring and tensile load estimation.” In: *Mechanical Systems and Signal Processing* 60 (2015), pp. 512–534. DOI: <https://doi.org/10.1016/j.ymsp.2015.01.019>.
- [166] Quaranta, G., C. Demartino, and Y. Xiao. “Experimental dynamic characterization of a new composite glulam-steel truss structure.” In: *Journal of Building Engineering* 25 (2019), p. 100773. DOI: <https://doi.org/10.1016/j.jobbe.2019.100773>.
- [167] Aloisio, A., R. Alaggio, and M. Fragiaco. “Dynamic identification and model updating of full-scale concrete box girders based on the experimental torsional response.” In: *Construction and Building Materials* 264 (2020), p. 120146. DOI: <https://doi.org/10.1016/j.conbuildmat.2020.120146>.
- [168] Alaggio, R., A. Aloisio, E. Antonacci, and R. Cirella. “Two-years static and dynamic monitoring of the Santa Maria di Collemaggio basilica.” In: *Construction and Building Materials* 268 (2021), p. 121069. DOI: <https://doi.org/10.1016/j.conbuildmat.2020.121069>.
- [169] Priori, C., M. De Angelis, and R. Betti. “On the selection of user-defined parameters in data-driven stochastic subspace identification.” In: *Mechanical Systems and Signal Processing* 100 (2018), pp. 501–523. DOI: <https://doi.org/10.1016/j.ymsp.2017.07.045>.
- [170] Civera, M., L. Sibille, L. Z. Fragonara, and R. Ceravolo. “A dbSCAN-based automated operational modal analysis algorithm for bridge monitoring.” In: *Measurement* (2023), p. 112451. DOI: <https://doi.org/10.1016/j.measurement.2023.112451>.
- [171] Zonno, G., R. Aguilar, R. Boroschek, and P. B. Lourenço. “Automated long-term dynamic monitoring using hierarchical clustering and adaptive modal tracking: validation and applications.” In: *Journal of Civil Structural Health Monitoring* 8 (2018), pp. 791–808. DOI: <https://doi.org/10.1007/s13349-018-0306-3>.

- [172] Garcia-Macias, E. and F. Ubertini. “MOVA/MOSS: Two integrated software solutions for comprehensive Structural Health Monitoring of structures.” In: *Mechanical Systems and Signal Processing* 143 (2020). DOI: <https://doi.org/10.1016/j.ymsp.2020.106830>.
- [173] Verboven, P., E. Parloo, P. Guillaume, and M. Van Overmeire. “Autonomous structural health monitoring—part I: modal parameter estimation and tracking.” In: *Mechanical Systems and Signal Processing* 16.4 (2002), pp. 637–657. DOI: <https://doi.org/10.1006/mssp.2002.1492>.
- [174] Scionti, M. and J. Lanslots. “Stabilisation diagrams: Pole identification using fuzzy clustering techniques.” In: *Advances in Engineering Software* 36.11-12 (2005), pp. 768–779. DOI: <https://doi.org/10.1016/j.advengsoft.2005.03.029>.
- [175] Neu, E., F. Janser, A. Khatibi, and A. Orifici. “Fully Automated Operational Modal Analysis using multi-stage clustering.” In: *Mechanical Systems and Signal Processing* 84 (2017). cited By 75, pp. 308–323. DOI: <https://doi.org/10.1016/j.ymsp.2016.07.031>.
- [176] Mugnaini, V., L. Z. Fragonara, and M. Civera. “A machine learning approach for automatic operational modal analysis.” In: *Mechanical Systems and Signal Processing* 170 (2022), p. 108813. DOI: <https://doi.org/10.1016/j.ymsp.2022.108813>.
- [177] Hasan, M. D. A., Z. Ahmad, M. S. Leong, L. Hee, and M. H. M. Idris. “Cluster analysis for automated operational modal analysis: A review.” In: *MATEC Web of Conferences*. Vol. 255. EDP Sciences. 2019, p. 02012. DOI: <https://doi.org/10.1051/mateconf/201925502012>.
- [178] Chauhan, S. and D. Tcherniak. “Clustering approaches to automatic modal parameter estimation.” In: *Proceedings, International Modal Analysis Conference (IMAC)*. 2008. URL: <https://www.bksv.com/media/doc/bn0561.pdf>.
- [179] Liu, D., Y. Bao, and H. Li. “Machine learning-based stochastic subspace identification method for structural modal parameters.” In: *Engineering Structures* 274 (2023), p. 115178. DOI: <https://doi.org/10.1016/j.engstruct.2022.115178>.
- [180] Reynders, E., R. Pintelon, and G. De Roeck. “Uncertainty bounds on modal parameters obtained from stochastic subspace identification.” In: *Mechanical systems and signal processing* 22.4 (2008), pp. 948–969. DOI: <https://doi.org/10.1016/j.ymsp.2007.10.009>.
- [181] Pintelon, R., P. Guillaume, and J. Schoukens. “Uncertainty calculation in (operational) modal analysis.” In: *Mechanical Systems and Signal Processing* 21.6 (2007), pp. 2359–2373. DOI: <https://doi.org/10.1016/j.ymsp.2006.11.007>.
- [182] Reynders, E. P. “Uncertainty quantification in data-driven stochastic subspace identification.” In: *Mechanical Systems and Signal Processing* 151 (2021), p. 107338. DOI: <http://dx.doi.org/10.1016/j.ymsp.2020.107338>.
- [183] Rainieri, C. and G. Fabbrocino. “Influence of model order and number of block rows on accuracy and precision of modal parameter estimates in stochastic subspace identification.” In: *International Journal of Lifecycle Performance Engineering* 1.4 (2014), pp. 317–334. DOI: <http://dx.doi.org/10.1504/IJLCPE.2014.064099>.
- [184] Zhou, K., Q.-S. Li, and X.-L. Han. “Modal Identification of Civil Structures via Stochastic Subspace Algorithm with Monte Carlo-Based Stabilization Diagram.” In: *Journal of Structural Engineering* 148.6 (2022), p. 04022066. DOI: [https://doi.org/10.1061/\(ASCE\)ST.1943-541X.0003353](https://doi.org/10.1061/(ASCE)ST.1943-541X.0003353).

-
- [185] Zhou, K. and Q.-S. Li. “Modal identification of high-rise buildings under earthquake excitations via an improved subspace methodology.” In: *Journal of Building Engineering* 52 (2022), p. 104373. DOI: <https://doi.org/10.1016/j.jobbe.2022.104373>.
- [186] Owen, A. B. “A randomized Halton algorithm in R.” In: *arXiv preprint arXiv:1706.02808* (2017). DOI: <https://doi.org/10.48550/arXiv.1706.02808>.
- [187] Hou, T., D. Nuyens, S. Roels, and H. Janssen. “Quasi-Monte Carlo based uncertainty analysis: Sampling efficiency and error estimation in engineering applications.” In: *Reliability Engineering & System Safety* 191 (2019), p. 106549. DOI: <https://doi.org/10.1016/j.res.s.2019.106549>.
- [188] Chatzi, E. N., M. D. Spiridonakos, and A. W. Smyth. “Implementation of Parametric Methods for the Treatment of Uncertainties in Online Identification.” In: *Identification Methods for Structural Health Monitoring* (2016), pp. 51–87. DOI: https://doi.org/10.1007/978-3-319-32077-9_3.
- [189] Gramacki, A. *Nonparametric kernel density estimation and its computational aspects*. Vol. 37. Springer, 2018. DOI: <https://doi.org/10.1007/978-3-319-71688-6>.
- [190] Silverman, B. W. *Density estimation for statistics and data analysis*. Routledge, 2018. ISBN: 9781351456173. URL: <https://books.google.it/books?id=wLQPEAAQBAJ>.
- [191] Wand, M. P. and M. C. Jones. *Kernel smoothing*. CRC press, 1994. DOI: <https://doi.org/10.1201/b14876>.
- [192] Botev, Z. I., J. F. Grotowski, and D. P. Kroese. “Kernel density estimation via diffusion.” In: *Ann. Statist.* 38.5 (2010), pp. 2916–2957. DOI: <https://doi.org/10.1214/10-AOS799>.
- [193] Odland, T. *tommyod/KDEpy: Kernel Density Estimation in Python*. Version v0.9.10. Dec. 2018. DOI: [10.5281/zenodo.2392268](https://doi.org/10.5281/zenodo.2392268).
- [194] Ziegel, E. R. “Methods of Multivariate Analysis.” In: *Technometrics* 45.1 (2003), p. 109. DOI: <https://doi.org/10.1198/tech.2003.s29>.
- [195] Ata, M. Y. “A convergence criterion for the Monte Carlo estimates.” In: *Simulation Modelling Practice and Theory* 15.3 (2007), pp. 237–246. DOI: <http://dx.doi.org/10.1016/j.simpat.2006.12.002>.
- [196] Chan, P.-H., J. Stebbins, and A. B. Zavatsky. “Efficacy of quantifying marker-cluster rigidity in a multi-segment foot model: a Monte-Carlo based global sensitivity analysis and regression model.” In: *Computer Methods in Biomechanics and Biomedical Engineering* 25.3 (2022), pp. 308–319. DOI: <https://doi.org/10.1080/10255842.2021.1954170>.
- [197] Benedetti, L., F. Claeys, I. Nopens, and P. A. Vanrolleghem. “Assessing the convergence of LHS Monte Carlo simulations of wastewater treatment models.” In: *Water Science and Technology* 63.10 (2011), pp. 2219–2224. DOI: <https://doi.org/10.2166/wst.2011.453>.
- [198] Frigge, M., D. C. Hoaglin, and B. Iglewicz. “Some implementations of the boxplot.” In: *The American Statistician* 43.1 (1989), pp. 50–54. DOI: <https://doi.org/10.1080/00031305.1989.10475612>.
- [199] Wickham, H. and L. Stryjewski. “40 years of boxplots.” In: *Am. Statistician* (2011). URL: <http://vita.had.co.nz/papers/boxplots.pdf>.

- [200] Petersen, Ø. W., O. Øiseth, and E.-M. Lourens. “The use of inverse methods for response estimation of long-span suspension bridges with uncertain wind loading conditions: Practical implementation and results for the Hardanger Bridge.” In: *Journal of civil structural health monitoring* 9 (2019), pp. 21–36. DOI: <https://doi.org/10.1007/s13349-018-0319-y>.
- [201] Petersen, Ø. W., O. Øiseth, and E. Lourens. “Investigation of dynamic wind loads on a long-span suspension bridge identified from measured acceleration data.” In: *Journal of Wind Engineering and Industrial Aerodynamics* 196 (2020), p. 104045. DOI: <https://doi.org/10.1016/j.jweia.2019.104045>.
- [202] Fenerci, A., K. Andreas Kvåle, Ø. Wiig Petersen, A. Rønnquist, and O. Øiseth. “Data set from long-term wind and acceleration monitoring of the hardanger bridge.” In: *Journal of Structural Engineering* 147.5 (2021), p. 04721003. DOI: [https://doi.org/10.1061/\(ASCE\)ST.1943-541X.0002997](https://doi.org/10.1061/(ASCE)ST.1943-541X.0002997).
- [203] Dederichs, A. C. and O. Øiseth. “Experimental comparison of automatic operational modal analysis algorithms for application to long-span road bridges.” In: *Mechanical Systems and Signal Processing* 199 (2023), p. 110485. DOI: <https://doi.org/10.1016/j.ymsp.2023.110485>.
- [204] Øiseth, O., A. Rønnquist, K. A. Kvåle, and R. Sigbjörnsson. “Monitoring wind velocities and dynamic response of the Hardanger Bridge.” In: *Dynamics of Civil Structures, Volume 2: Proceedings of the 33rd IMAC, A Conference and Exposition on Structural Dynamics, 2015*. Springer. 2015, pp. 117–125. DOI: https://doi.org/10.1007/978-3-319-15248-6_13.
- [205] Petersen, Ø. W., O. Øiseth, T. S. Nord, and E. Lourens. “Inverse identification of buffeting and self-excited wind loads on the hardanger bridge from acceleration data.” In: *COMPADYN 2019: 7th ECCOMAS Thematic Conference on Computational Methods in Structural Dynamics and Earthquake Engineering*. Vol. 3. 2019. DOI: <http://dx.doi.org/10.7712/120119.7238.20007>.
- [206] Fenerci, A. and O. Øiseth. “The Hardanger Bridge monitoring project: Long-term monitoring results and implications on bridge design.” In: *Procedia engineering* 199 (2017), pp. 3115–3120. DOI: <https://doi.org/10.1016/j.proeng.2017.09.576>.
- [207] Petersen, Ø. W. and O. Øiseth. “Finite element model updating of a long span suspension bridge.” In: *Proceedings of the international conference on earthquake engineering and structural dynamics*. Springer. 2019, pp. 335–344. DOI: https://doi.org/10.1007/978-3-319-78187-7_25.
- [208] Rosso, M. M., A. Aloisio, J. Parol, G. C. Marano, and G. Quaranta. “Intelligent automatic operational modal analysis.” In: *Mechanical Systems and Signal Processing* 201 (2023), p. 110669. DOI: <https://doi.org/10.1016/j.ymsp.2023.110669>.
- [209] Cheynet, E., J. B. Jakobsen, and J. Snæbjörnsson. “Damping estimation of large wind-sensitive structures.” In: *Procedia engineering* 199 (2017), pp. 2047–2053. DOI: <https://doi.org/10.1016/j.proeng.2017.09.471>.
- [210] Fenerci, A. and O. Øiseth. “Strong wind characteristics and dynamic response of a long-span suspension bridge during a storm.” In: *Journal of Wind Engineering and Industrial Aerodynamics* 172 (2018), pp. 116–138. DOI: <https://doi.org/10.1016/j.jweia.2017.10.030>.

- [211] Sun, H., J. Al-Qazweeni, J. Parol, H. Kamal, Z. Chen, and O. Büyüköztürk. “Computational modeling of a unique tower in Kuwait for structural health monitoring: Numerical investigations.” In: *Structural Control and Health Monitoring* 26.3 (2019), e2317. DOI: <https://doi.org/10.1002/stc.2317>.
- [212] Parker, D. and A. Wood. *The tall buildings reference book*. Routledge, 2013. DOI: <https://doi.org/10.4324/9780203106464>.
- [213] Gu, C., G. A. Prieto, A. Al-Enezi, F. Al-Jeri, J. Al-Qazweeni, H. Kamal, S. Kuleli, A. Mordret, O. Büyüköztürk, and M. N. Toksöz. “Ground motion in Kuwait from regional and local earthquakes: Potential effects on tall buildings.” In: *Pure and Applied Geophysics* 175 (2018), pp. 4183–4195. DOI: <https://doi.org/10.1007/s00024-018-1943-5>.
- [214] Welch, P. “The use of fast Fourier transform for the estimation of power spectra: a method based on time averaging over short, modified periodograms.” In: *IEEE Transactions on audio and electroacoustics* 15.2 (1967), pp. 70–73. DOI: <https://doi.org/10.1109/TAU.1967.1161901>.
- [215] Dickey, D. A. and W. A. Fuller. “Distribution of the estimators for autoregressive time series with a unit root.” In: *Journal of the American statistical association* 74.366a (1979), pp. 427–431. DOI: <https://doi.org/10.1080/01621459.1979.10482531>.
- [216] Dickey, D. A. and W. A. Fuller. “Likelihood ratio statistics for autoregressive time series with a unit root.” In: *Econometrica: journal of the Econometric Society* (1981), pp. 1057–1072. DOI: <http://dx.doi.org/10.2307/1912517>.
- [217] Stepinski, T., T. Uhl, and W. Staszewski. *Advanced structural damage detection: from theory to engineering applications*. John Wiley & Sons, 2013. DOI: <https://doi.org/10.1002/9781118536148>.
- [218] Asso, R., R. Cucuzza, M. M. Rosso, D. Masera, and G. C. Marano. “Bridges monitoring: an application of ai with gaussian processes.” In: *14th International Conference on Evolutionary and Deterministic Methods for Design, Optimization and Control. Institute of Structural Analysis and Antiseismic Research National Technical University of Athens*. 2021. DOI: <https://doi.org/10.7712/140121.7964.18426>.
- [219] Rytter, A. *Vibrational Based Inspection of Civil Engineering Structures*. Vol. Fracture & dynamics Vol. R9314 No. 44. Ph.D. thesis. Dept. of Building Technology and Structural Engineering: Aalborg University, 1993. URL: <https://vbn.aau.dk/en/publications/vibrational-based-inspection-of-civil-engineering-structures>.
- [220] Frangopol, D. M. and S. Kim. “Prognosis and life-cycle assessment based on SHM information.” In: *Sensor technologies for civil infrastructures*. Elsevier, 2022, pp. 581–607. DOI: <https://doi.org/10.1016/B978-0-08-102696-0.00003-8>.
- [221] Lichtenstein, A. G. “The silver bridge collapse recounted.” In: *Journal of performance of constructed facilities* 7.4 (1993), pp. 249–261. DOI: [https://doi.org/10.1061/\(ASCE\)0887-3828\(1993\)7:4\(249\)](https://doi.org/10.1061/(ASCE)0887-3828(1993)7:4(249)).
- [222] Carpinteri, A., G. Lacidogna, and A. Manuello. “Damage mechanisms interpreted by acoustic emission signal analysis.” In: *Key Engineering Materials*. Vol. 347. Trans Tech Publ. 2007, pp. 577–582. DOI: <https://doi.org/10.4028/www.scientific.net/KEM.347.577>.

- [223] Behnia, A., H. K. Chai, and T. Shiotani. “Advanced structural health monitoring of concrete structures with the aid of acoustic emission.” In: *Construction and Building Materials* 65 (2014), pp. 282–302. DOI: <https://doi.org/10.1016/j.conbuildmat.2014.04.103>.
- [224] Melchiorre, J., A. Manuello Bertetto, M. M. Rosso, and G. C. Marano. “Acoustic Emission and Artificial Intelligence Procedure for Crack Source Localization.” In: *Sensors* 23.2 (2023), p. 693. DOI: <https://doi.org/10.3390/s23020693>.
- [225] Cardarelli, E., C. Marrone, and L. Orlando. “Evaluation of tunnel stability using integrated geophysical methods.” In: *Journal of Applied Geophysics* 52.2 (2003), pp. 93–102. ISSN: 0926-9851. DOI: [https://doi.org/10.1016/S0926-9851\(02\)00242-2](https://doi.org/10.1016/S0926-9851(02)00242-2).
- [226] Rosso, M. M., A. Aloisio, V. Randazzo, L. Tanzi, G. Cirrincione, and G. C. Marano. “Comparative deep learning studies for indirect tunnel monitoring with and without Fourier pre-processing.” In: *Integrated Computer-Aided Engineering* Preprint (2023), pp. 1–20. DOI: <https://doi.org/10.3233/ICA-230709>.
- [227] Chapman, D. N., N. Metje, and A. Stark. *Introduction to tunnel construction*. Crc Press, 2017. DOI: <https://doi.org/10.1201/9781315120164>.
- [228] Society, B. T. et al. *Tunnel lining design guide*. Thomas Telford, 2004. DOI: <https://doi.org/10.1680/tldg.29866.0001>.
- [229] Jiang, Y., X. Zhang, and T. Taniguchi. “Quantitative condition inspection and assessment of tunnel lining.” In: *Automation in Construction* 102 (2019), pp. 258–269. ISSN: 0926-5805. DOI: <https://doi.org/10.1016/j.autcon.2019.03.001>.
- [230] Bhalla, S., Y. Yang, J. Zhao, and C. Soh. “Structural health monitoring of underground facilities – Technological issues and challenges.” In: *Tunnelling and Underground Space Technology* 20.5 (2005), pp. 487–500. ISSN: 0886-7798. DOI: <https://doi.org/10.1016/j.tust.2005.03.003>.
- [231] Tosti, F. and C. Ferrante. “Using ground penetrating radar methods to investigate reinforced concrete structures.” In: *Surveys in Geophysics* 41.3 (2020), pp. 485–530. DOI: <https://doi.org/10.1007/s10712-019-09565-5>.
- [232] Al-Nuaimy, W., Y. Huang, M. Nakhkash, M. Fang, V. Nguyen, and A. Eriksen. “Automatic detection of buried utilities and solid objects with GPR using neural networks and pattern recognition.” In: *Journal of Applied Geophysics* 43.2 (2000), pp. 157–165. ISSN: 0926-9851. DOI: [https://doi.org/10.1016/S0926-9851\(99\)00055-5](https://doi.org/10.1016/S0926-9851(99)00055-5).
- [233] Solomon, C. and T. Breckon. *Fundamentals of Digital Image Processing: A practical approach with examples in Matlab*. John Wiley & Sons, 2011. DOI: <https://doi.org/10.1002/9780470689776>.
- [234] Broughton, S. A. and K. Bryan. *Discrete Fourier analysis and wavelets: applications to signal and image processing*. John Wiley & Sons, 2018. DOI: <https://doi.org/10.1002/9781118032442>.
- [235] Fisher, R., S. Perkins, A. Walker, and E. Wolfart. *Hypermedia image processing reference*. 1996, pp. 118–130. ISBN: 9780471962434. URL: <https://www.dsi.unive.it/~atorsell/Hipr.pdf>.
- [236] He, K., X. Zhang, S. Ren, and J. Sun. “Deep Residual Learning for Image Recognition.” In: *2016 IEEE Conference on Computer Vision and Pattern Recognition (CVPR)*. 2016, pp. 770–778. DOI: <https://doi.org/10.1109/CVPR.2016.90>.

- [237] Tan, M. and Q. Le. “Efficientnet: Rethinking model scaling for convolutional neural networks.” In: *International conference on machine learning*. PMLR. 2019, pp. 6105–6114. DOI: <https://doi.org/10.48550/arXiv.1905.11946>.
- [238] Dosovitskiy, A., L. Beyer, A. Kolesnikov, D. Weissenborn, X. Zhai, T. Unterthiner, M. Dehghani, M. Minderer, G. Heigold, S. Gelly, et al. “An image is worth 16x16 words: Transformers for image recognition at scale.” In: vol. abs/2010.11929. 2020. DOI: <https://doi.org/10.48550/arXiv.2010.11929>.
- [239] Hassani, A., S. Walton, N. Shah, A. Abuduweili, J. Li, and H. Shi. “Escaping the Big Data Paradigm with Compact Transformers.” In: 2021. DOI: <https://doi.org/10.48550/arXiv.2104.05704>.
- [240] Chollet, F. et al. *Keras*. 2015. URL: <https://keras.io>.
- [241] Zhou, B., A. Khosla, A. Lapedriza, A. Oliva, and A. Torralba. “Learning deep features for discriminative localization.” In: *Proceedings of the IEEE conference on computer vision and pattern recognition*. 2016, pp. 2921–2929. DOI: <https://doi.org/10.48550/arXiv.1512.04150>.
- [242] Selvaraju, R. R., M. Cogswell, A. Das, R. Vedantam, D. Parikh, and D. Batra. “Grad-cam: Visual explanations from deep networks via gradient-based localization.” In: *Proceedings of the IEEE international conference on computer vision*. 2017, pp. 618–626. DOI: <https://doi.org/10.48550/arXiv.1512.04150>.
- [243] Wang, H., M. Du, F. Yang, and Z. Zhang. “Score-cam: Improved visual explanations via score-weighted class activation mapping.” In: 2019. DOI: <https://doi.org/10.48550/arXiv.1910.01279>.
- [244] Itakura, K. *Explainable-AI-interpreting-the-classification-performed-by-deep-learning-with-LIME-using-MATLAB*. 2021. URL: <https://github.com/KentaItakura/Explainable-AI-interpreting-the-classification-performed-by-deep-learning-with-LIME-using-MATLAB>.
- [245] Limongelli, M. P., E. Manoach, S. Quqa, P. F. Giordano, B. Bhowmik, V. Pakrashi, and A. Cigada. “Vibration Response-Based Damage Detection.” In: *Structural Health Monitoring Damage Detection Systems for Aerospace*. Cham: Springer International Publishing, 2021, pp. 133–173. DOI: https://doi.org/10.1007/978-3-030-72192-3_6.
- [246] Aloisio, A., L. Di Battista, R. Alaggio, and M. Fragiaco. “Sensitivity analysis of subspace-based damage indicators under changes in ambient excitation covariance, severity and location of damage.” In: *Engineering Structures* 208 (2020), p. 110235. DOI: <https://doi.org/10.1016/j.engstruct.2020.110235>.
- [247] Döhler, M., F. Hille, and L. Mevel. “Vibration-based monitoring of civil structures with subspace-based damage detection.” In: *Mechatronics for Cultural Heritage and Civil Engineering*. Springer, 2018, pp. 307–326. DOI: https://doi.org/10.1007/978-3-319-68646-2_14.
- [248] Yan, A.-M., P. De Boe, and J.-C. Golinval. “Structural damage diagnosis by Kalman model based on stochastic subspace identification.” In: *Structural Health Monitoring* 3.2 (2004), pp. 103–119. DOI: <https://doi.org/10.1177/1475921704042545>.
- [249] Gautier, G., R. Serra, and J.-M. Mencik. “Roller Bearing Monitoring by New Subspace-Based Damage Indicator.” In: *Hindawi Shock and Vibration* 2015 (2008), p. 11. DOI: <https://doi.org/10.1155/2015/828093>.

- [250] Balmès, E., M. Basseville, L. Mevel, H. Nasser, and W. Zhou. “Statistical model-based damage localization: A combined subspace-based and substructuring approach.” In: *Structural Control and Health Monitoring* 15.6 (2008), pp. 857–875. DOI: <https://doi.org/10.1002/stc.223>.
- [251] Rosso, M. M., A. Aloisio, G. Cirrincione, and G. C. Marano. “Subspace features and statistical indicators for neural network-based damage detection.” In: 56 (2023), p. 104792. DOI: <https://doi.org/10.1016/j.istruc.2023.06.123>.
- [252] Rosso, M. M., A. Aloisio, J. Melchiorre, F. Huo, and G. C. Marano. “Noise effects analysis on subspace-based damage detection with neural networks.” In: 54 (2023), pp. 23–37. DOI: <https://doi.org/10.1016/j.istruc.2023.05.024>.
- [253] Yan, A.-M. and J.-C. Golinval. “Null subspace-based damage detection of structures using vibration measurements.” In: *Mechanical Systems and Signal Processing* 20.3 (2006), pp. 611–626. ISSN: 0888-3270. DOI: <https://doi.org/10.1016/j.ymsp.2005.04.010>.
- [254] Basseville, M., M. Abdelghani, and A. Benveniste. “Subspace-based fault detection algorithms for vibration monitoring.” In: *Automatica* 36.1 (2000), pp. 101–109. ISSN: 0005-1098. DOI: [https://doi.org/10.1016/S0005-1098\(99\)00093-X](https://doi.org/10.1016/S0005-1098(99)00093-X).
- [255] Basseville, M., L. Mevel, and M. Goursat. “Statistical model-based damage detection and localization: subspace-based residuals and damage-to-noise sensitivity ratios.” In: *Journal of Sound and Vibration* 275.3 (2004), pp. 769–794. ISSN: 0022-460X. DOI: <https://doi.org/10.1016/j.jsv.2003.07.016>.
- [256] Döhler, M., L. Mevel, and F. Hille. “Subspace-based damage detection under changes in the ambient excitation statistics.” In: *Mechanical Systems and Signal Processing* 45.1 (2014), pp. 207–224. ISSN: 0888-3270. DOI: <https://doi.org/10.1016/j.ymsp.2013.10.023>.
- [257] Finotti, R. P., A. A. Cury, and F. d. S. Barbosa. “An SHM approach using machine learning and statistical indicators extracted from raw dynamic measurements.” In: *Latin American Journal of Solids and Structures* 16.2 (2019). DOI: <https://doi.org/10.1590/1679-78254942>.
- [258] Saeed, K., N. Mechbal, G. Coffignal, and M. Vergé. “Subspace-based damage localization using Artificial Neural Network.” In: *18th Mediterranean Conference on Control and Automation, MED’10*. 2010, pp. 563–568. DOI: <https://doi.org/10.1109/MED.2010.5547729>.
- [259] Zhu, M., F. McKenna, and M. H. Scott. “OpenSeesPy: Python library for the OpenSees finite element framework.” In: *SoftwareX* 7 (2018), pp. 6–11. DOI: <https://doi.org/10.1016/j.softx.2017.10.009>.
- [260] Dasar, A., H. Hamada, Y. Sagawa, and D. Yamamoto. “Deterioration progress and performance reduction of 40-year-old reinforced concrete beams in natural corrosion environments.” In: *Construction and Building Materials* 149 (2017), pp. 690–704. DOI: <https://doi.org/10.1016/j.conbuildmat.2017.05.162>.
- [261] Fu, C., N. Jin, H. Ye, X. Jin, and W. Dai. “Corrosion characteristics of a 4-year naturally corroded reinforced concrete beam with load-induced transverse cracks.” In: *Corrosion Science* 117 (2017), pp. 11–23. DOI: <https://doi.org/10.1016/j.corsci.2017.01.002>.
- [262] Kreislova, K. and H. Geiplova. “Evaluation of corrosion protection of steel bridges.” In: *Procedia Engineering* 40 (2012), pp. 229–234. DOI: <https://doi.org/10.1016/j.proeng.2012.07.085>.

- [263] Dang, V. H. and R. Francois. “Influence of long-term corrosion in chloride environment on mechanical behaviour of RC beam.” In: *Engineering Structures* 48 (2013), pp. 558–568. DOI: <https://doi.org/10.1016/j.engstruct.2012.09.021>.
- [264] Carpinteri, A. *Advanced structural mechanics*. CRC Press, 2017. ISBN: 9781315375298. DOI: <https://doi.org/10.1201/9781315375298>.
- [265] Barrias, A., J. R. Casas, and S. Villalba. “A review of distributed optical fiber sensors for civil engineering applications.” In: *Sensors* 16.5 (2016), p. 748. DOI: <https://doi.org/10.3390/s16050748>.
- [266] Kullaa, J. “Detection, identification, and quantification of sensor fault in a sensor network.” In: *Mechanical Systems and Signal Processing* 40 (2013), pp. 208–221. DOI: <https://doi.org/10.1016/j.ymsp.2013.05.007>.
- [267] Rahaman, A., C. H. Park, and B. Kim. “Design and characterization of a MEMS piezoelectric acoustic sensor with the enhanced signal-to-noise ratio.” In: *Sensors and Actuators A: Physical* 311 (2020), p. 112087. DOI: <https://doi.org/10.1016/j.sna.2020.112087>.
- [268] Andre, J., A. Kiremidjian, Y. Liao, C. Georgakis, and R. Rajagopal. “Structural health monitoring approach for detecting ice accretion on bridge cable using the Haar Wavelet Transform.” In: *Sensors and Smart Structures Technologies for Civil, Mechanical, and Aerospace Systems 2016*. Vol. 9803. SPIE, 2016, pp. 107–114. DOI: <https://doi.org/10.1117/12.2219392>.
- [269] Andre, J., A. Kiremidjian, Y. Liao, R. Rajagopal, and C. Georgakis. “Structural health monitoring approach for detecting ice accretion on bridge cables using the autoregressive model.” In: *Maintenance, Monitoring, Safety, Risk and Resilience of Bridges and Bridge Networks*. CRC Press, 2016, pp. 431–431. DOI: <https://doi.org/10.1201/9781315207681-252>.
- [270] Haddad, W. M. and V. Chellaboina. *Nonlinear dynamical systems and control: a Lyapunov-based approach*. Princeton university press, 2008. DOI: <https://doi.org/10.1515/9781400841042>.
- [271] Tarbouriech, S., I. Queinnec, and C. Prieur. “Stability analysis and stabilization of systems with input backlash.” In: *IEEE Transactions on Automatic Control* 59.2 (2013), pp. 488–494.
- [272] To, C. W. *Nonlinear random vibration: Analytical techniques and applications*. Crc Press, 2000. DOI: <https://doi.org/10.1201/9781482287264>.
- [273] Varanis, M., A. L. Silva, J. M. Balthazar, and R. Pederiva. “A tutorial review on time-frequency analysis of non-stationary vibration signals with nonlinear dynamics applications.” In: *Brazilian Journal of Physics* 51 (2021), pp. 859–877. DOI: <https://doi.org/10.1007/s13538-020-00842-y>.
- [274] Pai, P. F. “Nonlinear vibration characterization by signal decomposition.” In: *Journal of sound and vibration* 307.3-5 (2007), pp. 527–544. DOI: <https://doi.org/10.1016/j.jsv.2007.06.056>.
- [275] Huang, N. E. *Hilbert-Huang transform and its applications*. Vol. 16. Interdisciplinary Mathematical Sciences. World Scientific, 2014. ISBN: 9789814508254. URL: <https://books.google.it/books?id=jTG7CgAAQBAJ>.
- [276] Rao, A. R. and E.-C. Hsu. *Hilbert-Huang transform analysis of hydrological and environmental time series*. Vol. 60. Springer Science & Business Media, 2008. DOI: <https://doi.org/10.1007/978-1-4020-6454-8>.

- [277] Weng, J.-H. and C.-H. Loh. “Recursive subspace identification for on-line tracking of structural modal parameter.” In: *Mechanical Systems and Signal Processing* 25.8 (2011), pp. 2923–2937. DOI: <https://doi.org/10.1016/j.ymsp.2011.05.013>.
- [278] Loh, C.-H., J.-H. Weng, Y.-C. Liu, P.-Y. Lin, and S.-K. Huang. “Structural damage diagnosis based on on-line recursive stochastic subspace identification.” In: *Smart materials and structures* 20.5 (2011), p. 055004. DOI: <https://doi.org/10.1088/0964-1726/20/5/055004>.
- [279] Loh, C.-H. and J.-D. Chen. “Tracking modal parameters from building seismic response data using recursive subspace identification algorithm.” In: *Earthquake Engineering & Structural Dynamics* 46.13 (2017), pp. 2163–2183. DOI: <https://doi.org/10.1002/eqe.2900>.
- [280] Zhou, S., D. Y. Yang, G. Cai, L. Wang, Z. Chen, J. Ma, and B. Wang. “Ambient data-driven online tracking of electromechanical modes using recursive subspace dynamic mode decomposition.” In: *IEEE Transactions on Power Systems* 38.6 (2022), pp. 5257–5266. DOI: <https://doi.org/10.1109/TPWRS.2022.3229651>.
- [281] Chauhan, S. “Subspace algorithms in modal parameter estimation for operational modal analysis: perspectives and practices.” In: *Rotating Machinery, Hybrid Test Methods, Vibro-Acoustics & Laser Vibrometry, Volume 8: Proceedings of the 34th IMAC, A Conference and Exposition on Structural Dynamics 2016*. Springer. 2016, pp. 295–301.

Appendix A

Output block Hankel matrix in stochastic subspace identification

The block output Hankel matrix (a matrix which is constant along the anti-diagonals) of measured data represents the true starting point of both covariance-driven and data-driven stochastic subspace identification methods [101, 96]. Specifically, considering l measurement channels from the sensor layout deployed on a structure, the discrete-time sampled recordings are a collection of arrays $\{\mathbf{y}_0, \mathbf{y}_1, \dots, \mathbf{y}_r, \dots, \mathbf{y}_{N_t}\}$, with $\mathbf{y}_r \in \mathbb{R}^l$. The subscripts refers to the time instant in which those samples have been recorded, i.e. $0, 1, \dots, r, \dots, N_t$, thus determining an experimental vibration recording session with a total duration in time N_t or with a total number of data arrays equal to $N_d = N_t + 1$. In subspace identification methods, the user must set in advance a positive integer time lag parameter i , respectful of the condition in Eq. (2.96). Afterward, the output data can be rearranged in a output block Hankel matrix $\mathbf{Y}_{0|2i-1}$ by imposing a number of block rows equal to $2i$, i.e. with a total rows size of $2li$, and considering a one-time shift for two subsequent columns until using all available data. As a consequence, the number of columns j of output block Hankel matrix is automatically defined once known the total recording length N_d or N_t , and the time shift parameter i , i.e.

$$j = N_d - 2i + 1 \quad \text{or} \quad j = N_t - 2i + 2 \quad (\text{A.1})$$

Therefore output block Hankel matrix $\mathbf{Y}_{0|2i-1} \in \mathbb{R}^{2li \times j}$ can be split into two submatrices denoted as past outputs \mathbf{Y}_p and future outputs \mathbf{Y}_f as follows:

$$\mathbf{Y}_{0|2i-1} = \frac{1}{\sqrt{j}} \begin{bmatrix} \mathbf{y}_0 & \mathbf{y}_1 & \mathbf{y}_2 & \cdots & \cdots & \mathbf{y}_{N_t-2i+1} \\ \mathbf{y}_1 & \mathbf{y}_2 & \mathbf{y}_3 & \ddots & \ddots & \mathbf{y}_{N_t-2i+2} \\ \mathbf{y}_2 & \mathbf{y}_3 & \ddots & \ddots & \ddots & \mathbf{y}_{N_t-2i+3} \\ \vdots & \ddots & \ddots & \ddots & \ddots & \vdots \\ \vdots & \ddots & \ddots & \ddots & \ddots & \mathbf{y}_{N_t-i-1} \\ \mathbf{y}_{i-1} & \mathbf{y}_i & \ddots & \ddots & \ddots & \mathbf{y}_{N_t-i} \\ \hline \mathbf{y}_i & \mathbf{y}_{i+1} & \ddots & \ddots & \ddots & \mathbf{y}_{N_t-i+1} \\ \mathbf{y}_{i+1} & \mathbf{y}_{i+2} & \ddots & \ddots & \ddots & \mathbf{y}_{N_t-i+2} \\ \vdots & \ddots & \ddots & \ddots & \ddots & \vdots \\ \mathbf{y}_{2i-2} & \mathbf{y}_{2i-1} & \ddots & \ddots & \ddots & \mathbf{y}_{N_t-1} \\ \mathbf{y}_{2i-1} & \mathbf{y}_{2i} & \cdots & \cdots & \mathbf{y}_{N_t-1} & \mathbf{y}_{N_t} \end{bmatrix} = \begin{bmatrix} \mathbf{Y}_p \\ \mathbf{Y}_f \end{bmatrix} \quad (\text{A.2})$$

$$\mathbf{Y}_p = \frac{1}{\sqrt{j}} \begin{bmatrix} \mathbf{y}_0 & \mathbf{y}_1 & \mathbf{y}_2 & \cdots & \cdots & \mathbf{y}_{N_t-2i+1} \\ \mathbf{y}_1 & \mathbf{y}_2 & \mathbf{y}_3 & \ddots & \ddots & \mathbf{y}_{N_t-2i+2} \\ \mathbf{y}_2 & \mathbf{y}_3 & \ddots & \ddots & \ddots & \mathbf{y}_{N_t-2i+3} \\ \vdots & \ddots & \ddots & \ddots & \ddots & \vdots \\ \vdots & \ddots & \ddots & \ddots & \ddots & \mathbf{y}_{N_t-i-1} \\ \mathbf{y}_{i-1} & \mathbf{y}_i & \ddots & \ddots & \ddots & \mathbf{y}_{N_t-i} \end{bmatrix} \quad (\text{A.3})$$

$$\mathbf{Y}_p^T = \frac{1}{\sqrt{j}} \begin{bmatrix} \mathbf{y}_0 & & \mathbf{y}_1 & & \mathbf{y}_2 & & \cdots & \cdots & \mathbf{y}_{i-1} \\ \mathbf{y}_1 & & \mathbf{y}_2 & & \mathbf{y}_3 & & \cdots & \cdots & \mathbf{y}_i \\ \mathbf{y}_2 & & \mathbf{y}_3 & & \ddots & & \ddots & \ddots & \vdots \\ \vdots & & \ddots & & \ddots & & \ddots & \ddots & \vdots \\ \vdots & & \ddots & & \ddots & & \ddots & \ddots & \vdots \\ \mathbf{y}_{N_t-2i+1} & \mathbf{y}_{N_t-2i+2} & \mathbf{y}_{N_t-2i+3} & \cdots & \mathbf{y}_{N_t-i-1} & \mathbf{y}_{N_t-i} \end{bmatrix} \quad (\text{A.4})$$

$$\mathbf{Y}_f = \frac{1}{\sqrt{j}} \begin{bmatrix} \mathbf{y}_i & \mathbf{y}_{i+1} & \ddots & \ddots & \ddots & \mathbf{y}_{N_t-i+1} \\ \mathbf{y}_{i+1} & \mathbf{y}_{i+2} & \ddots & \ddots & \ddots & \mathbf{y}_{N_t-i+2} \\ \vdots & \ddots & \ddots & \ddots & \ddots & \vdots \\ \mathbf{y}_{2i-2} & \mathbf{y}_{2i-1} & \ddots & \ddots & \ddots & \mathbf{y}_{N_t-1} \\ \mathbf{y}_{2i-1} & \mathbf{y}_{2i} & \cdots & \cdots & \mathbf{y}_{N_t-1} & \mathbf{y}_{N_t} \end{bmatrix} \quad (\text{A.5})$$

The subscript in $\mathbf{Y}_{0|2i-1}$ indicates the indices of the first column of the matrix [101]. Under the hypothesis of ergodicity, and considering an infinite long data sequence ($N_t \rightarrow \infty$), it is possible to demonstrate that the output covariance Toeplitz matrix of SSI-cov approach provided in section 2.2.3.2 in Eq. (2.95) is derived from the output block Hankel submatrices \mathbf{Y}_p and \mathbf{Y}_f [281, 101]:

$$\mathbf{T}_{1|i} = \mathbb{E} [\mathbf{Y}_f \mathbf{Y}_p^T] \quad (\text{A.6})$$

It is possible to demonstrate the above relationship by firstly reminding the theoretical general definition of the output covariance matrices with finite time lag i

already provided in Eq. (2.72), i.e.

$$\mathbf{R}_i = \mathbb{E} [\mathbf{y}_{r+i} \mathbf{y}_r^T].$$

To demonstrate the validity of Eq. (A.6), it is possible to notice that computing it term-by-term as below, each of them can be traced back to output covariance definition of Eq. (2.72). For instance, the term in position (1,1) can be written as the row-column product rule from linear algebra matrices multiplication, i.e.

$$\begin{aligned} \mathbf{T}_{1|i(1,1)} &= \mathbb{E} \left[\mathbf{Y}_{f(1,:)} \mathbf{Y}_{p(:,1)}^T \right] \\ &= \mathbb{E} \left[\frac{1}{\sqrt{j}} \frac{1}{\sqrt{j}} [\mathbf{y}_i \quad \mathbf{y}_{i+1} \quad \dots \quad \mathbf{y}_{N_t-i+1}] \cdot \begin{bmatrix} \mathbf{y}_0 \\ \mathbf{y}_1 \\ \vdots \\ \mathbf{y}_{N_t-2i+1} \end{bmatrix} \right] \\ &= \frac{1}{j} \mathbb{E} [\mathbf{y}_i \mathbf{y}_0 + \mathbf{y}_{i+1} \mathbf{y}_1 + \dots + \mathbf{y}_{N_t-i+1} \mathbf{y}_{N_t-2i+1}] \\ &= \frac{1}{j} (\mathbb{E} [\mathbf{y}_{0+i} \mathbf{y}_0] + \mathbb{E} [\mathbf{y}_{1+i} \mathbf{y}_1] + \dots + \mathbb{E} [\mathbf{y}_{N_t-i+1+i-i} \mathbf{y}_{N_t-2i+1}]) \quad (\text{A.7}) \\ &= \frac{1}{j} (\mathbb{E} [\mathbf{y}_{0+i} \mathbf{y}_0] + \mathbb{E} [\mathbf{y}_{1+i} \mathbf{y}_1] + \dots + \mathbb{E} [\mathbf{y}_{(N_t-2i+1)+i} \mathbf{y}_{N_t-2i+1}]) \\ &= \frac{1}{j} (\mathbf{R}_i + \mathbf{R}_i + \dots + \mathbf{R}_i) \\ &= \frac{1}{j} j \mathbf{R}_i \\ &= \mathbf{R}_i \end{aligned}$$

Noting that all terms of the row-column product refer to different time instants which span always about a finite lag i . Similarly, the term in position (1,2) can be

obtained as below:

$$\begin{aligned}
 \mathbf{T}_{1|i(1,2)} &= \mathbb{E} \left[\mathbf{Y}_{f(1,:)} \mathbf{Y}_{p(:,2)}^T \right] \\
 &= \mathbb{E} \left[\frac{1}{\sqrt{j}} \frac{1}{\sqrt{j}} [\mathbf{y}_i \quad \mathbf{y}_{i+1} \quad \cdots \quad \mathbf{y}_{N_t-i+1}] \cdot \begin{bmatrix} \mathbf{y}_1 \\ \mathbf{y}_2 \\ \vdots \\ \mathbf{y}_{N_t-2i+2} \end{bmatrix} \right] \\
 &= \frac{1}{j} \mathbb{E} [\mathbf{y}_i \mathbf{y}_1 + \mathbf{y}_{i+1} \mathbf{y}_2 + \cdots + \mathbf{y}_{N_t-i+1} \mathbf{y}_{N_t-2i+2}] \\
 &= \frac{1}{j} \left(\mathbb{E} [\mathbf{y}_{0+i+1-1} \mathbf{y}_1] + \mathbb{E} [\mathbf{y}_{1+i+1-1} \mathbf{y}_2] + \cdots + \mathbb{E} [\mathbf{y}_{N_t-i+1+i-i+1-1} \mathbf{y}_{N_t-2i+2}] \right) \\
 &= \frac{1}{j} \left(\mathbb{E} [\mathbf{y}_{1+(i-1)} \mathbf{y}_1] + \mathbb{E} [\mathbf{y}_{2+(i-1)} \mathbf{y}_2] + \cdots + \mathbb{E} [\mathbf{y}_{(N_t-2i+2)+(i-1)} \mathbf{y}_{N_t-2i+2}] \right) \\
 &= \frac{1}{j} (\mathbf{R}_{i-1} + \mathbf{R}_{i-1} + \cdots + \mathbf{R}_{i-1}) \\
 &= \frac{1}{j} j \mathbf{R}_{i-1} \\
 &= \mathbf{R}_{i-1}
 \end{aligned} \tag{A.8}$$

Similarly, all the other terms can be computed, demonstrating that the output covariance Toeplitz matrix of SSI-cov method can be found by the expected value of the product between future measurements and past data matrices, eventually finding again the definition reported in Eq. (2.95), i.e.

$$\mathbf{T}_{1|i} = \mathbb{E} [\mathbf{Y}_f \mathbf{Y}_p^T] = \begin{bmatrix} \mathbf{R}_i & \mathbf{R}_{i-1} & \cdots & \mathbf{R}_2 & \mathbf{R}_1 \\ \mathbf{R}_{i+1} & \mathbf{R}_i & \ddots & \ddots & \mathbf{R}_2 \\ \vdots & \ddots & \ddots & \ddots & \vdots \\ \vdots & \ddots & \ddots & \ddots & \mathbf{R}_{i-1} \\ \mathbf{R}_{2i-1} & \mathbf{R}_{2i-2} & \cdots & \mathbf{R}_{i+1} & \mathbf{R}_i \end{bmatrix}$$

Theoretically, the output covariance matrices are related to the state matrices as in Eq. (2.75), i.e.

$$\mathbf{R}_i = \mathbf{C} \mathbf{A}^{i-1} \mathbf{G}.$$

Therefore, the Toeplitz matrix defined as in Eq. (2.95) making explicit the factorization according to the observability matrix \mathbf{O}_i and reversed controllability matrix

Γ_i , i.e.

$$\begin{aligned}
 \mathbf{T}_{1|i} &= \begin{bmatrix} \mathbf{R}_i & \mathbf{R}_{i-1} & \dots & \mathbf{R}_2 & \mathbf{R}_1 \\ \mathbf{R}_{i+1} & \mathbf{R}_i & \ddots & \ddots & \mathbf{R}_2 \\ \vdots & \ddots & \ddots & \ddots & \vdots \\ \vdots & \ddots & \ddots & \ddots & \mathbf{R}_{i-1} \\ \mathbf{R}_{2i-1} & \mathbf{R}_{2i-2} & \dots & \mathbf{R}_{i+1} & \mathbf{R}_i \end{bmatrix} \\
 &= \begin{bmatrix} \mathbf{C}\mathbf{A}^{i-1}\mathbf{G} & \mathbf{C}\mathbf{A}^{i-2}\mathbf{G} & \dots & \mathbf{C}\mathbf{A}\mathbf{G} & \mathbf{C}\mathbf{G} \\ \mathbf{C}\mathbf{A}^i\mathbf{G} & \mathbf{R}_i & \ddots & \ddots & \mathbf{C}\mathbf{A}\mathbf{G} \\ \vdots & \ddots & \ddots & \ddots & \vdots \\ \vdots & \ddots & \ddots & \ddots & \mathbf{C}\mathbf{A}^{i-2}\mathbf{G} \\ \mathbf{C}\mathbf{A}^{2i-2}\mathbf{G} & \mathbf{C}\mathbf{A}^{2i-3}\mathbf{G} & \dots & \mathbf{C}\mathbf{A}^i\mathbf{G} & \mathbf{C}\mathbf{A}^{i-1}\mathbf{G} \end{bmatrix} \\
 &= \begin{bmatrix} \mathbf{C} \\ \mathbf{C}\mathbf{A} \\ \vdots \\ \mathbf{C}\mathbf{A}^{i-1} \end{bmatrix} [\mathbf{A}^{i-1}\mathbf{G} \dots \mathbf{A}\mathbf{G} \mathbf{G}] \\
 &= \mathbf{O}_i\Gamma_i.
 \end{aligned}$$

Nevertheless, the state matrices \mathbf{A} , \mathbf{C} , and \mathbf{G} are not known in advance because they are comprised within the target of the parametric dynamic identification approach through the stochastic state space formulation. Additionally, considering that the monitored data sequence are not infinite ($N_t < \infty$), the Toeplitz matrix should be constructed numerically using output-only data by estimating the output covariances as reported in Eq. (2.94) [96], i.e.

$$\hat{\mathbf{R}}_i = \frac{1}{N_d - i} \mathbf{Y}_{1:N_d-i} \mathbf{Y}_{i:N_d}^T,$$

Alternatively, instead of setting up a Toeplitz matrix from reasoning based on output data Hankel matrices, it is possible to set a block Hankel matrix of the theoretical output covariance matrices as below [111, 108]. This alternative formulation provides a similar factorization because the same observability matrix \mathbf{O}_i

appear, whilst a new controllability matrix $\underline{\Gamma}_i$ is obtained.

$$\begin{aligned}
 H_R &= \begin{bmatrix} R_1 & R_2 & R_3 & \dots & R_i \\ R_2 & R_3 & \ddots & \ddots & R_{i+1} \\ R_3 & \ddots & \ddots & \ddots & \vdots \\ \vdots & \ddots & \ddots & \ddots & R_{2i-1} \\ R_i & R_{i+1} & \dots & R_{2i-1} & R_{2i} \end{bmatrix} \\
 &= \begin{bmatrix} CG & CAG & CA^2G & \dots & CA^{i-1}G \\ CAG & CA^2G & \ddots & \ddots & CA^iG \\ CA^2G & \ddots & \ddots & \ddots & \vdots \\ \vdots & \ddots & \ddots & \ddots & CA^{2i-2}G \\ CA^{i-1}G & CA^iG & \dots & CA^{2i-2}G & CA^{2i-1}G \end{bmatrix} \quad (\text{A.9}) \\
 &= \begin{bmatrix} C \\ CA \\ \vdots \\ CA^{i-1} \end{bmatrix} [G \quad AG \quad \dots \quad A^{i-1}G] \\
 &= O_i \underline{\Gamma}_i.
 \end{aligned}$$

Therefore, now it is clear the reason why $\underline{\Gamma}_i$ is called reversed controllability matrix, in contrast to the controllability matrix $\underline{\Gamma}_i$.

Appendix B

Tunnel linings damage detection: training curves and interpretable maps

B.1 Training curves

B.1.1 Convergence curves for ResNet-50

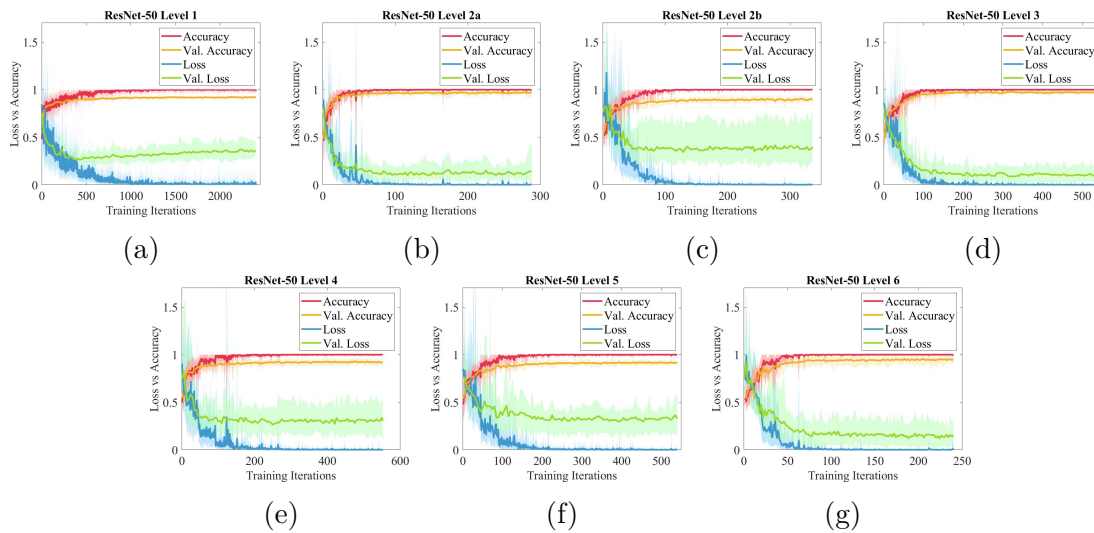


Figure B.1: (a-g) ResNet-50 trained with raw images: loss versus accuracy during the training iterations.

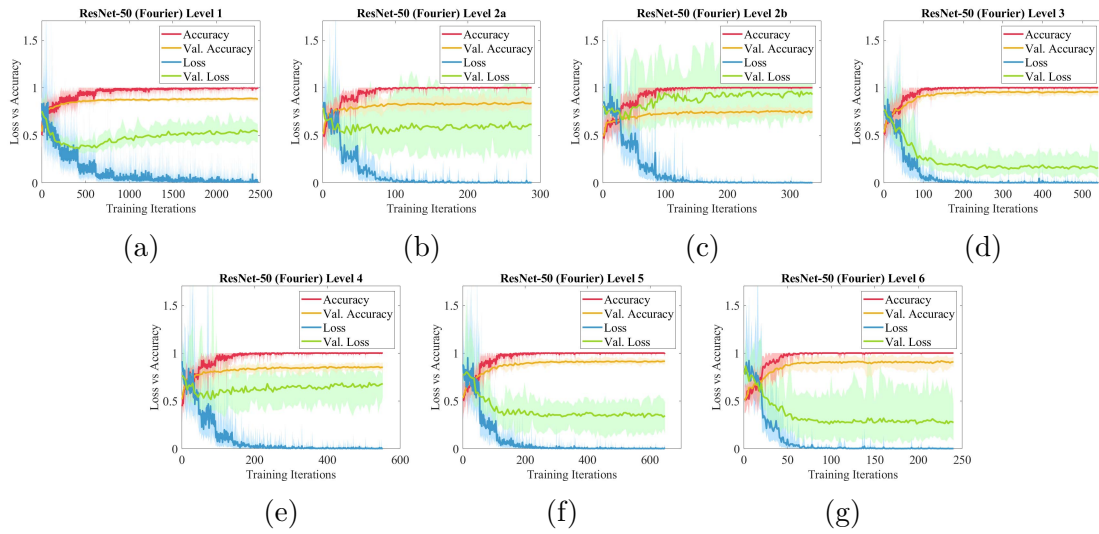


Figure B.2: (a-g) ResNet-50 trained with Fourier pre-processed images: loss versus accuracy during the training iterations.

B.1.2 Convergence curves for EfficientNet-B0

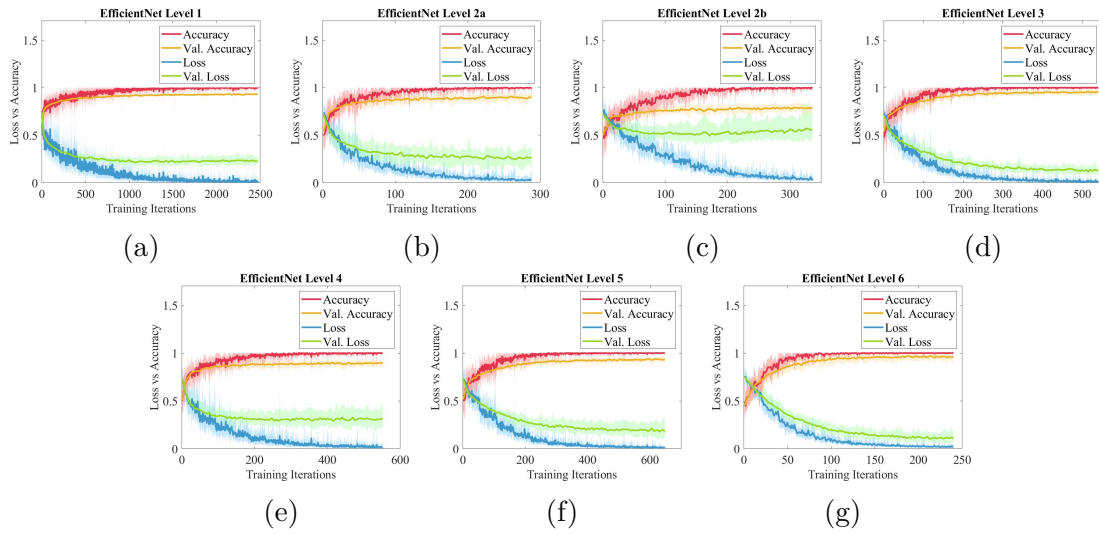


Figure B.3: (a-g) EfficientNet-B0 trained with raw images: loss versus accuracy during the training iterations.

B.1 – Training curves

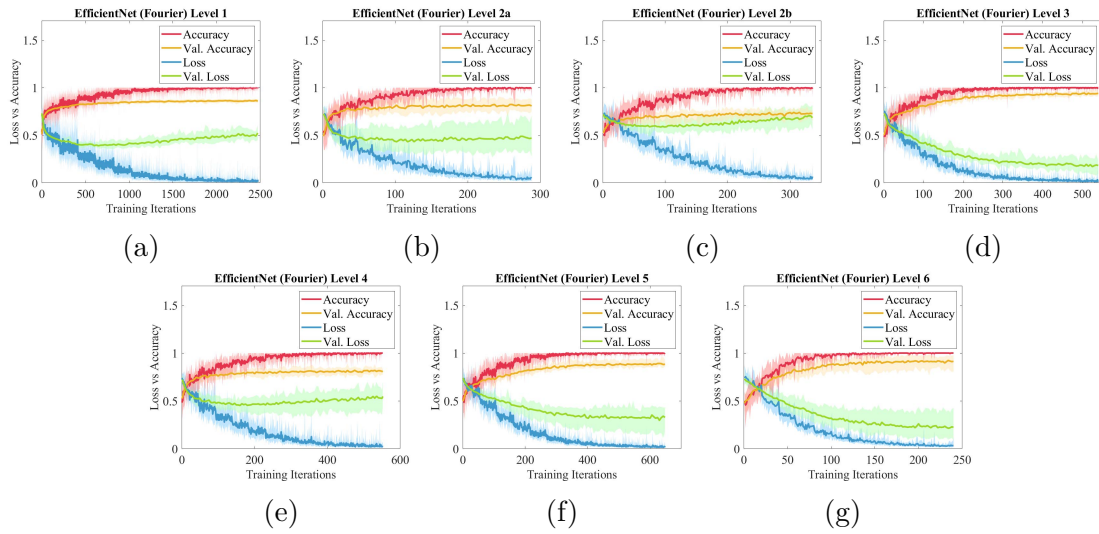


Figure B.4: (a-g) EfficientNet-B0 trained with Fourier pre-processed images: loss versus accuracy during the training iterations.

B.1.3 Convergence curves for ViT

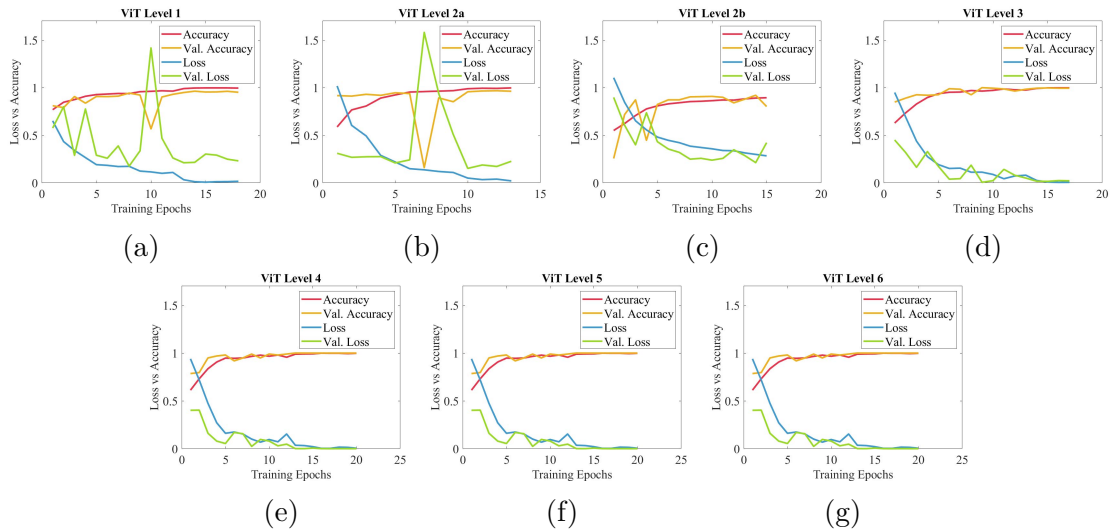


Figure B.5: (a-g) ViT trained with raw images: loss versus accuracy during the training epochs.

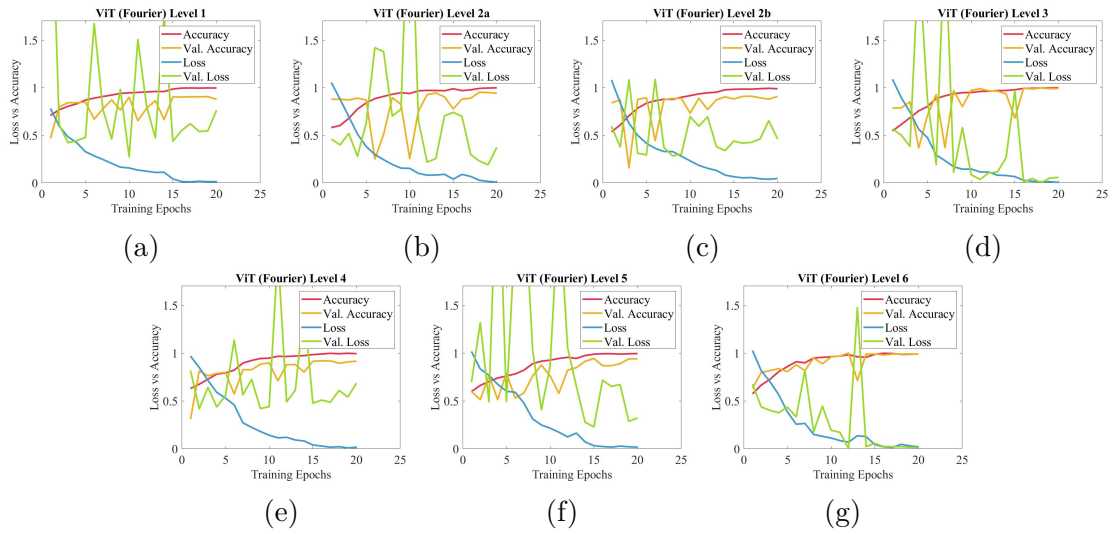


Figure B.6: (a-g) ViT trained with Fourier pre-processed images: loss versus accuracy during the training epochs.

B.1.4 Convergence curves for CCT

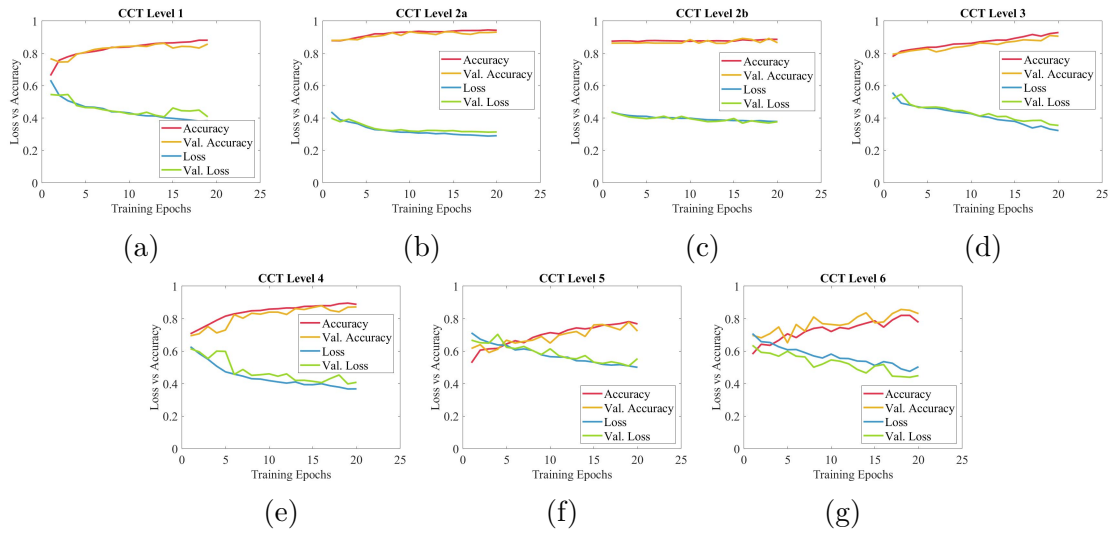


Figure B.7: (a-g) CCT trained with raw images: loss versus accuracy during the training epochs.

B.1 – Training curves

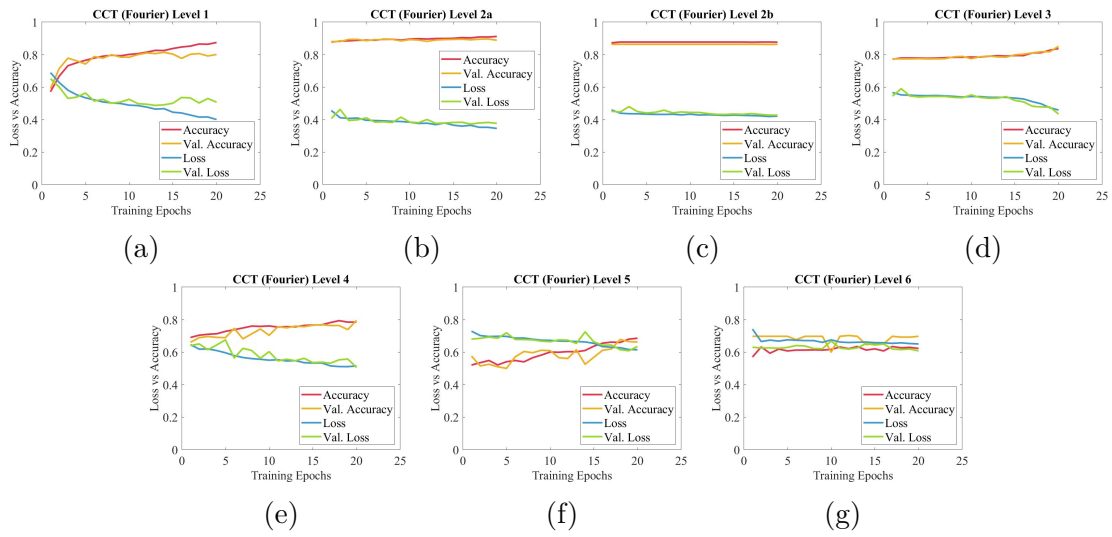


Figure B.8: (a-g) CCT trained with Fourier pre-processed images: loss versus accuracy during the training epochs.

B.2 Interpretable class activation maps and attention maps

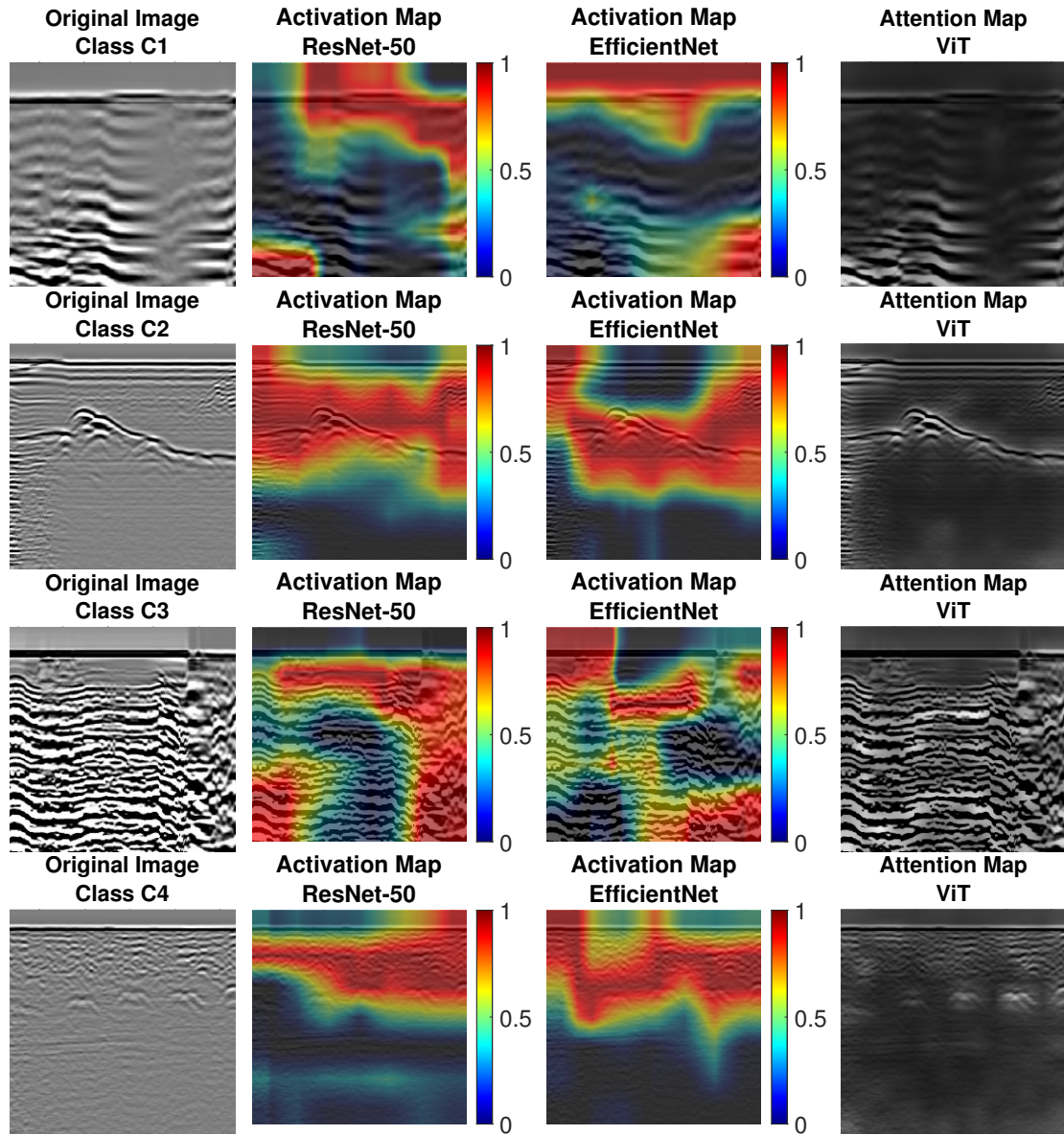


Figure B.9: Class activation maps for ResNet-50 and EfficientNet, and attention maps for ViT compared to original images for each class.

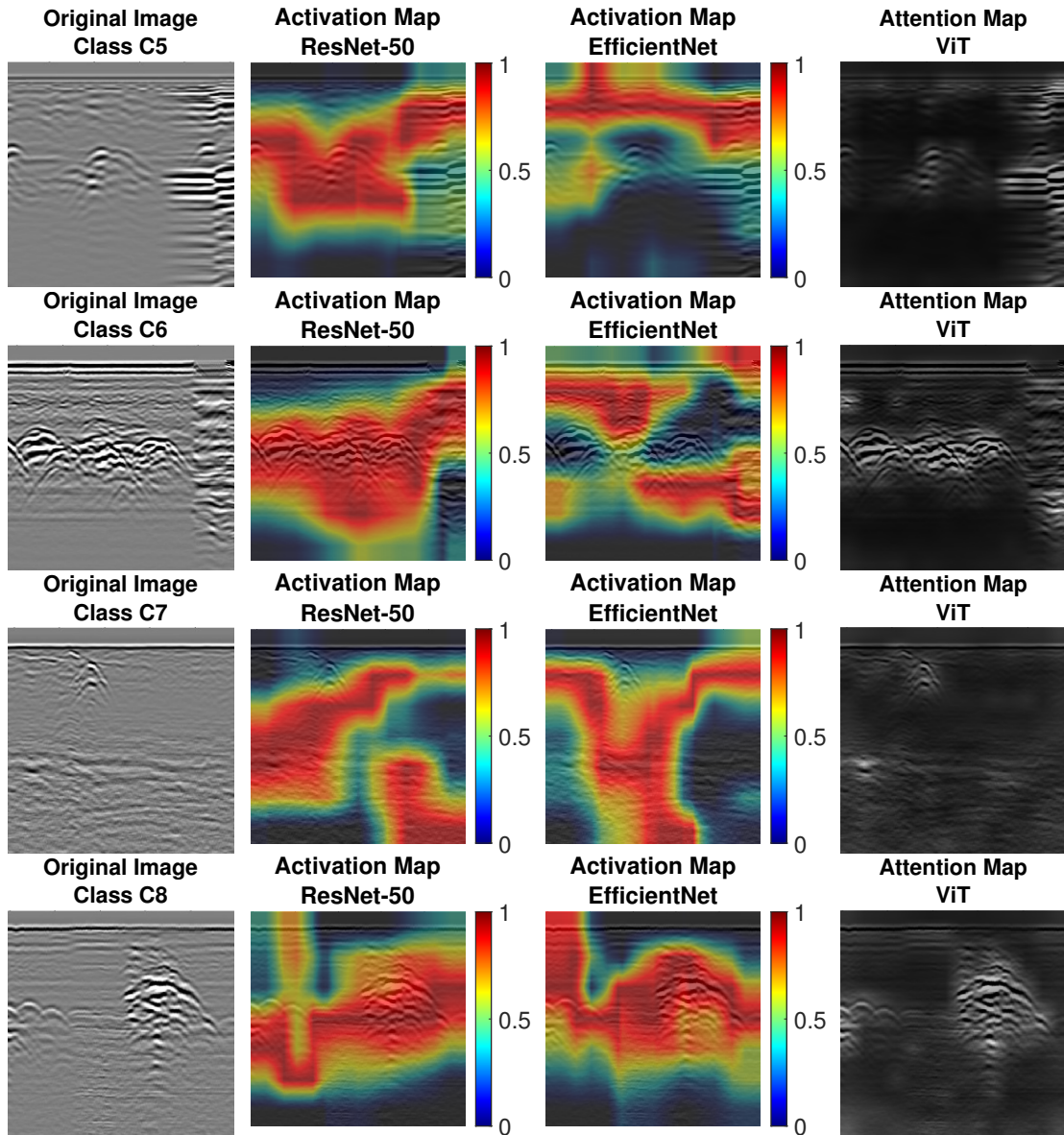


Figure B.9: Class activation maps for ResNet-50 and EfficientNet, and attention maps for ViT compared to original images for each class.

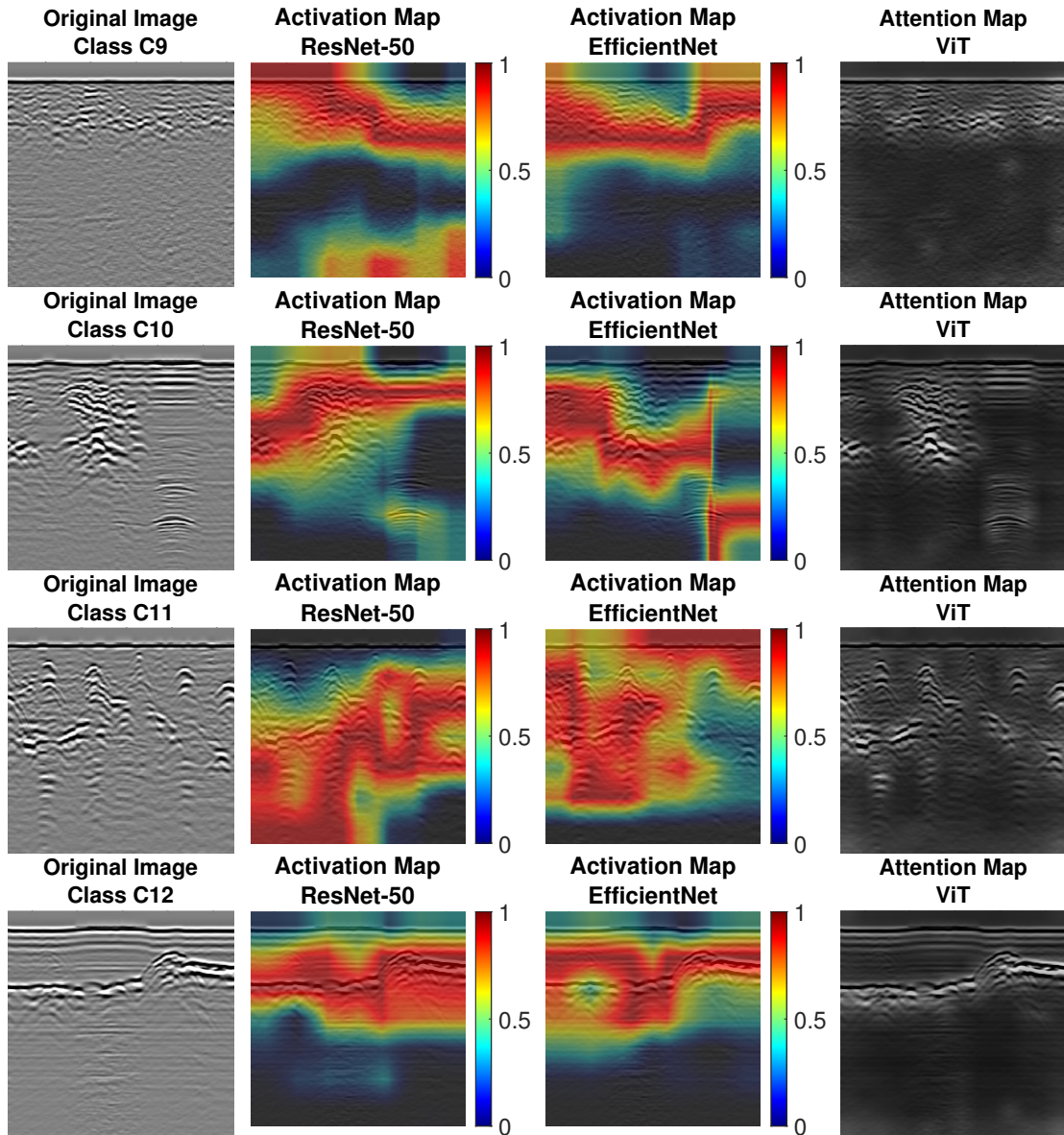


Figure B.9: Class activation maps for ResNet-50 and EfficientNet, and attention maps for ViT compared to original images for each class.

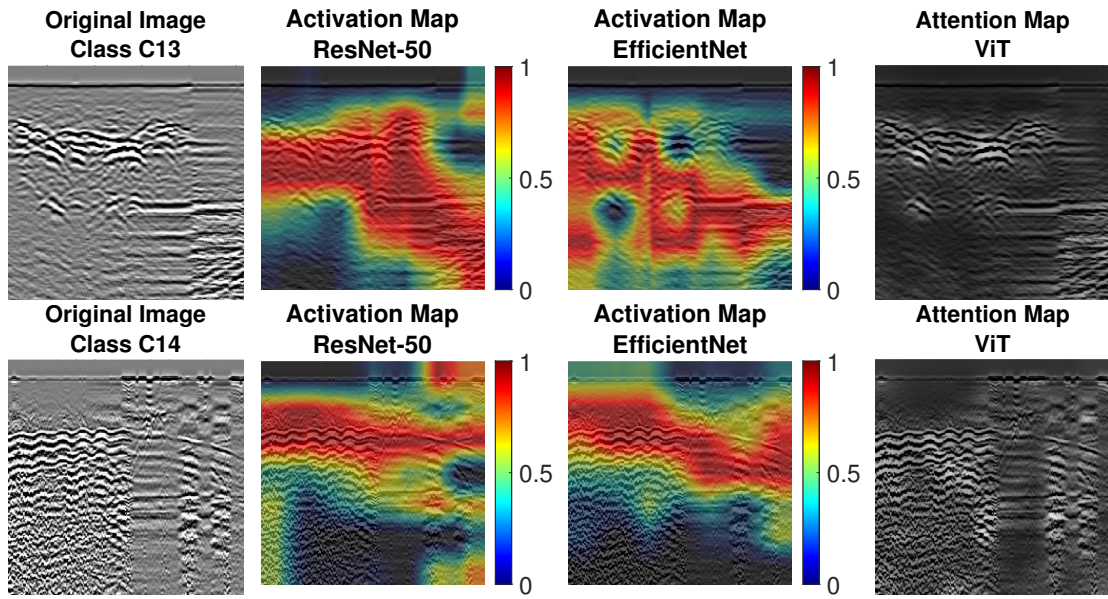


Figure B.9: Class activation maps for ResNet-50 and EfficientNet, and attention maps for ViT compared to original images for each class.

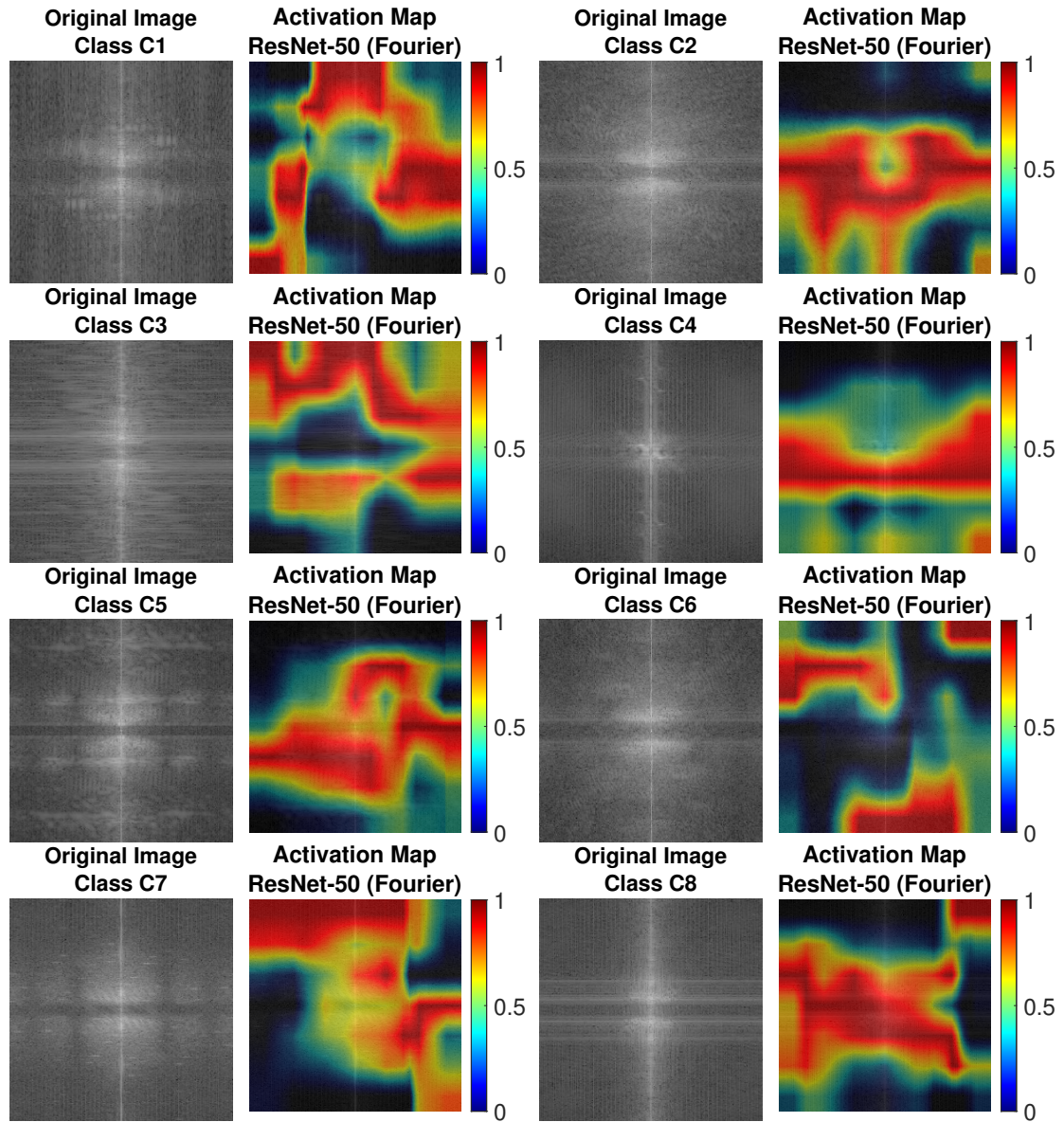


Figure B.9: Class activation maps for ResNet-50 with Fourier pre-processing compared to Fourier pre-processed images for each class.

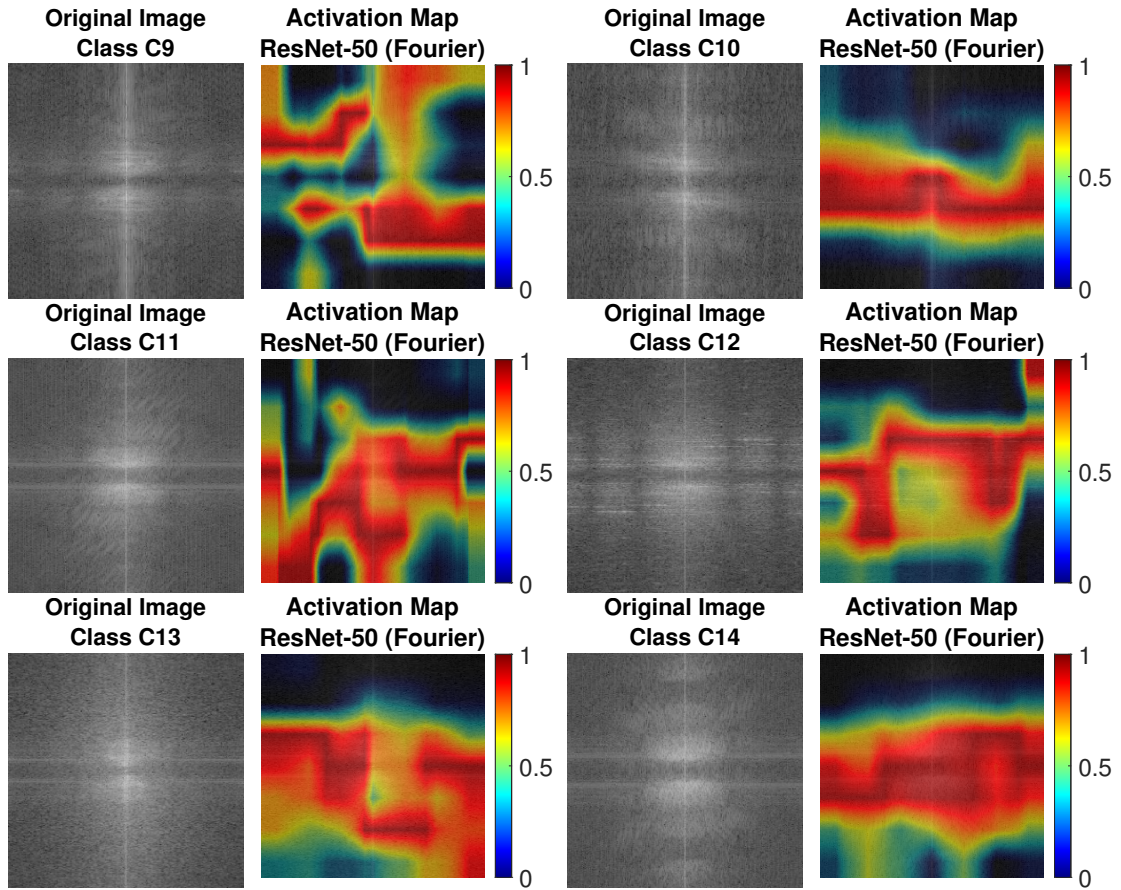


Figure B.9: Class activation maps for ResNet-50 with Fourier pre-processing compared to Fourier pre-processed images for each class.

Appendix C

Dissemination activity

Throughout the current Ph.D. three-year program in Politecnico di Torino, and within the context of the present Ph.D. thesis document, the papers listed below were published.

C.1 Journal Papers

- [J1] **Rosso, M. M.**, R. Cucuzza, F. Di Trapani, and G. C. Marano. “Nonpenalty machine learning constraint handling using PSO-SVM for structural optimization.” In: *Advances in Civil Engineering* 2021 (2021), pp. 1–17. DOI: <https://doi.org/10.1155/2021/6617750>.
- [J2] Cucuzza, R., **M. M. Rosso**, and G. C. Marano. “Optimal preliminary design of variable section beams criterion.” In: *SN Applied Sciences* 3.8 (2021), p. 745. DOI: <https://doi.org/10.1007/s42452-021-04702-5>.
- [J3] Aloisio, A., D. P. Pasca, L. Di Battista, **M. M. Rosso**, R. Cucuzza, G. C. Marano, and R. Alaggio. “Indirect assessment of concrete resistance from FE model updating and Young’s modulus estimation of a multi-span PSC viaduct: Experimental tests and validation.” In: 37 (2022), pp. 686–697. DOI: <https://doi.org/10.1016/j.istruc.2022.01.045>.
- [J4] **Rosso, M. M.**, R. Cucuzza, A. Aloisio, and G. C. Marano. “Enhanced Multi-Strategy Particle Swarm Optimization for Constrained Problems with an Evolutionary-Strategies-Based Unfeasible Local Search Operator.” In: *Applied Sciences* 12.5 (2022), p. 2285. DOI: <https://doi.org/10.3390/app12052285>.
- [J5] Cucuzza, R., **M. M. Rosso**, A. Aloisio, J. Melchiorre, M. L. Giudice, and G. C. Marano. “Size and Shape Optimization of a Guyed Mast Structure under Wind, Ice and Seismic Loading.” In: *Applied Sciences* 12.10 (2022), p. 4875. DOI: <https://doi.org/10.3390/app12104875>.
- [J6] Aloisio, A., **M. M. Rosso**, A. Iqbal, and M. Fragiaco. “Hysteresis modeling of timber-based structural systems using a combined data and model-driven approach.” In: *Computers & Structures* 269 (2022), p. 106830. DOI: <https://doi.org/10.1016/j.compstruc.2022.106830>.

- [J7] Cucuzza, R., G. Devillanova, A. Aloisio, **M. M. Rosso**, and G. C. Marano. “Analytical solutions for piles’ lateral deformations: The nonlinear stiffness case.” In: *International Journal of Mechanical Sciences* 229 (2022), p. 107505. DOI: <https://doi.org/10.1016/j.ijmecsci.2022.107505>.
- [J8] Aloisio, A., **M. M. Rosso**, and R. Alaggio. “Experimental and Analytical Investigation into the Effect of Ballasted Track on the Dynamic Response of Railway Bridges under Moving Loads.” In: *Journal of Bridge Engineering* 27.10 (2022), p. 04022085. DOI: [https://doi.org/10.1061/\(ASCE\)BE.1943-5592.0001934](https://doi.org/10.1061/(ASCE)BE.1943-5592.0001934).
- [J9] **Rosso, M. M.**, R. Asso, A. Aloisio, M. Di Benedetto, R. Cucuzza, and R. Greco. “Corrosion effects on the capacity and ductility of concrete half-joint bridges.” In: *Construction and Building Materials* 360 (2022), p. 129555. DOI: <https://doi.org/10.1016/j.conbuildmat.2022.129555>.
- [J10] Pasca, D. P., A. Aloisio, **M. M. Rosso**, and S. Sotiropoulos. “PyOMA and PyOMA_GUI: A Python module and software for Operational Modal Analysis.” In: *SoftwareX* 20 (2022), p. 101216. DOI: <https://doi.org/10.1016/j.softx.2022.101216>.
- [J11] **Rosso, M. M.**, G. Marasco, S. Aiello, A. Aloisio, B. Chiaia, and G. C. Marano. “Convolutional networks and transformers for intelligent road tunnel investigations.” In: *Computers & Structures* 275 (2023), p. 106918. DOI: <https://doi.org/10.1016/j.compstruc.2022.106918>.
- [J12] Aloisio, A., **M. M. Rosso**, D. Huang, A. Iqbal, M. Fragiaco, and S. Pei. “Nonlinear analytical modeling of mass-timber buildings with post-tensioned rocking walls.” In: *Bulletin of Earthquake Engineering* 21.1 (2023), pp. 473–502. DOI: <https://doi.org/10.1007/s10518-022-01553-2>.
- [J13] Melchiorre, J., A. Manuella Bertetto, **M. M. Rosso**, and G. C. Marano. “Acoustic Emission and Artificial Intelligence Procedure for Crack Source Localization.” In: *Sensors* 23.2 (2023), p. 693. DOI: <https://doi.org/10.3390/s23020693>.
- [J14] Aloisio, A., **M. M. Rosso**, M. Fragiaco, and R. Alaggio. “Fragility estimate of railway bridges due to concrete fatigue.” In: 49 (2023), pp. 70–87. DOI: https://doi.org/10.1007/978-3-031-21187-4_8.
- [J15] Marano, G. C., **M. M. Rosso**, A. Aloisio, and G. Cirrincione. “Generative adversarial networks review in earthquake-related engineering fields.” In: *Bulletin of Earthquake Engineering* (2023), pp. 1–52. DOI: <https://doi.org/10.1007/s10518-023-01645-7>.
- [J16] Aloisio, A., Y. De Santis, M. Pellicciari, **M. M. Rosso**, M. Fragiaco, and R. Tomasi. “Buckling capacity model for timber screws loaded in compression: Experimental, analytical and FE investigations.” In: *Construction and Building Materials* 379 (2023), p. 131225. DOI: <https://doi.org/10.1016/j.conbuildmat.2023.131225>.
- [J17] Aloisio, A., D. P. Pasca, **M. M. Rosso**, and B. Briseghella. “Role of Cable Forces in the Model Updating of Cable-Stayed Bridges.” In: *Journal of Bridge Engineering* 28.7 (2023), p. 05023002. DOI: <https://doi.org/10.1061/JBENF2.BEENG-6168>.
- [J18] **Rosso, M. M.**, A. Aloisio, V. Randazzo, L. Tanzi, G. Cirrincione, and G. C. Marano. “Comparative deep learning studies for indirect tunnel monitoring with and without Fourier pre-processing.” In: *Integrated Computer-Aided Engineering* Preprint (2023), pp. 1–20. DOI: <https://doi.org/10.3233/ICA-230709>.
- [J19] **Rosso, M. M.**, A. Aloisio, J. Melchiorre, F. Huo, and G. C. Marano. “Noise effects analysis on subspace-based damage detection with neural networks.” In: 54 (2023), pp. 23–37. DOI: <https://doi.org/10.1016/j.istruc.2023.05.024>.

- [J20] Aloisio, A., D. P. Pasca, Y. De Santis, T. Hillberger, P. F. Giordano, **M. M. Rosso**, R. Tomasi, M. P. Limongelli, and C. Bedon. “Vibration issues in timber structures: A state-of-the-art review.” In: *Journal of Building Engineering* (2023), p. 107098. DOI: <https://doi.org/10.1016/j.jobbe.2023.107098>.
- [J21] **Rosso, M. M.**, A. Aloisio, G. Cirrincione, and G. C. Marano. “Subspace features and statistical indicators for neural network-based damage detection.” In: 56 (2023), p. 104792. DOI: <https://doi.org/10.1016/j.istruc.2023.06.123>.
- [J22] **Rosso, M. M.**, A. Aloisio, J. Parol, G. C. Marano, and G. Quaranta. “Intelligent automatic operational modal analysis.” In: *Mechanical Systems and Signal Processing* 201 (2023), p. 110669. DOI: <https://doi.org/10.1016/j.ymsp.2023.110669>.
- [J23] Aloisio, A., **M. M. Rosso**, A. M. De Leo, M. Fragiaco, and M. Basi. “Damage classification after the 2009 L’Aquila earthquake using multinomial logistic regression and neural networks.” In: *International Journal of Disaster Risk Reduction* 96 (2023), p. 103959. DOI: <https://doi.org/10.1016/j.ijdr.2023.103959>.
- [J24] De Biagi, V., A. Reggio, **M. M. Rosso**, and L. Sardone. “Nondimensional Shape Optimization of Nonprismatic Beams with Sinusoidal Lateral Profile.” In: *Journal of Structural Engineering* 150.1 (2024), p. 04023191. DOI: <https://doi.org/10.1061/JSENDH.STENG-12493>.

C.2 Conference Papers

- [C1] Sardone, L., **M. M. Rosso**, R. Cucuzza, R. Greco, and G. C. Marano. “Computational Design of Comparative Models and Geometrically Constrained Optimization of A Multi Domain Variable Section Beam Based on Timoshenko Model.” In: *Proceedings of the EUROGEN2021, 14TH ECCOMAS Thematic Conference on Evolutionary and Deterministic Methods for Design, Optimization and Control, Athens, Greece*. 2021, pp. 28–30. DOI: <https://doi.org/10.7712/140121.7961.18535>.
- [C2] Asso, R., R. Cucuzza, **M. M. Rosso**, D. Masera, and G. C. Marano. “Bridges monitoring: an application of ai with gaussian processes.” In: *14th International Conference on Evolutionary and Deterministic Methods for Design, Optimization and Control. Institute of Structural Analysis and Antiseismic Research National Technical University of Athens*. 2021. DOI: <https://doi.org/10.7712/140121.7964.18426>.
- [C3] Di Trapani, F., G. Tomaselli, A. P. Sberna, **M. M. Rosso**, G. C. Marano, L. Cavaleri, and G. Bertagnoli. “Dynamic response of infilled frames subject to accidental column losses.” In: *Proceedings of the 1st Conference of the European Association on Quality Control of Bridges and Structures: EUROSTRUCT 2021 1*. Springer International Publishing. 2022, pp. 1100–1107. DOI: https://doi.org/10.1007/978-3-030-91877-4_125.
- [C4] Marasco, G., **M. M. Rosso**, S. Aiello, A. Aloisio, G. Cirrincione, B. Chiaia, and G. C. Marano. “Ground penetrating radar fourier pre-processing for deep learning tunnel defects’ automated classification.” In: *International Conference on Engineering Applications of Neural Networks*. Springer International Publishing Cham. 2022, pp. 165–176. DOI: https://doi.org/10.1007/978-3-031-08223-8_14.

- [C5] **Rosso, M. M.**, A. Aloisio, R. Cucuzza, G. C. Marano, and R. Alaggio. “Train-track-bridge interaction analytical model with non-proportional damping: Sensitivity analysis and experimental validation.” In: *European Workshop on Structural Health Monitoring*. Springer International Publishing Cham. 2022, pp. 223–232. DOI: https://doi.org/10.1007/978-3-031-07254-3_22.
- [C6] **Rosso, M. M.**, J. Melchiorre, R. Cucuzza, A. Manuello, and G. C. Marano. “Estimation of Distribution Algorithm for Constrained Optimization in Structural Design.” In: *WCCM-APCOM 2022, Yokohama, July 31 to August 5, 2022*. 2022. DOI: <http://dx.doi.org/10.23967/wccm-apcom.2022.048>.
- [C7] Cucuzza, R., **M. M. Rosso**, M. Domaneschi, and G. Marano. “Retrofitting of prestressed concrete decks by arch steel trusses for different degradation levels.” In: *Bridge Safety, Maintenance, Management, Life-Cycle, Resilience and Sustainability*. CRC Press, 2022, pp. 587–595. DOI: <http://dx.doi.org/10.1201/9781003322641-69>.
- [C8] **Rosso, M. M.**, R. Cucuzza, G. C. Marano, A. Aloisio, and G. Cirrincione. “Review on deep learning in structural health monitoring.” In: *Bridge Safety, Maintenance, Management, Life-Cycle, Resilience and Sustainability*. CRC Press, 2022, pp. 309–315. DOI: <http://dx.doi.org/10.1201/9781003322641-34>.
- [C9] **Rosso, M. M.**, R. Cucuzza, G. C. Marano, A. Aloisio, and D. P. Pasca. “Indirect estimate of concrete compression strength framework with FE model updating and operational modal analysis.” In: *IABSE Symposium: Challenges for Existing and Oncoming Structures, Prague, Czech Republic, 25-27 May 2022*. IABSE Symposium Prague 2022, International Association for Bridge and ... 2022, pp. 1611–1618. DOI: <http://dx.doi.org/10.2749/prague.2022.1611>.
- [C10] **Rosso, M. M.**, A. Aloisio, R. Cucuzza, D. P. Pasca, G. Cirrincione, and G. C. Marano. “Structural health monitoring with artificial neural network and subspace-based damage indicators.” In: *International Conference on Trends on Construction in the Post-Digital Era*. Springer International Publishing Cham. 2022, pp. 524–537. DOI: https://doi.org/10.1007/978-3-031-20241-4_37.
- [C11] Di Benedetto, M., R. Asso, R. Cucuzza, **M. M. Rosso**, D. Masera, and G. C. Marano. “Concrete half-joints: Corrosion damage analysis with numerical simulation.” In: *2nd fib Italy YMG Symposium on Concrete and Concrete Structures, 2021 Rome Code 273519*. Vol. 273519. fib. The International Federation for Structural Concrete, Del Zoppo M ... 2021, pp. 297–304. URL: <https://www.scopus.com/inward/record.uri?eid=2-s2.0-85134811676&partnerID=40&md5=c8de42127e2b651373f03cd92b59309e>.
- [C12] **Rosso, M. M.**, G. Marasco, L. Tanzi, S. Aiello, A. Aloisio, R. Cucuzza, B. Chiaia, G. Cirrincione, and G. Marano. “Advanced deep learning comparisons for non-invasive tunnel lining assessment from ground penetrating radar profiles.” In: *8th European Congress on Computational Methods in Applied Sciences and Engineering*. CIMNE. 2022. DOI: <http://dx.doi.org/10.23967/eccomas.2022.038>.
- [C13] Marano, G. C., **M. M. Rosso**, and J. Melchiorre. “Optimization as a Tool for Seismic Protection of Structures.” In: *World Conference on Seismic Isolation*. Springer International Publishing Cham. 2022, pp. 100–113.
- [C14] **Rosso, M. M.**, A. Aloisio, R. Cucuzza, R. Asso, and G. C. Marano. “Structural Optimization With the Multistrategy PSO-ES Unfeasible Local Search Operator.” In: *Proceedings of International Conference on Data Science and Applications: ICDSA 2022, Volume 1*. Springer. 2023, pp. 215–229. DOI: https://doi.org/10.1007/978-981-19-6631-6_16.

- [C15] Melchiorre, J., **M. M. Rosso**, G. Cirrincione, and G. C. Marano. “Compact Convolutional Transformer Fourier analysis for GPR tunnels assessment.” In: *2023 International Conference on Control, Automation and Diagnosis (ICCAD)*. IEEE, 2023, pp. 1–6. DOI: <https://doi.org/10.1109/ICCAD57653.2023.10152455>.
- [C16] Melchiorre, J., L. Sardone, **M. M. Rosso**, and A. Aloisio. “Intelligent Structural Damage Detection with MEMS-Like Sensors Noisy Data.” In: *International Conference on Communication and Intelligent Systems*. Springer, 2022, pp. 631–642. DOI: https://doi.org/10.1007/978-981-99-2322-9_48.
- [C17] Aloisio, A., R. Tomasi, Y. De Santis, T. Hillberg, D. P. Pasca, P. F. Giordano, **M. M. Rosso**, M. P. Limongelli, and C. Bedon. “Serviceability Criteria for the Dynamic Response of Timber Floors.” In: *International Conference on Experimental Vibration Analysis for Civil Engineering Structures*. Springer, 2023, pp. 560–568. DOI: https://doi.org/10.1007/978-3-031-39109-5_57.
- [C18] Melchiorre, J., **M. M. Rosso**, R. Cucuzza, E. D’Alto, A. Manuello, and G. C. Marano. “Deep acoustic emission detection trained on seismic signals.” In: *Applications of Artificial Intelligence and Neural Systems to Data Science*. Springer, 2023, pp. 83–92. DOI: https://doi.org/10.1007/978-981-99-3592-5_8.
- [C19] **Rosso, M. M.**, A. Aloisio, D. P. Pasca, G. C. Marano, and B. Briseghella. “FE Model Updating of Cable-Stayed Bridges Based on the Experimental Estimate of Cable Forces and Modal Parameters.” In: *International Conference on Experimental Vibration Analysis for Civil Engineering Structures*. Springer, 2023, pp. 71–80. DOI: https://doi.org/10.1007/978-3-031-39117-0_8.
- [C20] Aloisio, A., G. Quaranta, A. Contento, and **M. M. Rosso**. “Physics-Based and Machine-Learning Models for Braking Impact Factors.” In: *International Conference on Experimental Vibration Analysis for Civil Engineering Structures*. Springer, 2023, pp. 81–88. DOI: https://doi.org/10.1007/978-3-031-39117-0_9.
- [C21] Troise, A., E. Bruschi, **M. M. Rosso**, A. Alosio, A. Rizzo, N. D. Lagaros, V. Quaglini, and G. C. Marano. “Variable orifice damper implementation for seismic semi-active control of civil structures.” In: *9th ECCOMAS Thematic Conference on Computational Methods in Structural Dynamics and Earthquake Engineering (COMPdyn)*. Athens, Grece, June 2023.
- [C22] **Rosso, M. M.**, A. Aloisio, C. Bedon, and G. C. Marano. “Laminated glass slabs design challenges: dynamic identification of a fractured pedestrian walkway.” In: vol. 6. 5. Wiley Online Library, 2023, pp. 286–291. DOI: <http://dx.doi.org/10.1002/cepa.2084>.
- [C23] Cucuzza, R., M. Domaneschi, **M. M. Rosso**, L. Martinelli, and G. C. Marano. “Cutting Stock Problem (CSP) applied to Structural Optimization for the minimum waste cost.” In: *ce/papers* 6.5 (2023), pp. 1066–1073. DOI: <http://dx.doi.org/10.1002/cepa.2208>.

This Ph.D. thesis has been typeset by means of the \TeX -system facilities. The typesetting engine was \LaTeX . The document class was `toptesi`, by Claudio Beccari, with option `tipotesi=scudo`. This class is available in every up-to-date and complete \TeX -system installation.